169(2), 2017

COMBUSTION ENGINES

Emissions laboratories: facilities for certification and R&D work at the Euro 6d/RDE level

BOSMAL®

Laboratory No. 1

- Euro 6d-compliant emissions testing system for both certification and R&D activities
- Climate control for testing in the range +14 to +30°C
- 2WD single-roll 48" chassis dynamometer with slope simulation
- Bag and dilute emissions measurements (all regulated emissions, NO/NO_2)
- Raw emissions measurements (all regulated emissions, NO/NO_2) – 2 modal lines with high-accuracy dilution air measurement
- Filter (PM) and particle counter (PN) for measuring particulate emissions
- Opacimeter, soot sensor and size distribution counter available for R&D activities
- Direct engine speed monitoring
- Power analyser for RCB correction available
- NH_3 and FTIR analyser available
- Additional devices (thermocouples, analog signals, etc.) supported
- All common driving cycles available; custom cycles can be implemented

Laboratory No. 2

- Euro 5/6/6d-compliant emissions testing system for both certification and R&D activities
- Climate control for testing in the range -35 to +60°C
- 4WD single-roll 48" chassis dynamometer with slope simulation and motorcycle mounting system
- Bag and dilute emissions measurements (all regulated emissions)
- Raw emissions measurements (all regulated emissions, NO/NO_2) – 2 modal lines
- EGR measurement
- Filter (PM) and particle counter (PN) for measuring particulate emissions
- Opacimeter, soot sensor and size distribution counter available for R&D activities
- Additional devices (thermocouples, analog signals, etc.) supported
- ECU data logging via OBD port
- Power analyser for RCB correction available
- NH_3 and FTIR analyser available
- All common driving cycles available; custom cycles can be implemented

PEMS system

- Mobile emissions analysis system for testing emissions and fuel consumption under real driving conditions (RDE)
- Conforms to all applicable EU legislation; suitable for use of both light- and heavy-duty vehicles for both certification and R&D
- Equipped with high-accuracy exhaust flow meter, weather station and GPS
- Includes THC measurement and particle number (PN) measurement
- Data post-processing, elaboration of results, planning and analysis of test routes, etc.

BOSMAL Automotive Research and Development Institute Ltd
Sarni Stok 93, 43-300 Bielsko-Biała, POLAND
phone: +48 33 81 30 539, +48 33 81 30 598
www.bosmal.com.pl, e-mail: bosmal@bosmal.com.pl

PTNSS Supporting Members
Członkowie wspierający PTNSS

BOSMAL Automotive Research and Development Institute Ltd
Instytut Badań i Rozwoju Motoryzacji BOSMAL Sp. z o.o

Motor Transport Institute
Instytut Transportu Samochodowego

The Institute for Sustainable Technologies
Instytut Technologii Eksploatacji

Institute of Aviation
Instytut Lotnictwa

Automotive Industry Institute
Przemysłowy Instytut Motoryzacji

The Rail Vehicles Institute TABOR
Instytut Pojazdów Szynowych TABOR

Institute of Mechanised Construction and Rock Mining
Instytut Mechanizacji Budownictwa i Górnictwa Skalnego

Institute of Logistics and Warehousing
Instytut Logistyki i Magazynowania

Industrial Institute of Agricultural Engineering
Przemysłowy Instytut Maszyn Rolniczych

AVL List GmbH

Solaris Bus & Coach S.A.

Air Force Institute of Technology
Instytut Techniczny Wojsk Lotniczych

COMBUSTION ENGINES

A Scientific Magazine

2017, 169(2)

Year LVI

PL ISSN 2300-9896

Editor:

Polskie Towarzystwo Naukowe Silników Spalinowych
43-300 Bielsko-Biała, Sarni Stok 93 Street, Poland
tel.: +48 33 8130402, fax: +48 33 8125038
E-mail: sekretariat@ptnss.pl
WebSite: http://www.ptnss.pl
Papers available on-line: http://combustion-engines.eu

Editorial:
Institute of Combustion Engines and Transport
Poznan University of Technology
60-965 Poznan, Piotrowo 3 Street
tel.: +48 61 2244505, +48 61 2244502
E-mail: papers@ptnss.pl

Prof. Jerzy Merkisz, DSc., DEng. (Editor-in-chief)
Miłosław Kozak, DSc., DEng. (Editorial Secretary for Science) – papers@ptnss.pl
Ireneusz Pielecha, DSc., DEng. (Technical Editor)
Krystyna Bubacz, MSc. (Proofreading Editor)
Wojciech Serdecki, DSc., DEng. (Statistical Editor)
and Associate Editors

Contents

Editor
Polish Scientific Society of Combustion Engines
43-300 Bielsko-Biała, Sarni Stok 93 Street, Poland
tel.: +48 33 8130402, fax: +48 33 8125038
E-mail: sekretariat@ptnss.pl
WebSite: http://www.ptnss.pl

Subscriptions
Send subscription requests to the Publisher's address.
Cost of a single issue PLZ30 + VAT.

Preparation for print
ARS NOVA Publishing House
60-782 Poznań, ul. Grunwaldzka 17/10A

Circulation: 700 copies.

Printing and binding
Zakład Poligraficzny Moś i Łuczak, sp. j., Poznań, ul. Piwna 1

The journal is registered in the Polish technical journals content database – **BAZTECH** www.baztech.icm.edu.pl

The journal is listed in the international database **IC Journal Master List** – **Index Copernicus** www.indexcopernicus.com

Declaration of the original version
The original version of the Combustion Engines journal is the printed version.

Papers published in the ***Combustion Engines*** quarterly receive 13 points as stated by the Notification of the Minister of Science and Higher Education dated 31 December 2015.

Cover
I – Audi 3.0 V6 TFSI engine (*fot. www.canadianautoreview.ca*), background (© Sashkin – *pl.fotolia.com*)
IV – Camless Engine (*fot. freevalve.com*)

Article citation info:
GRÜNEBERGER, P., JOCHAM, B., WINKLHOFER, E. Diesel combustion in high load situations: a visual analysis of mixture formation and air utilization. *Combustion Engines*. 2017, **169**(2), 3-6. DOI: 10.19206/CE-2017-201

Patrick GRÜNEBERGER
Bernhard JOCHAM
Ernst WINKLHOFER

CE-2017-201

Diesel combustion in high load situations: a visual analysis of mixture formation and air utilization

As fuel injection pressures keep rising, questions focus on additional benefits to be gained from the considerable efforts to achieve and handle the fuel pressure increments. The aim of fuel injection processes is to support the mixing of fuel molecules with oxygen. The steps towards this goal include fuel atomization, evaporation, heat transfer from air into the liquid or vaporized fuel together with transport of fuel for best air utilization. Engineering degrees of freedom include the parameters of the fuel injection system and handling of in-cylinder gas conditions. The paper describes basic high pressure flow processes, spray propagation, evaporation and combustion and the mixing of flame clouds with in-cylinder air for oxidation of high temperature soot particles. Experimental evidence of such processes is derived from laboratory flow tests as well as from optically accessed engines operated under conditions relevant for today's passenger car and heavy duty engines.

Key words: *diesel engine, combustion, visual analysis*

1. Introduction

Fuel injection pressures have been rising to well above 2000 bar as such high pressure injection still provides benefits for both fuel efficiency and emissions which outperform the efforts related to provide and control such high pressure systems. What is the reason that combustion benefits from the degrees of freedom provided by such high pressure injection systems? Which mechanisms relate the pressure drop along the nozzle hole with improvements then seen in the entire combustion chamber?

This paper gives a summary of effects studied in various experimental configurations, see Fig. 1, which are related to high pressure flow through the nozzle holes, the propagation and atomization of sprays as they enter the combustion chamber, heat and momentum transfer between in-cylinder gas and spray as well as ignition and combustion in normal Diesel engine combustion chambers.

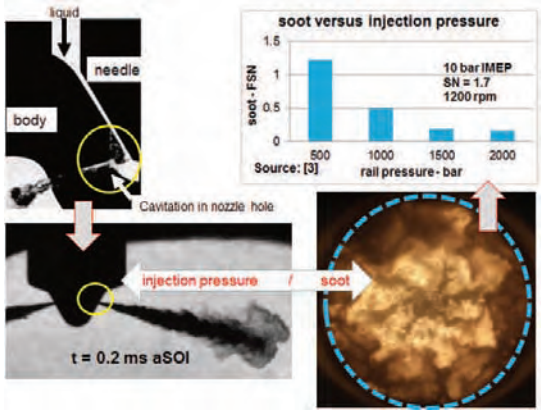

Fig. 1. The Diesel engine injection and combustion sequence. Example snapshots of cavitation in nozzle hole, spray injection, flame at end of injection and soot emissions trends related to injection pressure.

2. Diesel flames

The high luminosity of Diesel flames provides best conditions for flame observation by means of endoscopes together with high speed cameras. Endoscope access needs design adaptations and machining of the cylinder head, the technique is well established and suitable also for multicylinder engines. A comparison of diesel flames in a passenger car engine is given in Fig. 2. The examples for 4 and 8 bar IMEP give a view into the piston bowl and show the flame clouds rotating in the main, outer part of the bowl. In the 8 bar IMEP example with longer injection duration, there is a backflow of flame clouds into the center of the bowl.

The Diesel flame clouds as we see them in such movies or photographs comprise of soot particles being heated by the combustion process at a temperature of typically 2000 K. Soot particles are formed in the fuel rich areas of the spray, their luminosity and spectral content reflect the temperature of their reactive environment. Soot clouds, consequently, form a 3D structure surrounding the initial spray and being propelled by the turbulent motion of the spray and gas phase. Soot oxidation takes place in oxygen rich high temperature areas of the combustion chamber. For effective soot oxidation, this implies the necessity to bring soot particles in contact with oxygen at a time well before combustion chamber temperature starts to decrease.

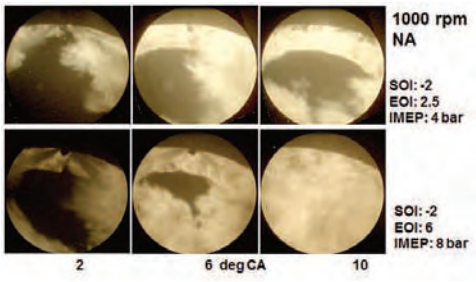

Fig. 2. Diesel flame motion in NA engine at 1000 rpm, view into piston bowl with endoscope and high speed camera

3. Premixed flame in diesel combustion

Ignition of Diesel flames occurs prior to the formation of soot clouds in a "premixed flame" giving rise to the typical premixed pressure peak followed by the main part of heat release. Such ignition is a gas phase event following the evaporation of fuel droplets and the further heating of fuel vapor in the hot surrounding air. Upon ignition, a typi-

cal blue premixed flame is established. As is seen in Fig. 3, such premixed flames appear per each spray with some minor timing fluctuation due to the individual sprays' propagation and mixing fluctuations. In the Fig. 3 example, premixed flames are seen for about 100 µs before very luminous diffusion flame radiation starts to dominate.

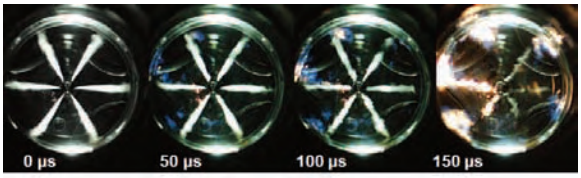

Fig. 3. Spray and flame sequence from a high speed movie with 50 µs frame intervals taken at start of combustion. The premixed Diesel flame shows self ignition locations. Luminosity of these blue flames is very low. See also ref. [1]

4. Spray evaporation

Heat transfer from in-cylinder gas into the spray first off all yields fuel vapor before vapor then undergoes self ignition or is consumed by ongoing combustion. The evaporation process as shown in Fig. 4 (A) is accessible in optical research engines with Schlieren imaging techniques showing the boundaries between in –cylinder gas, fuel vapor and the optically dense spray core area. The time sequence in Fig. 4 shows stages of initial spray formation, fuel evaporation especially at the spray front and along the spray boundaries and finally the appearance of soot clouds at the spray tip. In this Schlieren imaging configuration soot is seen by its absorption of the background illumination.

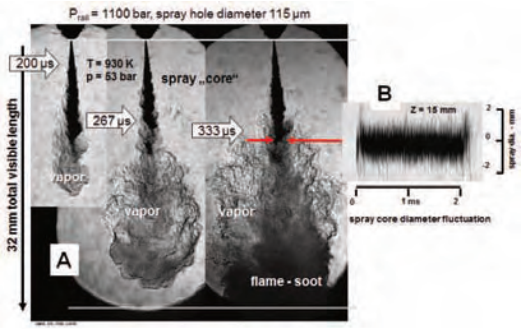

Fig. 4. (A) Diesel spray in an optical research engine with spray „core" comprising fuel droplets, fuel vapor seen with Schlieren illumination and shadow of soot clouds. (B) spray core diameter fluctuations show spray turbulence effects introduced at the injection process. Via heat and momentum transfer, compressed hot in-cylinder air controls spray core length, vapor formation and ignition

5. Spray atomization

Spray atomization is initiated as liquid fuel passes through the nozzle hole. The high pressure flow events introduce turbulence which results in the macroscopic spray cone angle downstream of the orifice and in the turbulent flow of spray ligaments and droplets forming the "spray core". Spray core diameter fluctuations are then a consequence of turbulence, an example is shown in Fig. 4 (B).

The source of spray turbulence is related to the high pressure fuel flow into and through the nozzle hole. At injection pressures above a few 100 bar and with usual nozzle hole geometry configurations, the local pressure gradients inside the nozzle hole give rise to cavitation [2 ilass]. The gas bubbles created at this cavitation process, their collapse inside the nozzle hole or otherwise their transport into the combustion chamber contribute to turbulent spray motion introducing spray breakup and atomization. Spray core diameter fluctuations as shown in Fig. 4 (B) are a consequence of such turbulent spray motion.

6. Spray core

With above described spray features, the definition of "spray core" is essentially related to observations in optical research engines. Spray core length as seen in the photographs of Fig. 4 or in the time resolved shadow traces of Fig. 5 are related to the attenuation of light used for back illumination of the spray. With this pragmatic definition of a spray core, its length is under the influence of spray evaporation and thus heat transfer from the compressed gas into the spray.

A practical consequence of such gas temperature and heat transfer effects is the absence or presence of liquid fuel film deposition on a piston bowl wall, see Fig. 5 (C). At low engine temperature with slow fuel evaporation, the spray core over many injection and combustion cycles can establish a wetted piston surface. The same engine at normal temperature shows only marginal impingement of liquid fuel.

The influence of injection pressure on spray core length is shown in Fig. 6 with examples collected in a research engine. At constant, compressed, hot gas conditions, injection pressure has very low influence on spray core length. However, injection pressure transfers to spray momentum. This momentum is preserved with the spray vapor and finally the soot cloud penetrating deeper into the combustion chamber.

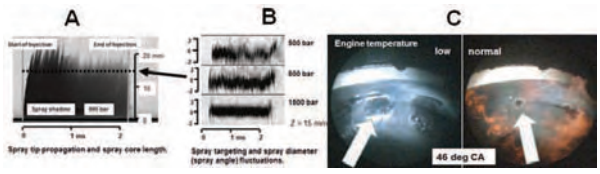

Fig. 5. spray core dynamics recorded (A) along and (B) across the spray axis from start to end of injection. Injection pressure has influence on fluctuation frequency of spray core diameter. In normal engine (C) temperature influence on spray core length is responsible for piston surface wetting in cold engine

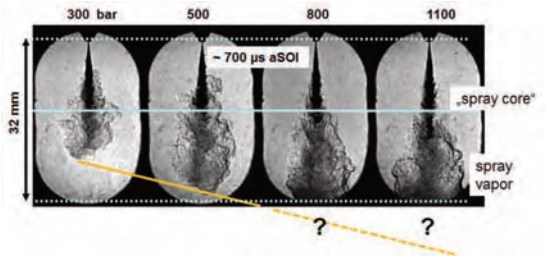

Fig. 6. spray core and spray vapor plumes under influence of injection pressure. Snapshots at about 700 µs aSOI

7. Injection pressure – air utilization – soot emissions

Flame motion in the entire piston bowl area can be observed in optical Diesel engines with elongated piston configurations and optical windows forming the bottom part of the piston bowl. Such engine designs can provide original

combustion chamber geometry conditions as well as highly realistic combustion cycles as is described in ref. [1].

Recording the diffusion flame patterns with a high speed camera shows formation and growth of the soot clouds related to each spray and the transport of these soot clouds under the influence of injection and in-cylinder gas motion. Finally, the visible soot clouds disappear as a combined result of soot oxidation and cooling of surviving soot particles.

Engine out soot, thus is the result of soot format and oxidation. With ignition delay in normal Diesel combustion systems much shorter than injection duration, there is massive formation of soot particles as mixing prior to combustion is ineffective. Consequently, the focus on achieving low engine out soot levels is on enabling maximum soot oxidation.

This oxidation needs the soot particles which are formed in the fuel rich flame areas to meet with oxygen or with oxidizer molecules such as OH. The soot – oxygen mixing furthermore must be supported by sufficiently high temperatures to initiate the oxidation process.

When following the flame formation and flame propagation events as are easily seen in high speed movies, it is evident that diffusion flame clouds formed along the spray plumes need to mix with the air present between the individual flame clouds and between flame clouds and combustion chamber surfaces.

A simple way to visualize the flow field related to the growth, transport and mixing of the complex 3D flame "surface" structure is to apply PIV evaluation software to subsequent frames of flame movies. This method has been introduced by Dembinski [3]. Application of such method to combustion cycles with short and long duration of injection is shown in the examples of Fig. 7.

The flame flow fields during injection in Fig. 7 (A) show the growth of the flame clouds and their radial motion towards the piston bowl wall. Near the wall the flame clouds respond to the swirl rotation of the in-cylinder air and bend into a rotational motion along the piston bowl wall.

In the high load examples of Fig. 7 (C), with more than twice as long injection duration, the flame clouds are reflected off the piston bowl wall and move back into the center of the combustion chamber. The flow field taken just after the end of injection now shows the backflow motion and a speedup of flame rotation in the combustion chamber center. This speedup of the central swirl motion has been explained by Dembinski to be caused by conservation of angular momentum as rotating gas is moving into the swirl center [3].

The effect of injection pressure on these flame transport and mixing events arises from the sprays' momentum. As this momentum is transferred into the vapor and flame clouds, reflection of a high velocity flame cloud back off the piston bowl wall yields faster mixing of the flame cloud with air in the bowl center.

Together with this large scale flame transport mechanism, turbulent flame and gas motion adds to the small scale mixing of soot particles and reactive gas.

Evaluation of the flame flow field data for turbulence effects has been done by Dembinski [1, 3]. His examples are reproduced in Fig. 8. They compare local turbulence distribution for combustion cycles with 500 and 1000 bar injection pressure, respectively. Clearly, higher injection pressure yields higher turbulence activity. The benefit of high turbulence, however is just present during injection and for a very short period after the end of injection. The mean kinetic energy plot over crank angle degrees shows kinetic energy to dissipate within about 5 deg CA following the end of injection.

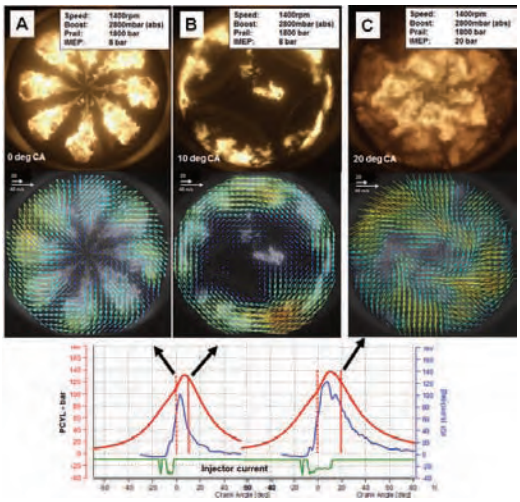

Fig. 7. Diesel flames and flame velocity fields in the piston bowl of an optically accessed heavy duty Diesel engine. Same injection pressure at 10 and 20 bar IMEP. Long DOI at 20 bar IMEP result in backflow of flames into the bowl center and speedup of center swirl motion

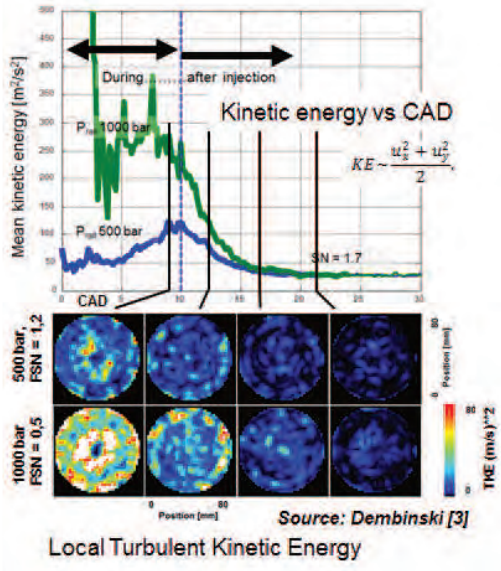

Fig. 8. Turbulent kinetic energy evaluation on basis of flame flow field data for 500 and 1000 bar injection pressure [1, 3]. Notice the fast decay of turbulence after end of injection

8. Injection for fast soot oxidation – summary

Above examples summarize experimental evidence on Diesel fuel injection and combustion with focus given to the clarification of mechanisms starting with the injection process and leading up to soot oxidation and emission of soot particles.

Fuel injection pressure has been shown to be one of the means available to engine development in controlling the

mixing of the reactants during and after injection. Following points have been emphasized:

– The formation of a highly turbulent spray supported by flow cavitation as fuel is injected at pressures exceeding a few hundred bar.
– Formation of the spray core mainly comprising fuel droplets.
– Formation of a fuel vapor plume as the spray core evaporates.
– Ignition of fuel vapor in a premixed flame being followed by combustion in the fuel rich part of the spray.
– Formation of the luminous Diesel flame with soot particles acting as very bright tracers of high temperature activity.
– Transport of the diffusion flames as given by the combined influence of spray momentum, in-cylinder air motion and combustion chamber surfaces.

The role of spray momentum and thus of fuel injection pressure for transport and mixing processes and especially the importance of fast mixing of reactants for effective soot oxidation was explained with experimental material collected in realistic Diesel engine combustion situations.

9. Experimental facilities – summary

Diesel combustion situations have been studied in optically access engines as shown in Fig. 9. Engine concepts and design details allow for maximum optical access with a glass liner ring and a full optical piston, or access to the piston bowl with a metal piston and a bottom glass window. Such engines have been used at cylinder pressures up to 160 bar.

In normal engines, optical access is achieved with endoscope inserts into the cylinder head. Endoscope windows are designed to allow cylinder pressures above 200 bar.

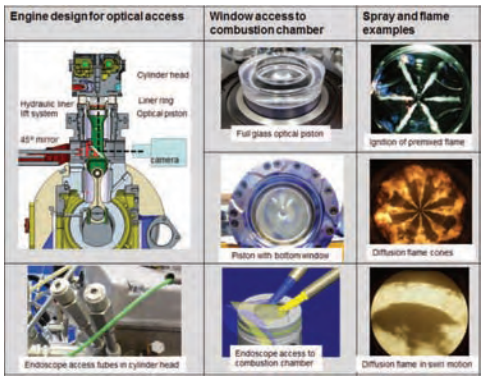

Fig. 9. Optical access in research Diesel engines with elongated piston and piston bowl windows. Endoscope access in cylinder head of normal engines. Visualization examples for each of these engines

Operation of such engines, especially in high load conditions requires frequent cleaning of window surfaces. In order to minimize the need for cleaning, such engines are preconditioned for target temperatures. They are furthermore operated in motored mode until engine speed and intake manifold pressure have stabilized. Then, for a few cycles, injection is activated with simultaneous recording of all data and camera records of interest.

In high load tests after start of fired operation, only the first few cycles are used for data evaluation Progressive blackening of window surfaces prohibits useful operation for more than about 10 fired cycles.

Access to the combustion chamber for removing the soot layers and cleaning window surfaces is achieved with hydraulic cylinder liner lift devices. The total time from stopping such optical engine, cleaning the combustion chamber and preparing the engine for re-start can be as short as 6 minutes.

Nomenclature

aSOI, SOI	(after) start of injection
EOI	end of injection
DOI	duration of injection
IMEP	indicated mean effective pressure
SN	swirl number
FSN	filter smoke number
NA	naturally aspirated
CA, CAD	crank angle (degree)
TKE, KE	(turbulent) kinetic energy
Prail	fuel rail pressure

Bibliography

[1] DEMBINSKI, H., ANGSTROM, H.-E., WINKLHOFER, E. Injection pressure as a means to guide air utilization in Diesel engine combustion. Fuel systems for IC engines. *Institution of Mechanical Engineers*. 2014.

[2] WINKLHOFER, E., KELZ, E., MOROZOV, A. Basic flow processes in high pressure fuel injection equipment. *ICLASS*. 2003, Italy.

[3] DEMBINSKI, H. In-cylinder flow characterization of heavy duty diesel engines using combustion image velocimetry. *Doctoral thesis, Royal Institute of Technology*. Stockholm, 2013.

Dipl.-Ing. Patrick Grüneberger – Development Engineer Optical Analysis,AVL List GmbH, Graz, Austria.

Dipl.-Ing. Bernhard Jocham – Development Engineer Optical Analysis, AVL List GmbH, Graz, Austria.

Ernst Winklhofer, DEng. – Manager Combustion Measurement and Optical Technologies, AVL List GmbH, Graz, Austria.

e-mail: *Ernst.Winklhofer@avl.com*

Article citation info:
GĘCA, M., CZYŻ, Z., SUŁEK, M. Diesel engine for aircraft propulsion system. *Combustion Engines*. 2017, **169**(2), 7-13. DOI: 10.19206/CE-2017-202

Michał GĘCA
Zbigniew CZYŻ
Mariusz SUŁEK

CE-2017-202

Diesel engine for aircraft propulsion system

Stricter requirements for power in engines and difficulties in fueling gasoline engines at the airport make aircraft engine manufacturers design new engines capable of combusting fuel derived from JET-A1. New materials used in compression-ignition engines enable weight reduction, whereas the technologies of a Common Rail system, supercharging and 2-stroke working cycle enable us to increase the power generated by an engine of a given displacement. The paper discusses the parameters of about 40 types of aircraft compression ignition engines. The parameters of these engines are compared to the spark-ignition Rotax 912 and the turboprop. The paper also shows trends in developing aircraft compression-ignition engines.

Key words: *diesel engine, aircraft propulsion system, power-to-weight ratio, specific fuel consumption*

1. Introduction

The choice of the engine for light aircraft depends on several factors: power, weight, power-to-weight ratio, specific fuel consumption, power density out of which fuel consumption and engine power are fundamental. The power-to-weight ratio is important, but detailed investigations show that higher specific fuel consumption can have a greater impact on the overall aircraft design than the engine weight so engines with low specific fuel consumption which also satisfy power requirements are more often chosen [1].

The beginnings of aviation particularly preferred lightweight engines that were designed as water-cooled, in-line spark ignition engines. Optimum performance was achieved for the aircraft piston engine, always spark ignition during the Second World War. Currently, reciprocating engines are found in sports, emergency, agricultural and recreation aviation. Technically, they are mostly at a pre-war knowledge of the theory of operation, design and manufacturing technology, especially if compared to that high level of development of automotive engines. Typically, these engines are driven by carburetors of a quite primitive desing. At present, due to environmental requirements and the need to deal with climate change, it is beneficial to develop aircraft piston engines and adopt the achievements of automotive engineering such as computer-controlled Common Rail high pressure injection systems and variable pressure turbochargers.

Compression-ignition engines show several advantages. They are *single-level* drive units, i.e. they do not need a fuel-air mixture to be supplied, they do not need an external fuel pump and ignition source like spark plugs and magneto. The fact that there is no ignition system eliminates electromagnetic noise and reduces disturbances in aircraft navigation and radio communication. The diesel engine design is more wear-resistant due to lubricating properties of diesel fuel.

Ecological requirements and climate change make a significant opportunity to develop aircraft piston engines even by adopting the achievements in the automotive industry. Regardless of this, the introduction of diesel engines running on the unified fuel [5]. Less toxic exhaust gas results from fuel composition free from toxic substances such as lead, benzene or solvents. Their reliability and low maintenance costs result from eliminated carburetor icing, ignition system failures, and vapor jams [2].

Aircraft compression-ignition engines run on diesel and JET fuel. These fuels are also favorably low flammable and cheaper than AVGAS 100LL. Fuel, or rather its cost, plays a very important role in the life of the engine. Meanwhile, the price of diesel fuel (diesel or JET A-1) is about half the price of aviation fuel – AVGAS 100 LL [12]. The second problem is that most flights do not terminate on stations where refueling with aviation fuel is possible. This, in turn, is caused by the high expense of all required procedures to undertake a refueling - landing, refueling and scheduling for further flight, which takes up to several hours. For example, aviation fuel in Poland is available at 34 stations located in 28 cities. Diesel engine responds to customers preferences – easy access to the automotive diesel at no additional cost and the supply of aircraft engine diesel fuel.

Their primary disadvantage is their weight and troublesome low-temperature start-up and higher operating temperature range. However, fuel consumption in diesel engines is lower than in spark ignition ones, which reduces the amount of fuel to fly the same distance, enabling a larger cargo to be transported despite these engines are heavier.

The General Aviation claims that the market of ultralight aircraft is more than 3,500 units worldwide, of which Rotax provides approx. 3,000 engines for ultralight aircraft only. Maximum power of its units is near 100 kW. Rotax provides approx. 75-80% of all aircraft engines manufactured worldwide to be dedicated to single- and double-seat aircraft. The rest is supplied by Jabiru (Australia), Continental and Lycoming (USA) and a small percentage by HKS (Japan) [14].

The light engine is also dedicated to the autogyro and ultralight aircraft. Over the last fifteen years, the autogyro has been rediscovered because as one of few aircraft it has not been subject to very strict regulations on construction and certification of new constructions as a result of little interest by uniformed services [18].

Our research focused on compression ignition engine parameters and compared them with those of aircraft spark-

ignition and turboproped engines so the compression-ignition engine to drive the lightweight airframe was defined.

2. Overview of aircraft compression-ignition engine designs

Many companies like AustroEngines, Continental Motors, WilkschAirmotive LTD, SMA have decided to re-apply the diesel engine and are successfully investing their money to develop this technology. These engines have been produced and certified. Some aircraft diesels, including DeltaHawk, WilkschAirmotive LTD, ZocheAerodiesels and Superior remained prototypes.

The Austro Engine is owned by Diamond, an aircraft manufacturer who developed and certified the AE300, a 93 kW diesel engine based on the Mercedes-Benz engine to be installed on two types of aircraft. This 4-cylinder engine has a Common Rail system, 2 camshafts in the cylinder head and 16 valves. The propeller is driven with a reduction gear with torsion damper (Fig. 1).

Fig. 1. Austro Engine AE 300 diesel aircraft piston engine [7]

The Safran SR305 (Fig. 2) is a 4-cylinder engine of 169 kW at a 3 bar inlet pressure. The boxer engine has 2 turbochargers to maintain flight parameters at an altitude of 3.8 km, and its TBO is 2,400 hours. So its fuel consumption is by 40% lower than comparable Avgas turbocharged engines and its noise is lower by 4dB. Fuel consumption per one-hour flight for Cessna 182's cruise speed is 38 liters of diesel fuel compared to 51 liters of Avgas.

Fig. 2. Safran SR 460 diesel aircraft piston engine [16]

The engine has been certified by the EASA and the FAA. About one-third of engine cooling is provided by cylinder fins, whereas the rest by oil flowing along channels around the cylinder liner and oil coolers. The engine has no gear so power is transmitted directly to the propeller with varied stroke and a constant speed of 2,200 rpm. The French manufacturer of this engine also has on offer the SR460 which is a 6-cylinder engine of 270 kW.

2-stroke WAM engines are 3-cylinder (WAM 165BB – see Fig. 3) and 4-cylinder (WAM 167BB) engines of different maximum power. They have an indirect injection system known as IDI that unlike in structures with a direct injection system (DI) results in a slower combustion and a delayed cylinder pressure increase. So combustion occurs in a separate chamber above the piston and there is a slight loss in efficiency but a significantly smoother combustion and a lower vibration of torque.

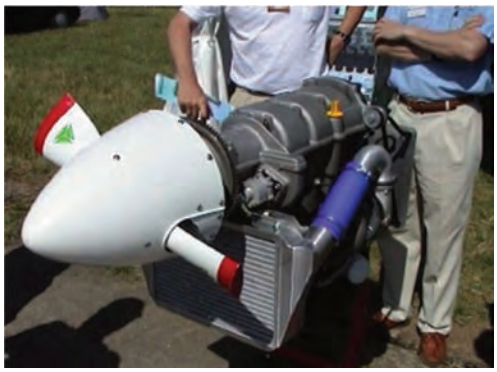

Fig. 3. WAM-165BB diesel aircraft piston engine [19]

Based on a car engine design, Subaru EE20, the boxer engine by CKT Aero Engines Ltd., England is fitted with a turbocharger, an intercooler and FADEC. It is a liquid-cooled engine with an aluminum frame with steel-casting reinforced main shaft bearings. It is combined with a gearbox that drives a 3-bladed hydraulic adjustable propeller, a hub shield and its mounting. The engine has separate cooling and oil systems. The engine consumes by 40-45% less fuel, which means 50% of fuel saved compared to AVGAS engines. There is a hydraulic damping flywheel. All of its parts come from the automotive industry. The compressor is driven by multiple-V-belt.

Fig. 4. CKT-240 TD diesel aircraft piston engine [8]

The Continental Motors CD series 100 (Fig. 5) is a row, 4-cylinder, turbocharged engine of 99 kW and 114 kW. The engine is a Mercedes-Benz A-class-sourced item. It is liquid-cooled with a Common Rail system.

The Superior Gemini 100 is a 2-stroke, liquid-cooled diesel engine with 3 cylinders and 6 opposed pistons. Each cylinder is fitted with a Common Rail injector and a glow

plug. Its steel liners are inside a die cast aluminum block. The opposite piston engine is driven by 6 pistons and 2 crankshafts mounted at the sides of the engine. The crankshafts are made of high quality steel *EN40* used primarily at Formula One. Inside, there is a gearbox to reduce speed (4,000 rpm) transmitted to a propeller (2,500 rpm). There is a dry sump lubrication system. Figure 6 shows the cover of sliding cylinder liners with its intake and exhaust systems. A compressed air fuel mixture goes through small holes on the left side of the liner, and the outlet is on the right side (larger holes).

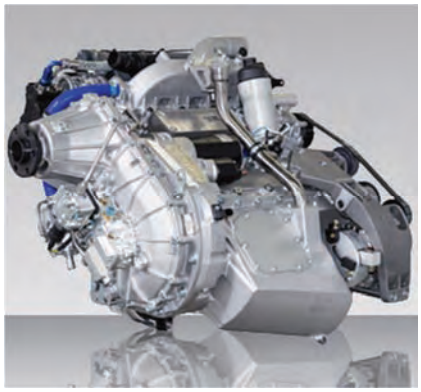

Fig. 5. CD-135/155 diesel aircraft piston engine [9]

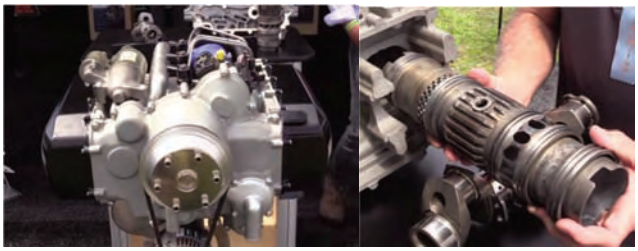

Fig. 6. Gemini 100 diesel aircraft opposite piston engine (right) and its cylinder liner (left) [6]

The DAIR-100 (Fig. 7) is a 75 kW, 2-stroke opposed-piston OPOS engine design with 4 pistons, 2 cylinders and 2 crankshafts coupled with a gearbox to drive a propeller. Its design is similar to that of the Gemini. Its cylinder intakes and outlets are rings opened by moving pistons. This is a liquid cooled engine powered by a high pressure fuel pump. In each cylinder there are two fuel injectors. The engine is supercharged with a centrifugal compressor.

Fig. 7. DAIR 100 diesel aircraft piston engine [10]

The Weslake A80 (Fig. 8), a 2-stroke opposed-piston engine has a special large-diameter flywheel in front of the engine. It is just where a propeller, an alternator drive and a compressor are installed. This 2-stroke engine with 2 cylinders reaches 60 kW at a speed of 4,800 rpm. The liquid-cooled engine is powered by an in-line fuel pump.

Fig. 8. Weslake A80 diesel aircraft opposite piston engine [17]

The DeltaHawk DH series (Fig. 9) is a 2-stroke V4 engine. Its cylinders are supplied with 4 separate unit injectors (137 MPa) and a supply pump (0.6 MPa). Its supply system is completely mechanical. Its charge system consists of a v-belt-driven compressor from a shaft, a supercharger with a by-pass valve and an intercooler. Its mechanical compressor provides for 50% of power and is used at a start-up and in emergency. In other states, its compressor does not work. There are inlet widows instead of valves. This engine with a dry sump is pressure-lubricated.

Fig. 9. Delta Hawk diesel aircraft piston engine [11]

Zoche aero-diesels, a German manufacturer, constructed three modular engines of different configurations of cylinders and power (Fig. 10). Its air-cooled 2-stroke engine directly drives a propeller. It is based on a direct fuel injection system. It uses a 2-stage supercharging system, i.e. a turbine and a supercharger as well as an intercooler to provide an intake air absolute pressure of 3 bars. A quad scroll compressor is installed inside an intercoller body. Low noise is achieved by a 2-stroke cycle and supercharging. There is dry sump pressure lubrication. The alternator is directly driven. There is no starter (a start-up by compressed air) and rubber parts.

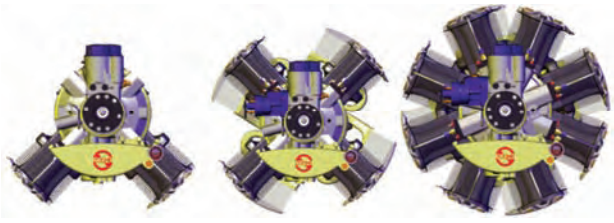

Fig. 10. Zoche aero-diesel ZO series diesel aircraft piston engines [20]

3. Aircraft diesel engine basic parameters

There have been created a database of about 40 diesel piston engines installed in light airframes and gyroplanes. The database provides basic parameters of available engines. Piston compression-ignition engines are in the former part, whereas opposed-piston compression-ignition ones in the latter one. For example, the parameters of the most popular engines like the Rotax and the turboshaft engine are investigated. There are compared the power, weight and brake specific fuel consumption (BSFC) of the 180-Watt turboshaft PBS TP-100 and gasoline, piston Rotax engines. In the turboshaft engine, the pilot controls power with a variable blade angle propeller. Its planetary gearing reduces turbine shaft speed at an outlet shaft from 61,000 rpm to 2,750 rpm. The engine weighs 62 kg and have fuel consumption equal to 525 g/kWh.

The air and liquid cooled (heads) Rotax 912-ULS has a power of 75 kW at 5,800 rpm and weighs 55 kg. Its fuel consumption is equal to 285 g/kWh. The engine is 4-cylinder boxer engine that operates in a 4-stroke cycle. The engine has a turbocharger and an electric valve. There is a dry sump lubrication system with an extra oil tank.

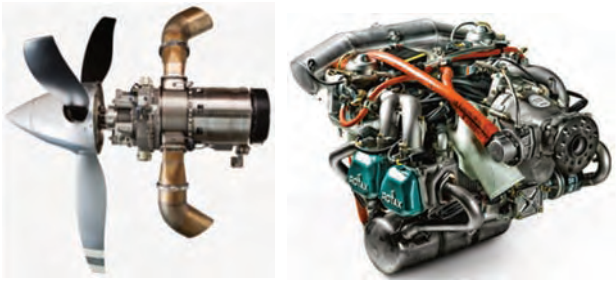

Fig. 11. Aircraft turboshaft TP- 100 engine (right) [15] and Rotax 912-ULS spark ignition engine (left) [13]

Some compression-ignition engines are based on car engines so the following technical parameters are examined: cylinder arrangement, engine power, weight, fuel consumption, etc. Our examination enabled us to define the configuration of the aircraft compression-ignition engine. The examined parameters included the main dimensions of the engine (stroke, bore), cylinder configuration, a crankshaft speed range and basic operating parameters. There were described the tendencies of the average value of a given parameter.

3.1. Operating cycle

Diesel engines are heavier than gasoline ones due to the nature of their operating cycle, i.e. much higher compression pressures, higher combustion pressures and larger gas forces. If these forces increase, the engine construction needs to be strengthened and more rigid so an engine block, crank-piston systems and a crankshaft are heavier. Their larger weight can be compensated for their more powerful charging systems.

The 2-stroke cycle allows for a significantly better power-to-weight ratio than it is in the 4-stroke cycle. The 2-stroke engine design is mechanically simpler so more reliable due to fewer moving parts. camshafts, valves, timing gear system were replaced by a port timing with inlet windows to be opened with a reciprocating piston. Engine weight is also reduced as there is no valve system. A regular operation and a very low vibration of a 2-stroke engine results from its single stroke in the cylinder per rotation.

It is important to note that 2-stroke engines due to their double firing frequency versus 4-stroke engines, have 30-40% reduced cylinder pressure and gas temperature than the 4-stroke engine at the same power rating [3]. This translates to the 2-stroke engine having approximately 30% lower NO_x emissions than the 4-stroke engine.

The 2-stroke cycle is, however, less efficient because the air-fuel mixture is diluted by exhaust gas and partially released through the exhaust window. Some difficulties occur when the 2-stroke engine is lubricated and cooled [6].

More than 30% of the modern aircraft diesel engines are 2-stroke. All opposed-piston designs are 2-stroke, whereas the rest are 4-stroke car engines.

3.2. Cylinder arrangement

Cylinder arrangement in aircraft engines enables us to minimize engine weight and a front surface area behind a propeller. Different types of cylinder arrangement are abbreviated as follows: B (boxer), R (in-line), G (radial), V (V-type), the V90 (V-type engine with cylinders at an angle of 90°), V180 (V-type engine with cylinders at an angle of 180°), OPE (opposite-piston engine). A dominant configuration is flat cylinder arrangement, i.e. boxer (10 engines) and opposed-piston arrangement (7 engines).

OPE engines have two opposed cylinders per one module of the crankshaft between them and two pistons oppositely reciprocating per each cylinder. Accordingly, the cylinder head and valves can be removed so such an engine design is much more efficient and simpler, with much less parts than in the other engines.

This type of engines is lighter because its cylinders/pistons are opposite each other so they are able to balance inertia forces and no extra balancing masses are necessary to improve rotational speed uniformity.

Our examination of aircraft engine designs shows that aircraft compression-ignition engines based on car engine designs are in-line (8 engines) and V90° (7 engines). This is the most compact type of design capable of achieving the lowest weight-to-power ratio. In addition, the V-type design is compact and easy to be installed in gyrocopters and helicopters. The crankshaft with 90° cranks enables us to minimize fluctuations of instantaneous torque.

The in-line engine design makes the engine heavier because of its long and heavy crankshaft. However, if applied in airframes, it has the smallest frontal surface.

The radial engine has the most lightweight crank system and the largest frontal surface. The two engines here have such a cylinder arrangement only.

3.3. Number and displacement of cylinders

Figure 3.1 summarizes the number of cylinders in each type of aircraft compression-ignition engines. The red frame indicates opposed-piston engines. Our research indicates that the engines have on average 4 cylinders and opposed-piston engines on average 3 cylinders (6 pistons). High power V-type and radial engines have 6 or 8 cylinders.

The opposed-piston (3 cylinders and 6 pistons) engine is a well-balanced engine, which is its advantage. Charge exchange there is optimal due to its dynamics, i.e. charge exchange is undisturbed so there is a continuous stream of exhaust gas mass that drives a turbine and compressor-based air supercharge is efficient. The 2-cylinder (4 pistons) engine design shows, however, long breaks in charge exchange resulting in turbocharger power loss, particularly at low load and speed. Therefore, a mechanical compressor is necessary but engine performance is reduced [4].

An average displacement of a single cylinder reaches 290 cm^3, 660 cm^3 and 690 cm^3 in gasoline, OPE and other aircraft diesel engines, respectively. It should be pointed out that a displacement of a single cylinder in the OPE engine results from a movement of two pistons (stroke of 2 pistons). Therefore, a displacement of a half of a single cylinder produced by a movement of a single piston is 330 cm^3. A displacement of supercharged engines is less than an average level.

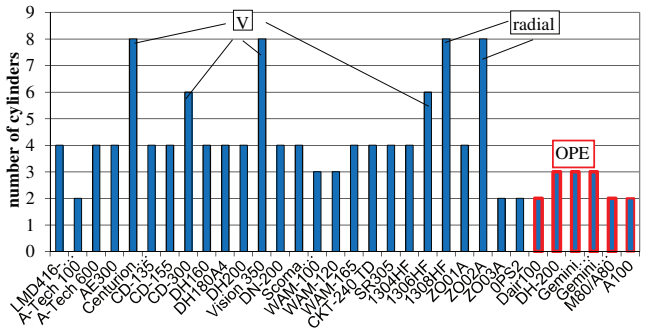

Fig. 12. Cylinder arrangement in diesel aircraft engines.

3.4. Engine power and weight

Figure 13 summarizes the specific engine output (power/unit displacement ratio) of individual aircraft engines This parameter describes the efficiency of an engine in terms of the brake horsepower it outputs relative to its displacement. and is around 50 kW/dm^3. One liter of displacement generates 66 kW in gasoline engines, 52 kW in OPR engines and 64 kW/dm^3 in the other diesel engines.

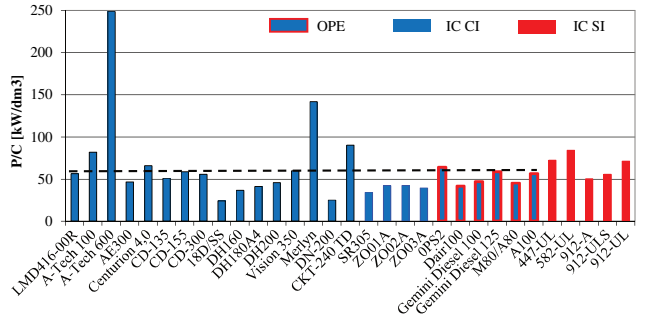

Fig. 13. Power/unit displacement ratio for aircraft piston engines

Figure 14 summarizes power-to weight ratio P/W (specific power), so the correlation between power density and weight for models of each aircraft engine. This parameter is very important for aircraft engines and should be as high as possible approaching 1 kW/kg as indicated by the dotted line. All gasoline Rotax engines and turboshaft engines achieve higher values. Modern classic diesel engines are not able to achieve such a good value of P/W. Our research shows that currently manufactured OPE engines can achieve a good value of this parameter near 1 kW/kg, and the best values are reached by the radial Zoche Aerodiesels ZO02A (1,8 kW/kg). A most of engines has power below 200 kW. The engines marked above the dotted line are high power lightweight engines. Their power density, P/M, is more than 1 kW/kg. This group of engines includes gasoline Rotax engines, turboshaft engines and most OPE engines.

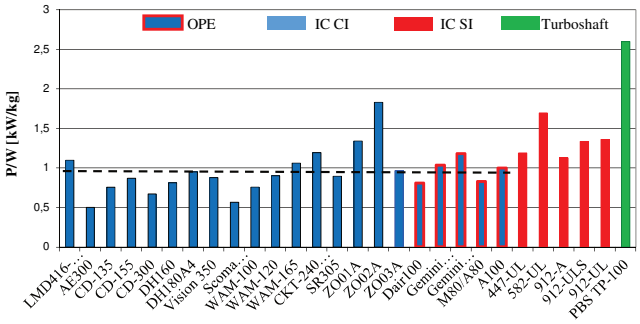

Fig. 14. Power-to-weight ratio for aircraft engines

Most of the engine designs studied here is liquid-cooled so their total weight is significantly higher but a defined level of engine temperature is better maintained and noise emission is lower than in air-cooled engines, which is their strong point. Moreover, the maximum efficiency can be achieved while monitoring coolant temperature depending on load. The group of air-cooled engines includes gasoline engines, the SMA, the VM Italy, the Zoche Aerodiesel and the Achates Power.

Aircraft engine power can substantially improve the use of a supercharging system. Typically, the lightweight turbine is used to achieve a defined level of power or to normalize the engine (to maintain the sea level pressure level regardless of the altitude). Engines capable of operating at an altitude above 2,000 m need a supercharging system as a mechanical compressor, pressure wave supercharging (dynamic charging) or a turbocharger. The last solution applied in engines based on car engine designs is most popular. Their power output is proportional to the mass of air that fills cylinders. The application of a mechanical compressor is most frequent in all of the analyzed OPE engines, and some of them are fitted with a turbocharger.

3.5. Fuel consumption

Here we summarizes Economy Cruise break specific fuel consumption (BSFC) in g/kWh for each of the aircraft engines. This value can be achieved for the 0.65 to 0.75 nominal power flight. Figures 15 and 16 depict power and weight as a function of the BSFC of the diesel engine designs studied here. The compression-ignition engines stud-

ied here have their Economy Cruise BSFC close to 200 g/kWh. Our research shows that the ZO03A Zoche and the Rotax 912 are the best designs in terms of their BSFC and power-to-weight ratio.

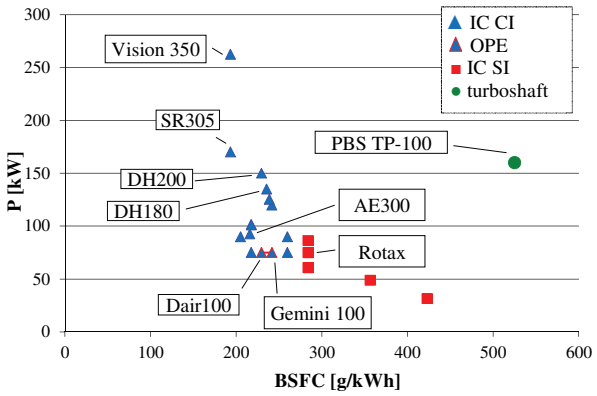

Fig. 15. Power vs. BSFC for the aircraft engines studied here

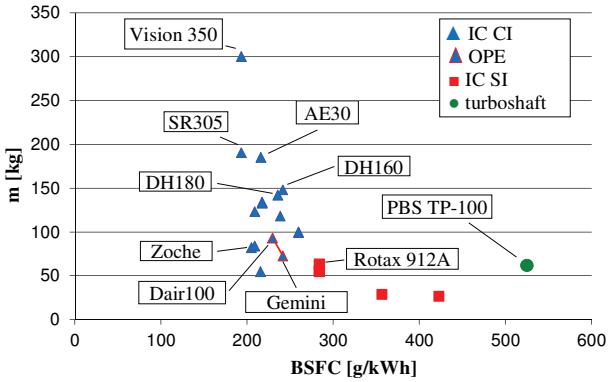

Fig. 16. Weight vs. BSFC for the aircraft engines studied here

3.6. Chamber dimensions

The engine chamber is defined by the stroke S and the bore D (diameter of cylinder liner). The chamber in a typical engine is limited by the head, the moving piston crown and cylinder liner walls. The chamber of OPE engine is shaped by two moving pistons and cylinder liner walls. The stroke-to-bore ratio, indicated as S/D, specifies engine main dimensions. Figure 17 summarizes the values of S/D for the aircraft engines studied here. S/D for today's compression-ignition engines ranges from 0.9 to 1.1, whereas that for gasoline aircraft ones is less than 0.8. Achates with AVL examined in detail S/D while designing a 2-stroke opposed-piston engine and concluded as follows [3]:

- the in-chamber heat exchange reduces with increasing the S/D ratio because the chamber area/volume ratio is reduced. Such reduced heat exchange directly improves engine thermal efficiency and reduces heat transfer to a cooling medium.
- an engine flush is more efficient if the S/D ratio increases, and pumping increases below 1.1 of the S/D ratio.
- friction in the engine is non-linearly correlated to the S/D ratio so friction increases when the S/D ratio reaches 1.15 although it is much less than heat transfer and pumping.

Compression ratio ε for compression-ignition engines ranges between 12 and 21. Figure 18 summarizes the theoretical compression ratio for the models of the aircraft engines. Compression ratio for gasoline engines ranges from 7 to 8.5, for diesel engines its average value is 18.

Heat generated by increased pressure is high enough to ignite the fuel in the chamber. Increased compression ratio results in higher power because of pressure and temperature at the end of the compression stroke. Too high compression ε, however, has an adverse impact on load of the crank-piston system so geometric compression ratio ε should not be more than 22 due to thermal and mechanical loads that have an impact on lifetime. Too low compression ratio, on the other hand, has an adverse impact on performance and fuel consumption.

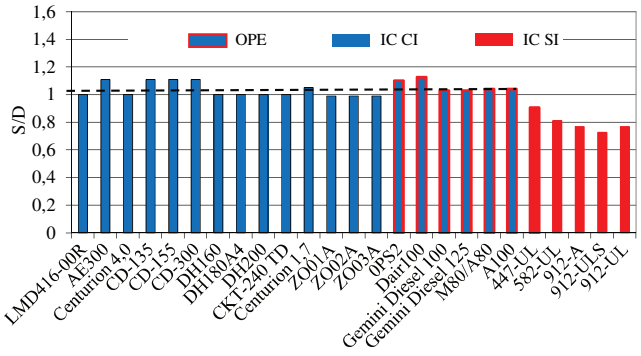

Fig. 17. Stroke vs. bore as S/D ratio for the aircraft piston engines studied here

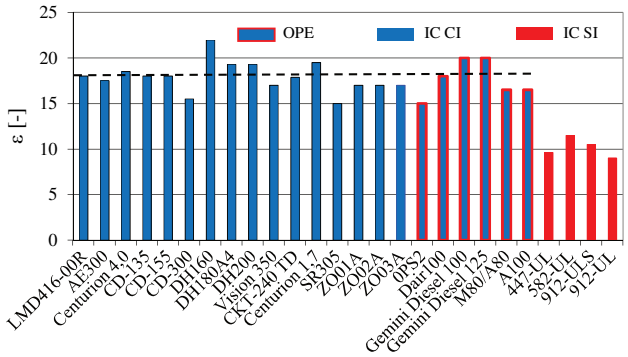

Fig. 18. Compression ratio for the models of the aircraft piston engines studied here

Summary

The development tendencies for aircraft compression-ignition engine are twofold, i.e. modifying car engine designs and designing completely new engines, generally 2-stroke opposed-piston engines. Our investigation of available aircraft compression-ignition engines shows that they are chiefly 4-stroke, 4-piston, liquid-cooled, and supercharged. The average displacement for analyzed diesel aircraft engines is 3,640 cm^3, whereas for the Rotax 912-UL it is 1,211 cm^3. The average displacement per cylinder is 812 cm^3, and for the Rotax 912-UL reaches 303 cm^3. The disadvantage of diesel engines is power-to-weight-ratio, which has average value equal to 0.97 kW/kg, while for the Rotax 912-UL is about 1.34 kW/kg. If these values are compared with the values of other engines, diesel engines

clearly stand out from their competition. But our comparative investigation shows that diesel engines consume much less fuel than spark-ignition engines and turboprops. The average fuel consumption amounts to 237 g/kWh and to 332 g/kWh and 548 g/kWh for the spark ignition Rotax 912-UL and turboshaft PBS TP100 respectively.

The average rotational speed for diesel engines is 2,827 rpm and for the Rotax 912-UL – 5,800 rpm. So diesel engines can run without reduction gear and the same decrease mass of the whole aircraft power plant.

Power, size, and better use of displacement are now the greatest challenges faced by today's engine designers to design compression-ignition engines capable of holding a dominant position in the aviation market. Diesel engines in the aviation industry are quite new compared to spark ignition engines but they have already managed to outrun much competing engines in reduced fuel consumption and toxic emissions. Accordingly, in the forthcoming years, investors are inspected to be more interested in these designs which can crowd out spark-ignition engines.

Acknowledgement

This work has been realized in the cooperation with The Construction Office of WSK "PZL-KALISZ" S.A." and is part of Grant Agreement No. POIR.01.02.00-00-0002/15 financed by the Polish National Centre for Research and Development.

Nomenclature

TBO	time between overhaul
FAA	Federal Aviation Administration
EASA	European Aviation Safety Agency
IDI	indirect injection
BSFC	brake specific fuel consumption
OPE	opposite piston engine
RPM	revolutions per minute
ICE	internal combustion engine
CI	compression ignition
SI	spark ignition
P/C	power-to-displacement ratio
P/W	power-to-weight ratio
ε	compression ratio

Bibliography

[1] DONOVAN, R. The design of an uninhabited air vehicle for remote sensing in the cryosphere. University of Kansas 2007.
[2] FAROKHI, S. Aircraft propulsion. ISBN: 978-1-118-80677-7, 2004.
[3] FLINT, M., PIRAULT, J.P. Opposed piston engines: evolution, use, and future applications. *SAE International.* PA ISBN 978-0-7680-1800-4, Warrendale 2009.
[4] REGNER, G., JOHNSON, D., KOSZEWNIK, J., DION, E. et al. Modernizing the opposed piston, two stroke engine for clean, efficient transportation. *SAE Technical Paper.* 2013, 2013-26-0114.
[5] Revised IPCC Guidelines for National Greenhouse Gas Inventories, 1996.
[6] www.achatespower.com
[7] www.austroengine.at
[8] www.cktaeroengines.com/
[9] www.continentalmotors.aero
[10] www.dair.co.uk
[11] www.deltahawkengines.com
[12] www.dlapilota.pl/wiadomosci/dlapilota/aktualizacja-ceny-paliw-lotniczych-na-polskich-lotniskach
[13] www.faston.pl
[14] www.generalaviationnews.com/2015/01/01/measuring-growth-in-lsa/
[15] www.pbsvb.com
[16] www.smaengines.com
[17] www.weslake.eu
[18] www.wiatrakowce.org
[19] www.wilksch.net
[20] www.zoche.de

Michał Gęca, DEng. – Faculty of Mechanical Engineering at the Lublin University of Technology.

e-mail: *M.Geca@pollub.pl*

Zbigniew Czyż, MEng. – Faculty of Mechanical Engineering at the Lublin University of Technology.

e-mail: *Z.Czyz@pollub.pl*

Mariusz Sułek, Eng. – Faculty of Mechanical Engineering at the Lublin University of Technology.

e-mail: *M.Sulek@pollub.pl*

BORKOWSKA, J., KAŹMIERCZAK, A. Research and analysis of the results from the tribotester test for piston. *Combustion Engines*. 2017, **169**(2), 14-17. DOI: 10.19206/CE-2017-203

Joanna BORKOWSKA
Andrzej KAŹMIERCZAK

CE-2017-203

Research and analysis of the results from the tribotester test for piston

Piston – ring – cylinder assembly of combustion engine has a lot of friction pairs examples, also one of them which decide about fastness to wear, it means first sealing ring – cylinder, called further very simply ring – cylinder unit. During work of this unit we can observe wear of piston, precisely – of coating which is deposited on ring to prolong service life. Objective of this work was to realize a test of roll-block type on tribotester to set durability of piston sample. Within the framework of this test were investigated a prototyped piston's rings with diamond embankment. Piston rings are made of diamond coating technology with a porous chromium coating, where in pores is deposited on said diamond powder with a grain size about 1 micron. The work will be carried out of an analysis of collaboration piston – rings – cylinder unit in internal combustion engine and an analysis of the use of hard materials in friction pairs, including powders. The work aims to show the possibilities and benefits of the application of new protective coatings to reduce their wearing, which is consistent with the observed trend of technology development.

Key words: *piston, diamond, coating, tribotester, friction*

1. Introduction

This article presents one of the stages in the research of the newly developed vacuum seal consisting of a sealing piston ring and a cylinder designed for an internal combustion engine, in which the novelty is an innovative diamond-derivative coating with very good anti-wear properties.

The purpose of the coating is not only to protect the item against wear, but also to improve its integrity. Diamond-coated coating is classified as hard coatings. Diamond copolymer coatings are amorphous raw materials with very thin layers and their properties depend on the conditions and the type of technology used in the production. For the first time, they were made by Aisenberg and Chabot in 1969 to produce an amorphous layer without hydrogen, thanks to the argon in which carbon beam beams were previously cooled. This has led to the ever-increasing use of this material as a tough, anti-wear coating with high resistivity. These coatings are named in various ways. The most common name is DLC. The name, precisely the structure of the DLC coating is derived from the high number of sp3 bonds present in the amorphous carbon, which at the same time affects the properties of the coating. This coating is characterized by high hardness, stability and smooth surface. Coatings can undergo some modifications by using such metal elements as vanadium, chrome, titanium or molybdenum, thereby obtaining suitable structures that interfere with parameters such as coefficient of friction, stress, adhesion and wear. In our case, the coating contains addition of chromium.

In general, the characteristics of diamond-shaped coatings are:

- higher hardness than traditional materials, within 10–60 GPa,
- high adhesion to the substrate,
- High mechanical, physical and chemical stability,
- coefficient of friction below 0.1,
- high electrical resistance up to 1016 Ω,
- high abrasion resistance up to 10^{-7} mm^3/Nm^{-1},
- as well as optical transparency.

Comparative research on tribotester test at model stations is considered as exploratory because many simplifications are used. The purpose of these studies is to compare the results of the tribological processes (wearing) that occur in the material connections in friction pairs.

The research was done on a roll-block type tribotester. The test elements are a rotating countersample in the form of a roll and a fixed sample in the form of a block. Key loads in this type of friction pair test are unit pressure [MPa] and linear speed [m/s]. High pressure and low speed produce extremely difficult conditions in the engine.

2. Test on tribotester

2.1. Preparation

The test was performed on a tribotester marked with the T05 symbol in Radom, which is suitable for tests of low-friction coatings. The sample is in the form of an annular roller, while the sample is characterized by a concave test surface, thereby adhering to the roll and simultaneously forming a contact of 100 mm^2. The working surfaces of the samples are covered with a diamond-like coating deposited by physical gas phase deposition in various ratios with chromium addition.

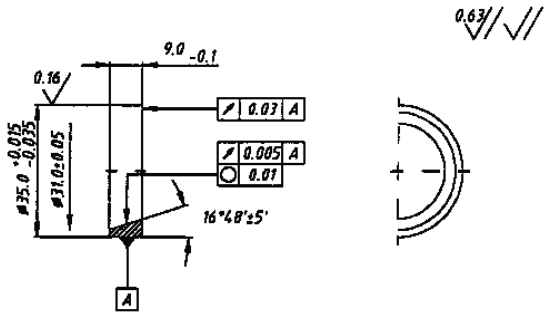

Fig. 1. Sample intended to tribotester test

A linear velocity of 1.25 m/s and a unit pressure of 5 MPa have been used for the tests, resulting in very severe operating conditions (very much in excess of normal operating conditions) which are very similar to those that occur at the beginning of the expansion stroke of 4 – with internal combustion engine in the vicinity of the ZZ of the first

sealing piston ring. The phenomenon of mixed friction appeared here, as evidenced by the excess of 0.01 typical of liquid friction. The friction was done in a synthetic oil environment named GOLD SINTHESIS VENOL 5W-40. In test we considered 6 samples, but after the research we typed sample T-2 as the best composition of % diamond and % of chromium.

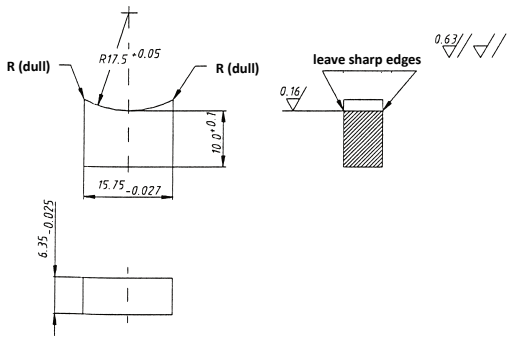

Fig. 2. Countersample intended to tribotester test

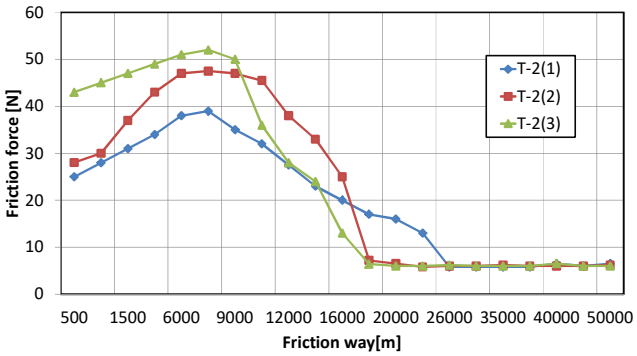

Fig. 3. Course of variation of friction force from road for samples marked T-2

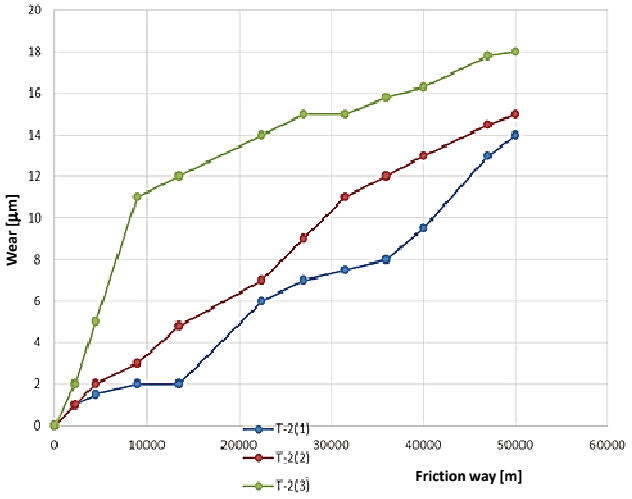

Fig. 4. Sum of wearing graph for T-2 friction node

The friction force measurements at the testing node were recorded at a certain time interval, and on this basis was compiled a source graph for 50,000 meters long of run in 3 trials (Fig. 3).

The aggregate wear of rings and blocks was performed directly on the T-05 tester during breaks and at a steady-state temperature of 25°C. Measurement was done without disassembly of the friction node and at a load of 5 MPa. For measurements, a clock sensor is used in the value of the parcel We = 0.002 mm, in the same angular position to eliminate the ring error. It should be noted here that the aggregate wear of the friction node is also burdened by the wear of bearings in the spindle and the angular position of the spheres. The results shows the Fig. 4.

2.2. Results

Of course, these studies do not fully reflect the working conditions of the steamed piston ring cylinder. First of all, there is no burning process. The material from which the piston ring model was made, was made of steel from which the piston rings were made and chrome-plated. Were designed and made 6 variants of the coating. The block was made of gray cast iron – typical metarial of the cylinder. Thus, the cooperation of the materials in the model of the same steamed pair, which are used in the tested for combustion engines, has been ensured. The selected motion parameters during the tribotester test result in extremely difficult operating conditions, ie a load close to the maximum working cycle of the actual steam seal ring cylinder, at the same time a rotational speed of only about 30% of idle speed for individual motors. The trial was conducted in the gears (according to test procedure on tribotester type T05), each of which has a friction path of 1250 meters. For each test sample count is 40 gears, which means a friction path of 50 000 meters. Experience shows that friction coefficient stabilizes after this friction path. The tests are conducted in the presence of Synthese Venol 5W40 synthetic elf lubricant. As a result of the research work we have obtained the variation of the frictional forces as a function of the friction path, from which it is possible to calculate friction coefficient values and friction coefficient sum values. Fig. 3 illustrates, for example, the course of friction force as a function of the friction path for a sample of T-2, the composition of which is the most favorable from the viewpoint of co-operation with the counterpart (carbon percentage in the chromium coating was about 1%).

Analyzes of the measurement results allowed to determine the final form of the diamond embankment. First of all, the percentage of diamond crystals in the shell was decided. Based on the above research was decided to have a content of about 0.75 mass%, which means 1.47% by volume diamond fill in the shell.

Within this task, material, shape and other rings and cooperating cylinders were also carried. It had examined piston rings with a diamond filler of 0.5 to 4.5 µm in diameter and a blend of corundum.

The final composition of the coating is the result of optimization work and its sample composition is shown in the table below.

Tab. 1. Sample composition of PCD coating

Elem %	**C**	**Al**	**Cr**
Min:	0.640	0.000	98.020
Max:	0.900	0.090	98.570
Mean:	0.770	0.047	98.306
StdDev:	0.096	0.030	0.195
% MAS	0.75	0.09	99.20
% V	1.49	0.14	98.36

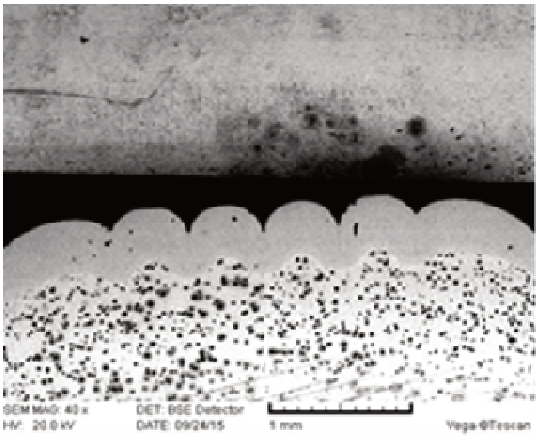

Fig. 5. A cross sectional view of the top layer of an engine ring with a PCD coating

Linear wear of rings and blocks was also measured on the Carl Zaiss Jena vertical optimizer, ring and block measurements were made before and after friction tests. The dimension difference should be treated as linear consumption. Measurement uncertainty is 0.001 mm. Results obtained in this way are presented in the form of bar charts in the table below, where we can observe that the smallest difference of linear wear in case of sample T-2.

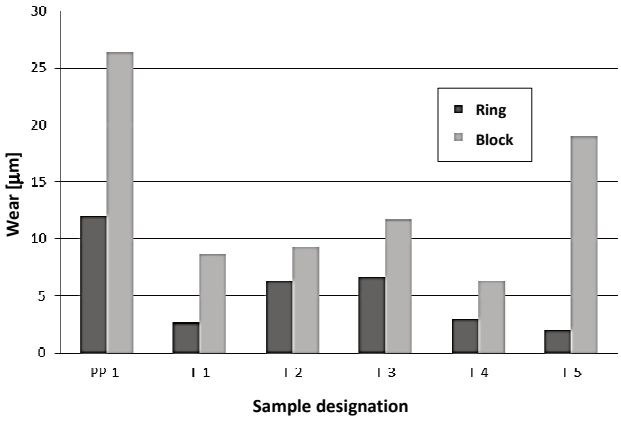

Fig. 6. Linear wear of rings and blocks after friction test

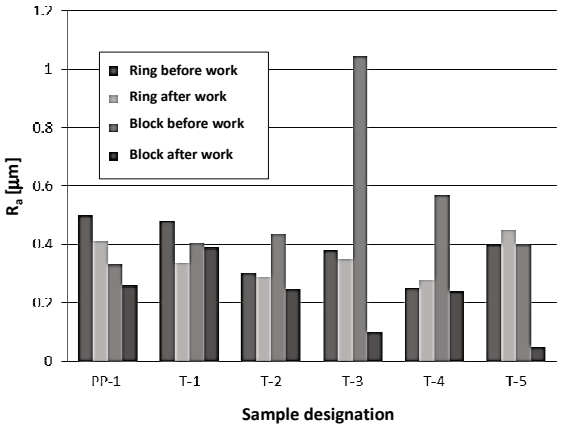

Fig. 7. Bar chart of the change of the roughness parameter

Roughness measurements of samples and counters were also carried out before and after the friction test on a computerized profilograph L50 topography produced by Advanced Manufacturing Technology in Cracow. The results of Ra parameter changes are presented in the form of bar graphs below, where we can see that the smallest change in roughness parameter between before and after the test appear in case of sample T-2:

Due to the relatively low linear wear of accelerated comparative tests, the friction path has been extended to 50,000 meters. In the oil exchanged after each series of tests, was observed a black precipitate.

In addition, micro hardness was measured by Vicers methodolody and performed at load of 100 G. The results of the measurements are shown in the bar graph in Fig. 8.

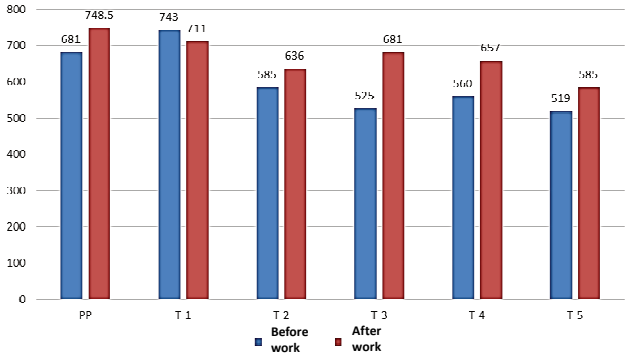

Fig. 8. Bar chart of the hardness of the rings before and after the friction test

The best sample turned out to be T-2, but to compare we can see f.ex. the results of the next sample with the less quantity of diamond powder in coating, where we can observe that the course of variation of friction force from the road for samples marked T-3 is very uneven:

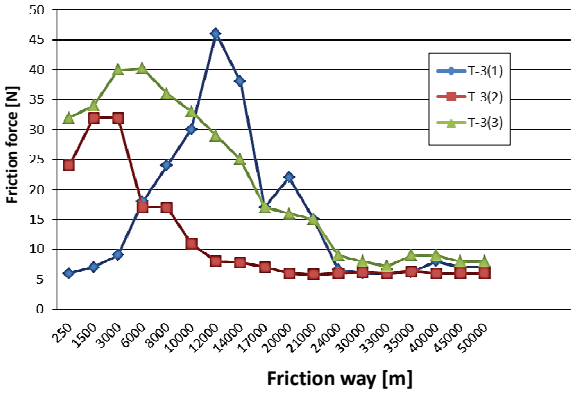

Fig. 9. Course of variation of friction force from road for samples marked T-2

3. Conclusion

Diamond – derivative coatings are mainly characterized by a lower friction coefficient and a much greater resistance to wear in comparison to rings that are covered by the common superhard coatings. Without a doubt, the application of such coatings will have an impact not only to extend the life of system piston – ring – cylinder, but also will reduce fuel consumption even under the most strenuous conditions of work of the unit.

Solutions to the given research problem is based on the results of these studies of tribotester test for piston. They allow to acquire new knowledge and skills in the manufacture of coatings PDC, in particular the constitution layers of diamond coating with a specific weight percentage composition. Positive test results realized in tribotester pose a real chance to increase the quantities of produced rings with diamond coating for f.e. large combustion engines powering locomotives or small inland waterway vessels (very positive results in the endurance tests) and in the future perhaps for small internal combustion engines for use in vehicles like a cars, thus extending their life.

Studies show that with % increasing of the carbon in the coating composition and decreasing of the hydrogen amount is related to improved strength and wear resistance at the time of no lubricating function of the lubricant. The use of diamond – derivative coatings is a new direction in the development of technology for internal combustion engines. Replacement of worn parts of the piston – ring – cylinder set would decrease considerably their properties and their improvement has a definite dimension, so the use of such modern shells prolonging the life could change a lot on what evidence may be carried out research and very promising results. These the hardest coatings available on the market today are increasingly used, mainly in the automotive and electronic equipment. The properties of these coatings and getting their increased popularity also contribute to the decrease in costs associated with their production, and the problem of their insufficient thickness will likely be solved with the most modern methods of hardfacing on components.

Diamond – derivative coatings can be applied to elements working in high-speed diesel engines and because of the opportunity to work at very high temperatures. They also exhibit good adhesion to the substrate steel and cast iron, and less stress their own, so they seem to be a breakthrough in the use of materials with excellent tribological properties. A complete set of advantages of applying diamond – derivative coatings contains very high hardness (70 GPa), high value electrical resistance, relatively low weight, and most importantly, low coefficient of friction and excellent wear resistance.

The diamond-based coating, exemplified by the DLC coating, is an example of a very hard surface coating that protects the element from wear. This layer of the coating affects tribological cooperation in the friction node and interaction with the environment. In turn, the core of such a coating is designed to provide adequate hardness, durability or thermal conductivity.

In a modern approach to coatings, coatings are used, which in the base composition contains carbon capable of crystallizing into graphite or diamond. A number of studies are being conducted based on the use of a diamond-based hard coating and successive research is being increasingly analyzed. Undoubtedly, the knot elements that are covered with diamond-coated coatings and cooperate with each other frictionally have less resistance. This, in turn, has a moderate linear wear on the parts and, what is important – a low friction coefficient, thus improving the mechanical properties of the system and therefore being used in all industries where there is a high risk of wear and high friction. There are several barriers to the widespread use of diamond-based coatings in the automotive sector. These coatings are small in thickness and this lowers its durability and it is difficult to obtain a smooth finish that improves tribological properties. Therefore, the DLC layer works with a layer of another origin and is applied eg in the presence of a chromium coating.

An important feature is that abrasive wear resistance increases with increasing hardness, which has a similar value on both working surfaces. This was the beginning of the discussion on diamond-based coatings, which is considered to be the hardest material.

Bibliography

[1] BUCKMASTER, J., CLAVIN, P., LINAN, A. et al. Combustion theory and modeling. *Proceedings of the Combustion Institute,* Vol. 30, pp. 1-19, Pittsburgh 2005.

[2] BURAKOWSKI, T., Wierzchoń, T. Inżynieria powierzchni metali, *Wydawnictwo Naukowo-Techniczne*. Warszawa 2004.

[3] ISKRA, A. Symulacja parametrów pracy pierścienia na stanowisku modelowym. *Materiały konferencyjne Konmot '94 Silniki Spalinowe – konstrukcja i badania*, Kraków – Raba Niżna 1994, 93-104.

[4] MADEJ, M. Właściwości systemów tribologicznych z powłokami diamentopochopdnymi. *Wydawnictwo Politechniki Świętokrzyskiej*. Kielce 2013.

Borkowska Joanna – Faculty of Mechanical Engineering at Wrocław University of Technology.

e-mail: *Joanna.Borkowska@pwr.edu.pl*

Kaźmierczak Andrzej, DSc., DEng. – Faculty of Mechanical Engineering at Wrocław University of Technology.

e-mail: *Andrzej.Kazmierczak@pwr.edu.pl*

Article citation info:
MERKISZ, J., WALIGÓRSKI, M. Recognition of combustion process irregularities in small volume displacement diesel engines with the use of non-dimensional characteristics of the vibration signal. Combustion Engines. 2017, **169**(2), 18-23. DOI: 10.19206/CE-2017-204

Jerzy MERKISZ
Marek WALIGÓRSKI

CE-2017-204

Recognition of combustion process irregularities in small volume displacement diesel engines with the use of non-dimensional characteristics of the vibration signal

The subject of the considerations described in the paper is the problem of early detection of abnormalities and damages during operation process of the turbo diesel engine with small volume displacement and direct fuel injection, which is used in modern LDV vehicles dedicated especially for urban areas, in the context of present and future requirements for a technical object diagnostics, taking into account the criteria of optimizing overall efficiency, toxic compound emission and safety of the object in real conditions of its operation. The paper presents the results of empirical research of vibroacoustic signal application to the diagnostic evaluation of correctness of short-time engine main processes. The evaluation of the combustion process variability from structural and operational abnormalities by using dimensionless estimates of a vibration process was conducted, and functional characteristics necessary to built the diagnostic algorithm in accordance with the requirements of on-board diagnostics were obtained.

Key words: *LDV vehicles, diesel engine, diagnostics, vibroacoustic methods, faults detection*

1. Introduction

Social, industrial, economic and environmental changes affecting societies have driven increased mobility, with increasing interest in road, water and air transport systems of the high performance and efficiency. Contemporary vehicles and their sources of a drive have to keep up with the new demands of the user, operating conditions and law regulations.

Among the requirements particularly relevant for new engine designs is to achieve the highest possible overall efficiency and the minimum emissions of toxic exhaust gases [11]. New regulations on emissions from means of transport force vehicle manufacturers to seek solutions that will enable them to achieve lower and lower emissions limits for their internal combustion engines. As a result, vehicles with engines with lower engine displacements with increasing their useful power are increasingly common. LDV vehicles with small displacement engines are particularly important for the urban agglomeration, where the importance of toxic gas and acoustic emissions and the optimization of fuel consumption for traction conditions are paramount for such a limited area of industrial, service and social activities. For this reason, the subject matter of the paper is up to date with regard to the issues being presented, going forward with contemporary and future transport trends in the areas of urban agglomerations.

In modern transport systems the main sources of their propulsions are modern combustion engines, among which the compression-ignition engines are of a significant importance. Their widespread use in various applications of means of transport and stationary machines results from the many advantages they have. The tendency of using engines with ever smaller displacement is also related to the CI engine, which continues to be the beneficial and most preferred source of a vehicle propulsion. However, the characteristics of the internal combustion engine not only define its state functions, defined by its structural properties, but also the process and conditions of use of the object for specific purposes.

Degradation of structure of an engine and the wrongly adjusted regulating parameters may cause - deterioration of work effectiveness of a combustion engine, engine brake power decrease, reduction of the mechanical and heat efficiency, lowering of overall engine efficiency (increase of fuel consumption), growth of an toxic compounds emission, possibility of damaging to the combustion engine elements. Recognizing the importance of the proper facility use and the need to monitor constantly the correctness of all the work functions assigned to the vehicle during the design phase, it is essential to diagnose this object continually, and in particular its superior power generation system and its conversion into useful work (the internal combustion engine).

Achievements in the field of the vibroacoustic diagnostics of combustion engines allow to state that: research works on the use of vibration signal parameters for assessment of technical condition of combustion engine units or processes occurring had been carried out, research works had concerned methodical issues and modeling issues, in those research works the simple methods for describing signals and also complicated techniques of converting signal were used [14].

The above advantages of vibroacoustic methods in the context of diagnostics of compression-ignition engines of LDV vehicles make possible to assess the possibility of monitoring the correct operation of the object under traction conditions and detection of main process abnormalities and damages of specified engine components. This task was undertaken by the authors of this work by analyzing the diagnosis of combustion abnormality in small displacement CI engines, using non-dimensional vibration signal estimators.

2. Methodology of the empirical process

The overriding postulate of obtaining the unambiguous functional relations during vibroacoustic testing of machines, especially of internal combustion engines, is the proper post-processing of complex measuring signals. In this case, the proper separation of the useful vibroacoustic signal, and then the optimum selection of the characteristic

signal characteristics from the accompanying process, eg. sensitive to damage, is of major importance [6, 7, 18, 19].

The timing of a vibroacoustic signal allows a qualitative assessment of the course of a change occurring in an object, referring to the evaluated fragment of its behavior with a specific characteristic. In this context, the degree of determinism, periodicity, occurrence or non-occurrence of certain fragments of the process and their relation to other phenomena occurring in the object is assessed. And in this case close interdependence with the kinematics of the object is necessary. The proper separation of active signal components from the recorded physical waveform and its properties relative to the source process allows the search for a diagnostic parameter in close relation with the evaluated dynamic process [3–4, 10, 12–13].

Research methodology was based on the active experiment. As the input parameters, changes in injection and combustion processes related to their correctness were taken into account. As the parameters being controlled, engine speed and torque were chosen. As the output parameters, vibration accelerations of engine head were taken into consideration. An original methodology was developed by the authors for diagnostic assessment of combustion process runs in CI engines of LDV vehicles, in order to get an accurate and non-intrusive method of combustion process description, comparable to cylinder pressure characterization. The processed data in time and frequency domains allowed to extract the components mainly related to the combustion events and these having irregularities or working cycles with misfires.

The accelerometer was put on the engine block. Such a position was selected to obtain a high vibration signal sensitivity in regard to the combustion process and a low sensitivity to the other vibrations. Placements and orientations of the accelerometer on the engine block were considered. The optimal position for the transducer was selected based on the analysis of the combustion related signal to noise ratio (passive part of a measured signal from other process sources). The research dimensions of digital signals were chosen as: X dimension – parallel to the diameter of a cylinder, Y dimension – perpendicular to X and Z dimensions, Z dimension – parallel to the cylinder axis.

Values of the engine speed and load were selected within the engine operative area. Digital data was sampled during experiments once coolant and temperatures were stabilized. A software algorithms were developed by the authors and were used to manage the data post-processing analysis. The sampling frequency range during research process was 0.1 Hz to 25.4 kHz for each channel of the measurement system. The sound pressure level was measured as well.

Measurement of selected parameters of the vibroacoustic process for specific engine performance was carried out in accordance with the principle of finding a reliable diagnostic parameter for accurate evaluation of the engine operating processes (injection and combustion). Such a postulate is relevant for the accurate assessment of the correctness of the functions, processes and performance of the components, in line with the criterion of ensuring optimum operation of the facility throughout its service life, taking into account its minimal environmental impact (emission of harmful exhaust gas compounds). Hence, the use of test results may take place in vehicles on-board diagnostics at traction work conditions (stationary and non-stationary).

3. Research test stand and devices

All researches were performed for the engine test stand conditions, and working points of the engine were chosen from the engine speed and torque operating ranges (Fig. 2).

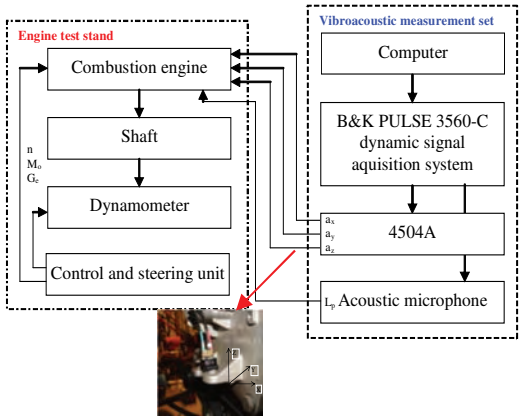

Fig. 2. The functional scheme of the measurement test stand

The compression-ignition engine taken into account in a research process is a small LDV (*Light Duty Vehicle)* source of a drive, that is an important share of means of transport used in urban areas. The paper considers research conducted on an common rail 4-stroke compression-ignition engine of Fiat, type 1.3 JTD with the following chosen specifications [17]: engine displacement 1251 cm^3, bore and stroke 69.6 x 82.0 mm, nominal brake effective power 55 kW for 4000 rpm, maximum torque 170 N·m for 1750–2500 rpm, compression ratio 18.1:1, CO_2 emission 113 g/km, average fuel consumption 4.24 dm^3/100 km.

The placement of the vibration acceleration transducer (Bruel&Kjær 4504A with its features: frequency 1–10000 Hz, sensitivity 10 mV/g, temperature range -50−125°C, resonance frequency 50 kHz) was located on the engine block, nearby the generated dynamic combustion processes [2]. Measurements were done for 3 perpendicular dimensions with the use of the Bruel&Kjær Pulse 3560-C system [15].

4. Diagnostic parameters and research conditions

The following non-dimensional vibroacoustic signal point measures were taken into consideration in the research analyses [1–2, 5, 8–9, 16]:

a) shape coefficient

$$K = \frac{u_{sk}}{u_{śr}} = \frac{\left[\frac{1}{T}\int_0^T u^2(t,\theta)\,dt\right]^{1/2}}{\frac{1}{T}\int_0^T |u(t,\theta)|\,dt} \tag{1}$$

b) peak coefficient

$$C = \frac{u_{sz}}{u_{sk}} = \frac{E\left\{\underset{0<t<T}{\text{Max}}\,|u(t,\theta)|\right\}}{\left[\frac{1}{T}\int_0^T u^2(t,\theta)\,dt\right]^{1/2}} \tag{2}$$

c) impulse coefficient

$$I = \frac{u_{sz}}{u_{śr}} = \frac{E\left\{\underset{0<t<T}{\text{Max}}\left|u(t,\theta)\right|\right\}}{\frac{1}{T}\int_0^T \left|u(t,\theta)\right| dt} \tag{3}$$

d) clearance coefficient

$$L = \frac{u_{sz}}{u_p} = \frac{E\left\{\underset{0<t<T}{\text{Max}}\left|u(t,\theta)\right|\right\}}{\left[\frac{1}{T}\int_0^T \left|u(t,\theta)\right|^{1/2} dt\right]^2} \tag{4}$$

e) kurtosis

$$\beta = \frac{\frac{1}{T}\int_0^T \left|u(t,\theta) - u_{śr}(\theta)\right|^4 dt}{\left[\frac{1}{T}\int_0^T \left|u(t,\theta) - u_{śr}(\theta)\right|^2 dt\right]^2} \tag{5}$$

Measurements were done in the following research conditions:

- termodynamic ambient conditions at the engine test stand area: $t_o = 15^oC$ and $p_o = 1013$ hPa,
- engine work conditions: stationary, for each constant engine speed values and for constant torque (7 engine speed values from the range 750–3000 rpm) and for load characteristics the torque values from 10−150 N·m,
- vibroacoustic measurement conditions: vibration acceleration frequency range: 1–10000 Hz, sampling rate: 25.6 kHz,
- placement of a vibration transducer: on the engine block (measurement in the 3 perpendicular dimensions), microphone placement – perpendicularly to the engine surface.

The measurement signals were fed to the analog inputs of the data acquisition card. Measurement signals were filtered inside the card with the help of analog and digital filters and then were converted from analog to digital. The signals obtained in the data acquisition card in a digital form were stored in a computer memory. The recorded all time history courses of the measurement signals were subjected to the time selection process. In the above selection all recorded signals were divided into signal sequences including single working cycles of the internal combustion engine.

5. Description of the research conditions and process

Measurements were made for different engine speed and torque values according to the following characteristics:

a) $y_1 = f(N_e)$ – screw characteristics;
b) $y_2 = f(n, M_o = \text{const.})$ – speed characteristics for constant torque values,
c) $y_3 = f(M_o, n = \text{const.})$ – load characteristics.

The following diagnostic parameters were taken into account in the analysis:

a) parameters of work processes: fuel injection pressure (p_{inj}) and cylinder pressure (p_c), fuel consumption (G_e, g_e), total efficiency (η),
b) parameters of accompanying processes: vibration accelerations in three dimensions (a_x, a_y, a_z), sound pressure level (L_p).

6. Assessment of the measurements results

Analysis of the engine working area during testing included the following overall engine efficiency ranges for the characteristics:

- partial power: 22–27%,
- load: 14–37%,
- screw: 19–38%.

If the engine speed values increase equivalent value of the sound pressure level and instantaneous peak sound pressure level are also raised (Fig. 3) – for L_{Aeq} increase up to 44% (depends from the working point). It means that the intensity of the dynamic processes taking place in internal combustion engines rises and level of the energy release from the process is transferred by the block material structure.

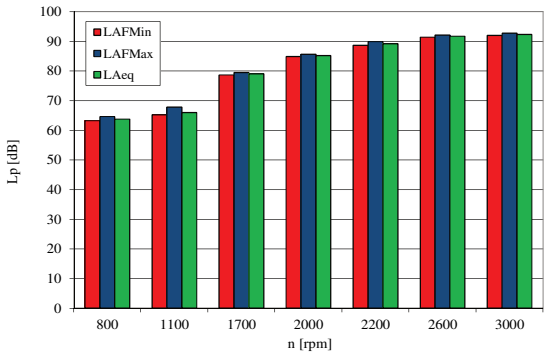

Fig. 3. The equivalent acoustic pressure level (L_{Aeq}) changes for different engine speeds

Observing the mean, RMS, peak, peak-to-peak point estimators of the vibration accelerations one can find that there is a strict function relation between the engine speed increase and the change of the above point measure (Figs 4–6). The point measures values, obtained for a combustion process, increases when engine speed rises, no matter what measurement dimension is considered. The highest values were obtained for Z dimension. Comparing such results with the peak and peak-to-peak values for the combustion process time run sections it is obvious the above two dimensional point measures of the vibration accelerations have the highest sensitivity for combustion process changes in the relation with the engine speed factor.

Comparing of all point measures taken into consideration for a Z dimension one can perceive the peak and peak-to-peak values are the most sensitive measures for combustion process changes resulting from engine speed increase. That means also the incorrect processes that might appear in the normal combustion engine operation will be unequivocally detected and described.

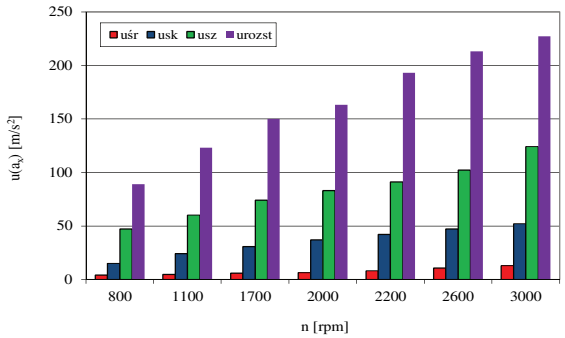

Fig. 4. Mean, RMS, peak and peak-to-peak value of vibration accelerations for X dimension and different engine speeds

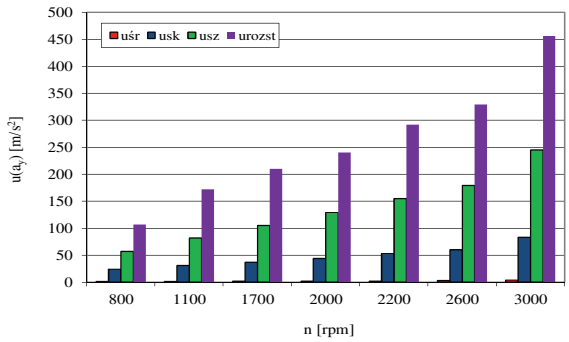

Fig. 5. Mean, RMS, peak and peak-to-peak value of vibration accelerations for Y dimension and different engine speeds

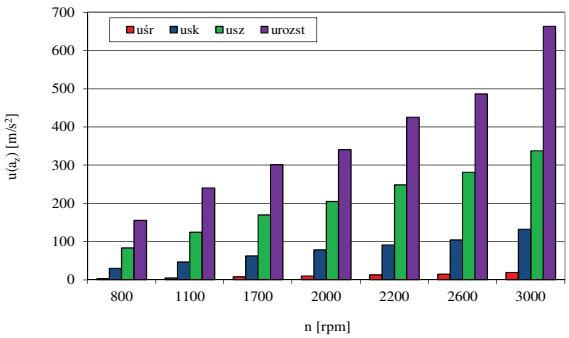

Fig. 6. Mean, RMS, peak and peak-to-peak value of vibration accelerations for Z dimension and different engine speeds

Determination of the variance function of the mentioned dimensional point estimates for empirical data with respect to the engine speed indicates simple mathematical functions that can be described for Z dimension as:

$$L_{Aeq}(n) = 16.83\ln(n) + 60.496 \ (R^2 = 0.95) \quad (6)$$

$$a_{z,sk}\ (n) = 16.107n + 13.143 \ (R^2 = 0.99) \quad (7)$$

$$a_{z,sz}\ (n) = 41.25n + 41.571 \ (R^2 = 0.99) \quad (8)$$

$$a_{z,rozst}\ (n) = 76.429n + 67.143 \ (R^2 = 0.96) \quad (9)$$

However, the question is how sensitive the non-dimensional vibroacoustic indicators are to the changes in engine speed. They are the point estimators independent of the momentary value of vibration amplitude. In addition, they allow to study the effects of the main process and its amplitude and energy values on the assumption of periodicity and relatively faithful reflection of the vibration characteristics for the engine fuel injection and combustion process. This makes it is possible to assess indirectly the determinants of the vibroacoustic process with the diagnostic nature, taking into account the reliability and unambiguity of the diagnosis (Figs 7–11).

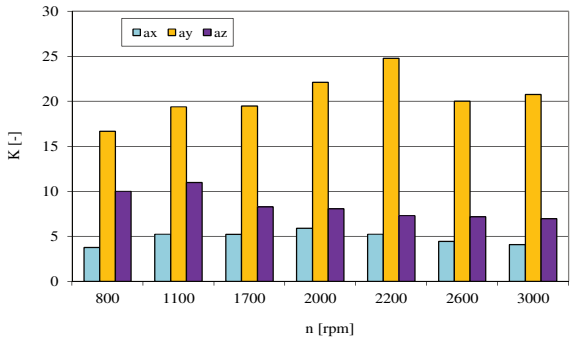

Fig. 7. Shape coefficient of vibration accelerations for X, Y and Z dimensions and different engine speeds

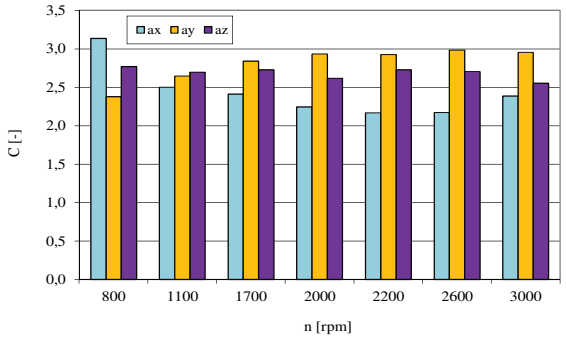

Fig. 8. Peak coefficient of vibration accelerations for X, Y and Z dimensions and different engine speeds

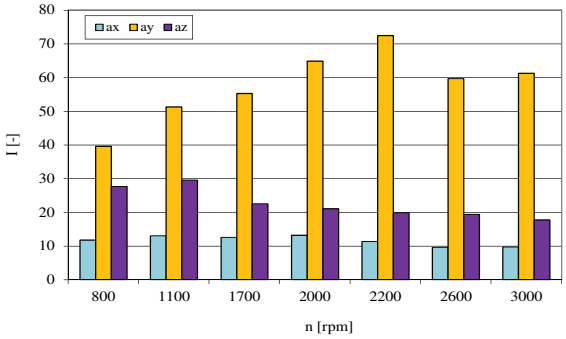

Fig. 9. Impulse coefficient of vibration accelerations for X, Y and Z dimensions and different engine speeds

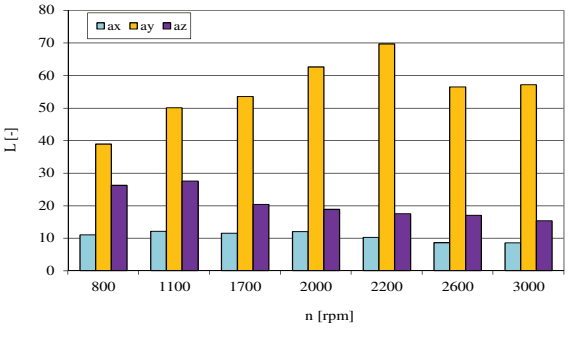

Fig. 10. Clearance coefficient of vibration accelerations for X, Y and Z dimensions and different engine speeds

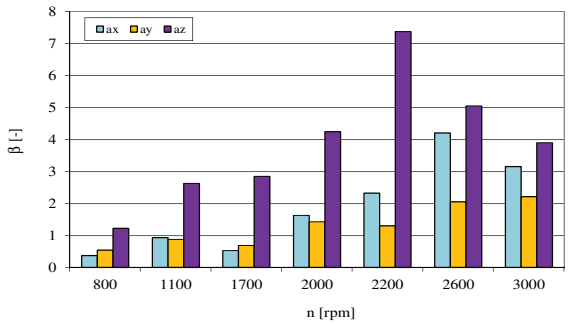

Fig. 11. Kurtosis of vibration accelerations for X, Y and Z dimensions and different engine speeds

The obtained waveforms of the selected non-dimensional measures of vibroacoustic process are not as clear as in the case of the first ones. Undoubtedly, the shape, pulse and slope coefficients for the Z direction have been found to be sensitive to combustion but with less reflection.

$$K_{az}(n) = -0.6323n + 10.909 \ (R^2 = 0.80) \tag{10}$$

$$C_{az}(n) = -0.0225n + 2.7732 \ (R^2 = 0.43) \tag{11}$$

$$I_{az}(n) = -5.874\ln(n) + 29.684 \ (R^2 = 0.82) \tag{12}$$

$$L_{az}(n) = -2.0206n + 28.448 \ (R^2 = 0.86) \tag{13}$$

$$\beta_{az}(n) = -0.1186n^3 + 1.1617n^2 - 2.147n + 2.5369 \ (R^2 = 0.84) \tag{14}$$

Analysis of the dimensionless estimates along with the increase of the engine speed indicates the uniqueness of the changes for the Z dimension for the shape, impulse and clearance coefficients. For the Y dimention, both the shape, the peak, impulse and the clearance are similar to the index change (increase in the measure to n = 2200 rpm). The above increase in value for a Z dimension is due to the significant increase in amplitude and energy emitted by the accompanying process from the working process. This results in a change in peak, RMS and mean values. The first of them concerns the increase of the impulse interaction of the dynamic process on the structure of the object, the second refers to the energy transfer from the main process to the object, the mean value on the increase, the amplitude of the signal, the energy emitted during the combustion process and the influence of the combustion nature of the increased fuel dose on the vibration acceleration time signal. Selecting a Z dimension as sensitive for combustion of the mixture in the cylinder determines the choice of K, I and L coefficients, according to the criterion of their uniqueness. The K factor determines the shape of a periodic waveform, and I factor how much the amplitude pulse value is relevant throughout the sample signal reflecting the dynamic process. The peak factor illustrates the relationship between the peak value and the global level of the whole measurement. Increasing the value of the clearance coefficient shows the accumulation of energy or occurs when the scattering of the measurement data changes.

Kurtosis is a measure of the flattening of a characteristic value distribution. It specifies the location and concentration of data values near the mean estimator. It occurs in the form of a fourth-degree central torque, referenced to a standard deviation raised to the fourth power. The higher the value of the kurtosis, the greater is the concentration of the population of data around the mean value (the slope of the distribution curve is greater). Its small value gives the opposite effect, which means a greater spread of values. The above indicator is higher with increasing rotational speed, showing the intensification of the dynamic impact from the combustion process (increase of the central torque), until the amount of emitted energy affects the average acceleration value.

Conclusions

The presented work is a new research carried out by its authors within the study of the influence of selected characteristics for CI engine with small engine displacement and relatively high brake power on non-dimensional vibroacoustic parameters. Comparison of selected dimensional and non-dimensional points measures allowed the diagnostic parameter and its reliability to be evaluated for the study of such vehicle sources of a drive, and its results can be used in their assessment in the real vehicles streams.

Due to the area of these measures analysis, limited to the field of time and value of the process, frequency analysis is of major importance. Modern engine diagnostics requires more and more detailed parametric and functional assessments. Changes to the regulations for vehicles of this category will affect their choice with a multi-criterion rating. Reliable characteristics and estimators will be put to the future diagnostic algorithms, which will be able to do the complex evaluation of the real technical state of objects even in non-stationary work conditions. That is why the specified diagnostic algorithms that use non-dimensional vibration signal point measures and improved frequency domain analyses should be created in the on-board diagnostics procedures basing on such methods of an empirical signal assessment.

Nomenclature

a	vibration acceleration
β	kurtosis
C	peak coefficient
CI	compression-ignition
CO_2	carbon dioxide
η	overall efficiency
G_e	stream mass of fuel consumption
g_e	specific fuel consumption
I	impulse coefficient
K	shape coefficient
L	clearance coefficient
LDV	light duty vehicle
L_p	sound pressure level
M_o	torque
n	engine speed
N_e	engine brake power

p_{inj} fuel injection pressure
p_o ambient pressure
θ lifetime of an object
t duration of dynamic processes
T signal period
t_o ambient temperature
$u(t, \theta)$ instantaneous signal value
u_p square root signal value
$u_{śr}$ mean signal value
u_{sz} peak signal value
u_{sk} root mean square signal value

Bibliography

[1] BARTELMUS, W., ZIMROZ, R. A new feature for monitoring the condition of gear- boxes in nonstationary operating conditions. *Mechanical Systems and Signal Processing*. 2009, **23**, 1528-1534.
[2] CEMPEL, C. Vibroacoustic machines diagnostics. *National Scientific Publishing Houses*, Warsaw 1989.
[3] CZECH, P., ŁAZARZ, B., WOJNAR, G. Detection of local gears of gear wheel gear using artificial neural networks and genetic algorithms. *ITE*, 2007, Radom.
[4] CZECH, P., MADEJ, H. Application of cepstrum and spectrum histograms of vibration engine body for setting up the clearance model of the piston-cylinder assembly for RBF neural classifier. *Maintenance and Reliability*. 2011, **4**, 15-20.
[5] CZECH, P., WOJNAR, G., FOLĘGA, P. Vibroacoustic diagnosing of disturbances in the car ignition system by amplitude estimates. *Scientific Journals of Silesian University of Technology*. Series: Transport. 2014, 83, 1904, 59-64.
[6] DESBAZEILLE, M., RANDALL, R.B., GUILLET, F. et al. Model-based diagnosis of large diesel engines based on angular speed variations of the crankshaft. *Mechanical Systems and Signal Processing*. 2010, **5**, 1529-1541.
[7] FIGLUS, T. Diagnosing the engine valve clearance, on the basis of the energy changes of the vibratory signal. *Maintenance Problems*. 2009, **1**, 75-84.
[8] KORBICZ, J., KOŚCIELNY, J. Modeling, diagnostics, and mastering processes. DiaSter implementation. *Scientific and Technical Publishing House*. Warsaw 2010.
[9] KORBICZ, J., KOŚCIELNY, J.M., KOWALCZUK, Z., CHOLEWA, W. Process diagnostics. *Science and Technology Publishing House*. 2002, **3**.
[10] MADEJ, H., CZECH, P. Discrete wavelet transform and probabilistic neural network in IC engine fault diagnosis. *Maintenance and Reliability*. 2010, **4**, 47-54.
[11] MERKISZ, J., JACYNA, M., MERKISZ-GURANOWSKA, A., PIELECHA, J. The parameters of passenger cars engine in terms of real drive emission test. *Archives of Transport*. 2014,. **32**(4), 43-50.
[12] PUŠKÁR, M., BIGOŠ, P., PUŠKÁROVÁ, P. Accurate measurements of output characteristics and detonations of motorbike high-speed racing engine and their optimization at actual atmospheric conditions and combusted mixture composition. *Measurement*. 2012, **45**, 1067-1076.
[13] QINGHUA, W., YOUYUN, Z., LEI, C., YONG-SHENG, Z. Fault diagnosis for diesel valve trains based on non-negative matrix factorization and neural network ensemble. *Mechanical Systems and Signal Processing*. 2009, **23**, 1683-1695.
[14] SZYMAŃSKI, G.M., TOMASZEWSKI, F. Application of impact tests to diagnose internal combustion engines. *Proceedings of the 17th International Congress on Sound and Vibration*. 2010, 2, 1282-1289.
[15] www.bksv.com.
[16] www.neur.am.put.poznan.pl/dwm/3.5.3.pdf.
[17] www.springerprofessional.de.
[18] YADAV, S.K., KALRA, P.K. Fault diagnosis of internal combustion engine using empirical mode decomposition. *Proceedings of the IEEE 6th International Symposium on Image and Signal Processing and Analysis*. ISPA 2009, 40-46.
[19] YILDIRIM, H., ÇINAR, A., SAYLI, O., KOYLU, H. Vibration and noise analysis of an engine fuelled with diesel and biodiesel blends. ICAME'15: *International Conference on Advances in Mechanical Engineering*. 13th–15th May 2015, Istambul.

Prof. Jerzy Merkisz, DSc., DEng. – Faculty of Machines and Transport at Poznan University of Technology.

e-mail: *Jerzy.Merkisz@put.poznan.pl*

Marek Waligórski, DSc., DEng. – Faculty of Machines and Transport at Poznan University of Technology.

e-mail: *Marek.Waligorski@put.poznan.pl*

Article citation info:
STELMASIAK, Z., LARISCH, J., PIETRAS, D. Issues related to naturally aspirated and supercharged CI engines fueled with diesel oil and CNG gas. *Combustion Engines*. 2017, **169**(2), 24-31. DOI: 10.19206/CE-2017-205

Zdzisław STELMASIAK
Jerzy LARISCH
Dariusz PIETRAS

CE-2017-205

Issues related to naturally aspirated and supercharged CI engines fueled with diesel oil and CNG gas

The study presents results of a research work on two various Diesel engines adapted for dual fuel feeding with CNG gas and diesel oil. The first engine is naturally aspirated, medium-sized engine, corresponding to engines mounted as power units in trucks and buses. Natural gas was used as the main fuel to this engine, and amount of diesel oil was reduced to minimum according to criterion of correct operation of injection system and reliable ignition of gaseous mixture. The second engine was a high-speed, supercharged engine of Fiat 1.3 MJT type, destined to powering of passenger cars. This engine is equipped with modern engine technologies, high-pressure injection system of Common Rail type with division of fuel dose and recirculation of exhaust gases, with catalytic converter and DPF filter. To fueling of this engine was used small additive of gas, aimed at reduction of smokiness of exhaust gases. Performed research has shown beneficial effect of gas on engine efficiency, reduction of concentration of nitrogen oxides, smokiness of exhaust gases and emission of particulate matter. Simultaneously, however, emissions of carbon monoxide and hydrocarbons had increased, especially in area of partial engine loads. Results of the study are pointing at possibility of installation of dual fuel system in traction engines with different size.

Key words: *compressed natural gas, dual fuel engine, work parameters, toxicity, smoke, engine controlling*

1. Introduction

In course of the recent decades, worldwide, it has been carried out intense research work on use of alternative fuels in relation to traditional, petroleum fuels [1, 11, 17]. It is connected with gradual scarcity of crude oil, diversification of energy sources, as well as environmental concerns. Such pursuit has resulted in legal regulations connected with gradual introduction of bio-fuels and gaseous fuels to combustion engines. Nowadays, ethyl and methyl alcohols, as bio-fuels, are used mainly in spark ignition engines, while processed fatty acid esters are used in Diesel engines as bio-fuels. Difficulties of blending simple alcohols with gasoline and diesel oil, and limited market supply of fatty acid esters, in Polish domestic conditions produced from rape oil, result in fact that anticipated future maximal market share will amount to 10% of total volume of consumed fuels. Use of gaseous fuels, mainly natural gas, bio-gases (of fermentation and landfill origin) and mine gas, belongs to completely different issue. Resources of natural gas, calculated energetically, are many times bigger than documented resources of crude oil, while degree of processing of the gas is significantly smaller, what have effects both on price of unit energy and total energetic loss. Use of waste, fermentation and mine gases is enforced by environmental reasons, because combustion of such gases in a torches or energetic boilers leads to environmental pollution and energy losses. Due to the above, it is anticipated that in the nearest future the CNG gas and the LNG gas will become the second fuel after liquid petroleum fuels, and their market share in European Union will reach level of about 20% of total consumed fuels [11, 16]. Nowadays, waste gases are used in co-generation systems, but emerging recently commercial installations to enrichment of methane in these gases can result in use of such gases in traction engines.

The natural gas, both CNG and LNG, can be used both in spark ignition and compression ignition engines [2, 3, 7]. Smaller-size automotive compression ignition engines operate mainly in bi-fuel system and can be alternatively fueled with gasoline or CNG gas, what results from limited network of CNG filling stations. In such engines the compression ratio remains unchanged due to need of fueling with gasoline. Bigger-size engines for powering of trucks and buses are built as adaptations of compression ignition engines to fueling with CNG or LNG gas. In such configuration the engines can operate according to spark ignition system or in so called Dual Fuel (DF) system with self-acting ignition of gaseous mixture [4–6, 8, 9].

In Dual Fuel Diesel engines, combustion process is initiated by self-ignition of small dose of liquid fuel. In majority of adaptations a small volume of initial dose is used, regardless of engine load [1, 4, 5, 7, 8, 11, 16, 17]. The aim is to minimize the initial dose, which due to considerable differences in price of liquid fuel and gas can lead to reduction of operational costs of the engines.

Issue of operational interchangeability of diesel oil with gas in DF engines can be analyzed from two points of view. In the first one, the CNG gas is considered as a main fuel, while quantity of consumed diesel oil results from reliable ignition of the gas only. Scope of adaptation of such engine should be significant; fueling with neat diesel oil can be treated as emergency fueling in case of shortage of gas or breakdown of gaseous installation. In the second case, quantity of gaseous fuel is small and the main objective is to reduce smoke of exhaust gases when the engine is operated in adverse urban conditions [10, 12–14, 19–21]. Scope of the adaptation in such case is significantly smaller, and the engine can be run alternatively on neat diesel oil or fueled in DF system [22, 23]. With such approach, the DF system can be implemented even in small-sized, high-speed automotive engines. With both types of the adaptation, compression ratio remains on unchanged level, what have beneficial effect on conditions of self-ignition of diesel oil and engine efficiency.

In dual fuel engine, it is important to maintain correct quality of charge, what will assure reliable ignition of gas-air mixture and correct course of its combustion. Quality of the charge is affected by size of initial dose and composition of gas-air mixture. At constant initial dose, reduction of

engine load occurs by reduction of quantity of gas. This results in leaning of the gas-air mixture, leading to worsening of combustion rate of the mixture, what effects in reduction of overall engine efficiency and increase of emissions of carbon monoxide and unburned hydrocarbons [7, 9, 11, 16]. Widespread use of Common Rail systems to liquid fuel injection can facilitate, to some extent, problems with excessive leaning of gaseous mixture, but can generate additional difficulties connected with advantages of division of the dose [21, 23]. The gas-air mixture is ignited by the first initial dose, *Pilot* or *Pre* dose, which determines course of entire combustion process. For this reason, initial dose should be injected with an advance suitable to combustion of gaseous mixture, considerably later relative to run on neat diesel oil. Too early advance angles of initial doses, what occurs when liquid fuel dose is divided, have unfavorable effect on combustion of gaseous mixture. On the other hand, too late injections of big dose of liquid fuel during advanced combustion process of gaseous mixture results in worsening of combustion conditions of liquid fuel [23].

Maintaining the correct quality of the charge depends also on whether the adaptation is made on naturally aspirated or supercharged engine. Leaning of gaseous mixture in naturally aspirated engine is caused by reduction of engine load, what distinctly affects worsening of combustion process. Situations of misfire can occur at extreme leaning of gaseous mixture, what affects worsening of smoothness of engine operation [2, 3, 6, 8, 16]. In supercharged engines, maintaining correct composition of gaseous mixture can be partially achieved by changed ratio of supercharging.

In the presented study are depicted results of research work on dual fuel, medium-sized, naturally aspirated engine (size of cylinders corresponds with engines used in trucks and buses) and high-speed supercharged engine to passenger cars. In the first investigated engine, the CNG gas was used as the main fuel, in the second engine the CNG gas was used as additive, reducing smokiness of exhaust gases. Comparison of the test results of these different fueling concepts and different engines can be helpful in taking decisions about use of dual fuel systems in traction engines.

2. Engine test bed

The tests were performed on a single-cylinder experimental engine of SB3.1 type with compression ignition and direct injection system, produced by WSK Mielec, and on automotive engine of Fiat 1.3 MJT type manufactured by Fiat-GM plant in Bielsko-Biała.

In the SB3.1 engine it were used Common Rail system to injection of diesel oil, and injection system of gas to inlet manifold located near aspiration valve. The both electronically controlled systems, allowed for free shaping of doses size and fuel shares according with assumed criteria of fueling and optimization of parameters. View of the test bed and the SB3.1 engine after the adaptation is presented in the Fig. 1, while technical parameters of this engine are listed in the Table 1.

a)

b)

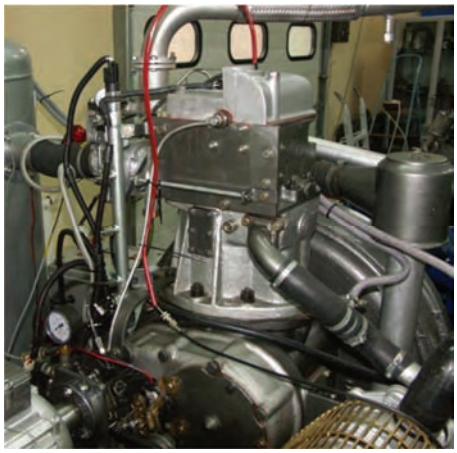

Fig. 1. General view of the test bed: a) engine test bed, b) view of the engine with assembled Common Rail system and with gas injectors on inlet manifold

Table 1. Technical data of of SB3.1 engine

Number of cylinder	1
Bore x stroke	127 x 146 mm
Displacement	1848 cm^3
Compression ratio	15.8
Maximum power/Engine revolution	22.8 kW/2200 rpm
Type of combustion chamber	Direct injection Toroidal combustion chamber in the piston
Injection system	Common Rail f-my Bosch
Injector Bosch	0986435 004 090
Injection system of CNG	IC
Gas injector Bosch	F465 151 72
Gas injection pressure	1 MPa

As the second engine was used in the investigations compression ignition, supercharged, four cylinder engine of FIAT 1.3 MJT type with swept capacity of 1248 ccm. Direct fuel injection in this engine was accomplished by second generation Common Rail system, so called Multi Jet. The engine was adapted to dual fuel operation in the Department of Combustion Engines and Vehicles in the ATH in Bielsko-Biała. Technical parameters of the engine are presented in the Table 2.

Table 2. Technical specification of Fiat 1.3 MJT engine [24]

Engine type	1.3 MJT
Bore x stroke	69.6 x 82 mm
Displacement	1248 cm^3
Number of cylinder	4
Compression ratio	18
Maximum power	51 kW at 4000 rpm
Maximum torque	180 Nm at 1750 rpm
Injection system	Common Rail
Number of valve per cylinder	4
Timing system	DOHC
Exhaust gas recirculation	EGR valve

a)

b)

Fig. 2. Intake manifold and test stand of Fiat 1.3 MJT engine:a) intake manifold, b) test stand

Control of the dual fuel engine was performed by factory made electronic control unit (ECU) of MJD.6F3 type produced by Magneti Marelli. When adding the gas, the ECU controller automatically reduces dose of diesel oil to maintain required engine torque. With considerable changes in unit dose of diesel oil, output of the air is also reduced.

3. Analysis of the test results

In dual fuel, naturally aspirated engine, in which CNG gas is the main fuel, constant initial dose is used, size of this dose is determined by reliable ignition of gas. With maintained condition of engine operation on neat diesel oil, or in dual fuel operation, original injectors are not replaced as a rule, what means that possible minimal dose is usually bigger than the dose required to reliable ignition of gas. This results in lower interchangeability of diesel oil with gas. Changes in engine load are obtained by reduction of amount of gas (reduction of opening time of gas injectors) what results in leaning of gaseous mixture and reduction of share of gas at partial engine loads, Fig. 3a. The biggest share of gas is present at maximal engine load; in case of tested SB3.1 engine such share amounted to 80–85%, depending on engine speed, Fig. 3a.

a)

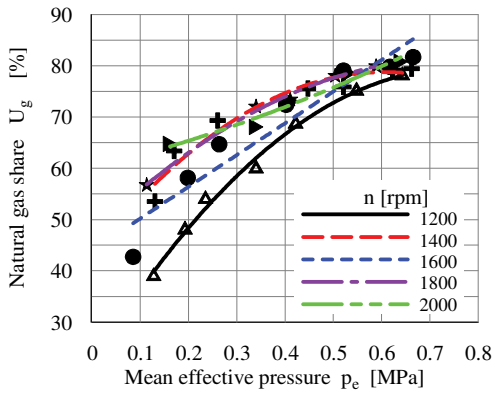

b)

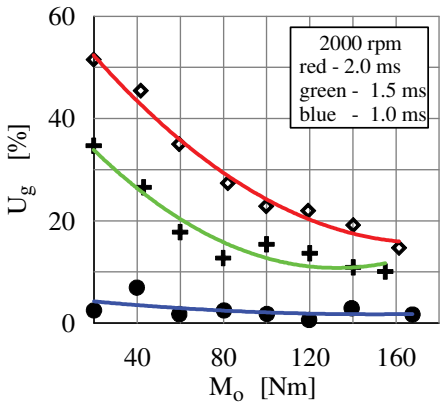

Fig 3. Influence of engine load on energetic share of gas in total dose of energy supplied to the engine: a) SB3.1 engine, different engine speeds, initial dose q = 19.8 mm3/cycle, injection advance angle 22oCA before TDC; b) Fiat 1.3 MJT engine, variable opening time of gas injectors, constant pressure of gas 4.5 bar

A different situation occurs in supercharged engine with small addition of gas, while change in engine load was accomplished by reduction of total dose of diesel oil. Small shares of gas were obtained at full engine load, while a bigger ones at partial loads, Fig. 3b. In the engine of Fiat 1.3 MJT type, for opening time of gas injectors of 2 ms, at low engine loads it has been obtained energetic share of gas in range of 40÷50%, while in case of maximal load of about 15%. In supercharged engine, reduced engine load is accompanied by reduced ratio of supercharging, what at constant amount of gas results in enrichment of gaseous mixture and improvement of conditions of its combustion. As automotive engines in majority of their operational life are running at partial engine loads, course of interchangeability of fuels shown in the Fig. 3b is favorable in terms of increased operational interchangeability of diesel oil, and improved ecological features of the engine. It concerns especially a cars running in big cities.

Use of gaseous fueling in naturally aspirated engine can lead to reduction of maximal brake power with 8÷10%, what can discourage to gaseous fueling. Engines which require maintained rated brake power at engine load of 90–100% N_{ezn} should be run on neat diesel oil. Additional argument for such concept is fact that modern traction engines feature high compression ratios and high ratios of supercharging. In some engines this promotes occurrence of knocking combustion when the engine is run on gas with minimal initial dose. Moreover, keeping the brake power on unchanged level requires reduction of average excess air factor λ, what can lead to thermal overloading of the engine.

In modern dual fuel engines are preferred C*ommon Rail* type injection systems of liquid fuel and multipoint injection of gas to inlet manifold. The both systems, controlled electronically, facilitate maintaining of proper composition of charge in any point of engine operation, and enable automatic change-over of operational mode of the engine (traditional or dual fuel) independently on will of a driver. With such systems it is possible to use such ranges of traction engine operation as shown in the Fig. 4. Due to small portion of time when traction engine is operated at maximal loads, use of traditional fueling system shouldn't have any significant effect on reduction of interchangeability of liquid fuel with gas. In engines for which reduction of maximal brake power is acceptable to customers, dual fuel feeding can be accomplished within range of engine load change of 20–100%.

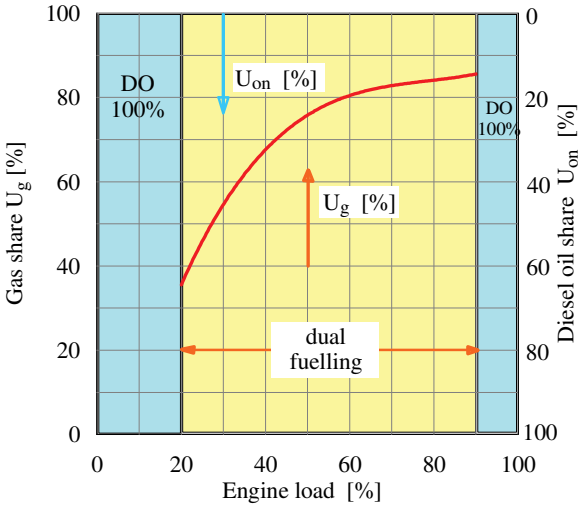

Fig. 4. Proposed range of gaseous fueling in dual fuel traction engine [18]

Dual fuel feeding advantageously affects engine efficiency in range of maximal loads, when the engine is run on rich gaseous mixture. Composition of gaseous mixture depends on size of initial dose, while maintaining the same $M_{oDO} = M_{oDF}$ engine load, the gaseous mixture undergoes enrichment as the initial dose decreases. In the tested engine of SB3.1 type for the dose of q = 14.6 mm^3/cycle at maximal engine load, overall efficiency increased in complete range of change of engine speed, Fig. 5a. Absolute growth of the efficiency has amounted to 0.9–2.1%, depending on engine speed.

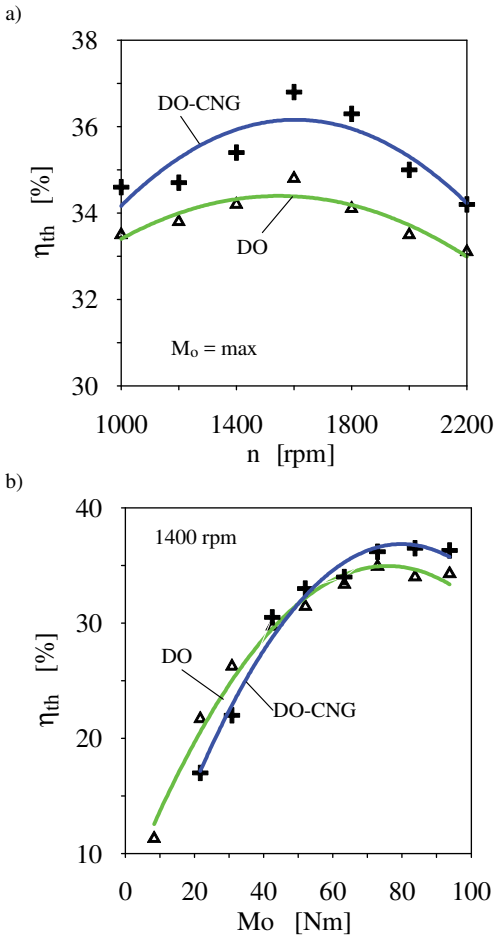

Fig. 5. Comparison of overall efficiency of SB3.1 engine run on diesel oil (DO) and in dual fuel system run on diesel oil and CNG gas (DO-CNG): initial dose q = 14.6 mm^3/cycle

Comparison of the efficiency shown in the Fig. 5b indicates that increase of efficiency occurs for a higher loads, in range of engine torque > $0.5 \cdot M_{o\,max}$. With low engine loads, excessive leaning of gaseous mixture leads to prolonged time of its combustion, what results in reduction of the efficiency. As a result, overall efficiency of dual fuel engine is lower than efficiency of the engine run on neat diesel oil.

In the engine controlled electronically, quantity of supplied gas can be adjusted by change of opening time of gas injector. In modern engines with *Common Rail* injection system and with original controller, small additive of gas, amounting to 25–35% of energetic share, doesn't change division method of diesel oil dose. Therefore, in the controllers to dual fuel engines it is possible to make use of control algorithms from traditionally fueled engine, only size of the main doses should be suitably corrected.

In the tested Fiat 1.3 MJT engine, at constant gas pressure of 1 bar in range of short opening time of the injectors 0–2 ms, gas outflow is small, what assures shares of gas smaller than about 5%. This is probably due to inertia of assembled gas injectors, which are not entirely open in case of such short times, but also results from inertia of stream of gas. Only for opening times longer than 3 ms, a distinct increase in share of gas in total energy supplied to the engine can be seen, Fig. 6a.

Amount of gas addition has significant effect on concentration of toxic components of exhaust gases emitted from Fiat 1.3 MJT engine, especially advantageously affects NO_x concentrations. Addition of 30% of gas resulted in nearly twice reduction of NO_x in exhaust gases of the investigated engine, Fig. 6b. Simultaneously, however, concentrations of carbon monoxide and unburned hydrocarbons increase. At 30% additive of gas, increase of concentration of CO was nearly fourfold, and aggregated hydrocarbons nearly eightfold, Fig. 6b. It is worth underlining, however, that in supercharged engines with indirect injection of gas to inlet manifold, a part of hydrocarbons enters into exhaust system due to valve overlapping. The main component of measured hydrocarbons is methane, considered as harmless, but having impact on greenhouse effect, similarly like CO_2.

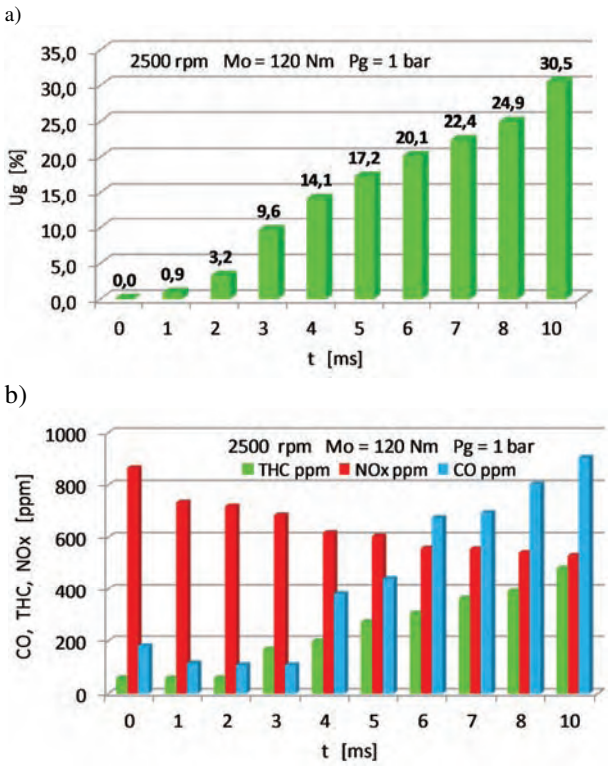

Fig. 6. Changes the gas energy share U_g and the concentration toxic components of exhaust gases of engine Fiat 1.3 MTI depending on gas injectors opening time: fixed gas supply pressure 1 bar

During testing of Fiat 1.3 MJT engine it had been used original ECU controller from this engine running on neat diesel oil. With small addition of gas at constant openings of gas injectors, 1.5 ms and 2.0 ms, controlling algorithms of diesel oil injection (method of division of the dose and angle of beginning of their injection) remained unchanged. Only size of the main doses was changed, they were decreased proportionally to quantity of energy supplied with gas. This affected course of toxic components concentration in exhaust gases according to engine load, what is shown in the Fig. 7.

Additive of gas almost in complete range of engine load change results in increased concentration of carbon monoxide and aggregated hydrocarbons (Fig. 7a and 7b), and decrease in concentration of nitrogen oxides, Fig. 7c.

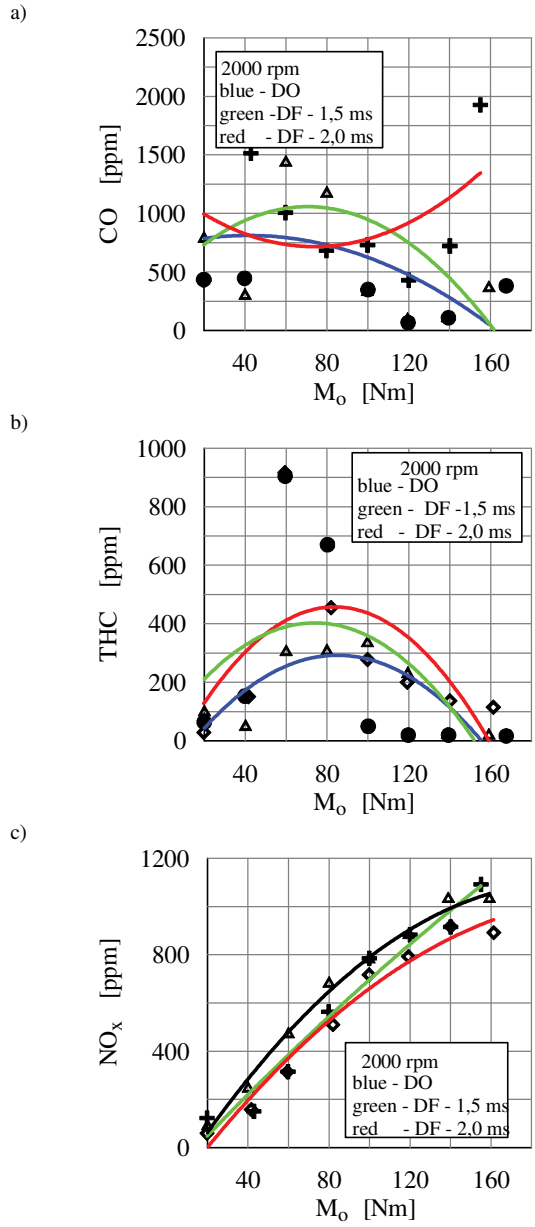

Fig. 7. Comparison the concentration of toxic component in exhaust Fiat 1.3 MJT engine fuelled with diesel oil and dual fuel for varies times of gas injectors opening: engine speed 2000 rpm, times of gas injectors opening 1.5 ms, 2.0 ms

In testing of modern passenger cars are performed measurements of toxic components of exhaust gases under conditions equivalent to driving conditions on road, i.e. at changing engine speed, load and time. Such tests are performed on chassis dynamometer, in European countries according to NEDC cycle. In the tests discussed in this paper, 20 points of static engine operation on engine dynamometer in conditions of (n, M_o = const) were used, simulating the NEDC road test. During selection of these points were used methods of static analysis described in the study [15].

Effect of additive of gas on smokiness of exhaust gases and emission of particulate matter was discussed basing on comparison with traditional fueling in these 20 selected points, simulating NEDC test.

To measurement of smokiness of exhaust gases it was used opacimeter made by AVL, model 415 SE, with FSN (Filter Smoke Number) scale or mg/m^3 scale. Size of particulate matter was measured with use of 3090 EEPS (*Engine Exhaust Particle Sizer™ Spectrometer*) analyzer produced by the TSI Incorporated Company. The analyzer had enabled analysis of continuous dimensional distribution of particulate matter emitted by the engine. The spectrometer enabled measurement of particulate matter's size in range of 5.6–560 nm of their diameter (22 measuring channels) with frequency 10 Hz.

In the Fig. 8 is presented effect of addition of gas in range of 24.6–35.6% of energetic share on reduction of smokiness of exhaust gases. It should be underlined that in case of dual fuel feeding a correction of boost factor was used so that air excess ratio was the same as for traditional fueling. The smokiness of exhaust gases underwent reduction in nearly all tested points.

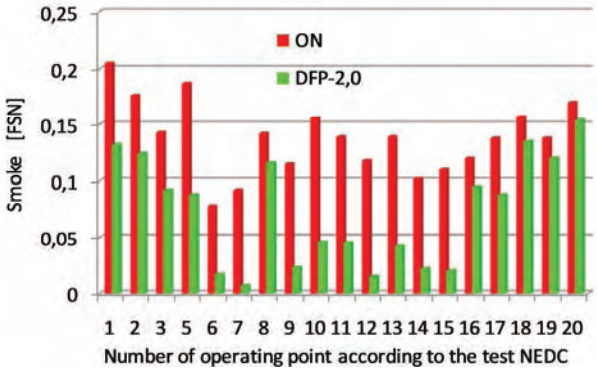

Fig 8. Comparison of smokiness of exhaust gases of Fiat 1.3 MJT engine fueled traditionally and in dual fuel system with correction of output of air: air output at duel fuel feeding was the same as at fueling with diesel oil, opening time of gas injectors 2.0 ms

Emission of particulate matter (PM), due to their hygroscopicity and density lower than density of air, is a serious hazard for the environment and generates important problems of modern compression ignition automotive engines [1, 13, 17, 20]. For this reason, during the last two decades, emission of the PM was the most intensively reduced, comparing to other toxic components of exhaust gases. Contemporary legal regulations restrict not only mass emissions of the particulate matter expressed in [mg/m^3], but also their PN number [13, 20]. It results from the fact that together with high number of emitted particulates, percentage of the particulates with small diameter increases, what according to opinion of epidemiologists is particularly dangerous for living organisms, because small particulate matter can stay in atmosphere much longer than particulate matter with a bigger size. For this reason, emissions of particulate matter, considering their PN number and fractional distribution, were also measured in course of the research at the points corresponding to NEDC test.

From comparison shown in the Fig. 9 it is seen that in dual fuel feeding, almost in all investigated measuring points also total number of emitted particulate matter is lower than emissions in case of traditional fueling.

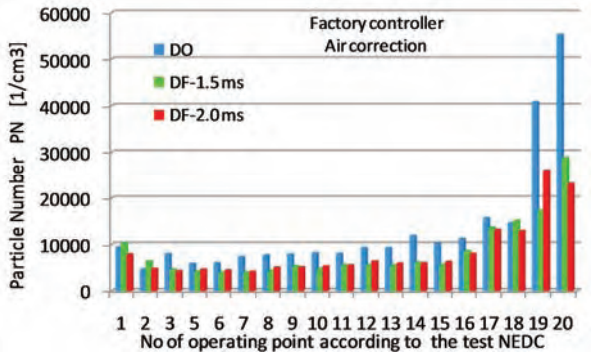

Fig 9. Comparison of total number of particulate matter (PN) in exhaust gases of Fiat 1.3 MJT engine fueled traditionally and in dual fuel system, with correction of air output: factory made ECU controller, constant opening time of gas injectors 1.5 ms and 2.0 ms

It is also worth noting, that in a big number of measuring points, differences in number of emitted particulate matter for opening time of injectors equal 1.5 ms and 2.0 ms are small, while in some points even for the time of 2.0 ms, number of the particulate matter is bigger than for the time of 1.5 ms. Simultaneously, in all analyzed points the smokiness of exhaust emissions for the time of 2.0 ms was distinctly lower than the smokiness for the time of 1.5 ms. It can therefore be assumed that at such points increased share of gas leads to emission of bigger number of particulate matter with small sizes.

Fundamental differences in quantity of emitted particulate matter for dual fuel feeding refer to particulate matter with average size, Fig. 10. In range of small and big particulate matter, quantities of emitted particulate matter for the both fueling systems are comparable.

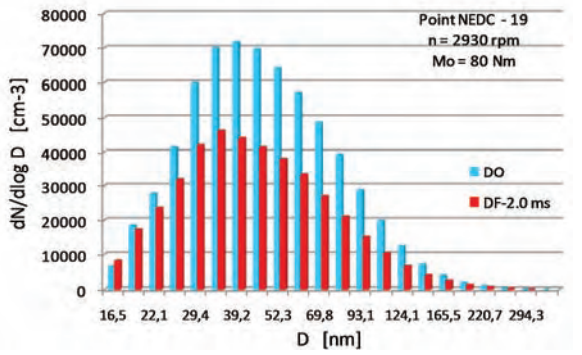

Fig 10. Comparison of fractional distribution of particulate matter dN/dlogD of the Fiat 1.3 MultiJet engine fueled traditionally and in dual fuel system: point 19 according to NEDC test, n = 2930 rpm, Mo = 80 Nm, opening time of gas injectors 2.0 ms

4. Summary

The study performed on two engines: medium-sized, naturally aspirated engine similar to engines as mounted to trucks and buses, and high-speed supercharged engine destined to passenger cars, has enabled to draw a general-nature conclusions concerning both strategy of dual fuel supply and effects of such supply on engine performance.

– Controlling strategy of dual fuel engine depends on whether full interchangeability of fuels is assured – traditional fueling with diesel oil or in dual fuel system. Maintaining this condition, it is essential to remain un-

changed components of serial injection system of the engine, which limits value of minimal initial dose and reduces interchangeability of diesel oil with gas. This applies both to engines equipped with inline, piston-type pumps as well pumps as used in Common Rail injection systems.

– For medium-sized traction engines, during period of introduction of gaseous fueling systems and shortage of CNG filling stations, complete interchangeability of the fuels should be absolutely assured. With assumption that CNG gas is the main fuel, minimal doses to be used will depend on injection systems of liquid fuel. For the sake of correct engine operation and proper operational life of injectors, the minimal doses shouldn't be smaller than:
  – 20% of nominal dose for piston-type pumps,
  – 15% of nominal dose for *Common Rail* systems.
– Application of the above mentioned doses enables, in conditions of engine load higher than 20% of its nominal torque, interchangeability of liquid fuel in scope of 40÷80% for piston-type pumps, and 55÷85% for *Common Rail* systems. Due to considerable difference in price of the fuels, engine adaptation is profitable both in case of already operated older engines, as well as modern engines with electronic injection systems of liquid fuel.
– Due to worsened combustion conditions of lean mixture in traction engines, the engine should be fed with neat diesel oil when the engine load is lower than 20% of rated load. This will allow reduction of CO and THC emissions and will improve overall efficiency of the engine.
– In medium-sized engines controlled electronically, with dual fuel systems and with assumption that CNG gas is the main fuel, maximal brake power of the engines should be limited to about 90–95%, what results from needs of unchanged durability of injection equipment and condition of non-thermal overloading of the engine. In engines where the maximal brake power should be maintained at engine loads higher than 90%, the engine should be supplied with neat diesel oil. Interchangeability of liquid fuel with gas will depend on method of engine operation. However, due to small percentage of minimal and maximal loads in total time of engine operation, interchangeability of liquid fuel shouldn't be significantly reduced.
– Supply of gas should be correlated with closing time of exhaust valve. Long opening times of gas injectors could impede to meet such condition at higher rotational speeds. In systems with injection of gas to inlet manifold, quantity of gas supplied to the engine can be adjusted by opening time of injectors and pressure of gaseous supply. In tested Fiat 1.3 MJT engine, at supply pressure of 1 bar, obtaining 30% share of gas required opening time of injectors of about 4 ms at average engine loads, and about 10 ms at maximal loads. Use of higher supply pressures of gas enables considerable reduction of required injection time of the gas. The investigations have shown that at supply pressure of 4.5 bar, opening time of injectors equal to 2.0 ms has allowed obtainment of about 20% of energetic share of gas at maximal engine load in complete range of variations of engine speed.
– It seems that for engines in which gaseous fuel is not used as the main fuel, it is possible to implement constant opening times of gas injectors, set on the base of assumed share of gas at maximal engine load. Increasing share of gas at partial engine loads promotes interchangeability of liquid fuel with gas in traction engines, and reduces running costs of the engine. Investigations of Fiat 1.3 MJT engine have shown that this engine can operate correctly in range of partial engine loads with share of gas of about 60%.
– Original ECU controller optimized to fueling with diesel oil in presence of gas causes reduction of boost pressure according to reduction of diesel oil dose. As a result, unit air dose per single engine cycle decreases. At comparable doses of energy supplied to engine together with diesel oil and gas, this negatively affects combustion process and results in increased CO and THC emissions, and emission of smoke in exhaust gases. This requires changed setting values of ECU controller, adjusting boost pressure, requires special control algorithms for dual fuel supply, and controllers adapted to such type of fueling.
– Small additive of CNG gas to diesel oil has effect on reduction of smokiness of exhaust gases and emission of particulate matter in modern automotive engines with Common Rail injection systems. Reduction of smokiness of exhaust gases amounted to 12–92%, reduction of total number of particulate matter amounted to 30–40%, depending on operational conditions of the engine. Especially important is reduction of particulate matter at a higher engine speeds and high engine loads, when emission of exhaust gases is the highest.
– Dual fuel supply in modern compression ignition engines can contribute to reduction of particulate matter emissions, especially in urban traffic conditions. This should result in increased intervals between subsequent regenerations of DPF filters, increased life of the filters and improved reliability of automotive engines.

Acknowledgment

The study was performed within framework of Research Project No. PBS1/A6/13/2012 *„Reduction of smoke and particulate matter in exhaust gases of automotive engines with compression ignition, accomplished with use of CNG gas addition"* financed by NCBiR.

Bibliography

[1] BARROSO, P., RIBAS, X., DOMINGUES, J., et al. Study of dual-fuel (diesel+natural gas) particle mater and CO_2 emissions of a heavy-duty diesel engine during transient operation. *Combustion Engines*. 2013, **153**(2), 28-39.

[2] BEROUN, S., BLAŻEK, J. The possibility of the improvement of the combustion process stability in gas engines. *VI*

Międzynarodowa Konferencja Gazowa "SILNIKI GAZOWE 2003", Częstochowa 2003.
[3] BEROUN, S., MARTINS, J. The development of gas (CNG, LPG and H2) engines for buses and trucks and their emission and cycle variability characteristics. *SAE Technical Paper*. 2001, 2001-01-0144.
[4] Clark, N.N., Atkinson, C.M., Atkinson, R.J. et al. Optimized emission reduction strategies for dual fuel compression ignition engines running on natural gas and diesel. www.cemr.wvu.edu, 2002, 1-6.
[5] Daisho, Y., Takahashi, K. Controlling combustion and exhaust emissions in a direct-injection diesel engine dual fueled with natural gas. *SAE Technical Paper*. 1995, 952436.
[6] EHSAN, M., BHUIJAN, S. Dual fuel performance of a small diesel engine for applications with less frequent load variations. *International Journal of Mechanical & Mechatronics Engineering*. 2011, **9**(10).
[7] FRIEDEMAN, Z. Gasmotoren. *Vogel Buchverlag* Wurzburg, 2001.
[8] GEBERT, K., BECK, J., BARKHIMER, R.L., WONG, H.C. Strategies to improve combustion and emission characteristics of dual-fuel pilot ignited natural gas engines. *SAE Technical Paper*. 1997, 971712.
[9] KOWALEWICZ, A. Adaptacja silnika wysokoprężnego do zasilania gazem naturalnym. *Czasopismo Techniczne Wydawnictwo Politechniki Krakowskiej*. 2008, **7**, 67-78.
[10] KOZAK, M. Studium wpływu komponentów tlenowych oleju napędowego na emisję toksycznych składników spalin z silników o zapłonie samoczynnym. *Monografia habilitacyjna*. Wydawnictwo Politechniki Poznańskiej, 2013.
[11] MATYJASIK, M. Aktywizacja procesu spalania mieszaniny gaz-powietrze w silnikach dwupaliwowych przez podział dawki inicjującej oleju napędowego. *Praca doktorska*, Bielsko-Biała 2012.
[12] MERKISZ, J., DASZKIEWICZ, P., IDZIOR, M., et al. Analiza ograniczenia emisji toksycznych składników spalin dwupaliwowego silnika o zapłonie samoczynnym. *Logistyka*. 2014, **6**, 7260-7269.
[13] MERKISZ, J., PIELECHA, J. Emisja cząstek stałych ze źródeł motoryzacyjnych. *Wydawnictwo Politechniki Poznańskiej*. Poznań 2014.
[14] MERKISZ, J., PIELECHA, J., ŁABĘDŹ, K., STOJECKI, A. Badania emisji spalin pojazdów o różnej klasie emisyjnej zasilanych gazem ziemnym. *Prace Naukowe Politechniki Warszawskiej. Transport*. 2013, **98**, 463-472.
[15] PIETRAS, D., SOBIESZCZAŃSKI, M., ŚWIĄTEK, A., PAJDOWSKI, P. Dobór parametrów pracy silnika 1.3 multijet charakterystycznych dla testu jezdnego NEDC do badań rozwojowych. *PTNSS Kongres* P05-C065, 2005.
[16] STELMASIAK, Z. Studium procesu spalania gazu w dwupaliwowym silniku o zapłonie samoczynnym zasilanym gazem ziemnym i olejem napędowym. Wydawnictwo ATH, *Praca habilitacyjna*, Bielsko-Biała 2003.
[17] STELMASIAK, Z. Dwupaliwowe silniki o zapłonie samoczynnym. *Wydawnictwo Naukowe Instytutu Technologii Eksploatacji*. Radom 2013.
[18] STELMASIAK, Z. Impact of engine control on the energetic interchangeability of diesel oil by gas in dual fuel CI engine. *Journal of KONES Powertrain and Transport*. 2013, **20**(1), 425-434.
[19] STELMASIAK, Z., LARISCH, J. Dwupaliwowe zasilanie silnika Fiat 1.3 MultiJet. *Logistyka*. 2014, **6**.
[20] STELMASIAK, Z., LARISCH, J., PIETRAS, D. Wpływ dodatku gazu ziemnego na zadymienie spalin samochodowego silnika ZS. *Combustion Engines*. 2015, **3**.
[21] STELMASIAK, Z., LARISCH, J., PIETRAS, D. Wpływ dodatku gazu ziemnego na wybrane parametry pracy silnika Fiat 1.3 MultiJet zasilanego dwupaliwowo. *Combustion Engines*. 2015, **3**.
[22] STELMASIAK, Z., LARISCH, J., PIETRAS, D. Wybrane problemy adaptacji samochodowego silnika o zapłonie samoczynnym do zasilania dwupaliwowego. *Combustion Engines*. 2015, **3**.
[23] STELMASIAK, Z., LARISCH, J., PIETRAS, D. Some problems of controlling the car diesel engine powered dual fuel. Combustion Engines no. 3/2015 (162) pp. 1070-1081.
[24] Materiały firmy FIAT AUTO POLAND, 2014.
[25] Materiały techniczne firmy EuropeGAS, 2013.

Prof. Zdzislaw Stelmasiak, DSc., DEng. – Faculty of Mechanical Engineering and Computer Science at University of Bielsko-Biala.

e-mail: *ZStelmasiak@ath.bielsko.pl*

Jerzy Larisch, DEng. – Faculty of Mechanical Engineering and Computer Science at University of Bielsko-Biala.

e-mail: *JLarisch@ath.bielsko.pl*

Dariusz Pietras, DEng. – Faculty of Mechanical Engineering and Computer Science at University of Bielsko-Biala.

e-mail: *Pietras@ath.bielsko.pl*

Article citation info:
SKRZEK, T. The analysis of the possibilities of increasing the share of propane in the fuel mixture supplied to a dual fuel diesel engine. *Combustion Engines*. 2017, **169**(2), 32-37. DOI: 10.19206/CE-2017-206

Tomasz SKRZEK

CE-2017-206

The analysis of the possibilities of increasing the share of propane in the fuel mixture supplied to a dual fuel diesel engine

The paper presents the main reasons for the limitations as to the share of gaseous fuel in dual fueling in commercial engine applications. It also indicates the proposals of solutions aiming at increasing of the share of this fuel. The investigations were conducted in two stages. The first stage of the investigations involved gradual increase in the share of propane at a simultaneous phasing out of the amount of diesel fuel so that the excess air coefficient remained on the same level. The second stage of the investigations involved a maximum possible share of propane with a simultaneous adjustment of the diesel fuel injection parameters. The investigations were performed for three different values of the charging pressure: 200, 400, 600 mbar and for a naturally aspirated variant. The obtained results led to a conclusion that modifying diesel fuel injection parameters and increasing the charging pressure allow a significant increase in the share of gaseous fuel up to 70% of the total energy contained in both fuels.

Key words: *dual fuel, supercharged engine, propane, combustion process, exhaust emissions*

1. Introduction

The concept of duel fuel engine fueled with diesel fuel and an additional fuel of low cetane number (propane, LPG, methane, ethanol, gasoline) assumes the greatest possible share of the additional fuel in the combusted mixture. Solutions already exist, in which the energy share of the additional fuel reaches 99%. These solutions, however, are used in large powertrains usually applied in marine transport. The solutions that enable using such great share of additional gaseous fuel (most often natural gas) have not yet been loaned to smaller units used in road transport. The specificity of transport of liquefied gas by sea forced the necessity to utilize the evaporated part of gas, which is a natural consequence of gas in a liquid state. This is how gas has become a fuel powering the engines of a transporting vessel. An additional benefit resulting from this type of fueling is the improvement of the environmental performance mainly by a reduction of the emission of particulate matter [5, 6, 8, 10, 14]. The economic factor is also important due to the difference in the prices of diesel oil and gaseous fuels. There is little wonder that the number of duel fuel vehicles is growing. This is particularly the case for heavy-duty vehicles. Compared to passenger vehicles or light duty trucks there are no stringent limitations as to the location of the additional fuel cylinder, hence the lower percentage share of the weight of such a fuel tank in the weight of the vehicle, particularly if steel high-pressure gas containers are applied. Besides, the need to reduce the costs of operation appears to be a decisive factor if a dual fuel system is to be installed. Given the difference in the prices of diesel fuel and the mixture of propane/butane that can successfully be applied in dual fuel systems, a well developed network of distribution, easy transport and storage make it a very attractive source of energy resulting in a growing number of users of duel fuel systems [3]. Current solutions used in motor vehicles, however, allow a mere 30% energy share of LPG, which, from the economic point of view is less attractive and distant from the solutions offered for marine transport. Hence, comes the question of the reason for the fact that the share of energy obtained from additional fuel is not as significant as it should be and whether the limitation responsible for such a status quo may perhaps be eliminated without the need of costly modifications of the power train. For many years, research on this type of fueling has been dealing with analyses of the phenomena occurring during the process of combustion in dual fuel engines [4, 9, 14]. This contributed to solving problems characteristics of duel fueling - the course of the combustion process. The aim of this paper is to indicate the main reasons for the limitation of the share of additional LPG fuel and propose solutions that would enable increasing this share.

2. Research procedure

The investigations were carried out on a 511 cm^3 dual fuel (diesel fuel and propane) single cylinder diesel research engine (AVL 5402) of the compression ratio of ε 17.5 Fig. 1. In the investigations, the most commonplace system of supply of indirectly injected evaporated propane was used. The gas was fed via an injector fitted near the intake valve. The opening time of the injector was synchronized with the cylinder filling cycle, which prevented the loss of cylinder charge at valve overlap [12]. The investigations were performed in two stages. The first stage consisted in a gradual increase in the share of propane with the diesel fuel being phased out to keep the excess air coefficient on a steady level. The investigations were performed for three different charging pressures: 200, 400, 600 mbar and for the naturally aspirated variant. The parameters of the injection of diesel fuel such as pressure, start of injection of the pilot and the main doses were constant irrespective of the share of propane in the mixture or the variations in the charging pressure, which corresponded to the original settings applied in diesel fueling alone. Only the value of the main fuel dose was changed, which resulted from the need to maintain a steady level of excess air coefficient at the moment of increasing of the share of propane in the mixture. The increase in the share of propane with the reduction of the share of diesel fuel was continued until the maximum pressure increment exceeded 1 MPa/deg. The second stage of the investigations consisted in applying the greatest possible share of propane for different levels of the charging pressure, as in the first stage, with a simultaneous

adjustment of the injection parameters of diesel fuel still preserving the above-mentioned criterion of pressure increment rate and the highest possible overall engine efficiency.

a)

b)

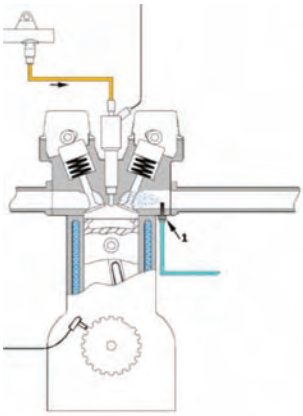

Fig. 1. a) Engine dynamometer by AVL, b) The method of propane supply to the engine

3. Possibilities of increasing of the share of propane in the mixture of fuels while preserving the excess air coefficient

As earlier research has shown, the main limitation for high shares of propane is the abruptness of the course of combustion that is characterized by a high pressure increment rate, much more exceeding the values obtained for diesel fuel alone. By gradually increasing the share of propane and reducing the share of diesel fuel while maintaining the injection parameters optimum for conventional fueling (performance of the first stage of the investigations), one can observe a clear growth of the maximum pressure increment rates Fig. 2. The maximum share of propane for which this parameter did not exceed 1 MPa/deg is merely 30% for the naturally aspirated engine and 50% for the highest charging pressure applied during the investigations. When analyzing the influence of the share of propane on the pressure increment rate, one can clearly observe that the addition of propane for all cases under analysis results in an increase in the pressure increment rate and a delayed self-ignition. The physicochemical changes of the compressed mixture of propane and air more significantly influence the delay of the start of combustion when the share of the gaseous fuel is greater Fig. 3. The increase in the share of the gaseous fuel is accompanied by the increase in the specific heat of the compressed mixture [12–14], the effect of which is a lower temperature of the medium in the compression phase leading to a delay in the start of combustion. The lower concentration of oxygen in the compressed mixture, being a consequence of the portion of propane fed to the cylinder, is another reason for the delay of the start of combustion. Hence, the growing delay of ignition will directly affect the pressure increment rate in the combustion process because a significant portion of energy coming from the pilot dose of diesel fuel and part of the dose of propane is released in a shorter time compared to conventional fueling [1, 6, 15, 16]. Changes in the pressure increment rate in the combustion process are tightly related to the changes of the charging pressure. Maintaining the parameters of diesel fuel injection, the excess air coefficient and increasing the charging pressure one may observe a very conspicuous and at the same time advantageous phenomenon. An increase in the charging pressure results in a reduction of the maximum pressure increment rates. This means that the disadvantageous consequences following the addition of propane can be eliminated by a change in the charging pressure. According to the theory contained in [2], an increase in the charging pressure results in a growth of the temperature of the compressed mixture, thus, a reduction of the delay in self-ignition. Consequently, it causes a less abrupt course of combustion, the result of which is a drop in the maximum pressure increment rates. Wherever the delay of self-ignition grows distorting the combustion process, it is possible to influence that by increasing the charging pressure. For the naturally aspirate variant, a merely 30% share of propane gave average values (from the recorded test cycles) of the pressure increment rate of 8.9 bar/deg and, at times, exceeding 15 bar/deg. Therefore, the increase in the share of propane under these conditions should not be continued mainly due to the risk of damaging the engine, which is why the authors gave up supplying more gaseous fuel to a naturally aspirated engine. The presented 70% share of propane was obtainable only after changing the parameters of the diesel fuel injection exclusively in the turbocharged engine. The most conspicuous effect of the impact of the charging pressure on the pressure increment rate can be seen on the example of the 30% share of propane, for which the charging pressure from 0 to 600 mbar resulted in almost a double reduction of the pressure increment rate. When analyzing the parameter of maximum pressure increment rate, which is the fundamental criterion in selecting the shares of both fuels, one has to note the very desired effect of reduction of the pressure increment rates following the increase in the charging pressure. Maintaining the excess air coefficient on the same level when increasing the charging pressure must lead to an increase in the amount of energy supplied with the fuel. Despite the greatest portion of energy for the case of the maximum charging pressure, the maximum pressure increment rates are the lowest and even though this parameter increases with the growing share of propane, the increment is the smallest out of all the cases under analysis.

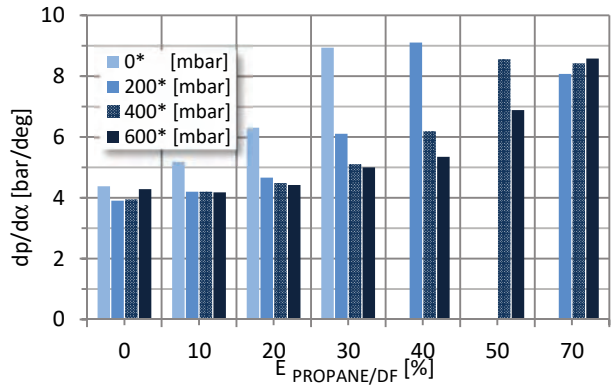

Fig. 2. Maximum pressure increment rates for conventional fueling and dual fueling with a growing share of propane for 4 values of the charging pressure

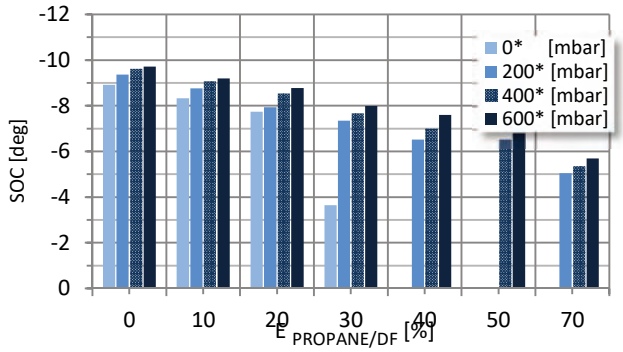

Fig. 3. Start of combustion for conventional fueling and dual fueling with a growing share of propane for 4 values of the charging pressure

The dropping trend of the maximum pressure increment rates following the increase in the charging pressure continues starting from a 10% and ending with a 50% share of propane except the greatest (70%) share of this gas, for which the parameters of the diesel fuel injection were modified. When analyzing the pressure curves inside the cylinder for different shares of propane Fig. 4., one can see a clear impact of the changed thermodynamic properties of the compressed mixture. Following the increase in the share of the gaseous fuel, one can observe a gradual decrease of the pressure of the charge in the compression phase. Since this trend is maintained in all the cases under analysis, only the results obtained for the highest charging pressure (600 mbar) have been presented Fig. 4. The lower pressure of the compressed mixture, the lower temperature at the moment of injection of the pilot fuel dose and the lower oxygen concentration in the compressed mixture due to the growing amount of propane pushing out the air fed to the cylinder result in a clear delay of the start of combustion, thus influencing the heat evolution curves shown in Fig. 5.

Comparing the course of combustion obtained for conventional fueling with the course of combustion for duel fueling, it can be confirmed that the growing share of the gaseous fuel clearly influences the first phase of the combustion, in which the pilot dose plays an important role. For conventional fueling, the pilot fuel dose, whose start o injection is at 18° before TDC, definitely initiates the process of combustion as can be seen on the graph of the cylinder pressure curve Fig. 4. and on the heat evolution curve Fig. 5. The increase in the share of the gaseous fuel results in a much different start of combustion and heat evolution rate in the initial phase of the combustion process compared to diesel fuel alone. When a small (10%) share of propane results in a small (0.5°) CA. self-ignition delay compared to conventional fueling and the heat evolution curve has two phases, the 50% share results in a delayed start of combustion by 3° and the boundary between the phases of the combustion process fades Fig. 5. This means that along the increase in the share of propane, despite the growing delay in self-ignition, the portion of energy released in the initial phase of the combustion process (started by the pilot dose) is much greater than that obtained for diesel fuel alone. The consequence is the increase in the charge-burning rate Fig. 6. and a shift of the peak value of the pressure towards TDC Fig. 4.

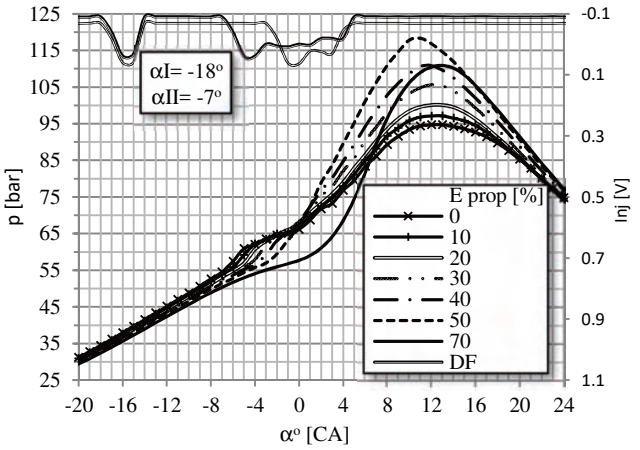

Fig. 4. Pressure curves taken from inside the cylinder for conventional fueling and dual fueling with a growing share of propane for the charging pressure of 600 mbar. Angle of the start of injection of the pilot fuel dose –18°, angle of the start of injection of the main fuel dose –7° (constant for the 0%–50% share of propane), angle of the start of injection of the main fuel dose –3° (for the 70% share of propane)

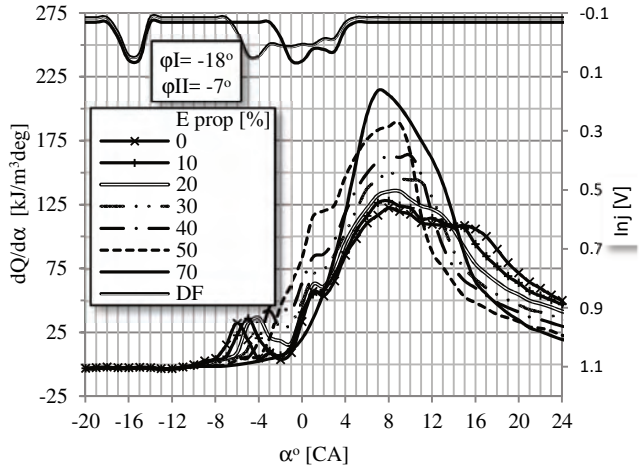

Fig. 5. Heat evolution curves taken from inside the cylinder for conventional fueling and dual fueling with a growing share of propane for the charging pressure of 600 mbar. Angle of the start of injection of the pilot fuel dose –18°, angle of the start of injection of the main fuel dose –7° (constant for the 0%–50% share of propane), angle of the start of injection of the main fuel dose –3° (for the 70% share of propane)

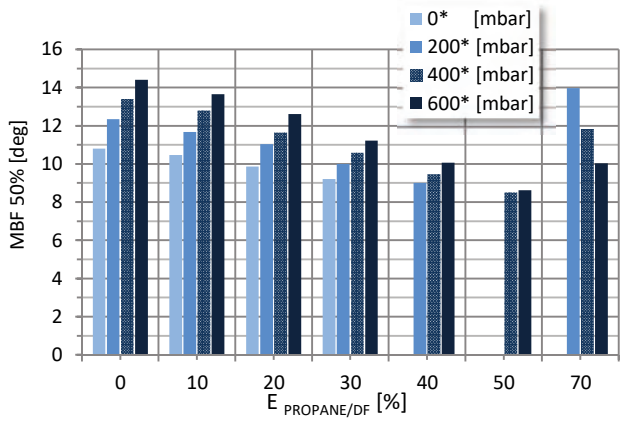

Fig. 6. Burning of 50% of the charge for conventional fueling and dual fueling with a growing share of propane for 4 values of the charging pressure

Analyzing the course of the combustion process based on the charge burn described with a 50% burn in the scale of CA. Fig. 6. a diversity is observed compared with the first phase of the combustion process Fig. 3, where the increase in the share of propane resulted in a delay of the self-ignition in all cases under analysis and the phase of the charger half-burn indicates a significant growth of the combustion dynamics. This process is almost linear; the trend of growth of the charge burn intensity clearly depends on the proportions of both fuels and the charging pressure. Only in the case of the highest (70%) share of propane was this process different, which resulted mainly from: the combination of the influence of a significant share of propane, the influence of the changes of the charge temperature and the delay of the angle of the start of diesel fuel injection. The greatest differences in the time needed to burn 50% of the charge were for conventional fueling. The increase in the share of the gaseous fuel gradually reduces these differences. From the analysis of the above graph, one may infer that along the increase in the charging pressure, the combustion time extends. This phenomenon is to be explained by the fact that the growing charging pressure is tantamount to the increase in the amount of fuel (maintaining constant excess air coefficient), thus, to the prolonged reactions accompanying the combustion process. Hence, when maintaining the injection pressure and the angle of the start of injection of the pilot fuel dose, it is necessary to extend the duration of the injection of the diesel fuel. A greater portion of injected fuel at a decreasing difference of the pressures (higher compression and constant injection pressure) caused by the growing pressure inside the cylinder due to supercharging translates into a deteriorated atomization, therefore leading to the extension of the time of combustion. A substitution of part of the conventional fuel with gaseous fuel accelerates the combustion process and the differences in the time to burn 50% of the charge for different charging pressures become less clear Fig. 6. Burning of 50% of the charge with a 50% share of propane despite a late start of combustion falls at approx. 8.5^{o} after TDC i.e. almost 6^{o} earlier compared to diesel fueling alone. As a consequence, this leads to an increase in the maximum pressure increment rates, increase in the maximum pressures of the combustion process and a shift of the peak pressure towards TDC.

The changes that are observed in the course of the combustion process under conventional and dual fueling become so conspicuous that they may have impact on the actual use of such an engine. As a consequence, this may lead to an accelerated wear of components due to excess mechanical and thermal loads. A question arises, whether it is possible to increase the share of the gaseous fuel at a simultaneous preservation of the overall efficiency and the combustion parameters obtained under conventional fueling. The fact that no engine modifications are performed before the increase in the share of the gaseous fuel is also significant. The performed investigations have shown that the objective is to delay the combustion process in duel fueling so that the parameters of this process such as the maximum pressure increment rates and the maximum pressure are not significantly divergent from the ones of conventional fueling. The fulfillment of these conditions will eliminate the risk of premature engine wear. The application of a common rail based fuel system allows a very precise control of the course of combustion by the possibility of a very extensive change of the diesel fuel injection parameters. In dual fueling it is very important to be able to control the way of releasing the energy contained in the gaseous fuel. The application of a great share of the gaseous fuel and the introduction of a single ignition-initiating fuel dose of the compressed mixture is characterized by a very abrupt nature of the combustion process including knock combustion. [9, 13] A properly selected angle of the start of injection for conventional fueling will not be optimum for dual fueling. The introduction of the possibility of dividing of the diesel fuel dose, however, makes the process of combustion in a dual fueling scenario (even with the 70% share of propane) less abrupt than the combustion with a 30% share of propane with a single dose of diesel fuel. Besides, the possibility of a precise adjustment of the pilot and the main fuel doses and the angle of the start of injection of these fuel doses results in a situation that despite significant differences between the conventional and dual fueling combustion, it is possible to eliminate disadvantageous phenomena such as: knock combustion, limitation of the maximum pressure increment rates and maximum pressure.

4. Investigating the possibilities of reaching the greatest share of propane in the mixture of fuels for different charging pressures with adjustment of diesel fuel parameters

In the second stage of the investigations, the authors attempted to increase the energy share of propane while reducing the share of diesel fuel. The maximum share that was applied was 70% of propane for three charging pressures: 200, 400, 600 mbar and 50% for the naturally aspirate variant. The selection of such propane to diesel fuel ratio was not a coincidence and was determined by a series of previously performed trials that allowed indicating a safe boundary of the share of the gaseous fuel. Similarly to the first part of the investigations, the fundamental criterion was the maximum pressure increment rate whose value should not exceed 1 MPa/deg. In order to meet this condi-

tion, the angle of the start of injection of the diesel fuel had to be delayed. The presented results in the form of the pressure (Fig. 7) and the heat evolution (Fig. 8) curves pertain to cases with the most beneficial adjustment of the angle of the start of injection of both the pilot and the main fuel doses that led to the obtainment of the highest overall efficiency of the investigated engine.

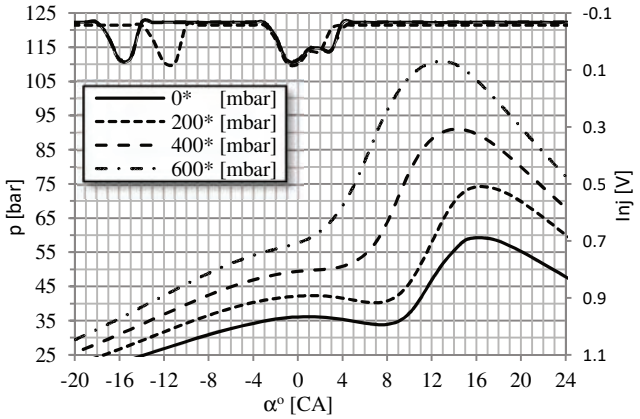

Fig. 7. Cylinder pressure curves for dual fueling with a 70% share of propane for three different charging pressures 200, 400, 600 mbar ad for the naturally aspirated variant with a 50% share of propane with the introduced change of the angle of the start of injection of the pilot and the main fuel doses

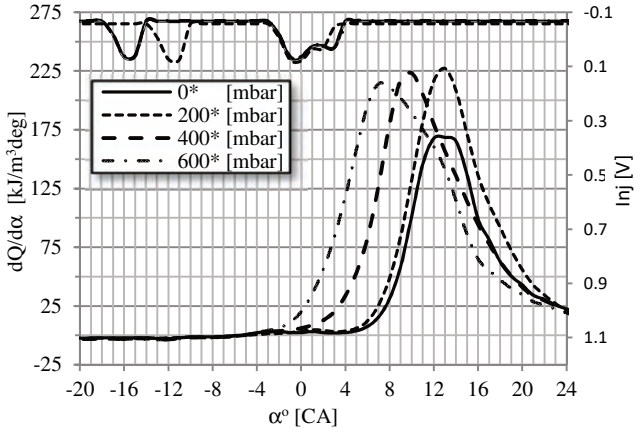

Fig. 8. Heat evolution curves for dual fueling with a 70% share of propane for three different charging pressures 200, 400, 600 mbar ad for the naturally aspirated variant with a 50% share of propane with the introduced change of the angle of the start of injection of the pilot and the main fuel doses

At the charging pressure of 600 mbar, the angle of the start of injection of the main fuel dose was changed from –7° to –3°. This delayed the course of combustion, prevented the excess of the maximum pressure increment rate and limited the maximum pressures by approx. 10 bar compared to the maximum pressures obtained for the 50% share of propane without modifying the injection parameters. The application of such a great share of propane resulted in a 1% drop of the overall efficiency compared to conventional fueling, the reason for which may have been: greater heat loss (higher temperatures in the combustion process, greater heat release area), escape of part of the gaseous fuel due to valve overlap and incomplete combustion of part of propane particularly in the area where diesel fuel had no access because of limited spray penetration. A small drop in the overall efficiency has been observed for the other variant of the charging pressure. Because of the similar nature of the course of combustion, the reasons for deterioration of the efficiency will also be similar. Another analyzed case for the charging pressure of 400 mbar indicates a need of maintaining the same angles of the start of injection of the main fuel dose only. Similarly to the higher charging pressure, a small drop in the efficiency is observed. For the pressure of 200 mbar the angle of the start of injection of both the pilot and the main dose was changed. A small delay in the injection of the pilot fuel dose gives it a greater chance of taking on the combustion due to a higher temperature of the medium, to which it is fed. A change of this parameter appears justified, particularly if, following the growing share of propane, the temperature of the compressed medium drops, which was discussed in the first part of the investigations. Out of the analyzed cases, the most beneficial is the one with the highest charging pressure. When analyzing the course of combustion it may be indicated that for both the conventional and dual fueling, the peak value of pressure occurs in the same position of the crankshaft (approx. 12° after TDC). In the other supercharging variants the maximums of the pressures drift from the TDC, thus shifting the center of the combustion process, the consequence of which is a slight drop in the efficiency compared to the efficiency obtained for diesel fueling only. Despite the fact that the change in the angle of the start of injection of the main fuel dose is capable of accelerating this process, it cannot be applied due to the accompanying increase in the maximum pressure increment rates exceeding the assumed value of 1 MPa/deg.

Despite significant differences in the course of combustion for the conventional and dual fueling variants, it is possible to control the fuel combustion in such a way that even a 70% share of propane does not result in a significant drop in the efficiency or excess pressure increment rate. For the naturally aspirated engines, the obtainment of such a great share of propane was impossible. The combustion process with the share of propane above 50% was characterized by a significant unrepeatability, a clear delay of combustion or even combustion deficiency. The attempt of an earlier initiation of combustion by changing the angle of the start of injection led to an increase in the maximum pressure increment rates and a 'jagged' pressure curve taken from inside the cylinder, which is characteristic of knock combustion. Therefore, despite corrections of the injection parameters widely implemented for the pilot and the main fuel doses, the maximum share of propane while still maintaining proper engine operation was 50%. This means that for dual fueling in the naturally aspirated variant, the range of influence on the course of the combustion by a modification of the angle of the start of diesel fuel injection is significantly limited compared to the turbocharged version of the engine.

Conclusions

Because of the way the fuel is supplied to the cylinder in a dual fuel system, the formation of mixture subjected to high temperatures in the compression process and, addi-

tionally, no diesel fuel dose division (diesel fuel initiates the ignition), the energy share of the additional fuel does not exceed 30%. The performed investigations related to dual fueling have shown that a significant increase in the share of the gaseous fuel (propane or a mixture of propane and butane) is possible up to the level of 70%. With such a significant share of propane used in the tests, the main limitation was the pressure increment rate.

The potential of modern common rail systems such as fuel dose division, adjustment of the amounts of these fuel doses and the pressure of their injection make the process of energy release a gradual one, hence, it is possible to eliminate the adverse effects such as excess pressure increment rate, or excessively delayed start of combustion. With such high amounts of the gaseous fuel in the mixture, an adjustment of parameters of the diesel fuel injection is necessary. Besides, during dual fuel combustion with great shares of propane, an increase in the charging pressure gives very good results. It could, thus, be clearly stated that a combination of the adjustment of the diesel fuel injection parameters and the adjustment of the charging pressure provides a wide range of opportunities influencing the course of combustion if a great share of the gaseous fuel is the case, which ensures an effective combustion of two types of fuel in a compression ignition engine.

Nomenclature

CI	compression ignition
LPG	liquified petrolum gas
DF	diesel fuel
TDC	top dead center
SOC	start of combustion
MBF	mass burned fraction

Bibliography

[1] KYUNGHYUN, R. Effects of pilot injection timing on the combustion and emissions characteristics in a diesel engine using biodiesel–CNG dual fuel *Appl. Energy*. 2013, **111**, 721-730.

[2] LEE, J., CHOI, S., KIM, H. et al. Reduction of emissions with propane addition to a diesel engine *Int. J. Automotive Technol.* 2013, **14**(4), 551-558.

[3] LE FEVRE, C. The prospects for natural gas as a transportation fuel in Europe. *Oxford Institute for Energy Studies* paper NG84, March 2014.

[4] LUFT, S. Analysis of combustion process in a dual-fuel compression ignition engine fuelled with LPG in liquid phase. *J. KONES Power Train Transp*. 2007, **14**(4).

[5] OGAWA, H., ZHAO, P., KATO, T., SHIBATA, G. Improvement of combustion and emissions in a dual fuel compression ignition engine with natural gas as the main fuel. *SAE Technical Paper*. 2015, 2015-01-0863.

[6] PAPAGIANNAKIS, R.G., HOUNTALAS, D.T. Theoretical study of the effects of pilot fuel quantity and its injection timing on the performance and emissions of a dual fuel diesel engine. *Energy Convers. Manage*. 2007, 48, 2951-2961.

[7] PAYKANI, A., KAKAEE, A-H., RAHNAMA, P., REITZ, R.D. Effects of diesel injection strategy on natural gas/diesel reactivity controlled compression ignition combustion. *Energy*. 2015, **90**, 814-826.

[8] RAO, G.A., RAJU, A.V.S., MOHAN RAO, C.V., GOVINDA RAJULU, K. Effect of LPG content on the performance and emission characteristic of a diesel–LPG dual fuel engine. *Eng. Today Quart. J.* 2010, **2**(4), 69-74.

[9] RÓŻYCKI, A. Analysis of performances of a dual-fuel turbocharged compression ignition engine. *Journal of KONES Powertrain and Transport*. 2010, **17**(3).

[10] SAYIN, C, CANAKCI, M. Effects of injection timing on the engine performance and exhaust emissions of a dual-fuel diesel engine. *Energy Conversion and Management*. 2009, **50**.

[11] SELIM MOHAMED, Y.E. Sensitivity of dual fuel engine combustion and knocking limits to gaseous fuel composition. *Energy Convers. Manage*. 2004, **45**, 411-425.

[12] SKRZEK, T. Assessment of the effect of gaseous fuel delivery mode on thermal efficiency and fuel losses during the valve overlap period in a dual-fuel compression ignition engine *IOP Conf. Series: Materials Science and Engineering* 2016, **148**.

[13] SKRZEK, T. Effect of the diesel fuel dose division and the injection angle on operating parameters of a dual-fuel compression ignition engine. *Combustion Engines*. 2015, **162**(3), PTNSS-2015-3480.

[14] STELMASIAK, Z., MATYJASIK, M. Exhaust emissions of dual fuel self-ignition engine with divided initial dose. *Combustion Engines*. 2013, **154**(3), 144.

[15] STELMASIAK, Z. The combustion controlling in the dual fuel CI engine by pilot dose division. *Combustion engine*. 2011, 146(3).

[16] WIERZBICKI, S. Effect of the parameters of pilot dose injection in a dual fuel diesel engine on the combustion process. *Journal of KONES Powertrain and Transport*. 2011, **18**(3), 499-506.

Tomasz Skrzek, DEng. – Mechanical Engineering Faculty at Radom University of Technology and Humanities.

e-mail: *T.Skrzek@uthrad.pl*

Article citation info:
AMBROSEWICZ-WALACIK, M., TAŃSKA, M., WALACIK, M. Fatty acid composition as a parameter of using vegetable oils for biofuel production. *Combustion Engines*. 2017, **169**(2), 38-42. DOI: 10.19206/CE-2017-207

Marta AMBROSEWICZ-WALACIK
Małgorzata TAŃSKA
Marek WALACIK

CE-2017-207

Fatty acid composition as a parameter of using vegetable oils for biofuel production

The aim of the study was to show the validity of determining the quality of oils intendent for the biofuels production. One of the main discriminant that should be used to assess the suitability of oil raw materials for the fuel purposes is the composition of fatty acids. The research was conducted on 13 different samples of vegetable oils, that were cold-pressed from the seeds of various species, including rape, camelina, flax (light and dark), mustard, milk thistle, hemp, evening primrose oil, amaranth, sunflower, soybean, and cumin. The analysis of the fatty acid composition showed significant differences between the analysed oil samples, both within the species and varieties of oilseeds. The results indicate the need for continuous quality control of oils and fats led to the production of biodiesel in the small households and large commercial enterprises, because as it was indicated by the analysis of fatty acids composition rape seeds of different varieties are characterized by the diverse quality.

Key words: *vegetable oils, quality, fatty acids composition, biofuels production*

1. Introduction

The term biodiesel is defined as the fatty acid alkyl monoesters derived from the renewable sources, such as edible and non-edible vegetable oils and animal fats [1]. The availability of oil-based raw material is dependent on the regional geography, native soil, climate and vegetation [2]. On the other hand, the main factors determining the biodiesel properties are: an oil quality [3], oil refinement (for example pretreatment step), conditions of transesterification and quality of phases in the purification step [4]. Among the presented factors, the content and quality of oil intendent for the biodiesel production, seems to be one of the most important. Edible and non-edible oils are characterized by the different oil seed content (wt%). In case of the first group, content of this constitute varies for the seeds of rapeseed between 38-46 wt%, cameline approx. 32-36.0 wt%, milk thistle 20-35 wt%, evening primrose 18-25 wt%, hemp 25-35 wt%, sunflower 25-35 wt% and soybean 15-20 wt% [5–8]. On the other hand, the value of this discriminant in the non-edible plant oils was estimated on 65 wt% for nyamplung, between 43-59 wt% for jatropha, between 45-50 wt% for castor and between 40-60 wt% for rubber [9]. An oil molecule is composed of a gycerin backbone of three carbons, and each of these carbon atoms is attached to a long chain of fatty acids. The chemistry of oleaginous raw material is similar and is presented by the fatty acids with carbon atoms between 12-22. Some of these compounds are saturated and others are unsaturated. The number of the double bounds determines the level of unsaturation (one double bonds means mono-unsaturation, two or more poly-unsaturation) [10]. The vegetable oils and animal fats are differentiated by saturated, mono- and poly-unsaturated share of these compounds. As Ramos et al. pointed the fatty acids profile of raw materials does not change during the transesterification process, that is way it is important to control this parameter [4]. Mittelbach and Remschmidt found that using biofuels characterized by the high content of glycerides, especially triglycerides, generates the formation of deposits at the injection nozzles and on the valves [11]. The same authors pointed that to achieve the biodiesel with a low presence of glycerides it is necessary to select appropriate reagents and reaction conditions. Cited authors, Pinzi et al. and Knothe and Steidley reported that the composition of these constitutes has an important impact during the estimation of some biodiesel discriminants, such as rate of FAME conversion, kinematic viscosity, stability of oxidation, cetane number, iodine number, cold filter plugging point, exhaust emission, lubricity and heat of combustion [12, 13]. Richards et al. reported that the saturated fatty acids, having a natural preference for the first and third positions in the molecules of triglyceride, were transestrificated at the beginning of the process, while during the reaction progression the amount of unsaturated fatty acids esters increased [14]. Moreover, Pinzi et al., analysing the influence of vegetable oils fatty acid composition on the reaction temperature and glycerides conversion to the biodiesel during the transesterification, found that the conversion of mono-glycerides in FAME took place faster in case of the oils characterized by the higher degree of unsaturation (for example sunflower oil), then for these the most saturated (for example palm oil and maize oil) [15]. What is more, the cited authors reported that the optimal reaction temperature increased with a mean chain length increase and a number of polyunsaturated bonds decrease.

The main raw material for the biodiesel production in the most UE countries is rapeseed. However, is worth to mention that the seeds currently used in the oil manufacturing industry are a mixture of several winter varieties which do not guarantee a stable quality of the obtained oils, what affects the economic aspect of production. The same situation is observed in case of the other seed species, that are cultivated in other countries and continents. Therefore, it is so important to carry out a continuous control of the oil seeds quality. What is more, it is believed that estimating the fatty acids profile will allow to quickly verify the suitability on the individual plant oil for the biofuels production and thus let to avoid conducting other costly and time-consuming and chemical analysis. Taking into account the above the aim of the study was to show the validity of determining the fatty acids composition of the different oleaginous plant oils.

2. Material and analytical methods

2.1. Material

The raw material was presented by the group of vegetable oils, among others, oils pressed from the seeds of spring and winter varieties of rape, camelina, light and dark flax, mustard, milk thistle, hemp, evening primrose oil, amaranth, sunflower, soybean, and black seed.

2.2. Analytical methods

The composition of fatty acids in oils was determined according to the Polish Standard PN-EN ISO 12966-2:2011 [16] using the methyl esters that had been previously prepared as described by Zadernowski and Sosulski [17]. The quality analysis of fatty acids was performed on a GC 8000 FISONS series gas chromatograph with a flame-ion detector and a DB-225 type column (30 m × 0.25 mm × 0.15 μm) and helium as a carrier gas. Fatty acids were identified based on the retention times determined for fatty acid models. Obtained results of researches were presented as the arithmetic mean (from three replicates).

3. Results and discussion

The conducted analysis of the fatty acids composition indicated on the significant differences in the profile of these compounds. The shares of individual fatty acids in the samples of two rapeseed varieties and two flax samples were diverse. Tańska et al. having analysed the fatty acids composition of three different varieties of rapeseed (winter hybrid variety Pomorzanin, winter pollinated variety Kana and spring pollinated variety Bios) also found differences in the profile of these compounds. The oil sample obtained from seeds of spring variety of rapeseed, in comparison to the winter varieties, was characterized by the lower share of oleic acid, while higher linolenic acid (Table 1).

The fatty acids composition of the oils obtained from the seeds of the different plant species was also differential. The most noticeable differences were found in case of the palmitic acid, oleic acid, linoleic acid, alfa-linolenic and gamma-linolenic acids, and eicosenic acid (Table 1).

The highest share of palmitic acid was noticed in the amaranthus oil (19.56%), while the lowest in the sample of mustard oil (3.85%). The high concentration of that compound was also found in the oil samples of soybean and black seed, while for the other 10 samples the share of palmitic acid did not exceed 10%. One the other hand, the share of palmitooleic acid for the all analysed samples was below 0.3%, while the stearic acids below 5.5%.

One of the fatty acids, that most differentiated the analysed oil samples were oleic acid. Its share ranged from 6.75% for the evening primrose oil to 65.38% for the mustard oil. The rapeseed oils were also characterized by the high concentration of that compound (> 59%). In the other 3 samples (cameline oil, dark flax oil and hemp oil) the share of oleic acid was almost on a similar level (approx. 15-19%), while in the other 4 (light flax oil, amaranthus oil, soybean oil and black seed oil) it was about 22%. The last 2 samples of the milk thistle and sunflower oils were characterized by the, respectively, 28.42 and 31.96% share of that fatty acid (Table 1).

Table 1. The composition of fatty acids of analyzed vegetable oil (%)

	winter variety of rapeseed	spring variety of rapeseed	cameline	light flax	dark flax	mustard	milk thistle	hemp	evening primrose	amaranthus	sunflower	soybean	black seed
myristic ($C_{14:0}$)	nd.	nd.	nd.	nd.	nd.	nd.	nd.	0.74	nd.	nd.	0.03	0.00	nd.
palmitic ($C_{16:0}$)	4.22	4.68	5.39	7.45	7.05	3.85	6.83	8.78	7.97	19.56	9.88	15.02	16.81
palmitooleic ($C_{16:1}$)	0.18	0.14	0.11	nd.	nd.	0.19	nd.	0.11	0.03	0.19	0.05	0.00	0.28
stearic ($C_{18:0}$)	1.09	1.57	2.33	3.69	5.20	2.09	4.30	3.67	2.08	2.76	2.56	3.76	3.80
oleic ($C_{18:1}$)	65.28	59.55	15.79	22.24	18.63	65.38	28.42	15.49	6.75	22.54	31.96	21.34	22.54
linoleic ($C_{18:2}$)	19.73	20.76	16.54	17.46	16.31	9.85	55.24	52.90	76.08	53.61	47.73	55.26	52.16
α-linolenic ($C1_{8:3}$ n-3)	8.11	10.86	37.32	48.86	52.55	15.47	0.15	0.46	0.00	0.64	0.27	4.35	0.36
linolenic ($C_{18:3}$ n-6)	nd.	nd.	1.74	nd.	nd.	nd.	nd.	15.90	7.09	nd.	nd.	nd.	nd.
stearidonic ($C_{18:4}$)	nd.	nd.	nd.	nd.	nd.	nd.	nd.	0.37	nd.	nd.	nd.	nd.	nd.
arachidic ($C_{20:0}$)	0.35	0.41	1.33	0.12	0.16	0.59	2.63	0.71	nd.	0.58	0.30	0.27	0.25
eicosenoic ($C_{20:1}$)	0.76	1.83	15.32	0.18	0.10	2.58	0.64	0.40	nd.	0.12	nd.	nd.	0.29
eicosadienoic ($C_{20:2}$)	nd.	nd.	2.16	nd.	nd.	nd.	nd.	nd.	nd.	nd.	nd.	nd.	3.51
behenic ($C_{22:0}$)	0.15	0.19	0.23	nd.	nd.	nd.	1.71	0.28	nd.	nd.	nd.	nd.	nd.
erucic ($C_{22:1}$)	0.13	0.01	1.74	nd.	nd.	nd.	0.08	0.22	nd.	nd.	nd.	nd.	nd.

nd. – not detected or present in trace amounts

Taking into the consideration the share of main polyunsaturated fatty acids, linoleic and alfa-linolenic, it was impossible to unequivocally state, which of them dominated in the analysed oils. Among the 13 samples of oils, 9 of them (oils of the two rapeseed varieties, milk thistle, hemp, evening primrose, amaranthus, sunflower, soybean and black seed) were characterized by the higher share of the linoleic acid. The concentration of that compound ranged from 9.85% for the mustard oil to 76.08% for the evening primrose oil. One the other hand, other 4 samples were characterized by the higher share of alfa-linolenic acid, in comparison to linoleic share. That group of oils was presented by the cameline, light and dark flax and mustard oils. The shares of that compound in the mentioned samples were from 15.47 to 52.55%. One the other hand, the evening primrose sample was characterized by the trace amount of that compound, while in the other 5 samples (milk thistle oil, hemp oil, amaranthus oil, sunflower oil and black seed oil) the share of alfa-linolenic fatty acids did not exceed 1% and in the next 3 ones (two sample of rapeseed oil and soybean oil) 11%. Moreover, the oils of cameline, hemp and evening primrose seeds were characterized by the presence of the gamma-linolenic fatty acids. The highest share of that compound was noticed in the hemp oil, which was also the only sample with the presence of the stearidonic fatty acids (Table 1).

The share of arachidonic fatty acid did not exceed 1% for 10 of the analysed samples, while the trace amount was observed in the evening primrose oil. The oils of cameline and milk thistle were characterized by the, respectively 1.33 and 2.63% share of that compound.

In case of the eicosenoic fatty acid, it was found that the cameline oil was characterized by the significant higher share of that compound (15.32%), while in the other 9 samples the concentration of that fatty acid did not exceed 2.6%, and in the last 3 samples its amount was trace.

Among the 13 oil samples only 2 of them – the cameline oil and black seed oil, were characterized by the presence of the eicosadienoic fatty acid, while the behenic and erucic fatty acids were noticed in the 5 analysed oils (2 rapeseed oil samples, cameline oil, milk thistle oil and hemp oil). The concentration of these compounds in the other samples was trace (Table 1).

The total share of saturated fatty acids, represented by the myristic, palmitic, stearic, arachidic and behenic fatty acids were differentiated. The higher concentration of these compound was observed for the amaranthus oil (22.90%), black seed oil (20.86%) and soybean oil (19.05%), while the lower for the both samples of rapeseed (approx. 5.8%) and for the mustard oil (6.53%) (Table 2).

One the other hand, the total share of the palmitooleic, oleic and erucic fatty acids, that belong to the group of monounsaturated fatty acids, was significantly higher in the rapeseed and mustard samples. The lowest total share of listed fatty acids were found in the evening primrose oil, that in turn was characterized by the highest total share of the polyunsaturated fatty acids (83.17%). The increased share of that fatty acids group was also noticed for the oils of cameline (73.08%), hemp (70.03%), dark and light flax (respectively, 66.50 and 68.96%). In turn, the samples of rapeseed and mustard were characterized by the lower (approx. 27%) concentration of these compounds (Table 2).

Table 2. Total share of the individual groups of fatty acids (%)

	winter variety of rapeseed	spring variety of rapeseed	cameline	light flax	dark flax	mustard	milk thistle	hemp	evening primrose	amaranthus	sunflower	soybean	black seed
total share of saturated fatty acids	5.81	5.85	9.28	11.26	12.41	6.53	15.47	14.17	10.05	22.90	12.77	19.05	20.86
total share of monounsaturated fatty acids	65.59	67.70	17.64	22.24	18.63	65.57	28.50	15.81	6.78	22.73	32.01	21.34	22.82
total share of polyunsaturated fatty acids	28.60	26.45	73.08	66.50	68.96	27.90	56.03	70.03	83.17	54.37	48.00	59.61	56.32

During analysing the influence of fatty acids composition of the raw material properties for the biofuel production, it should be remembered that there is no single fatty acid that is responsible for any particular fuel characteristics. The physico-chemical properties of the biodiesel dependent on the fatty acid structural features, among other, a chain length, degree of unsaturation and branching of the chain [18].

High amounts mono-, di, and triglycerides in fuels cause that these products are prone to the coking and may lead to the formation of deposits to the injector nozzles, pistons and valves. Share of these compounds in thetransesterified oil – biodiesel has an important influence on its yield, or as Vicente at al. stated on the purity of biodiesel [19]. Pinzi et al., analysing, effect of the fatty acid composition of vegetable oils on the biodiesel optimization found that oils with a high unsaturated fatty acids content shown a proportional dependence between the catalyst concentration and yield [15]. Moreover, cited authors found that the fatty acid chain length influences the biodiesel conversion. Oils characterized by the longer fatty acid chains needed half of the re-

quested reaction time, compared to samples with the shorter fatty acids chains.

One of the discriminant that determine the number of double bonds (unsaturated ones) presented in the oil is an iodine number [20]. Islam et al. reported, that the higher share of unsaturated fatty acid in raw material, the higher value of that discriminant [18]. Altun found that biodiesel characterized by the lowest iodine number leads to the highest cetane number and as a consequence, reduces nitrogen oxides emissions [21].

The ignition quality of biofuel is related to the cetane number, that determines the ability of the fuel to ignite quickly after being injected - a higher value indicates a getter ignition quality of fuel [22]. Value of that discriminant decreases with a decreasing chain length, increasing branching, and increased saturation in the fatty acid chain [23]. As cited author found the higher cetane number, the better quality of ignition whereas the saturated esters, which are advantageous for mentioned discriminant possess poor cold-flow properties. The biofuels produced from the raw material characterized by the high share of the polyunsaturated fatty acids let to obtain the esters improving a cold-flow, due to their low melting point, what is considered as desirable. However, a high amount of polyunsaturated fatty esters contributes (undesirable for fuel) the lower cetan number and oxidative stability. The oxidation of biodiesel may induce the polymerisation of esters and form insoluble gums, which contribute to clogging of the fuel filters [24].

Muniyappa et al., analysing possibility of using the soybean and tallow oil for biodiesel production, found that that methyl esters from the beef tallow oil were characterized by the high cold point, what was involved with the high concentration of saturated fatty acid methyl esters [25]. Mittelbach and Remschmidt, Wang et al. and Chuah et al. explained that during the biodiesel cooling, the first fraction to precipitate is the stearic and palmitic methyl esters [11, 26, 27]. What is more, these components constitute a substantial share of material that are recovered from clogged biodiesel fuel filters. Moreover, Knothe and Steideley, analysing the dependence of biodiesel viscosity on the structure of fatty acid alkyl esters, found that with an increasing chain length and saturation of fatty acids the viscosity of obtained esters increased [13]. The cited authors also reported that *cis* double bonds contribute to a reduction of esters viscosity, while *trans* ones display this parameter similar to their saturated counterparts.

4. Conclusions

During the selection of a suitable raw material for the biofuel production, the attention should not be paid only on the oil content, but also on its quality. One of the discriminant, which lets to quickly verify the usefulness of individual raw material is the composition of fatty acids. As assessed, such oil samples as the evening primrose oil, cameline oil, hemp oil, light and dark oils, that were characterized by the increased share of the polyunsaturated fatty acids should not be used as a self-contained fuel, due to the low oxidative stability. On the other hand, biofuels that would be produced from oils with a high share of saturated fatty acids, such as amaranthus oil, black seed oil would be characterized by high cold point.

Bibliography

[1] MEHER, L.C.X., VIDYA SAGAR, D., NAIK, S.N. Technical aspects of biodiesel production by transestrification – a review. *Renewable and Sustainable Energy Reviews*. 2006, **10**(3), 248-268.

[2] SANJID, A., MASJUKI, H.H., KALAM, M.A. et al. Impact of palm, mustard, waste cooking oil and Calophyllum inophyllum biofuels on performance and emission of CI engine. *Renewable and Sustainable Energy Reviews*. 2013, **27**, 664-682.

[3] KULKARNI, M.G., DALAI, A.K. Waste cooking oil an economical source for biodiesel: a review. *Industrial & Engineering Chemistry Research*. 2006, **45**(9), 2901-2913.

[4] RAMOS, M.J., FERNÁNDEZ, C.M., CASAS, A. et al. Influence of fatty acid composition of raw materials on biodiesel properties. *Bioresource Technology*. 2009, **100**(1), 261-268.

[5] DEFERNE, J.L., PATE, D.W. Hemp seed oil: A source of valuable essential fatty acids. *Journal of the International Hemp Association*. 1996, **3**(1), 4-7.

[6] CHRISTIE, W.W. The analysis of evening primrose oil. *Industrial Crops and Products*. 1999, **10**(2), 73-83.

[7] RAMASAMY, K., AGARWAL, R. Multitargeted therapy of cancer by Silymarin. *Cancer Letters*. 2008, **269**(2), 352-362.

[8] TAŃSKA, M., ROTKIEWICZ, D., AMBROSEWICZ-WALACIK, M. Effect of industrial conditions of heat treatment of rape, mustard, flax and camelina seeds on the quality of oils intended for biodiesel production. *Polish Journal of Natural Sciences*. 2013, **28**(4), 449-462.

[9] ATABANI, A.E., SILITONGA, A.S., BADRUDDIN, I.A. et al. A comprehensive review in biodiesel as an alternative Energy resource and its characteristics. *Renewable and Sustainable Energy Reviews*. 2012, **16**(4), 2070-2093.

[10] US DEPARTMENT OF ENERGY. Biodiesel handling and use quidelines, US Department of Energy, Energy efficiency and renewable energy, Third edition. September 2006.

[11] MITTELBACH, M., REMSCHMIDT, C. Biodiesel: The Comprehensive Handbook Boersedruck GmbH, 2004, Vienna, Austria.

[12] PINZI, S., GARCIA, I.L., LOPEZ-GIMENEZ, F.J. et al. The ideal vegetable oil-based biodiesel composition: a review of social, economical and technical implications. *Energy & Fuels*. 2009, **23**(5), 2325-2341.

[13] KNOTHE, G., STEIDLEY, K.R. Kinematic viscosity of biodiesel fuel components and related compounds. Influence of compound structure and comparision to petrodiesel fuel components. *Fuel*. 2005, **84**(9), 1059-1065.

[14] RICHARDS, A., WIJESUNDERA, C., PALMER, M., SALISBURY, P. PAOCS. 2002, *Australian Workshop*, Sydney.

[15] PINZI, S., GANDÍA, L.M., ARZAMENDI, G. et al. Influence of vegetable oils fatty acid composition on reaction temperature and glycerides conversion to biodiesel during transestrification. *Bioresource Technology*. 2011, **102**(2), 1044-1050.

[16] PN-EN ISO 12966-2:2011. Animal and vegetable fats and oils – Analysis by gas chromatography of methyl esters of fatty acids.

[17] ZADERNOWSKI, R., SOSULSKI, F. Composition of total lipids in rapeseed. *Journal of American Oil Chemistry Society*. 1978, **55**(12), 870-872.
[18] ISLAM, M.A., AYOKO, G.A., BROWN, R. et al. Influence of fatty acid structure on fuel properties of algae derived biodiesel. *Procedia Engineering*. 2013, **56**, 591-596.
[19] VICENTE, G., MARTINEZ, M., ARACIL, J. Optimisation of integrated biodiesel production Part I. A study of the biodiesel purity and yield. *Bioresource Technology*. 2007, **98**(9),1724-1733.
[20] ROCHA, M.V.P., LIMA DE MATOS, L.J.B., PINTO DE LIMA, L. et al. Ultrasound-assisted production of biodiesel and ethanol from spent coffee grounds. *Bioresource Technology*. 2014, **167**, 343-348.
[21] ALTUN, S. Effect of the degree of unsaturation of biodiesel fuels on the exhaust emission of a diesel power generator. *Fuel*. 2014, **117**(A), 450-457.
[22] ABBASI, S., DIWEKAR, U.M. Characterization and stochastic modeling of uncertainties in the biodiesel production. *Clean Technologies and Environmental Policy*. 2014, **16**(1), 79-94.
[23] KNOTHE, G. „Designer" biodiesel: optimalizing fatty ester composition to improve fuel properties. *Energy & Fuels*. 2008, **22**(2), 1358-1364.
[24] JAIN, S., SHARMA, M.P. Effect of metal contents on oxidation stability of biodiesel/diesel blends. *Fuel*. 2014, **116**, 14-18.
[25] MUNIYAPPA, P.R., BRAMMER, S.C., NOUREDDINI, H. Improved conversion of plant oils and animal fats into biodiesel and co-product. *Bioresource Technology*. 1996, **56**(1), 19-24.
[26] WANG, L.B., YU, H.Y., HE, X.H., LIU, R.Y. Influence of fatty acid composition of woody biodiesel plants on the fuel properties. *Journal of Fuel Chemistry and Technology*. 2012, **40**(4), 397-404.
[27] CHUAH, L.F., YUSUP, S., AZIZ, A.R.A. et al. Influence of fatty acid content in non-edible oil for biodiesel properties. *Clean Technologies and Environmental Policy*. 2016, **18**(2), 473-482.

Marta Ambrosewicz-Walacik, DEng. – Faculty of the Technical Sciences, University of Warmia and Mazury in Olsztyn.

e-mail: *Marta.Ambrosewicz@uwm.edu.pl*

MałgorzataTańska, DEng. – Faculty of Food Sciences, University of Warmia and Mazury in Olsztyn.

e-mail: *M.Tanska@uwm.edu.pl*

Marek Walacik, DEng. – Faculty of Geodesy, Geospatial and Civil Engineering, University of Warmia and Mazury in Olsztyn.

e-mail: *Marek.Walacik@uwm.edu.pl*

Article citation info:
VANHAELST, R., BANNACK, C., KLOSE, M. Comparison of two measurement methods for the determination of extended turbine maps at the eATL test bench of the Ostfalia UAS. *Combustion Engines*. 2017, **169**(2), 43-48. DOI: 10.19206/CE-2017-208

Robin VANHAELST
Caroline BANNACK
Maik KLOSE

CE-2017-208

Comparison of two measurement methods for the determination of extended turbine maps at the eATL test bench of the Ostfalia UAS

This document compares two measurement methods for the determination of extended turbine maps. One method is to minimize heat flows and thus to maintain the assumption of adiabatic processes even in low speed ranges of turbines. The results obtained were compared with those of the Ostfalia eATL method. Here, is slowed down electrically by an electric motor. The direct comparison of the measurement results shows considerable differences in the turbine efficiency. Furthermore, the graphical comparison illustrates clear advantages of the eATL concept for the evaluation, which result from the width and the position of the generated measurement points.

Key words: *turbocharger, hot gas test bench, heat flows, extended turbine maps*

1. Introduction and motivation

Because of exhaust emission laws, which become more and more strictly, it is necessary to optimize the current engines until alternate engine concepts are competitive. In recent years downsizing of combustion engines become established. Turbochargers are mainly used to compensate the horsepower losses resulting from the reduced engine sizes.

Turbine maps and compressor maps are required for choosing a turbocharger well-matched to the selected engine. These maps commonly were generated on hot gas test benches. In praxis it's proposed to approximate engine requirements for measuring. But there are no standardized norms for generating turbine and compressor maps. In many cases the measurements are performed as descripted in guidelines such as SAE J922 [7] or SAE J1826 [8]. But in both guidelines are missing detailed descriptions about the setup of the section of measurements and measuring point assembly. They equally leave recommendation on minimizing heat flows of turbochargers out of consideration [5].

Various influences have an impact on turbocharger parameters during generating the maps. However these parameters cannot determine straightaway. They have to calculate from the steady conditions pressure, temperature, mass flow and air humidity. Ideally the parameters can describe the thermo- and aerodynamic performance of the turbocharger. Likewise the reproducibility and comparability have to be exactly. But in practice this could be a conflict of goals, because of the differences of each turbocharger and the associated differences in measuring tubes, metrology and system boundaries (Fig. 1) [9].

Heat flows within the turbocharger have a wide influence on the level of efficiency of compressor and turbine. For generating the turbine and compressor maps it is generally adopted, that turbine and compressor are adiabatic units. This method achieves reliable results at high speeds. If the rotational speed decelerates (less than 30% of maximum rotational speed) the turbine efficiency will falsify the results because of heat flows. Similarly the adiabatic adoption for turbine and compressor declines. Therefore special measuring methods are required in low speed ranges. [1] The maps with low speed ranges are so-called extended turbine maps. The additional data points of the diagrams enable detailed und quite extrapolations of the turbine efficiency. Furthermore, the information is needed to characterize the behaviour of the turbine within its entire speed range. So it's possible to optimize the engine process simulation.

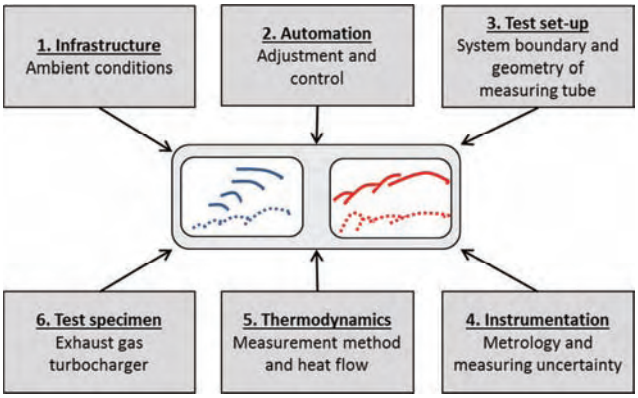

Fig. 1. Ranking of the influencing factors of parameters of a turbocharger on a hot gas test bench by generating characteristing maps, based on [5]

This document compares two measurement methods directly and indicates the obtained results. Both methods intend to reduce the effects of heat transfer on turbine efficiency at low speed ranges. The first approach used for the comparison is based on conventional procedures on hot gas test benches. As on common configurations the turbine is braked down by the compressor. As opposed to common measurements, adiabatic conditions are aspired to reduce heat flows within the turbocharger. On the second procedure the compressor is replaced by an electric motor, so the influences of heat flows on the compressor side are completely eliminated.

2. Mathematical method

According to custom on common test benches, both experiments were run under steady-state conditions. [3] The pictured turbine maps are based on calculated turbine efficiencies. The specific ways the turbine efficiencies are determined are explained below.

Adiabatic: The turbine efficiency of turbochargers commonly is defined by the ratio of outputs of turbine and compressor on standard test benches [2]. For the adiabatic criterion the isentropic turbine efficiency $\eta_{ts,T,is}$ is defined as the dividend of measured compressor output P_C and the calculated isentropic turbine output $P_{ts,T,is}$:

$$\eta_{ts,T,is} = \frac{P_C}{P_{ts,T,is}} \tag{2.1}$$

The compressor output computates from the specific heat capacity $c_{p,C}$ and the air mass flow $\dot{m}_C$ multiplied with the difference of the measured temperatures $T_{t,2}$ and $T_{t,1}$:

$$P_C = \dot{m}_C \cdot c_{p,C} \cdot (T_{t,2} - T_{t,1}) \tag{2.2}$$

The isentropic turbine output $P_{ts,T,is}$ computates from the specific heat capacity $c_{p,3}$, the measured temperature $T_{t,3}$ and the inverted turbine pressure ratio $\Pi_{ts,T}$, which substitutes the isentropic turbine temperature:

$$P_{ts,T,is} = \dot{m}_T \cdot c_{p,3} \cdot T_{t,3} \cdot \left(1 - \left(\frac{1}{\Pi_{ts,T}}\right)^{\frac{\kappa-1}{\kappa}}\right) \tag{2.3}$$

Equation (2.2) combined with equation (2.3) results in the turbine efficiency $\eta_{ts,T,is}$:

$$\eta_{ts,T,is} = \frac{\dot{m}_C \cdot c_{p,C} \cdot (T_{t,2} - T_{t,1})}{\dot{m}_T \cdot c_{p,3} \cdot T_{t,3} \cdot \left(1 - \left(\frac{1}{\Pi_{ts,T}}\right)^{\frac{\kappa-1}{\kappa}}\right)} \tag{2.4}$$

The measured values used for calculating the isentropic turbine output yield solid results. But the compressor power can be manipulate the measured data because of heat flows. Especially in test bench operation with hot gas at low rotational speeds, the measured compressor output is incorrect for the reason that there are heat flows by the warmer turbine side. As a result the turbine efficiency is also distorted. Because of the heat input the adiabatic method operates with fluids approximated to ambient temperature. So it's possible to reduce the error risk.

Ostfalia eATL: In this setup an electric motor displaces the compressor housing and rotor. So it's possible to get the isentropic turbine efficiency directly from the electrical power $P_{T,eATL}$ divided by the isentropic turbine output:

$$\eta_{T,eATL} = \frac{P_{T,eATL}}{P_{ts,T,is}} \tag{2.5}$$

To calculate the electrical power it is simply necessary to measure the torque M_{ATL} und rotational speed n_{ATL} of the turbocharger shaft:

$$P_{T,eATL} = 2 \cdot \pi \cdot M_{ATL} \cdot n_{ATL} \tag{2.6}$$

Equation (2.6) combined with equation (2.3) results in the turbine efficiency:

$$\eta_{T,eATL} = \frac{2 \cdot \pi \cdot M_{ATL} \cdot n_{ATL}}{\dot{m}_T \cdot c_{p,3} \cdot T_{t,3} \cdot \left(1 - \left(\frac{1}{\Pi_{ts,T}}\right)^{\frac{\kappa-1}{\kappa}}\right)} \tag{2.7}$$

3. Creation of turbine maps

There is a certain range to create turbine maps. An established method is to plot the turbine efficiency as a function of velocity ratio φ_T. The velocity ratio can be calculated as a quotient of peripheral speed of turbine wheel u_T and flow velocity c_0.[2]

$$\varphi_T = \frac{u_T}{c_0} \tag{3.1}$$

The peripheral speed of the turbine wheel is the product of turbine wheel diameter d_T and rotational speed of turbocharger n_{ATL}.

$$u_T = \pi \cdot d_T \cdot n_{ATL} \tag{3.2}$$

With the isentropic turbine output $P_{T,is}$ and the air mass flow of turbine $\dot{m}_T$ the flow velocity can be compute.

$$c_0 = \sqrt{\frac{2 \cdot P_{T,is}}{\dot{m}_T}} \tag{3.3}$$

Two more points are needed for generating the characteristic curve for the turbine efficiency. These two points stand for a turbine efficiency level of 0%.

4. Test bench setup

For the comparison of both methods the setups were operated with the same turbocharger on the Ostfalia University of Applied Sciences (Ostfalia UAS). The general structure of the test bench corresponds largely to conventional hot gas test benches. To supply the turbocharger turbine with air a Root's compressor compresses ambient air. Optional it is possible to heat the air in a heating chamber which is operated by electricity. All required parameters for the calculation were measured accurately. A high-precision measuring device records ambient pressure p_0, ambeint temperature T_0, humidity φ_0 and the mass flow $\dot{m}_T$. These paremeters are the basis for setting the desired measuring point. It is also possible to modify pressure and temperature of the oil for the turbocharger bearing by using an oil conditioner. The specific test setup for each method is explained below.

Adiabatic: The setup for the adiabatic measurement of the Ostfalia UAS test bench is shown in Fig. 2.

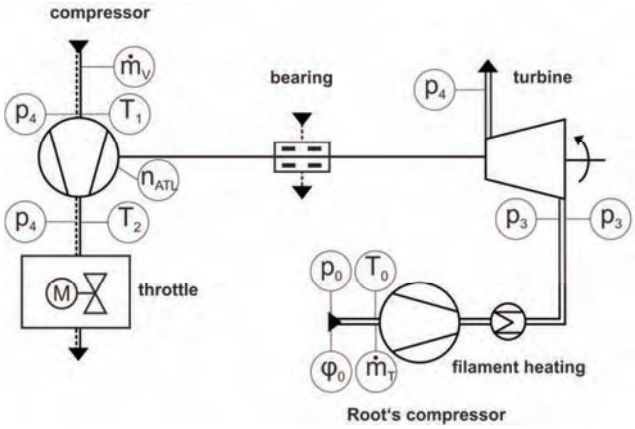

Fig. 2. Test bench setup "adiabatic"

The entire turbocharger is built in the test bench. So the compressor breaks down the turbine. The compressor output is adjusted by a throttle which is arranged behind. So it's possible to modify the compressor mass flow for adjusting the compressor output. Because of the adiabatic criterion, the heating chamber is not in use. But because of the compression of the gas a heat build-up is resulting. In this setup of the test bench it is not possible to act contrary to the heating of the air. But there were the possibility for using the inertness of the heating chamber. The tube following this chamber includes the measuring points for pressure and temperature in front of the turbine. The turbine exhaust contains a temperature measuring point, too. On the compressor side are measuring points for temperature and pressure behind and in front of the compressor wheel. In front of the compressor is a longer tube to succeed a steady flow. So the precision of measurements of airflow increases. An airflow sensor is determined in front of the compressor. The compressor housing features a sensor, which detects the rotational frequency of the compressor wheel.

eATL: The setup for the eATL measurement of the Ostfalia UAS test bench is shown in Fig. 3. Instead of the compressor wheel and the compressor housing an electric motor is installed. For this configuration the compressor housing is dismantled and the compressor wheel is eroded. A coupling combines the shafts of the turbocharger and the electric motor. In combination with an electric load the e-motor can be switched to a generator. So it's possible to break down the turbine. The torque generated by breaking down the turbine is measured with a torque sensor. The shaft torque is measured by the reaction force of the e-motor. Sensor and e-motor are fixed permanently, so the reaction force is measured with a Wheatstone bridge with resistive wire strain. The shaft frequency is measured with an inductive speed sensor. The e-motor features a water-cooled cladding, which protects it from overheating because of much power ratings resulting from high rotational speeds or high electrical loads. To compensate axial and radial offsets of both shafts (e-motor and turbocharger shafts) a special socket is appointed. On this socket e-motor and torque sensor are applied. The seating consists of three linear units, which enable axial alignment on x-, y- and z-axis. The measuring points behind and in front of the turbine are identically equal to the adiabatic test bench setup. But the measuring points around the compressor are omitted.

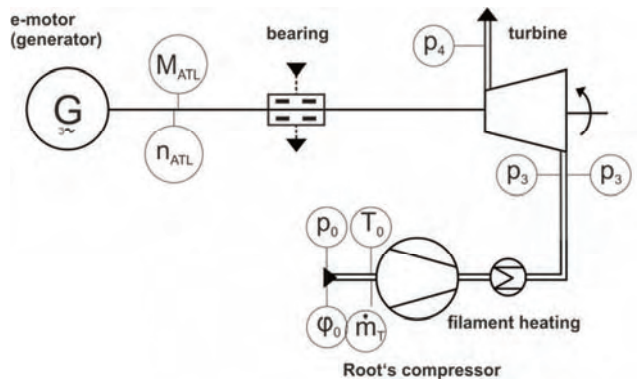

Fig. 3. Test bench setup "eATL"

Measurement conditions: The tested turbocharger is one with wastegate adjustment. Because of the comparability of both measurement methods, the terms and conditions of the eATL were transferred to the adiabatic setup. So all fluids were unheated and round about ambient conditions (approximately 20°C). Sole exception is the compacted air for the turbine. It increased because of the pressure rise resulting from the Root's compressor. But the temperature was not higher than 32°C.

For generating extended turbine maps in low speed levels the rotational speeds 20000; 40000; 60000 and 80000 rpm were investigated.

5. Measurement results

The test readings are shown in diagrams with velocity ratio on x-coordinate and isentropic turbine efficiency on y-axis. Because of increasing the brakeload of each series of measurement, the maps and graphs have to be read from right side to left side. For the beginning the results of both measurement methods are shown separately.

Adiabatic: The generated meter points are shown in Fig. 4. The increase in the efficiency with the increase of the rotational speed seems to be plausible and corresponds to the expectation. The maximum efficiency is around 48 % and is reached with 80000 rpm as expected at the highest speed. You can see that the measured points of all series are located in a narrow margin. This results from the low braking power which the compressor is able to provide. For illustrating the compressor outputs, the first and the last measured point are exemplarily shown for the rotational speeds 20000 rpm and 80000 rpm.

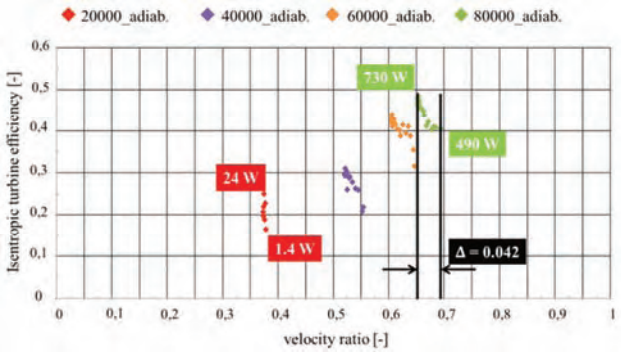

Fig. 4. Measured points – adiabatic

But for generating continuous rising efficiencies in the evaluation, the meter points were reassessed. In this case, only those measured points were used, in which an increased brake load is also accompanied by an increase in the determined turbine efficiency, while the velocity ratio is reduced at the same time. As a further criterion the compressor power was used. Here, only the measured points were turned to account, where the increase of the brake load is accompanied by a steady increased compressor power. The result of the reassessment is shown in Fig. 5. The revised measurement results provide a more steady progress due to a reduced dispersion of the measured points. So the course of the turbine efficiency is more obvious. At the rotational speeds 20000 and 40000 rpm the expected typical characteristic curve can be derived from the position of the

measured points. The positions of the measured points at the speeds 60000 rpm and 80000 rpm are more inconsistent. At 60000 rpm the first measured point gets out of the ordinary run. This one has a low efficiency or a too low velocity ratio. The other points allow realizing the expected run. The measured points for 80000 rpm allow indicating an opposed run for the turbine efficiency.

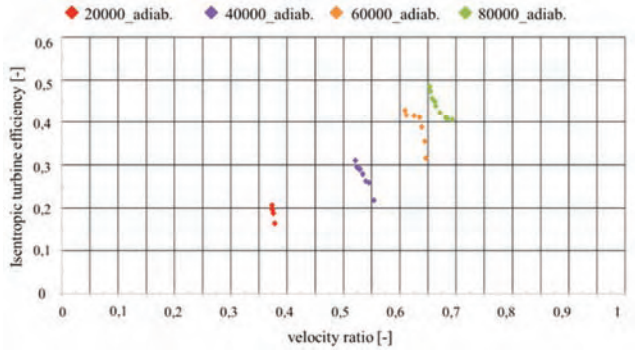

Fig. 5. Revised measuring points – adiabatic

eATL: The generated meter points are shown in Fig. 6. The measurements provide plausible results. As expected, the maximum efficiency is reached at the highest speed at 80000 rpm and is about 49 %.

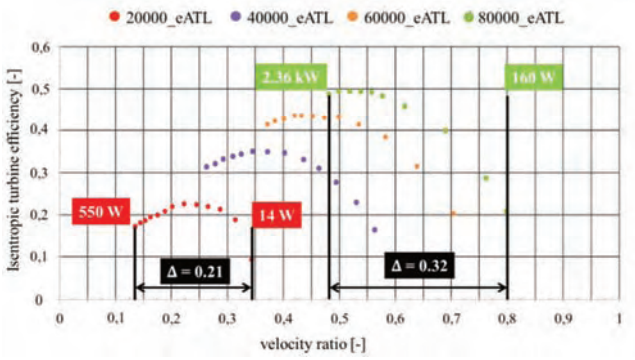

Fig. 6. Measured points - eATL

It is apparent that all measured points have a wide range for generating a reliable run for the turbine efficiency. This wide range is perfectly good to describe the increasing and decreasing efficiency for each measuring graph. The performance of the e-motor allows decelerating the turbine with an output up to 4 kilowatts. For detailed explanation, the outputs for each speed are shown in Fig. 6. The lowest output at 20000 rpm is 14 watts and the major output is 550 watts. The outputs at 80000 rpm are 160 watts and 2.36 kilowatts. The difference between the lowest and highest velocity ratio at 20000 rpm is 0.21 and at 80000 rpm 0.32. According to [2], the typically measured velocity ratio is between 0.4 and 0.8 for manufacturers. The results shown in Fig. 6 approximately correspond to the velocity ratio covered by the Ostfalia eATL configuration at the speed of 80000 rpm. The lowest velocity ratio provided by the Ostfalia eATL method is 0.135 at the speed of 20000 rpm.

5.1. Preparation of measurement results

The extrapolated characteristic curve of turbine efficiency is generated with two additional points. Each point represents a turbine efficiency of 0. The first point with turbine efficiency 0 is in point of origin. It results from a non-rotating turbine. That means that the turbine is braked down by the e-motor and the air mass flow is not able to bring the shaft into rotation. The other point is when velocity of air mass flow rate and circumferential speed of turbine are in balance. Turbine shaft and e-motor are disconnected and so there is no effective work, because turbine output is determined by braking down the friction power of turbocharger bearing. With these two supporting points and the measuring points it's feasible to extrapolate a graph for illustrating the isentropic turbine efficiency. The extrapolation method is a cubic equation. In the following charts the graphs are named as "Poly".

5.2. Analysis of measurement results

Figure 7 shows the extrapolated graph of turbine efficiency of the eATL configuration. It highlights that the extrapolation method is almost perfect. In general the measurement produce plausible and repeatable results. The isentropic turbine efficiencies are similar with results which could be found in literature. But in literature are efficiencies around 60 to 70% in higher rotational speeds [1]. There is a divergence from the first measured points and the extrapolated graph. The reason for the difference could be the low output paired with the low rotational speed. Because of that the influence of troubles is highly and so the turbine efficiency varies in value. For instance, a minimal axially offset of both shafts has a bigger impact in low rotational speeds than in higher speeds. So the influence becomes less in higher rotational speeds. Typically the velocity ratio of turbochargers is between 0.4 and 0.8 [2]. This is comparable with the results of the Ostfalia eATL at 80000 rpm.

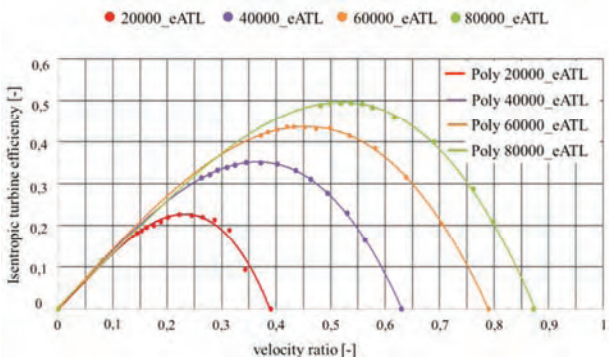

Fig. 7. Extrapolated graph – eATL

Figure 8 shows the comparison of adiabatic and eATL measurement. It's for evaluation of the turbine efficiencies which were obtained with adiabatic configuration. As already said, the revised measurement points were used. It highlights, that the adiabatic method has a high offset to the eATL method. The measured points of 80000 rpm have the largest alignment with the extrapolated graph and the slimmest alignment. For better illustration the offset for each rotational speed of adiabatic method is shown. So the largest difference is in the speed of 20000 rpm. There is a dis-

crepancy of 16.1 percent. The speeds 40000 rpm and 60000 rpm exhibit a discrepancy of round about 7%. The highest nonconformity at 80000 rpm is 4.6 percent. But in all speeds the variance becomes more by increasing the braking power. But the expectation is that the influence of heat flows becomes less with increasing the air mass flow [4].

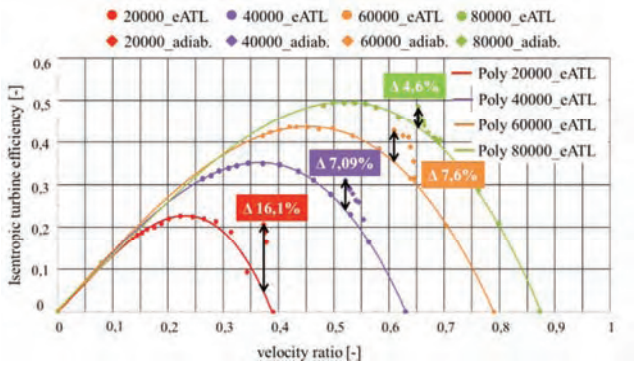

Fig. 8. Extrapolated graph and measuring points of eATL and adiabatic technique

The line graph in Figure 9 deals with the direct comparison of the extrapolated graphs of both methods. The measured points of the adiabatic method were extrapolated, too. But in this case it happened only with an equation of the second degree. The two sampling points with turbine efficiency of zero were used too. But the point with balancing air mass flow ratio and circumferential turbine speed was manually generated. For that reason the highest alignment of measured points and graph were taken as a basis. The line graph clearly shows that the extrapolated turbine efficiencies of adiabatic method for each rotational speed are higher than the extrapolated efficiencies of eATL method. Only a part of the adiabatic 80000 rpm graph matches with the turbine efficiency at the same rotational speed. But an extrapolation without the sampling points would generate a contrary graph run of the adiabatic method. So the results are not really surprising.

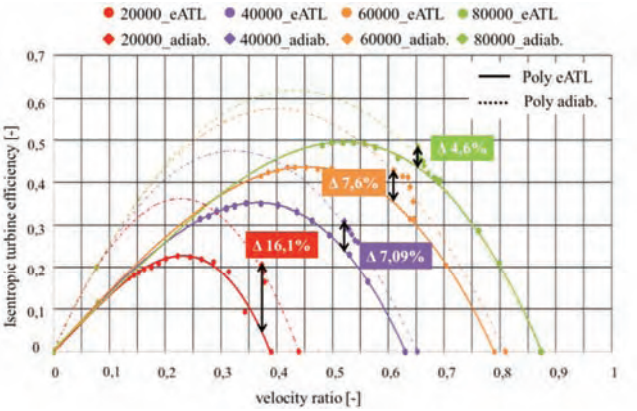

Fig. 9. Direct comparison of extrapolated graphs

6. Conclusion and prospects

The methods for measuring turbine efficiencies explained in this paper generate different results. The first is the eATL method and is about an electrical braked down turbine in combination with a torque sensor. With the gained magnitudes it's possible to calculate the isentropic turbine efficiency very easily. On the other hand is the adiabatic method with braking down the turbine with the compressor, as usual. Both techniques conduce for generating turbine maps at low rotational speed ranges. These areas are used for detailed motor process simulations for each operating range. Commonly generated turbine maps on hot gas test benches are not able to acquire measuring points in speed ranges less than 80000 rpm.

The adiabatic technique results in higher turbine efficiencies than the Ostfalia eATL. This impact seems to be caused by heat flows from the warmer turbine side into compressor side. At low rotational speeds the heat flows have the biggest influence. Another issue is the narrow range of achievable measuring points using the adiabatic method. One reason is the low air mass flow rate in low speed ranges. Because of the limited maximum braking power of compressor it is not possible to get low velocity ratios. And so it is not possible to get the maximum turbine efficiency. In contrast the eATL is able to gain measurement points from low to high turbine efficiencies. With these results reliable extrapolations of turbine efficiency are feasible. The results of both test procedures include the friction power of the bearing. There is a separate test bench for measuring the friction power of turbocharger bearings of the Ostfalia UAS. With this test bench it is possible to determine friction power for different rotational speeds as well as axial force. In combination of these two test benches the turbine efficiencies without friction power can be determined.

For improving the test procedure of the adiabatic method the compressor air mass flow has to be increased. There is the capability of using the Closed Compressor Loop (CCL) procedure. In CCL procedure the compressed air mass flow returns to the compressor inlet. So it's possible to increase the flow rate at low speed near surge line. Moreover the increasing air mass flow reduces the influences of heat flows on turbine efficiencies. Another possibility is to cool down the compressed turbine air mass flow. With compression the air the temperature increases. A recuperator could be installed in the tube. If necessary a speed controlled fan could be installed additionally. But best solution would be the combination of CCL and active cooling of turbine air mass flow. Integration of these techniques is future development.

Nomenclature

CCL	closed compressor loop
ATL	turbocharger
$c_{p,C}$	specific heat capacity at the compressor
$c_{p,3}$	specific heat capacity at the entrance of the turbine
M_{ATL}	torque at the shaft
$\dot{m}_C$	compressor air mass flow

$\dot{m}_T$	turbine air mass flow
n_{ATL}	rotational speed of the shaft
P_C	compressor power
$P_{T,eATL}$	braking power of the electric motor
$P_{ts,T,is}$	isentropic turbine power, total-to-static
p_0	atmospheric pressure
T_0	ambient air temperature
$T_{t,1}$	total temperature at the entrance of the compressor
$T_{t,2}$	total temperature at the outlet of the compressor
$T_{t,3}$	total temperature at the entrance of the turbine
$\eta_{ts,T,is}$	isentropic turbine efficiency, total-to-static
κ	heat capacity ratio
$\Pi_{ts,T}$	turbine pressure ratio, total-to-static
φ_0	humidity
φ_T	velocity ratio
u_T	peripheral speed of the turbine wheel
c_0	approach velocity

Bibliography

[1] VAN BASSHUYSEN, R., SCHÄFER, F. Handbuch Verbrennungsmotor. Grundlagen, Komponenten, Systeme, Perspektiven. 2015, **7**, 554-558.

[2] PISCHINGER, S., SCHARF, J.S., FUNKEN, B., SMILJANOWSKI, V., SCHORN, N. Measurement of turbine efficiency at low turbocharger speeds. *13th Supercharging Conference*. 2008, 7.

[3] LÜDDECKE, B. Stationary and non-stationary operating behavior of exhaust gas turbo-chargers. *Scientific Series Vehicle Technology*. University of Stuttgart, 2016, **1**.

[4] GRIGORIADIS, P., BINDER, E., BÖTTCHER, L., BENZ, A., SENS, M. Advanced turbocharger model for 1D ICE simulation – part I. *SAE Technical Paper*. 2013, 2013-01-0581.

[5] MAI, H., BOLZ, H. Validierung von Turboladerkennfeldern auf Heißgasprüfständen. *ATZ Extra*. 2015, **8**.

[6] SINAN, Ö. Wärmestromanalyse der Radialturbinenstufe eines PKW-Abgasturboladers mittels numerischer Simulation. *Dissertation*. 2017.

[7] SAE International; Turbocharger Nomenclature and Terminology SAE J922. 1995.

[8] SAE International, Turbocharger Gas Stand Test code SAE J1826. 1995.

[9] NICKEL, J.; GRIGORIADIS, P., Verfahren und Messmethoden zur Erfassung von Turboladerkennfeldern an Turboladerprüfständen. In: Lechmann, A. (Hrsg.):Simulation und Aufladung von Verbrennungsmotoren. *Berlin, Heidelberg: Springer*. 2008, 227-244.

Robin Vanhaelst, DSc., DEng. – Faculty of Automotive Engineering at University of Applied Sciences.

e-mail: *R.Vanhaelst@ostfalia.de*

Maik Klose, BEng. – Faculty of Automotive Engineering at University of Applied Sciences.

Caroline Bannack, BEng. – Faculty of Automotive Engineering at University of Applied Sciences.

e-mail: *Ca.Bannack@ostfalia.de*

Article citation info:
ADAMSKI, W., POLAK, S. Investigations of the influence of engine thermal state on the fuel consumption of passenger vehicles. *Combustion Engines*. 2017, **169**(2), 49-52. DOI: 10.19206/CE-2017-209

Wojciech ADAMSKI
Stanisław POLAK

CE-2017-209

Investigations of the influence of engine thermal state on the fuel consumption of passenger vehicles

The paper presents the results of investigations of the fuel consumption of two vehicles performed for non-stabilized engine temperature in the start and warm up phases. The measurements were performed in a wide range of ambient temperatures from –18°C to +25°C. In order to obtain such conditions the tests were carried out in a climate chamber.

Key words: *passenger vehicle, fuel consumption, engine thermal state*

1. Introduction

A start-up of a cold engine and its operation in the first moments that follow are a specific state of its operation characterized by, inter alia, increased fuel consumption and exhaust emissions.

A cold start of an engine denotes a state when it operates under the conditions when the temperature of the engine coolant, the lubricating oil and the engine components (including their subassemblies) equals that of the ambient air. In the next stage of the engine operation, the warm up phase of the said components takes place until the optimum operating temperature is reached [1].

The fuel consumption and exhaust emissions upon a cold start depend on the engine thermal state (ambient temperature), the fuel system (diesel spark, ignition), the engine displacement and the exhaust emissions standard.

The fuel consumption and exhaust emissions at cold start become particularly significant if a given routine engine operation involves a high number of starts. The operation of vehicles at cold start predominantly takes place in urban areas and is characterized by an increasing trend of idle operation at very low loads [2]. Literature [3] indicates that up to 45% of engine starts are cold starts. [1] indicates that in Europe, 50% of the routes realized in urban areas by passenger vehicles and light-duty trucks (LDV), is shorter than 5 km.

The aim of the research work presented in this paper was to determine the fuel consumption of a combustion engine at cold start and warm up for different ambient temperatures. The warm up process was carried out at minimum loads at idle, which are the least advantageous conditions for quick obtainment of optimum operating conditions. The measurements were performed for two passenger vehicles fitted with engines of different fuel systems (spark ignition and diesel).

2. Methods of reduction of the fuel consumption of a cold engine

For a cold engine operating at low loads, an efficient way to reduce the fuel consumption is the reduction of the mechanical resistance or application of solutions providing engine heating prior to its start and accelerating the warm up process of a cold engine during its operation.

Solutions reducing the mechanical resistance of an engine include:

- introduction of design solutions that reduce friction in the piston-crank assembly as well as in the timing system,
- application of low viscosity engine lubricants,
- application of engine aggregates of lower energy consumption, e.g. electrically driven fuel pumps, oil and coolant pumps (or components of variable flow rate) or intelligent charging alternators.

The engine pre-heat and subsequent warm up can be obtained through:

- the application of electric heaters powered from external sources used to heat the oil, or the coolant, or
- the application of electric or combustion-based integrated engine heaters (parking heating).

The application of these solutions requires a supply of a certain amount of electrical energy or fuel, which should be allowed for in the total energy balance. The fundamental reason for applying these systems is to facilitate the engine start at low ambient temperatures as well as improve the thermal comfort in the cockpit immediately after engine ignition.

Solutions that indirectly assist the engine heating process are:

- intelligent blinds preventing the chilling of the engine compartment including the engine itself,
- cooling systems fitted with electronic pumps (during start and warm up, the pump does not operate or works with at reduced flow rate),
- lubrication systems of variable oil capacity in the circuit allowing a reduction of the amount of circulating oil in the phase of engine warm up,
- devices utilizing the exhaust gas energy,
- heat accumulator in the cooling systems that returns the heat accumulated in previous driving cycles.

3. The test conditions

The tests have been performed for two passenger vehicles of the below-given characteristics.

LANCIA Ypsilon

- spark ignition engine (SI)
- number of cylinders: 4
- displacement: 1242 cm^3
- maximum power/rpm: 51 kW/5500 rpm

– maximum torque/rpm: 102 Nm/3000 rpm
– number of valves per cylinder: 2
– turbocharging: no
– fuel system: indirect injection, Multipoint
– emission standard: Euro 6
– lubricating oil: SAE 5W40
– fuel: unleaded gasoline 95.

FIAT Doblo

– diesel engine (CI)
– number of cylinders: 4
– displacement: 1598 cm^3
– maximum power/rpm: 77 kW/4000 rpm
– maximum torque/rpm: 290 Nm/1500 rpm
– number of valves per cylinder: 4
– turbocharging: yes
– fuel system: direct injection, Multijet, common rail
– emission standard: Euro 5
– lubricating oil: SAE 5W30
– fuel: diesel fuel.

The tests were performed in a climate chamber of the Division of Road Tests at Research and Development Institute BOSMAL in Bielsko-Biała. The chamber has the following parameters:

– temperature range: –45°C … + 75°C
– dimensions: length 870 cm, width 710 cm, height 315 cm.

The fuel consumption measurement was based on the volumetric method utilizing the PLU116H by Pierburg flow meters of the following parameters:

– measurement range: up to 60 l/h,
– measurement accuracy: ±1.5% of the measured value.

The temperatures of the fluids were measured with the type K (NiCr-NiAl) thermocouples. Additionally, the basic engine operating parameters were recorded with dedicated diagnostic devices connected to the EOBD port.

The tests were performed for selected ambient temperatures: –18°C, –10°C, 0°C, +10°C, +25°C. Prior to each trial the vehicle was conditioned at the required temperature for approx. 24 hours. The criterion for the engine thermal stability was the difference of the engine oil/coolant temperature and the ambient air that was not to exceed 2°C. The applied fuels had specifications appropriate for the temperature of the trial and the engine oil and coolant were applied as recommended by the manufacturer.

The engine start was performed as recommended by the vehicle manufacturer. For the diesel engine, the glow plug heating procedure was first carried out. Upon start, the engine operated at the minimum idle speed and all additional energy receivers such as heating, air conditioning, lighting etc. were off during the trial. The test ended after 20 minutes from the start (turning on the ignition).

4. Results

Figures 1 and 2 present the total amount of consumed fuel [l] after a given time from the engine start for different temperatures.

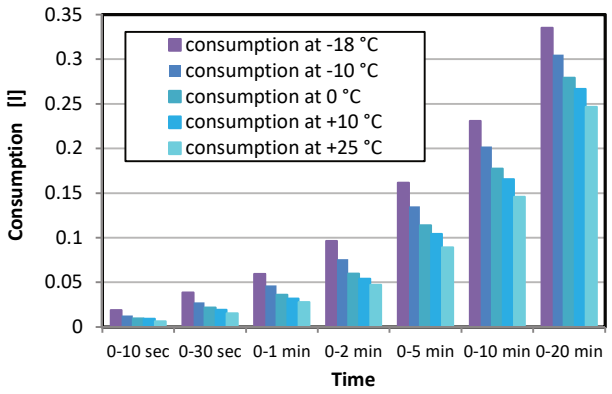

Fig. 1. The amount of fuel consumed by LANCIA Ypsilon (SI)

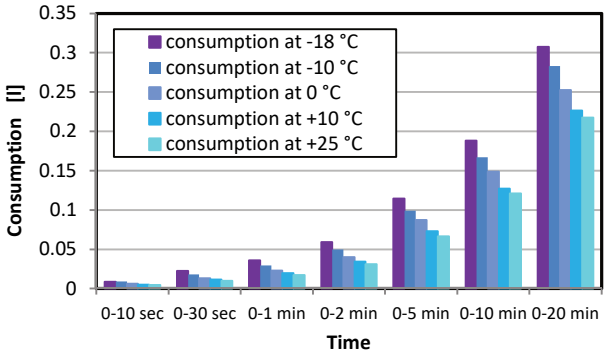

Fig. 2. The amount of fuel consumed by FIAT Doblo (CI)

The Instantaneous fuel consumption [l/h] as a function of time for selected temperatures has been shown in Figs 3–5.

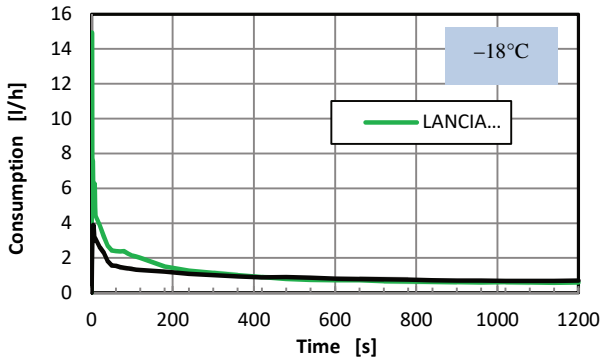

Fig. 3. Instantaneous fuel consumption at the temperature of –18°C

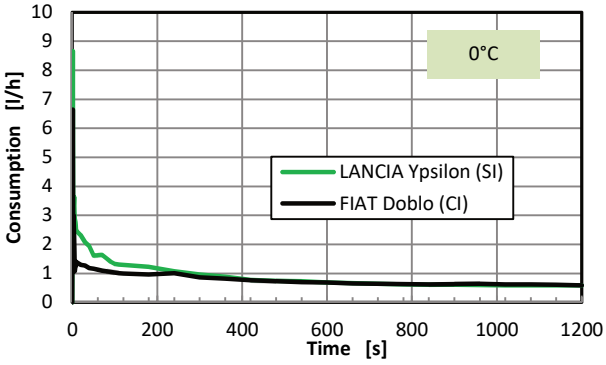

Fig. 4. Instantaneous fuel consumption at the temperature of 0°C

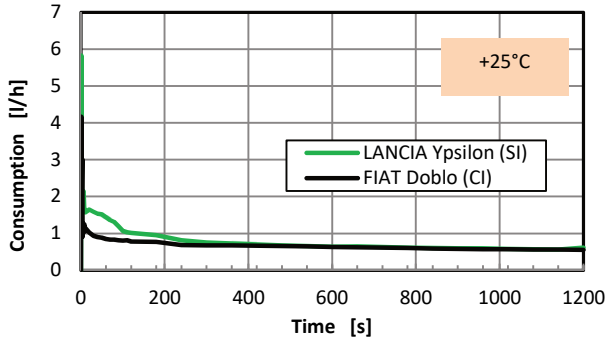

Fig. 5. Instantaneous fuel consumption at the temperature of +25°C

For better presentation of the differences in the fuel consumption, Figs 6–8 show the averaged fuel consumption values [l/h] in selected time intervals (of different width).

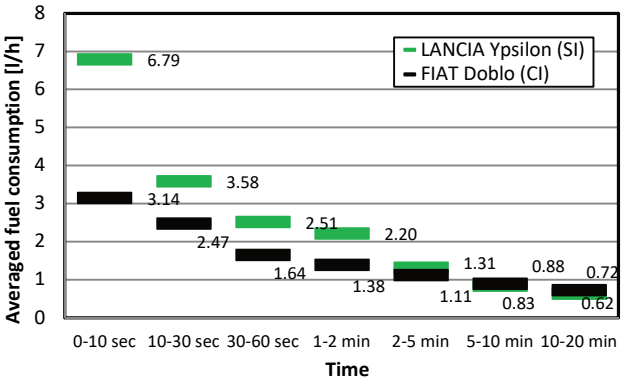

Fig. 6. Averaged fuel consumption at the temperature –18°C

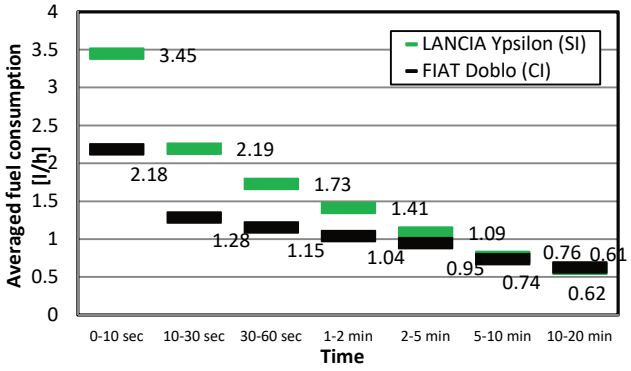

Fig. 7. Averaged fuel consumption at the temperature 0°C

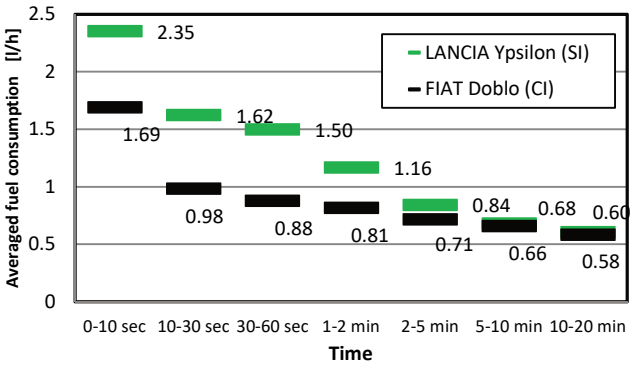

Fig. 8. Averaged fuel consumption at the temperature +25°C

The engine warm up during operation at idle is a long process, particularly if diesel engine is the case. The curve of the coolant temperature as a function of time has been shown in Figs 9–11.

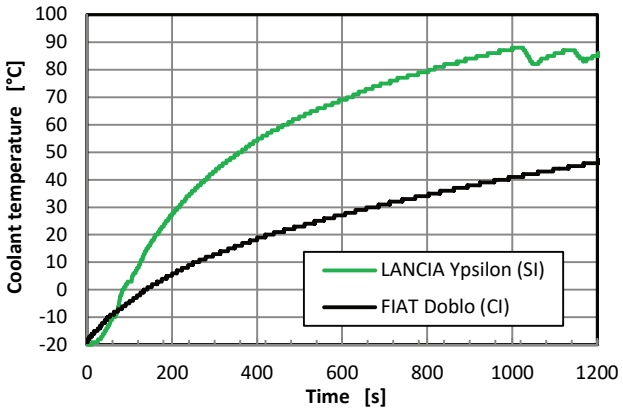

Fig. 9. The coolant temperature at the ambient temperature –18°C

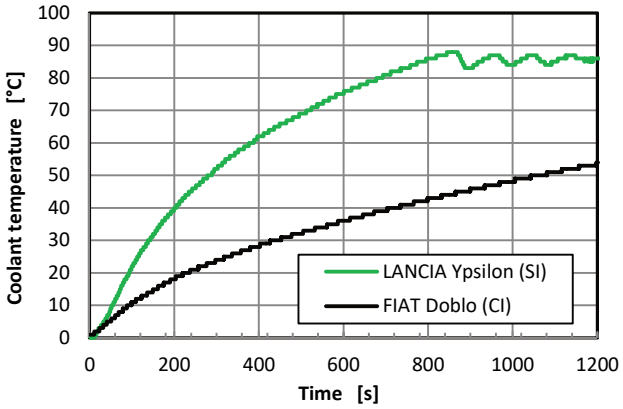

Fig. 10. The coolant temperature at the ambient temperature 0°C

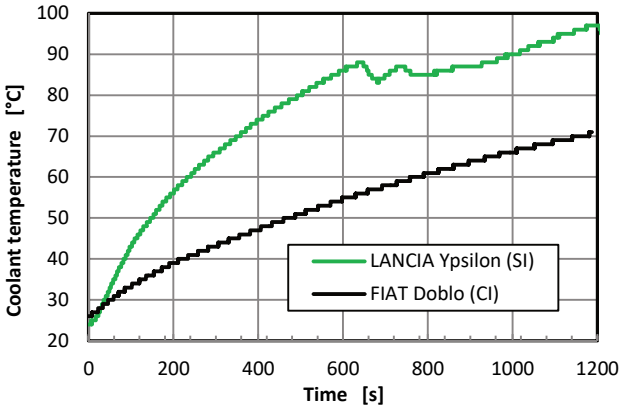

Fig. 11. The coolant temperature at the ambient temperature +25°C

5. Results and discussion

1. For both tested vehicles (engines) increased fuel consumption has been observed during the engine start and immediately after ignition. Depending on the ambient temperature, already after several seconds, the fuel consumption decreased significantly and asymptotically reached its steady value.

The increased fuel consumption, particularly under low ambient temperatures, is caused by increased friction inside the engine and unstable combustion e.g. impossibility to form proper air/fuel mixture, misfires, the chilling effect of the combustion chamber walls etc.

2. The influence of the reduced ambient temperature on the fuel consumption in the first phase of engine operation is more conspicuous for spark ignition engines. Comparing the fuel consumption measured in the initial period of 10 seconds after the start of a spark ignition engine in the ambient temperature of –18°C with the fuel consumption of the ambient temperature of +25°C, we can observe the it grows three times while for the diesel engine this fuel consumption grows only twice.

In a spark ignition engine, it is necessary to enrich the mixture to evaporate the fuel while filling the cylinder. Besides, in indirect injection systems (as was in the case of the tested engine) increased condensation of vapors occurs on the walls of the intake manifold. The process of mixture enrichment is necessary to quickly reach the readiness of the fuel/air mixture control system to properly activate the closed loop operation based on the signals from the oxygen sensor and to heat up the catalytic converter to its light-off temperature.

When analyzing the results, we need to allow for the differences in the engine displacement of the investigated engines (1242 cm^3 spark ignition engine and 1598 cm^3 diesel engine).

The engine mechanical resistance is heavily influenced by the temperature and viscosity of the lubricating oil. Oil of the same 5W parameter was applied in the investigated engines, characterizing the viscosity under low ambient temperatures. Therefore, when comparing the results, this factor could be omitted.

3. As the engine thermal state stabilizes, the fuel consumption in both engines equalizes. After the start at the temperature of –18°C, the spark ignition engine stabilizes thermally (reaches the temperature of approx. +90°C) after the time of approx. 17 minutes while the diesel engine after the same time, reaches only the temperature of +40°C.

As described in [4], for the diesel engine, a significant share in the engine mechanical friction is attributed to the drive of the high-pressure injection pump. During idle operation, up to 50% accumulated mechanical resistance may occur.

Conclusions

The performed research allowed determining how great the increase of fuel consumption is during the cold start and warm up phases and what the ranges of this value are depending on the ambient temperature. Variable vehicle operating conditions, particularly in the urban cycle make the share of the warm up phase in the entire time of operation increasingly prevalent.

It is recommended that in the further stages of the research, an assessment is carried out of the solutions that may contribute to the reduction of fuel consumption in the warm up phase either through the reduction of engine mechanical resistance or acceleration of the warm-up process. When analyzing the changes in the fuel consumption, it will also be necessary to evaluate the impact of the applied solutions on the exhaust emissions and thermal comfort of the passengers.

A topic of separate analyses (particularly for spark ignition engines) may be the assessment of the applied injection control algorithm (calibration) in terms of air/fuel mixture enrichment in the start and warm-up phases of an engine.

The planned expansion of the BOSMAL climate chamber by a dynamometric roller test bench will enable the performance of tests under conditions close to actual – after the engine start, the engine will warm up in selected driving cycles.

Bibliography

[1] BIELACZYC, P., MERKISZ, J., PIELECHA, J. Stan cieplny silnika spalinowego a emisja związków szkodliwych. *Wydawnictwo Politechniki Poznańskiej*. Poznań 2001.

[2] ISKRA, A., KAŁUŻNY, J., BABIAK, M. Charaktery-styka biegu jałowego w fazie nagrzewania silnika. *Wydawnictwo Politechniki Krakowskiej*. Kraków 2008.

[3] JOUMARD, R., ANDRE, M. Cold start emissions of traffic. *The Science of the Total Environment*. 1990, **93**, 175-182.

[4] KARCZEWSKI, M., SZCZĘCH, L. Pomiary oporów wewnętrznych silnika spalinowego. *Zeszyty Naukowe Akademii Marynarki Wojennej*. 2013, **2**(193).

Wojciech Adamski, MEng. – BOSMAL Automotive Research & Development Institute Ltd in Bielsko-Biała.

e-mail: *Wojciech.Adamski@bosmal.com.pl*

Stanisław Polak, Eng. – BOSMAL Automotive Research & Development Institute Ltd in Bielsko-Biała.

e-mail: *Stanislaw.Polak@bosmal.com.pl*

Article citation info:
PYSZCZEK, R., MAZURO, P., JACH, A., TEODORCZYK, A. Numerical investigation on low calorific syngas combustion in the opposed-piston engine. *Combustion Engines*. 2017, **169**(2), 53-63. DOI: 10.19206/CE-2017-210

Rafał PYSZCZEK
Paweł MAZURO
Agnieszka JACH
Andrzej TEODORCZYK

CE-2017-210

Numerical investigation on low calorific syngas combustion in the opposed-piston engine

The aim of this study was to investigate a possibility of using gaseous fuels of a low calorific value as a fuel for internal combustion engines. Such fuels can come from organic matter decomposition (biogas), oil production (flare gas) or gasification of materials containing carbon (syngas). The utilization of syngas in the barrel type Opposed-Piston (OP) engine arrangement is of particular interest for the authors. A robust design, high mechanical efficiency and relatively easy incorporation of Variable Compression Ratio (VCR) makes the OP engine an ideal candidate for running on a low calorific fuel of various compostion. Furthermore, the possibility of online compression ratio adjustment allows for engine the operation in Controlled Auto-Ignition (CAI) mode for high efficiency and low emission. In order to investigate engine operation on low calorific gaseous fuel authors performed 3D CFD numerical simulations of scavenging and combustion processes in the 2-stroke barrel type Opposed-Piston engine with use of the AVL Fire solver. Firstly, engine operation on natural gas with ignition from diesel pilot was analysed as a reference. Then, combustion of syngas in two different modes was investigated – with ignition from diesel pilot and with Controlled Auto-Ignition. Final engine operating points were specified and corresponding emissions were calculated and compared. Results suggest that engine operation on syngas might be limited due to misfire of diesel pilot or excessive heat releas which might lead to knock. A solution proposed by authors for syngas is CAI combustion which can be controlled with application of VCR and with adjustment of air excess ratio. Based on preformed simulations it was shown that low calorific syngas can be used as a fuel for power generation in the Opposed-Piston engine which is currently under development at Warsaw University of Technology.

Key words: *opposed-piston, syngas, combustion, CAI, CFD*

1. Introduction

The development of the industrial sector became the reason of the emissions growth. In order to counterbalance the harmful effect of pollutants on the environment, emission regulations are becoming more and more strict. This trend forces engine manufacturers to constantly improve their devices and develop new solutions that will help to meet new emission standards. In recent years research in clean internal combustion (IC) engine technology is focused on renewable energy sources such as natural gas and alternative gaseous fuels. Such fuels can come from organic matter decomposition (biogas), oil production (flare gas) or gasification of materials containing carbon (syngas). Additionally, when fuel is considered as a waste it needs to be utilized due to environmental regulations what raises additional costs. Under present conditions, economic factors provide the strongest argument for the use of syngas as fuel [1].

In areas where the price of petroleum fuels is high, or where supplies are unreliable, syngas can provide an economically viable solution. Syngas consists of about 40% combustible gases, mainly carbon monoxide (CO), hydrogen (H_2) and methane (CH_4). The remainder is made up of non-combustible gases, primarily nitrogen (N_2) and carbon dioxide (CO_2). The presence of H_2 in gaseous fuel increases flame propagation speed and widen flammability limits extending the lean limit of gas operation without entering the lean misfire region. With the lean mixture combustion higher thermal efficiency and low NO_x emission are possible to attain [2]. Despite advantages of utilizing syngas as a fuel in internal combustion engines, there are still several challenges problems that researchers are trying to overcome. One of the biggest problems is varying composition of syngas depending on the source of the fuel. Since main components of the syngas have considerably different combustion properties, the overall behaviour of the fuel can be significantly changed with change of the $CH_4/H_2/CO$ proportions. Furthermore, with increasing of the H_2 fraction in the fuel, the minimum energy required for ignition is reduced leading to increased probability of mixture auto-ignition in the region of end gas in the combustion chamber.

There are several works dedicated to investigation of syngas utilization in IC engines. Some of them consider spark-ignition (SI) combustion system [3–5]. However, under high load conditions, SI is not suitable for this kind of fuel due to the fluctuation of the syngas composition which makes it difficult to obtain stable combustion. In order to achieve reliable ignition and low cycle-to-cycle variations it is beneficial to utilize syngas in IC engine that operate in dual-fuel mode under compression ignition with a lean mixture, using a pilot injection of diesel fuel. Firstly, a pilot diesel fuel is injected, resulting in ignition and a subsequent temperature rise in the combustion chamber. Then, the primary gaseous fuel (syngas) is ignited due to temperature increase in the chamber with subsequent combustion.

Dual-fuel engines powered by syngas have been widely studied by several research groups. Tomita et al. [6] studied the combustion characteristics in a supercharged dual-fuel engine with syngas as primary fuel and ignition from micro-pilot. They stated that a premixed flame of syngas-air mixture develops from multiple flame kernels produced by the ignition of diesel pilot. It was also determined that a certain increase in the hydrogen content of the syngas allows the engine to operate even at equivalence ratios as low as $\Phi = 0.45$ with stable combustion and high efficiency.

In a series of papers Roy et al. [7–9] performed experimental studies of performance and characteristics of supercharged dual-fuel engine fuelled by producer gases with varying hydrogen content and by hydrogen-rich coke oven gas. In their work, authors also studied the effect of fuel injection parameters on engine performance and emissions. They detected characteristic two-stage heat release during the combustion of syngas at a pilot fuel injection pressure of 40 MPa and 10° before top dead centre (BTDC). With further advance of pilot injection more than 13.5° BTDC knocking combustion occurred. When the injection pressure was increased to 80 MPa, two-stage heat release combustion was observed at 9° BTDC, and knock occurred after 11° BTDC. Moreover, authors also studied the effect of hydrogen content in the fuel and the effect of exhaust gas recirculation (EGR) on the performance and exhaust emissions of a dual-fuel engine. They found that the engine power obtained from syngas with high H_2 content was 12% greater than that obtained from syngas with low H_2 content. They also showed that high H_2 content is superior to low H_2 content for leaner syngas operation.

Azimov et al. [10–12] performed experimental and numerical investigation of ignition, combustion and exhaust emission characteristics of Micro-Piloti-Ignited (MPI) dual-fuel (DF) engine fuelled with natural gas, syngas and hydrogen. Authors also reported characteristic two-stage heat release profile. The first stage is gaseous fuel flame propagation and the second is end-gas mixture auto-ignition. The second stage can be mainly controlled by the pilot fuel injection timing, gaseous fuel equivalence ratio, and EGR rate. Authors named this combustion mode as PREMIER (PREmixed Mixture Ignition in the End-gas Region) and stated that an increase in the fuel mass fraction burned in the second stage of heat release affects the rate of maximum pressure rise. Furthermore, increase in hydrogen content in syngas induces an increase in the mean combustion temperature, IMEP and efficiency, but also a significant increase in NO_x emissions.

The most recent concept is to run IC engine fuelled with syngas in Homogeneous Charge Compression Ignition (HCCI)/Controlled Auto-Ignition (CAI) combustion mode for high thermal efficiency and low emissions. It is a unique form of combustion based on charge auto-ignition at desired crank angle. It has been demonstrated that HCCI gasoline engine can achieve fuel economy levels comparable to those of a Compression Ignition (CI) engines, while producing engine-out NO_x emissions that are as low as tail-pipe NO_x emissions from a conventional SI engine equipped with a three-way catalyst [13].

Although the idea of HCCI/CAI combustion is desirable, it is also very challenging to implement in an IC engine due to absence of direct ignition timing control (i.e. spark). In order to guarantee correct combustion timing, closed-loop combustion control is necessary. This type of control is supposed to vicariously influence the ignition timing via different measures (i.e. VCR). Additionally, in case of utilizing syngas as a fuel in HCCI engine it would be possible to become independent from diesel fuel conventionally used for ignition, since ignition in HCCI is controlled only by in-cylinder conditions. Although there have been many studies on HCCI combustion of gasoline, HCCI of syngas is still not well investigated. It is probably due to the fact, that varying composition of syngas might be very challenging for adopting HCCI combustion. Nevertheless, in one of the recent studies Bhaduri et al. [14] performed experimental study of running IC engine fuelled with impure syngas in HCCI mode. Authors proved stability of their concept with 24-hour test. However, relatively low IMEP (2.5 bar) and high NO_x emission (150 ppm) were achieved. The conclusion was that the concept requires further improvement to make commercially viable.

The aim of the current work is to investigate a possibility of utilizing low calorific syngas as a fuel in the barrel type Opposed-Piston engine which is currently under development at Warsaw University of Technology. The engine is equipped with diesel pilot injection for direct ignition timing control, as well as with an online VCR and water injection systems for indirect ignition timing control. The goal is to achieve high performance and low emissions in order to make the engine commercially viable. Such a complex combustion control system is challenging to implement in the real engine. Therefore, numerical simulations can become a useful tool for better understanding of the combustion process and can shorten the time span for engine development. In this study 3D CFD numerical simulations of the scavenging, injection and combustion processes were performed. With numerical simulation it was possible to determine engine operating points in dual-fuel mode with diesel pilot ignition and in CAI mode.

2. Opposed-Piston engines

There are several types of OP engine configurations (cranckless, single crankshaft, multiple crankshaft, rotary or barrel) [15]. The barrel type OP engine is of particular interest for the authors because of its robust design, high mechanical efficiency and relatively easy incorporation of a Variable Compression Ratio. In the barrel type OP engine cylinders' axes are parallel to the drive shaft axis. Linear to rotary motion is changed through the special plate with connecting rods mounted on ball bearings. An 8-cylinder barrel type OP piston engine concept is presented in Fig. 1.

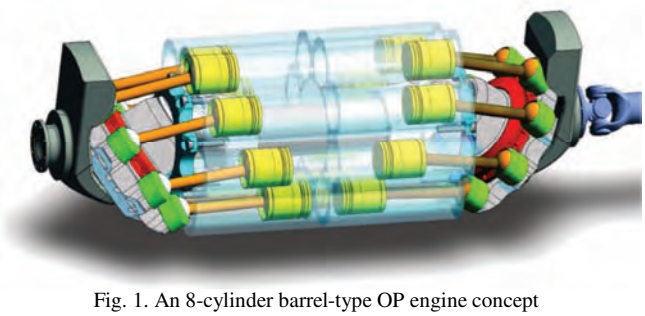

Fig. 1. An 8-cylinder barrel-type OP engine concept

The possibility of achieving high thermal efficiency brings Opposed-Piston (OP) engines back into interest of research centres. An advantage of such design is that combustion chamber is formed between moving pistons. The main thermal benefits arise from the geometrical shape of the combustion chamber. The ratio of the area to the volume of the combustion chamber A/V in the OP engine is

twice lower than in conventional IC engines [15] resulting in low heat losses and increased thermal efficiency. In the OP engine designed as a 2-stroke the poppet valves become redundant and with adapting a uniflow scavenging, the volumetric, trapping and scavenging efficiency become comparable with a 4-stroke. Because of the lack of the cylinder head, a scavenging process need to be handled differently than in a conventional 4-stroke engine. In the OP engine usually intake and exhaust ports in the cylinder liner are responsible for the scavenging. When pistons reach their Bottom Dead Centre (BDC), ports are opened and charge is exchanged due to pressure difference between the intake and exhaust manifolds.

Several studies have been dedicated to investigation of thermal benefits of OP engine configuration. For example in [16] authors performed detailed thermodynamic analysis to demonstrate the fundamental efficiency advantage of a 2-stroke OP engine over a standard 4-stroke engine. They found that the 4-stroke OP have increased indicated thermal efficiency compared to the 4-storke conventional engine. Furthermore, the 2-stroke OP engine additionally benefitted from doubled firing frequency, which allowed for leaner operating conditions and reduced energy release densities resulting in shorter combustion durations without exceeding maximum rate of pressure rise constraints. When evaluated over a representative engine speed/load operating map, the 2-stroke OP engine achieved 10.4% lower specific fuel consumption than the 4-stroke OP engine.

3. Syngas combustion modelling

In order to properly predict ignition and combustion processes in dual-fuel engine running on syngas it is necessary to account for diesel pilot spray, variable composition of the fuel, charge stratification or wall interaction, what leads to multi-dimensional CFD modelling with detailed kinetic schemes for fuel oxidation. Furthermore, modelling ignition process from diesel pilot requires to use kinetic scheme which incorporates chemical reactions for $CH_4/CO/H_2$ as well as for diesel surrogate, n-heptane (n-C_7H_{16}). Although, this kind of mechanisms are available, they usually have too many species to be directly used for 3D CFD numerical simulations of IC engine. For example POLIMI_TOT kinetic mechanism [17] comprises 484 species and 19341 reactions, while mechanism that can be used 3D CFD engine simulations should be the size of less than 100 species and 500 reactions in order to provide reasonable computation times.

During recent years several kinetic schemes for oxidation of $CH_4/CO/H_2$ mixtures that could be used for 3D CFD modelling of syngas combustion have been developed. Some of them are GRImech-3.0 [18], USC Mech 2.0 [19], POLIMI_C1C3 [20] or Sandiego [21]. However, as already mentioned, they are not suitable for dual-fuel engine simulations due to lack of n-C_7H_{16} oxidation chemistry. In order to overcome this problem, Azimov et al. [12] developed their own mechanism for multidimensional CFD simulation of syngas combustion in a micro-pilot-ignited dual-fuel engine. They combined simple mechanisms for CH_4, H_2/CO and $H_2/CO/O_2$ oxidation and included a single-step reaction chemistry of n-C_7H_{16}. The mechanism was validated by using a chemical kinetics code and a multidimensional CFD code, and the results were compared with experimental data of combustion in a supercharged dual-fuel engine. The mechanism predicted the engine performance well, including the cylinder pressure history, heat-release rate data with respect to syngas composition equivalence ratio, and injection timing.

4. Construction and validation of syngas/n-heptane kinetic mechanism

In current work authors decided that the best way to model syngas combustion in pilot-ignited dual-fuel engine is to combine GRImech-3.0 [18], which is well known and validated kinetic scheme for $CH_4/CO/H_2$ oxidation, with chemistry of n-C_7H_{16}. However, instead of using only single reaction chemistry like in [12], a simple and validated scheme for n-C_7H_{16} oxidation from Wisconsin ERC [22] was combined with GRImech-3.0. Any duplicate reactions were eliminated from n-C_7H_{16} scheme resulting in final mechanism comprising 61 species and 347 reactions. The new mechanism ERC-GRI was validated against experimental data of ignition delay times (IDT) of methane/air [23] and n-heptane/air [24] mixtures, as well as against experimental data of laminar burning velocity (LBV) of methane/air [25] and n-heptane/air [26] mixtures. Ignition delay time simulations were performed in a constant volume reactor with adaptive time step in Cantera 2.3.0. in Matlab R2016b environment. Laminar burning velocities were calculated in Cantera 2.3.0. in Python 3.6. environment using free flame model and automatic refinement of a grid. Results of validation are given in Fig. 2, Fig. 3, Fig. 4 and Fig. 5.

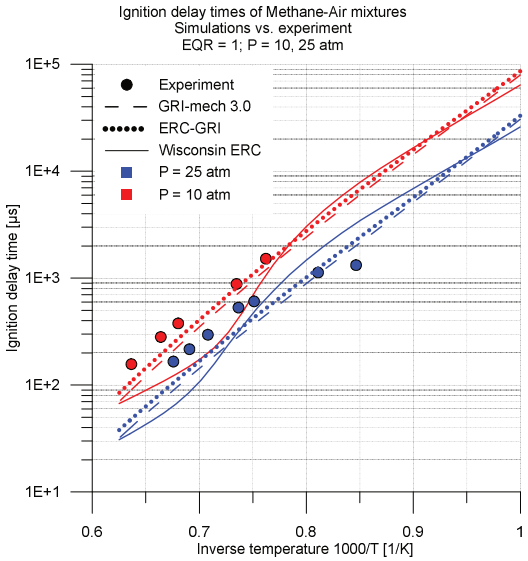

Fig. 2. Validation of IDTs for methane/air mixtures

Results of validation show that Wisconsin ERC mechanism was able to predict IDTs of n-heptane/air mixtures with reasonable agreement. On the other hand, it predicted LBVs to be twice as high as experimental values for n-heptane/air mixtures. Interestingly, combination of mechanisms in a single ERC-GRI mechanism resulted in an improvement of both IDTs and LBVs agreement for n-heptane/air mixtures. Furthermore, the ability of correct

prediction of IDTs and LBVs for methane/air mixtures from GRImech was remained. Overall, results suggest that new mechanism shows reasonable agreement with experimental IDTs and LBVs and can be used for multidimensional CFD simulations in a dual-fuel engine.

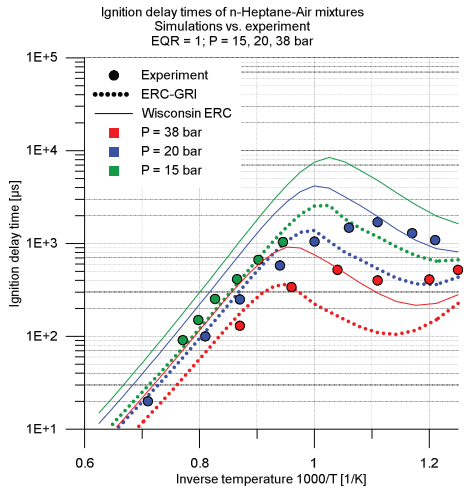

Fig. 3. Validation of IDTs for n-heptane/air mixtures

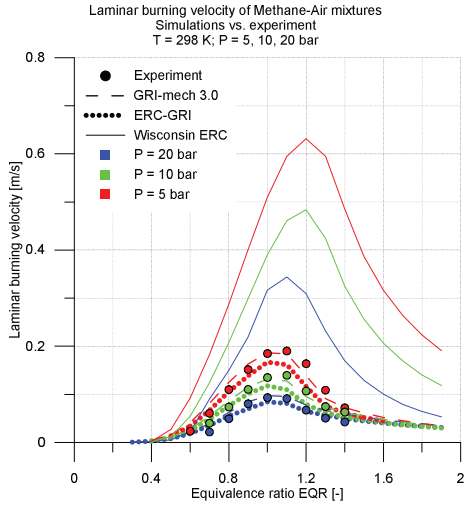

Fig. 4. Validation of LBVs for methane/air mixtures

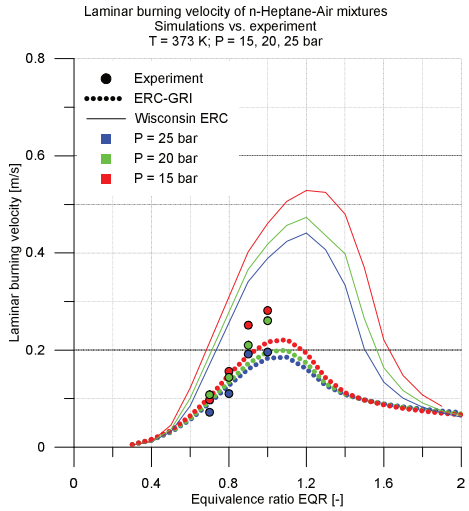

Fig. 5. Validation of LBVs for n-heptane/air mixtures

5. Engine setup

The engine considered in this study is a 2-cylinder, 2-stroke, barrel-type OP engine with cylinders' axes parallel to the shaft axis. It is a research engine being currently developed at Warsaw University of Technology. The engine is mainly developed for power generation application with utilization of low calorific syngas as a fuel. However, the construction of the engine allows for operation on different kind of fuels with different ignition modes. Namely, it is possible to run the engine in SI mode, micro-pilot-ignition mode or CAI mode. The basic engine parameters are given in Table 1.

Table 1. Engine parameters

Engine type	2-stroke Opposed-Piston Turbocharged
Number of cylinders	2
Bore	0.055 m
Stroke	0.2 m
Engine speed	1500 rpm
Compression ratio	VCR 8÷18
Fuel	Syngas Natural gas Gasoline Diesel
Ignition	SI MPI CAI
Injector type	Hollow Cone
Injection pressure	25 MPa

Although it is possible to utilize different fuels in the engine, this study is focused on syngas combustion simulations. A composition of the syngas considered in this work is given in Table 2. One can notice significant amount of inert gases in the fuel. Hence, the Lower Heating Value of the fuel is only 4.74 MJ/kg. Additionally, engine operation on pure methane was modelled in order to have a comparison between low calorific syngas and methane which is well known and investigated fuel.

Table 2. Syngas composition

Species	Mass fraction	Mole fraction
CH_4	0.02640	0.04586
H_2	0.00519	0.07175
CO_2	0.24403	0.15453
H_2O	0.01289	0.01994
CO	0.17435	0.17346
C_2H_2	0.00186	0.00199
C_2H_4	0.02007	0.01994
N_2	0.51521	0.51254

The biggest challenge associated with syngas combustion is its variable composition which can influence the ignition and combustion processes. In order to assure reliable ignition, diesel-pilot is utilized for initiation of combustion. As for the combustion process itself, the engine runs with VCR which can be adjusted according to current load and fuel composition. The goal is to work always with the

highest possible compression ratio for high efficiency and on the same time avoid knock, which is related to the excessive heat release rate.

In case of CAI operation, which is also possible with the OP engine, additional issue of the ignition timing control has to be taken into account. A proposed solution is closed-loop control based on VCR. However, application of CAI for syngas with variable composition still can be very challenging. Hence, the investigated engine is equipped with the following solutions that will allow CAI combustion control:

- Variable Compression Ratio for indirect ignition timing control,
- Variable Port Timing for scavenging and EGR control,
- Direct fuel injection for fuel stratification and limiting the heat release rate,
- Manifold Water Injection for indirect ignition timing control and limiting knock,
- Direct Water Injection for ignition control through direct internal EGR cooling,
- Turbocharging for increased engines IMEP and wider operation area.

6. Simulations setup

6.1. Operating conditions in simulations

Numerical simulations of combustion in this study were performed using the AVL Fire 3D CFD solver based on Finite Volume Method (FVM) discretization. For turbulence modelling, the k-ζ-f turbulence model was used [27]. For hydrocarbon oxidation, the kinetic scheme described in section 4. was used. Simulations were performed for two types of ignition – Micro-Pilot-Ignition and CAI. In case of MPI both CH_4 and syngas fuels were considered. As for CAI, only cases with syngas were calculated in order to define possible operating points of the engine running on this fuel. Summary of operating conditions considered in simulations is given in Table 3. It includes three different boost pressures P_b and corresponding intake temperatures as well as equivalence ratios, compression ratios and energy fraction of the pilot which were defined in simulations.

Table 3. Operating conditions

Boost pressure P_b	3.0 bar (absolute) 2.5 bar (absolute) 2.0 bar (absolute)
Intake temperature	410 K (at 3.0 bar) 390 K (at 2.5 bar) 365 K (at 2.0 bar)
Equivalence ratio	0.5 1.0
Compression Ratio	8–14
Fuel in simulations	Syngas Methane
Ignition	MPI CAI
Pilot energy fraction	5.0–10.0%
EGR mass fraction	6.5%

6.2. Numerical mesh and boundary conditions

Before setting up simulations, numerical mesh was prepared for one cylinder and half of the intake and exhaust manifolds. Two types of meshes were defined – steady mesh for intake/exhaust manifolds and moving mesh for cylinder volume. Movement of the cylinder mesh was handled by changing positions of the nodes representing intake-side and exhaust-side pistons separately according to the given piston displacement curves. Simultaneously, positions of the nodes between pistons were interpolated every time step according to the pistons displacement. Meshes of the cylinder and intake/exhaust manifolds were connected with *Arbitrary Interface* at the contact of the cylinder wall and intake/exhaust ports. Total number of mesh elements for the entire model was of 1 200 000, while mesh for the cylinder itself consisted of 200 000 elements. The mesh of the cylinder used for simulations together with applied temperature boundary conditions is presented in Fig. 6. In this study temperature boundary condition was assumed to be dependent on the load, which is related to the boost pressure. Different temperatures were assumed on the intake-side and exhaust-side pistons. On the cylinder wall a temperature profile was defined. Summary of temperature boundary conditions is given in Table 4.

Table 4. Temperature at boundary walls

	Intake-side piston T_{in}	Exhaust-side piston T_{ex}	Cylinder wall T_{cyl}
P_b = 2.0 bar	550 K	605 K	400–550 K
P_b = 2.5 bar	600 K	660 K	400–600 K
P_b = 3.0 bar	650 K	715 K	400–650 K

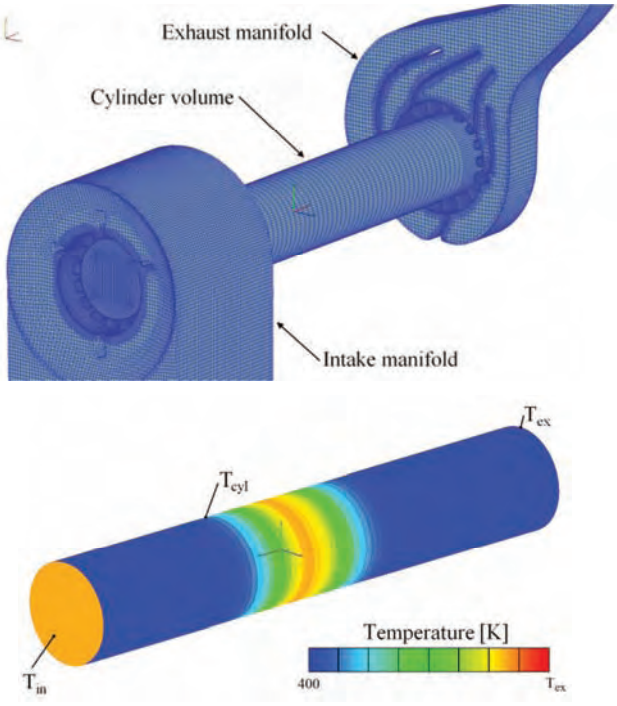

Fig. 6. Numerical mesh and temperature boundary conditions

6.3. Operation targets and summary of cases

Simulations were performed for different compression ratios, equivalence ratios and different amounts of directly or indirectly injected water. For each case two engine cycles were calculated. For the first cycle approximate initial conditions in the cylinder before the scavenging were assumed. At the end of the first cycle realistic conditions in

the cylinder were obtained for the second cycle scavenging and combustion. Only results from the second cycle are presented and compared in this study.

In order to compare the results and draw conclusion specific targets for the combustion results need to be assumed. In this study following parameters are considered:

– Crank angle of 50% accumulated heat release (CA50) was considered as a measure of combustion timing. Target for CA50 in this study was 5.0°CA ATDC;
– Maximum pressure rise dP/dCA was assumed as the limiting parameter for the knock, since the knock itself was not modelled in this work. Target for maximum dP/dCA was of 10 bar/CA;
– Delay between start of pilot injection and crank angle of 5% accumulated heat release (CA5D). Although no target was defined for CA5D time, it helped to compare delay of the primary fuel ignition between cases.

For each type of ignition (MPI or CAI) different procedures for combustion timing control were adopted. In case of MPI injection timing of the pilot was adjusted in order to meet the CA50 target, while for CAI adjustment of compression ratio was performed for each calculated case to match the CA50 target.

A combination of two different fuels, different compression ratios, different equivalence ratios, different boost pressures and different ignition/combustion modes resulted in a number of calculated cases, which are summarized in Table 5. The case naming follows the pattern XCR000ER00P00, where X stands for fuel (M for methane and S for syngas), CR000 is compression ratio with one decimal place, ER00 is equivalence ratio with one decimal place and P00 is boost pressure with one decimal place.

Table 5. Summary of investigated cases

	P_b = 2.0 bar	P_b = 2.5 bar	P_b = 3.0 bar
METHANE MPI	MCR110ER10P20 MCR120ER10P20 MCR130ER10P20 MCR130ER05P20	MCR090ER10P25 MCR100ER10P25 MCR110ER10P25 MCR100ER05P25	MCR080ER10P30 MCR090ER10P30 MCR080ER05P30
SYNGAS MPI	SCR110ER10P20 SCR120ER10P20 SCR130ER10P20 SCR130ER05P20	SCR090ER10P25 SCR100ER10P25 SCR110ER10P25 SCR100ER05P25	SCR080ER10P30 SCR090ER10P30 SCR080ER05P30
SYNGAS CAI	SCR140ER05P20	SCR112ER05P25	SCR092ER05P30

7. Results and discussion

7.1. Scavenging results

Presentation of the results should start with results of the scavenging process. During the scavenging in a 2-stroke engine the exhaust gases are removed from the combustion chamber which is filled with the fresh charge at the same time. During this process it is important to remove as much of combustion products from the previous cycle as possible and not to let fuel reach the exhaust. If any fuel reaches the exhaust it is considered as HC emission. Investigated engine is equipped with specially designed intake and exhaust systems which allow for charge stratification and minimize fuel mass lost to the exhaust. Results of the scavenging process for boost pressure of P_b = 3.0 bar and compression ratio CR = 9.0 are given in Fig. 7. It can be noticed that temperature stratification of the charge is related to the EGR, which was left in the chamber after the scavenging. Although noticeable amount of exhaust gases concentration is visible close to the exhaust-side piston, the overall EGR mass fraction in the engine can be reduced up to 5%. The advantage of the incorporated intake/exhaust system can be seen on the plots of equivalence ratio in Fig. 7. Generally combustion chamber is divided in 4 zones. Starting from the left side (intake-side) the zones are air/fuel/air/exhaust. Thanks to this separation it was possible to reduce fuel lost to exhaust and increase charge stratification. Highly stratified charge is supposed to limit excessive heat release and allow engine operation at increased compression ratios for high efficiency.

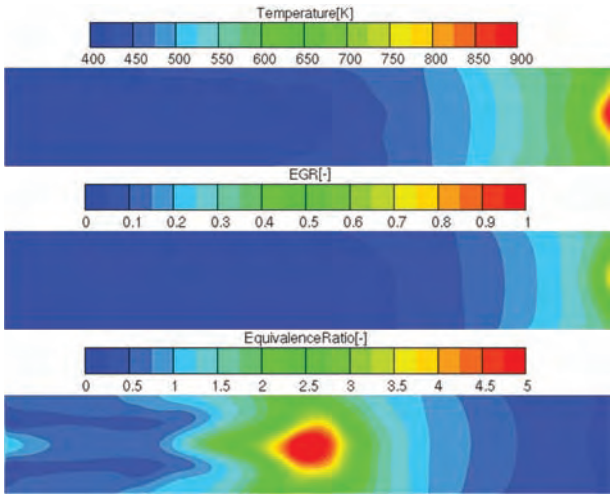

Fig. 7. Results of temperature, EGR fraction and equivalence ratio in cross-section along the cylinder

7.2. Combustion with ϕ = 1.0 and MPI mode

The determination of the possible operation points of the OP engine running in dual-fuel mode started with simulations of stoichiometric mixtures. Calculations were performed for both methane and syngas to have a comparison between these fuels. The goal was to meet CA50 timing and work with the highest possible compression ratio at which pressure rise dP/dCA will not exceed 10.0 bar/CAD. The CA5D time was also monitored in order to know how given conditions influence the delay time between start of pilot injection and ignition of the primary fuel. The injected mass of the pilot was adjusted for each case to contain 5% of the total energy released in one cycle. Results of calculated cases are given in Table 6. Cases which fulfilled both defined targets are marked with green color. For methane it should be possible to work with P_b = 3.0 bar and CR = 8.0, P_b = 2.5 bar and CR = 9.0, P_b = 2.0 bar and CR = 11.0. The lower were intake pressure and temperature, the higher compression ratio could be set. For syngas it was not possible to determine suitable operating points.

The main problem was to adjust CA50 timing. It was mainly because of the delay time CA5D which normally was much longer than in corresponding cases with methane. The reason for this behavior was probably composition of the combustible mixture. For syngas, significant fraction of the inert gases (N_2, CO_2, H_2O) in the fuel resulted low O_2 mass fraction in the final mixture, which was of ~12.8% in

all cases, while for methane O_2 mass fraction in the mixture was of ~20.6% in all cases. This difference resulted in longer delay of pilot ignition and difficulties in controlling combustion timing. On the other hand, one can notice that in some cases CA5D delay time was shorter for syngas than for methane (e.g. case CR080ER10P30). It was caused by auto-ignition of the mixture before or during the pilot injection, which also did not allow to control timing of combustion. Finally, when conditions in the chamber allowed to obtain correct CA50 timing, they caused excessive heat release rate and maximum pressure rise dP/dCA beyond the specified limit.

Table 6. Cases calculated with ϕ = 1.0 and MPI mode

Case	P_b [bar]	CR [–]	Pilot [CA]	Pilot [mg]	CA5D [CAD]	CA50 [CA]	dP/dCA [bar/CAD]
MCR080ER10P30	3.0	8.0	–13.2	5.0	12.0	5.2	9.48
SCR080ER10P30			–13.2	3.7	22.7	16.5	7.6
MCR090ER10P30		9.0	–9.2	5.0	8.6	5.1	15.27
SCR090ER10P30			–6.6	3.7	4.6	3.1	13.8
MCR090ER10P25	2.5	9.0	–14.6	4.5	13.1	4.9	9.14
SCR090ER10P25			–14.6	3.3	35.8	37.8	0.86
MCR100ER10P25		10.0	–10.2	4.5	9.3	5.0	11.72
SCR100ER10P25			–14.6	3.3	15.0	5.2	16.9
MCR110ER10P25		11.0	–8.0	4.5	7.4	5.0	17.28
SCR110ER10P25			–7.0	3.3	7.2	3.6	22.77
MCR110ER10P20	2.0	11.0	–13.2	3.8	11.8	4.8	9.58
SCR110ER10P20			–13.2	2.8	34.2	38.3	0.99
MCR120ER10P20		12.0	–9.8	3.8	9.0	5.1	11.51
SCR120ER10P20			–15.2	2.8	15.7	5.4	20.6
MCR130ER10P20		13.0	–8.2	3.8	7.5	4.9	15.8
SCR130ER10P20			–9.0	2.8	9.8	4.8	24.12

7.3. Combustion with ϕ = 0.5 and MPI mode

Due to problems with combustion control of stoichiometric syngas mixture it was decided to calculate cases with equivalence ratio reduced to ϕ = 0.5. Only cases for which it was possible to determine operating points in previous section were recalculated. Mass of the diesel-pilot remained the same and now it contains ~10.0% of the total energy released in the cycle for methane fuel and ~8.0% of the total energy released in the cycle for syngas fuel. Results are given in Table 7, plots of pressure trace and ROHR are given in Fig. 8 and Fig. 9, visualization of ignition and combustion processes is shown in Fig. 10 and Fig. 11. Reduction of equivalence ratio resulted in increase of the O_2 mass fraction in the methane mixture to ~21.2% and in the syngas mixture to ~16.6%. This increase is supposed to shorten ignition delay of diesel-pilot and improve ignition process of the syngas. Eventually, it was possible to meet CA50 and dP/dCA targets for all recalculated cases. Although CA5D times were still longer for syngas mixture, it was possible to control combustion timing for reduced equivalence ratios.

It is interesting to compare pressure trace and ROHR between calculated cases. In Fig. 8 and Fig. 9 one can notice characteristic profile of the heat release which was also reported by other researchers in [7–12]. Heat release is divided in two stages. The first stage is ignition of the diesel-pilot followed by the flame propagation of the primary fuel. The second stage is auto-ignition of the end gas, that results in the secondary peak of the heat release. Generally, heat release profile is similar in considered cases for methane and syngas combustion. However, some differences can be noticed. For methane the primary peak of heat release is higher which is caused by faster combustion of the diesel-pilot, as well as larger dose of the pilot. For syngas the secondary peak of heat release is higher, what suggests that syngas is more prone to auto-ignition.

Table 7. Cases calculated with ϕ = 0.5 and MPI mode

Case	P_b [bar]	CR [–]	Pilot [CA]	Pilot [mg]	CA5D [CAD]	CA50 [CA]	dP/dCA [bar/CAD]
MCR080ER05P30	3.0	8.0	–14.0	5.0	8.3	5.1	7.6
SCR080ER05P30	3.0	8.0	–16.7	3.7	16.2	4.8	6.7
MCR110ER05P25	2.5	11.0	–12.2	4.5	6.9	4.9	8.2
SCR110ER05P25	2.5	11.0	–11.2	3.3	8.6	5.0	6.1
MCR130ER05P20	2.0	13.0	–11.2	3.8	5.8	4.8	9.3
SCR130ER05P20	2.0	13.0	–8.2	2.8	6.6	4.9	9.0

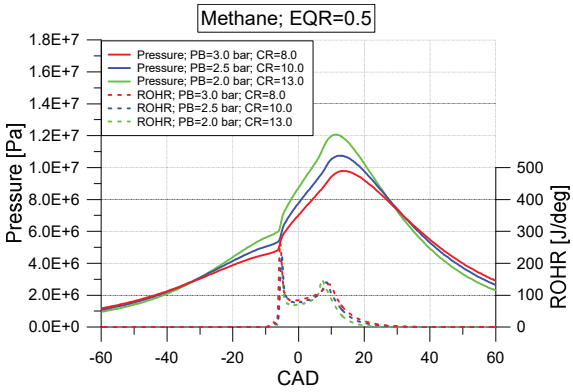

Fig. 8. Pressure trace and ROHR for methane and MPI mode

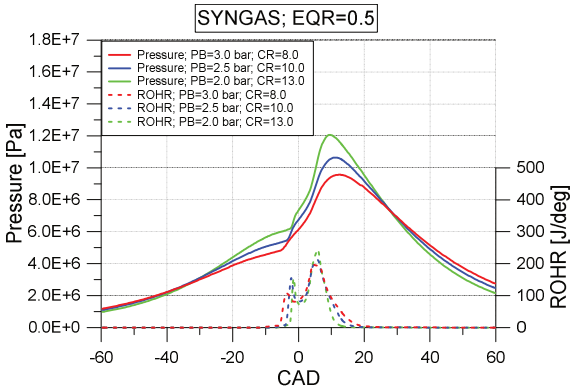

Fig. 9. Pressure trace and ROHR for syngas and MPI mode

Similar observation can be made based on ignition and combustion visualization presented in Fig. 10 and Fig. 11. In these figures 3D results of spray, temperature in a plane along the cylinder and flame surface are shown. Surface that represents the flame is an iso-surface of the temperature of 1200 K. In case of syngas longer delay between start

of pilot injection and ignition of the primary fuel can be distinguished as well as slower flame propagation in early stage of combustion process. Also auto-ignition of the end gas is more clear for syngas than for methane. End gas always ignites at the exhaust-side piston, in the region of high temperature EGR which was left from previous cycle.

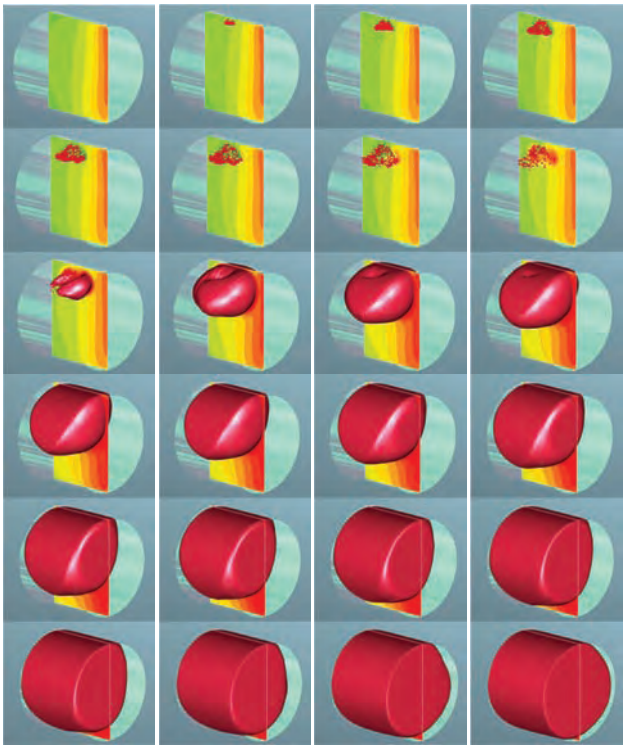

Fig. 10. Visualisation of ignition and combustion for case MCR080ER05P30 (methane MPI)

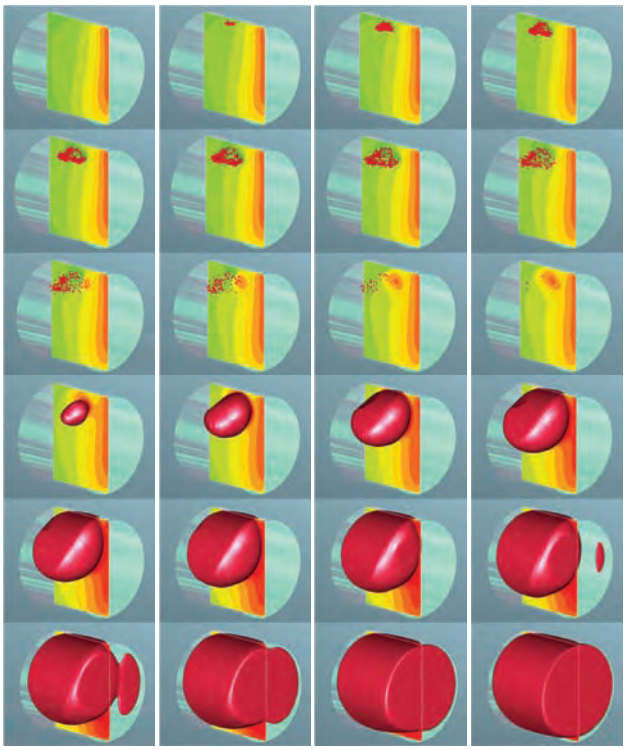

Fig. 11. Visualisation of ignition and combustion for case SCR080ER05P30 (syngas MPI)

7.4. Combustion with ϕ = 0.5 and CAI mode

The last calculated set of cases considered syngas combustion in CAI mode. The benefits arising from engine running in CAI mode are: independence on diesel fuel (no pilot), increased efficiency and low emissions. The procedure for simulations was to start with cases calculated with MPI mode and equivalence ratio of ϕ = 0.5, remove injection of diesel pilot and adjust compression ratio in order to meet the CA50 target. Based on results given in Table 8 it should be possible to run the engine in CAI mode with P_b = 3.0 bar and CR = 9.2, P_b = 2.5 bar and CR = 11.2, P_b = 2.0 bar and CR = 14.0. Only for case SCR140ER05P20 pressure rise limit was exceed. However, it was still very close to 10.0 bar/CA and it should be possible to reach this limit with further adjustment of equivalence ratio.

Table 8. Cases calculated with ϕ = 0.5 and CAI mode

Case	P_b [bar]	CR [–]	CA50 [CA]	dP/dCA [bar/CAD]
SCR092ER05P30	3.0	9.2	5.5	5.2
SCR112ER05P25	2.5	11.2	4.6	7.3
SCR140ER05P20	2.0	14.0	5.3	11.8

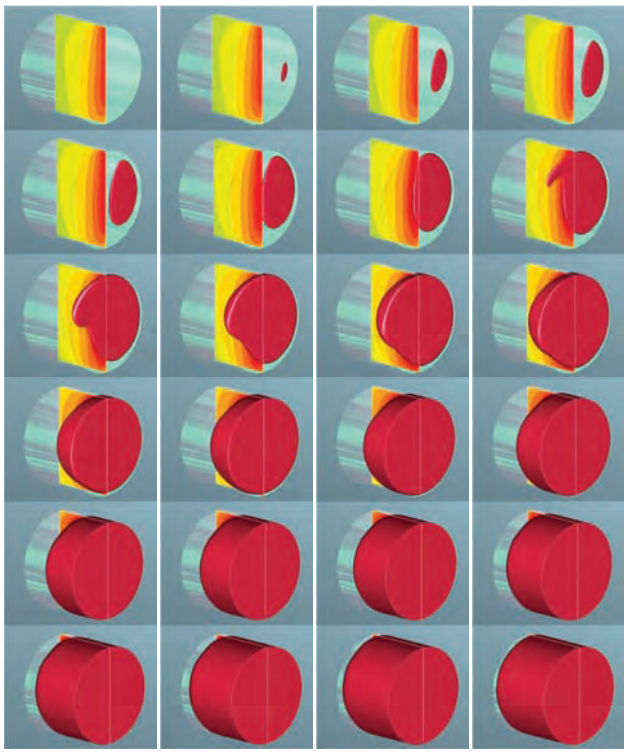

Fig. 12. Pressure trace and ROHR for syngas and CAI mode

Results of pressure trace, ROHR and visualization of CAI combustion are given in Fig. 12 and Fig. 13. It is interesting to see difference between CAI combustion mode and MPI dual-fuel mode. In case CAI mode mixture always ignites at the exhaust-side piston in a region of high temperature EGR. Then flame propagates from the exhaust-side piston to the intake-side piston through stratified mixture. Because there is no secondary auto-ignition, there is also no secondary peak in the heat release.

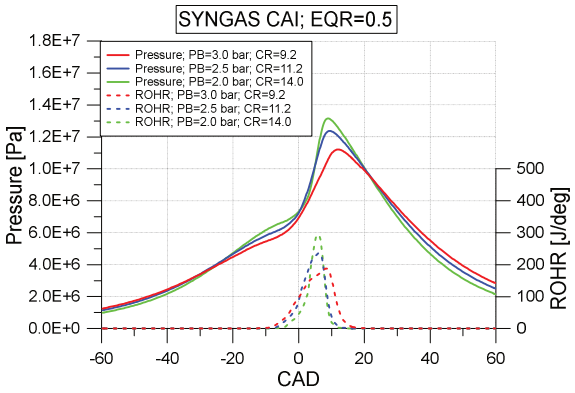

Fig. 13.Visualisation of ignition and combustion for case SCR092ER05P30 (syngas CAI)

7.5. Performance and emissions

This section contains comparison between possible operating points in terms of performance and emissions. Results are also referred to EU regulations on pollutant emission in Non-Road Mobile Machinery [28]. Investigated engine fits in NRE-v/c-5 category of Stage V standards, for which CO emission limit is of 5.0 g/kWh, HC emission limit is of 0.19 g/kWh and NO_x emission limit is of 0.4 g/kWh. Results of IMEP, Indicated power, Thermal efficiency and emission of CO, HC and NO_x are given in Fig. 14–Fig. 19. When it comes to results of IMEP and power, it is clear that reduction of equivalence ratio for methane caused significant decrease in performance. For equivalence ratio ϕ = 0.5 and MPI combustion there is visible difference between methane and syngas, which comes from low LHV of syngas. Performance results for syngas combustion in MPI and CAI modes are comparable.

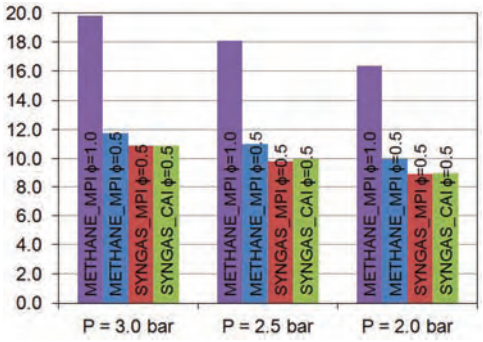

Fig. 14. Results of IMEP for final operating points

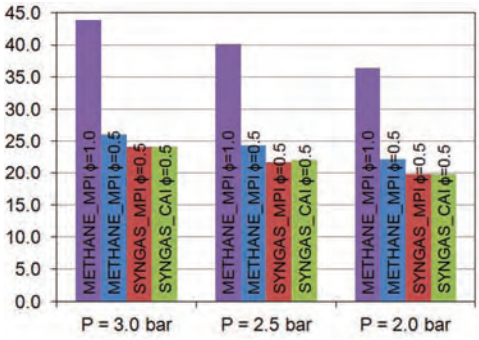

Fig. 15. Results of power for final operating points

In case of thermal efficiency again differences between equivalence ratio ϕ = 1.0 and ϕ = 0.5 for methane can be noticed. It can be related to the fact that for the lowered equivalence ratio, temperatures in the combustion chamber were also reduced. With reduced temperatures heat loses were lower and thermal efficiency increased. Furthermore, thermal efficiency generally increased with compression ratio and the highest obtained efficiency was of 47.8% for case MCR130ER05P20.

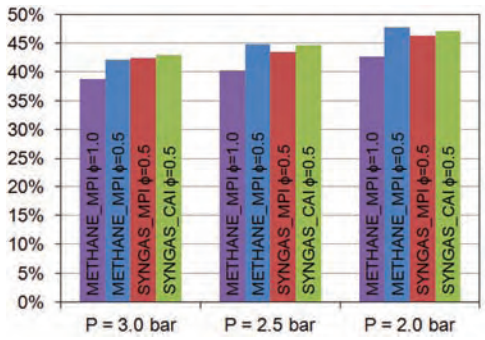

Fig. 16. Results of thermal efficiency for final operating points

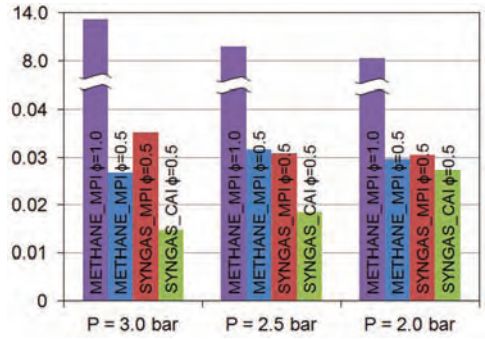

Fig. 17. Results of CO emission for final operating points

CO emission was the highest for cases with equivalence ratio of ϕ = 1.0. Change of equivalence ratio for methane to ϕ = 0.5 resulted in drastic reduction of CO emission. Then comparable results were obtained for methane and syngas with MPI mode. The lowest CO emission was obtained for syngas combustion in CAI mode and was much lower than EU regulations limit.

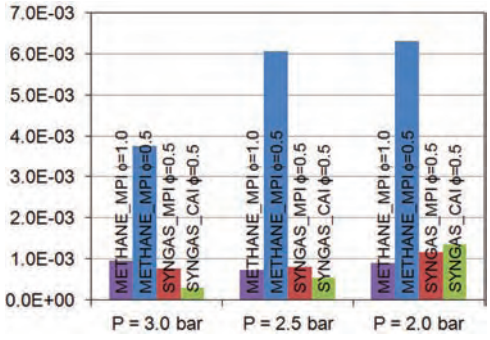

Fig. 18. Results of HC emission for final operating points

HC emission was very low in all investigated cases. The reason for this result is probably simplified geometry, which did not include piston ring pack and other crevice. In

real engine some parts of the charge are forced into narrow regions during the compression stroke and returned to the combustion chamber during the expansion stroke to be expelled with the exhaust gases and contribute to HC emission.

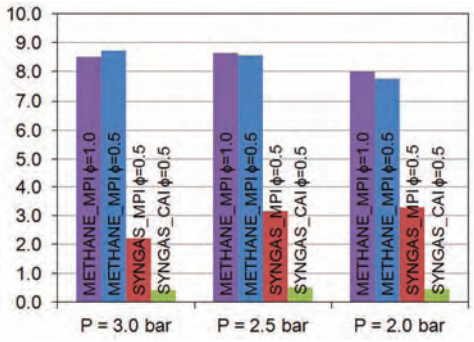

Fig. 19. Results of NO_x emission for final operating points

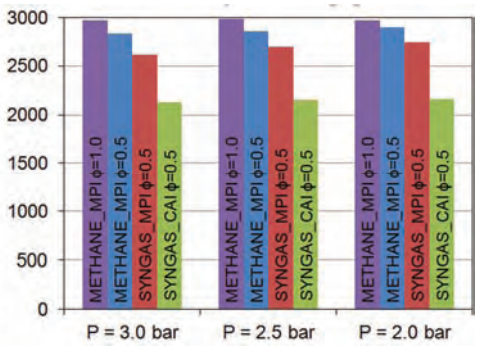

Fig. 20. Maximum temperatures in the combustion chamber

The last presented result is NO_x emission. For methane combustion very similar NO_x emission was obtained for equivalence ratio $\phi = 1.0$ and $\phi = 0.5$. Although maximum temperatures in the combustion chamber and NO_x mass were reduced with lower equivalence ratio, the power output was also reduced and final NO_x emission in g/kWh was not improved. NO_x emission for syngas with MPI mode was over 50% lower than for methane, which can be related to lower maximum temperatures in the combustion chamber in case of syngas. The lowest maximum temperatures in the combustion chamber were obtained for syngas combustion with CAI mode, what contributed to very low final NO_x emission, comparable to EU regulation limits of 0.4 g/kWh.

8. Conclusions

In this work multidimensional CFD combustion simulations for the 2-stroke, 2-cylinder barrel-type Opposed-Piston engine were performed. Engine operation in dual-fuel mode with MPI was considered for methane or syngas utilized as a primary fuel. Additionally, engine operation on syngas in CAI mode was analyzed. The following conclusions can be drawn:

– It should be possible to operate the engine on methane with stoichiometric mixtures and ignition from diesel-pilot;
– Significant content of inert gases in syngas and low oxygen mass fraction in the final stoichiometric mixture resulted in long ignition delays of diesel-pilot and problems with combustion timing control in some of investigated cases. In cases where it was possible to control the combustion timing, auto-ignition of end gas and excessive heat release occurred. Finally, it was not possible to establish suitable operating point for engine running on stoichiometric mixtures of syngas;
– Reduction of equivalence ratio to $\phi = 0.5$ allowed for engine operation in dual-fuel mode for both methane and syngas with ignition from diesel-pilot. The drawback was decrease in performance, but advantage was reduction of CO emission and increase in efficiency;
– The lowest emissions were obtained for engine operation on syngas in CAI mode with reduced equivalence ratios. Very low NO_x emission were obtained due to limited maximum temperatures in the combustion chamber. Final engine-out emissions in CAI mode were within limits of current EU regulations.

Acknowledgements

This work is a part of Applied Research Programme of the National Centre for Research and Development within the scope of applied research in industry branches (programme path B) „Badania wysokosprawnego silnika wykorzystującego technologię HCCI do zastosowań w energetyce rozproszonej" (GENEKO).

The Fire calculation code was used as per the AVL AST University Partnership Program.

Nomenclature

ATDC	after top dead center
BTDC	before top dead center
CA	crank angle
CA50	crank angle of 50% accumulated heat
CA5D	delay of 5% accumulated heat
CAD	crank angle degrees
CAI	controlled auto ignition
CI	compression ignition
CFD	computational fluid dynamics
CR	compression ratio
DF	dual fuel
EGR	exhaust gas recirculation
HCCI	homogeneous charge compression ignition
IDT	ignition delay time
IC	internal combustion
IMEP	indicated mean effective pressure
LBV	laminar burning velocity
LHV	lower heating value
LPG	liquified petrolum gas
MPI	micro pilot ignition
OP	opposed piston
ROHR	rate of heat release
SI	spark ignition
VCR	variable compression ratio

Bibliography

[1] LIEUWEN, T., YANG, V., YETTER, R. Synthesis gas combustion: fundamentals and applications. Taylor & Francis Group; 2010.

[2] BADE SHRESTHA, S.O., KARIM, G.A. Hydrogen as an additive to methane for spark ignition engine applications. *International Journal of Hydrogen Energy*. **24**(6), 577-586.

[3] PUSHP, M., MANDE, S. Development of 100% producer gas engine and field testing with pid governor mechanism for variable load operation. *SAE Technical Paper*. 2008, 2008-28-0035.

[4] YAMASAKI, Y., TOMATSU, G., NAGATA, Y., KANEKO, S. Development of a small size gas engine system with biomass gas (combustion characteristics of the wood chip pyrolysis gas). *SAE Technical Paper*. 2007, 2007-01-3612.

[5] ANDO, Y., YOSHIKAWA, K., BECK, M., ENDO, H. Research and development of a low-BTU gas-driven engine for waste gasification and power generation. *Energy*. **30**(11–12), 2206-2218.

[6] TOMITA, E., FUKATANI, N., KAWAHARA, N. et al. Combustion characteristics and performance of supercharged pyrolysis gas engine with micro-pilot ignition. *CIMAC congress*. 2007. Paper No. 178.

[7] ROY, M.M., TOMITA, E., KAWAHARA, N. et al. Effect of fuel injection parameters on engine performance and emissions of a supercharged producer gas-diesel dual fuel engine. *SAE Technical Paper*. 2009, 2009-01-1848.

[8] ROY, M.M., TOMITA E., KAWAHARA N. et al. Performance and emission comparison of a supercharged dual-fuel engine fueled by producer gases with varying hydrogen content. *International Journal of Hydrogen Energy*. 2009.

[9] ROY, M.M., TOMITA, E., KAWAHARA N. et al. Performance and emissions of a supercharged dual-fuel engine fueled by hydrogen-rich coke oven gas. *International Journal of Hydrogen Energy*. 2009.

[10] AZIMOV, U., TOMITA, E., KAWAHARA, N. Ignition, Combustion and exhaust emission characteristics of micro-pilot ignited dual-fuel engine operated under PREMIER combustion mode. *SAE Technical Paper*. 2011, 2011-01-1764.

[11] AZIMOV U., TOMITA E., KAWAHARA N., HARADA Y. Effect of syngas composition on combustion and exhaust emission characteristics in a pilot-ignited dual-fuel engine operated in PREMIER combustion mode. *International Journal of Hydrogen Energy*. 2011, 36, 11985–11996.

[12] AZIMOV, U., OKUNO, M., TSUBOI, K. et al. Multidimensional CFD simulation of syngas combustion in a micro-pilot-ignited dual-fuel engine using a constructed chemical kinetics mechanism. *International Journal of Hydrogen Energy*. 2011, **36**, 13793–13807.

[13] ZHAO, H. HCCI and CAI engines for the automotive industry. *Woodhead Publishing*. 2007.

[14] BHADURI, S., BERGER, B., POCHET, M. et al. HCCI engine operated with unscrubbed biomass syngas. *Fuel Processing Technology*. 2017, **157**, 52-58.

[15] FLINT M. Opposed Piston Engines: Evolution, Use, and Future Applications. *Warrendale: SAE International*. 2010

[16] HEROLD, R.E., WAHL, M.H., REGNER, G. et al. Thermodynamic benefits of opposed-piston two stroke engines. *SAE Technical Paper*. 2011, 2011-01-2216.

[17] RANZI, E., FRASSOLDATI, A., GRANA, R. et al. Hierarchical and comparative kinetic modeling of laminar flame speeds of hydrocarbon and oxygenated fuels. *Progress in Energy and Combustion Science*. 2012, **38**(4), 468-501.

[18] SMITH, G.P., GOLDEN, D.M., FRENKLACH, M. et al. "GRI-Mech 3.0."

[19] WANG, H., YOU, X., JOSHI, A.V. et al. USC Mech Version II. High-Temperature Combustion Reaction Model of H2/CO/C1-C4 Compounds.

[20] RANZI, E., FRASSOLDATI, A., GRANA, R. et al. Hierarchical and comparative kinetic modeling of laminar flame speeds of hydrocarbon and oxygenated fuels. *Progress in Energy and Combustion Science*. 2012, **38**(4), 468-501.

[21] Mechanical and Aerospace Engineering (Combustion Research) – University of California at San Diego, "Chemical-Kinetic Mechanisms for Combustion Applications, San Diego Mechanism web page."

[22] PATEL, A., KONG, S., REITZ, R. Development and validation of a reduced reaction mechanism for HCCI engine simulations. *SAE Technical Paper*. 2004, 2004-01-0558.

[23] BURKE, U., SOMERS, K.P., O'TOOLE, P. et al. An ignition delay and kinetic modeling study of methane, dimethyl ether, and their mixtures at high pressures. *Combustion and Flame*. 2015, **162**(2) 315-330.

[24] ZHANG, K., BANYON, C., BUGLER, J., et al. An updated experimental and kinetic modeling study of n-heptane oxidation. *Combustion and Flame*. 2016, **172**, 116-135.

[25] ROZENCHAN, G., ZHU, D.L., LAW, C.K., TSE, S.D. Outward propagation, burning velocities, and chemical effects of methane flames up to 60 ATM. *Proceedings of the Combustion Institute*. 2002, **29**(2), 1461-1470.

[26] JERZEMBECK, S., PETERS, N., PEPIOT-DESJARDINS, P., PITSCH, H. Laminar burning velocities at high pressure for primary reference fuels and gasoline: Experimental and numerical investigation. *Combustion and Flame*. 2009, **156**(2), 292-301.

[27] HANJALIĆ, K., POPOVAC, M., HADZIABDIĆ, M. A robust near-wall elliptic-relaxation eddy-viscosity turbulence model for CFD. *International Journal of Heat and Fluid Flow*. 2004, **25**(6), 1047-1051.

[28] Regulation (EU) 2016/1628 of the European Parliament and of the Council of 14 September 2016 on requirements relating to gaseous and particulate pollutant emission limits and type-approval for internal combustion engines for non-road mobile machinery.

Rafał Pyszczek, MSc. – Faculty of Power and Aeronautical Engineering at Warsaw University of Technology.

e-mail: *Rafal.Pyszczek@itc.pw.edu.pl*

Agnieszka Jach, MSc. – Faculty of Power and Aeronautical Engineering at Warsaw University of Technology.

e-mail: *Agnieszka.Jach@itc.pw.edu.pl*

Paweł Mazuro, DEng. – Faculty of Power and Aeronautical Engineering at Warsaw University of Technology.

e-mail: *Pawel.Mazuro@itc.pw.edu.pl*

Prof. Teodorczyk Andrzej DSc., DEng.– Faculty of Power and Aeronautical Engineering at Warsaw University of Technology.

e-mail: *Andrzej.Teodorczyk@itc.pw.edu.pl*

Article citation info:
BUCZEK, K., LAUER, S. Firing order selection for a V20 commercial diesel engine with FEV Virtual Engine. *Combustion Engines*. 2017, **169**(2), 64-70. DOI: 10.19206/CE-2017-211

Konrad BUCZEK
Sven LAUER

CE-2017-211

Firing order selection for a V20 commercial diesel engine with FEV Virtual Engine

The continuously increasing mechanical and thermal loads of modern engines require optimization of the designs with incorporation of a wide range of different aspects. Application of advanced computer simulations in the development process for most engine components is well established, leading to the creation of well optimized products. However, the optimization of such design variables like the firing order, which influences engine operation in several disciplines, is still challenging. Considering the ever increasing peak firing pressure requirements, the layout of the firing order in multi-cylinder commercial engines is an efficient way to reduce crank train / overall engine vibration and main bearing loads, whilst controlling engine balancing and preserving adequate gas exchange dynamics.

The proposed general firing order selection process for four-stroke engines and, in particular, its first part being the optimization of the firing order based on crank train torsional vibration, is the main topic of this paper. The exemplary study for a V20 high speed commercial Diesel engine regarding the influence of the firing sequence on crank train torsional vibration has been conducted with the multibody dynamics simulation software "FEV Virtual Engine". It addresses various engine crankshaft layouts and engine applications.

Key words: *firing order, torsional vibration, commercial engine powertrain*

1. Introduction

Selection of the firing order for typical automotive engine, having only few cylinders, is relatively simple task, since the number of alternatives is limited. However, the number of feasible firing orders rises strongly with the number of cylinders and for multi-cylinder engines having more than 12 cylinders (being currently almost exclusively commercial diesel or gas engines) it reaches thousands of possibilities. Due to this, as well as due to strong influence of the firing order on several aspects of engine operation, the selection of the firing order is since decades an engineering challenge [3, 9].

The exceptional increase of computational speed in the last years allows for an investigation of firing order influence to a higher extend than ever before. In particular, the torsional vibration simulation of the crankshaft in frequency domain, which may currently return the basic results of one specific case within few seconds, enables the full factorial considerations on a big set of alternative firing orders. This is especially convenient, since the application of typical optimization techniques having an algorithm, which decides how to explore the design space in order to find the optimum, is not feasible, because of the integer valued nature of the firing order as specific design variables (a set of cylinder numbers with assigned firing angles or firing intervals).

There are certain boundary conditions, which limits the above-mentioned design variable space. For typical commercial vee engines, one such is the crankshaft layout, which defines engine internal/external balancing, while enabling realization of hundreds or thousands of alternative firing sequences.

2. Proposed firing order selection process [5, 6]

An overview of the proposed general firing order selection process is shown in Fig. 1. The process starts with the definition of an initial crank train design. For these basic data, alternative crankshaft layouts can be defined, including verification of engine external and internal balancing.

Subsequently, all alternative firing orders are to be generated. The set of alternative firing orders should contain only those firing orders which are possible within the considered crankshaft designs. This significantly reduces the number of cases to be subjected to further considerations.

Since in case of engines with crankshafts having several crank throws (e.g. V16 or V20 high speed commercial engines), crank train torsional vibration is one of the most challenging aspects to be controlled in engine bottom end design, the set of torsional vibration simulations in the frequency domain or 1D crankshaft simulations which additionally include quasi-static bending analysis of crank throws are to be performed subsequently. This full factorial investigation of the firing order influence is the first, torsional vibration-based, firing order optimization loop leading to a preselected set of beneficial firing orders.

Following the selection process, the preselected firing orders are to be subjected to further engine concept analyses which are hydrodynamic bearing simulation and gas dynamics simulation in the intake and exhaust ducts. As a result, a second firing order optimization loop is performed. In the last step, one or few final firing orders are to be considered in the time consuming detailed design engine simulations, to finally confirm the proper selection of the optimal firing order. This includes the analysis of crankshaft axial vibration being a new rising concern in development of high speed commercial engines [1].

Within such a firing order selection process, several backward loops are possible, including revision of base engine dimensions and change of the optimization objective targets.

The Firing Order Investigation Tool, enabling the investigation according to above-mentioned methodology, is already implemented for commercial software "FEV Virtual Engine". In its initial form, it allows the end user to automatically generate alternative firing orders for the predefined crankshaft layout, to run series of 1D crankshaft simulations by application of a known and proven functionality called Crank Concept Analysis and to evaluate the.

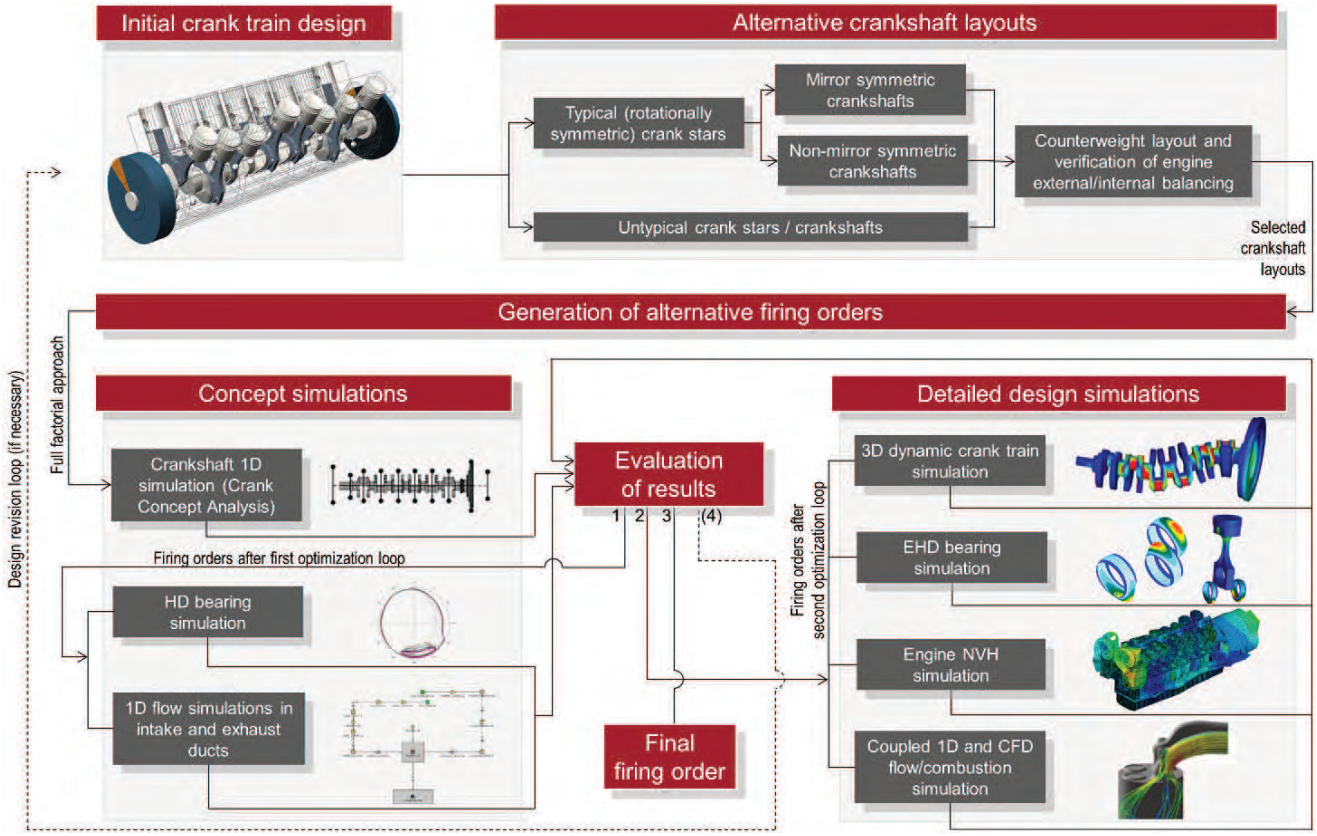

Fig. 1. General firing order selection process

results by use of multi-criteria optimization techniques popularized by Derringer and Suich [10The alternative firing orders are determined by execution of a specialized algorithm, which predecessor has been described in [4]. The procedure implemented for the "FEV Virtual Engine" has been significantly improved, enabling the generation of all feasible firing sequences for any defined crankshaft layout and engine configuration.

3. Exemplary investigation of the firing order influence on crank train torsional vibration

The above-mentioned approach has been applied in order to investigate the influence of the firing order in an exemplary V20 four-stroke high speed commercial Diesel engine taking into account torsional vibration aspects. The considered engine has a bore of 180 mm, a bank angle of 60 degrees and a rated speed of 1900 rpm. The crankshaft base dimensions have been defined basing on experience from development of engines of similar size and type in order to enable safe crankshaft operation with a peak cylinder pressure of 240 bar.

The influence of the firing order on crankshaft torsional vibration was investigated considering typical crankshaft layouts having rotationally symmetric crank stars and lengthwise mirror symmetric arrangement of crank throws (so called fully symmetric crankshafts). Such approach ensures inherent engine external balancing and minimizes engine torque fluctuations. The marine engine application with torsionally highly elastic flywheel coupling and an appropriately tuned leaf spring type torsional vibration damper was taken into account.

The applied crank train torsional vibration excitation due to gas forces for various engine speeds corresponds to a so-called overload propeller curve.

3.1. Number of considered crankshaft layouts and firing orders

The number of feasible firing orders for the considered V20 engine has been determined by use of equation (1):

$$n_{FO} = 2^{\left(\frac{n_{CT}}{2}-1\right)} \cdot \left[2^{\left(\frac{n_{CT}}{2}\right)}\right]^{(n_b-1)} \cdot \left(\frac{n_{CT}}{2}-1\right)! \qquad (1)$$

where n_{CT} is number of crank throws and n_b is the number of engine banks. The equation (1) can be applied for any typical engine configuration having fully symmetric crankshaft. It consists of three general parts:

$$n_{FO} = n_{FO_{i,1}} \cdot \left[n_{FO_{i,j}}\right]^{(n_b-1)} \cdot n_{csh} \qquad (2)$$

which describes accordingly: number of firing orders in first cylinder bank $n_{FO_{i,1}}$, number of firing orders in next cylinder bank(s) $n_{FO_{i,j}}$ and number of possible crankshaft layouts n_{csh}.

The results of application of equation (1) for the considered V20 engine are summarized in Table 1. A V12, V16 and V24 engines have been added for a reference.

Table 1. Number of alternative firing orders for a VEE engines with fully symmetric crankshaft layouts

Engine type	Number of firing orders for single crankshaft layout			Number of crankshaft layouts	Total number of firing orders
	in first bank	in second bank	total		
V12	4	8	32	2	64
V16	8	16	128	6	768
V20	16	32	**512**	**24**	**12288**
V24	32	64	2048	120	245760

3.2. Evaluation of crankshaft layouts and balancing concept

Since the study has been reduced to fully symmetric crankshaft layouts, all 24 considered crankshafts for V20 engine are externally inherently balanced. However, relative angular arrangement of a consecutive crank throws have significant influence on a crankshaft internal balancing. An internal bending moment caused either by rotating or oscillating forces bends the crankshaft during rotation, resulting in an increased bearing loads. Therefore, the evaluation of crankshaft layout has been performed considering crankshaft internal balancing determined acc. to approach described in [2].

The course of non-dimensional internal bending moment caused by rotating masses over crankshaft length for two selected crankshaft layouts is shown in Fig. 2 and Fig. 3. In both cases, the internal bending moments have been determined prior to the application of counterweights, which enables evaluation of the inherent internal unbalance.

The crank throw arrangement in crankshaft layout No. 15 depicted in Fig. 2 leads to small bending in the parallel ($Mb_{XZ\text{-}un}$) as well as in perpendicular ($Mb_{YZ\text{-}un}$) plane to the first crank throw. Therefore, the maximum of the non-dimensional resultant bending moment ($Mb_{tot\text{-}un}$) over crankshaft length with a value of 1.29 is also on the low level (the lowest over all considered crankshafts).

Contrary to the above-mentioned crankshaft layout, the crankshaft layout No. 4, depicted in Fig. 3, leads to significant bending in plane parallel to the first crank throw ($Mb_{XZ\text{-}un}$). The maximum value of non-dimensional resultant bending moment ($Mb_{tot\text{-}un}$) equal to 4.98 is the biggest over all considered crankshafts and almost four times bigger than in case of crankshaft layout No. 15.

The Table 2 summarizes the considerations regarding crankshaft internal balancing of fully symmetric crankshafts due to rotating masses, showing 3 best and 3 worst crankshaft layouts.

The internal bending of the crankshaft due to rotating masses can be noticeably reduced or even cancelled out by appropriate counterweight layout. For the purpose of this paper, a most straightforward and a historically proven counterweight layout have been applied, where each crank throw is balanced separately by two counterweights. The balancing ratio of 100% has been chosen. Therefore, the internal bending due to rotating masses has been eliminated and internal bending due to oscillating masses has remained unchanged for all 24 considered crankshaft layouts. Since in the considered engine the internal bending due to first order oscillating masses follows similar rules as in case of already considered rotating masses, the evaluation shown in Table 2 can be directly extrapolated to final engine internal balancing.

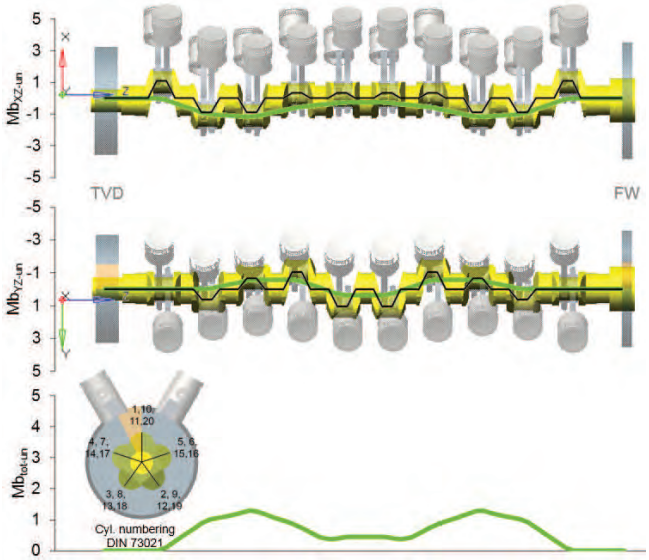

Fig. 2. Non-dimensional internal bending moment due to rotating masses of crankshaft layout No. 15

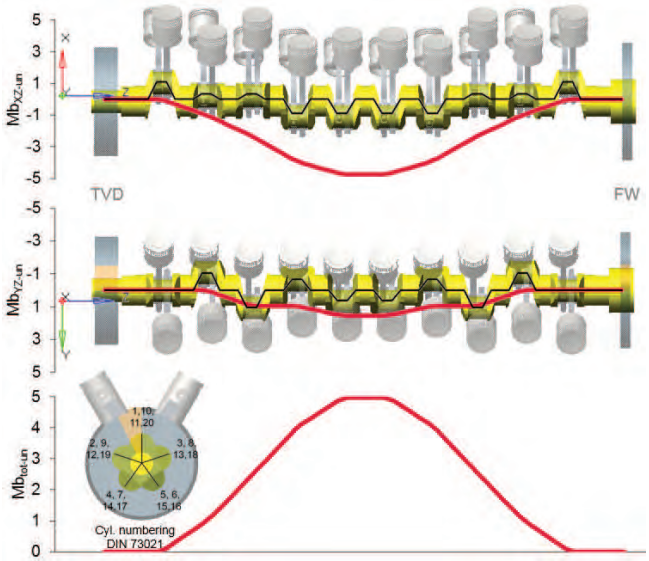

Fig. 3. Non-dimensional internal bending moment due to rotating masses of crankshaft layout No. 4

The applied counterweight layout compromises crankshaft weight and therefore crankshaft natural frequencies of torsional and axial eigenmodes are relatively low. The same balancing effect can be obtained by smaller number/size of counterweights but it requires optimization of counterweight layout for each considered engine and crankshaft configuration. Therefore, the balancing of each crank throw separately is still preferred by some engine manufacturers since it simplifies crankshafts designs during development of commercial engine family. For the firing order investigation, such approach is also a convenient starting point, since mass moment of inertia of each lump mass in crankshaft torsional 1D model remains unchanged for any crankshaft layout.

Table 2. Peak non-dimensional internal bending moments for selected crankshaft layouts

	Crank stars with small internal bending moment		
ID	CS15	CS13	CS20
Crank star	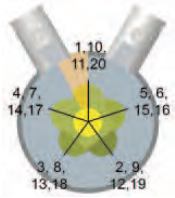	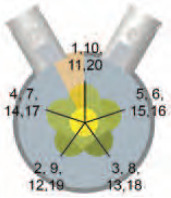	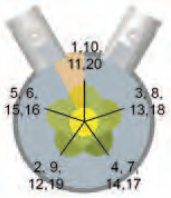
Mb_{tot_un}	1.29	1.56	1.67
	Crank stars with big internal bending moment		
ID	CS2	CS6	CS4
Crank star	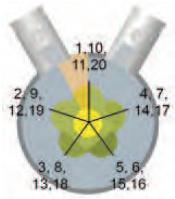	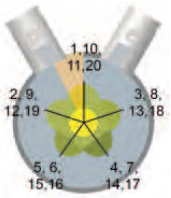	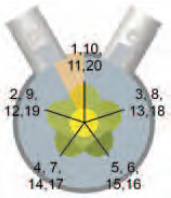
Mb_{tot_un}	4.75	4.75	4.98

Remark: cylinder numbering acc. to DIN 73021

It is to be mentioned, that application of semi-symmetric crankshafts (having rotationally symmetric crank stars but no lengthwise mirror symmetric arrangement of crank throws) becomes to be an interesting alternative for current, highly loaded multi-cylinder commercial engines [8]. Regardless of introduction of usually unavoidable engine external unbalance and required comprehensive balancing investigations, they may finally lead to good compromise between all crankshaft and firing order related aspects. The additional balancing topics for semi-symmetric crankshafts are introduction of crankshaft intentional unbalance as well as verification of balancing potential by balancing drillings, which are required to ensure feasibility to remove crankshaft unbalance caused by forging and manufacturing tolerances in a dedicated counterweights on a balancing machine.

3.3. Torsional vibration damper tuning [6]

For the considered engine, the engine speed of the highest torsional vibration excitation due to gas forces is between 1700 and 2000 rpm. Especially in this speed range, excessive vibration should be avoided either by system tuning, appropriate damping or reduction of the resultant excitation of selected eigenmodes by proper phasing of excitation caused by individual cylinders. The means for the first two points are provided by the application of the leaf spring damper, while the last one can be addressed by appropriate selection of the firing order.

The layout of the leaf spring damper has been performed taking into account in parallel the physical damper limitations and possible further influence by the firing order alteration. Regarding the damper size, the mass moment of inertia of the outer part was defined as less than 45% of the complete crank train mass moment of inertia without a damper. The selected stiffness of the damper, which is in the middle of the known range, leads to the split of the 1st crank train eigenmode into two crank train – damper modes, with natural frequencies being possibly far from one another. This effect is shown in Fig. 4.

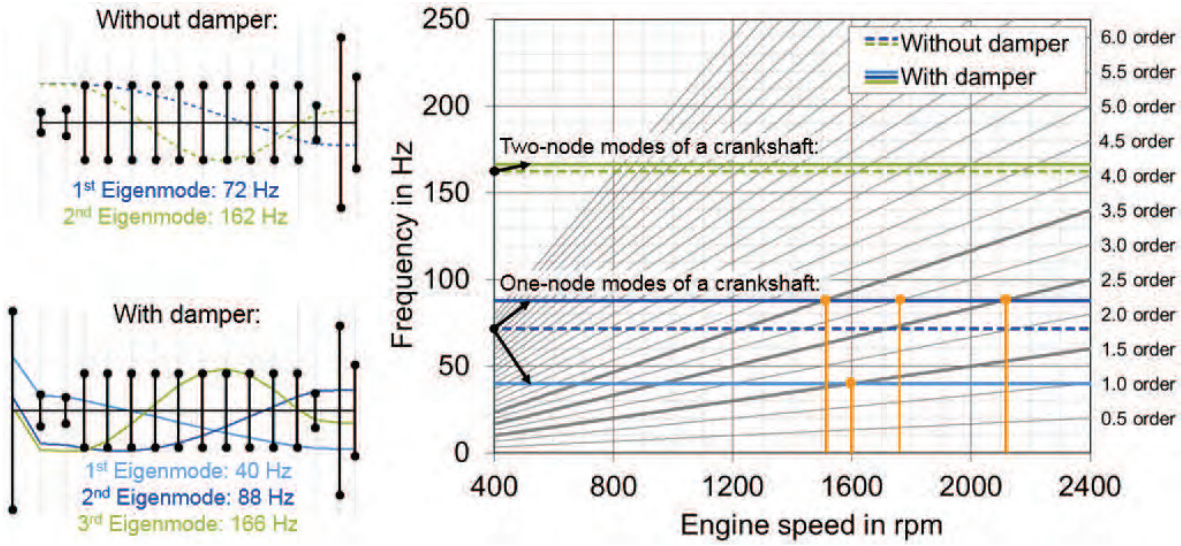

Fig. 4. Leaf spring damper tuning prior to the firing order influence investigation

For the considered engine with any fully symmetric crankshaft, taking into account lower excitation harmonic orders which are the strongest, the alteration of a firing order influences the resultant excitation of the 1.5th, 2.5th and 3.5th order. With the applied damper tuning, these resonances have been moved out of the engine speed range of

high torsional vibration excitation of each single engine cylinder (from 1700 to 2000 rpm).

The only resonance, which according to the Campbell diagram may occur in the above-mentioned speed range is the resonance of the 3rd excitation harmonic order with the 2nd crank train – damper mode (88 Hz). However, due to the combination of the selected engine bank angle and the mirror symmetry of the crankshaft, regardless of the chosen firing order, the resultant torsional vibration excitation of this eigenmode is zero for the 3rd excitation harmonic order.

3.4. Influence of the firing order on crank train torsional vibration

The influence of a firing order on crank train torsional vibration of the considered V20 engine has been analyzed by use of conceptual firing order investigation tools, which uses FEV Virtual Engine's Crank Concept Analysis as a 1D crankshaft simulation solver. The torsional vibration simulations of the crankshaft have been performed for a determined 12288 alternative firing orders (512 per each of 24 crankshaft layouts) on a currently available business class PC in about 6 hours of computational time by use of multiprocessing (8 parallel processes).

The tolerable torsional vibration level of the crank train is limited in relation to several aspects. The most important are crankshaft fatigue strength, design limitations of the torsional vibration damper, couplings, driven system(s) and accessory drives [7]. For the purpose of this paper, the presented signals are reduced to the crankshaft nominal vibratory stress amplitude and the torsional vibration damper load. The figures are divided into two groups, where the first one (Figure 5 to 8) depicts the results of historical firing orders from engine literature [3, 9] or a known engines and the second one (Figure 9 to 12) depicts the optimized results derived by multi-criteria optimization according to weighted desirability function approach popularized by Derringer and Suich [10].

All above-mentioned figures involve the so-called "Max./min. over FOs" zone which is defined by the upper and lower envelope of all simulation results. The zones show a strong influence of the firing order on the resultant torsional vibration excitation of the 1st eigenmode by the 1.5th, 2.5th and 3.5th excitation harmonic order, as well as not fully developed due to fuel cut-off resonance of the 2nd eigenmode with the 2.5th excitation harmonic order and the 3rd eigenmode with the 4.5th excitation harmonic order. The resonance of the 1st eigenmode with the 1.5th excitation harmonic order is exceptionally strong, therefore it was depicted separately in Figure 6 and 10.

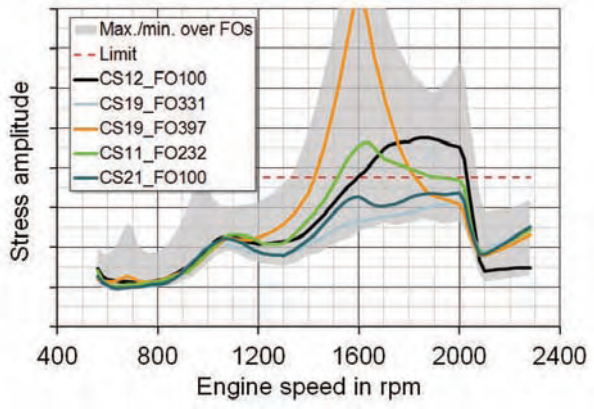

Fig. 5. Crankshaft nominal vibratory stress amplitude (synthetized) for historical firing orders

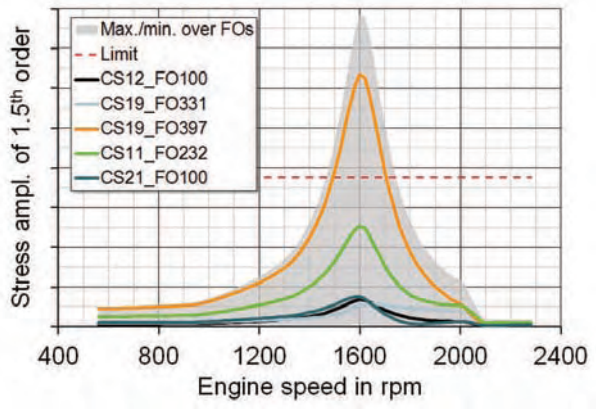

Fig. 6. Crankshaft nominal vibratory stress amplitude (1.5th order) for historical firing orders

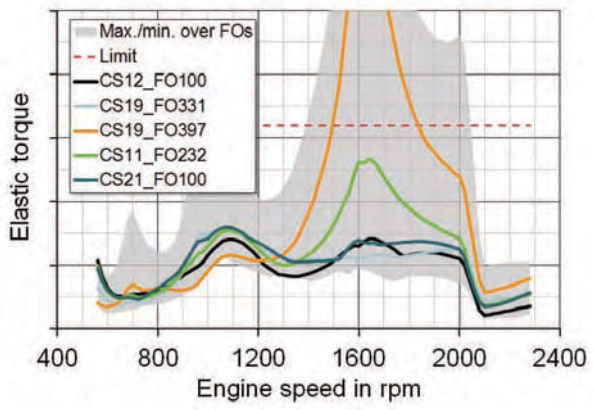

Fig. 7. Torsional vibration damper elastic torque for historical firing orders

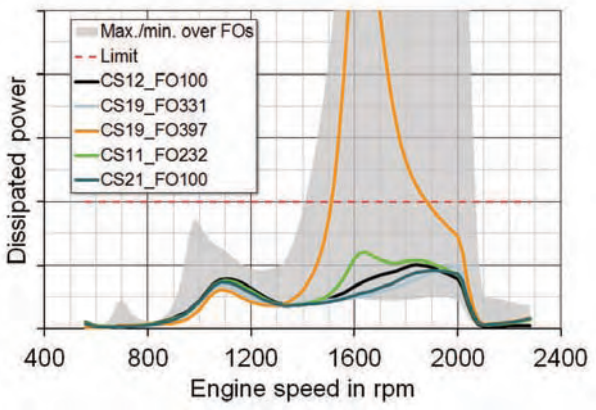

Fig. 8. Torsional vibration damper dissipated power for historical firing orders

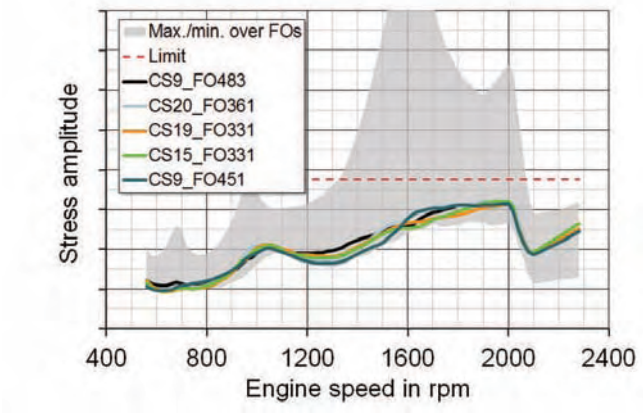

Fig. 9. Crankshaft nominal vibratory stress amplitude (synthetized) for optimum firing orders

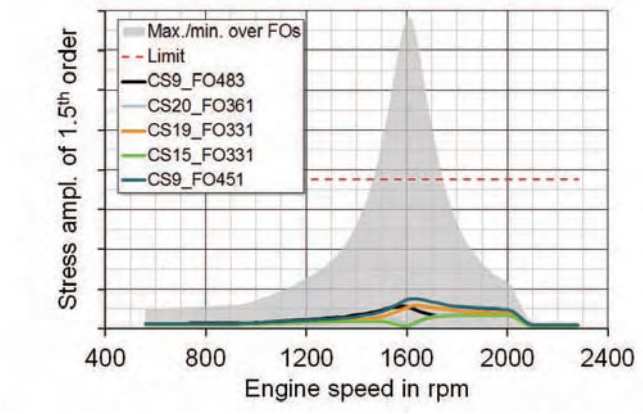

Fig. 10. Crankshaft nominal vibratory stress amplitude (1.5th order) for optimum firing orders

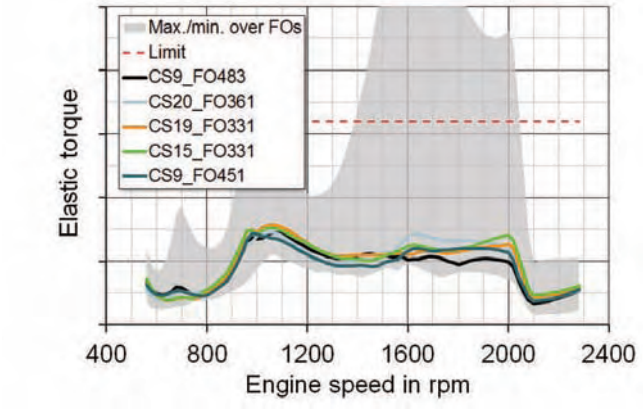

Fig. 11. Torsional vibration damper elastic torque for optimum firing orders

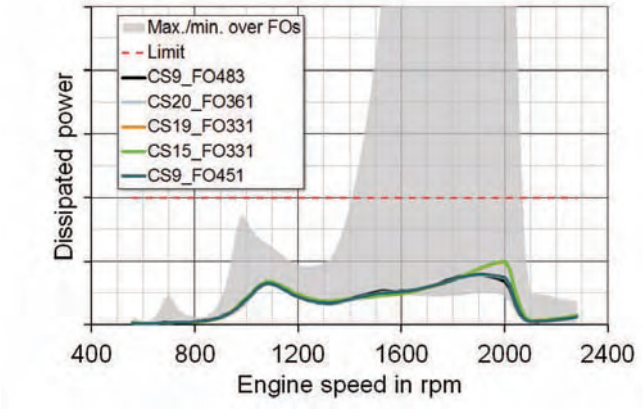

Fig. 12. Torsional vibration damper dissipated power for optimum firing orders

The two from depicted historical firing orders, CS19_FO331 (crank star No. 19, firing order No. 331) and CS21_FO100 enables to satisfy the criteria for nominal vibratory stress amplitude of the crankshaft but only CS19_FO331 passed the multi-criteria optimization. In case of firing order CS19_FO397 and CS11_FO232, exceeding the limit of crankshaft nominal vibratory stress is caused by strong vibration according to the 1st eigenmode excited by the 1.5th harmonic order, while in case of firing order CS12_FO100, this is caused by the common contribution of the resonance of the 3rd eigenmode with 5th, 5.5th and 6th excitation harmonic order.

The only 35 from 12288 firing orders were able to satisfy all of the considered vibratory and engine balancing limits. The results for the 5 most beneficial firing orders per crankshaft layout are shown individually in Figures 9 to 12. They are listed in the chart legend in ascending order (the firing order CS9_FO451 has the biggest value of the desirability function).

All of the beneficial firing orders leads to low crankshaft nominal vibratory stress amplitude (Fig. 9) and weakly excites the vibration according to the 1st eigenmode by the 1.5th harmonic order (Fig. 10). In addition, the damper load (Fig. 11 and 12) is also in the lower range. It is worth to notice, that historical firing order CS19_FO331 is in one of top 5 firing orders.

4. Summary

The torsional vibration part of the proposed firing order selection process has been performed for the purpose of this paper on an exemplary V20 high speed commercial Diesel engine. The taken into consideration aspects of engine balancing, torsional vibration damper tuning, definition of the number of alternative firing orders and crankshaft torsional vibration simulation depicts the significance and the complexity of this engineering challenge already in the concept phase of an engine development.

The results prove the sensitivity of the resultant torsional vibration excitation of crank train eigenmodes by particular excitation harmonic orders for different firing orders. From over 12000 of alternative firing sequences feasible to be realized by 24 fully symmetric crankshaft layouts (typical crankshafts for V20 engines), only 35 firing orders were able to satisfy all crankshaft torsional vibration and balancing criteria. Such preselection supported by multi-criteria optimization gives a good basis for further concept and detailed design simulations.

Applicability of historical firing orders for current highly loaded high speed commercial engines have been exceptionally considered. It was indicated, that historical firing orders might not be an optimum choice for a newly developed engines and detailed firing order optimization be-

comes an important part of commercial engine development.

The basic functionality of the conceptual firing order investigation tools which applications have been briefly presented in the paper is already implemented for a commercial multi-body simulation software "FEV Virtual Engine". It allows the firing order investigation based on crankshaft 1D simulation. The list of alternative firing orders feasible to be realized by pre-defined crankshaft layout is generated by dedicated algorithm. The obtained results can be subsequently analyzed in the evaluator which allows multi-criteria optimization according to weighted desirability function approach.

Acknowledgements

Authors would like to thank Dr. Ir. Antonius Voncken (FEV Europe GmbH), Dipl.-Ing. Michael Heinen (FEV Europe GmbH), Dipl.-Ing. Carsten Thorenz (FEV Europe GmbH) and M.Sc. Eng. Maciej Bartosik (FEV Polska Sp. z o.o.) for their valuable contribution in the development of procedures and methods supporting the firing order optimization process.

Nomenclature

CS	crankshaft/crank star
FO	firing order
FW	flywheel
TVD	crankshaft torsional vibration damper

Bibliography

[1] MOKDAD, B., HENNINGER, C. Avoiding Crankshaft Axial Vibrations: Influencing Parameters, Simulation and Solutions. *25th Aachen Colloquium Automobile and Engine Technology*. 2016.

[2] MAASS, H., KLIER, H. Die Verbrennungskraftmaschine, Band 2: Kräfte, Momente und deren Ausgleich in der Verbrennungskraftmaschine. *Springer*. 1981.

[3] SCHEUERMEYER, M. Einfluß der Zündfolge auf die Drehschwingungen von Reihenmotoren. *Technical University of Munich*. 1932.

[4] BUCZEK, K., LAUER, S. Firing order optimization in FEV Virtual Engine. *Torsional Vibration Symposium.* 2014.

[5] BUCZEK, K., LAUER, S. Firing order optimization in FEV Virtual Engine. *Cimac Congress*. 2016.

[6] BUCZEK, K., LAUER, S. Firing order selection for commercial engines with FEV Virtual Engine. *Torsional Vibration Symposium*. 2017.

[7] HENNINGER, C. Firing sequence optimization for a V20 cylinder diesel engine. *Torsional Vibration Symposium.* 2014.

[8] MOKDAD, B., HENNINGER, C. Irregularity instead of harmony – Ways to improve torsional performance of a V20 engine. *Torsional Vibration Symposium*. 2017.

[9] WILSON, W.K., Practical solution of torsional vibration problems. *John Wiley & Sons Inc*. 1942

[10] MYERS, R.H., MONTGOMERY, D.C., ANDERSON-COOK, M.C. Response surface methodology: process and product optimization using designed experiments. *Wiley Series in Probability and Statistics*. 2009.

Konrad Buczek, MEng. – FEV Polska Sp. z o.o.

e-mail: *Buczek@fev.com*

Sven Lauer, Dr.-Ing. – FEV Europe GmbH.

e-mail: *Lauer@fev.com*

Article citation info:
OWCZUK, M., MATUSZEWSKA, A., ODZIEMKOWSKA, M. et al. Evaluation of the impact of the hydration degree of bioethanol on the operation parameters of the spark-ignition engine. *Combustion Engines*. 2017, **169**(2), 71-75. DOI: 10.19206/CE-2017-212

CE-2017-212

Marlena OWCZUK
Anna MATUSZEWSKA
Małgorzata ODZIEMKOWSKA
Mateusz BEDNARSKI
Marcin Krzysztof WOJS
Jakub LASOCKI

Evaluation of the impact of the hydration degree of bioethanol on the operation parameters of the spark-ignition engine

The article presents an overview of methods for the production of bioethanol and the possibility of its use to power internal combustion engines. The effects of supplying spark-ignition engine with bioethanol having various degrees of hydration were examined experimentally on the engine dynamometer. The measurement results were referred to the anhydrous bioethanol, which is used widely as petrol biocomponent and compared in terms of the course of the pressure in the combustion chamber of the engine as well as engine performance parameters – torque and power. It was found that with the decrease in alcohol concentration, the performance of the spark-ignition engine deteriorated. The reduction of in-cylinder pressure was proportional to the increase in the water content in the fuel. No significant changes in the general shape of in-cylinder pressure curves were observed. Engine torque and power decreased with an increase in the water content in the fuel, especially at high engine speed. It has been stated that supplying the engine with bioethanol containing up to 6% (v/v) of water does not result in significant losses in engine performance.

Key words: *bioethanol, water content, spark-ignition engine, engine performance*

1. Bioethanol production

Bioethanol is an alcohol that is produced from many different types of carbohydrate-rich biomass, during alcoholic digestion. For its production are commonly used:

a) plants containing directly digesting sugars such as sucrose, glucose, fructose (e.g.: fruits, vegetables, sugar beets, sugar cane),
b) plants and wastes containing polysaccharides, degraded during hydrolysis into the fermentable mono- and disaccharides (e.g.: cereals, potatoes, industrial waste, lignocellulosic biomass).

The bioethanol production process is carried out in several stages depending on a type of the raw material involved and a degree of purification of the product (Fig. 1).

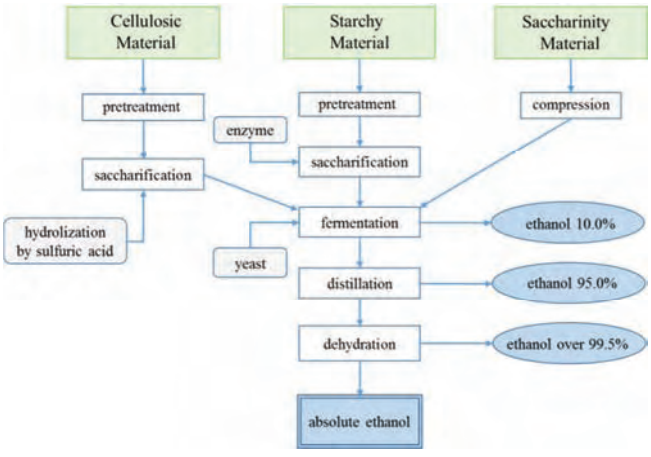

Fig. 1. Schema of bioethanol production processes depending on the raw material and the degree of purification of the product

There are four main stages in the ethanol production process: pretreatment, hydrolysis, fermentation and purification of the main product. The first stage is very important especially when the lignocellulosic raw material (extremely resistant to biodegradation) is used as a feedstock [16]. The appropriate methods used to pretreatment of the substrate can increase the efficiency of hydrolysis phase. Furthermore, such pretreatment limits the formation of toxic compounds that inhibit the metabolism of microorganisms involved in fermentation steps [4].

They are many methods of lignocellulosic biomass decomposition that break down the lignocellulosic fibers, reducing the degree of polymerization and crystallization of lignin-cellulose [23]. These methods can be divided into [7, 14, 15, 25]:

a) mechanical (the action of various kinds of shearing forces or changes in pressure are used, e.g. steam explosion),
b) non-mechanical: physical (e.g.: high or low temperature cellular destruction, treatment with detergents), chemical (oxidation processes, acid or alkaline hydrolysis) and biological (the use of special hydrolysis enzymes capable of degrading lignin and hemicellulose).

The disintegration of lignocellulosic biomass allows to hydrolyse of cellulose and hemicellulose into the simple sugars (C5 and C6) that are transformed into ethanol and carbon dioxide by *Saccharomyces cerevisiae* yeast or *Zymamonas mobilis* bacteria during alcoholic digestion [2, 6]. Digestion is sensitive to changes of process conditions:

a) temperature (optimum range 30–38°C),
b) acidity (optimum pH range 4.5–4.7),
c) sugar concentration (typically in the range of 12–20%),
d) oxygen content (a small amount of oxygen dissolved in the fermenting solution favorably affects the yeast growth rate and kinetics of the process),
e) alcohol concentration (more than 10–12% concentration of ethanol in digestion solution affects negatively on the growth of microorganisms and the process is discontinued [24]).

Besides ethanol, the post-fermentation mixture contains a lot of others compounds, for example: methyl esters, aldehydes (e.g. acetaldehyde), methanol, higher alcohols

(amyl alcohol, propanol, isobutanol, so-called fusel oil), organic acids (acetic, butyric), glycerine, sulphur, not decomposed sugars, residues of substrates, microorganisms [10]. Moreover, the water content in this mixture is very high (above 80%) and concentration process of ethanol up to 96% and higher requires a lot of energy and generates high costs [19]. As shown in Figure 2, the cost of ethanol dehydration above 70% rapidly grows.

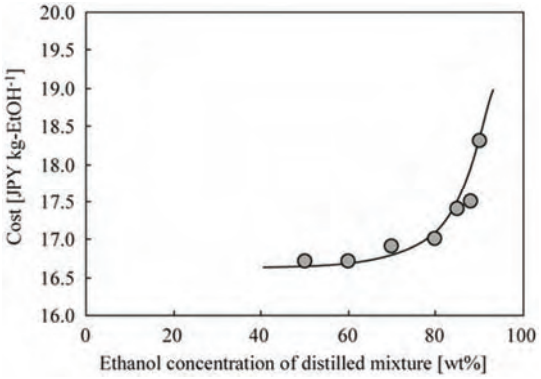

Fig. 2. The cost of ethanol dehydration [21]

Ethanol has a high affinity to water and their mixtures form an azeotrope with a boiling point at 78.2°C, which is lower than either of its components. Ethanol for fuel applications should be anhydrous. With the use of conventional distillation under atmospheric pressure it is impossible to obtain a product containing more than 80.4 mol% of ethanol [18]. Therefore, to get an anhydrous ethanol the special processes are required. There are several such processes [18, 22]: chemical dehydration, dehydration by vacuum distillation, azeotropic distillation, diffusion distillation, extractive methods, membrane methods, adsorption methods. Some of these methods have been suppressed e.g. chemical dehydration due to high energy demand (high cost), or azeotropic distillation with benzene because of its carcinogenic effect. Others have some disadvantages like high cost connected with recycling big quantities of ethanol to the process (dehydration on molecular sieves), environmental pollution by losses of the azeotropic agent (azeotropic distillation) or high energy consumption (extractive distillation) [17, 18]. In recent years more and more attention has been paid to the membrane technique, particularly to pervaporation. The separation is caused by differences in the solubility of particular components in the membrane (sorption) and differences in the diffusion rate through the membrane. Water permeates through the membrane, while dehydrated ethanol remains as the retentate.

2. Bioethanol application for fuel purposes

Biofuels are considered as good substitutes for fossil fuels. The use of them gives environmental and economic benefits. Bioethanol as a biofuel in the transport sector has gained interest all over the world. The use of bioethanol as a transportation fuel has been promoted in the USA, Brazil and Australia. The development of fuels contained bioethanol is promoted in the European Union as well. Detailed information on this subject can be found in the literature [3, 18, 20].

Due to combustion and antiknock benefits, ethanol has been used as a fuel for many years. It can be used directly in an internal combustion engine or it can be blended with petrol or diesel. Pure alcohol needs some modifications in the area of engine design and fuel system [5], especially in the case of compression-ignition engines (initially, ethanol was not intended for combustion in this type of engine). Nowadays, mainly petrol with bioethanol admixture in various ratio has commercial importance. In the European Union bioethanol can be used as a 5% or 10% (by volume) blends with petrol without engine modification. After modification of spark-ignition engine, bioethanol can be used at higher levels, for example, E85 (a blended fuel of 85% bioethanol and 15% petrol). In Brazil bioethanol is used as a pure fuel or as a mixture with petrol in the flexible range from 20% to 25% by volume [3, 11]. Ethanol/petrol blend (so-called E10) is the standard fuel in the US market. By 2030 the bioethanol content in petrol will increase to 15% [12].

The chemical characteristic of ethyl alcohol is very different from that of hydrocarbon fuels. Typical properties of bioethanol in comparison with petrol are given in Table 1.

Table 1. Bioethanol and petrol characteristics [18]

Characteristics	Bioethanol	Petrol
Chemistry	C_2H_5OH	Mixture of hydrocarbons
Density at 15°C [g/cm^3]	0.785	0.72–0.75
Distillation temperature [°C]	78.4	32–210
Flashpoint [°C]	12	13
Flame temperature at 101.3 kPa [°C]	478	392
Reid vapour pressure at 37.8°C [kPa]	17	35–60
Research octane number	111	91–100
Motor octane number	92	82–92
Net heat of combustion [MJ/kg (MJ/dm^3)]	27.0 (21.2)	43.5 (32.2)
Heat of vaporization [kJ/kg]	900	400
Oxygen content [%, w/w]	34.7	0
Stoichiometric air/fuel ratio [w/w]	8.97	14.6
Water solubility	∞	0
Vapour flammability limits [%, v/v]	3.5–15	0.6–8
Maximum flame speed [m/s]	0.40	0.33

In comparison with petrol, bioethanol is characterized by higher research octane number, higher heat of vaporization, lower vapor pressure (due to strong intermolecular hydrogen bonding interaction between alcohol molecules [8], lower heat of combustion (per unit volume, bioethanol has 68% of petrol energy). Ethanol, unlike petrol, contains 35% (w/w) oxygen, so stoichiometric air/fuel ratio for this compound is lower that for fossil fuel [18]. The above mentioned properties affect engine performance and exhaust emissions. A higher octane number, wider flammability limits, higher flame speeds and higher heat of vaporization allow for a higher compression ratio and shorter burn time, which lead to theoretical efficiency advantages over petrol in an internal combustion engine [3]. High octane number prevents pre-ignition and it helps to run vehicle smoothly. On the other hand, the higher evaporation heat negatively influences the start of the cold engine. Low vapor pressure adversely influences cold start, too. The lower heating value of ethyl alcohol results in increased

specific fuel consumption in comparison with petrol – a higher mass amount of alcohol is required per unit of output power [9].

Bioethanol, as oxygenate compound, reduces engine emissions. Leaning of fuel/air ratio causes the reduce nitrogen oxides and as well as carbon monoxide emissions [1, 18]. In comparison with petrol, alcohol combustion generates a higher volume of gaseous products, thus increasing cylinder pressure and the work done on the piston [9].

Disadvantages of bioethanol, besides the previously listed, are: its corrosiveness, toxicity to ecosystems, increase in exhaust emissions of acetaldehyde and increase in vapor pressure (and evaporative emissions), miscibility with water when blending with petrol. The addition of ethanol to hydrocarbons can significantly affect the properties of the resulting ethanol/petrol blend, among others: Reid vapor pressure and distillation characteristic. The increase in vapor pressure sharply rises until it reaches a maximum at approximately 4%–5% (v/v) bioethanol and gradually decreases at levels higher than 4%–5% (v/v). Whereas all levels of ethanol addition tend to lower the boiling temperatures in the mid-range and back-end of the distillation curve [3, 8, 13].

Most of the published research papers are referred to mixtures of fossil fuels with bioethanol. There is lack of results concerning combustion of pure bioethanol with different water content. Therefore, it is difficult to assess the influence of water content in bioethanol on the engine characteristics. Such research may be important from the viewpoint of necessity of bioethanol dehydration, which is a costly process. Therefore, the purpose of the presented research was a determination of water content effect on the operation of a bioethanol-powered engine.

3. Experiment and research results

This work was aimed at determining the operating parameters of the spark-ignition engine powered by water-alcohol blends. The blends were prepared under laboratory conditions by adding of specified amount of water to dehydrated ethanol (99.8%, v/v). The real water content was estimated with the use of Karl-Fisher method. The obtained concentrations of ethanol and chosen physicochemical parameters of tested samples are shown in Table 2.

Table 2. Characterization of research samples of bioethanol

Characteristics	Bioethanol			
	1	2	3	4
Ethyl alcohol content [%, v/v]	99.8	94.0	92.4	87.3
Water content [mg/kg]	0.3	5.8	7.4	12.5
Density at 15°C [g/cm^3]	794.4	810.5	819.3	829.1
Vapor pressure [kPa]	16.6	15.7	15.0	14.7

The study was carried out on a single cylinder research engine with spark-ignition. It worked according to the speed characteristics, which allowed to determine the rotational speeds of the maximum power and torque. The engine capacity was 50 cm^3 and the compression ratio was 1:4. Valve system made in pneumatic technology, a parameter of valve opening and closing time, fuel injection timing and length was electronically controlled. During testing, the torque generated by the engine, the rotational speed and the pressure in the combustion chamber were recorded. The test stand consisted of an electric brake, a spark-ignition engine, an indicator system, and a computer that recorded data. The block diagram of the test bench is shown in Fig. 3.

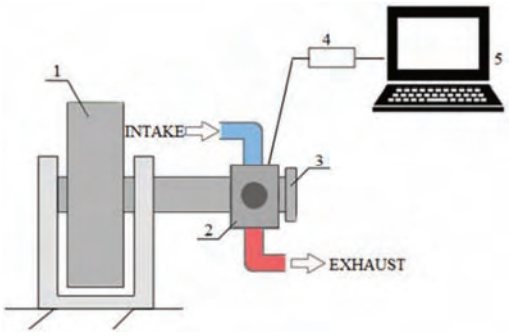

Fig. 3. Block diagram of the test stand 1 – engine brake, 2 – single cylinder spark-ignition engine, 3 – crank revolution angle recorder, 4 – indicator system, 5 - computer

Figure 4 shows the dependence of pressure in combustion chamber on a crank angle during supplying the engine with alcohol fuels with different water concentrations. This characteristic was created for the rotational speed of maximum power. Figures 5 and 6 present, respectively, the courses of engine torque and power as functions of engine speed for tested fuel samples.

As shown in Figure 4, it is clear that the increase in water concentration in ethanol causes the reduction of in-cylinder pressure during fuels combustion up to approximately 22% (from 9.6 MPa for 99.8% ethanol content to 7.5 MPa for 87.3% ethanol content). The observed reduction of in-cylinder pressure was proportional to the increase in the water content in the fuel. It should be noticed, that the pressure reduction affects power and torque of research engine. It should be emphasized that curves for 94.0% and 92,4% of bioethanol concentrations have a similar run from a 10º crank angle.

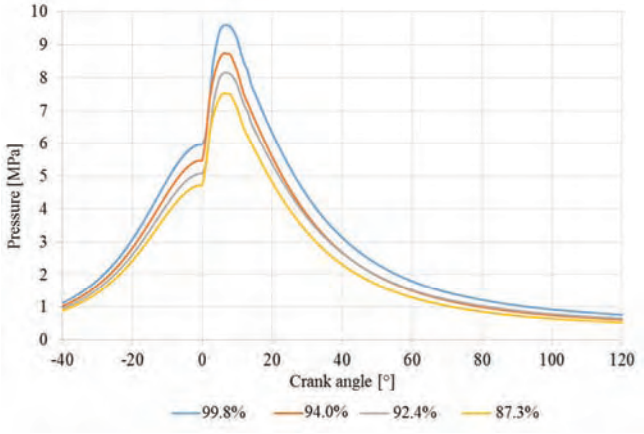

Fig. 4. Dependence of in-cylinder pressure on crank angle during combustion of the ethanol fuels with different content of water

The analysis of torque curves showed that observed changes are similar independently on water content in samples. The increase in engine speed caused the increase in torque. The maximum value of torque was at 2200 rpm for all bioethanol concentrations. Then, the slight decrease in that parameter was observed. Higher content of water in

fuels causes lowering of torque of the engine, especially in the range of higher engine speed. For example, at 1200 rpm the torque changed from 0.45 Nm to 0.32 Nm and at 2200 rpm from 1.01 Nm to 0.74 Nm, depending on the water concentrations (Fig. 5).

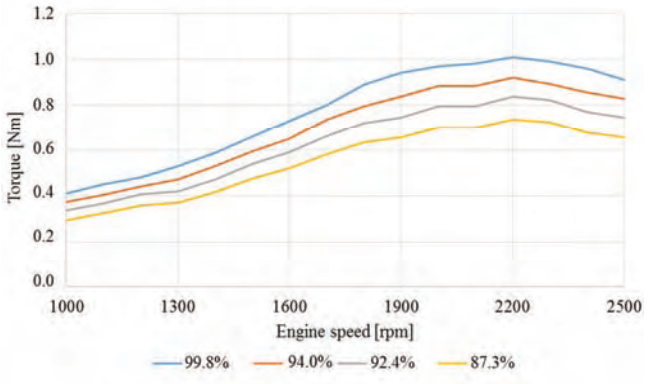

Fig. 5. Engine torque as a function of speed for the ethanol fuels with different content of water

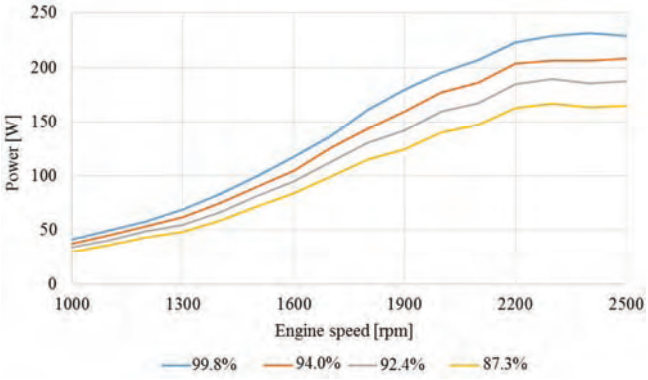

Fig. 6. Engine power as a function of speed for the ethanol fuels with different content of water

The influence of water content on the engine power was similar as it was observed in the case of parameter mentioned above. The higher engine speed, the higher value of engine power for all tested fuels. However, water addition changes the maximum power point. The highest power (232 W) showed engine supplied with 99.8% bioethanol at 2400 rpm (Fig. 6). The lower content of ethanol in fuel caused a movement of maximum power point to the lower value of engine speed (2300 rpm). Additionally, it caused a decrease in the value of maximum power to 206 W, 190 W and 167 W for 94.0%, 92.4% and 87.3% bioethanol samples respectively. Compared to dehydrated ethanol, for samples containing water, the decrease in the power by 9% (for 94.0%), 20% (for 92.4%) and 30% (for 87.3%) was observed at 2400 rpm.

Carried out research showed that it is possible to supply the engine with ethanol fuel containing up to 6% of water without major losses in the engine's operating parameters. This solution will reduce the financial costs and energy consumption connected with anhydrous ethanol production [17, 18].

In conclusion, the present study can be regarded as a preliminary work, that highlights some qualitative tendencies in terms of the relationship between water content in ethanol fuel and the engine performance.

4. Summary

Bioethanol can be a good substitute for fossil fuels, that use allows for environmental and economic benefits. It is primarily used as a biocomponent for gasoline. The ethanol used as a biofuel should be anhydrous, but the process of its concentration up to 96% (v/v) and higher requires a lot of energy and generates high costs.

Research carried out by authors showed that with the increase of water in ethanol fuel up to 13% (v/v) the decrease in power, pressure and torque of engine occurred. It has been stated that up to 6% (v/v) of water concentration the losses in engine performance are not significant. It allows concluding that it is possible to supply the engine with the ethanol fuel containing water. This solution permits to reduce the costs of anhydrous ethanol production.

Bibliography

[1] AGARWAL, A.K. Biofuels (alcohols and biodiesel) applications as fuels for internal combustion engines. *Progress in Energy and Combustion Science*. 2007, **233**, 233-271.

[2] BALAT, M., BALAT, H., ÖZ, C. Progress in bioethanol processing. *Progress in Energy and Combustion Science*. 2008, **34**, 551-554.

[3] BALAT, M., BALAT, H. Recent trends in global production and utilization of bio-ethanol fuel. *Applied Energy*. 2009, **86**, 2273-2282.

[4] BALAT, M. Production of bioethanol from lignocellulosic materials via biochemical pathway: A review. *Energy Conversion and Management*. 2011, **52**, 858-875.

[5] BAYRAKTAR, H. Experimental and theoretical investigation of using gasoline–ethanol blends in spark-ignition engines. *Renewable Energy*. 2005, **30**(11), 1733-1747.

[6] CHANDRA, R. et al. Methane production from lignocellulosic agricultural crop wastes: A review in context to second generation of biofuel production. *Renewable and Sustainable Energy Reviews*. 2012, **16**, 1462-1476.

[7] CHANDRA, R., TAKEUCHI, H., HAGESAWA, T., Hydrothermal pretreatment of rice straw biomass: a potential and promising method for enhanced methane production. *Applied Energy*. 2012, **94**, 129-140.

[8] CONCAWE REPORT 3/08 Guidelines for blending and handling motor gasoline containing up to 10% v/v ethanol. Available online: www.concawe.eu/publications/137/40/report-no-3-08 (accessed on 27.03.2016).

[9] COSTA, R.C., SODRE, J.R. Compression ratio effects on an ethanol/gasoline fuelled engine performance. *Applied Thermal Engineering*. 2011, **31**, 278-283.

[10] CZUPRYŃSKI, B., KOTARSKA, K. Zanieczyszczenia chemiczne spirytusów surowych związkami karbonylowym. *Inżynieria i Aparatura Chemiczna*. 2009, **48**, 31-32.

[11] DE FREITAS, L.C., KANEKO, S., Ethanol demand under the flex-fuel technology regime in Brazil. *Energy Economics*. 2011, **33**, 1146-1154.

[12] European Biofuels technology Platform available online: www.biofuelstp.eu/bioethanol.html (accessed on 27.03. 2016).
[13] FRENCH, R., MALONE, P. Phase equilibria of ethanol fuel blends. *Fluid Phase Equilibria*. 2005, **228-229**, 27-40.
[14] HATAKKA, A. Lignin-modifying enzymes from selected white-rot fungi: production and role from in lignin degradation. *FEMS Microbiology Reviews*. 1994, **13**, 125-135.
[15] HENRICS, A.T.W.M., ZEEMAN, G. Pretreatments to enhance the digestibility of lignocellulosic biomass. *Bioresource Technology*. 2009, **100**, 10-18.
[16] JORGENSEN, H., KRISTENSEN, J.B., FELBY, C. Enzymatic conversion of lignocellulose into fermentable sugars: challenges and opportunities. *Journal of Biofuels, Bioproducts and Biorafinering*. 2007, **1**(2), 119-134.
[17] KAMINSKI, W., MARSZALEK, J., CIOLKOWSKA, A. Renewable energy source—dehydrated ethanol. *Chemical Engineering Journal.* 2008, **135**, 95-102.
[18] KUMAR, S., SINGH, N., PRASAD, R. Anhydrous ethanol: A renewable source of energy. *Renewable and Sustainable Energy Reviews.* 2010, **14**, 1830-1844.
[19] LEJA, K, LEWANDOWICZ, G., GRAJEK, G., Produkcja bioetanolu z surowców celulozowych. *Biotechnologia*. 2009, **87**, 88-101.
[20] ODZIEMKOWSKA, M., MATUSZEWSKA, A., CZARNOCKA, J. Bioethanol as a fuel for compression-ignition engines. *Applied Energy*. 2016, **184**, 1264-1272.
[21] OKABE, K., et al. Energy and cost evaluation for the concentration and dehydration process of bioethanol by zeolite membranes. *Kagaku Kogaku Ronbunshu.* 2010, **36**, 486-493.
[22] RAKOCZY, J., KUPIEC, K., BŁĄK, A., LARWA, T. Usuwanie wody ze spirytusu gorzelnianego w celu otrzymania bioetanolu paliwowego. *Czasopismo Techniczne Chemia.* 2008, **1**, 115-124.
[23] SUN, Y., CHENG, J., Hydrolysis of lignocellulosic material for ethanol production: a review. *Bioresource Technology*. 2002, **83**, 1-11.
[24] SZYMCZYK, E. Stan badań i perspektywy wdrożeń technologii do produkcji bioetanolu paliwowego z surowców lignocelulozowych. Praca dyplomowa. Kraków 2008/2009.
[25] ZHANG, B., SHAHBAZI, A. Recent developments in pretreatment technologies for production of lignocellulosic biofuels. *Journal of Petroleum & Environmental Biotechnology*. 2011, **2**(2), 1-8.

Marlena Owczuk, MEng. – Department of Fuels and Renewable Energy, Automotive Industry Institute in Warsaw.

e-mail: *M.Owczuk@pimot.eu*

Marcin Krzysztof Wojs, DEng. – Faculty of Automotive and Construction Machinery Engineering at Warsaw University of Technology.

e-mail: *Marcin.Wojs@simr.pw.edu.pl*

Anna Matuszewska, DEng. – Department of Fuels and Renewable Energy, Automotive Industry Institute and Cardinal Stefan Wyszynski University.

e-mail: *A.Matuszewska@pimot.eu*

Mateusz Bednarski, MEng. – Institute of Vehicles, Department of Combustion Engines, Warsaw University of Technology.

e-mail: *Mateusz.Bednarski@simr.pw.edu.pl*

Małgorzata Odziemkowska, MEng. – Department of Fuels and Renewable Energy, Automotive Industry Institute in Warsaw.

e-mail: *M.Odziemkowska@pimot.eu*

Jakub Lasocki, DEng. – Faculty of Automotive and Construction Machinery Engineering at Warsaw University of Technology.

e-mail: *J.Lasocki@simr.pw.edu.pl*

Article citation info:
KALKE, J., OPALIŃSKI, M., MAZURO, P. Combustion and heat release analysis in an opposed-piston engine. *Combustion Engines*. 2017, **169**(2), 76-82. DOI: 10.19206/CE-2017-213

Jakub KALKE
Marcin OPALIŃSKI
Paweł MAZURO

CE-2017-213

Experimental test stand for development of an opposed-piston engine and initial results

The article presents the reason for developing a 0D predictive and diagnostic model for opposed-piston (OP) engines. Firstly, a description of OP engines, together with their most important advantages and challenges are given together with current research work. Secondly, a PAMAR-4 engine characteristic is presented. After that the proposed 0D predictive model is described and compared with the commercially availible software. Test stand with most important sensors and solutions are presented. After that the custom Engine Control Unit software is characterized together with a 0D diagnostic model. Next part discusses specific challenges that still have to be solved. After that the preliminary test bed results are presented and compared to the 0D simulations. Finally, the summary together with possible future improvement of both 0D predictive model and test bed capabilities are given.

Key words: *opposed-piston, combustion, heat release, 2-stroke*

1. Introduction

Opposed-piston engines allows achieving high thermodynamic efficiency inter alia due to lack of a cylinder head and better shape of the combustion chamber [1, 2]. During PAMAR-4 project it turned out that there are no ready-made tools which can be used for analyzing the 2-stroke opposed-piston engine operation, neither in design phase nor during measurements on the test bed. A set of supportive numerical tools has been developed, concerning mainly modelling 3D scavenging and heat transfer calculations using CFD. Unfortunately, those tools are very computationally expensive and not particularly useful for transient operation simulations or as a part of prediction control system which could be used for a HCCI control. It has been assumed that a simple 0D predictive and diagnostic custom tailored model will address the needs of improving the efficiency of the future opposed-piston engines and allow implementing closed-loop control basing on cylinder pressure signal.

2. Opposed-piston engines

2.1. Geometry

An opposed-piston engine is a subtype of internal combustion engine with no cylinder head. Two pistons are reciprocating opposite to each other, both working in one cylinder (Fig. 1). They can work as 4-stroke, but most of them are 2-stroke engines and scavenging is usually controlled by piston-ported valves. Combustion chamber is formed between moving pistons.

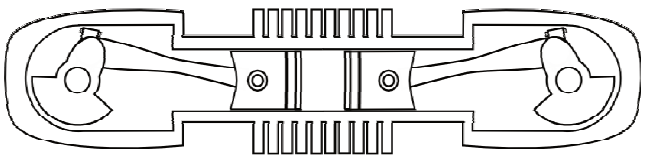

Fig. 1. Opposed-piston engine

First opposed-piston engines emerged in the late XIX century [1], while the most famous of them were used during the WWII (Jumo series by Junkers company). In the 1946 Sulzer 8G18 Series achieved 39.5% brake thermal efficiency.

2.2. Advantages of OP engines

Shape of a combustion chamber: Heat generated is proportional to the volume (V) of a combustion chamber, while heat loses are proportional to the surface area (SA). The SA/V factor is nearly twice lower in OP engines than in conventional, leading to higher thermal efficiency [1, 2].

Lack of a cylinder head: Cylinder head heat loses are significant due to necessity of cooling poppet valves. Eliminating cylinder head simply eliminates these loses, which improves thermodynamic efficiency. Moreover, it leads to reducing the emission of unburned hydrocarbons and carbon monoxide, mainly formed at the cold walls of the head, where flame is being quenched.

Possible high stroke/bore ratio: Engines with higher S/B have smaller surface area exposed to combustion gases which improves thermal efficiency. Also mechanical efficiency is affected: while increasing S/B factor the bearing friction decreases proportionally to the lower forces (lower piston area, same pressure). In OP engines the stroke is split between two pistons, which gives high S/B without increasing mean piston speed (lower the speed – better the efficiency) [12].

2.3. Challenges connected with the OP engines

High thermal load: 2-stroke engines have no additional two strokes to exchange the charge (during which the engine is cooled). Also, high power concentration leads to problems with exhaust ports durability (usually they have to be water cooled) and piston head wear.

Changing linear to rotary motion: Classical engines inherently have one shaft. The challenge with the OP is to take the power from 2 pistons and transfer it in effective way to one shaft. There are single, double or multishift solutions [1], rotary or barrel engines [6] but it is hard to achieve comparable or better mechanical efficiency than in crankshaft mechanism without in-depth analysis.

Side injection: In the OP engines injection is being made perpendicularly to the piston motion while in stand-

ard engines injection is parallel and central. Classical injectors have problem with even fuel distribution in a combustion chamber of the OP engines which can lead to an inefficient combustion. Moreover, there is a risk of cylinder liner or piston rings fuel impingement – that makes charge non-uniform and generates local high thermal loads. Fuel impingement can also destroy lubrication film, leading to increased emission, oil consumption and faster piston-cylinder wear.

2.4. Current research work in the world

Kharkiv Morozov Machine Building Design Bureau designed and introduced a 2-stroke, 6-cylinder, liquid-cooled multi-fuel diesel engine 6TD-2 with horizontal placement of cylinders and opposed pistons with 882 kW, being able to use diesel, jet engine fuel, petrol or any mixtures of them. This engine is used in T-84 main battle tank since 1990.

Achates Power is an American company founded in 2004, developing a 2-stroke, 3 cylinder, OP compression ignition engine (4,9 L, 205 kW power). In 2016 they surpassed 7,000 hours of dynamometer testing. They best brake thermal efficiency point is at the moment is 44% (191 g/kWh) and they are predicting a possibility to achieve 180 g/kWh in production level engine [3] while meeting exhaust emissions US2010 EPA requirements using conventional after-treatment system.

EcoMotors is an American company founded in 2008 developing and commercializing an opposed-piston opposed-cylinder (OPOC) engine. In 2011 they struck a partnership with Generac (large manufacturer of backup power generators) and they are developing together a 240 kW power pack. They created their second R&D center in China (main target market) to adapt technology and engine to local reality.

Pinnacle Engines is a start-up with an idea of commercializing a 4-stroke, SI, opposed-piston engine. It uses "Cleeves" cycle [4], changing constant volume combustion to constant pressure combustion depending on operating condition. The production of 110 cm^3 scooter engines will be started in 2017 in Asia [5].

2.5. Applications

In authors opinion there are three main reasonable applications for OP engines utilizing adequate advantages:

- distributed power generation (high fuel efficiency, good power-to-weight and power-to-bulk ratio),
- military (multifuel potential and high power-to-bulk ratio),
- automotive, as a range extender for hybrids (high fuel efficiency and good power-to-weight ratio).

The 2-stroke OP engine could be a worse solution than normal 4-stroke for direct propulsion of a car as scavenging process can be only optimized properly for a given load and rotation speed.

3. Object of study – PAMAR type engine

A PAMAR-4 engine is a 2-cylinder, opposed-piston, 2-stroke barrel engine (Fig. 2, 3). It has been designed under the Polish-Norwegian Cooperation Research conducted by the National Research and Development Centre, project: Investigations of HCCI in an innovative barrel engine.

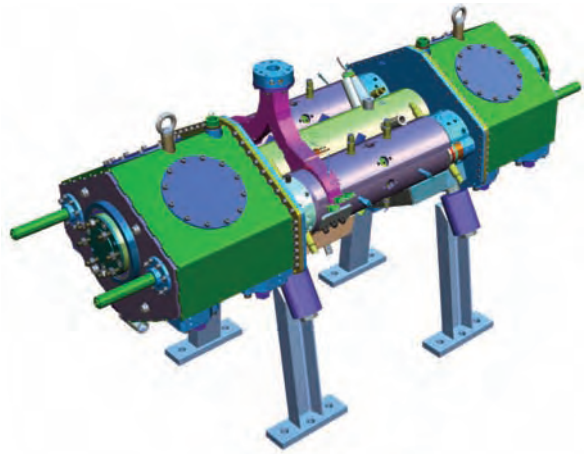

Fig. 2. PAMAR-4 CAD model without auxiliary equipment

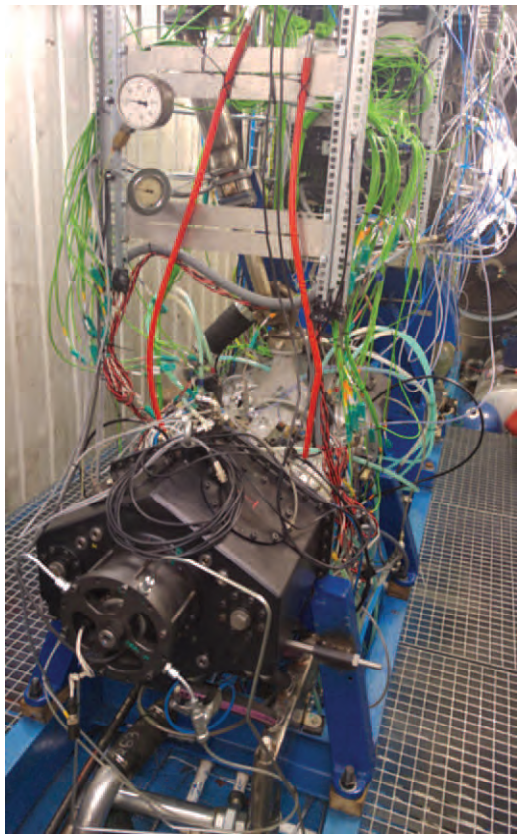

Fig. 3. PAMAR-4 on the test bed

Main properties:

- HCCI combustion on gasoline under various loads,
- 100 kW@1500 rpm, 1700 dm^3, 640 Nm@1500 rpm,
- multifuel potential (both liquid and gaseous),
- variable compression ratio,
- variable valve timing,
- variable phase shift.

PAMAR-4 is using a wobble plate mechanism. Shaft is not straight but bended with a proper angle – this makes plate rotate in other axis than shaft. The plate has a special pin (crosshead) which moves on the crosshead guide. This slider is blocking the plate's rotation and makes the shaft rotate while the plate pin is only having a pendulum like motion (wobbling) (Fig. 4).

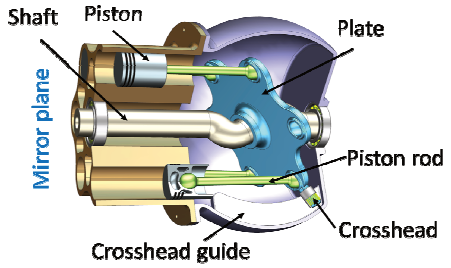

Fig. 4. PAMAR-4 wobble plate (blocked by crosshead, half of the engine)

The combustion chamber has mounted:

- piezoelectric gasoline direct injector (VDO Siemens 1353 7565137-03 - also used for direct water injection),
- piezoelectric diesel direct injector (Delphi A6510701287),
- piezoelectric pressure transducer (Kistler 6055C80),
- spark plug (NGK ER9EHIX),
- glow plug (NGK D-Power CZ303).

4. Heat release in 0D model

4.1. Introduction

The main reason for developing a 0D model is a need to have a simple prediction algorithm for controlling a HCCI combustion on gasoline under various loads from cycle to cycle. The solver is based on a Single Zone Model, which is a common approach in modelling SI in commercial software [11]. The system is balanced using the first law of thermodynamics for a stationary open system:

$$dU = \delta Q - \delta W + h_j dm_j \tag{1}$$

where: dU – change in the total internal energy of in-cylinder charge, δQ – total heat transfer across the cylinder boundary, δW = pdV – work transfer rate out of the system, h_j – specific enthalpy of gas mixture flowing through the boundary j (intlet, outlet, blowby, injection etc.).

On the other hand the dU term can be expressed as:

$$dU = m_i c_{vi} dT + u_i m_i \tag{2}$$

where: i – specie index. Mass conversion is assumed by Wiebe function.

Mass flow through ports is approximated by equation for compressible flow through an orifice derived from a one-dimensional isentropic flow. Non-isentropic effects are modelled by discharge coefficient C_d. Coefficient of discharge is usually in range from 0.75 to 0.85 [8] and is also parametrized as a function of port open fraction.

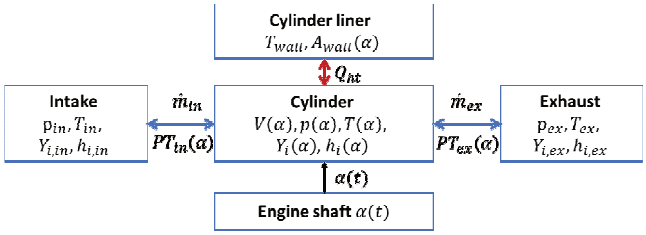

Fig. 5. Diagram of developed simple thermodynamic 0D model

Table 1. Description of the Fig.5

Value	Unit	Meaning
$V(\alpha)$	m^3	Volume of cylinder
$p(\alpha)$	Pa	Mass-averaged in-cylinder pressure
$T(\alpha)$	K	Mass-averaged in-cylinder temperature
$Y_i(\alpha)$	-	Species mass fractions
$h_i(\alpha)$	J/kg	Enthalpy
$PT_{in}(\alpha)$, $PT_{ex}(\alpha)$	$m^2\alpha$	Port timing
$m_{in}(\alpha)$, $m_{ex}(\alpha)$	kg/s	Mass flow through ports
T_{wall}, $A_{wall}(\alpha)$	K, m^2	Reference area and temperature for Woschni correlation

4.2. Geometry

In 2-stroke, opposed-piston engine the volume and valve timing is directly connected with the port geometry. A computer program has been prepared to calculate effective compression ratio, effective stroke volume, valve timing, combustion chamber surface area etc. for a given port geometry. Additionally, the variable systems are taken into consideration – they are implemented as the change of piston motion function. The program return volume function and timing. The piston displacement in PAMAR-4 engine can be described by (3) and (4). F is a function of wobble plate mechanism, VCR is a shift from variable compression ratio system and VVT is a shift from variable valve timing (in this came a variable piston timing). Exhaust piston leads intake piston by phase ϕ to allow charge exchange.

$$x_{in}(\alpha) = F(\alpha - \phi/2) + VCR + VVT \tag{3}$$

$$x_{ex}(\alpha) = F(\alpha + \phi/2) + VVT \tag{4}$$

4.3. Thermodynamic data

NASA 7-coefficient polynomial parametrization is used to compute the species reference-state thermodynamic properties: heat capacity at constant pressure J/kmolK, specific standard molar enthalpy of formation kJ/mol and specific standard molar entropy: J/kmolK [7]. Assuming ideal gas model for working medium (standard assumption basing on [8]) all needed thermodynamic properties like heat capacity at constant pressure, volume, heat capacity ratio are calculated with a help of Cantera.

4.4. Heat transfer

As only cylinder volume is taken into consideration the conduction is not modeled. Radiation is omitted (the engine is working on gasoline, there is no radiating soot like in diesel-fueled compression ignition engines). The convection is modeled by Newton's law (5) with instantaneous special average coefficient for convective heat-transfer calculated using Woschni formula (6) [9, 10]:

$$Q = h_k(T_g - T_w) \tag{5}$$

$$h_k = 110B^{-0.2}p^{0.8}v^{0.8}T^{-0.55} \tag{6}$$

where: B – cylinder bore [m], p – in-cylinder pressure [bar], v – characteristic velocity connected with (7) mean piston speed S_p, constants C_1 and C_2 depending on cycle's period and difference between current (p) and motoring pressure (p_m) [m/s], C_{ref} is calculated from known reference state and displaced volume, T_g – in-cylinder gas temperature [K].

$$v = (C_1 S_p + C_{ref} C_2 (p - p_m)) \quad (7)$$

In the 0D model there are four distinguished areas (Fig. 6):

- intake piston area and its reference temperature,
- exhaust piston area and its reference temperature (exhaust piston is hotter as intake piston is cooled by fresh charge),
- combustion chamber area and its reference temperature,
- cylinder liner area vs angle and its reference temperature.

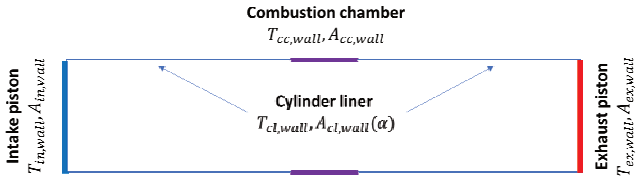

Fig. 6. Boundary conditions for heat-transfer calculations

4.5. Heat release

Heat release is modelled by S-shaped mass fraction burned profile described by Wiebe function. Wiebe function (8) is widely used in engine software packages [11], e.g. GT Power uses single Wiebe function for SI engine and multi-Wiebe function for CI engine modelling. AVL Boost uses single Wiebe function for combustion process and two-zone Wiebe for NOx calculations. Ricardo Wave has a SI Wiebe combustion model and CI Wiebe based semi-predictive model with pilot injection.

$$x_b = 1 - \exp(-a((\theta - \theta_0)/\Delta\theta)^{m+1}) \quad (8)$$

where: x_b – mass fraction burned, θ – current crank angle, θ_0 – start of the combustion (ignition in SI, approximately injection in CI), $\Delta\theta$ – combustion duration, a, m – adjustable parameters.

4.6. Calculation solver

Calculation algorithm:

1. If ports are open calculate mass change through the boundaries (intake/exhaust).
2. Recalculate gas composition Y_i change due to mass flow through the boundaries (using scavenging model).
3. Calculate new gas composition Y_i according to Wiebe function.
4. Update gas properties (new composition).
5. Get current volume V and calculate dV.
6. Calculate components of the equation (1): work, change in internal energy due to combustion, mass flow through the boundaries and change in internal energy due to heat transfer through the boundaries using Woschni correlations.
7. Calculate dT and new temperature from equation (2).
8. Calculate pressure from ideal gas law.
8. Proceed to the next time step (time step is 0.1 CAD)

5. Test stand

PAMAR-4 engine together with whole dyno is encapsulated in a 40 feet High Cube Pallet Wide marine-type container enabling transport.

5.1. Engine indication

Engine crank position is measured by two Heidenhein ERN 130 3600 HTL quad incremental encoders connected to NI 9411 module. PXI-7853R FPGA couples encoder signal with pressure acquisition to precisely gather pressure vs crank angle characteristic with 0.1 CAD resolution.

In cylinder pressure is measured by piezoelectric Kistler 6055C80 pressure transducer with diaphragm that allows measurements during engine knocking. Piezoelectric sensors outputs charge, in case of 6055C80 it is –20 pC/bar (output range is from 0 to 5000 pC as measuring range is 0-250 bar). Dewetron Charge B charge module is used to read the charge and convert it to voltage signal (–5 V to 5 V) which can be further analyzed. It has built-in Bessel or Butterworth (software programmable) filter and grounds each engine cycle to help keep data from drifting out of digitiser range. Charge modules are stored in Dewe-800 mainframe (special model prepared for DAQP isolated analog input amplifier modules).

Pressure signal is acquired by both Dewetron and National Instruments system. Dewetron uses DEWE-ORION-1616-500 A/D card (with 16 simultaneous sampled single-ended channels at 500 kSamples/s each), controlled by DeweSoft which is used for simple in-cylinder pressure and heat release analysis. National Instruments system uses NI PXI-7853R LX85 Multifunction RIO (8 analog inputs, 750 kHz, 16-bit) under control of LabView-written custom data acquisition software, tailored for opposed-piston engines.

5.2. Torque measurement and power absorption

Torque is measured by load cell of Froude Hofmann's AG400 eddy current dynamometer with a capacity of 400 kW and 2000 Nm (inertia is 1.107 kg m^2). Load cell is connected to Texcel V4 Controller, measurement accuracy is 0.25%. The speed is measured by a Hall-effect sensor counting slopes on a toothed wheel mounted on the shaft half coupling hub (accuracy is ± 1 rpm). Engine is coupled to the dynamometer with an Elbe 100 Cardan shaft of 8,200 Nm capacity which has been dynamically balanced.

5.3. Fuel system

Injection system is patent pending solution (P-419918, "Device for providing and very precise measuring of small amounts of liquids under high pressure") which allows precise measurement of very low flows (even less than 0.001 LPM) under very high pressure (up to 300 bar). The double acting piston pumps the gasoline out of the hydraulic cylinder under pressure generated by the hydraulic oil. The piston position is measured using TK LA46K magnetostrictive linear encoder thus volumetric flow is known (Fig. 7). Injectors are controlled by NI 9751 Direct Injector

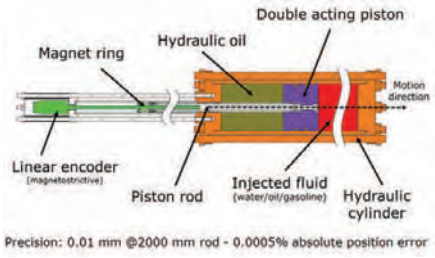

Fig. 7. PAMAR-4 fuel consumption measurement module

Driver Module, ignition is set by NI 9403 TTL Digital Input/Output Module.

5.4. Air charging

Air intake system is 2-stage boosted. 1-st stage is Garrett GT1749V variable nozzle turbocharger, 2-nd stage is Eaton TVS R410 5th generation mechanical supercharger powered by an electrical inverter-controlled engine. Air is water intercooled to improve charging efficiency. Pressure is regulated by bypasses controlled by throttles.

Air mass flow is measured using Bosch air-mass meter (0 281 002 802 – a typical automotive measurement, about 3% error) and Rosemount Annubar 3051SFA (industrial grade flow meter, less than 1% error). Temperatures are measured using K-type 1.5 mm thermocouples connected to NI PXIe-4353 32-Ch Thermocouple Input (accuracy 0.3 ºC). Pressure is measured using NXP MPX4250AP (1.5% accuracy) or NXP MPX5500DP (2.5% accuracy) accordingly to the pressure range.

5.5. Exhaust system

The pressure in exhaust is measured using a fast, water cooled Kulite EWCTV-312M-25bar A pressure transducer (range 0-25 bar, accuracy ±0.1% FSO BFSL). The emissions are measured using Bosch BEA 460: CO (0.001% vol resolution), HC (1 ppm resolution), CO2 (0.01% vol resolution), NO/NO_2 (1 ppm resolution), and O_2 (0.01% vol resolution). There is no catalyzer at the moment.

6. Data acquisition system

Dewesoft, supplied with Dewetron charge amplifiers, has capabilities of measuring in-cylinder data, calculating simple heat generation and knock detection. Unfortunately, it's neither possible to control the engine with it nor to make more sophisticated thermodynamic calculations. This forced authors to develop a custom Engine Control Unit in LabView, which will allow both data acquisition and closed-loop control.

6.1. Data acquisition system configuration

Data acquisition hardware is based on National Instruments PXI platform with auxiliary units (Fig. 8). System has:

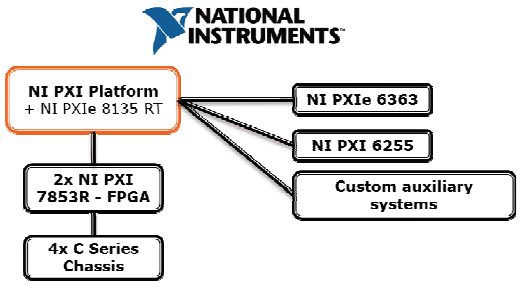

Fig. 8. Block diagram of data acquisition system

- 96 thermocouple inputs, 64 of them used for measuring the temperature of the engine parts (Fig. 9),
- 16 fast analog inputs with independent sampling rate up to 750 kHz, 16-bit,
- 112 analog inputs,
- 22 analog outputs,
- 104 digital in/out channels,
- digital interfaces (CAN Bus, RS-485, TCP/IP, UDP),
- C Series drivers for direct and port injectors, spark plugs, throttles and encoders.

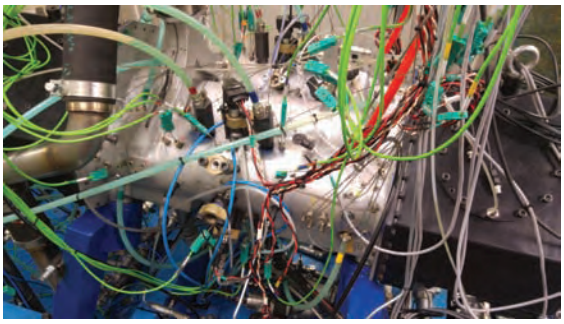

Fig. 9. 64 thermocouples embedded in PAMAR-4 engines

6.2. Software overview

Application is split between PC, PXI and 2xFPGA (Fig. 10). A communication between PC and PXI is solved by using Network Streams over the Ethernet. PXI and FPGA communicates using Direct Memory Access or Front Panel Communication depending on data. Application consists of 4 main modules:

- PX – user module, which allows results visualization and control,
- PXI – real time computer which makes the data acquisition and automatic control by using feedback loops,
- FPGA1/FPGA2 – FPGA matrixes used for fast channel data acquisition (in-cylinder pressure, Kulite pressure transducers, vibrations, knock sensor, encoder) and controlling C Series drivers (ignition, injection).

Texcel V4 (dynamometer controller) and Dewetron's amplifiers are controlled over RS-485 while Bosch BEA gas analyzer 460 over RS-232. As engine response is not known in advance the main role of the ECU is to protect the prototype engine and not allow user to break it down by accident. Every command from automatic control (PID-based) or given by the user is being filtered by so called Watchdog system. This system verifies if either control given by user can be executed or system has to be put in a safe-state (no ignition/injection allowed, engine slowed down aggressively by the dynamometer). PID controls are implemented on the real time computer. There is an independent loop for every PID-controlled actuator. The PID's can be automatically calibrated using Ziegler-Nichols tuning method (heuristic iterative method) or manually by typing P, I and D values.

6.3. 0D diagnostic model

A Single Zone Model has been assumed for calculating heat release from the pressure signal. Gas composition, pressure and temperature is assumed uniform, fuel is evaporated and perfectly mixed. For a diagnostic model the gas exchange phase is not calculated, heat release calculation starts at Inlet Valve Closing (IVC) and ends at Exhaust Valve Opening (EVO). Net heat release rate is calculating using standard formula (9) as in Heywood [8]:

$$dQ_{chem}/d\theta = k/(k-1)PdV/d\theta + 1/(k-1)VdP/d\theta \qquad (9)$$

The polytropic constant k is calculated from logP–logV where compression and expansion curves can be approxi-

mated by linear function. The model calculates work, power, torque, IMEP, heat release and temperature.

7. Additional remarks and future challenges

7.1. TDC

It is not possible to use a Top Dead Center (TDC) sensor due to combustion chamber construction. A wrongly set TDC can lead to serious errors (Fig. 10) while calculating volume-based quantities (dV/dθ). In PAMAR-4 engine the volume function resulting from piston motion (3), (4) has inherent ϕ phase, which can be changed during engine operation resulting in Variable Valve Timing. By using 2 encoders, one correlated with intake piston motion and second one with exhaust piston motion the difference between their indications allows measuring current ϕ. The base offset and TDC position is measured with dial gauges with hand-rotating the shaft. Dewesoft also allows TDC detection while motoring the shaft (without combustion). Pegging (referencing the output to absolute pressure) is currently done by measuring the reference pressure using additional absolute pressure sensor, but there are many more possibilities [14].

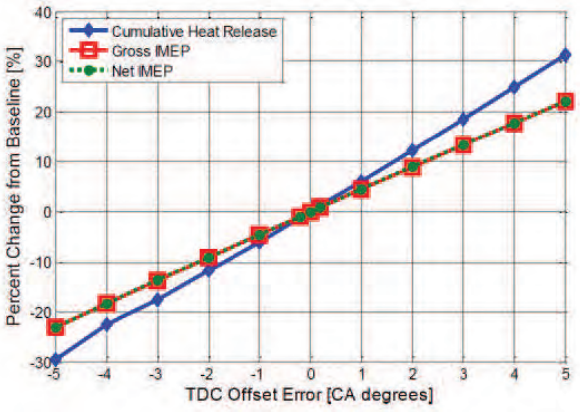

Fig. 10. Effect of TDC offset on cumulative heat release and IMEP [13]

7.2. Scavenging and trapped mass

Currently there is no equipment available on the test stand to measure precisely trapping and scavenging efficiency. This makes trapped mass and concentration uncertain and, as it is a 2-stroke, using an oxygen sensor is questionable (air used for scavenging would disturb it's indication) and then AFR ratio is not known precisely.

8. Preliminary test bed results

The PAMAR-4 has been preliminarily tested on gasoline with direct injection into the combustion chamber with spark ignition. For initial tests the rotational speed has been limited to 800 RPM and Eaton was used only to start an with 20% power, then bypassed. Start of ignition was about 5 deg aTDC and lasted for 40 deg. Maximum pressure was 68 bar with IMEPn 19.2 bar and torque 160 Nm@770 rpm, work per cycle was 997 J thus engine power was 28 kW@770 rpm.

Maximum pressure was observed at 20 deg aTDC, while maximum pressure rise rate was about 5.4 bar/deg. The Fig 11 presents in-cylinder pressure and heat release. As it can be seen there is a need to improve signal filtering and signal processing resolution as heat release is oscillating. Because the pressure signal wat not smoothed the heat release, which has a component proportional to the pressure derivative (9) and thus is very sensitive to the signal quality, was giving false results in range (–80:–20) and (70–90) CAD. The p–V graph (Fig. 12) can be used for calculating mean polytrophic exponent for compression and expansion.

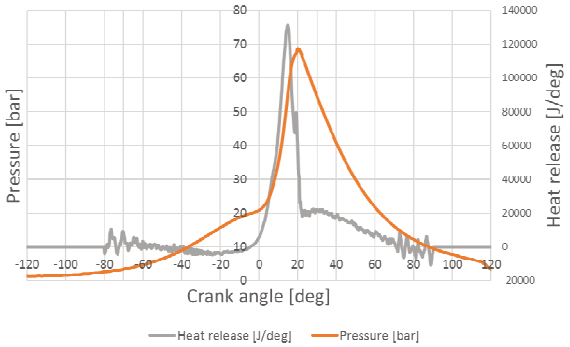

Fig. 11. Preliminary results from PAMAR-4 engine – pressure [Pa] vs crank angle [deg]

The conformance of numerical model with test bed results is not satisfactory yet (Fig. 13). Big discrepancies can be seen for compression and expansion. In author's opinion it can be caused by wrong heat transfer calculations. The Woschni's formula has been taken as is and cylinder liner temperature has been assumed constant. In PAMAR-4 engine total stroke to bore ratio is more than 7 (for 2 pistons), the exhaust-side liner is cooled while the intake one not. Additionally, the initial gas composition is not known exactly at the moment for a 0D model, which leads to errors in results depending on specific gas constant or c_p.

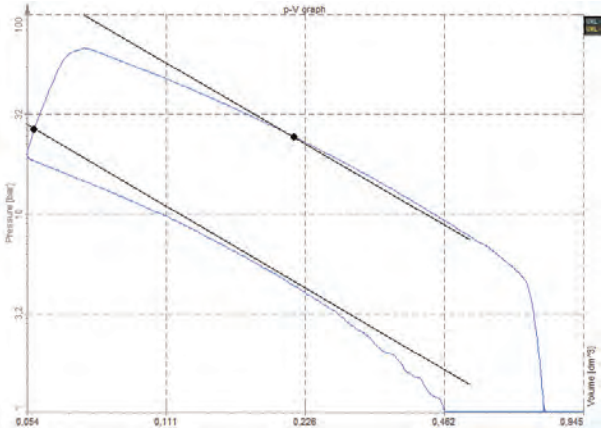

Fig. 12. Preliminary results from PAMAR-4 engine – pressure [Pa] vs volume [dm^3]

9. Summary and future work

A PAMAR-4, 2-stroke, opposed-piston barrel engine, has been designed, build and mounted on the specially designed test bed. As there were no ready-made tools which can be used for analyzing the 2-stroke opposed-piston engine operation authors developed two Single Zone Models (predictive and diagnostic). The equipment and software of the test bed were presented.

Further work will mainly cover the development of a predictive model, which will be upgraded, calibrated and validated with test bed results for various loads and fuels and finally re-written from Matlab to LabView. It will be used for implementing a closed-loop predictive control system basing on cylinder pressure signal. Second model (diagnostic) will be expanded by taking into account fuel injection and blow-by loses. Engine injection and ignition map will be optimized for efficiency.

A test bed should be extended with additional sensors and equipment to allow gas marking to accurately determine scavenging efficiency, trapping efficiency and purity vs delivery ratio for given rotational speed and load. It will allow determining the in-cylinder gas composition.

The measured torque and IMEPn testify to the possibility of obtaining a high power-to-volume ratio in the future while working under the full load. After optimizing the injection and ignition map there will be a possibility to find out what is the achievable efficiency.

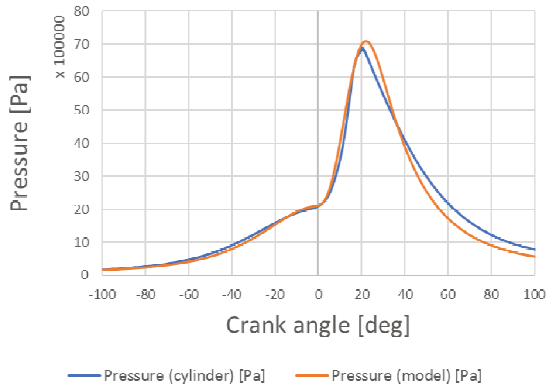

Fig. 13 Preliminary results from PAMAR-4 engine vs 0D model

Nomenclature

OP	opposed-piston
DI	direct injection
SI	spark ignition
TDC	top dead center
FPGA	field-programmable gate array
ECU	engine control unit

Bibliography

[1] PIRAULT, J.P., FLINT, M. Opposed piston engines: evolution, use, and future applications. Warrendale: *SAE International*. 2009.

[2] HEROLD, R.E., WAHL, M.H., REGNER, G. et al. Thermodynamic benefits of opposed-piston two-stroke engines. *SAE Technical Paper*. 2011, 2011-01–2216.

[3] SHARMA, A., REDON, F. Multi-cylinder opposed-piston engine results on transient test cycle. *SAE Technical Paper*. 2016, 2016-01-1019.

[4] Pinnacle Engines, Inc. [Internet]. 2016. Available from: www.pinnacle-engines.com.

[5] KANELLOS, M. New vehicle engines almost here: this time for real [Internet]. Available from: www.forbes.com/sites/michaelkanellos/2015/07/15/new-vehicle-engines-almost-here-this-time-for-real.

[6] MAZURO, P., Rychter, T., Teodorczyk, A. Piston engines with cylinder axis parallel to drive shaft axix – classification and review. *Journal of KONES Powertrain and Transport*. 2007, **13**(3).

[7] GUPTA, R.N., YOS, J.M., THOMPSON, R.A. A review of reaction rates and thermodynamic and transport properties for the 11-species air model for chemical and thermal nonequilibrium calculations to 30000 K. Nasa Technical Memorandum 1989; Available from: ntrs.nasa.gov/search.jsp?R=19890011822.

[8] HEYWOOD, J.B. Internal combustion engine fundamentals. New York, *McGraw-Hill*. 1988.

[9] WOSCHNI, G. A universally acceptable equation for the instantaneous heat transfer coefficient in the internal combustion engine. *SAE Technical Paper*. 1967, 670931.

[10] SIHLING, K., WOSCHNI, G. Experimental investigation of the instantaneous heat transfer in the cylinder of a high speed diesel engine. *SAE Technical Paper*. 1979, 790833.

[11] GHOJEL, J. Review of the development and applications of the Wiebe function : A tribute to the contribution of Ivan Wiebe to engine research Review of the development and applications of the Wiebe function : a tribute to the contribution of Ivan Wiebe to engine research. *International Journal of Engine Research*. 2010, **11**(4).

[12] REGNER, G., JOHNSON, D., KOSZEWNIK, J. et al. Modernizing the opposed piston, two stroke engine for clean, efficient transportation. *SAE Technical Paper*. 2013, 2013-26-0114.

[13] KAUL, B., LAWLER, B., FINNEY, C. et al. Effects of data quality reduction on feedback metrics for advanced combustion control. *SAE Technical Paper*. 2014, 2014-01-2707.

[14] RANDOLPH, A. Methods of processing cylinder-pressure transducer signals to maximize data accuracy. *SAE Technical Paper*. 1990, 900170.

Jakub Kalke, MSc. – Faculty of Power and Aeronautical Engineering at Warsaw University of Technology.

e-mail: *Jakub.Kalke@itc.pw.edu.pl*

Marcin Opaliński, MSc. – Faculty of Power and Aeronautical Engineering at Warsaw University of Technology.

e-mail: *Marcin.Opalinski@itc.pw.edu.pl*

Paweł Mazuro, DSc. – Faculty of Power and Aeronautical Engineering at Warsaw University of Technology.

e-mail: *Pawel.Mazuro@itc.pw.edu.pl*

Article citation info:
SKRĘTOWICZ, M., WOŹNIAK, J., WRÓBEL, R. Evaluation of the efficiency of the three-way catalytic converter of a spark ignition engine of the chosen aromatic hydrocarbons removing. *Combustion Engines*. 2017, **169**(2), 83-86. DOI: 10.19206/CE-2017-214

Maria SKRĘTOWICZ
Joanna WOŹNIAK
Radosław WRÓBEL

CE-2017-214

Evaluation of the efficiency of the three-way catalytic converter of a spark ignition engine of the chosen aromatic hydrocarbons removing

In the paper the results of measurement of the most popular aromatic hydrocarbons (benzene, toluene and xylenes) in the exhaust of spark ignition engine before and after three-way catalytic reactor were presented. The investigations have been conducted at fixed rotational speed, 2500 rpm and at a few different values of torque in range 0 – 80 Nm, every 10 Nm. Based on obtained results, the calculations of catalytic reactor efficiency in removing analysed components have been made. The measurements showed high efficiency of the catalytic converter in reduction of that pollutants in exhaust gases.

Key words: *hydrocarbons, TWC, exhaust, BTX, spark ignition engines*

1. Introduction

Photochemical air pollution is mostly caused by volatile organic compounds (VOCs) from vehicle evaporative emissions. The most significant way of VOCs emissions by vehicle is tailpipe effect, which is characterized by expulsion from the system a large amount of unburned fuel vapours and exhaust fumes from fuel combustion generated during engine operation. Another cause of VOCs emission is evaporative impact, which results in vaporization of fuels regardless of whether the vehicle is moving or not. In addition, volatile organic compounds are emitted from vehicle equipment, such as leather seats, plastics and tires [1]. Generally, the composition of exhaust gases depends on many factors, one of them is type of an engine and its ignition. Self-ignition and spark-ignition have influence on concentration of low boiling hydrocarbons (the greater part of volatile organic compounds) and another gaseous toxic compounds of exhaust gases and solid particles with the fact that higher concentration of VOCs and lower solid particles emission is typical for spark-ignition engines [2]. Main reason of such a state of affairs is less gasoline tendency to create soot regard to diesel fuel [3]. In case of VOCs concentration, it is determined by the course of combustion process which consists complex chemical and physical reactions and phenomena. The best option in this case is total combustion, which prevents the unburned hydrocarbons escape from the system. The impact on these processes has composition of air-fuel mixture in the combustion chamber characterized by the air-fuel ratio λ [4]. The air-fuel ratio in spark-ignition engines closely determines fuel consumption, power, and also exhaust composition in each state of engine's operation. Rich mixture of air-fuel composition ($\lambda < 1$), when the oxygen level is low, causes increased number of unburned hydrocarbons. As the amount of air increases ($\lambda > 1$) the combustion of hydrocarbons is more effective, simultaneously temperature inside combustion chamber increases as well, which supports termination of the reactions, as shown in Fig. 1 [3].

From one year to another increase in the concentration of VOCs in the environment due to the increasing number of total vehicles has major impact on formation of surface ozone [5] and secondary organic aerosols (SOAs) [6]. However, particular importance has their direct toxicity on human health and all living organism in general. The most hazardous compounds from VOCs group are low boiling single aromatic hydrocarbons shown in figure 2, such as benzene, toluene and xylene isomers, known as BTX group [7]. BTX group consists single aromatic hydrocarbons which exist mainly in the gasoline fraction of the petroleum hydrocarbons that mostly are emitted with exhausts from automobiles [8].

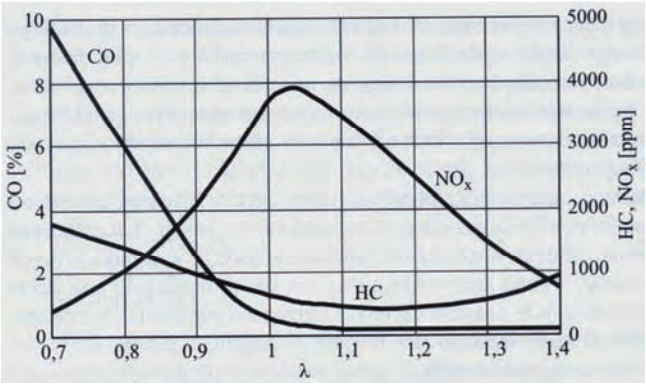

Fig. 1. Carbon monoxide CO, hydrocarbons HC and nitrogen oxides NO_x concentration values depending on the air-fuel ratio [3]

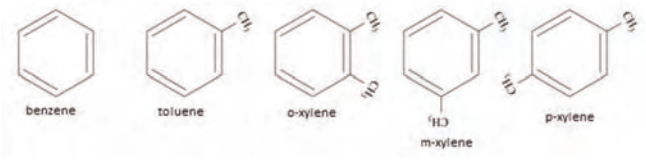

Fig. 2. Skeletal formulas of aromatic hydrocarbons molecules belonging to BTX group

The BTX group is highly toxic, especially benzene. Due to its specific chemical and physical properties, as shown in Table 1, exposure to the BTX group is constantly human health concern. Because of facilitated inhalation of these volatile compounds the health effects begin with general distress (drowsiness, headaches, dizziness) to more severe anomalies in the living organism. Within the long exposure to these compounds BTX group appears to be mutagenic and carcinogenic for the cells of respiratory system [9].

Table 1. Physical and chemical properties of BTX group [10]

	Benzene	Toluene	Xylene		
			orto-	meta-	para-
Chemical formula	C_6H_6	C_6H_5CH	$C_6H_4(CH_3)_2$		
Molar mass, g/mol	78.11	92.14	106.17		
Form	colorless, transparent liquid with characteristic odor				
Density[1)], g/cm^3	0.8737	0.8623	0.8759	0.8601	0.8566
Boiling point, °C	80.10	110.62	144.3	139.1	138.4

[1)] Density in 20°C

Because of the harmfulness of BTX group and other components of combustion fumes in general there is many methods of exhaust purification. Under real conditions of engine operation it is not possible to achieve adequate reaction rate therefore catalytic reactors are used to accelerate certain processes. Nowadays three-way catalytic reactors (TWC) are used for spark-ignition engines due to their possibility to remove three group of the most harmful compounds (carbon monoxide CO, hydrocarbons HC and nitrogen oxides NO_x) [11]. The principle of this type of catalytic reactors operation is based on the support for carbon monoxide and hydrocarbons conversion (oxidation) to non-toxic carbon dioxide as a result of total combustion while the group of nitrogen oxides is simultaneously converted to nitrogen and oxygen (reduction) [3]. Efficiency of TWC depends on many factors, especially its temperature, concentration of pollutants and time of contact with active layer. Temperature of reliable work of catalytic converter is between 250 and 900°C, and the maximum temperature is about 1100-1200°C [11].

2. Material and methods

The tests of three-way catalytic reactor (TWC) efficiency were conducted on the spark-ignition engine Fiat 1.2 on the engine test bench in the Department of Automotive Engineering, Wroclaw University of Science and Technology. It was 4 cylinders and 8 valves, multipoint injection and *natural aspirated* engine with maximum power 46 kW at 5500 rpm and maximum torque 105 Nm at 3200 rpm. The engine was used in the passenger cars such as Fiat Brava or Fiat Punto. The tested engine was coupled by the shaft with the water-cooled electromagnetic brake EMX 100/10000, which allowed applying the engine torque. In Figure 3 the test station was presented. The catalytic reactor was located at the exhaust manifold just after the cylinder outlet.

In the tests the engine was powered by the commercial gasoline with 95 octane number. Before investigations began, it was needed to wait when the engine and the catalyst reactor would achieve their operating temperature. In the tests load characteristic of engine with fixed rotational speed was performed. The rotational speed was set on the 2500 rpm value. The engine was loaded with the torque values from 0 to 80 Nm every 10 Nm. Samples were taken in almost the same time before and after TWC by special *measuring connectors*. After setting the next value of torque, it was needed to wait above 10 minutes before sampling for achieving the suitable temperature of catalytic reactor. Changing the engine's torque with constant rotational speed in spark ignition engine, the temperature of the combustion process and thus the temperature of exhaust fumes changes as well. Beside concentrations of BTX, additionally in the tests fuel consumption (in g/s) was measured.

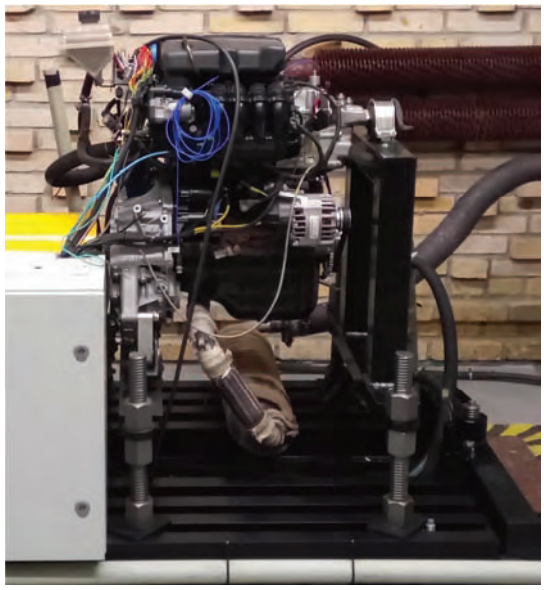

Fig. 3. The engine test station, Fiat 1.2

Concentrations of the aromatic hydrocarbons from BTX group were analysed using gas chromatography method. The samples of the fumes before and after TWC were taken to Teflon bags by the vacuum pump. It allowed for short-term BTX concentration measurement. Then, the content of the bags was given by semi-automatic aspirator ASP-3II into special tubes filled with active carbon. The aspirator was equipped with the pomp and flow controller. From each bag 10 dm^3 of exhausts were transferred with a fixed airflow rate set at 30 dm^3/h. Setting the same value of airflow and the fumes volume in each of samples enabled comparing the concentrations before and after TWC without any additional calculations. All samples were moved to the Laboratory of Emission Researches in the Department of Automotive Engineering, Wroclaw University of Science and Technology, where were analysed with a gas chromatography (GC) method.

In the Laboratory tube samples were prepared for further steps. The sorbent (active carbon) with fumes adsorbed on its surface was extracted from each tube correspondingly to 5 ml flasks. To the flasks was added 2 ml of carbon disulphide solvent and the flasks were tightly closed. The extraction proceeded for 20 minutes, including 5 minutes extraction inside ultrasound generator chamber in temperature about 30ºC. After 20 minutes each solution from over active carbon particles was moved respectively to 10 ml flask and attentively purified from carbon dust. For qualitative and quantitative analysis gas chromatograph Varian 450-GC with FID detector, autosampler and proper capillary column was used. On the chromatography column a

clear solutions were given at an established internal method for VOCs analysis, as follow:

– dispenser temperature: 200ºC,
– oven and capillary column temperature program: 110ºC, 10 minutes, isothermal program,
– FID detector temperature: 250ºC.

3. Results

As a results of gas chromatography analysis are concentration of aromatic hydrocarbons in ppm in solvent (CS_2). It was necessary to calculate these values for concentrations in the exhaust in µg/m^3. The calculations were made using the equation as follow:

$$C_{\mu g/m^3} = \frac{2 \cdot C_{ppm} \cdot 1{,}26 \cdot 10^{-3}}{0{,}8 \cdot V} \quad (1)$$

where: 2 – volume of solvent used in desorption, in cm^3, Cppm – concentration in ppm in solvent, 1,26 – density of CS2, in g/cm^3, 0,8 – error of desorption, V – volume of air, dm^3

Calculations have been made for the values of concentrations measured before and after catalyst reactor. In table 2 concentrations of analysed aromatic hydrocarbons in µg/m3 at 2500 rpm are shown. In figure 4 chart of concentrations of BTX before TWC are presented.

Table 2. Concentration (in µg/m^3) of BTX measured before and after catalyst reactor

Torque, Nm	Concentration before TWC, ug/m^3				Concentration after TWC, ug/m^3			
	Benzene	Toluene	Xylenes	Sum of BTX	Benzene	Toluene	Xylenes	Sum of BTX
0	7.25	22.18	10.53	44.78	1.46	4.90	5.55	14.29
10	5.21	15.35	8.01	32.22	1.87	7.54	7.16	19.59
20	5.99	18.96	10.59	40.23	1.42	4.28	4.91	12.72
30	1.14	4.18	3.01	9.01	0.04	0.25	0.41	0.78
40	1.17	4.19	2.78	8.77	0.17	0.92	1.22	2.56
50	1.21	4.36	3.02	9.32	0.18	1.04	1.41	2.95
60	0.31	1.03	0.55	2.01	0.01	0.05	0.04	0.10
70	1.17	3.95	2.37	8.03	0.03	0.08	0.10	0.24
80	0.50	1.35	0.64	2.64	0.02	0.00	0.01	0.03

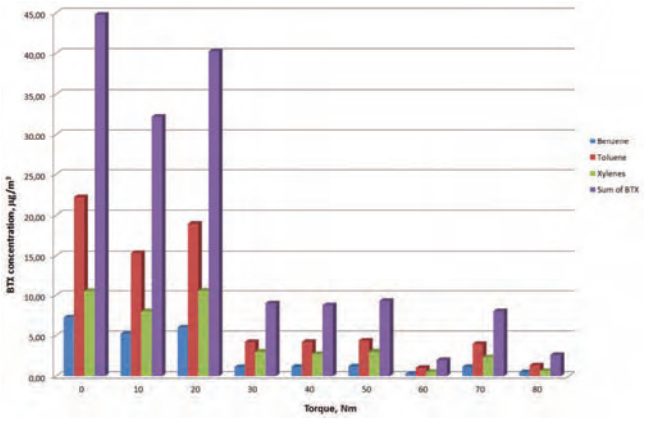

Fig. 4. Concentration of BTX (in µg/m^3) before catalyst reactor depending on the torque value

As it has been written above, one of the duty of the TWC is oxidation of hydrocarbons to carbon dioxide. In Figure 5 comparison of the concentrations before and after catalyst reactor on the example of benzene is shown.

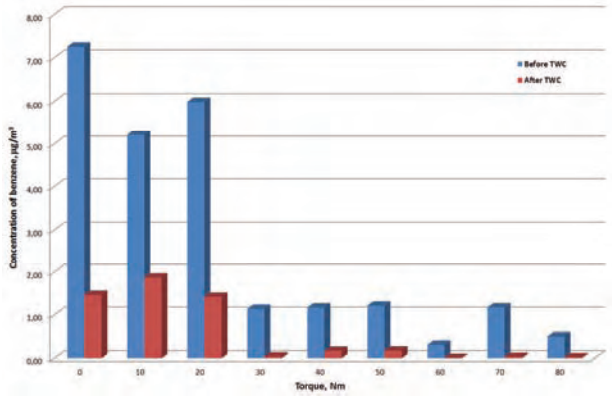

Fig. 5. Concentrations of benzene (µg/m^3) depending on the torque value before and after three-way catalyst reactor

In next step the efficiency of the three-way catalyst reactor has been determined according to the equation:

$$E_f = 1 - \frac{C_{a,i}}{C_{b,i}} \cdot 100\% \quad (2)$$

where: E_f – efficiency of TWC, %, C_a – concentration after TWC, ug/m^3, C_b – concentration before TWC, ug/m^3, i – component of HC

Calculated efficiency of analysed TWC for each of measured aromatic hydrocarbons is shown in Figure 6. In Figure 7 the efficiency of the sum of BTX is shown.

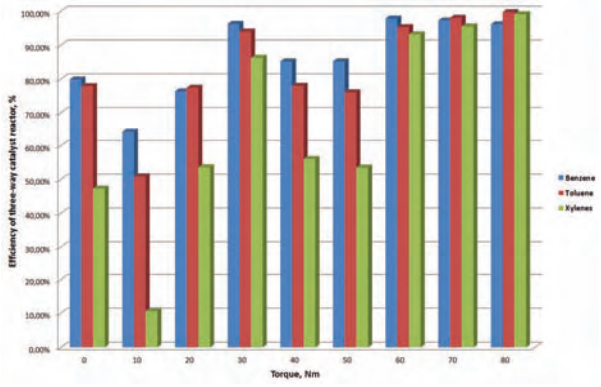

Fig. 6. Effectiveness of analysed aromatic hydrocarbons removal by TWC depending on the torque value

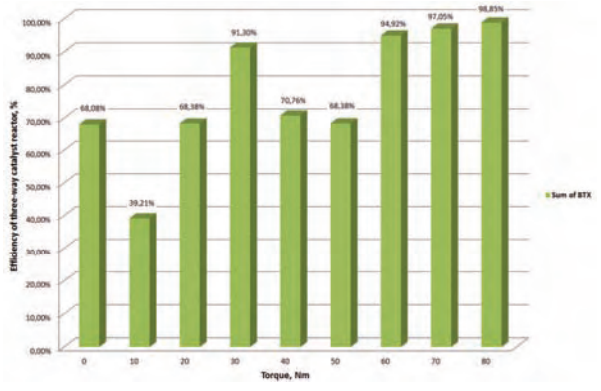

Fig. 7. Effectiveness of sum of BTX removal by TWC depending on the torque value

4. Discussions and conclusions

As it could be seen in Figures 6 and 7, except a few points of engine's work, generally the efficiency of the three-way catalyst reactor is growing with torque value. The figures also shows that the efficiency of the TWC is very high in all range of engine's loads at 2500 rpm. In the highest value of torque (80 Nm) it is almost 99%. The efficiency of the catalytic reactor increases with the torque at constant rotation speed because the higher load, the higher temperature of combustion of the fuel and higher temperature of exhaust (and the TWC simultaneously). In higher temperature of combustion there is less hydrocarbons in exhaust and also the efficiency of the TWC is growing. Disturbances of that trend are observed in several points of engine's work: at torque 0 and 10 Nm and also at 40 and 50 Nm. In the first case (at 0 and 10 Nm) the likely reason was cooling the TWC reactor in low value of torque. Before the measurements the engine was warmed up at 10 Nm for about 30 minutes. Next, the torque was lowered to 0 and waited about 10 minutes. In this time and during the measurement without load the temperature of the exhaust decreased and the TWC cooled down as well. Due to these events, the temperature of TWC during the measurement at 10 Nm could be lower than at 0 Nm, because at 0 Nm torque the TWC didn't cool down after heating up the engine.

In the second case, the reason of decreasing of the TWC efficiency could be disintegration of the higher hydrocarbons in the reactor and increasing of amount of lower hydrocarbons (such as BTX). Oxidation of the hydrocarbons, same as combustion of fuel in the combustion chamber occurs as many chain chemical reactions. It means that firstly the higher hydrocarbons are oxidized to lower ones and only in the final stage to carbon dioxide. In this regard TWC was working with high efficiency and reducing the higher hydrocarbons. Summarizing, obtained results showed that analysed catalytic reactor works well with high efficiency in measured range of engine's work.

Nomenclature

VOC volatile organic compounds
BTX benzene, toluene, xylenes
TWC three-way catalytic converter

Bibliography

[1] YUE, T., YUE, X., CHAI, F. et al. Characteristics of volatile organic compounds (VOCs) from the evaporative emissions of modern passenger cars. *Atmospheric Environment*. 2017, **151**, 62-69.

[2] MERKISZ, J. Wpływ motoryzacji na skażenie środowiska naturalnego. *Wydawnictwo Politechniki Poznańskiej*. Poznań, 1993.

[3] CHŁOPEK, Z. Ochrona środowiska naturalnego. Pojazdy samochodowe. *Wydawnictwa Komunikacji i Łączności*. Warszawa, 2002.

[4] KAŹMIERCZAK, A. Silniki pojazdów samochodowych. Podręcznik do nauki zawodu Technik pojazdów samochodowych, *Wydawnictwo REA*. Warszawa, 2010.

[5] CARTER, W.P.L. Development of ozone reactivity scales for volatile organic compounds. *Journal of the Air and Waste Management Association*. 1994, **44**, 881-899.

[6] ODUM, J.R., HOFFMANN, T., BOWMAN, F.A. et al. Gas/particle partitioning and secondary organic aerosol yields. *Environmental Science and Technology*. 1996, **30**, 2580-2585.

[7] Główny Urząd Statystyczny, Departament Badań Regionalnych i Środowiska: Ochrona Środowiska 2014. Informacje i opracowania statystyczne, Warszawa, 2014; materiał dostępny na stronie internetowej: www.stat.gov.pl.

[8] LIU, F.F., PENG, C., NG, J.C. BTEX in vitro exposure tool using human lung cells: trips and gains. *Chemosphere*. 2015, **128**, 321-326.

[9] JANICKA, A. Ocena toksyczności mikroatmosfery środowiska wnętrza pojazdu samochodowego. *Oficyna Wydawnicza Politechniki Wrocławskiej*, 2013.

[10] MIZERSKI, W., Tablice chemiczne, wyd. piąte zaktualizowane. *Wydawnictwo Adamantan*. Warszawa, 2008.

[11] MERKISZ, J., Ekologiczne aspekty stosowania silników spalinowych. *Wydawnictwo Politechniki Poznańskiej*, Poznań, 1994.

Maria Skrętowicz, DEng. – Faculty of Mechanical Engineering at Wroclaw University of Science Technology.

e-mail: *Maria.Skretowicz@pwr.edu.pl*

Joanna Woźniak, MEng. – Faculty of Mechanical Engenering at Wrocław Univesity of Science and Technology.

e-mail: *Joanna.Wozniak@pwr.edu.pl*

Radoslaw Wróbel, DEng. – Faculty of Mechanical Engineering at Wroclaw University of Science Technology.

e-mail: *Radoslaw.Wrobel@pwr.edu.pl*

Article citation info:
CHŁOPEK, Z., LASOCKI, J. Correlation investigations into pollutant emission and the operational states of compression-ignition engines in dynamic tests. *Combustion Engines*. 2017, **169**(2), 87-92. DOI: 10.19206/CE-2017-215

Zdzisław CHŁOPEK
Jakub LASOCKI

CE-2017-215

Correlation investigations into pollutant emission and the operational states of compression-ignition engines in dynamic tests

This study investigates the correlation dependences between pollutant emission intensity and the engine operational states determining these properties, in various conditions, both in relation to measurements of engine operational states and their dynamic nature. The research was carried out in a variety of dynamic tests. Investigations into the correlations of processes occurring in combustion engines make it possible to assess the impact of one process on another and the relationship between the various processes. In general, it was found that similar dependencies occur for carbon monoxide and hydrocarbons, but were often substantially different for nitrogen oxides.

Key words: *combustion engines, pollutant emission, correlation analysis*

1. Introduction

The objective of this study is to examine the correlation dependences between pollutant emission intensity and the internal combustion (IC) engine operational states determining these properties, in different conditions, both in relation to the values of the states and their dynamic nature. Diverse working conditions of IC engine are applied during engine testing, in a variety of dynamic tests.

The operational states of IC engines which determine pollutant emission from engines pre-heated to a stable temperature are described in this study by the following measures: engine rotational speed, engine torque and effective power. Pollutant emission intensity depending on engine operational states and the intensity of emission of individual pollutants relative to each other have been subjected to correlation research.

Due to the limited size of the article the published research uses only the Pearson's linear correlation [14], and reference is also made to the authors' own unpublished results using the non-parametric correlation theories Spearman's rank correlation [16], Kruskal's gamma correlation [12], and Kendall's tau correlation [10].

Most of the publications concerning correlation relationships between processes occurring in IC engines are associated with engine steering [5, 11] and diagnostics [17]. These publications are more practical than cognitive. Studies on correlation models of particulate matter emission and the quantities characterising smoke opacity [7] can also be met. In the work presented in [8] the sensitivity of pollutant emission to the different specifications of fuels in different areas of the static states of engine operation was investigated. In publication [9] the results of the analysis of particulate matter emission in the conditions of actual bus operation are presented. In that report, the results of investigations into the correlative effects of the particulate matter emission on, *inter alia*, engine operational states, have been published. The results of correlation investigations into pollutant emission from spark-ignition engines and compression-ignition engines have been presented in articles [4] and [3], respectively. Publication [2] deals with research into relationships between the intensity of pollutant emission from compression-ignition engines and the states determining the pollutant emission, carried out by employing the function of intercorrelation between the processes under investigation.

This study deals with research into pollutant emission processes and engine operational states determining the pollutant emission, in dynamic tests characterising the working conditions of compression-ignition engines in non-road machines.

2. Research results

Tests were carried out on a Cummins 6C8.3 engine. It is a four-cylinder turbocharged compression-ignition engine with an 8.3 dm^3 capacity. This engine meets the emission-level requirements of Euro III. The tests were carried out within the project reported in [1]. The engine was tested on a test stand equipped with a dynamometer bench that allows the testing of engines in dynamic conditions.

Research was carried out using dynamic tests:

- NRTC (Non-Road Transient Cycle), employed in type-approval procedures [18],
- BBDT (Bulldozer-Blade Dynamic Test) prepared within the project reported in [1],
- BRDT (Bulldozer-Ripper Dynamic Test) prepared within the project reported in [1].

BBDT and BRDT tests were developed in accordance with the principle of faithful simulations in real time [13]. The results of experiments carried out on a testing ground in the blade and ripper operating modes of a bulldozer were used for the synthesis of tests [1]. As fundamental criteria of similarity when developing the tests, the similarity of the average value and variance of the engine steering and torque in tests, and under empirical test conditions, were assumed.

Figures 1–6 show the time histories of the engine speed and torque in the individual tests. Figures 7–9 represent the set of IC engine operational states within the coordinate system: engine speed – torque, in individual tests. The points of coordinates of the average values of the engine speed and engine torque have also been marked on the graph. Figure 10 represents the points of coordinates: the average values of the engine speed and engine torque in individual tests against the background of full-load torque vs. engine speed curve.

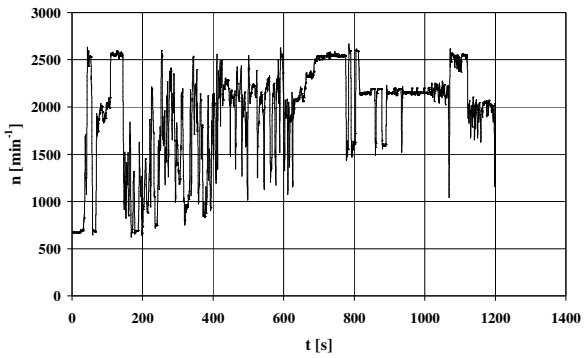

Fig. 1. Engine speed – n vs. time – t curve, recorded in the NRTC test

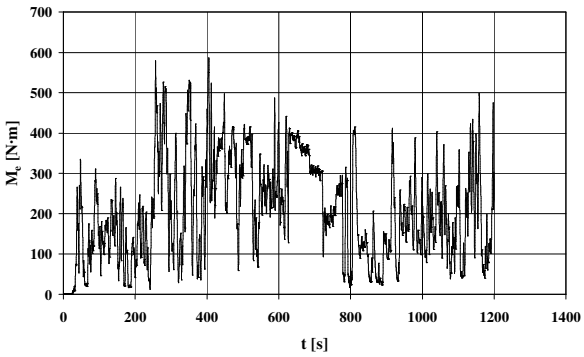

Fig. 2. Engine torque – M_e vs. time – t curve, recorded in the NRTC test

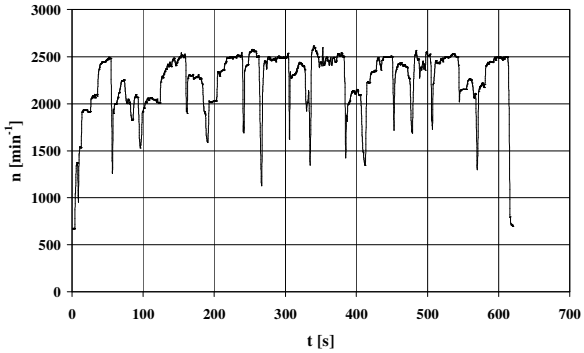

Fig. 3. Engine speed – n vs. time – t curve, recorded in the BBDT test

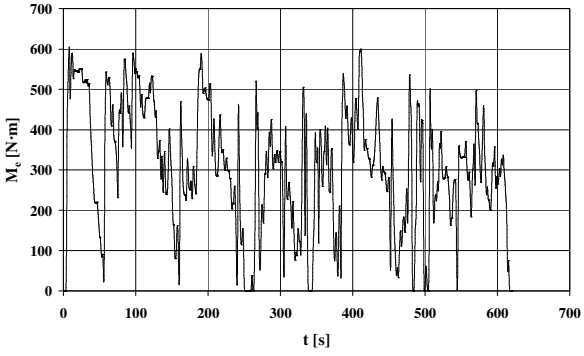

Fig. 4. Engine torque – M_e vs. time – t curve, recorded in the BBDT test

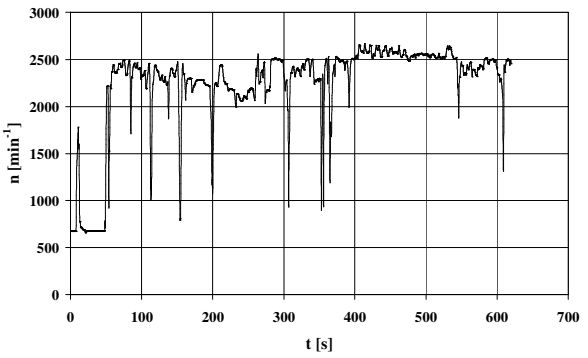

Fig. 5. Engine speed – n vs. time – t curve, recorded during the BRDT test

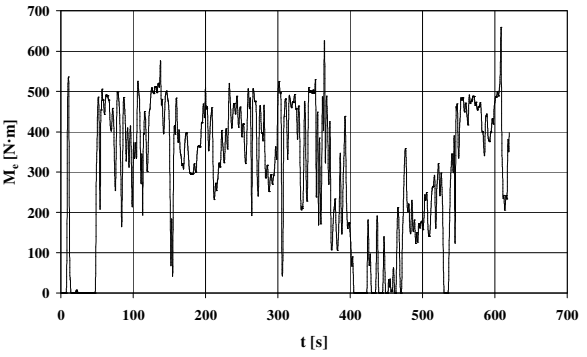

Fig. 6. Engine torque – M_e vs. time – t curve, recorded in the BRDT test

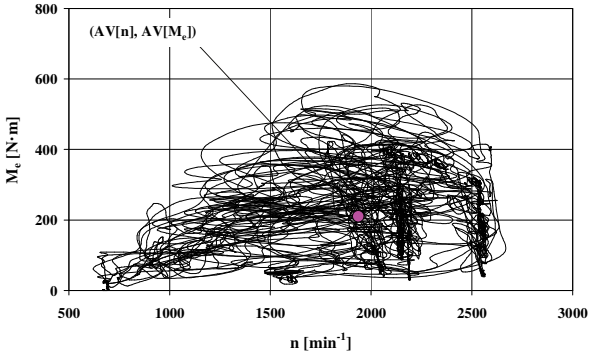

Fig. 7. The set of engine operational states: engine speed – n, torque – M_e in the NRTC test; (AV[n], AV[M_e]) – the coordinates of the average values of the engine speed and engine torque

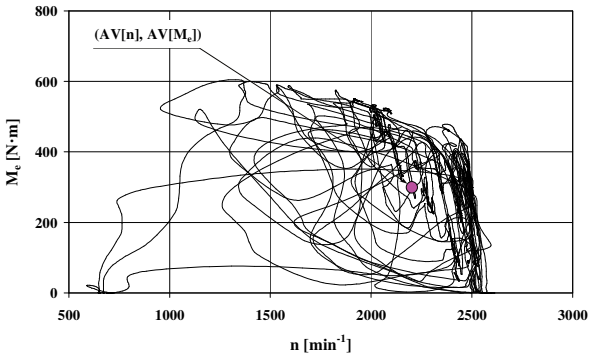

Fig. 8. The set of engine operational states: engine speed – n, torque – M_e in the BBDT test; (AV[n], AV[M_e]) – the coordinates of the average values of the engine speed and engine torque

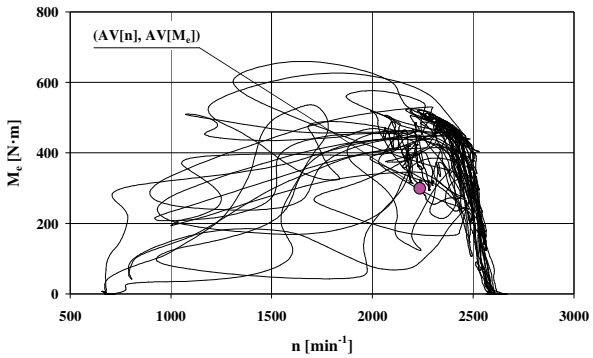

Fig. 9. The set of engine operational states engine speed – n, torque – M_e in the BRDT test; (AV[n], AV[M_e]) – the coordinates of the average values of the engine speed and engine torque

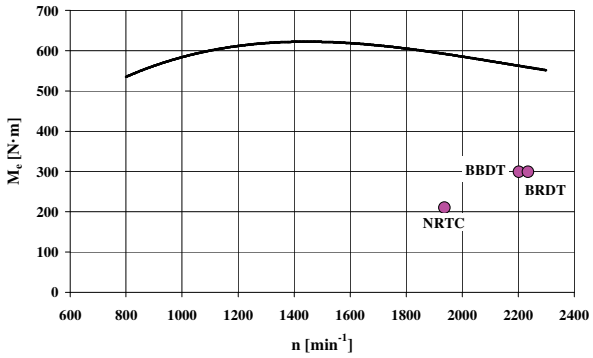

Fig. 10. Points of coordinates: the average value of the engine speed – n, the average value of the engine torque – M_e in tests against the background of full-load torque vs. speed curve

A big difference is clearly visible in the positions of the points of the coordinates: the average values of the engine speed and the engine torque, in individual tests. The BBDT and BRDT tests in respect of the static states of engine operation – according to the criterion of their average values – are close to each other. These tests are characterised by high speed and high loads.

The recorded signals of engine speed, engine torque and pollutant emission intensity were synchronised with taking into account the exhaust-gas tap-off location in the engine-exhaust system – the delays in individual signals, related to the exhaust-gas analysis, were taken into account. The measurement sampling frequency was 10 Hz. The signals were digitally processed to eliminate gross errors and to reduce the influence of high-frequency interference. The gross errors were identified by continuously analysing the variance of measurement results. To reduce the effects of high-frequency noise on the signals, a Golay-Savitzky low-pass filter [15] was used, with both-side approximation from 5 data points on each side to a polynomial of degree 2 being applied.

The graphs shown in Figures 11–13 represent in aggregate form the time histories of pollutant emission intensity in the tests.

Figure 14 shows the average values of pollutant emission intensity in individual tests.

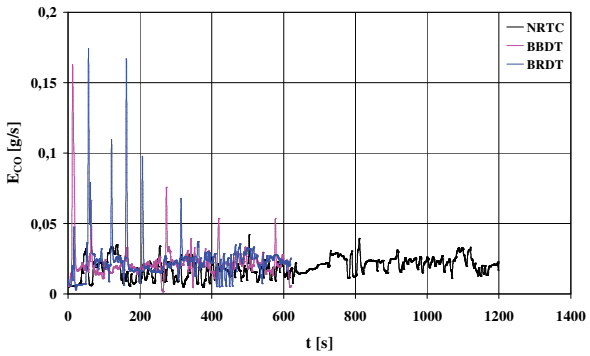

Fig. 11. Courses of the carbon monoxide emission intensity – E_{CO} in tests

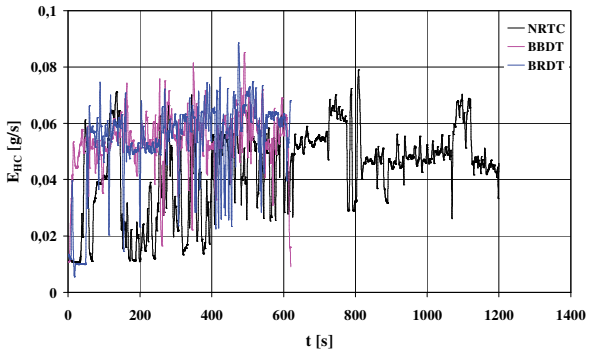

Fig. 12. Courses of the hydrocarbons emission intensity – E_{HC} in tests

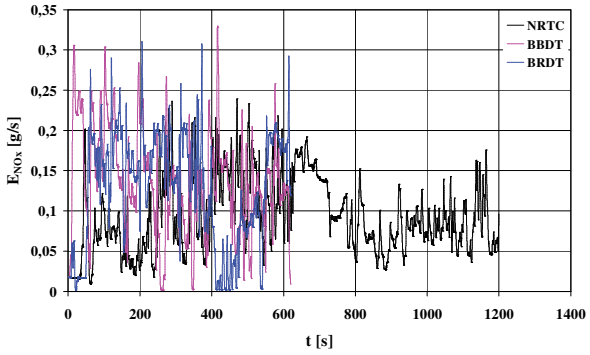

Fig. 13. Courses of the nitrogen oxides emission intensity – E_{NOx} in tests

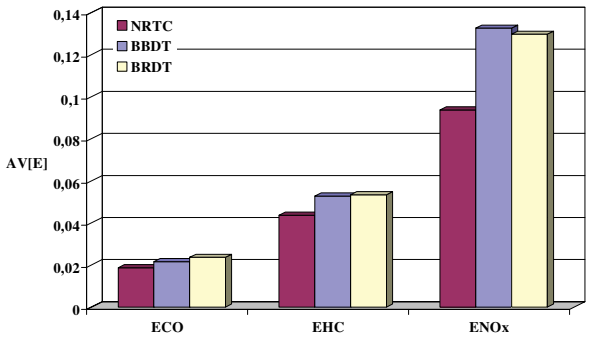

Fig. 14. The average value – AV[E] of pollutant emission intensity in individual tests

There is a clear differentiation between the average values of the pollutant emission intensity in the various tests. Tests with a larger engine load involve larger values of average pollutant emission intensity; particularly large differences occurs in the case of nitrogen oxides. The average values of the emission intensities of individual pollutants in BBDT and BRDT tests are close to each other.

Figs. 15, 16 and 17 show, respectively, the coefficient of Pearson's linear correlation between pollutant emission intensity and engine speed, torque and effective power.

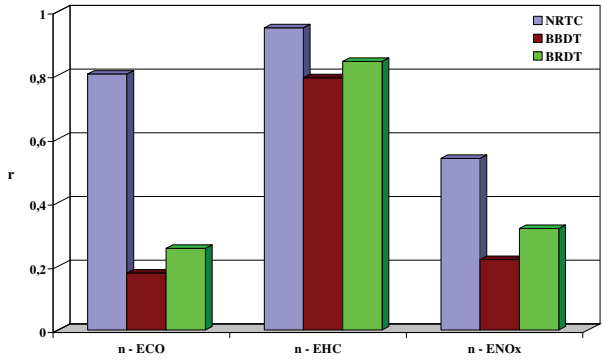

Fig. 15. The coefficient of Pearson's linear correlation – r between engine speed and pollutant emission intensity in individual tests

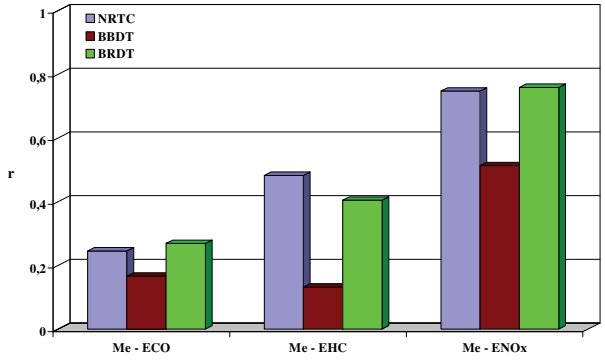

Fig. 16. The coefficient of Pearson's linear correlation – r between engine torque and pollutant emission intensity in individual tests

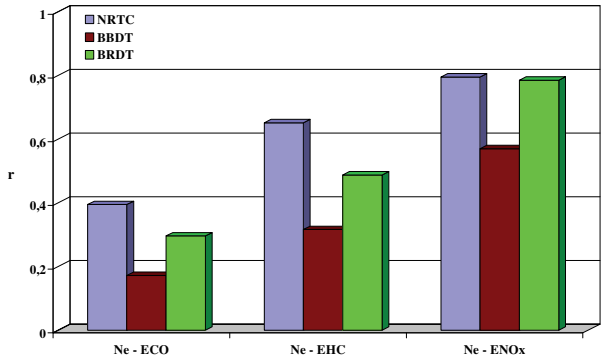

Fig. 17. The coefficient of Pearson's linear correlation – r between engine effective power and pollutant emission intensity in individual test

Although the correlation coefficient values are widely diverse (they range from 0.13 to 0.95), the probability that the hypothesis of the absence of a correlation would not be rejected is below 0.01, even for their lowest values. This can be explained by a very large size of the sets under investigation [6], which consist of about 12,000 elements for the NRTC test and 6,400 for the BBDT and BRDT tests.

The values of the coefficient of correlation between the engine speed and the pollutant emission intensity are the highest in NRTC test, and the lowest in the BBDT test. For torque and effective power the pattern is different: the NRTC and BRDT tests have similar correlation coefficient values, while the BBDT test has considerably lower correlation coefficient values.

Figs. 18–20 present the coefficient of the correlation between the emission intensity of individual pollutants and engine speed, torque and effective power.

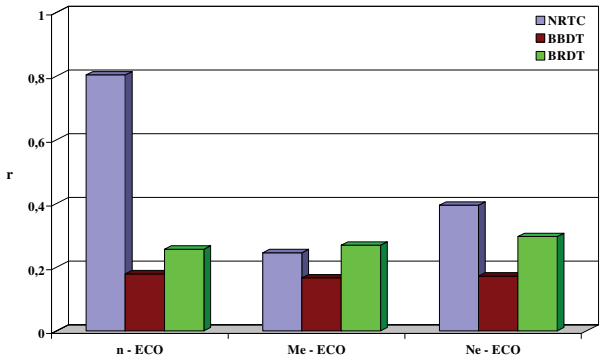

Fig. 18. The coefficient of Pearson's linear correlation – r of carbon monoxide emission intensity with engine speed, torque and effective power

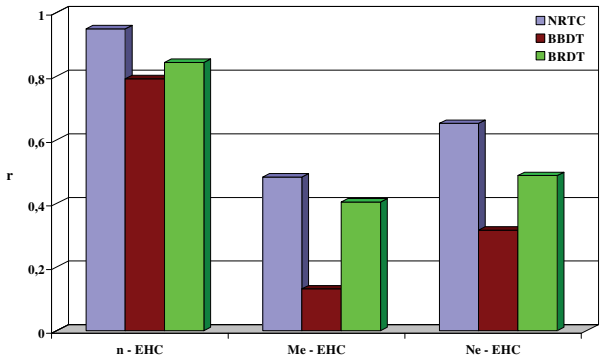

Fig. 19. The coefficient of Pearson's linear correlation – r of hydrocarbons emission intensity with engine speed, torque and effective power

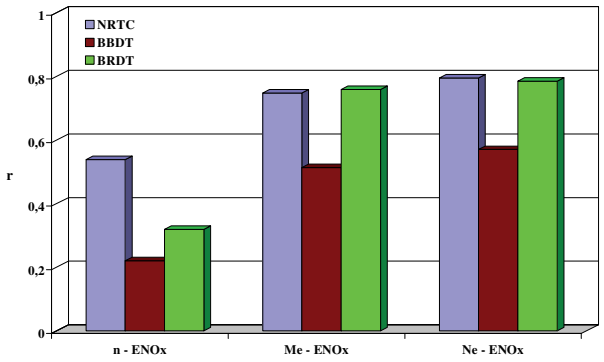

Fig. 20. The coefficient of Pearson's linear correlation – r of nitrogen oxide emission intensity with engine speed, torque and effective power

Similar trends exist for torque and effective power. It is characteristic that the dominant factor determining the emission intensity of hydrocarbons, and – less clearly – of carbon monoxide, is engine speed, whereas of nitrogen oxides – torque and effective power.

Figure 21 shows the correlation coefficient between the pollutant emission intensity in individual tests.

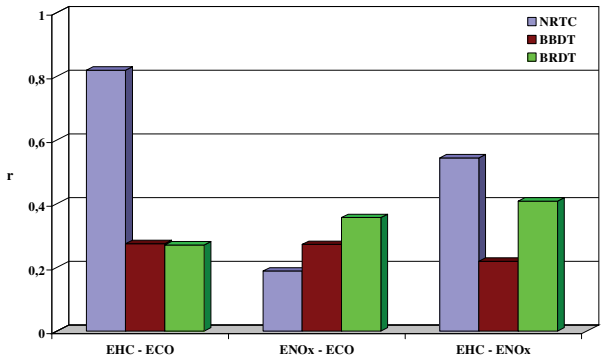

Fig. 21. The coefficient of Pearson's linear correlation – r between the pollutant emission intensity in individual tests

It was found that major differences exist in the values of the correlation coefficient between the pollutant emission intensity in individual tests. Also in this case, the probability that the hypothesis of the absence of a correlation would not be rejected is below 0.01 in all pairs of sets analysed. The correlation coefficient has the highest value for the hydrocarbons emission intensity and the carbon monoxide emission intensity in the NRTC test, while the lowest was in the same test – for the carbon monoxide emission intensity and the nitrogen oxide emission intensity. In all other cases, the differences between the values of the correlation coefficient are lower. In general there is a certain similarity because of the value of the correlation coefficient in the BBDT and BRDT tests.

3. Summary

The research work having been carried out may be recapitulated by formulating the following conclusions:

1. Wide differences between the values of the correlation coefficient for the examined quantities in the range of 0.13 to 0.95 were found. Nevertheless, even for the smallest values, the probability that the hypothesis of the absence of a correlation would not be rejected is below 0.01, which can be explained by the very large size of the sets under investigation.
2. The values of the correlation coefficient between the engine speed and the pollutant emission intensity are the highest in NRTC test, and the lowest in the BBDT test.
3. The NRTC and BRDT tests have the highest values of the correlation coefficient of torque and effective power with pollutant emission intensity, while the BBDT test has considerably lower correlation coefficient values.
4. The dominant factor determining the emission intensity of hydrocarbons and – less clearly – of carbon monoxide, is engine speed, whereas of nitrogen oxides – torque and effective power.
5. It was found that major differences exist in the values of the correlation coefficient between the pollutant emission intensity in individual tests: the correlation coefficient has the highest value for the hydrocarbon emission intensity and the carbon monoxide emission intensity in the NRTC test, while the lowest in the same test – for the carbon monoxide emission intensity and the nitrogen oxide emission intensity.

This paper presents the results of research using Pearson's linear correlation coefficient. Similar results can also be obtained for the coefficients of Spearman's rank correlation, Kruskal's gamma correlation, and Kendall's tau correlation.

Investigations into the correlations between the processes occurring in IC engines make it possible to assess the impact of one process on another and the relationships between the various processes. It is symptomatic of combustion engines that dynamic operating states affect in different ways the phenomenon of the emission of various pollutants. Generally, similar dependencies occur for carbon monoxide and hydrocarbons, but they are often substantially different for nitrogen oxides. The research was performed in three tests simulating the working conditions of IC engine in non-road machines. The authors' own work shows that similar trends apply in the case of other working conditions of IC engines.

Nomenclature

AV	average value
BBDT	Bulldozer-Blade Dynamic Test
BRDT	Bulldozer-Ripper Dynamic Test
E	emission intensity
E_{CO}	carbon monoxide emission intensity
E_{HC}	hydrocarbons emission intensity
E_{NOx}	nitrogen oxides emission intensity
IC	internal combustion
M_e	engine torque
n	engine rotational speed
NRTC	non-road transient cycle
r	the coefficient of Pearson's linear correlation
t	time

Bibliography

[1] BUDNY, E., CHŁOPEK, Z., CHŁOSTA, M. Ocena skuteczności zasilania silnika spalinowego gazem ziemnym w celu ograniczenie emisji zanieczyszczeń w warunkach użytkowania silnika w maszynie do robót ziemnych – ciągniku gąsienicowym (The evaluation of the effectiveness of supplying of combustion engine with natural gas to reduce pollutant emission in the conditions of the engine used in an earth mover – crawler tractor). Report of research

project No. 9 T12 D 013 23 sponsored by the State Committee for Scientific Research, Warsaw 2009 (not published).
[2] CHŁOPEK, Z., SZCZEPAŃSKI, T. Correlation research of combustion engines properties in dynamic states. *Combustion Engines*. 2013, **154**(3), 175-182.
[3] CHŁOPEK, Z. A correlation analysis of the pollutant emission from a self ignition engine. *Silniki Spalinowe – Combustion Engines*. 2010, **140**(1), 25-32.
[4] CHŁOPEK, Z. The correlation researches of a pollution emission from the internal combustion engine. *Czasopismo techniczne. Mechanika*. 2004, **101**(6-M), 151-156.
[5] EPA: The development of emission rates for light-duty vehicles in the motor vehicle emissions simulator (MOVES2009). Draft Report No. EPA-420-P-09-002. The U.S. Environmental Protection Agency, 2009.
[6] FISZ, M. Probability theory and mathematical statistics. *Wiley. New York*, 1963.
[7] JAGADISH, D., KUMAR, P.R., MURHTY, K.M. The performance and emission characteristics of diesel engines run on biofuels based on experimental and semi analytical methods. *International Journal of Energy and Environment*. 2011, **2**(5), 899-908.
[8] JEIHOUNI, Y., PISCHINGER, S., RUHKAMP, L., KOERFER, T. The relationship between fuel properties and sensitivity analyses of non-aromatic and aromatic fuels used in a single-cylinder heavy-duty diesel engine. *SAE Technical Paper*. 2011, 2011-01-0333.
[9] KAMARIANAKIS, Y., GAO, H.O. Diesel ultrafine/fine particle emissions in numbers: statistical modeling and evaluation of engine operating variables. Final Report No. 49777-33-19. The University Transportation Research Center, *The City College of New York*. New York, 2009.
[10] KENDALL, M.G. A new measure of rank correlation. *Biometrika*. 1938, **30**, 81-89.
[11] KITAMURA, Y., MOHAMMADI, A., ISHIYAMA, T., SHIOJI, M. Fundamental investigation of NO_x formation in diesel combustion under supercharged and EGR conditions. *SAE Technical Paper*. 2005, 2005-01-0364.
[12] KRUSKAL, H., WALLIS, W.A. Use of ranks in one-criterion variance analysis. *Journal of the American Statistical Association*. 1952, **260**(47), 583-621.
[13] MARECKA-CHŁOPEK, E., CHŁOPEK, Z. Synteza testów do badań silników spalinowych maszyn roboczych (A synthesis of tests for investigations into the combustion engines of non-road machines). A chapter in "Uwarunkowania ekorozwoju rekreacji i turystyki" (The conditions for the sustainable development of recreation and tourism). *Wydawnictwo Naukowe Gabriel Borowski*, Lublin, 2008, 258-267.
[14] PEARSON, K. On the theory of contingency and its relation to association and normal correlation. Drapers' Company Research Memoirs. *Biometric Ser. I, Dulau and Co.*, London, 1904.
[15] SAVITZKY, A., GOLAY, M.J.E. Smoothing and differentiation of data by simplified least squares procedures. *Analytical Chemistry*. 1964, **36**, 1627-1639.
[16] SPEARMAN, C. The proof and measurement of the association between two things. *American Journal of Psychology*. 1904, **15**, 72-101.
[17] SUAREZ-BERTOA, R., ZARDINI, A.A., ASTORGA, C. Ammonia exhaust emissions from spark-ignition vehicles over the New European Driving Cycle. *Atmospheric Environment*. 2014, **97**, 43-53.
[18] Worldwide emission standards. Heavy-duty & off-road vehicles. Delphi. Innovation for the real world. 2015/2016.

Zdzisław Chłopek, DSc., DEng. – Faculty of Automotive and Construction Machinery Engineering at Warsaw University of Technology.

e-mail: *Zdzislaw.Chlopek@simr.pw.edu.pl*

Jakub Lasocki, DEng. – Faculty of Automotive and Construction Machinery Engineering at Warsaw University of Technology.

e-mail: *J.Lasocki@simr.pw.edu.pl*

Article citation info:
CHWIST, M., SZWAJA, S., GRAB-ROGALIŃSKI, K., PYRC, M. Bio-oil blended butanol as a fuel to the spark ignition internal combustion reciprocating engine. *Combustion Engines*. 2017, **169**(2), 93-96. DOI: 10.19206/CE-2017-216

Mariusz CHWIST
Stanisław SZWAJA
Karol GRAB-ROGALIŃSKI
Michał PYRC

CE-2017-216

Bio-oil blended butanol as a fuel to the spark ignition internal combustion reciprocating engine

The article presents results on combustion of the bio-oil blended butanol in the spark ignition engine. Bio-oil is a mixture of hydrocarbons condensing to liquified phase while cooling it down to ambient temperature. In general, the liquid called bio-oil is a byproduct of the pyrolysis process of organic matter. Results from analysis presented in the manuscript include the following: in-cylinder pressure traces and toxic exhaust emissions. Finally, comparison of these results with results from combustion of n-butanol reference fuel were provided. Obtained results indicate satisfactory, eco-friendly possibility for utilization of bio-oil in the internal combustion engine

Key words: *bio-oil, pyrolysis, butanol, IC engine*

1. Introduction

Pyrolytic bio-oil is a mixture of hydrocarbons that arises as a result of the thermal processing of organic matter in the pyrolysis. During pyrolysis the substrate is heated to a temperature in the range 300-1000°C the absence of oxygen, the process is endothermic. Depending on the temperature, pressure, heating rate and the particle size of the parts, is obtained the various proportions of products in the form of: gases, liquids, solids. For low temperatures 300-450°C and longtime of the material in the reactor 600-6000s the largest share of the pyrolysis products are solids. In the medium temperature range (from 450-700°C) and a range time of from 1 to 5 seconds, most liquid products formed, and the maximum temperature (700-1000°C) and the shortest time less than 1 second are gaseous products. For the production of bio-oil by pyrolysis is used the middle range temperature as the most efficient. In other article, research into the production of bio-oil from pyrolysis of waste was carried out using: the worn out tires, plastics waste, fruit, fish waste, etc. [6, 8].

According to the authors in the world it is 29 million tons of tires recyclable, and only 6.6 million tonnes will be processed. The remaining waste is not processed due to the lack of cost-effective method. In the study, they carried out the pyrolysis of used tires, cut into pieces measuring about 10x10 cm, at a temperature of 450-500°C over a period of 8 hours. As a result of thermal decomposition of tires are: oil pyrolysis, pyrolysis gas, charred residue and steel wire. The pyrolysis bio-oil was distilled at three temperatures of 160°C, 204°C and 350°C. The most received medium fraction. Then, they compared the characteristics of the bio-oil and diesel parameters. The results were as follows: characterized pyrolysis oil is more viscous, which amounted to 2.12 mm^2/s, than diesel oil (3.54 mm^2/s). The distillation fractions were characterized by a lower viscosity, which ranged from 1.18 mm^2/s fraction light to 1.36 mm^2/s for fraction hard. The density of the pyrolysis oil was higher than 860 kg/m^3. Diesel oil fulfill the requirements of DIN EN 590 in the density range of the diesel fuel, which should not exceed 860 kg/m^3. Fractions of the distillation are a density of 825 kg/m^3 to 885 kg/m^3. Only light fraction fulfilled the requirement of the standard. Another parameter which is significant in terms of suitability of the fuel is the acid number. For commercial diesel oil amounted to less than 0.08 mg KOH/g, and the pyrolysis oil 4.33 mg KOH/g, a distillation fraction of bio-oil for this parameter was in the range 2.45-3.77 mg KOH/g. The standard allows the acid number of no greater than 0.5 mg KOH/g of oil, therefore, only diesel to meet this criterion. The next parameter comparable was the flash point for oil amounted to less than 55°C and fulfilled the requirements of the standard. Pyrolytic bio-oil also met this criterion and the ignition temperature was 53°C, and the fractions lit up at 5.5°C light fractions to 40°C heavy fractions. Based on the study, the authors found that the separated fractions of pyrolysis oil can not constitute an independent fuel, because they do not meet the standard requirements [12].

Other scientists have conducted studies on the pyrolysis oven, where the heat source is microwave, but Beneroso D., T. Monti, E.T. Kostas and J. Robisnos critically assessed the microwave pyrolysis process. They emphasize that the experiments in the laboratory scale will never be implemented in the industry, because there is no microwave source with adequate power and which will be worked continuously. And the second problem is to transfer energy from the electromagnetic wave to the material batch, which is not always efficient [2].

In Ghana, looking for alternative ways of obtaining fuel in order to become independent of fossil fuels. Potential see in the peel of oranges as a substrate for the production of bio-oil by pyrolysis. With the increase in demand for processed oranges and orange while increasing crop to 1.6 million hectares in the coming years they could replace 6.7% of all fuels, both diesel and gasoline to bio-fuel in the processing of 10% of waste from oranges. The authors pay more attention to one fact that bio-oil rather be used as a fuel additive and not as a stand-alone fuel. With the support of sector fruit processing by governments and increasing the production orange waste, production bio-oil from peel orange is the most real [1].

Successive authors see potential in waste from the fishing industry. In 2008, fish production reached 144 million tons, half of which is waste. The waste from the fish oil content ranges from 40-65%. Currently, the removal of fish

waste is costly in terms of both economic and ecological. The authors presented the properties of fish oil (waste from salmon). Moreover, they attempted mixed with pyrolysis oil produced from softwood sawdust. The experiment showed that the mixture separate after several minutes, a slight improvement of the miscibility of adding methanol [6].

Other ecological aspect which provide decrease in emission of exhaust gases is use of alcohol fuel in an engine. Using an alcohol in an CI engine is difficult because of its properties which not allow to ignite it as a single fuel. Use a hydrocarbon-alcohol blends in CI engine cause decrease in CO_2 and soot emissions what is discussed by Tutak et al. [9–11].

In the literature a studies can be found, were pyrolysis oil was successfully used to supply a diesel engine. The paper presents the results of the experiment on combustion of mixture pyrolysis bio-oil with alcohols in spark ignition engine [5, 13].

2. Description of the research stand

The test bed consists of the following:

- Single cylinder engine with variable compression ratio (b = 85 mm; s = 115 mm; V = 650 cm^3; ε = 6–14),
- Port fueled system for both gaseous and liquid fuels with heaters for warming up fuels (Fig. 1, 2),
- Dynanometer with breaking power of 5.5 kW,
- Electronic engine control system for spark timing and fuel control,
- Signal gas analysers,
- Data acquisition system with A/D converter resolution of 16 bits and sampling frequency of 100 kHz per each channel,
- Primary fuel applied to investigation was n-butanol due to satisfactory dilution rate of bio-oil in it.

The test stand outline is presented in Fig. 3.

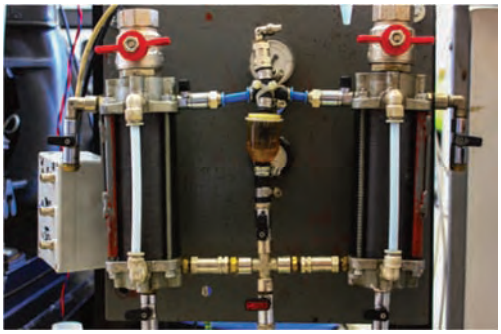

Fig. 1. Dual fuel supply system

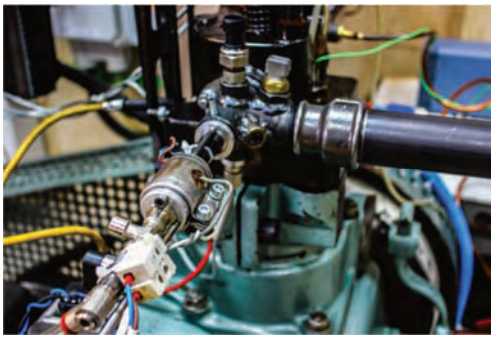

Fig. 2. Heating and fuel injection system

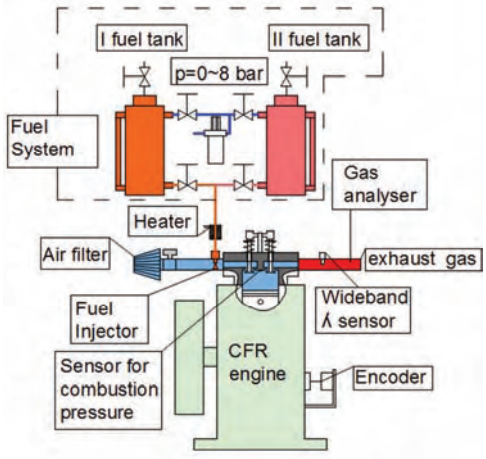

Fig. 3. Scheme of research test stand

3. Analysis of results

Tests were conducted to obtain the data as follows:

- In-cylinder pressure,
- Fuel and air temperature,
- Crank angle,
- Lambda ratio,
- THC, CO, NO_x emissions.

After data processing the following parameters were determined:

- Indicated mean effective pressure (IMEP) shown in Figure 4,
- NO_x, THC and CO from exhaust gases depicted in Figures 5,6 and 7, respectively,
- Combustion pressure (Fig. 8, 9) and its derivative over crank angle dp/dCA (Fig. 10),
- Pressure vs. volume plotted in Fig. 11.

As presented in Figure 4, the IMEP for pure butanol is approximately 20% higher when compared to butanol and 20% bio-oil blends. However, the IMEP for bio-oil blended butanol the characteristics is flat, hence this is less sensitive to spark timing.

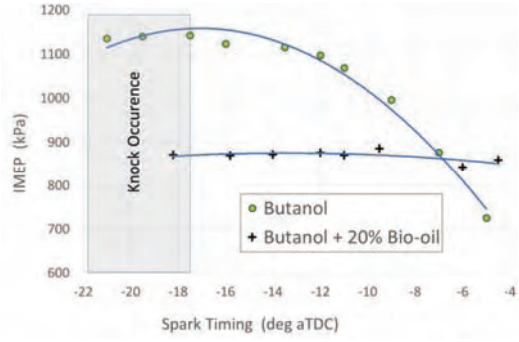

Fig. 4. Indicated mean effective pressure vs. spark timing

Concerning the toxic emissions, it is found that NO_x emission has its maximum at spark timing in the range from –12 to –6 CA deg after TDC. Total unburned hydrocarbons are at their minimum for spark timings from –16 to –10 CA deg aTDC. CO emission is low at spark timing from –12 to –6 CA deg aTDC. This is at the same spark timing range in which the NO_x is high. Thus, as seen in Figures 5-7 the exhaust emissions for THC, CO and NO_x characterizes with

trends typical for other common fuels used in the SI engine as eg. gasoline. However, THC look different what might be caused by several poly-aromatic hydrocarbons species diluted in water in the bio-oil. Thus, for their thermal dissociation longer time is required, that can be achieved by ignition discharge more advanced.

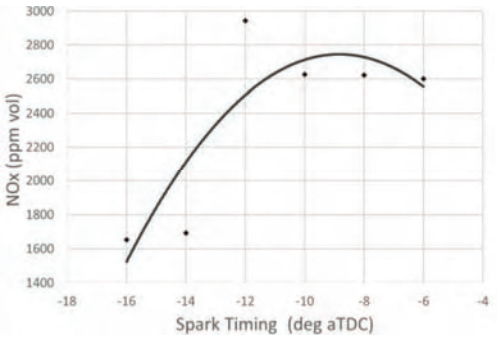

Fig. 5. NO_x emission as a function of the spark timing

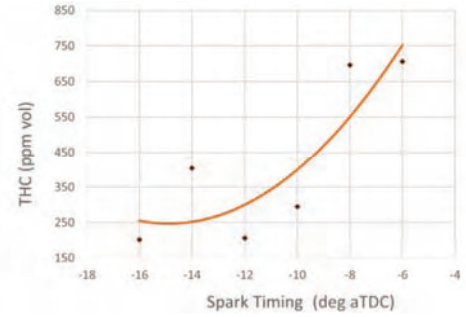

Fig. 6. THC emission as a function of the spark timing

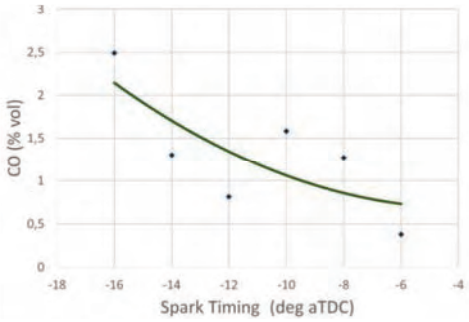

Fig. 7. CO emission as a function of the spark timing

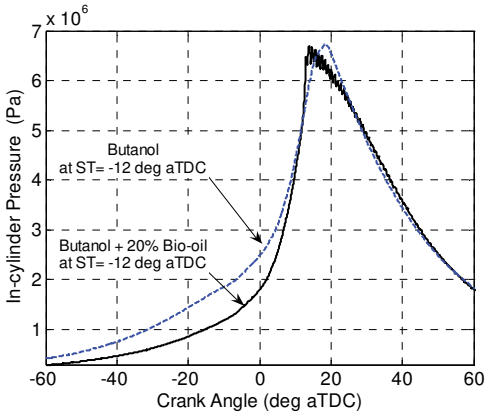

Fig. 8. In-cylinder pressure vs. crank angle

When butanol was blended bio-oil in 20%, anyone can observe tremendous increase in combustion pressure rate as presented in Figure 8 and after filtering in Figure 10. Figure 9 shows closer look on pulsations generated at the end of combustion. They resulted mainly from this high pressure rate observed at the main combustion phase.

As shown in Figure 8 and in Figure 9, pressure pulsations accompany the combustion event of butanol-bio-oil. The pressure pulsations are characterized with peak-to-peak of 400 kPa. Such intensity for pulsations can be considered as harmful to the engine [7].

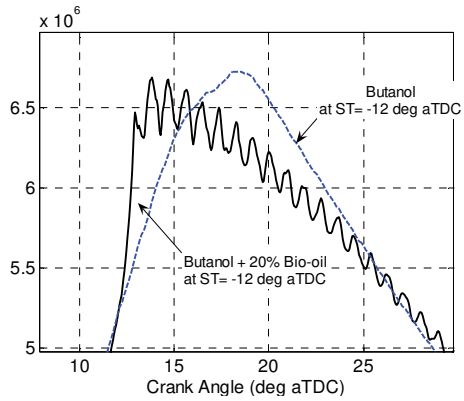

Fig. 9. Zoom on in-cylinder pressure vs. crank angle

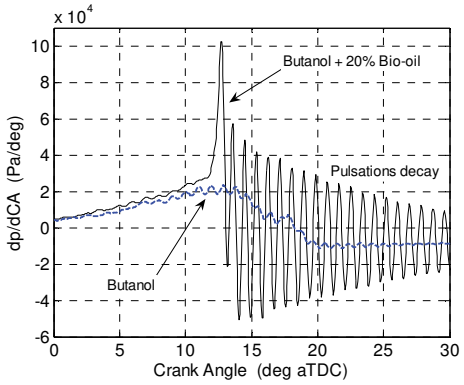

Fig. 10. Pressure rise rate in the function of the crank angle

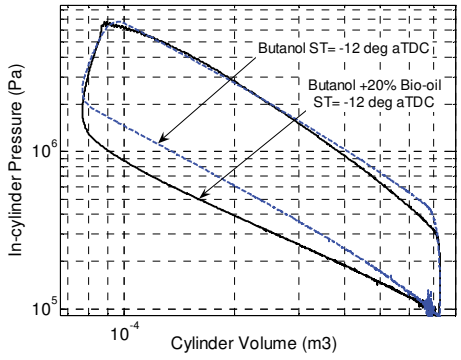

Fig. 11. In-cylinder pressure profile as a function of the cylinder volume

As presented in both Figures 8 and 11, one can conclude that to reduce pressure pulsations and reduce in this way knock intensity, the engine fueled with

butanol blended bio-oil had to work at lower load by approximately of 20%. Hence, the throttle was closed to the required position to maintain the specific engine load.

4. Conclusion

The following conclusions can be drawn from the research:

- Bio-oil can be combusted in the IC engine after its dilution in alcohol eg. n-butanol.
- Due to lower heating value if compared to other fuels the bio-oil in blends decreases overall heating value, so does engine performance.
- Bio-oil as additive to other fuels increases combustion rate, what can cause several symptoms of combustion knock, hence knock reduction measures are required to be implemented in this purpose.
- As far as toxic emission is concerned, addition of 20% bio-oil to butanol fuel reports similar emission as is typical for other fossil based fuels.

5. Acknowledgments

The present research was conducted in the frame of the project No. BIOSTRATEG1/270745/2/NCBR/2015, entitled: "Dietary, Power and Economic Potential of Sida Hermaphrodita Cultivation on Fallow Land" supported by the Polish National Centre for Research and Development.

Nomenclature

CA	crank angle
CI	compression ignition
CNG	compressed natural gas
DI	direct injection
IC	internal combustion
IMEP	indicated mean effective pressure
LPG	liquified petrolum gas
SI	spark ignition

Bibliography

[1] ABOAGYE, D., BANADDA, N., KIGGUNDU, N., KABENGE I. Assessment of orange peel waste availability in Ghana and potential bio-oil yeld using fast pyro-lysis. *Renewable and Sustainable Energy Reviews*. **70**, 2017, 814-821.

[2] BENEROSO, D., MONTI, T., KOSTAS, E.T., ROBINSOS J. Microwave pyrolysis of biomass for bio-oil production: Scalable processing concepts. *Chemical Engineering Journal.* 2017, **316**, 481-498.

[3] GRAB-ROGALINSKI, K., SZWAJA, S. The combustion properties analysis of various liquid fuels based on crude oil and renewables. *IOP Conference Series: Materials Science and Engineering*. **148(1)**, 012066.

[4] HASSAN, H., LIM, J.K., HAMEED, B.H. Recent progress on biomass co-pyrolysis conversion into high-quality bio-oil. *Bioresource Technology*. 2016, **221**, 645-655.

[5] KALARGARIS, I., TIAN, G., GU, S. Combustion, performance and emission analysis of a DI diesel engine using plastic pyrolysis oil. *Fuel Processing Technology*. 2017, **157,** 108-115.

[6] KRUTOF, A., HAWBOLDT, K. Blends of pyrolysis oil, petroleum, and other bio-based fuels: a review. *Renewable and Sustainable Energy Reviews*. 2016, **59**, 406-419.

[7] SZWAJA, S., NABER, J.D. Dual nature of hydrogen combustion knock. *International Journal of Hydrogen Energy*. 2013, **38**(28), 12489-12496.

[8] TANSY, WIGLEY, ALEX, C.K., YIP SHUSHENG, PANG. A detailed product analysis of bio-oil from fast pyrolysis of demineralised and torrefied biomass. *Journal of Analytical and Applied Pyrolysis*. 2017, **123**, 194-203.

[9] TUTAK, W., JAMROZIK, A., PYRC, M. Experimental investigations on combustion, performance and emissions characteristics of compression ignition engine powered by B100/ethanol blend. *Energy and Fuels*. 2016, E3S Web of Conferences 14, **02019**.

[10] TUTAK, W., JAMROZIK, A., PYRC, M. Co-combustion of biodiesel with oxygenated fuels in direct injection diesel engine. *Energy and Fuels*. 2016, E3S Web of Conferences 14, **02018**.

[11] TUTAK, W., SZWAJA, S. The effect of methanol–diesel combustion on performance and emissions of a direct injection diesel engine. *Journal of KONES Powertrain and Transport*. 2015, **22**(2), 259-266.

[12] VIHAR, BASKOWIĆ U.Z., SELJAK, T., KATRAŚNIK, T. Combustion and emission formation phenomena of tire pyrolysis oil in a common rail diesel engine. *Energy Conversion and Management*. 2017.

[13] YONGSHENG, FAN, YIXI CAI, XIAOHUA, LI LIHUA, JIAO JISHENG, XIA XIULI DENG. Effects of the cellulose, xylan and lignin constituents on biomass pyrolysis characteristics and bio-oil composition using the Simplex Lattice, *Mixture Design Method Energy Conversion and Management*. 2017, **138**, 106-118.

Mariusz Chwist, MSc. – Faculty of Mechanical Engineering and Computer Science at Czestochowa University of Technology.

e-mail: *Chwist@imc.pcz.pl*

Stanisław Szwaja, DSc., DEng. – Faculty of Mechanical Engineering and Computer Science at Częstochowa University of Technology.

e-mail: *Szwaja@imc.pcz.pl*

Karol Grab-Rogaliński, MSc. – Faculty of Mechanical Engineering and Computer Science at Czestochowa University of Technology.

e-mail: *Grab@imc.pcz.pl*

Michał Pyrc, MSc. – Faculty of Mechanical Engineering and Computer Science at Czestochowa University of Technology.

e-mail: *Pyrc@imc.pcz. pl*

Article citation info:
LESIAK, K., BRZEZANSKI, M. Concept of the exhaust system of combustion engines used in underground mining. 2017, **169**(2), 97-100. DOI: 10.19206/CE-2017-217

Krzysztof LESIAK
Marek BRZEZANSKI

CE-2017-217

Concept of the exhaust system of combustion engines used in underground mining

Analyses the problems occurring in the exploitation combustion engines used in mining have been presented in article. Design solutions used at present to protect the intake and exhaust systems of internal combustion engines operated in underground hard coal mines have been also described. A new design concept of exhaust system have been presented.

Key words: *exhaust system, temperature of exhaust gases, CI combustion engine, flame arrester, hard coal mining*

1. Introduction

The use of internal combustion engines in underground mining, and especially in hard coal mining, requires meeting a number of safety requirements. Safety requirements related to the use of internal combustion engines in potentially explosive atmospheres are described in a series of Standards EN 1834.

The article focuses on the requirements for Group I engines used in underground workings susceptible to methane firedamp and/or combustible dust (EN 1834-2: 2000 [1]) as regards the protection of the air intake and exhaust systems.

The main requirement for air intake and exhaust systems is a necessity of equipping them with the flame arrester, and additionally equipping the exhaust system with spark arrester. Another requirement for machines working in the presence of combustible dust is keeping the surface temperature below 150°C. The maximum temperature applies to the surface of the machine as well as to the exhaust gases emitted into the atmosphere directly behind the flame arrester.

Therefore, design solutions of flame arresters and the method of reducing the exhaust gases temperature to the required value are of vital importance.

An additional aspect that is particularly important in underground mine workings is the quality of emitted exhaust gases. Specific requirements in this regard depend on engine power and are described in the Standard EN 1679-1:1998+A1:2011 [2]. Table 1 shows the requirements of the Standard in terms of the emission limit applied to engines operating underground.

Table 1. Emission limits [2]

Power P [kW]	Carbon monoxide CO [g/kWh]	Hydrocarbons HC [g/kWh]	Nitrogenoxide NOx [g/kWh]	Particulates PT [g/kWh]
37 ≤ P < 75	6.5	1.3	9.2	0.85
75 ≤ P < 130	5.0	1.3	9.2	0.7
130 ≤ P < 560	5.0	1.3	9.2	0.54

Although internal combustion engines currently used in underground workings machines meet the above requirements, due to the limited cross-section, limited volume of mining workings and the health of mining personnel, any improvement in exhaust gas quality is justified.

2. Present solutions

2.1. Flame arresters

Flame arresters are designed to stop the flame that may occur in the intake and/or exhaust system before igniting the potentially explosive external atmosphere.

Extinguishing the flame can be achieved by eliminating one of the following components: fuel, oxygen, heat. Flame arresters eliminate heat and their principle of operation is based on gap effect (flame extinguishing in narrow gap through absorbed heat from a flame, below auto-ignition temperature). The gap effect is closely associated with Maximum Experimental Safe Gap (MESG). MESG is the result of standard measurement, described in the EN 60079-20-1:2010 Standard [3], aimed at determining the maximum gap at the standard length of 25 mm (and on the standard stand) that does not cause explosion transfer (it extinguishes the flame). Gases and vapors are classified according to their maximum experimental safe gaps into Groups I, IIA, IIB and IIC.

Group I includes equipment for mines susceptible to firedamp (MESG Methane (firedamp) = 1.14). Group II includes equipment for areas with an explosive gas atmosphere other than mines susceptible to firedamp. Group II equipment is subdivided and, for the purpose of classification of gases and vapors, the MESG limits are [3]:

– Group IIA: MESG ≥ 0.9 mm (exemplary gases: propane, acetone),
– Group IIB: 0.5 mm < MESG < 0.9 mm (exemplary gases: ethylene, formaldehyde),
– Group IIC: MESG ≤ 0.5 mm (exemplary gases: hydrogen, acetylene).

2.2. Examples of flame arresters

There are many manufacturers offering flame arresters of various types (end tubes, deflagration, detonation, etc.), certified for use in Group II Hazardous Areas. A typical function element (flame extinguishing) is shown in Fig. 1.

Important parameters for the proper operation of the flame arrester are the gap width, its length (thickness of the function element) and maximum working temperature (maximum working temperature is related to the possibility of absorbing heat from a flame, below the auto-ignition temperature).

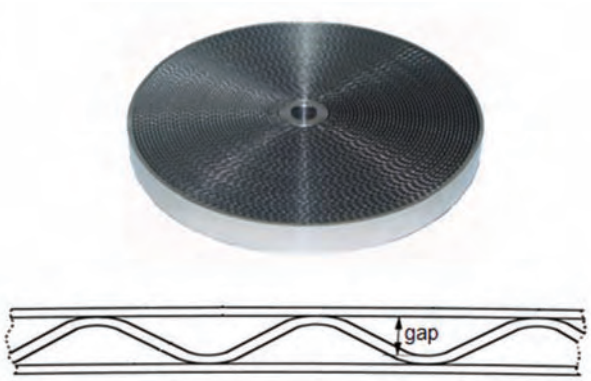

Fig. 1. Example of function element of a flame arrester [4]

There are no certified flame arresters for Group I (intended for an operation in underground mines).

Type tests of such flame arresters include testing of the whole "installation", from the flame arrester in the air inlet system to the flame arrester in the exhaust system. The requirements and the type approval process are described in EN 1834-2: 2010 Standard (for use in internal combustion engines). An example of the flame arrester, designed at the KOMAG Institute of Mining Technology, used in a mine combustion engine is shown in Fig. 2 and its functional element is shown in Fig. 3.

Fig. 2. Flame arrester used in a mine combustion engine

Fig. 3. Function element of a flame arrester, model (left), real view (right) [5]

2.3. Reduction of exhaust gas temperature

In accordance with the requirements of EN 1834-2 Standard, the exhaust gas temperature from the engine, in the presence of combustible dust in the atmosphere, measured directly behind the flame arrester cannot exceed 150°C. Two types of heat exchangers, used to reduce exhaust gas temperature to the required values, can be installed in the internal combustion engines. They include a wet heat exchanger (also called water washer) and a dry heat exchanger. In the first solution, the exhaust gas has direct contact with the coolant. In the second solution, the transmission of heat from the exhaust gases to the coolant is carried out through the walls separating the exhaust gas from the coolant [5]. So far the research and development work realized at the KOMAG Institute of Mining Technology has included both technical solutions (Figs 4 to 7).

Despite high efficiency of exhaust gas cooling with the use of wet heat exchanger, the disadvantage of using it consists in a necessity of monitoring the level of the cooling water and of making it up. As a consequence, dry heat exchangers are used more often. In a dry heat exchanger the coolant circulates in a closed loop system and after getting the heat from the exhaust gases it is cooled by an additional radiator with a forced air flow[6] .

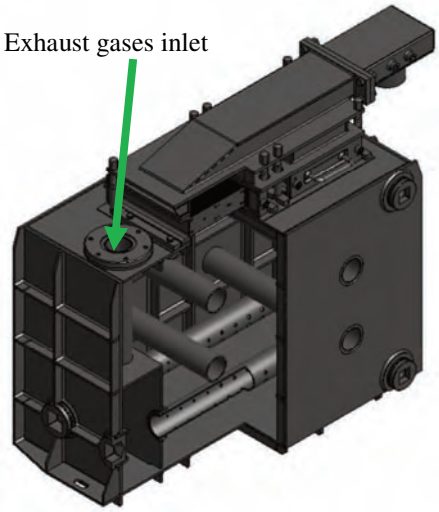

Fig. 4. Wet heat exchanger (model) [6]

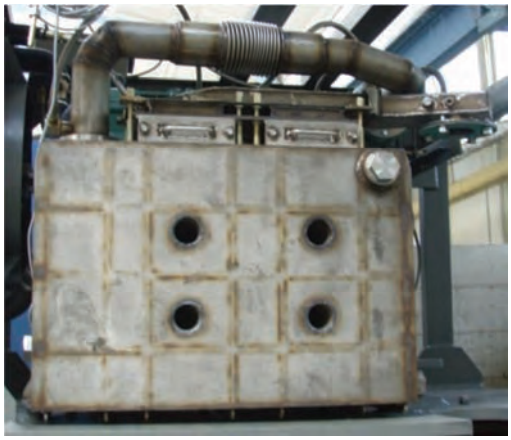

Fig. 5. Wet heat exchanger (real view) [6]

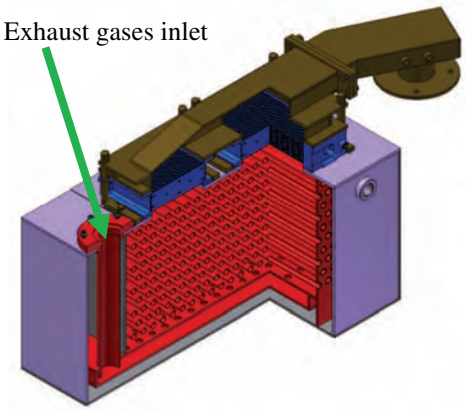

Fig. 6. Dry heat exchanger (model) [7]

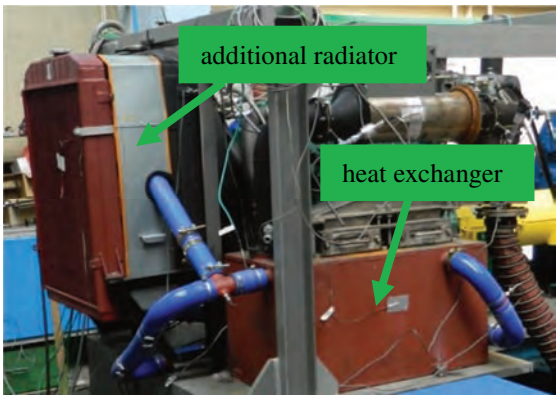

Fig. 7. Dry heat exchanger (real view) [7]

3. Concepts of the exhaust system and function element of the flame arrester

One of the basic disadvantages of cooling systems, used at present, is their big weight and dimensions. Additionally the wet heat exchanger requires constant monitoring of the level of the coolant as well as it gives additional resistance to the exhaust gases.

In order to improve the exhaust system, and at the same time to meet the safety requirements for combustion engines working in the hard coal mining industry, and with a purpose to improve exhaust gas quality, the authors have developed a new design concept of this system. A general view of the design concept is shown in Fig. 8.

In the presented design concept combustion products from the internal combustion engine are directed to the Diesel Oxidation Catalyst (DOC), where CO and HC oxidation occurs. The DOC reactor (in addition to air thermal insulation) is provided with a solid insulation (eg. mineral wool) to maintain its surface temperature below 150 °C (additional water cooling may be provided if necessary). To increase the oxidation, additional air (oxygen) is supplied before the catalytic reactor. The exhaust gas is cooled using compressed air from the environment. Mixing of cool air with hot exhaust gases is realized with an ejector. The control system, using temperature transducers, acts as a protection against excessive exhaust gas temperature and oxidation control in the DOC reactor (control of the amount of oxygen directed to the reactor input is considered). The use of pressure transducers in the intake air system for the engine is aimed at an early detection of the risk associated with the transfer of the explosion through the intake air system.

As a compressor providing additional air, the use of a second compressor powered by exhaust gases or a compressor powered by an autonomous source (eg. hydraulic drive) is considered.

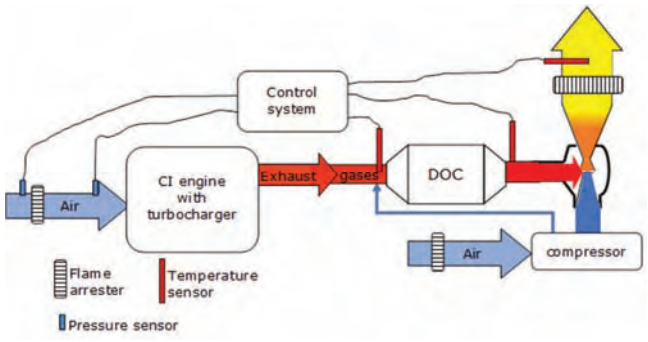

Fig. 8. Design concept of air cooling of exhaust gases with DOC reactor [8]

As a part of the planned research work on a development of the presented concept, an analysis of possibilities to use ceramic catalyst monoliths instead of currently used function element in flame arrester is also made. The ability to use such cores would be an alternative to the solutions used at present.

4. Summary

The article describes design solutions used at present to protect the intake and exhaust systems of internal combustion engines operated in underground hard coal mines. Special attention is paid to the risks resulting from high temperature and the transfer of flame. From the presented analyses the following conclusions can be drawn:

- Group IIA: MESG ≥ 0.9 mm (exemplary gases: propane, acetone),
- exhaust gas temperature reduction systems, used at present, are of large dimensions and weight,
- the wet heat exchanger requires constant monitoring of the coolant level, which is a hindrance in the day-to-day operation of machines,
- the wet heat exchanger is characterized by high resistance to exhaust gases,
- the dry heat exchanger does not require water replenishment for daily use,
- the dry heat exchanger requires an additional radiator and a pump for water circulation, in order to decrease the temperature of water.

This article presents the concept of the exhaust system. The expected benefits of this concept include:

- significant decrease of CO and HC content in exhaust gases (> 50%) [9],
- elimination of the heat exchanger,
- weight reduction of the entire exhaust system,
- increase of efficiency (by reducing weight in comparison with the systems used at present) and of engine power (reduction of exhaust resistance).

However, the disadvantages are as follows:

- possibility of increasing NO_x emissions,
- additional equipment, i.e. the second air compressor and another flame arrester.

As a part of the development work on the concept, numerical analyses are planned to determine the technical parameters of the compressor used for cooling the exhaust gases and the ejector element. As a part of the research work on the possible use of ceramic monoliths, the first step includes testing the abrasion resistance of ceramic material which, according to the requirements of EN 1834-2: 2002 Standard, must be equal to or better than for stainless steel 14404 or 14435.

Bibliography

[1] EN 1834-2:2000 Reciprocating internal combustion engines. Safety requirements for design and construction of engines for use in potentially explosive atmospheres. Group I engines for use in underground workings susceptible to firedamp and/or combustible dust.

[2] EN 1679-1:1998+A1:2011 Reciprocating internal combustion engines. Safety. Compression ignition engines.

[3] EN 60079-20-1:2010 Explosive atmospheres. Material characteristics for gas and vapour classification. Test methods and data.

[4] www.techmako.pl, Przerywacze płomieni/Zawory oddechowe

[5] KACZMARCZYK K., BRZEŻAŃSKI, M. Problemy ekologiczne silników spalinowych eksploatowanych w wyrobiskach podziemnych węgla kamiennego *Prace naukowe – Monografie*. Gliwice. 2015.

[6] DOBRZANIECKI, P. Modelowanie charakterystyk trakcyjnych napędów na przykładzie pojazdów górnictwa węglowego. *Praca doktorska*. Gliwice 2012.

[7] KACZMARCZYK, K. Metoda dostosowania silnika do wymagań stawianych górniczym napędom spalinowym. *Praca doktorska*. Gliwice 2014.

[8] LESIAK, K. Redukcja toksycznych składników w spalinach silników wysokoprężnych oraz optymalizacja układu wylotowego spalin. *ITG KOMAG*, Gliwice 2016, materiały niepublikowane.

[9] KRUCZYŃSKI, S., DANILCZYK, W. Ograniczanie szkodliwości gazów wylotowych silników spalinowych poprzez zastosowanie reaktorów katalitycznych. *MOTROL.* 2007, **9**, 93-102.

Marek Brzeżański, DSc., DEng. – Faculty of Mechanical Engineering at Cracow University of Technology.

e-mail: *MBrzez@pk.edu.pl*

Krzysztof Lesiak, MEng. – KOMAG Institute of Mining Technology.

e-mail: *KLesiak@komag.eu*

Article citation info:
KOWALSKI, J. The theoretical investigation on influence the fuel spray geometry on the combustion and emission characteristic of the marine diesel engine. *Combustion Engines*. 2017, **169**(2), 101-107. DOI: 10.19206/CE-2017-218

Jerzy KOWALSKI

CE-2017-218

The theoretical investigation on influence the fuel spray geometry on the combustion and emission characteristic of the marine diesel engine

The paper presents an analysis of the influence of the fuel spray geometry on the combustion and emission characteristic of the marine 4-stroke Diesel engine. Presented analysis was prepared based on computational fluid dynamic model (CFD). Initial and boundary conditions of the model as well as data used to model validation were collected during the laboratory study. Calculations were conducted for two different fuel injectors with changed nozzle holes diameters, the number of nozzle holes and the angle between holes axis. The increase of the fuel nozzle holes diameter causes the decrease of the fuel spray tip penetration, but simultaneously the decrease of holes number causes that auto-ignition delay is not changed. The increase of the angle between holes axis from 150° to 158° causes fuel ingintion near cylinder head wall. Result of this is the increase of CO fraction. The deterioration of fuel combustion causes the decrease of NO_x mass fraction in the cylinder also.

Key words: *marine engine, CFD, combustion model, fuel injection, emission*

1. Introduction

Commonly used sources of mechanical energy on ships are Diesel engines. The source of mentioned energy is the combustion process in engine cylinders. Products of combustion process are emitted into the atmosphere and due to large dimensions of marine engines and many weeks of continuous operation the air pollution is large. For example marine engine with nominal power of 20MW consumes almost 100 tons of fuel per day (on the assumption of value of specific fuel consumption of 200 g/kWh) and emits 300 tons of CO_2. Due to the significant air pollution and high costs of marine engines operation, scientific investigations are conducted to obtain the reduction of the fuel consumption. Moreover temperature of the combustion process should be reducing due to the nitric oxides emission reduction. The combustion process in Diesel engine cylinder is mainly determined by the fuel injection process [8]. Fuel delivered by the injector is brake-up and simultaneously evaporated and mixed with air/exhaust gas mixture and combusted. According to [16] non-reacting phase of fuel propagation is divided in two stages; primary and secondary brake-up. The course and parameters of mentioned phenomena are determined e.g. by fuel injection pressure, diameters of nozzle holes, the fuel flow, pressure in the engine cylinder and properties of fuel [6]. The fuel temperature change causes the change of fuel viscosity and fuel density. According to this, colder diesel fuel had a longer liquid tip penetration length and a narrower spray angle than the warm diesel fuel. This phenomenon attributed to the poor atomization [18] and the vaporization [7]. It should be noted that in the case of heavy fuel oil presented trend is not observed [17].

In the literature we can find a lot of work concerning parameters of the fuel injection and their impact of the combustion process and the characteristic of emission. According to [2] the increase of fuel injection pressure causes the increase of NO_x emission and the decrease of CO emission. The increase of injection pressure causes the decrease of SMD of fuel spray leads to better mixing on air and CO reduction. The shape of fuel nozzle holes has significant impact on the engine performance and emission characteristic [20]. The increase of fuel conicity causes the increase of the spray cone angle and the decrease of NO_x emission [21]. The key factor for the Diesel engine performance and the emission is the fuel injection timing. Early fuel injection causes the delay of the fuel ignition due to lower pressure and temperature in the engine cylinder. According to [9] the delay of fuel injection causes the increase of CO and NO_x emission. The sharpness of the fuel nozzle holes edge is important to the fuel atomization also [4, 19]. A method of fuel injector activation affects the parameters of fuel spray. On [26, 23] works measurement results for piezo- and solenoid driven fuel injectors were presented. The energizing of the fuel injector by piezoelectric system with fuel injection pressure equals 60MPa causes lower tip penetration and higher spray cone angle in relation to energizing by the solenoid system. It should be emphasized that available publications concerns fuel injectors and injection conditions in diesel engines with small dimensions in relation to marine engines [5]. Therefore the main target of paper is the theoretical analysis of the influence of fuel spray geometry on the combustion and the emission characteristic of the marine Diesel engine. Chosen research object is 3-cylinder, 4-stroke, supercharged and intercooled marine engine, operated at constant speed and constant power output.

2. Experiment description

2.1. Laboratory test

The study was carried out by using an AL25/30 Cegielski-Sulzer marine, installed in the Laboratory of Internal Combustion Engines, Gdynia Maritime University. The engine was loaded by a generator electrically connected to the water resistance and supercharged by the VTR 160 Brown-Boveri turbocharger. During the tests the engine was fueled with diesel oil of properties presented in Table 1, and operated at the constant speed of 750 rpm and constant output power of 250 kW. Important engine parameters are given in Table 2. The fueling system of the engine consisted of a Bosch type, mechanically controlled fuel pumps connected to injectors with multi-hole nozzles. Two types of nozzles with parameters presented in Table 3 are tested.

Close description of the laboratory test with the schematic diagram of the laboratory stand and the accuracy and ranges of measurement equipment are presented in [10].

Table 1. Fuel oil properties [10]

Parameter	Unit	Value
Density at 15°C	kg/m^3	827.3
Viscosity at 40°C	mm^2/s	2.636
Cetane number	–	53.2

Table 2. Laboratory engine properties [10]

Parameter	Unit	Value
Max. electric power	kW	250
Rotational speed	rpm	750
Cylinder number	–	3
Cylinder bore	mm	250
Stroke	mm	300
Compression ratio	–	12.7
Fuel nozzle opening pressure	MPa	25
Start of fuel injection	° before TDC	18

Table 3. Fuel nozzles parameters

Fuel nozzle	Nozzle 1	Nozzle 2
Number of holes	9	8
Holes diameter [mm]	0.325	0.375
Angle between holes axis [°]	150	158
Conicity K factor [22]	1	1

2.2. CFD model description

CFD model was prepared on the basis of the moving mesh of the engine cylinder. Mentioned mesh was prepared for overall volume of the engine cylinder and allows preparing the calculations for full crankshaft rotation. The moving mesh was prepared using "Fame Engine Plus" tool from the AVL Fire software. Quantitative characteristic of the fuel injection was calculated on the basis on measured crankshaft position of the injection start, the fuel consumption and fuel pressure measured behind the fuel injector. It should be noted that mentioned characteristic is different for both considered nozzles [3, 25]. The WAVE fuel brake-up model with the Wakisaka modification and the Dukowicz evaporation model were used. The 3Z-ECFM model of the auto-ignition and the combustion process, based on the Euler description was chosen. The amount and the composition of the mixture in each finite volumes of the moving mesh are based on the average of Navier-Stokes equations and continuity equations. The turbulent flow was iteratively calculated by the k-zeta-f model with pressure correction by the SIMPLE model. The "upwind" differential scheme was used to energy balances and turbulent flows calculation. The central scheme of differential equations was used to calculate the flow continuity equations. The Zeldowicz's, the Fenimore as well as fuel mechanisms of NO_x formation are used simultaneously. Detailed description of the model and the validation of calculation results are presented in [14]. The validation as well as the initial and the boundary conditions are collected during laboratory measurements [10]. Model was validated on the basis on measured combustion pressure in the cylinder and the NO_x and the oxygen fraction in the exhaust duct.

3. Results and discussion

The change of nozzles, presented in Table 3, causes the change of nozzle holes diameter and the number of holes as well as the angle between holes axis. The cross section area of holes of the nozzle 1 is 18.3% lower than the nozzle 2. According to results, presented in [12] the increase of fuel nozzle holes diameter (nozzle 2) causes the increase of the SMD in the initial stage of the injection process. The effect of this phenomenon is slowdown of the fuel evaporation and the auto-ignition. This situation promotes elongation of fuel tip penetration of not evaporated fuel but the quickness of the fuel propagation in the combustion chamber is lower. The result of this is decrease of both combustion temperature and pressure. According to [15] the decrease of the fuel nozzle holes number causes opposite changes in the intensity of the fuel evaporation and the auto-ignition in relation to the increase of the fuel nozzle holes diameter. The intensity of the combustion process increases also. The result of this is the increase of combustion temperature and NO_x formation. The analysis of the influence of the changing of the angle between fuel holes axis on the combustion process is presented in [13]. According to presented results the increase of mentioned angle causes the increase of intensity of the diffusion stage of combustion and the decrease of the intensity of the kinetic stage of the combustion. Result of this is the increase of both combustion temperature and pressure. The increase of the angle causes the intense of the NO_x formation also.

Presented analysis shows that changing the nozzle 1 to the nozzle 2 causes complex and in some part opposite influence of combustion and emission parameters. Fig. 1 presents measured values of fuel pressure behind fuel injector. According to presented results the change of nozzle geometry causes a little change of fuel pressure.

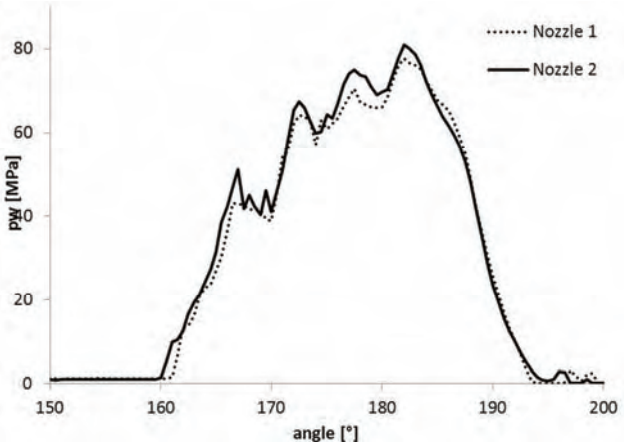

Fig. 1. Fuel pressure behind the injector

Figure 2 presents the fuel spray tip penetration, calculated for both nozzles. According to presented results the increase of the diameter and the angle between axis of nozzle holes and the decrease of the holes number causes the increase of the fuel tip penetration.

Deteriorations in the fuel tip penetration at the end of injection are the result of the fuel evaporation. It means, that presented geometrical changes in the fuel nozzle causes the

increase of the initial fuel droplets diameter. The simultaneous decrease of the nozzles number causes, that the initial quantity of evaporated fuel not changed. This phenomenon is presented on the Fig. 3.

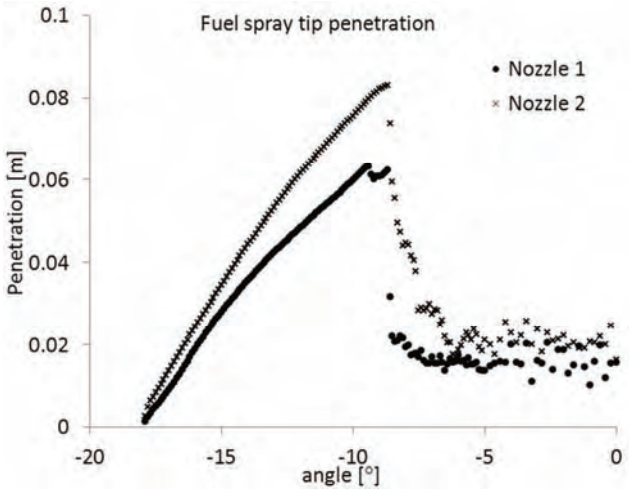

Fig. 2. Fuel tip penetration

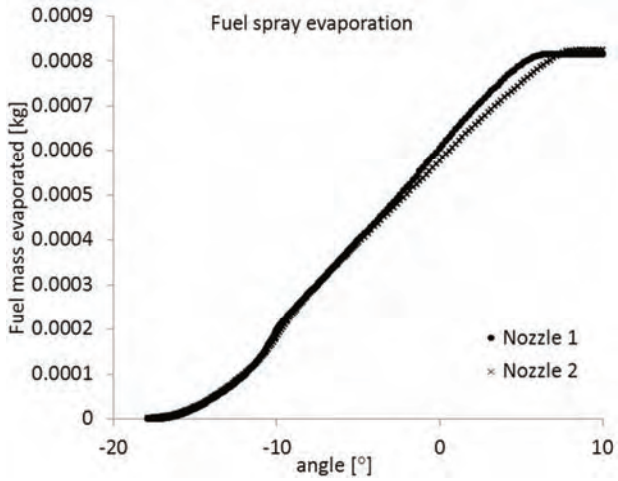

Fig. 3. Fuel spray evaporation

Use the nozzle 2 causes the delay of the fuel evaporation at the end stage of the fuel spray by 1.6° of the crankshaft angle position. According to the Fig. 4, the change of the fuel nozzle geometry influences on the heat release rate. The delay of the combustion kinetic stage and the shortening of the combustion diffusion stage are observed for the nozzle 2. It should be noted, that the maximum value of the heat release in the diffusion stage is decreased and the characteristic of the heat release for this stage of combustion is narrowed. Moreover, according to presented results the auto-ignition delay not changes. This is the result of the opposite influence of the fuel nozzle holes number and the diameter on the auto-ignition delay. It should be noted, that according to [24] the increase of the angle between holes axis causes shortening the auto-ignition delay, but in mentioned citation the maximum angle not exceed 30° value.

The result of heat release changes is the decrease of both combustion temperature and combustion pressure. It's interesting that according to results presented in the Fig. 5. the maximum combustion temperature decreases for the nozzle 2, but the value of the temperature near the exhaust valve opening (110° after TDC) increases in relation to calculation results for the nozzle 1. The advantage of the multidimensional calculations is the possibility of the calculation and the visualization of combustion process parameters in different areas of the cylinder.

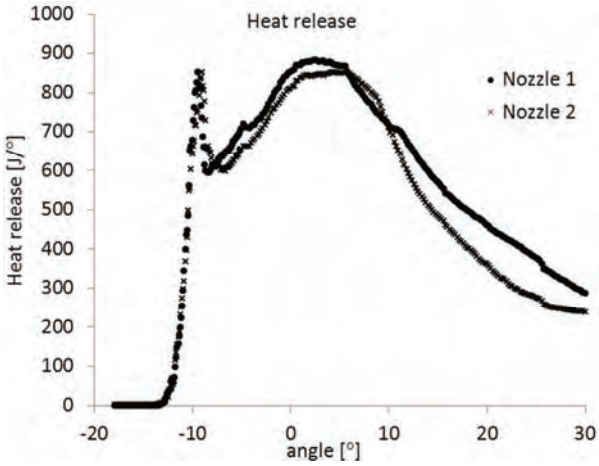

Fig. 4. Heat release rate

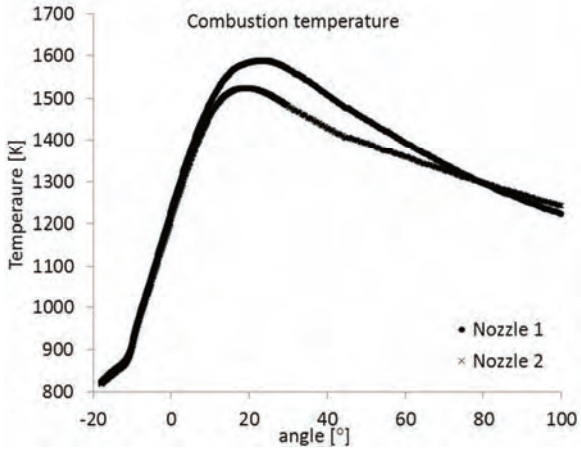

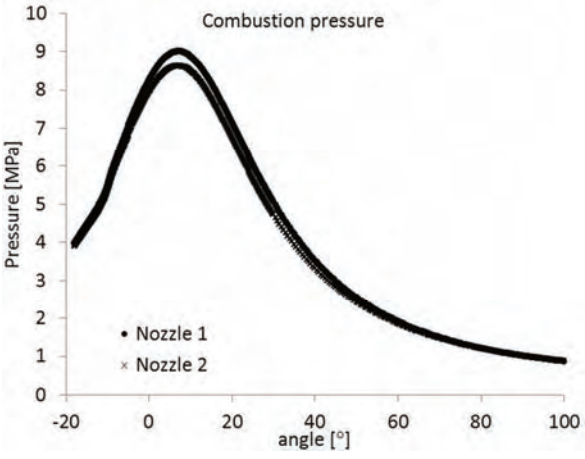

Fig. 5. Calculated temperature and pressure of combustion

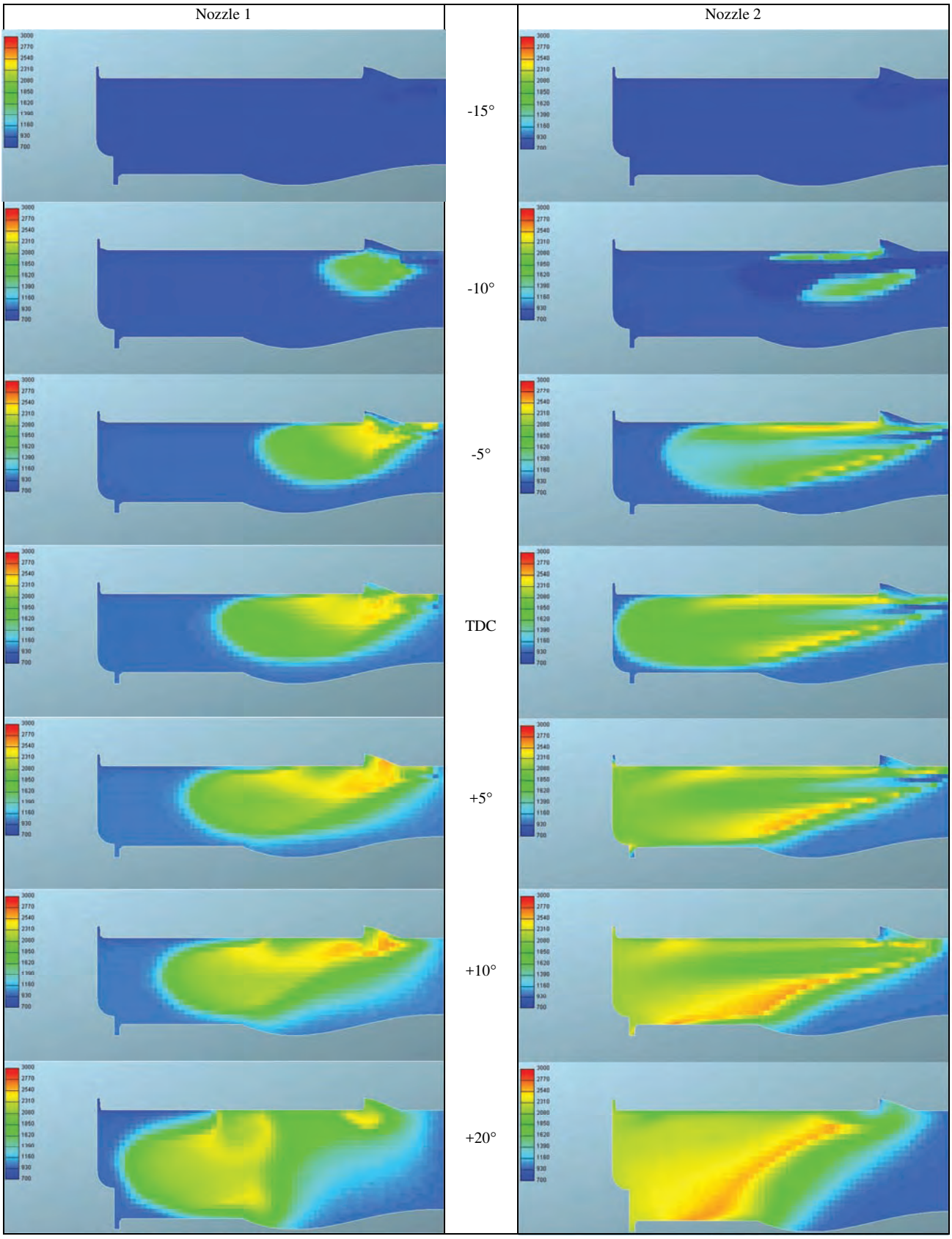

Fig. 6. Calculated temperature of combustion

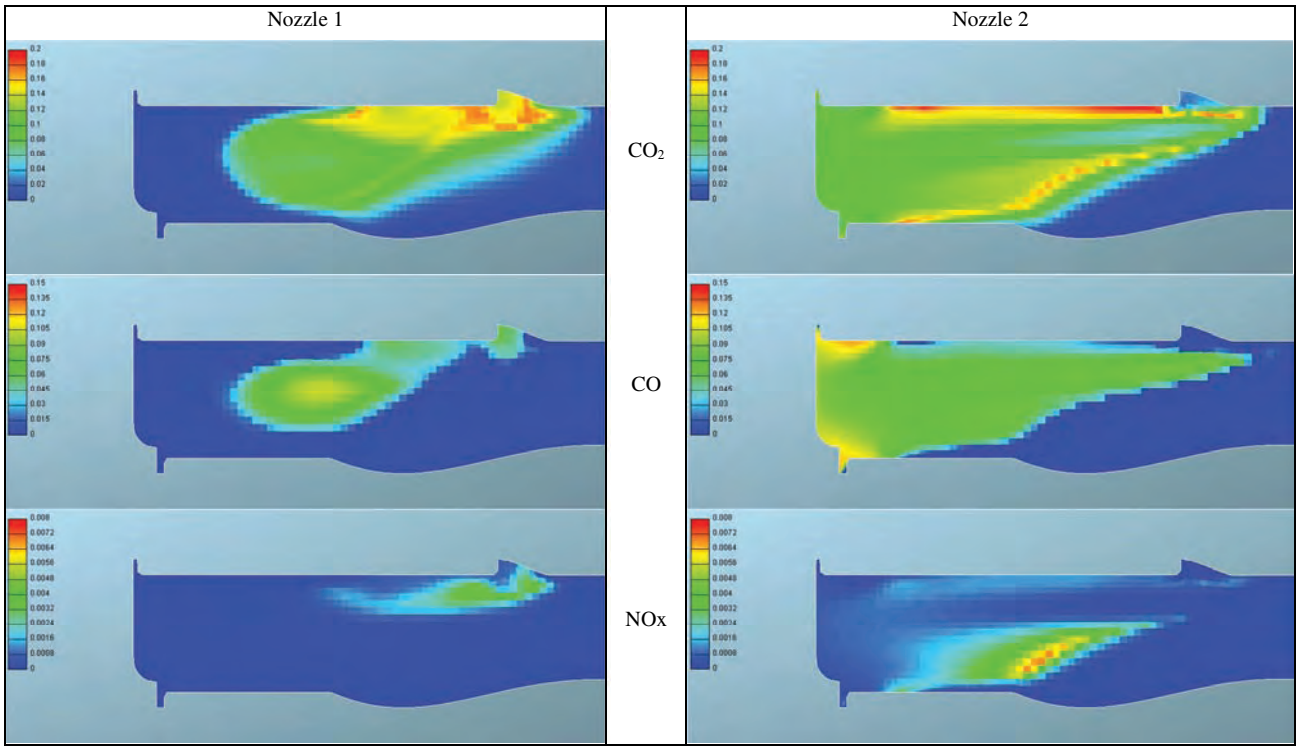

Fig. 7. Calculated fractions of chosen species for 10° after TDC of crankshaft position

The Fig. 6 presents the evolution of the combustion process based on temperature in the combustion chamber for both considered nozzles. Only the left side of the cross section area is presented due to the axial symmetry of the combustion chamber. According to presented results the increase of the diameter of fuel nozzle holes causes the increase of the fuel flow. The development of fire in the combustion chamber is different for both considered nozzles. 10° before TDC in the both cases the combustion process is started, but for the nozzle 1 the combustion is developed on the front of the fuel spray. The fuel injection for the nozzle 2 is more intense and the combustion is started near sides of the fuel spray. Moreover the higher temperature is observed near the wall of the cylinder head. Its result of increased the cone angle between the fuel nozzle axis from 150° for the nozzle 1 to 158° for the nozzle 2. For the nozzle 2 the combustion process reaches walls of the combustion chamber at the TDC crankshaft position and in opposite to the nozzle 1 the area with not evaporated fuel is observed near nozzle holes. The combustion process for the nozzle 1 riches the cylinder walls later (at 20° of the crankshaft position). The comparison of results of the temperature calculation from the Fig. 5 and the Fig. 6 for 20° of the crankshaft position after TDC shows that mean temperature for the overall cylinder volume is lower for the nozzle 2 but it is possible to observe areas with higher temperatures in relation to the combustion for the nozzle 1 due to extended combustion process. The Fig. 7 presents results of the fractions calculation of chosen chemical species for 10° after the TDC of crankshaft position.

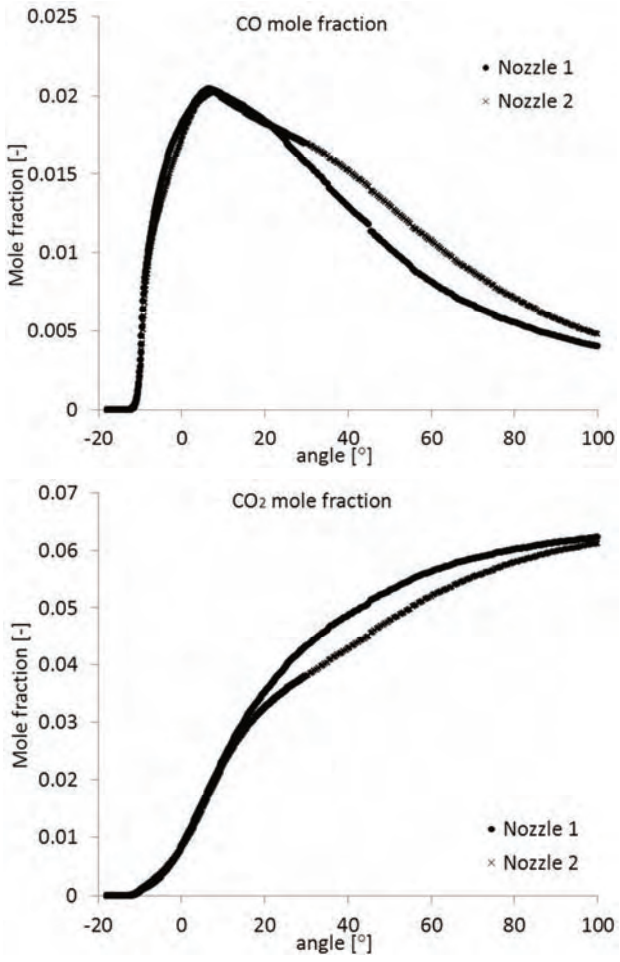

Fig. 8. CO and CO_2 mole fractions

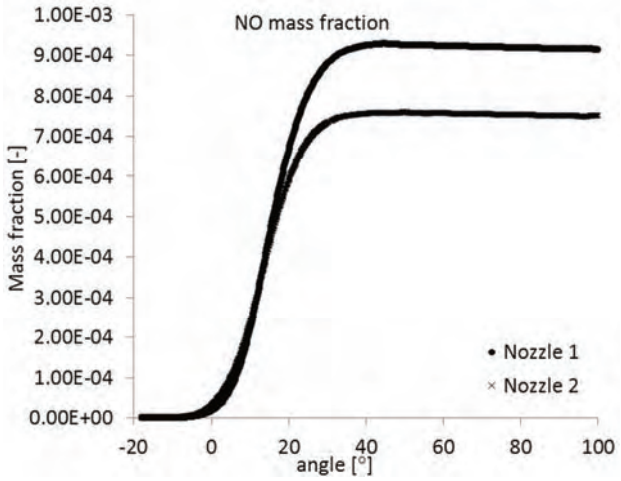

Fig. 9. NO_x mass fraction

Presented results confirm the extension of the combustion process for the nozzle 2. The area of the CO formation is located in largest part of the cylinder volume. Comparison of results presented in the Fig. 6 and the Fig. 7 shows that the NO_x formation area corresponds to areas with higher temperatures for both nozzles. According to results presented in the Fig. 7 the combustion process seems to be more homogeneous for the nozzle 2 in comparison to the nozzle 1, but it should be noted, that results are presented for cross section through the nozzle holes axis. Changes of mean fractions of CO and CO_2 for overall volume of cylinder are presented in the Fig. 8. The extension of the combustion process for the nozzle 2 causes the decrease of CO_2 formation during the combustion. The visible combustion near cylinder walls for the nozzle 2 causes the increase of the CO formation also. It should be noted that fractions of both considered species are similar for both nozzles near 100° after TDC (end of combustion). The Fig. 9 presents mean values of the NO mass fraction in the cylinder. The NO fraction equals 90-99% of the overall NO_x fraction in internal combustion engines [1]. According to presented results the increase of the fuel holes diameter and the angle between holes axis and simultaneous the decrease of the fuel holes number causes the decrease of the NO fraction. The reason of this is the decrease of combustion pressure and temperature. This result corresponds to measurement results [11] and results from the modeling [24].

4. Conclusions

The theoretical investigations of the combustion and the emission characteristic of the marine 4-stroke Diesel engine are presented. Mentioned investigations are based on the 3 dimensional, milti-zone CFD model. According to presented results following conclusions may be formulated:

– The increase of the fuel nozzles holes diameter causes slowdown of the fuel vaporization and auto-ignition but simultaneous the decrease of the fuel nozzle number causes that changes in the auto-ignition delay are not observed. The slowdown of vaporization process is observed only at the end of the injection process due to the increase of the angle between nozzle holes axis.
– The increase of the fuel nozzles holes diameter causes the increase of the fuel tip penetration. The result of this is the change of fire propagation. The combustion for the nozzle 2 start near the sides of the fuel spray, and is observed near the cylinder walls, meanwhile the combustion for the nozzle 1 is started on the top of the fuel spray.
– The change of the nozzle 1 to the nozzle 2 causes the delay of the combustion kinetic stage and the shortening of the combustion diffusion stage of the combustion. The maximum value of the heat release in the diffusion stage is decreased and the characteristic of the heat release for this stage of combustion is narrowed, but the auto-ignition delay is not changed.
– The result of the fuel nozzle geometry changing is the change of pressure and temperature of the combustion. The maximum temperature in the cylinder area is observed for the nozzle 2, but the mean value for overall cylinder volume is lower in the relation to results for the nozzle 1.
– The result of the decrease of temperature and pressure of combustion is the decrease of the NO_x fraction for the combustion for the nozzle 2.
– The CO fraction for the combustion with the nozzle 2 is lower than for the nozzle 1. This result should be treated with the great reserve due to unsatisfactory quantitative validation with measurement values of the presented model.

Acknowledgements

The project was supported by AVL Company according to University Partnership Program and license of AVL Fire software.

Nomenclature

NOx	nitric oxides
CO	carbon oxide
CO_2	carbon dioxide
CFD	computational Fluid Dynamic
SMD	Sauther's Mean Diameter
TDC	top dead center of crankshaft position
3Z-ECFM	three zone extended coherent flame model

Bibliography

[1] BENAJES, J., LÓPEZ, J.J., NOVELLA, R., REDÓN, P. Comprehensive modeling study analyzing the insights of the NO–NO_2 conversion process in current diesel engines. *Energy Conversion and Management*. 2014, **84** 691-700.

[2] ÇELIKTEN, I. An experimental investigation of the effect of the injection pressure on engine performance and exhaust emission in indirect injection diesel engines. *Applied Thermal Engineering*. 2003, **23** (16), 2051-2060.

[3] DESANTES, J.M., GARCÍA-OLIVER, J.M., PASTOR, J.M., RAMÍREZ-HERNÁNDEZ, J.G. Influence of nozzle

geometry on ignition and combustion for high-speed direct injection diesel engines under cold start conditions. *Fuel.* 2011 **90**(11) 3359-3368.
[4] GIMENO, J., BRACHO, G., MARTÍ-ALDARAVÍ, P., PERAZA, J.E. Experimental study of the injection conditions influence over n-dodecane and diesel sprays with two ECN single-hole nozzles. Part I: Inert atmosphere. *Energy Conversion and Management*. 2016, **126**, 1146-1156.
[5] HEYWOOD, J. B., SHER, E. The two-stroke cycle engine. its development, operation, and design. *Taylor&Francis* N.Y. 1999.
[6] HOSEINI, S.S., NAJAFI, G., GHOBADIANA, B. et al. The effect of combustion management on diesel engine emissions fueled with biodiesel-diesel blends. *Renewable and Sustainable Energy Reviews*. 2017, **73**, 307-331.
[7] KAPUSTA, Ł.J., PIELECHA, I., WISŁOCKI, K., TEODORCZYK, A. Autoignition and combustion of n-hexane spray in subcritical and supercritical environments. *J Therm Anal Calorim.* 2016, **123**(1), 819-828.
[8] KIM, H.J., PARK, S.H., LEE, C.S. Impact of fuel spray angles and injection timing on the combustion and emission characteristics of a high-speed diesel engine. *Energy*. 2016, **107,** 572-579.
[9] KIPLIMO, R., TOMITA, E., KAWAHARA, N., YOKOBE, S. Effects of spray impingement, injection parameters, and EGR on the combustion and emission characteristics of a PCCI diesel engine. *Appl Therm Eng*. 2012, **37**, 165-75.
[10] KOWALSKI, J. An experimental study of emission and combustion characteristics of marine diesel engine with fuel pump malfunctions. *Applied Thermal Engineering*. 2014, **65**, 469-476.
[11] KOWALSKI, J. An experimental study of emission and combustion Characteristics of marine diesel engine with fuel Injector malfunctions. *Polish Maritime Research.* 2016, **23**(1), 77-84.
[12] KOWALSKI, J. Influence of fuel injector holes diameter on parameters of combustion process in the cylinder of the marine 4-stroke diesel engine. *Journal of Polish CIMEEAC.* 2016, **11**(1), 95-102.
[13] KOWALSKI, J. The analysis of influence of fuel spray angle on NO_x fraction in the exhaust gas from marine 4-stroke diesel engine. *Journal of Kones*. 2015, **22**(3), 309-316.
[14] KOWALSKI, J. The model of combustion process in the marine 4-stroke engine for exhaust gas composition assessment. *Combustion Engines*. 2016, **165**(2), 60-69.
[15] KOWALSKI, J. Wykorzystanie składu spalin w diagnostyce czterosuwowych silników okrętowych. *Wydawnictwo Naukowe Instytutu Technologii Eksploatacji*. Radom 2015.
[16] NAGASAKA, K., TAKAGI, T., KOYANAGI, K., YAMAUCHI, T. The development of "ne atomization injector Kenzo. *JSAE Review*. 2000, **21,** 309-313.
[17] PARK, J., JANG, J.H., PARK, S. Effect of fuel temperature on heavy fuel oil spray characteristics in a common-rail fuel injection system for marine engines. *Ocean Eng*. 2015, **104**, 580-589.
[18] PARK, Y., HWANG, J., BAE, C. et al. Effects of diesel fuel temperature on fuel flow and spray characteristics. *Fuel.* 2015, **162**, 1-7.
[19] PAYRI, R., SALVADOR, F.J., GIMENO, J., PERAZA, J.E. Experimental study of the injection conditions influence over n-dodecane and diesel sprays with two ECN single-hole nozzles. Part II: Reactive atmosphere. *Energy Conversion and Management*. 2016, **126**, 1157-1167.
[20] PAYRI, R., TORMOS, B., SALVADOR, F.J., ARANEO L. Spray droplet velocity characterization for convergent nozzles with three different diameters. *Fuel*. 2008, **87**, 15-16.
[21] SOM, S., RAMIREZ, A.I., LONGMAN, D.E., AGGARWAL, S.K. Effect of nozzle orifice geometry on spray, combustion, and emission characteristics under diesel engine conditions. *Fuel*. 2011, **90**, 1267-1276.
[22] SOM, S., RAMIREZ, A.I., LONGMAN, D.E., AGGARWAL, S.K. Effect of nozzle orifice geometry on spray, combustion, and emission characteristics under diesel engine conditions. *Fuel*. 2011, **90**(3), 1267-1276.
[23] SUH, H.K., PARK, S.W., LEE, C.S. Effect of piezo-driven injection system on the macroscopic and microscopic atomization characteristics of diesel fuel spray. *Fuel*. 2007, **86**, 2833-2845.
[24] TAGHAVIFAR, H., KHALILARYA, S., JAFARMADAR, S., BAGHERY, F. 3-D numerical consideration of nozzle structure on combustion and emission characteristics of DI diesel injector. *Applied Mathematical Modelling*. 2016, **40**(19-20), 8630-8646.
[25] WU, X., DENG, J., CUI, H. et al. Numerical simulation of injection rate of each nozzle hole of multi-hole diesel injector. *Applied Thermal Engineering*. 2016, **108**(5), 793-797.
[26] YU, W., YANG, W., MOHAN, B. et al. Macroscopic spray characteristics of wide distillation fuel (WDF). *Appl. Energy*. 2017, **185**, 1372-1382.

Jerzy Kowalski, DSc., DEng. – Faculty of Marine Engineering at Gdynia Maritime University.

e-mail: *jerzy95@am.gdynia.pl*

Article citation info:
KLYUS, O., ZAMIATINA, N. Residual fuel atomization process simulation. *Combustion Engines*. 2017, **169**(2), 108-112. DOI: 10.19206/CE-2017-219

Oleh KLYUS
Nadezhda ZAMIATINA

CE-2017-219

Residual fuel atomization process simulation

The process of atomization of fuel in engines with compression ignition is determining in organization of the combustion process, the result of which are the economic and environmental performance of the engine. One of the main parameters of the spray jet fuel is the mean droplet diameter. The article presents the results of analytical and experimental studies by the definition of mean diameter of Sauter droplet of atomized residual fuel IFO380.

Key words: *diesel engines, residual fuel, mean diameter of Sauter*

1. Introduction

The decision to reduce the emission of toxic components in the exhaust gases of internal combustion engines can be considered in three stages depending on each other: the introduction of carbohydrate fuels into the combustion chamber, their burning out with the formation of incomplete combustion products, nitrogen and sulfur oxides, as well as their reduction and oxidation in the exhaust system. The main stage is the combustion process, which is determined by the fuel supply characteristic and the design parameters of the combustion chamber and the intake path. When the organization of a low-toxicity work process depends on the spraying of hydrocarbon fuels. Especially it concerns for heavy fuel grades used in low-speed marine diesel engines, the physical parameters of which are different from distilled fuels used in medium- and high-speed diesel engines. In the literature of the subject of research there are no results of scientific and experimental design work in this direction, so modeling the process of spraying heavy fuel is a very urgent task.

2. Fuel atomization in the diesel engines

As is known, the combustion of hydrocarbon fuel in compression-ignition engines is preceded by physical and chemical processes that can be represented in the following sequence: a volume of fuel is injected, jet break up into droplets, fuel droplets evaporate, fuel vapor mixes with hot air in cylinder, fuel molecules forms free radicals, ignition and combustion. It should be noted that each element in the presented sequence is determined by the specific physical parameters of the fuel: jet break up into droplets depend from fuel viscosity and surface tension; fuel droplets evaporate – from fuel specific heat; vapor pressure, heat of vaporization, and fuel vapor mixes with hot air in cylinder – from fuel vapor diffusivity [12, 15].

The main criterion for the quality of the atomized fuel is the droplet diameter. By spraying, the surface of the cyclic portion increases, thereby increasing the amount of perceived heat and the rate of evaporation of the droplets. When the diameter of the droplet determines the macrostructure (the opening angle and the range) and the microstructure (size and distribution of droplets) of the jet. In practice, a theoretical jet consisting of droplets of the same size is used to determine the quality of spraying and which has characteristics similar to the actual jet, for example the total number of drops, the sum of their surface, volume or diameter [5, 6].

For the conditions of heat exchange, evaporation and combustion of a drop corresponding to the conditions of the combustion chamber of diesel engines, the average diameter of the Sauter (D_{32} or SMD) is taken as the criterion for the quality of spraying, expressing the ratio of the volume to the surface of the drop in the theoretical jet [3, 15]:

$$SMD = \frac{\sum N_i D_i^3}{\sum N_i D_i^2} \tag{1}$$

In the literature of the subject of research, it is possible to find the equations determining the average droplet diameter according to Sauter (Table 1).

Table 1. Calculation formulas for determining the mean diameter of a drop

Equation		Author
$SMD = 3330 d_0^{0.3} \mu_L^{0.07} \rho_L^{-0.648} \times \times \sigma^{-0.15} U_L^{-0.55} \mu_G^{0.78} \rho_G^{-0.052}$	(2)	Harmon [1, 2]
$SMD = \frac{47 d_0 \sigma^{0,25} (1 + 331Oh)}{U_L \rho_G^{0.25}}$	(3)	Tanasawa and Toyoda [1, 5]
$SMD = 3.08 \upsilon_L^{0.385} (\sigma \rho_L)^{0.737} \times \times \rho_G^{0.06} \Delta P_L^{-0.54}$	(4)	Elkotb [1, 4]
$SMD = 0.38 d_0 \, Re^{0.25} \, We^{-0.32} \times \times \left(\frac{\mu_L}{\mu_G}\right)^{0.37} \left(\frac{\rho_L}{\rho_G}\right)^{-0.47}$	(5)	Hiroyasu and Arai [1, 7]
$SMD = 2330 \rho_G^{0.121} Q_L^{0.131} \Delta P_L^{-0.135}$	(6)	Hiroyasu and Kadota [1, 7]
$SMD = 0.53 \frac{Q_L^{0.27} d_0^{0.27} \mu_L^{0.69} \rho_G^{0.48} C_0^{0.97}}{\rho_L^{-0.21} \Delta P_L^{-0.21}}$	(7)	Hansmann [1]
$SMD = 0.158 \left(\frac{\sigma}{\rho_L}\right)^{0.354} \mu_L^{0.303} Q_L^{0.139}$	(8)	Mochida [1]
$SMD = \frac{10^6 E_{32} d_0 M^{0.0733}}{(\rho We)^{0.266}}$	(9)	Kuleshov [14]

Listed in the Table 1 equations, show a different approach of the authors to a mathematical description of the fuel atomization process. So, for example, in the equations there is a significant difference in the magnitude of the constant coefficients and the exponents for the same physical parameters – by equation 2, an increase in the surface tension leads to an increase in the SMD, according to equa-

tions 4 and 6, higher counterpressure values contribute to better sputtering, according to equation 7 – this relationship has the opposite meaning. Equations 6 and 7 do not take into account the effect of surface tension on SMD, although at spraying the fragmentation of droplets continues until the surface tension forces become larger than the total forces causing the jet to decay.

Constant coefficients and exponents in the above equations, taking into account the effect of various physical fuel parameters on the average droplet diameter, were obtained experimentally by various methods and means of measurement and indicate the depth of the processes that require further research. Especially this applies to heavy grades of fuel used in marine diesel engines and differing in physical parameters from light grades.

3. Experimental installation

Determination of the quality of the sprayed fuel was carried out on an experimental test bench consisting of three main elements (Fig. 1): Nozzle attachment unit, with the ability to move it vertically and horizontally, the Spraytec STP 5000 apparatus from Malvern Instruments and the EPS 200 installations from Bosch and PRW-3 fuel injector adjustment.

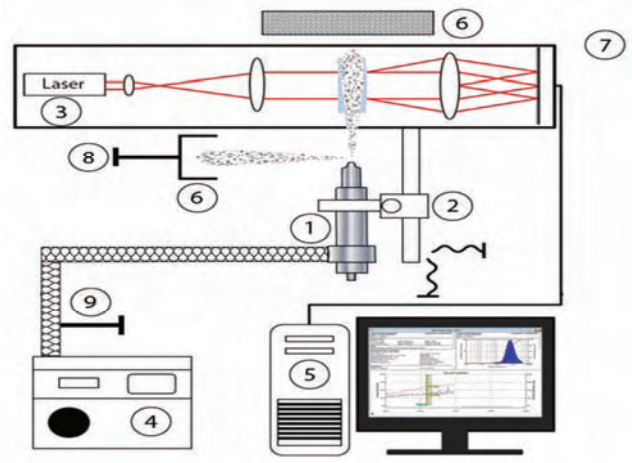

Fig. 1. Scheme of the experimental device for determining the quality of the atomized fuel: 1 – nozzle, 2 – nozzle attachment point, 3 – Spraytec STP 5000 device, 4 – EPS 200 installation, 5 – personal computer, 6 – spray catchers, 7 – fume hood, 8, 9 – thermocouples

The nozzle attachment unit was equipped with micrometric screws to control the position of a single fuel jet directed to the measurement zone, as well as traps of the remaining jets of sprayed fuel. Thus, it was possible to measure the parameters of the sprayed fuel only from one nozzle opening, and the remaining fuel jets did not affect the accuracy of the results obtained (Fig. 2).

To determine the distribution of the droplet size in a jet of sprayed fuel, an apparatus of the Spraytec STP 5000 type was used whose operation is based on the measurement of the scattering of the He-Ne laser beam (Fig. 3). The system consists of 30 detectors which detects light scattering on the drops and converts it into an electrical signal. The angle at which the drop disperses the light is inversely proportional to its diameter – while smaller droplets correspond to a larger angle. Each detector senses a light signal in a certain range of scattering angles. At present, the method of laser diffraction is the most accurate method for determining the droplet size in aerosols and liquids, which makes it possible to use it to determine the quality of spraying of diesel fuel.

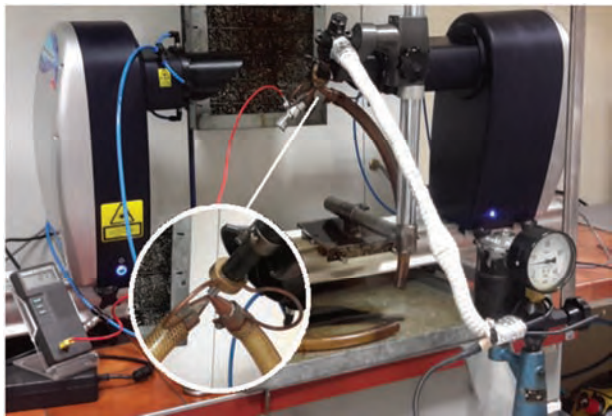

Fig. 2. Experimental installation with traps of separate jets of sprayed fuel

Fig. 3. Scattering beam light on fuel droplets

The main technical characteristics of the device Spraytec STP 5000 firm Malvern Instruments are listed in the Table 2 [9].

Table 2. Basic technical data of the Spraytec STP 5000

Method of measurement	Laser-diffraction (small-angle scattering)
Range of measured drops	0.1–900 μm, Dx(50): 0.5–600 μm
Optical model	The Mie theory and the Fraunhofer approximation
Aerosol concentration range	Multiple Dispersion Correction System
Light source	Laser type He-Ne, 2 mW, 632.8 nm
Measurement error	Does not exceed ±1% for Dx(50)

3. Results and Discussions

An important point in preparing fuel for combustion is to provide the necessary viscosity. If for diesel fuels the need for heating to reduce the viscosity is eliminated, then for heavy fuels, preheating in steam or electric heaters is a prerequisite for their preparation, since only this way it is possible to achieve the required viscosity. The effect of viscosity and compressibility on the injection characteristic, depending on the design of the fuel equipment, is different, but in all cases it affects to some extent the quality of

spraying and subsequent combustion of fuel. The viscosity, determined by the forces of the internal cohesion of the fuel, and the forces of its surface tension, have a direct effect on the decay of the jet of fuel flowing from the nozzle [10, 11, 13]. Before the test, heavy fuel was heated, during the experiment it gradually cooled down (Fig. 4). The temperature in the tank and the fuel trap was constantly measured by thermocouples of the Fluke 52II type.

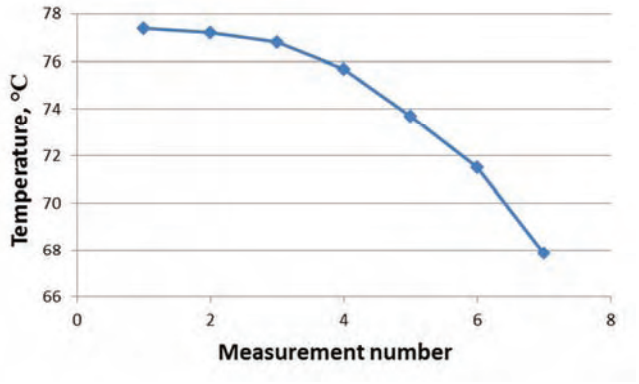

Fig. 4. Change in fuel temperature during the experiment.

The parameters of the test fuel that directly affect the average droplet diameter, such as density, viscosity and surface tension, as well as the characteristics of the injector and the injection conditions are shown in Table 3.

Table 3. Characteristics of the injector, fuel, environment.

Parameter	Unit	Value
Nozzle	Tipe	D1LMK 148/1
Nozzle hole diameter	mm	0.34
Axial length of nozzle	mm	1.2
Pressure difference	MPa	20
Air density, 20 °C	kg/m^3	1.16
Fuel density, 15 °C	kg/m^3	986
Fuel kinematic viscosity, 50 °C	cSt	380
Fuel surface tension, 20 °C	N/m	0.0369

Surface tension is an unregulated in the standards physical parameter of fuel, which affects the fineness of the spraying, thereby the combustion efficiency and the environmental performance of the engine. The smaller the surface tension of the fuel, the lower the resistance is to the forces that cause the jet to decay. During the experiment, the temperature of the fuel was constantly changing, along with its physical parameters. The change in surface tension from temperature is shown in Fig. 5.

As described above, many mathematical models of calculating SMD have been proposed in the literature. Figure 6 shows the curves for calculating the SMD from the temperature for fuel IFO-380 according to the equations of different authors and data on the Spraytec experiment. As can be seen from the figure, the calculation results range from 10 to 80 μm. In the temperature range from 68 to 72, the result is closer to the experiment by the Hansmana equation, but from 74°C the curves diverge, which means that the SMD dependences on temperature are different. SMD by Hiroyasu and Katoda as the temperature decreases, though slightly, but reduced, which contradicts the theory and other calculations. It should also be noted that the Hiroyasu and Katoda equation does not take into account such a parameter as the surface tension of the fuel. The results for the Elkotb and Mochida equations are close to each other, but they are very far from the results of the experiment. The equation of Tanasawa and Toyoda displays an almost parallel curve to the results of the experiment. According to the Kuleshov equation, the SMD coincides at a temperature of 68°C.

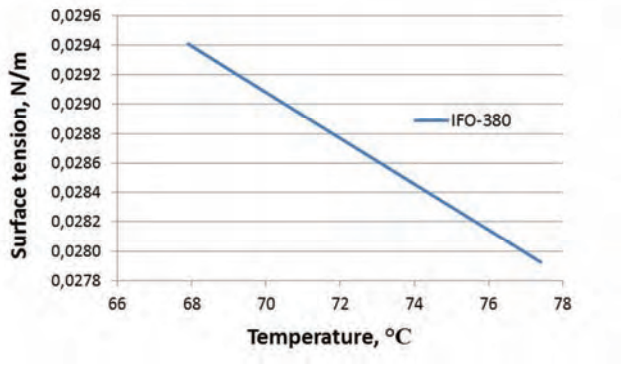

Fig. 5. Dependence of surface tension of fuel IFO-380 on temperature

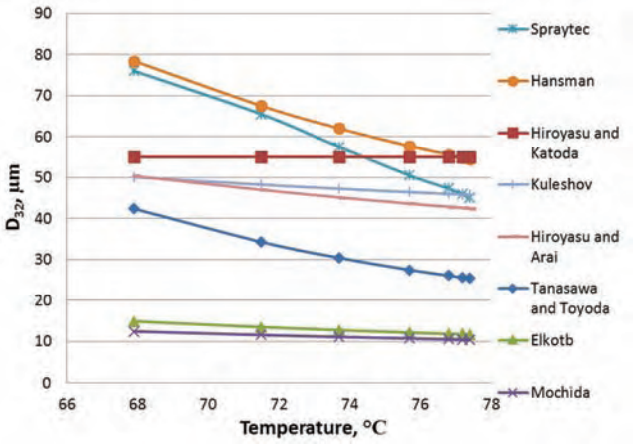

Fig. 6. Calculation of the SMD for mathematical models and the result of the experiment at different temperatures

Since there is an empirical coefficient in the Kuleshov equations, the value of which depends on the experimental conditions, we assume that it has a temperature dependence (Fig. 7).

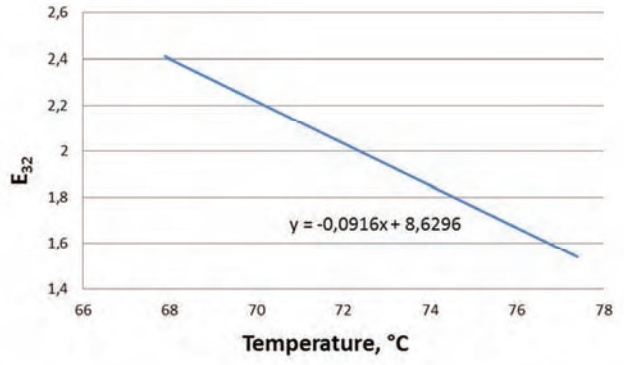

Fig. 7. The change in E_{32} from temperature

Calculation by the Kuleshov equation with a varying coefficient E_{32} shows good agreement with the result of the experiment. Also, when the coefficient of 1.83 is added to the Tanasawa and Toyoda equation, the calculation result is close to the experimental (Fig. 8).

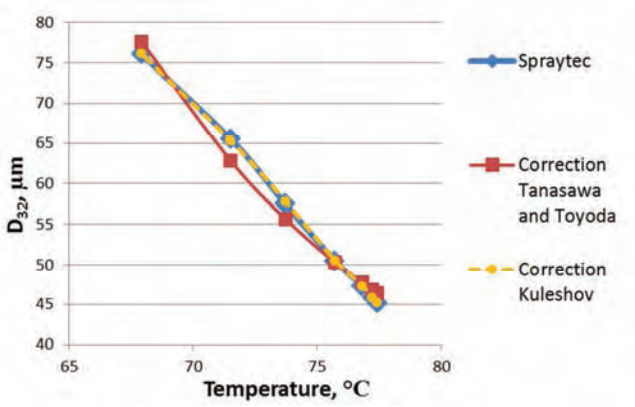

Fig. 8. SMD on experiment and on corrected mathematical models

Thus, for heavy fuel grades, we can recommend the determination of the mean Sauter diameter by the Kuleshov equation with the introduction of the correction $E_{32}(f_T)$, taking into account the temperature dependence:

$$SMD = \frac{10^6 E_{32}(f_T) d_0 M^{0.0733}}{(\rho We)^{0.266}} \tag{10}$$

At the same time, in the Tanasawa and Toyoda equations, a correction factor of 1.83 should be used. The use of these corrections leads to an approximation of the analytical dependences to the experimental data with a correlation coefficient of 0.99.

4. Conclusions

The process of fuel atomization is one of the most important stages in the complex of physical and chemical processes preceding the combustion and heat generation in the combustion chamber of compression-ignition engines. It is this stage that affects the magnitude of the ignition delay, the degree of buildup of pressure and temperature in the cylinder, thereby determining the economic and environmental parameters of the engine. The quality of fuel atomization is conveniently represented by the average diameter of droplet in the jet (SMD), and although this parameter is conditional, nevertheless its quantitative characteristic can be used in modeling the fuel delivery process in diesel engines. In recent years, instead of a full experimental study, modeling is becoming an attractive alternative for analyzing engine performance. This is especially true for heavy fuel grades, for which the results of calculations should be sufficiently detailed for the purpose of their subsequent comparison with experimental data and data from other calculation methods.

The equations of SMD calculation presented in the paper, which were encountered in the literature, were obtained for a specific type of liquid with certain physical parameters, but not all are suitable for heavy types of fuel. When choosing a mathematical model for heavy fuel, the Tanasawa and Toyoda and Kuleshov equations were chosen, since the results for the Tanasawa and Toyoda equation lie on the graph almost parallel to the experimental results, and in the Kuleshov equation there is a separate empirical coefficient, the value of which can be selected for heavy fuel. The corrected Tanasawa and Toyoda equation by a factor of 1.83 and calculation by the Kuleshov equation with a variable coefficient $E_{32}(f_T)$ showed good agreement with the results of the experiment.

Nomenclature

SMD	Sauter mean diameter, µm
Oh	Ohnesorge number
Re	Reynolds number
We	Weber number
C_0	discharge coefficient of the nozzle
N_i	number of drops with a given outer diameter
D_i	diameter of droplets of a given size, µm
d_0	initial jet diameter, m
μ_L	liquid dynamic viscosity, Pa·s
ρ_L	liquid density, kg/m^3
σ	surface tension, N/m
ν_L	liquid kinematic viscosity, m^2/s
U_L	liquid velocity, m/s
ΔP_L	pressure differential across nozzle, Pa
Q_L	mass flow rate, kg/s
μ_G	gas dynamic viscosity, Pa·s
ρ_G	gas density, kg/m^3
ρ	ρ_G/ρ_L
M	$\mu_L^2/(d_0\rho_L\sigma)$
E_{32}	empirical coefficient
$E_{32}(f_T)$	temperature dependence empirical coefficient

Bibliography

[1] ASHGRIZ, H. Handbook of atomization and sprays. Theory and applications. *Springer*. 2011.

[2] CAI, H., SONG, B., PEI, Y., SHI. S. Fuel leaking analysis of fuel tank by projectiles impact with mechanical properties of projectiles. *Advanced materials research*. 2013, **644**, 203-206.

[3] FILIPPA, L., TRENTO, A., ÁLVAREZ, A.M. Sauter mean diameter determination for the fine fraction of suspended sediments using a LISST-25X diffractometer. *Measurement*. 2012, **45**(3), 364-3687.

[4] KENNETH, W.R., KENNETH, M.B. Combustion engineering, Second edition. *CRC Press Taylor and Francis*. 2011.

[5] LEFEBVRE, A.H. Atomization and sprays. *Hemisphere Publishing Corporation*. New York. 1989.

[6] LIU, H. Science and engineering of droplets – fundamentals and applications. *William Andrew Publishing*, New York, USA. 2000.

[7] SANTOS, F.D., MOYNE, L.L. Spray atomization models in engine applications, from correlations to direct numerical

simulations. *Oil & Gas Science and Technology – Rev. IFP Energies nouvelles*. 2011, **66**(5), 801-822.
[9] Spraytec user manual. Malvern Instruments Ltd. MAN0368 issue 3.0. 2007.
[10] TOTTEN, E.G., WESTBROOK, R.S., SHAH, J.R. Fuels and lubricants handbook: technology, properties, performance and testing. ASTM manual series: MNL37WCD, USA. 2003, 1087.
[11] QING, S., JIXIAN, G., YUHUI, L. et al. Estimation of the sauter mean diameter for biodiesels by the mixture topological index. *Renewable energy*. 2011, **36**(2), 482-487.
[12] ZABŁOCKI M. Wtrysk i spalanie paliwa w silnikach wysokoprężnych. *WKiŁ*, Warszawa. 1976.
[13] ЗАРЕЦКАЯ, А.К. Технология использования топлива, масла и воды. *Конспект лекций*, Керчь. 2014.
[14] КУЛЕШОВ, А.С. Программа расчета и оптимизации двигателей внутреннего сгорания ДИЗЕЛЬ-РК. Описание математических моделей, решение оптимизационных задач. *МГТУим. Н.Э.Баумана*. 2004.
[15] РАЗЛЕЙЦЕВ, Н.Ф. Моделирование и оптимизация процесса сгорания в дизелях. Вища школа: *Изд-во при Харьк*. ун-те. 1980.

Prof. Oleh Klyus, DSc., DEng., D.h.c. – Maritime University of Szczecin.

e-mail: *olegklus@o2.pl*

Nadezhda Zamiatina – Faculty of Marine Technology and Natural Sciences at Klaipeda University.

e-mail: *Nadezda.Zamiatina@ku.lt*

Article citation info:
KNEFEL, T., NOWAKOWSKI, J. Calculated injection times of divided fuel dose in a compression ignition engine. *Combustion Engines*. 2017, **169**(2), 113-119. DOI: 10.19206/CE-2017-220

Tomasz KNEFEL
Jacek NOWAKOWSKI

CE-2017-220

Calculated injection times of divided fuel dose in a compression ignition engine

This study presents analyses concerning control processes of injection times of divided dose of fuel, startning from setting of injection time in controller up to moment of execution in compression ignition engine. Multiple injection doses were analyzed taking into consideration both sums of individual portions of doses as well as gaps between the doses. Studies were performed for various configurations of the doses, with different values of injection times and gaps between the injections. Measurements were performed for three measuring groups containing single-, two-, and five-portion doses. At constant values of time in a given group it have been applied variable injection pressures. The most important factors determining division of fuel dose were discussed.

Key words: *diesel engine, common rail injection system, indicator of injection, fuel injection rate, injection time*

1. Introduction

Permanent strive for development of more and more perfect automotive combustion engines is caused by necessity of assurance of high efficiency, durability and compliance with increasingly stringent regulations on harmful exhaust emissions. Perfection of combustion process proves natural pursuance of development of more efficient and better-controlled systems of fuel supply. Use of suitable control algorithms and selection of appropriate injection times make it possible to achieve both required parameters of engine performance and compliance with legal standards concerning purity of exhaust gases.

Vast majority of Diesel engines manufactured nowadays is equipped with high-pressure Common Rail systems. The main advantage of such systems is ability of controlling in wide range of engine operation, such parameters as time and pressure of injection, as well as form of the injection. Knowledge of injection time is important, because during operation of injection system, amount of fuel supplied to cylinder of engine is changed basing on this value.

Analyzes of injection processes which are performed by fuel supply systems with Common Rail have showed significant differences between injection times preset by controller and times of the injection. The authors have undertaken attempt to assess these differences, their causes and directions of change.

Nowadays, issues related to the analysis of multiple injection rate are discussed in terms of the effect of individual injection parts on the injection process. These tasks are carried out both by means of model analyzes [1] and by experiments carried out on test beds [2]. Rarely you can see analyzes of the multiple injection rates, especially in terms of changes in both time and fuel mass delivered in the parts.

This paper is the third publication devoted to analysis of injection times of multiple fuel dose. In the first publication [3] are presented characteristic injection times in function of operational parameters of injection system, while in the second publication are discussed controlled injection times and times of needle lift [5].

2. Scope of the analysis

With fixed pressure values in fuel rail, injection times determine amounts of injected fuel and form of the injection.

These times, which were input to read-only memory of the controller of the engine (ECU unit), or to internal memory of experimental controller are called as preset times of injection. The concept of „calculated times" was also introduced to the considerations. Under this concept is meant injection time of individual portion of dose and time of gap between the doses, determined on the basis of pressure increase in indicator of injected dose and on the basis of calculated courses of injection. With such approach it is necessary to use dependencies resulting from equation of mass conservation, needed to carry out approximations of measured courses and to take into consideration changes in parameters of injected fuel. These are not, therefore, the times obtained directly, for instance by measuring of needle lift, but obtained indirectly, based on recalculations with taking into consideration additional quantities. Calculated injection times are the response of the system to the preset times. Calculated injection times and characteristic parameters of fuel outflow rate from the injector directly result from determined courses of injections.

Thus, it is possible to determine relationships between preset, electric courses which control injectors in fuel supply system, and calculated injection times, reflecting changes in fuel stream supplied to cylinder. The comparison is especially significant in optimization of combustion process in cases where various forms of injection are used, and hence where divided injection doses are supplied. Therefore, the studies were undertaken to explain a reasons and to determine direction of changes of these quantities.

The objective of the study was to determine differences between preset times of injection and calculated times of injection, and hence, quantities necessary during development and modification of controlling algorithms to compression ignition engines. Proper selection of these quantities is necessary to ensure low operational fuel consumption. This knowledge is also useful for modeling of working cycle of compression ignition engine.

In turn, due to need to assure long operational life of vehicle with unchanged operational parameters, it is necessary that injection system should comply with high requirements, such as: stability of multiple doses supply, proper response of the system to preset, differentiated times, and unchanged accuracy of injection process during complete operational life of the system [8]. Assessment of

dosing process is impossible without knowledge of preset times of injection and response to such enforcement, i.e. calculated injection times.

Considering the above, it was necessary to determine dependence between differences in the above mentioned injection times and pressure in fuel rail, and method of division of fuel dose into portions.

As already mentioned above, multiple doses of injection were analyzed. Therefore, in each measuring case the comparisons were performed in two ways:

– for sums of times of individual portions of dose, and
– for total injection times, i.e. for sum of times of individual portions of the doses and gaps between them.

The considerations were accomplished for various configurations of multiple doses, with different values of injection times and gaps. Measurements were performed for three measuring groups. The first group, with two-portion division of the dose, consisted of short, uniform values of the preset times and low, variable pressures of injection.

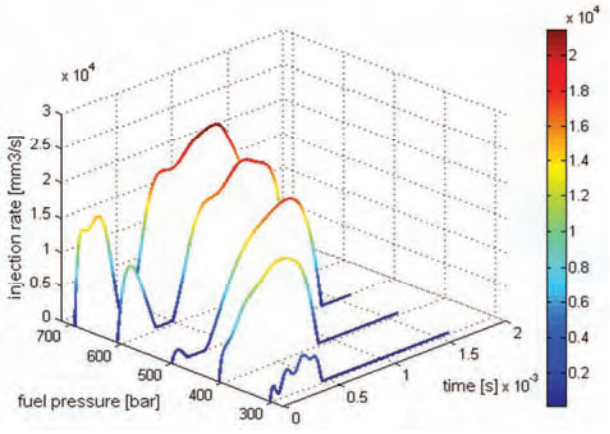

Fig. 1. Injection courses of two-portion dose (first measuring group)

The second group with values of different preset times, with three-, two-, and single-portion division and different pressures. In these cases, the aim was to obtain similar values of aggregated dose of the fuel 50 mg/injection. Values measured in the test bed differed from assumed values from –1.8% to 5.1%.

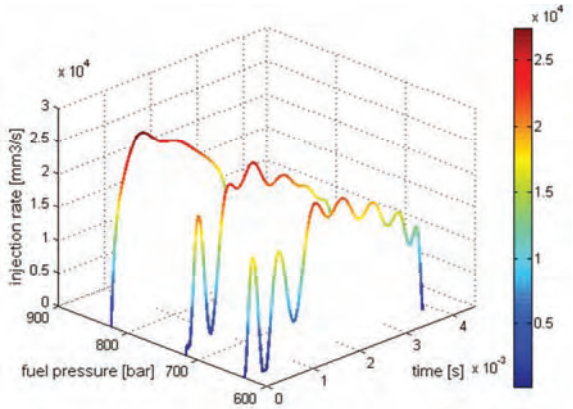

Fig. 2. Injection courses of the doses with constant value (second measuring group)

The third group consisted of identical values of times, preset for five-portion division and variable values of fuel pressure in the rail, selected from range of average values as used during operation of vehicles.

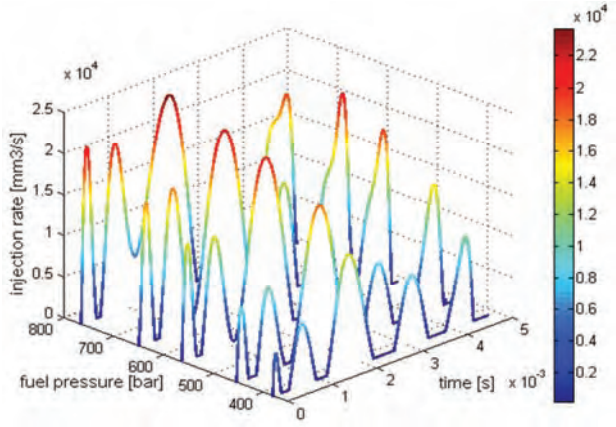

Fig. 3. Injection course of five-portion dose (third measuring group)

In turn, in the Fig. 4–6, for each from the groups, are presented ranges of the changes, both preset parameters and form of the injection.

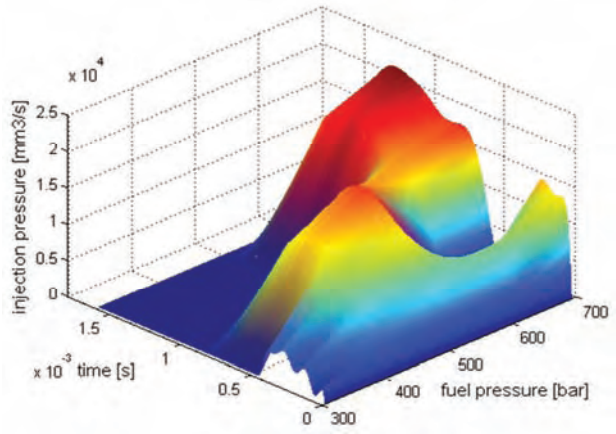

Fig. 4. Changes in parameters and forms of injection of two-portion dose (first measuring group)

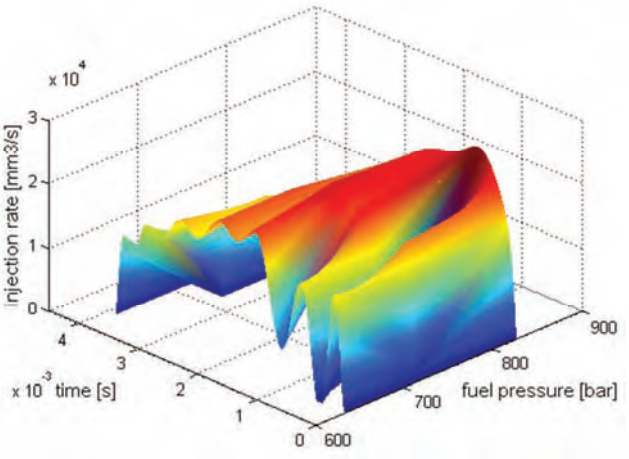

Fig. 5. Changes in parameters and forms of injection of the doses with constant value (second measuring group)

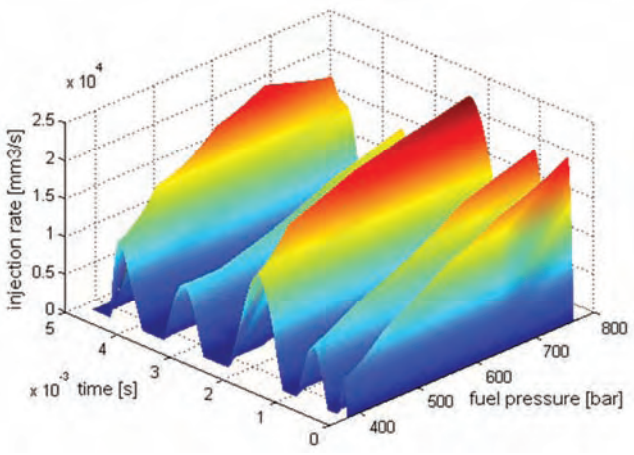

Fig. 6. Changes in parameters and forms of injection of five-portion dose (third measuring group)

Investigated injection system with Common Rail was controlled by KSSiP-2 controller, developed and produced in the Department of Combustion Engines and Vehicles [5]. Calculated injection times were determined based on courses of voltage change in piezo-quartz GU-21D transmitter produced by AVL, located in chamber of electronically controlled indicator of injection dose [6]. The voltage was measured at the output from the transmitter, using Tektronix TDS-3014 electronic oscilloscope. Based on measured voltage were evaluated calculated injection times and characteristic quantities connected with injection course of divided dose.

3. Comparative analysis of preset and calculated injection times

Injection time accomplished by injection system can be determined by various methods. To this purpose, in the study [4], effect of fuel injection in form of pressure growth in chamber of electronically controlled indicator of injection dose was used. Determined in such way courses were called as times of needle lift. Courses of pressure variations can be also used as a basis for calculations of injection course, and these in turn to evaluation of calculated injection times. It might seem that since comparisons of preset times and needle lift were carried out earlier [4], there is no needed to compare the preset times and calculated times. However, times of the lift and calculated times are different. Necessity of approximation of measured signals should be recognized as the most significant reason, because measured courses are not smooth, and this causes difficulties in calculations of derivative of pressure in function of time, needed to evaluation of calculated injection times. Sometimes there are also difficulties in evaluation of zero line of fuel outflow rate from atomizer. Moreover, division of the dose into portions is not always reflected on curve of injection course. For some values of time of the gap, the needle can not be settled in the seat, and only reduced fuel outflow rate can be observed. Therefore, the differences exist and comparative analysis between the times mentioned at the beginning is justified.

In the Fig. 7 is presented comparison of preset and calculated sums of individual portions of the dose. They were arranged in groups according to preset times and shapes of injection. It can be noticed a significant differences between preset and calculated times. The differences concern all analyzed cases. The biggest difference occurred for multi-portion times and higher pressure values, and amounted to 2354 μs. For much shorter, two-portion times and lower pressures much smaller value of the difference – 773 μs was recorded.

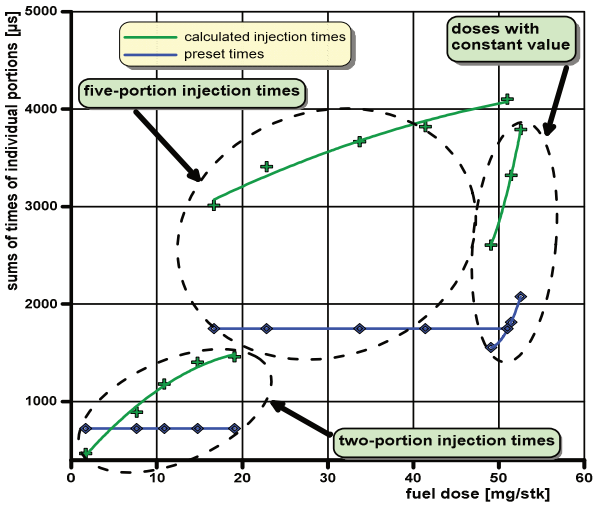

Fig. 7. Collation of sums of times of individual portions of the dose for the analyzed measuring cases

A similar comparison was performed for preset and calculated sums of total injection times. They were summarized in the Fig. 8. Here the absolute differences are lower than these analyzed above, and for five-portion times do not exceed 350 μs, and for two-portion 635 μs.

Because the analyzed quantities are characterized by considerable variability of values, in the comparative analysis were also used relative, percentage differences of analyzed times. They were calculated as quotient of difference of preset, total times of injection (preset sums of times of respective portions) and calculated, total times of injection (calculated sums of times of respective portions), related to preset, total times of injection (preset sums of times of respective portions).

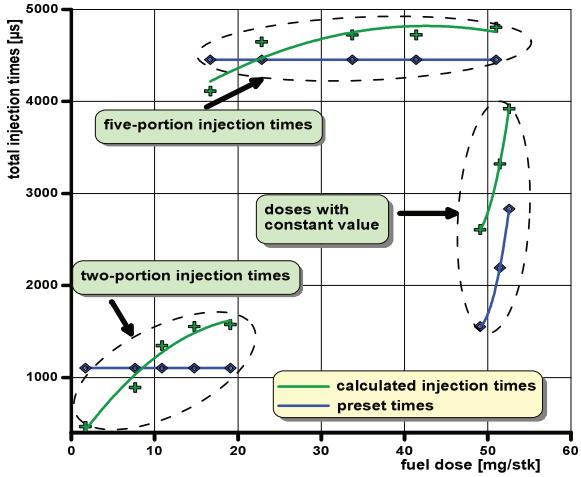

Fig. 8. Collation of sums of total times for the analyzed measuring cases

The results in function of total dose of the fuel are presented in the Fig. 9. The dashed lines indicate changes in total times, while solid lines depict changes of sums of respective portions. Nature of the changes of these courses is similar to linear.

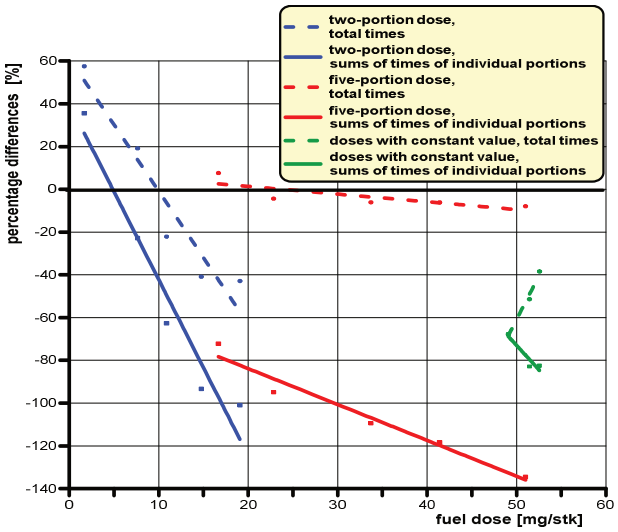

Fig. 9. Percentage differences between preset and calculated injection times, evaluated for two- and five-portion doses

As can be noticed, in majority of the cases the calculated times are greater than the preset times. Only for the short times and low pressures this regularity is not fulfilled. Distinct differences between preset and calculated times occur especially for the sum of individual portions of the dose (solid lines). In this case, values of the differences are growing rapidly as the dose increases, and for five-portion division, where percentage differences practically in complete analyzed range are bigger than 90%, and even can reach up to 140%. Such significant differences result mainly from the causes listed in performed earlier comparative analysis of preset injection times and times of needle lift [4], i.e. from increase rates of amperage controlling injectors, values of preset injection times of respective portions of the dose and gaps between the injections, delays in beginning and finishing of the injection. There are also others, resulting from calculations of injection course and associated necessity of interpretation of injection courses from indicator of injection dose. As already notices at beginning of the discussion, times of needle lift of individual portions of the dose were measured with arbitrarily taken assumption on beginning and ending of process of pressure growth in chamber of the device. Despite all the diligence, it is not possible to capture all small changes in course of injection which affect values of analyzed times. Process of evaluation of injection courses, which were the basis to calculation of injection times, is based on processes of approximation and differentiation of averaged, measured values. Particular attention is required in case of pressure courses obtained in result of injection of multi-portion doses. In these cases, to maintain accuracy of simulation of injection process, it is necessary to divide the courses into parts, and for each part to carefully select approximation function to differentiate it, and next reconnect the parts into a single course [7]. In particular, computation of the derivative reveals and enhances each recorded local change in the output course, and if it concerns the beginning and the ending of analyzed curve, it makes it difficult to evaluate the root-values. In these stages of the proceedings could be seen some sources of discrepancy between times of needle lift and calculated injection times, and in consequence, sources of increased percentage differences between preset and calculated injection times.

For two-portion division, when only one gap was preset, the differences are smaller, due to lower values of injection pressure and are resulting mainly from smaller values of injection pressure and connected with it – for some measuring points – lacking division of the dose into portions.

In the Fig. 9 are also presented percentage differences in preset and calculated injection times, evaluated for constant fuel dose (the second measuring group). From the course of changes of differences in sums of preset and calculated times of respective portions of the dose (solid line) is seen that in the analyzed range the sums of calculated times are bigger than the preset ones, and the differences reach 80%. The highest values of the differences are present for the biggest number of divisions of the dose, while the smallest ones for a single-portion dose. When performing analyzes for this measuring group it was possible to evaluate times of the lift for respective portions of the dose (based on course of pressure in chamber of the indicator), but in case of the calculated times it wasn't possible because only significant changes in fuel outflow rate were observed, none division of the dose into portion occurred. Thus, to evaluate percentage differences in the preset and calculated times of individual portions of the dose, it was necessary to take the total calculated injection times and refer them to sums of preset times of individual portions of the dose. For this reason, discussed percentage differences have a higher values than in case of comparison of preset injection times with needle lift.

Values of percentage differences of the total times (dotted lines) differ to a small extent with analogical, plotted earlier values for times of the lift [4]. This complies with expectations, because calculated total times were evaluated on the basis of total times of the lift. Here too, although to much smaller degree, can be applied the above presented remarks concerning discrepancy between preset and calculated times. The differences are mainly due to difficulties in evaluation of zero level of calculated courses, and referencing to times of the lift, the differences do not exceed 5%. A slight increase in total injection time is only noticeable for a bigger doses.

Verification of the calculations was comparison of the calculated unit dose of the fuel with the dose measured in testing station. In vast majority of the cases the differences between these values were included within interval 2.3–6.6%. Only in two cases of very small doses were observed a higher values: 12.7 and 30.4%. On this basis it was concluded that calculated curves, being the basis for analytical evaluation of size of the dose, accurately reflect duration of fuel supply process.

In the further part of the analysis consideration was given to share of calculated times of individual portions and

gaps in total calculated injection time. The analyzes were performed for the first and the third measuring groups. The share of individual portions of the dose in total mass of supplied fuel was also taken into account. Names of individual portions of the dose were adopted according to terminology used in the English language literature, that is: the first part is called „pilot", the second „pre", the third „main", the fourth „after" and the fifth „post".

And thus, in the Fig. 10, for the first measuring group and investigated values of fuel pressure in the rail, is presented percentage share of calculated times of individual portions and gaps in total, calculated injection time. Obtained values were referred to percentage share of the preset times of individual portions and gaps in total preset time of the injection. (left part of the drawing). In spite of significant shares of all preset values (the first portion – pilot – 23.8%, the second portion - main – 42.1%, gap – 34.2%) in the total preset injection time, from calculated courses of fuel outflow rate results that for two the lowest pressures the fuel was supplied in form of a single portion dose. For the next three values already occurred division into two portions, with domination of share of the second portion of calculated time of injection. For two the highest pressures its share was practically maintained on a constant level (about 68%). At these points, the changes occur for the first portion and for the gap, while the first portion of the dose was extended at the expense of the gap (occurs increase of share of the first portion from 22.4% to 25.2%).

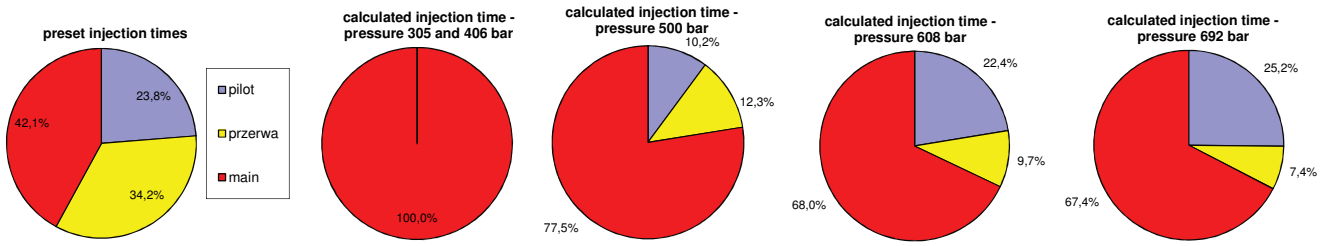

Fig. 10. Percentage shares of calculated times of individual portions and gaps in total, complete injection time for the first group of the measurements

Consequently, it would be expected a significant increase of mass of fuel supplied with the first portion of the dose. However, from summarization presented in the Fig. 11 is seen that this mass increases, but more slowly than indicated by share of the time. Thus, with increase of pressure, for the first portion of the dose is seen reported earlier increase of fuel outflow rate from the atomizer. However, it is not as much important that share of fuel mass of this portion in the total dose is comparable with share of time of this portion in total calculated time of the injection. This is insofar important observation, that when developing control algorithms of the engine (or when modeling working processes of the engine), it is important to take into considerations both calculated quantities of the fuel, evaluated for respective portions of the dose, as well as calculated times of the injection.

When injecting small doses at low injection pressures, the question arises what values of preset injection times should be used. Omitting issues connected with spraying of the fuel, based on the data presented above, it can be ascertained that divided times shouldn't be set, because division into portions will never be accomplished. However, from the point of view of need of proper and long-lasting operation of injector's valve, divided times should be used. In this way is reduced amount of energy required to controlling of the valve, and thus amount of heat generated in the valve and temperature of fuel flowing across the fuel overflow. It should be remembers, however, that times of gaps shouldn't be shorter than delay times of completion of the injection. Otherwise, process of needle lift, initiated by the first from preset portions, may be interrupted. With a higher fuel pressure, it is possible to use successfully divided times to modulate the stream of fuel supplied to the cylinder. This method seems especially effective for low and medium engine loads, where the first portion of the dose has a significant effect on level of emissions of nitrogen oxides, while the second portion on effective performance of the engine.

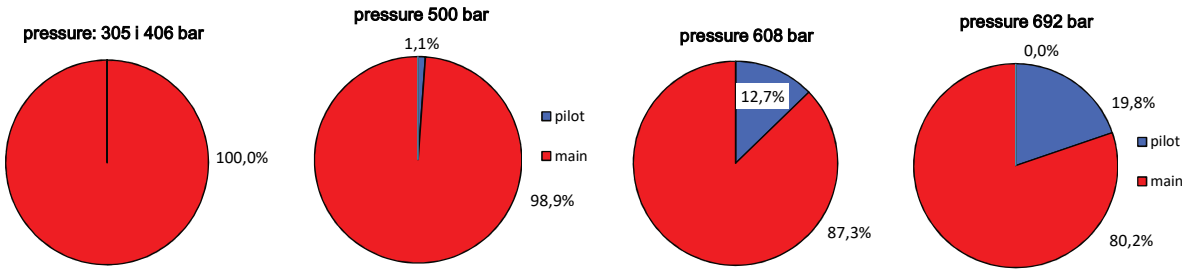

Figs. 11. Percentage share of individual portions of the dose in total amount of supplied fuel for the first group of the measurements

In turn, in the Fig 12 is shown, for the third group of the measurements and analyzed values of pressure in the rail, percentage share of calculated times of individual portions and gaps in the total calculated time of the injection. These values were compared with percentage share of preset times of individual portions and gaps, in the total preset time of injection (left part of the drawing).

Shares of preset times are significantly smaller than shares of calculated times. In the total preset injection time the biggest share – more than 60% – belongs to gaps. For calculated times the shares are significantly smaller and decrease with increase of pressure (from 28.5% to 14.6%). The share of the biggest portion – the main portion – increases significantly, especially when combined with Pre - portion (also Fig. 12). Phenomenon of linking the portions begins to occur for fuel pressures in the rail highest than 650 bar and was discussed earlier.

When considering amounts of fuel supplied in the individual portions (Fig. 13), the third portion of the dose (main) draws the attention, as dominating the others. As the pressure increases, share of fuel supplied by this portion increases from 45% up to 58%. The first portion of the dose (pilot) is the most stable. Its share amounts to about 7%.

Significant effect of times of gaps on injection process is seen when multi-portion dose of injection is used. By their proper selection, various forms of injection course can be created, without significant increase in total time of the injection. It is also possible to achieve maximal value of fuel outflow rate at predominated, in respect to beginning of injection, position. Fuel pressure fluctuations do not significantly affect this position, but at the same time they allow for changing dose and spraying quality of fuel.

Generally speaking, the longest gaps promote generation of divisions into portions, but considerations should be always given to pressure level of fuel in the rail, strongly impacted on form of the injection. Design features of a given type of injector, having effect on characteristic times of injection, are also important. Mostly, it should be listed here: mass and dimensions of the atomizer's nozzle, geometrical parameters of control piston and control chamber, and operational parameters of quick-toggling valve, the valve incorporated into upper part of the injector.

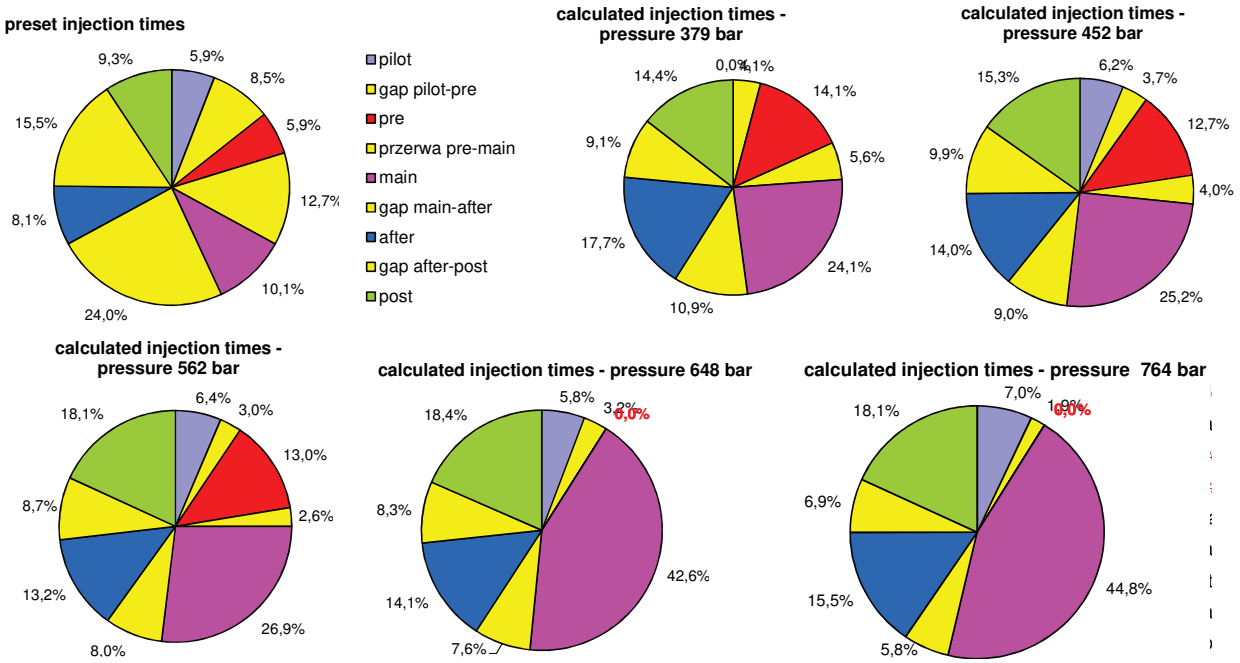

Fig. 12. Percentage shares of calculated times of individual portions and gaps in total, complete injection time for the third group of the measurements

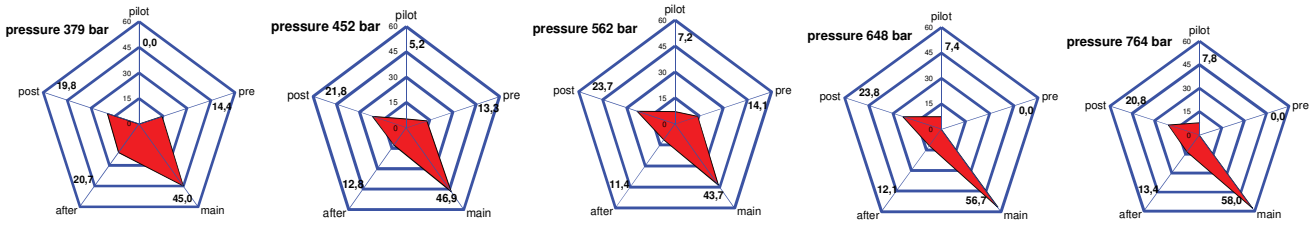

Fig. 13. Percentage share of individual portions of dose in total amount of supplied fuel for the third group of the measurements

Summary

Calculated injection times are different from preset times. This is decided by many factors, but the most important are: control method of electromagnetic valve (course control current flow), inertia of movable components of injector and pressure in high-pressure part of injection system. During injection are occurring factors causing both reduction and increase of injection time. Finally, however, the times during which the fuel is supplied are in the vast majority of cases higher than preset injection times. Exceptions are the cases where, at low fuel pressure in the rail, small doses of fuel are supplied. Therefore, for fixed surface area of outflow ports from the atomizer and fixed pressure of fuel injection the dose can not be equated with

preset injection times. They will depend both on features adequate to a given injector (operational parameters of control valve, moving masses of the injector, viscous resistance of motion, etc.) as well as values of injection times and gaps between injections, or number of portions to which the dose was divided.

Increasing duration of fuel supply is associated with increase of times of individual doses, constituting the fuel dose. Intensity of changes in time of the process depends on values of preset parameters. Thus, increasing supply pressure of fuel results in decrease of delay time of beginning of injection and increasing of delay time of termination of injection, and thus causing a high increase of time of needle lift. Similarly are affecting two phenomena: inductivity – associated with course of controlling electric current of the valve and magnetic residue of the valve, depending on preset injection time. The both ones increase delay times of injection ending. In turn, increasing the preset times of gap results in reduced delay times of injection ending and reduced time of needle lift. However, its effect is smaller than the others. As a result, injection times of individual portions, and the same entire injection cycle, are prolonged.

Clearly, the intervals between dose portions disappear. This phenomenon has an effect on the mass of fuel that is given in the individual parts of the dose. The share of fuel masses in the individual dose portions is greater than that calculated from the calculated injection times (differences up to 25 %).

The knowledge of calculated injection times is one of elements that allow development of control algorithms to compression ignition engines. It allows significant reduction of labour consumption needed for application of software in controller of the power unit. The results of performed comparative analysis of preset and calculated injection times may be used to calculation of energy stream supplied to combustion chamber during individual phases of the process. They can be also helpful in determining characteristic parameters of the injection, such as maximal injection pressure and fuel outflow from atomizer.

It should be remembered that use of multi-portion doses of the injection doesn't result in any significant increase in total, calculated values of injection time relative to the preset ones. However, under certain circumstances, calculated values of the times are significantly increased. This occurs when a small unit dose of fuel is supplied, and when high values of preset times are used. Calculated durations of individual portions of the dose are much longer than their preset counterparts. The differences are due to the same reasons, as these described during comparison of preset times with lift of the needle, and additionally are coming here discrepancies connected with transformations of measured coursed into smooth curves and resulted from their differentiation.

Division of fuel dose into portions can be accomplished under certain conditions. First and foremost, a sufficiently high fuel pressure should be generated and sufficiently long times of gaps should be set. When are set constant values of injection time, times of needle lift for individual portions of the dose increase together with increase of pressure. Such increase depends on size of the gap, because for longer gaps the delay time of injection ending increases, and the same time of the lift. This in turn reduces gaps.

Presented analyses concerning the processes governing injection times, starting from presetting in the controller up to moment of execution in compression ignition engine, could be a tool for research engineers, writing or modifying control algorithms to the power units. The comparisons, specifications and dependencies presented in this paper allow considerable reduction of time spent on work connected with selection and calibration of fuel supply system.

Bibliography

[1] BINGQI, T., LIYUN, F., XIUZHEN, M. et al. Investigation of main injection quantity fluctuation due to pilot injection in high pressure common rail fuel injection system. *International Journal on Smart Sensing and Intelligent Systems*. 2014, **7**(2), 820-836.

[2] HERFATMANESH, M. R., PENG, Z., IHRACSKA, A. et al. Characteristics of pressure wave in common rail fuel injection system of high-speed direct injection diesel engines. *Advances in Mechanical Engineering*. 2016, **8**(5), 1-8.

[3] KNEFEL, T. The evaluation and interpretation of the characteristic injection times of a multiple fuel dose. *Journal of KONES: Powertrain and Transport*. 2011, **18**(2), 205-213.

[4] KNEFEL, T. Analiza porównawcza wybranych czasów wtrysku wieloczęściowej dawki paliwa. *Czasopismo Techniczne*. 2012, **9**, 115-129.

[5] STELMASIAK, Z., KNEFEL, T., LARISCH, J. A development control unit for common rail injection system – KSSiP-1. *Combustion Engines*. 2005.

[6] KNEFEL, T. Electronically controlled indicator of injection. *Combustion Engines*. 2007, SC2, 74-79.

[7] KNEFEL, T. Methodology of determination diesel engine injection rate and dose with the assistance indicator of injection. *Combustion Engines*. 2009, SC2, 379-385.

[8] WANG, X., KIKUTANI, T., TAKEUCHI, K., NAKANE, N. Development toward "diesel revolution" using ultra high pressure CRS with closed-loop control system for heavy duty engine. *FISITA World Automotive Congress*, 2010, Budapest, F2010-A-164.

Tomasz Knefel, DSc., DEng. – Faculty of Mechanical Engineering and Computer Sciences at University of Bielsko-Biala.

e-mail: *Knefel@ath.bielsko.pl*

Jacek Nowakowski, DSc., DEng. – Faculty of Mechanical Engineering and Computer Sciences at University of Bielsko-Biala.

e-mail: *JNowakow@ath.bielsko.pl*

Article citation info:
LEWIŃSKA, J., KAPUSTA, Ł.J. Analysis of the microstructure of the fuel spray atomized by marine injector. *Combustion Engines*. 2017, **169**(2), 120-124. DOI: 10.19206/CE-2017-221

Joanna LEWIŃSKA
Łukasz Jan KAPUSTA

CE-2017-221

Analysis of the microstructure of the fuel spray atomized by marine injector

The process of the atomization and formation of the fuel spray can be described by macro- and microstructure parameters. Knowledge of these parameters may be a key information to conduct further optimization of the combustion process. This paper presents the research results of the microstructure parameters of the diesel oil spray atomized with marine engine injector. A measurement technique, named Laser Induced Fluorescence (LIF) in the combination with Mie scattering was used to determine LIF/Mie ratio across the spray. The fuel was injected into a constant volume vessel. LIF and Mie signals were recorded by two cameras at the same time. Nd:YAG pulsed laser was used to create light sheet for spray illumination. Wavelength of λ = 266 nm was used in this study.

Key words: *marine diesel engine, marine injector, microstructure spray parameters, optical method, LIF/Mie*

1. Introduction

Diesel engines are the main type of drive for large-sized marine vessels. Burning diesel oil by marine engines effects the emission of toxic compounds into the atmosphere. The emissions generated by engine, similar to a marine vessel engine, depending on various design feature are reported in the literature [1–3]. The amount of exhaust emissions are regulated and gradually tightened by International Maritime Organization (IMO) MARPOL 73/78 regulations, attachment VI including chapter 4 [4]. Stricter exhaust emission regulations are the main reason for optimizing the combustion process. The process of designing the marine engine and its units is aimed at maximizing engine efficiency while maintaining low emission of toxic compounds. High pressure of injection, controlled fuel delivery, and increased engine effectiveness are the advantages of the common rail system. Nevertheless, there is enormous number of engines equipped with conventional pressure-opened injectors. Retrofitting these engines with CR injection system in order to meet stricter emissions standards in most cases is not economically feasible. Therefore, more cost-effective method to optimize combustion process in engines in operation needs to be implemented.

The combustion of fuel in the combustion chamber of marine engine begins at certain time after start of injection. This time is necessary for creating the fuel-air mixture of proper parameters. This process is dependent on atomization, evaporation and diffusion. Payri et al. [5] defined five phases of creating combusting fuel spray: I) non-reacting, II) auto-ignition expansion, III) stabilization, IV) acceleration, and V) quasi-steady propagation. First phase contains atomization which includes primary and secondary brake-up [6]. The next following ones are strongly dependent on the first one, therefore injection process is of crucial importance. Atomization occurs as a result of internal turbulences (induced at inlet to the nozzle and by cavitation) and aerodynamic forces.

Creating proper macrostructure and microstructure [7] of diesel fuel spray may lead to decreased exhaust emissions and increased efficiency.

Injected fuel spray takes the shape of a cone with a spherical forehead described with parameters: tip penetration and spray cone angle. Tip penetration and spray cone angle demonstrate droplets ability to penetrate gaseous environment in the combustion chamber. Droplets in the fuel spray are usually non-homogeneous in terms of size, which is characterized by a large spread of droplet diameters. Droplets diameters in the fuel spray define the microstructure [6, 8–10]. The size of fuel droplets depends on many factors, so the process of their formation is often referred to as the statistical process - the spray spectrum [7]. The most representative parameter used to assess spray quality is the mean diameter of the droplets. The average diameter of the droplets refers to number and diameter, surface or volume of droplets in the fuel spray. The most commonly used is the SMD – Sauter Mean Diameter [11]. SMD may be directly connected to evaporation and combustion of fuel droplets.

Recent research shows that the structure of the diesel fuel spray is influenced by the construction and technical condition of the injection system or the pressure in the combustion chamber [9, 12]. Studies presented in [13, 14] contain the comparison of fuel spray parameters obtained with piezoelectric and solenoid injector. The influence of injection pressure on fuel spray parameters is shown in [15], while backpressure in [16, 17]. The nozzle parameters influence are shown in [18]. While considering the fuel spray parameters, it is necessary to mention cavitation phenomena [19–21]. The increase in injection pressure and the cavitation effect cause a decrease of SMD [22]. Thus, the cavitation may improve quality of the combustion process.

One may notice that the spray formation process can be improved by changing number of parameters, which does not necessarily need to require high investments. The results of the modification need to be properly measured. Diesel spray however, pose a challenge in terms of droplet diameter measurements. Due to small droplets and high optical density of the diesel spray the number of techniques which can be used for spray microstructure characterization is limited. One of the methods is ballistic imaging [23–25]. This technique in a form of optical shadowgraphy was used to visualize breakup of the near-field of an atomizing Diesel spay by Linne et al. [23]. The other possible methods are based on X-ray absorption [26]. The technique which can provide SMD distribution across the spray cloud is LIF/Mie method – also called Laser Sheet Dropsizing (LSD). Pastor et al. [27] used this method to characterize droplet size

distribution in Diesel spays at three different engine relevant discharge densities. They conducted experiments using two different light sheet illumination wavelengths 355 nm and 532 nm. 355 nm signal was used to induce natural fluorescence of Diesel fuel while 532 nm signal was used to induce fluorescence of rhodamine B doped to Diesel fuel. They noticed dissymmetrical behavior of natural fluorescence signal. The signal emitted by the Rhodamine B didn't reveal such behavior. They concluded that the observed dissymmetrical behavior of the natural fluorescence signal made this solution unreliable for quantifying the droplet diameter via the LIF/Mie ratio, and indicated second approach as appropriate one. In this study, we used LIF/Mie method to quantify SMD distribution across the marine injector spray at engine relevant pressures. Fluorescence signal in our study was induced at 266 nm in order to overcome dissymmetrical behavior reported by Pastor et al. [27].

2. Experimental setup

Laboratory studies presented in this article were carried out at Warsaw University of Technology. The constant volume vessel was used to observe sprays at elevated pressure. constant volume vessel is shown in Fig. 1.

Fig. 1. Constant volume vessel with injector on the top

The parameters of the combustion vessel were summarized in Table 1.

Table 1. The parameters of constant volume vessel

Dimensions	200 x 200	mm
Optical view	100	mm
Under pressure	3.2	MPa
Measurement space	nitrogen	-
Number observation windows	3 (all 4)	-

The injector used in this study is a conventional pressure opened diesel injector from marine engine Sulzer Al 25/30 type, equipped with UPS (Unit pump system) injection system. The injector was located at the top of the vessel in a way to observe single jet evolution at a distance of almost 100 mm (half of the cylinder bore). The tested spray of diesel oil was made by one active injector nozzle. Rest of the nozzles was plugged. The diameter of the nozzle was 0.320 mm. The fuel was supplied to the injector by a high pressure common rail system equipped with fast-acting electromagnetic valve releasing fuel flow to the injector. The pressure behind the injector was measured by means of Kistler type 4067E [28] piezorezistive pressure sensor. The specifications of the pressure sensor are shown in Tab. 2.

Table 2. Kistler type 4067E pressure transducer specifications according to [28]

Parameter	**Value**
Measuring range / MPa	0–300
Overload /MPa	350 MPa
Reference temperature (T ref) / °C	25
Sensor temperature, min./max. / °C	–40/200
Temperat. compensation range / °C	25–180
Max. deviation pressure / %FSO	≤ ±0.8
Max. deviation temperature / °C	≤ ±4
Linearity at Tref (LSQ) / %FSO	≤ ±0.3
Natural frequency / kHz	> 200

The fuel pressure in common rail system was of 50 MPa. The opening pressure was set to 35 MPa. The pressure in the vessel was of 3.2 MPa. Instead of air, pure nitrogen was used. The research was conducted at room temperature. Each measurement point was repeated 10 times.

Measured diesel oil viscosity and density at 40°C was of 2.35 mPa·s and 816.1 kg/m^3 respectively.

In this work, the laser-based system was used for the purpose of simultaneous imaging of fluorescence and Mie scattering. The laser beam was generated by Spectra-Physics Nd:YAG pulsed laser of the maximal energy of the signal 220 mJ (at 266 nm) [29]. Generated fuel spray was illuminated by a collimated laser beam. The lights sheet height was of 50 mm.

The experimental setup system is shown in Fig. 2.

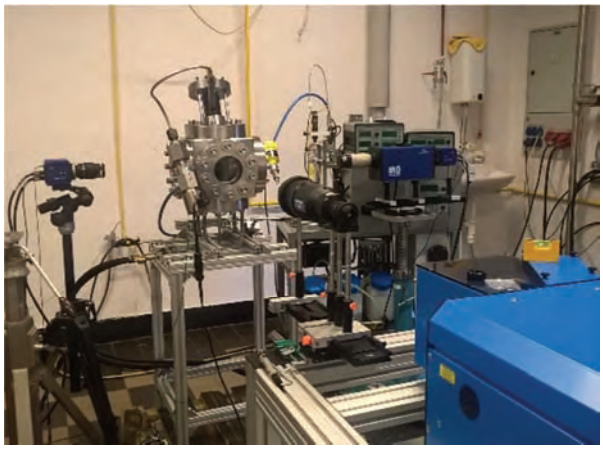

Fig. 2. Experimental setup

The intensity of the signal of LIF and Mie was registered simultaneously with two video cameras sCMOS manufactured by La Vision. The parameters of the video cameras were presented in Tab. 3.

Table 3. The parameters of sCMOS Camera

Frequency	10	Hz
Min. exposure	15	µs
Spectral range	370–1100	nm
Number of pixels	2560 x 2160	Pixels
Pixel size	6.5 x 6.5	µm
Active area	16.6 x 14.0	mm
A/D converter	16	bit

The cameras were set oppositely in one axis (Fig. 3), directed towards illuminated plane of diesel spray. The signals of LIF and Mie were separated with the adequate optical filters. In order to capture 266nm Mie signal the videocamera registering the image of Mie signals was coupled with the IRO La Vision intensifier. IRO caused the intensification of Mie signal before it was projected onto the matrix of camera sCMOS La Vision.

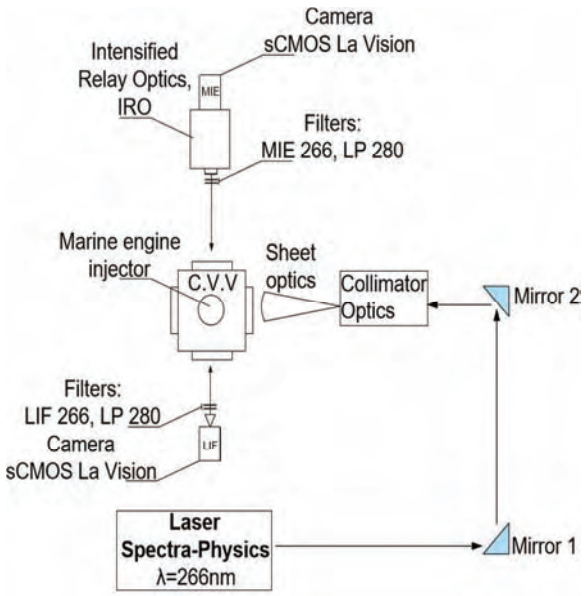

Fig. 3. Experimental setup of the LIF/Mie optical arrangement, C.V.V – Constant Volume Vessel

3. Results

The principle of LIF/Mie technique is based on the assumption that the intensity of scattered light on the surface of the droplets is proportional to their surface, while the fluorescence intensity is proportional to their volume. The ratio of the intensity of fluorescence to Mie signal therefore represents the Sauter Mean Diameter (SMD). Note, that this is true for spherical droplets, thus the spray region close to the nozzle, where ligaments and strongly deformed droplets are present, cannot be characterized with this technique. One needs to be aware that LIF/Mie ratio are not correlated linearly with SMD as explained by Berrocal et al. [30]. Another important aspect of using laser sheet imaging techniques for dense sprays is multiple scattering. According to Berrocal et al [30] in non-reacting diesel spray usually more than 65% of the received signal may come from multiple scattering. Therefore, the results presented here shall be treated as qualitative ones.

As a result of the measurements, we received LIF and Mie diesel spray images. Using the appropriate image processing allows obtaining LIF/Mie ratio 2D map that serves as the basis to determine SMD.

Before acquisition of LIF and Mie signals coming from the illuminated spray at first background and laser light sheet images were taken. These were important in proper image processing. The background and light sheet images are shown in Fig. 4. Note that all images presented here are shown using the same colormap, however the range of the scale differs depending on the image.

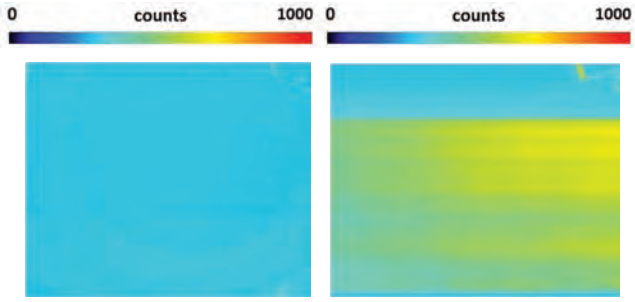

Fig. 4. Background and light sheet images, respectively from left

The first step of results processing included background subtraction from acquired raw LIF and Mie images. Instantaneous LIF and Mie images recorder during one of the injections after background subtraction are shown in Fig. 5 and Fig. 6 respectively.

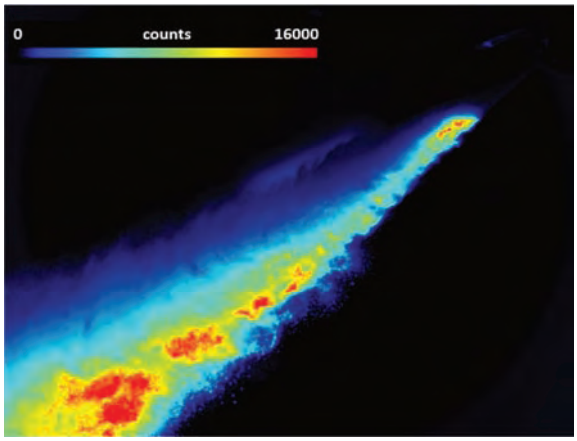

Fig. 5. Instantaneous LIF image after background subtraction

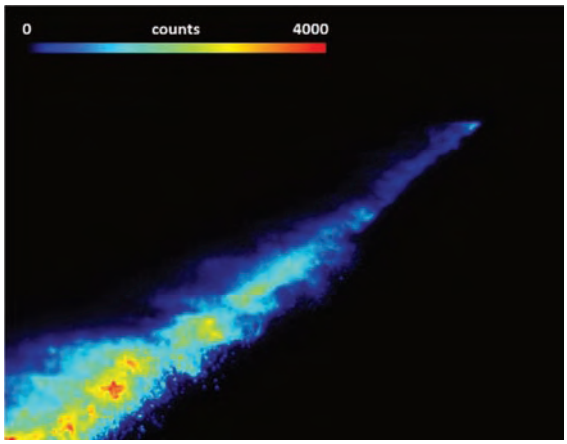

Fig. 6. Instantaneous Mie image after background subtraction

10 instantaneous images for each signal after background subtraction were averaged. The averaged images of LIF and Mie signal are shown in Fig. 6 and Fig. 7 respectively.

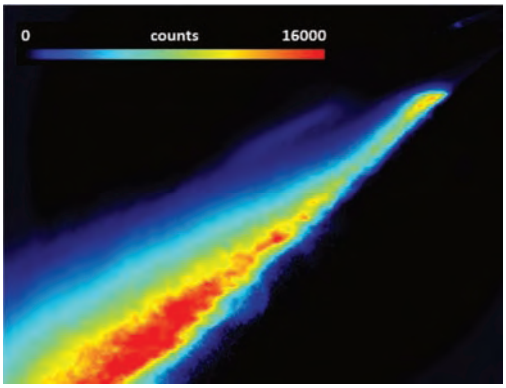

Fig. 7. Instantaneous LIF image after background subtraction

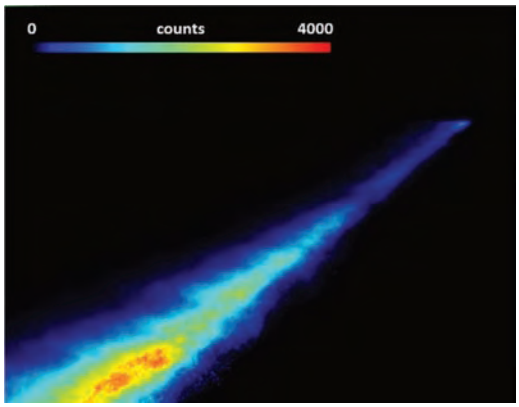

Fig. 8. Instantaneous Mie image after background subtraction

As explained earlier only 10 instantaneous images were used to create average image. The averaged images are still influenced by unsteady turbulent structures what indicates that the number of images should be higher in order to create smooth LIF and Mie images. Nevertheless, comparing to instantaneous images the unsteady turbulent structures were strongly limited. The averaged images were used to create LIF/Mie ratio 2D map which is shown in Fig. 9. LIF/Mie ratio shown in Fig. 9. was multiplied by 100.

Superimposing the images of Mie and LIF signals results in the visualization of created liquid and gas phase in the diesel spray. Basing on received visualizations, it is possible to determine the shape of diesel spray. The analysis of drops distribution in the gas and liquid phase is a quite important aspect in case of the marine internal combustion engine because it is connected to the quality of created air-fuel mixture and the ignition process. Fig. 7. and Fig. 8. show that the intensity of signal decreases in a radial direction outside the diesel spray cone. Reduction of signal intensity proclaims the decrease in density of drops distribution and a decrease in diameter. It is important to remember that the diesel spray was created under back pressure conditions – 3.2 MPa. The back pressure in the constant volume vessel contributes to increase in appearing aerodynamic forces and at the same time to the breakup of the drops. The highest concentration occurs in the axial part, which indicates the presence of a liquid phase and a dense distribution of droplets. The images of LIF signal (Fig. 7) show high intensity in the middle part of a spray cone and at a minor distance from the nozzle. However, Mie images (Fig. 8) present significant intensity at the end of the spray cone and relatively small intensity at the short distance from the nozzle. LIF imaging through the fluorescence excited by the laser light wave may lead to obtaining the fluorescent signal in the gas part. The involvement of fluorescence from the gas phase should be minimal.

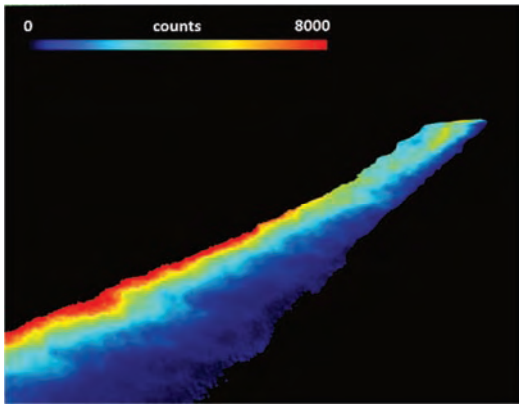

Fig. 9. LIF/Mie ratio (based on averaged images)

4. Conclusions

The results presented here show that the dissymmetrical behaviour of natural frequency concerns also 266 nm excitation wavelength. Mie signal in distinguish to LIF signal was much more symmetrical. Nevertheless, the ratio of LIF/Mie was strongly dissymmetrical and could not be used for SMD determination. The determined LIF/Mie ratio suggests that large droplets are on one side of the spray while the small ones are on the opposite side, which is untrue.

Although the results obtained here cannot be used to conclude on droplet size distribution they are highly valuable. It is proven here that dissymmetrical behavior of the natural fluorescence, noticed by Pastor et al [27] for 355 nm wavelength, cannot be overcome by switching from 3rd to 4th harmonic of Nd:YAG laser. This in turn indicate that the proper approach to SMD determination in Diesel sprays shall be done using rhodamine B, as proposed by Pastor et al. [27].

Acknowledgements

The authors would like to thank Ph.D., D.Sc., Eng., Jerzy Kowalski Gdynia Maritime University and M.Sc., Eng., Piotr Jaworski Warsaw University of Technology for their technical support and valuable remarks to the optical research of the fuel injection parameters.

Nomenclature

SMD Sauter Mean Diameter

LIF Laser Induced Fluorescence

Bibliography

[1] SARVI, A., FOGELHOLM, C.J., ZEVENHOVEN, R. Emissions from large-scale medium-speed diesel engines: 1. Influence of engine operation mode and turbocharger. *Fuel Process Technol*. 2008, **89**, 510-519.

[2] SARVI, A., FOGELHOLM, C.J., ZEVENHOVEN, R. Emissions from large-scale medium-speed diesel engines: 2. Influence of fuel type and operating mode. *Fuel Process Technol*. 2008, **89**, 520-527.

[3] SARVI, A., KILPINEN, P., ZEVENHOVEN, R. Emissions from large-scale medium-speed diesel engines: 3. Influence of direct water injection and common rail. *Fuel Process Technol*. 2009, **90**, 222-231.

[4] IMO. IMO Marine Engine Resolutions, Greenhouse Gas Emissions 2017.

[5] PAYRI, R., GARCÍA-OLIVER, J.M., XUAN, T., BARDI, M. A study on diesel spray tip penetration and radial expansion under reacting conditions. *Appl Therm Eng*. 2015, **90**, 619-629.

[6] NAGASAKA, K., TAKAGI, T., KOYANAGI, K., YAMAUCHI, T. Development of fine atomization injector. *JSAE Rev*. 2000, **21**, 309-313.

[7] Orzechowski Z. Wytwarzanie i zastosowanie rozpylonej cieczy. *Wydawnictwo Naukowo Techniczne*. 2008.

[8] JU, D., JIA, X., HUANG, Z. et al. Comparison of atomization characteristics of model exhaust gas dissolved diesel and gasoline. *Fuel*. 2016, **182**, 928-934.

[9] WANG, Z., JIANG, C., XU, H., WYSZYNSKI, M.L. Macroscopic and microscopic characterization of diesel spray under room temperature and low temperature with split injection. *Fuel Process Technol*. 2016, 142, 71-85.

[10] PARK, S., WOO, S., KIM, H., LEE, K. The characteristic of spray using diesel water emulsified fuel in a diesel engine. *Appl Energy*. 2016, **176**, 209-220.

[11] MISHRA, Y.N., KRISTENSSON, E., BERROCAL, E. Reliable LIF/Mie droplet sizing in sprays using structured laser illumination planar imaging. *Opt Express*. 2014, **22**, 4480.

[12] LI, D., GAO, Y., LIU, S. et al. Effect of polyoxymethylene dimethyl ethers addition on spray and atomization characteristics using a common rail diesel injection system. *Fuel*. 2016, **186**, 235-247.

[13] YU, W., YANG, W., TAY, K. et al. Macroscopic spray characteristics of kerosene and diesel based on two different piezoelectric and solenoid injectors. *Exp Therm Fluid Sci*. 2016, **76**, 12-23.

[14] SUH, H.K., PARK, S.W., LEE, C.S. Effect of piezo-driven injection system on the macroscopic and microscopic atomization characteristics of diesel fuel spray. *Fuel*. 2007, **86**, 2833-2845.

[15] LEE, S., PARK, S. Spray atomization characteristics of a GDI injector equipped with a group-hole nozzle. *Fuel*. 2014, **137**, 50-59.

[16] PAYRI, R., VIERA, J.P., GOPALAKRISHNAN, V., SZYMKOWICZ, P.G. The effect of nozzle geometry over the evaporative spray formation for three different fuels. *Fuel*. 2017, **188**, 645-660.

[17] PAYRI, R., SALVADOR, F.J., GIMENO, J., DE LA MORENA, J. Effects of nozzle geometry on direct injection diesel engine combustion process. *Appl Therm Eng*. 2009, **29**, 2051-2060.

[18] PAYRI, R., SALVADOR, F.J., GIMENO, J., ZAPATA, L.D. Diesel nozzle geometry influence on spray liquid-phase fuel penetration in evaporative conditions. *Fuel*. 2008, **87**, 1165-1176.

[19] BADOCK, C., WIRTH, R., FATH, A., LEIPERTZ, A. Investigation of cavitation in real size diesel injection nozzles. *Int J Heat Fluid Flow*. 1999, **20**, 538-544.

[20] SOU, A., HOSOKAWA, S., TOMIYAMA, A. Effects of cavitation in a nozzle on liquid jet atomization. *Int J Heat Mass Transf*. 2007, **50**, 3575-3582.

[21] DESANTES, J.M., PAYRI, R., SALVADOR, F.J., DE LA MORENA, J. Influence of cavitation phenomenon on primary break-up and spray behavior at stationary conditions. *Fuel*. 2010, **89**, 3033-3041.

[22] SUH, H.K., LEE, C.S. Effect of cavitation in nozzle orifice on the diesel fuel atomization characteristics. *Int J Heat Fluid Flow*. 2008, **29**, 1001-1009.

[23] LINNE, M., PACIARONI, M., HALL, T., PARKER, T. Ballistic imaging of the near field in a diesel spray. *Exp Fluids*. 2006, **40**, 836-846.

[24] LINNE, M.A., PACIARONI, M., BERROCAL, E., SEDARSKY, D. Ballistic imaging of liquid breakup processes in dense sprays. *Proc Combust Inst*. 2009, **32 II**, 2147-2161.

[25] DURAN, S.P., PORTER, J.M., PARKER, T.E. Ballistic imaging of diesel sprays using a picosecond laser: characterization and demonstration. *Appl Opt*. 2015, **54**, 1743.

[26] POWELL, C.F., CIATTI, S.A., CHEONG, S.-K. et al. X-ray absorption measurements of diesel sprays and the effects of nozzle geometry. *SAE Technical Paper*. SAE International; 2004.

[27] PASTOR, J.V., PAYRI, R., SALAVERT, J.M., MANIN, J. Evaluation of natural and tracer fluorescent emission methods for droplet size measurements in a diesel spray. *Int J Automot Technol*. 2012, **13**, 713-724.

[28] Kistler. Piezoresistive high pressure sensor 2014. www.kistler.com/?type=669&fid=61054&model= document&callee=frontend (accessed March 5, 2017).

[29] KAPUSTA, Ł.J., JAWORSKI, P., TEODORCZYK, A., KOWALSKI, J. Laser based diagnostic system for spray measurements. *J KONES Powertrain Transp*. 2015, **22**, 91-98.

[30] BERROCAL, E., KRISTENSSON, E., HOTTENBACH, P. et al. Quantitative imaging of a non-combusting diesel spray using structured laser illumination planar imaging. *Appl Phys B*. 2012, **109**, 683-694.

Joanna Lewińska, MEng. – Faculty of Marine Engineering at Gdynia Maritime University.

e-mail: *J.Lewinska@wm.am.gdynia.pl*

Łukasz Jan Kapusta, DEng. – Faculty of Power and Aeronautical Engineering at Warsaw University of Technology.

e-mail: *Lukasz.Kapusta@itc.pw.edu.pl*

Article citation info:
ANTUNES, E., SILVA, A., BARATA, J. Modeling of transcritical and supercritical nitrogen jets. *Combustion Engines*. 2017, **169**(2), 125-132. DOI: 10.19206/CE-2017-222

Eduardo ANTUNES
Andre SILVA
Jorge BARATA

CE-2017-222

Modelling of transcritical and supercritical nitrogen jets

The present paper addresses the modelling of fuel injection at conditions of high pressure and temperature which occur in a variety of internal combustion engines such as liquid fuel rocket engines, gas turbines, and modern diesel engines. For this investigation a cryogenic nitrogen jet ranging from transcritical to supercritical conditions injected into a chamber at supercritical conditions was modelled. Previously a variable density approach, originally conceived for gaseous turbulent isothermal jets, employing the Favre averaged Navier-Stokes equations together with a "k-ε" turbulence model, and using Amagat's law for the determination of density was applied. This approach allows a good agreement with experiments mainly at supercritical injection conditions. However, some departure from experimental data was found at transcritical injection conditions. The present approach adds real fluid thermodynamics to the previous approach, and the effects of heat transfer. The results still show some disagreement at supercritical conditions mainly in the determination of the potential core length but significantly improve the prediction of the jet spreading angle at transcritical injection conditions.

Key words: *fuel injection, jets, critical point, supercritical flows, cryogenics*

1. Introduction

The increasing demand for higher efficiency and performance of power and propulsion systems lead to the practice of raising pressure and temperature inside the combustion chamber. Rocket engines combustion chambersare typically subjected to high values of pressure and temperature which commonly exceed the critical thermodynamic point of it working fluid. The widespread of turbocharging, high compression ratios and high pressure direct injection systems seen in diesel engines contributed to the increase of the operating pressures and temperatures inside the combustion chamber. Often, in these engines, fuel injection happens at pressures which exceed the critical value of the fuel. The development of more advanced materials used in gas turbines has led to higher compression ratios and allow for higher temperatures at the turbine inlet, in practice this translates in higher pressures and temperatures experienced by fuels when injected into the combustion chamber, conditions around and above the critical point are easier to be achieved. Finally, more recently, the policy of downsizing in small gasoline engines has led to the inclusion of much of the technologies already present in diesel engines, consequently causing an increase of operating pressures and temperatures as well.

The thermodynamic critical point of fuels and oxidizers is likely to be achieved in a large number of internal combustion engines. According to several authors this leads to fast variations of the fluid properties [1] which must be correctly understand and predicted in order to obtain the most efficient design of propulsion and power systems.

Recent studies have pointed in the direction of identifying four different regions around the critical point. When both pressure and temperature are below the critical point, the regime is called subcritical. When temperature is above critical point and the pressure bellow, the fluid behaves like an ideal gas. If only pressure is supercritical the regime can be called transcritical, regime which still raises a lot of questions to researchers since fluids appear to have mixed behaviour. Finally when both pressure and temperature are above the critical point the regime is called supercritical [2].

The present study is focused on the numerical investigation of injection under transcritical and supercritical conditions, a problematic that has been studied experimentally by several authors [3–14] as well as numerically [2, 9–11, 14–30]. As far as today, some conclusions have been reached and validated about the changes in the physical properties of fluids when they are around and above critical conditions. According to Bellan [1], at the critical point mass diffusivity, surface tension, and latent heat become zero. On the other hand, the heat capacity at constant pressure, Cp, the isentropic compressibility, k_s and the thermal conductivity, λ, all become infinite. At supercritical conditions a behavioural change is observed for the jet structure, which evolves from a liquid-gas injection to a gas-gas like injection [8, 10, 13, 31]. However bigger questions appear about fluid behaviour in conditions near critical for which it is still unknown if the fluid presents a behaviour closer to a gas, a liquid or a mix of the two. Also, the transcritical regime still constitutes an unknown in terms of fluid behaviour which deserves further studies.

To model transcritical and supercritical injection conditions a variable density approach, which employs the Favre Averaged Navier-Stokes equations and a $k-\varepsilon$ turbulence model was tested [32]. This approach originally developed for isothermal, incompressible, turbulent, gaseous jets. It was tested to model the injection of cold nitrogen at conditions ranging from transcritical to supercritical regime, into a chamber filled with gaseous nitrogen at supercritical conditions. Flow configuration can be observed in Fig. 1, while the test conditions are described in Table 1. The obtained results showed quite good accuracy of the simulations at supercritical injection conditions, when compared with experimental. However the agreement was worse for transcritical injection conditions. Reasons for this discrepancy with experimental data at transcritical injection conditions could be pointed to the fact that the used model didn't take in consideration the influence of heat transfer between the two fluids and also not including real fluid effect. In order

to address these drawbacks of the previous approach the Favre averaged energy equation was integrated in the existing formulation as well as real fluid equations of state. With these modifications the authors have the expectation to improve the model performance in the modelling of the jet at transcritical conditions as well as to introduce more understanding over the flow of study.

To do so, the same configuration used in previous investigation [32] was employed as well as the same test conditions. The results will be compared with experimental data [8, 9] as well as with other numerical approaches [19, 23].

2. Computational model

In the present work was used a mathematical model and numerical approach based on the model used by Barata et al. [15] and in previous works [29, 30, 32]. However, modifications were made, the Favre averaged energy conservation equation was introduced and the equation of state based of Amagat's law was replaced by real fluid equations of state.

2.1. Governing equations

The method to solve is based on the solution of the conservation equations for momentum and mass. Turbulence is modelled with the "k–ε" turbulence model. A similar method has been used for three-dimensional or axisymmetric flows and only the main features are summarized here.

Table 1. Conditions of the test cases

	Case 3	Case 4
Condition	Transcritical	Supercritical
Chamber Temperature [K]	298	298
Chamber Pressure [MPa]	3.97	3.97
Injection Temperature [K]	126.9	137
Injection Velocity [m/s]	4.9	5.4
ρ_0 [kg/m^3]	435	171
ρ_∞ [kg/m^3]	45.5	45.5
ω	0.1046	0.2661

In the conservation equations, mass weighted averaging is applied to avoid the appearance of many terms involving density fluctuations for which additional models are needed. A mass averaged quantity is defined as

$$\widetilde{\phi} = \frac{\overline{\rho\phi}}{\overline{\rho}} \tag{1}$$

For the governing equations the standard parabolic truncation is employed. The mass averaged continuity equation for the axisymmetric two-dimensional geometry can be written in cylindrical polar coordinates, and is given by

$$\frac{\partial \overline{\rho}.\widetilde{U}}{\partial x} + \frac{1}{r}\frac{\partial r\overline{\rho}.\widetilde{V}}{\partial r} = 0 \tag{2}$$

The momentum equations for axial and radial direction take the form

$$\frac{\partial \overline{\rho}.\widetilde{U}\widetilde{U}}{\partial x} + \frac{1}{r}\frac{\partial r\overline{\rho}.\widetilde{V}\widetilde{U}}{\partial r} = -\frac{\partial \overline{p}}{\partial x} - \frac{1}{r}\frac{\partial r\overline{\rho}.\widetilde{u''v''}}{\partial r} \tag{3}$$

and

$$\frac{\partial \overline{\rho}.\widetilde{U}\widetilde{V}}{\partial x} + \frac{1}{r}\frac{\partial r\overline{\rho}.\widetilde{V}\widetilde{V}}{\partial r} = -\frac{\partial \overline{p}}{\partial r} - \frac{1}{r}\frac{\partial r\overline{\rho}.\widetilde{v''v''}}{\partial r} + \frac{\overline{\rho}.\widetilde{w''w''}}{r} \tag{4}$$

The mixing of different fluids is described by introducing the scalar property of mixture fraction, F, this variable represents the mass fraction of the fluid at the injector. It obeys a convection-diffusion equation of the form

$$\frac{\partial \overline{\rho}.\widetilde{U}\widetilde{F}}{\partial x} + \frac{1}{r}\frac{\partial r\overline{\rho}.\widetilde{V}\widetilde{F}}{\partial r} = -\frac{1}{r}\frac{\partial r\overline{\rho}.\widetilde{v''f''}}{\partial r} \tag{5}$$

In "k–ε" turbulence model, the Reynolds stresses are expressed in terms of the local strain rate:

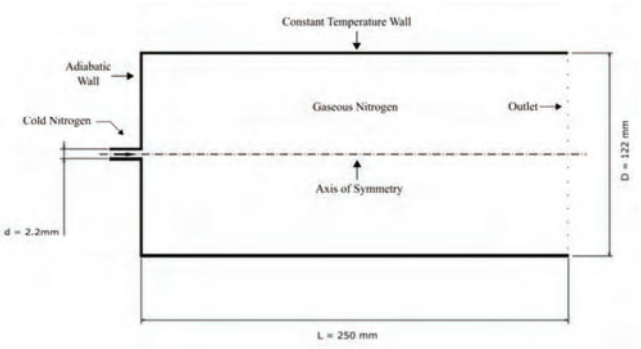

Fig. 1. Chamber geometry

$$-\overline{\rho}\widetilde{u_i''u_j''} = \overline{\rho}(\mu_t + \mu)\left(\frac{\partial \widetilde{u}_i}{\partial x_j} + \frac{\partial \widetilde{u}_j}{\partial x_i}\right) - \frac{2}{3}\delta_{ij}\left[\overline{\rho}\widetilde{k} + \overline{\rho}(\mu_t + \mu)\frac{\partial \widetilde{u_k}}{\partial x_k}\right] \tag{6}$$

with

$$\mu_t = C_\mu \frac{k^2}{\varepsilon} \tag{7}$$

The scalar flux in equation (5) is approximated with a gradient transport assumption

$$-\overline{\rho}\widetilde{u_i''f''} = -\frac{\mu_f}{\sigma_f}\frac{\partial \overline{F}}{\partial x_i} \tag{8}$$

From the foregoing we can deduced the parabolized set of equations in cylindrical coordinates where the generalized equation is

$$\frac{\partial}{\partial x}\left(\overline{\rho}.\widetilde{U}\widetilde{\phi}\right) + \frac{1}{r}\frac{\partial}{\partial r}\left(r\overline{\rho}.\widetilde{V}\widetilde{\phi}\right) = -\frac{1}{r}\frac{\partial}{\partial r}\left(r\overline{\rho}\Gamma\frac{\partial \widetilde{\phi}}{\partial r}\right) + S_\phi \tag{9}$$

where $\widetilde{\phi}$ may stand for any of the velocities, turbulent kinetic energy, dissipation, or scalar property, and S_ϕ take on different values for each particular $\widetilde{\phi}$ [33].

The previous works [29, 30, 32] didn't include in its formulation the conservation equation of energy. For the present investigation it had to be deduced and then integrated in the computational code. The Favre averaged energy equation for a steady flow in its vectorial form is represented by

$$\frac{\partial}{\partial x_j}\left(\overline{\rho}\widetilde{u}_j c_p \widetilde{T}\right) = -\frac{\partial}{\partial x_j}\left(c_p \frac{\mu}{Pr}\frac{\partial \widetilde{T}}{\partial x_j}\right) - \frac{\partial}{\partial x_j}\left[\underbrace{c_p\overline{\rho u_j'' T''}}_{(1)} + \frac{\overline{\rho}\widetilde{u}_j\widetilde{u}_k\widetilde{u}_k}{2} + \overline{\rho}\widetilde{u}_j\widetilde{k} + \underbrace{\widetilde{u}_k\overline{\rho u_j'' u_k''}}_{(2)} + \underbrace{\frac{\overline{\rho u_j'' u_k'' u_k''}}{2}}_{(3)} + \underbrace{c_p\frac{\mu}{Pr}\frac{\partial T''}{\partial x_j}}_{(4)} - \widetilde{u}_i\widetilde{\tau}_{ij} - \underbrace{\overline{u_i''\tau_{ij}}}_{(5)} + \underbrace{\widetilde{u}_i\overline{\tau_{ij}}''}_{(6)}\right] \tag{10}$$

The Favre averaged energy equation brings with it a large number of source terms, some of them can be solved directly, others, which are numbered, must be modelled.

Term (1), corresponding to turbulent transport of heat, can be modelled using a gradient approximation for the turbulent heat-flux:

$$c_p\overline{\rho u_j'' T''} \approx -c_p\frac{\mu_t}{Pr_t}\frac{\partial \widetilde{T}}{\partial x_j} \tag{11}$$

Term (2) is obtained from the turbulent-viscosity hypothesis expressed in equation (6)

$$\overline{\rho u_i'' u_j''} \approx \frac{2}{3}\rho\tilde{k}\delta_{ij} - \mu_t\left(\frac{\partial \widetilde{u}_i}{\partial x_j} + \frac{\partial \widetilde{u}_j}{\partial x_i} - \frac{2}{3}\frac{\partial \widetilde{u}_k}{\partial x_k}\delta_{ij}\right) \tag{12}$$

Terms (3) and (5), corresponding to turbulent transport and molecular diffusion of turbulent energy, can be neglected if the turbulent energy is small compared to the enthalpy, $k \ll \tilde{h}$. This is a reasonable approximation for most flows below the hyper-sonic regime. A better approximation might be a gradient expression of the form:

$$\frac{\overline{\rho u_j'' u_k'' u_k''}}{2} - \overline{u_i''\tau_{ij}} \approx -\left(\mu + \frac{\mu_t}{\sigma_k}\right)\frac{\partial k}{\partial x_k} \tag{13}$$

Term (4) is an artefact from the Favre averaging. It is related to heat conduction effects associated with temperature fluctuations. It can be neglected if $\left|\frac{\partial^2 \widetilde{T}}{\partial x_j^2}\right| \gg \left|\frac{\partial^2 \overline{T''}}{\partial x_j^2}\right|$, which is also true for virtually all flows.

And finally term (6) can also be neglected if $\left|\widetilde{\tau_{ij}}\right| \gg \left|\overline{\tau_{ij}''}\right|$, which is true to virtually all flows. The energy equation could also be put in the form of the general equation (9), it is not done here due to the fact of becoming a very long expression.

2.2. Real fluid equation of state

To obtain the mean density field an equation of state is employed. For many applications the ideal gas equation of state is the most common choice. However, as explained previously, the conditions of study of the present investigation escape the range of applicability of the concept of ideal gas. For this reason a real fluid equation of state seems to be a more convenient choice.

In the present investigation two different real fluid equations of state were analysed and employed in the numerical approach, the Soave-Redlich-Kwong and the Pend-Robinson equations of state.

The Soave-Redlich-Kwong equation can be expressed as

$$P = \frac{RT}{(V_m - b)} - \frac{a(T)}{V_m(V_m + b)} \tag{14}$$

where the coefficients a and b are described in detail in Soave [34].

The Peng-Robinson equation of state can be written as

$$P = \frac{RT}{(V_m - b)} - \frac{a(T)}{V_m(V_m + b) + b(V_m - b)} \tag{15}$$

once again the detailed formulation of coefficients a and b can be found in Peng and Robinson's work [35].

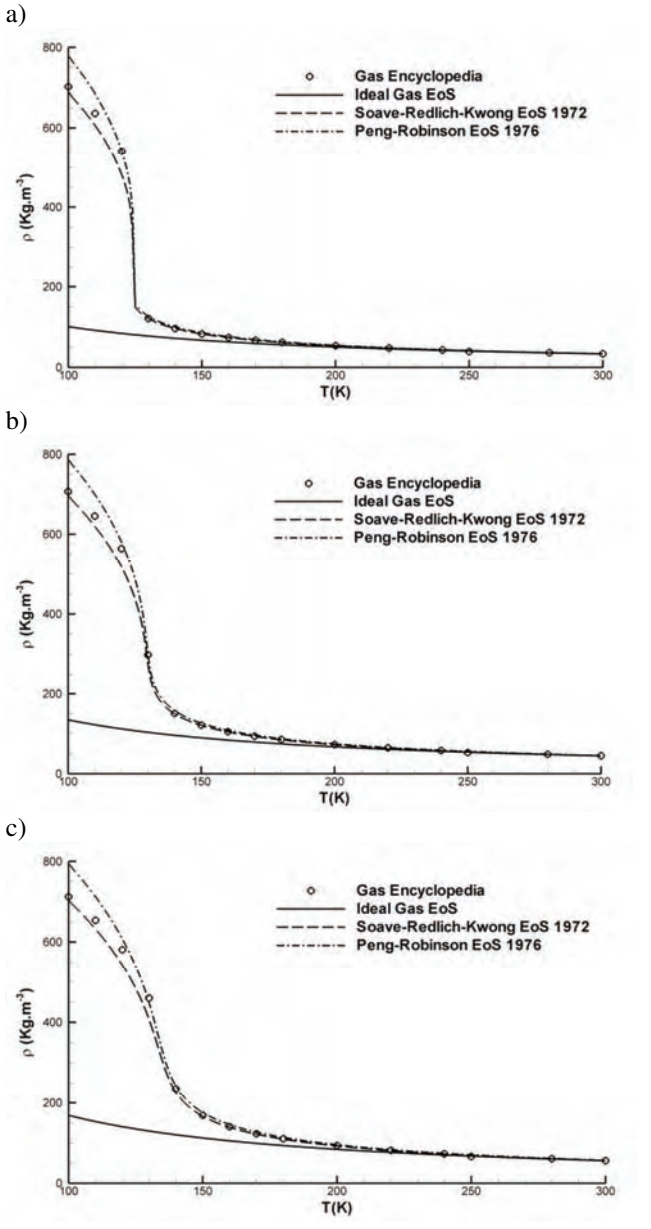

Fig. 2. Comparison of different equations of state at: a) 3 MPa; b) 4 MPa; c) 5 MPa

The performance of both equations of state was investigated in the present investigation. Fig. 2 shows the comparison, for three different pressures and under temperatures ranging from 100 K to 300 K, between the two real fluid equations of state and the data from gas encyclopaedia [36], having also as reference the performance of the ideal gas equation of state.

Results express very clearly the advantage that the two real fluid equations of state have over the ideal gas equation of state. What doesn't become so clear is which real fluid equation of state performs better. Thus, both equations of state were implemented into the computational approach in order to evaluate their performance in the modelling of the flow of interest.

In previous work [30, 32], fluid properties such as molecular viscosity, specific heat at constant pressure, and thermal conductivity had been assumed as constant. However, this was not the case for the present investigation. Experimental data from Gas Encyclopaedia [36] was used to generate linear functions which provide the value of such properties for different temperatures and pressures.

2.3. Numerical method

The governing equations are solved using a parabolized marching algorithm which resembles the (elliptic) TEACH code, and are described in detail in [33]. This approach was applied to variable density jets and then extended to the study of liquid cryogenic jets under sub-near critical pressures, and sub to supercritical temperatures in the present work.

2.4. Computational grid

An expansive grid in both directions was used, making it more refined when close to injector. In the axial direction a constant expansion rate is impose, as well as the domain length, due to this, the initial grid size is calculated by the grid construction routine. The determination of points in the radial direction is somewhat more complex. For the width of the injector, a fixed amount of points was set, which stablishes a constant distance between nodes. Outside of the injector radial size, the grid routine determines the expansion rate in order to fit the remaining points into the radial domain of the configuration. The grid has a size of 150 by 65 points, and for the injector 13 points are set in the radial direction. The rate of expansion in the axial direction is set as 2%.

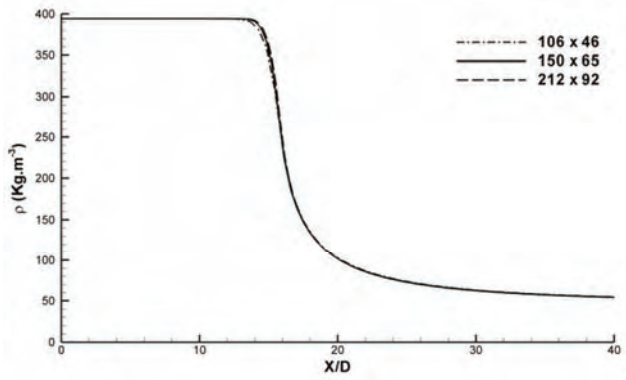

Fig. 3. Grid size dependency test based on the axial density distribution

In order to evaluate the influence of the grid on the converged solution grid dependency tests had to be performed. Figure 3 shows the grid dependency test, the used grid, of 150x65 points is compared with a more refined grid of 212x92 points and with a coarser grid of 106x46 points. The results used for comparison are the axial density variation in the centreline and its visible the independence of the solution from the grid size.

3. Results and discussion

Numerical results obtained in the present work are presented in this section and compared with the experimental data of Mayer et al. [9], the large eddy simulations of Schmitt et al. [19] and of Jarczyk and Pfitzner [23], and also with the results obtained using the unmodified approach [30, 32]. A discussion is also provided in order to reach the conclusions exposed in the next section.

Fig. 4 and 5 show the density field and streamlines for respectively the transcritical case and the supercritical case, in both figures image a) shows the results obtained while employing the Soave-Redlich-Kwong equation of state while image b) expresses the results achieved with the Peng-Robinson equation. Analysing Fig. 5 the most evident conclusion that can be taken is the appearance of a recirculation downstream of the injector, it is also evident the existence of entrainment of the chamber fluid into the injection fluid right after the injector. This jet structure is not affected by the choice of equation of state, both Fig.5 a) and b) show exactly the same jet structure. Comparing the results from both equations of state can be concluded that the Peng-Robinson equations produces higher values of density at the inlet, this is a result which could be anticipated by the results obtained in Fig. 2. It is also visible a longer potential core and deeper penetration of the jet into the chamber in the model with uses the PR equation. This can possibly be explained by the fact that the higher density at inlet causes a larger momentum, since velocity is the same, and this larger momentum takes longer to be dissipated. The supercritical case is represented in Fig. 6. A very similar jet structure is observed for this case when compared with transcritical injection conditions. There's also the appearance of entrainment close to the injector, and, further downstream, the existence of a recirculation. Comparing with Fig. 5 the potential core length and jet penetration is shorter for both equations of state. Like in the transcritical case also the Peng-Robinson equations of state produces higher values of density in the inlets which leads to a longer potential core.

Fig. 6 and 7 represent in better detail the evolution of density in the centreline of the jet. In Fig. 6 the axial density distribution for the transcritical case is shown for the current approach with both equations of state, these results are here compared with the experimental results from Mayer et al. [9] as well as with the results obtained with the previous approach, which obtained density from Amagat's law, and with two large eddy simulations of Schmitt et al. [19] and of Jarczyk and Pfitzner [23]. Both results of the different equations of state for the current approach show a much larger potential core than the one observed in the results of the other authors. With the Soave-Redlich-Kwong equation of state is obtained a potential core of 15.7 injector diameters, as for the Peng-Robinson equation a potential core of 16.4 injector diameters is obtained. For the same case Schmitt et al. reaches a potential core of 7.9 diameters while

Jarczyk and Pfitzner achieves a potential core with a length of around 9 diameters. These values of potential core length are also longer than the potential core of 11.8 obtained by the initial approach with Amagat's law. Further downstream the current approach keeps the difficulty in fitting the experimental data or the other LES investigations.

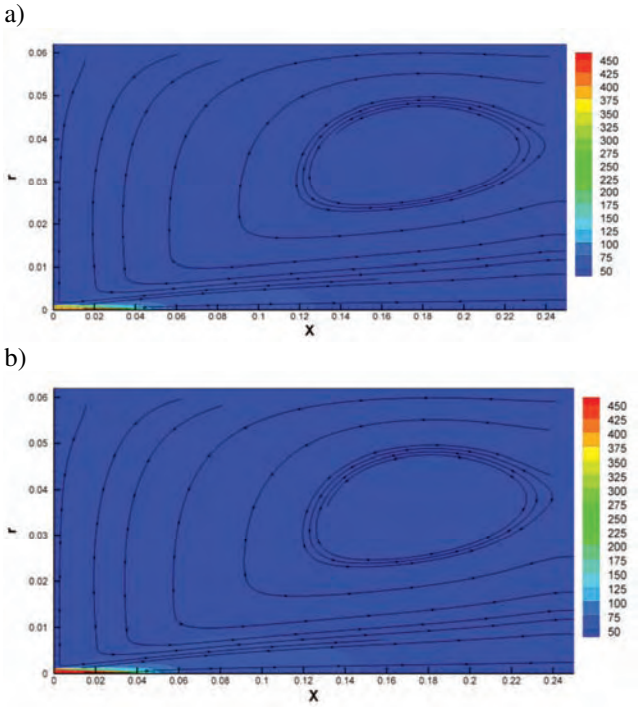

Fig. 4. Density field and streamlines for transcritical case, a) SRK EoS, b) PR EoS

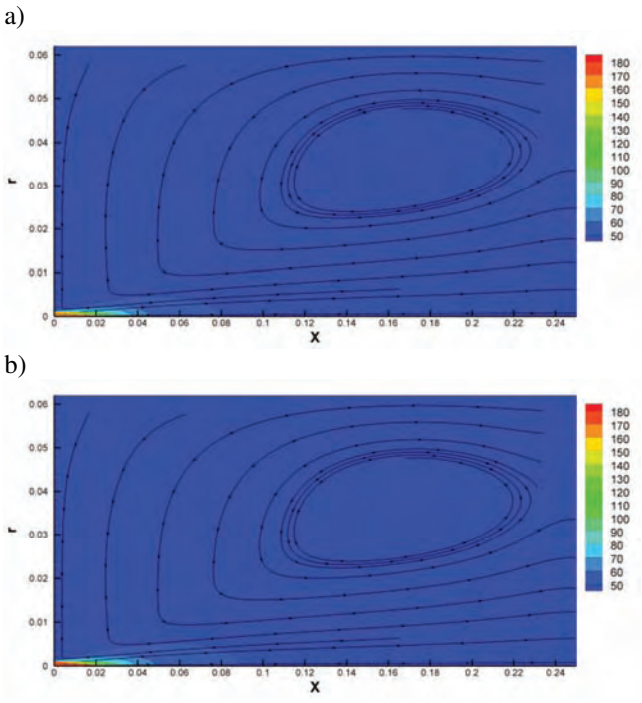

Fig. 5. Density field and streamlines for supercritical case, a) SRK EoS, b) PR EoS

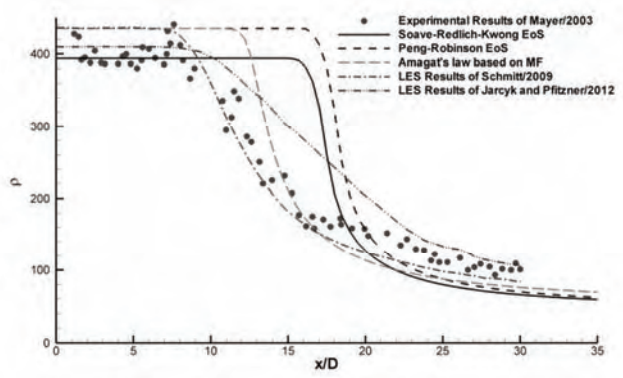

Fig. 6. Axial density distribution for transcritical case

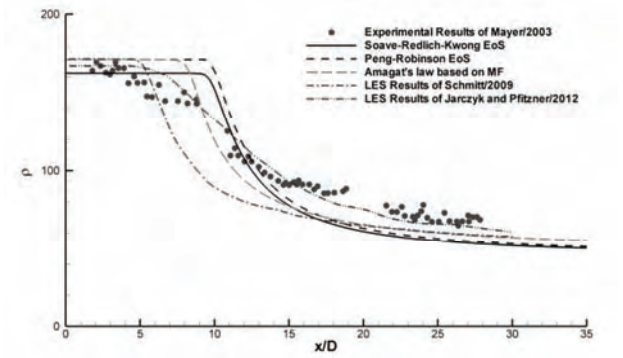

Fig. 7. Axial density distribution for supercritical case

The axial density distribution for the supercritical case is represented in Fig. 7. Again, the current approach employing the two different equations of state is compared with experimental and LES data as well as with the results obtained by the previous approach [30]. For the supercritical case a closer agreement with experimental data is obtained but the over prediction of the potential core length still exists. When using the Soave-Redlich-Kwong equation a potential core with a length of 9.4 injector diameters is observed, with the Peng-Robinson equation it increases to a length of 9.6 injector diameters. For the same test case the previous approach achieved a potential core length of 7.8 diameters, Schmitt et al. reached 5.1 while Jarczyk and Pfitzner predicted a potential core with a length of 6.0 injector diameters, it's important to refers that when analyzing the experimental results for this case the existence of a potential core is not evident. Downstream of the potential core is obtained a better agreement with experiments between 10 and 15 diameters but then there is a departure from the data provided by Mayer [9]. Still, for this condition, the LES from Schmitt et al. [19] is not able to provide superior agreement, while the previous approach provides a closer agreement. For this case is the large eddy simulation of Jarczyk and Pfitzner which provides the closest agreement.

The full width of half maximum of density is expressed for the transcritical and supercritical test cases respectively in Figures 8 and 9. In figure 8 are represented the values obtained by the previous and current approach as well as the experimental data provided by Mayer et al. [9]. Analyzing first the data from Mayer, it can be seen that initially the jet appears to have a radius of twice the radius of injector,

this is explained in the paper of Mayer [9] by the difficulty of the technique of Raman Scattering to provide accurate values of density when the values are high. There's then a decrease of the jet thickness until 10 x/D followed then by the expected expansion of the jet width. Similar evolution is observed by all the approaches presented in the present paper. However, when using the real fluid equations of state the potential core is longer thus delaying the expansion of the jet. In figure 12 only the results obtained by previous and current approach are exhibit since Mayer didn't provide results for this case. Nevertheless, the evolution of the full with of half maximum of density follows the same shape obtained for the transcritical case, with the previous approach showing wider expansion of jet.

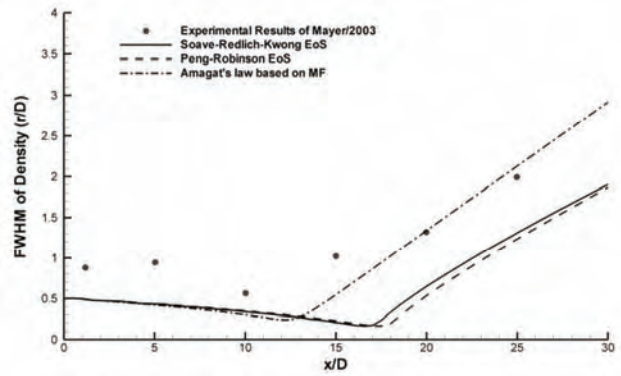

Fig. 8. Axial density distribution for transcritical case

From the results of the full width of half maximum of density, it can be obtained the tangent by linear interpolation which represents the jet expansion rate. The linear interpolation was performed by other authors between x/D = 15 and x/D = 25. In the present work these were generally the points chosen for the calculation, however as it is visible, for the current approach at transcritical conditions, the jet expansion starts only after x/D = 15, thus, for this situation the interpolation was performed between x/D = 20 and x/D = 30. These results are expressed in Table 2.

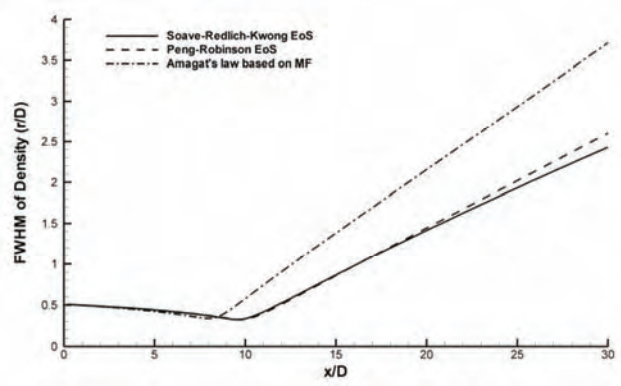

Fig. 9. Axial density distribution for supercritical case

For the transcritical case the experimental data of Mayer et al. [9] reached to a spreading rate of 0.196, a similar spreading rate was obtained by the experimental work of Oschwald and Micci [8]. The original approach used in the present investigation, for the same case predicted a spreading rate of 0.316 which is an over prediction of around 61% when compared with the data of Mayer. By the introduction of a real fluid equation of state a closer agreement for the spreading rate was reached, with values of 0.250 for the SRK equation and 0.266 with the PR equation of state, representing respectively a variation of 27.6% and 35.7% when compared with Mayer's work. The large eddy simulation of Schmitt et al. provides a spreading rate of 0.227 which is still closer to experimental data.

Table 2. Results of jet spreading rate

Case	First Approach Amagat's law	Current Approach		Mayer et al. 2003 [9]	Schmitt et al. 2009 [19]	Oschwald and Micci 2002 [8]
		SRK	PR			
Trans-critical	0.316	0.250	0.266	0.196	0.227	0.206
Super-critical	0.310	0.214	0.234	–	0.241	0.312

For the supercritical case Mayer et al. didn't provide results of the FWHM of Density thus not allowing the comparison of jet spreading angle. On the other hand Oschwald and Micci [8] as well as Schmitt et al. [19] did provide results allowing a comparison to be established. The results obtained from the first approach which makes use of Amagat's law replicate almost perfectly the jet spreading rate obtained by Oschwald and Micci [8]. Achieving a much better result that any of other predictions. The large eddy simulation of Schmitt et al. [19] provides an acceptable results as well, closely followed by the second approach when employing the Peng-Robinson equation of state and finally the furthest agreement comes from the second approach when employing the SRK equation of state.

4. Conclusions

With the objective of testing and developing new methodologies to model jets at conditions around the critical point, a methodology originally developed for the study of turbulent, variable density, isothermal jets was modified to include the effects of heat transfer and a real fluid equation of state. The effects of the variation of physical properties of fluid such as thermal conductivity, specific heat at costant pressure and molecular viscosity experienced with the variation of pressure and temperature were also included. To do so, in the present approach were introduced linear functions taken from the data provided by the Gas Encyclopaedia [36].

The original approach had already along this investigation proved his potential for the study of this kind of fluids, despite its simplicity and inexpensive computational requirements. It proved to provide good agreement with experimental data for supercritical injection conditions outperforming much more expensive large eddy simulations. However, it starts facing difficulties when dealing with flows in subcritical and transcritical conditions. By not accommodating the heat transfer and real fluid thermodynamics it fails to predict the correct behaviour of fluids in the transition to the two phase flow. The new approach intends overcome these lacks by the introduction of the Favre averaged energy equation and a real fluid equation of

state in the form of a Soave-Redlich-Kwong and a Peng-Robinson equations of state.

This new modified approach was able to improve the spreading angle results over the original approach under transcritical regime of injection, reaching a much closer agreement. The performance of the agreement at supercritical conditions unfortunately suffered a decrease.

Two different reasons could be pointed out to the decrease of accuracy at supercritical conditions. On one hand the data provided in Gas Encyclopaedia doesn't contain values of the properties in the critical point. The critical point represents a thermodynamic singularity, thus, the properties values at this point suffer a very pronounced variation which is not accessed by the present approach. On the other hand, the flow appears to be governed by the turbulent characteristics. The ratio between turbulent viscosity and turbulent thermal diffusivity is prone to suffer variations along the flow. Thus, the employment of a constant turbulent Prandtl number, Pr_t, may in fact not be the most efficient option. Future work will address these two points, expecting to obtain increased performance.

Acknowledgments

The present work has been performed under the scope of the activities of Aeronautics and Astronautics Research Center of the Associated Laboratory in Energy Transports and Aeronautics (AeroG-LAETA), UID/EMS/50022/2013.

The first authors would like to thanks to the Fundação para a Ciência e a Tecnologia (FCT), the Portuguese public agency for science and technology for the PhD scholarship SFRH/BD/87822/2012.

Nomenclature

a, b	real fluid equation of state coefficients
c_p	specific heat at constant pressure
C_μ	coefficient in turbulence model
D	injector diameter [m]
ε	dissipation rate of turbulent energy
f	mixture fraction
F	mean mixture fraction
i	axial direction index
j	radial direction index
k	turbulent kinetic energy
μ	molecular viscosity
μ_t	turbulent viscosity
ϕ	generalized variable
ω	chamber-to-injected fluid density ratio
P_{cr}	critical pressure [MPa]
P_∞	chamber ambient pressure [MPa]
P_r	reduced presure (P_∞/P_{cr})
Pr	Prandtl number
Pr_t	turbulent Prandtl number
ρ	density [kgm^{-3}]
ρ_0	injected fluid density [kgm^{-3}]
ρ_∞	injection chamber's fluid density [kgm^{-3}]
r	radial coordinate [m]
R	universal constant of gases
R/D	radial distance normalized by injector diameter
R_{diam}	injector radius [m]
R_e	Reynolds number
S_ϕ	source term
t	time [s]
T	temperature [K]
u	axial velocity [ms^{-1}]
U	mean axial velocity [ms^{-1}]
U_{in}	injection axial velocity [ms^{-1}]
v	radial velocity [ms^{-1}]
v_t	turbulent kinematic viscosity
V	mean radial velocity [ms^{-1}]
V_m	molar volume
X	axial coordinate [m]
x/D	axial distance normalized by injector diameter

Bibliography

[1] BELLAN, J. Supercritical (and subcritical) fluid behavior and modeling: drops, streams, shear and mixing layers, jets and sprays. *Prog. Energy Combust. Sci*. 2000, **26**, 329-366.

[2] LACAZE, G., OEFELEIN, J.C. A non-premixed combustion model based on flame structure analysis at supercritical pressures. *Combust. Flame*. 2012, 159, 2087-2103.

[3] NEWMAN, J.A., BRZUSTOWSKI T.A. Behavior of a liquid jet near the thermodynamic critical region. *AIAA J.* 1971, **9**, 1595-1602.

[4] MAYER, W.O.H. et al. Atomization and breakup of cryogenic propellants under high-pressure subcritical and supercritical conditions. *J. Propuls. Power*. 1998, **14**(5), 835-842.

[5] OSCHWALD, M., SCHIK, A. Supercritical nitrogen free jet investigated by spontaneous Raman scattering. *Exp. Fluids*. 1999, **27**, 497-506.

[6] CHEHROUDI, B., COHN, R., TALLEY, D. Gas behaviour of cryogenic fluids under sub- and supercritical conditions. Eighth International Conference on Liquid Atomization & Sprays Systems. *ICLASS-2000*, 2000.

[7] CHEHROUDI, B., COHN, R., TALLEY, D. Spray/gas behaviour of cryogenic fluids under sub- and supercritical conditions. Eighth International Conference on Liquid Atomization & Sprays Systems. *ICLASS-2000*, 2000.

[8] OSCHWALD, M., MICCI, M.M. Spreading angle and centerline variation of density of supercritical nitrogen jets. *Sprays*. 2002, **12**(1-3), 91-106.

[9] MAYER, W., TELAAR, J., BRANAM, R. et al. Raman measurements of cryogenic injection at supercritical pressure. *Heat Mass Transf.* 2003, **39**, 709-719.

[10] OSCHWALD, M. et al. Injection of fluids into supercritical environments. *Combust. Sci. Technol*. 2006, **178**, 908038079, 49-100.

[11] STAR A.M., EDWARDS J.R., LIN K.-C. et al. Numerical simulation of injection of supercritical ethylene into nitrogen. *J. Propuls. Power*. 2006, **22**(4), 809-819.

[12] MARTÍNEZ-MARTÍNEZ, S., SÁNCHEZ-CRUZ, F.A., RIESCO-ÁVILA, J.M. et al. Liquid penetration length in direct diesel fuel injection. *Appl. Therm. Eng*. 2008, 28, 1756-1762.

[13] SEGAL, C., POLIKHOV, S.A. Subcritical to supercritical mixing. *Phys. Fluids*. 2008, 20, 1-7.
[14] SCHMITT, T., RODRIGUEZ, J., LEYVA, I.A., CANDEL, S. Experiments and numerical simulation of mixing under supercritical conditions. *Phys. Fluids*. 2012, **24**.
[15] BARATA, J.M.M., SILVA, A.R.R., GOKALP, I. Numerical study of cryogenic jets under supercritical conditions. *Journal of Propulsion and Power*. 2003, **19**, 142-147.
[16] ZONG, N., MENG, H., HSIEH, S.Y., YANG, V. A numerical study of cryogenic fluid injection and mixing under supercritical conditions. *Phys. Fluids*. 2004, **16**, 4248-4261.
[17] ZONG, N., YANG, V. Cryogenic fluid jets and mixing layers in transcritical and supercritical environments. Combust. Sci. Technol. 2006, 178, 908038079, 193-227.
[18] AOUISSI, M., BOUNIF, A., BENSAYAH, K. Scalar turbulence model investigation with variable turbulent Prandtl number in heated jets and diffusion flames. Heat Mass Transf. und Stoffuebertragung. 2008, 44, 9, 1065–1077.
[19] SCHMITT, T., SELLE, L., CUENOT, B., POINSOT, T. Large-eddy simulation of transcritical flows. *Comptes Rendus - Mec*. 2009, **337**(6-7), 528-538.
[20] KIM, T., KIM, Y., KIM, S.K. Numerical study of cryogenic liquid nitrogen jets at supercritical pressures. *J. Supercrit. Fluids*. 2011, **56**(2), 152-163.
[21] ZHOU, L., XIE, M.-Z., JIA, M., SHI, J.-R. Large eddy simulation of fuel injection and mixing process in a diesel engine. *Acta Mech. Sin*. 2011, **27**, 519-530.
[22] NEGRO, S., BIANCHI, G.M. Superheated fuel injection modeling: An engineering approach. *Int. J. Therm. Sci.* 2011, 50(8), 1460-1471.
[23] JARCZYK, M., PFITZNER, M. Large eddy simulation of supercritical nitrogen jets. *50th AIAA Aerospace Sciences Meeting Including the New Horizons Forum and Aerospace Exposition*. 2012, **1**, 1-13.
[24] TERASHIMA, H., KOSHI, M. Approach for simulating gas-liquid-like flows under supercritical pressures using a high-order central differencing scheme. *J. Comput. Phys*. 2012, **231**(20), 6907-6923.
[25] TERASHIMA, H., KOSHI, M. Strategy for simulating supercritical cryogenic jets using high-order schemes. *Comput. Fluids*. 2013, **85**, 39-46.
[26] PARK, T.S. LES and RANS simulations of cryogenic liquid nitrogen jets. *J. Supercrit. Fluids*. 2012, 72, 232-247.
[27] Schuler, M.J., Rothenfluh, T., Von Rohr, P.R. Simulation of the thermal field of submerged supercritical water jets at near-critical pressures. *J. Supercrit. Fluids*. 2013, **75**, 128-137.
[28] PETIT, X., RIBERT, G., LARTIGUE, G., DOMINGO, P. Large-eddy simulation of supercritical fluid injection. *J. Supercrit. Fluids*. 2013, **84**, 61-73.
[29] ANTUNES, E., SILVA, A.R.R., BARATA, J.M.M. Evaluation of numerical variable density approach to cryogenic jets. *50th AIAA Aerospace Sciences Meeting Including the New Horizons Forum and Aerospace Exposition*. 2012, **1**, 1-14.
[30] ANTUNES, E., SILVA, A., BARATA, J. RANS modeling of transcritical and supercritical nitrogen jets. *53rd AIAA Aerospace Sciences Meeting*. 2015, **1**, 1-14.
[31] CHEHROUDI, B., COHN, R., TALLEY, D. Cryogenic shear layers: Experiments and phenomenological modeling of the initial growth rate under subcritical and supercritical conditions. *Int. J. Heat Fluid Flow*. 2002, **23**, 554-563.
[32] ANTUNES E., SILVA A., BARATA J. Variable density approach for modeling of transcritical and supercritical jets. *J. Eng. Appl. Sci.* 2017.
[33] SANDERS, J.P.H., SARH, B., GÖKALP, I. Variable density effects in axisymmetric isothermal turbulent jets: a comparison between a first- and a second-order turbulence model. *Int. J. Heat Mass Transf.* 1997, **40**, 823-842.
[34] SOAVE, G. Equilibrium constants from a modified Redlich-Kwong equation of state. *Chem. Eng. Sci*. 1972, **27**(6), 1197-1203.
[35] PENG, D.-Y., ROBINSON, D.B. A new two-constant equation. *Ind. Eng. Chem. Fundam*. 1976, **15**(1), 59-64.
[36] MEDARD L. Gas encyclopaedia, 1st ed. Amsterdam: *Elsevier Science*, 1976.

Eduardo Antunes, MEng. – Aeronautical Engineering at University of Beira Interior.

e-mail: *EduardoFariasAntunes@hotmail.com*

Prof. Jorge Barata, Habilitation – Aerospace Science Department at University of Beira Interior.

e-mail: *JBarata@ubi.pt*

André Silva, PhD. – Aerospace Science Department at University of Beira Interior.

e-mail: *Andre@ubi.pt*

Article citation info:
KRAKOWSKI, R. Modelling the impact of microbial contamination of fuel filtration efficiency. *Combustion Engines*. 2017, **169**(2), 133-136. DOI: 10.19206/CE-2017-223

Rafał KRAKOWSKI

CE-2017-223

Modelling the impact of microbial contamination of fuel filtration efficiency

In this paper the concept of filtration and the problem of microbial contamination occurring in the fuels and oils was presented. Then the factors influencing the growth of bacteria in petroleum products were described in detail. In the next part of the article modeling of the impact of fuel microbial contamination on filtration efficiency was performed. The modeling presented in the article is an example showing how undesirable phenomenon is the microbial contamination and how pollution affects the other elements of the entire system. As part of the modeling, numerical model of filtration with the solution was presented. Then analysis results on the basis of the impurities concentration characteristics in the fuel as a function of the fouling thickness in the partition of the filter is performed. The development of impurities was divided into three stages. In the article for one case the trend line was presented. The article was completed conclusions.

Key words: *modeling, filtration, microorganisms, petroleum products, fuel system, oil system*

1. Introduction

Filtration of diesel or lubricating oil consists in the separation of suspended particles, i.e. impurities, through the filter surface from a flow of diesel or lubricating oil. These impurities can be of very different sizes, and therefore the purification process itself is most often a complex process utilizing various physical phenomena. Physical phenomena that are most commonly used in filtration processes include: diffusion, barrier, sieve and electrostatic effects. However, in the filtering process may be involved, inter alia, gravitation, inertia, centrifugal and electrostatic interaction [5].

In the operation of internal combustion engines, the continuous filtration process, both diesel and lubricant, is extremely important. This is due to the fact that even in a properly operated piston engine, various types of pollution arise due to the deterioration of its technical condition. The deterioration of this condition is primarily due to all kinds of mechanical and chemical pollution. Out of all the various pollutants which different ways from the outside get into the engine and subassemblies of its equipment Various contaminants from different directions come from outside to the engine and subassemblies of its accessories or are formed inside the cylinders. The most harmful are the impurities contained in the fuel and the engine oil that is circulating in the engine lubrication circuit. Contamination of fuels and lubricating oils are all solid particles, water and dissolved chemicals (e.g. sulfur) that cause corrosion or undesired components (e.g. organic substances with high viscosity or gelatin content, etc.). The most harmful pollutants are mechanical impurities, and therefore mostly fine and hard particles of mineral substances of different graininess. Such impurities are partly a natural remnant of petrochemical processes, and partly pass to fuels and oils during distribution (transport, storage and transfer). The harmfulness of mechanical impurities in petroleum products results mainly from their hardness and compression resistance. Theoretically, all solids are classified as harmful, which in any way can mechanically affect for parts rinsed by fuel or exhaust [10].

Highly undesirable impurities of the diesel engine fuel are even small amounts of water that easily penetrates to the tank from the environment – most often in the form of water vapor, condensing on their walls due to lowering of temperature. Water due to much higher specific gravity, compared to diesel, collects in the lowest places inside pipelines and subassemblies of the fuel system. It often seriously interferes with their operation. As the ambient temperature drops even slightly below 0°C, the water in the fuel easily freezes. It then transforms into fine ice needles, which blinding the passageways and passages of fuel system components interferes with the power supply of the engine, and often precludes its operation [5, 11].

2. The problem of microbial contamination

In petroleum products is a major problem microbial contamination, which includes both fuel for automobiles, aviation, and marine, motor and transformer oils and lubricants and oil emulsions. As the industry and automotive industry expanded, including aviation and ships, the problem of microbial contamination has been found to be still current and becoming more widespread. Research has shown that living organisms of microorganisms can lead to work disruption and even damage to car engines, aircraft or ships [1, 4].

The increase in microbial contamination of fuels and oils can be caused by a number of factors, including: changes in fuel sources and their quality, increased use of fuel additives that can provide compounds for microbial growth, and changes in fuel management and storage. The presence of microorganisms in the system can cause:

- production of corrosive compounds, causing the destruction of tanks, and thus an increase in the amount of mechanical impurities,
- adverse changes in physicochemical properties due to decomposition of hydrocarbons and additives, resulting in a decrease in chemical and thermal stability,
- production of surfactants,
- formation of sediment and biological membranes on the walls of tanks and ducts that contaminate the product after detaching from the substrate,
- clogging of filters and wires during operation.

Fuel of good quality must be clear and transparent. Growth of microorganisms can often contribute to its cloudiness and darkening. The most obvious and easy to

understand consequence of microbial activity is the formation of sediments visible as solids, which are a mixture of living and dead cells and inorganic by-products [2, 8].

3. The impact of microbial contamination of fuel filtration efficiency

3.1. Concept of modeling

One of the methods of testing the dynamic properties of a system is to conduct an experiment directly on the system. In many cases, it is impossible to perform an experiment on a system, for technological reasons, or for the cost of an experiment. An important factor is the duration of the tests, which can be very long and take several years (for example, in the fatigue test) or very short, on the order of fractions of seconds (transients in electrical systems). It is difficult to record the courses of a individual values [6].

Another approach to the problem of testing properties of the system is to build a system model and testing the model. A system model is a representation of a system using mathematical relationships (abstract form of a system) or in a physical form (a layout model) that depicts, usually with some simplification, the properties of the system.

Mathematical model (abstract) is a collection of mathematical relations, based on which one can predict the behavior of a system. The mathematical model of the continuous system is usually the differential equation describing the operation of the system. Mathematical models are most often implemented by means of digital machines and electronic analogue machines. The main advantage of digital modeling is the ability to save the model and its parameters in the program form. This makes it possible to perform model tests flexibly.

Mathematical modeling provides the ability to quickly and accurately investigate courses in the most complex systems, with different combinations of parameters and with different kinds of extortion. One of the basic aims of modeling is to use a model in an adaptive system, which allows to select the structure and parameters of this model most similar to the behavior of the real system. The basic element of programming a digital machine (mathematical modeling) is to create an operational schema of the studied system. Because the operation of the continuous system is most often described by differential equations, the modeling of the system consists in creating an operating scheme for the differential equation or system of equations. The presented system is investigated by means of a process simulation method, using various methods for solving differential equations [9].

In the article, modeling the influence of pollutants on the efficiency of filtration using a numerical algorithm was presented.

3.2. Mathematical numerical filtration

In the process of filtering contaminants balance equation connects the change dynamics in the degree of contaminants in the fluid filtered with the change dynamics in the concentration contaminants accumulated in the porous baffle. On the basis of change in concentration of contaminants in the filtered liquid conducted to the desired depth baffle can be estimated concentration change deposits accumulated in the baffle of the filter at that depth. The concentration of the contaminants in the filtered liquid is expressed as a weight by volume. The mass balance equation, in the case of constant speed in a cross-section of the filtrating barrier and the one-dimensional flow, has the following form:

$$\frac{\partial\sigma(t,d)}{\partial t}+\varepsilon_o\frac{\partial C(t,d)}{\partial t}+v\frac{\partial C(t,d)}{\partial d}=D\frac{\partial^2 C(t,d)}{\partial d^2} \tag{1}$$

where: $\sigma(t,d)$ – mass concentration of impurities in the filter baffle at time "t"at a depth "d" g/m^3; C(t, d) – concentration of impurities in the liquid at time "t"at a depth "d" g/m^3, ε_o – porosity of the barrier filter, D – dispersion coefficients, m^2/s.

Assuming that the second component of equation (1) equals zero and ignoring dispersion the simplest form of mass balance equations is obtained [3]:

$$v\left(\frac{\partial C(t,d)}{\partial d}\right)+\left(\frac{\partial\sigma(t,d)}{\partial t}\right)=0 \tag{2}$$

The kinetic of the filtration process can be described in different ways. The simplest way to describe the kinetic of removal of contaminants from the filtered fluid as it passes through the barrier using the concept of filtration coefficient, determining the effectiveness of contaminant removal. One of the forms the kinetic equation is the change in the concentration of impurities in the filtered liquid per unit depth of the baffle proportional to the concentration. Kinetic equation is as follows:

$$a\frac{\partial C(t,d)}{\partial d}=-\lambda C(t,d) \tag{3}$$

where: λ – filtration coefficient, 1/m.

Filtration coefficient is a measure of the efficiency of the filter and is dependent on parameters such as the type and diameter of pores, filtration speed, physico-chemical properties of the liquid filtered and concentration of the contaminants retained in the baffle. The function has the following form:

$$\lambda=\lambda(\lambda_o,\sigma(t,d),v(t)) \tag{4}$$

expressing filtration coefficient by its initial value, where $v(t)$ is the filtration speed in m/h.

The most popular model is in the form [3]:

$$\lambda=\lambda_o\left(1+\frac{\beta\sigma(t,d)}{\varepsilon_o}\right)^x\left(1-\frac{\sigma(t,d)}{\varepsilon_o}\right)^y\left(1-\frac{\sigma(t,d)}{\sigma_u(v)}\right)^{z(v)} \tag{5}$$

where σ_u is the contractual concentration of pollutants for which $\lambda = 0$.

In this model, three types of factors that influence the value of filtration were included, and besides, its value depends on the exponents of power series of x, y, z, determined experimentally.

The first factor in parentheses included an increase in the specific surface area of the baffle filter, due to the contaminants deposited on the baffle. The second one takes into account the reduction of the porosity of the barrier at the time of filtration as compared to its initial porosity due to the deposition of contaminants in the pores of the baffle. The third factor takes into account the increase in the average filtration speed resulting from the reduction of the cross-section the pores by the deposition of impurities on

the baffle. In the description of the filtration process, assuming additivity of the pressure loss when flowing through the clean filtering barrier and the pressure losses resulting from the accumulation of contaminants in the baffle, the pressure equation is of the form [3]:

$$\frac{\partial p(t,d)}{\partial d} = 1 - \frac{K_o \mu v (1-\varepsilon_o)^2}{\rho g \varepsilon_o^3 \psi^2 d_s^2} - b_1 \left(\frac{6(1-\varepsilon_o)}{\psi d_s}\right)^{0,9} v^{0,4} \sigma_o(t,d) \quad (6)$$

where: p(t, d) – the pressure in the filter baffle at the time "t" at the depth "d" from the boundary condition h(t, 0) = h_o, where h_o is the pressure on the surface of the baffle, mH_2O, K_o – Kozeny constant, ρ – specific mass of the liquid, g/m^3, μ – the coefficient of dynamic viscosity of the liquid, g/m·s, ψ – the pores shape factor, ds – effective diameter of the pores in the filter baffle, mm, σo(t, d) – volume concentration contaminants, g/m^3, g – acceleration of gravity, m/s^2.

4. Numerical solution of equations of filtration and analysis of simulation results

Model of the filtration process is a set of three differential equations with partial derivatives, preset initial conditions and boundary, defining function C(t, d), σ(t, d) and h(t, d), whose arguments are continuous. For numerical solution of the model equations, as well as to identify its parameters, it is necessary discretization arguments occurring in these functions. According to the shape of the area where certain functions are considered, discretization on a uniform rectangular grid was adopted. The row number of the array corresponds to a fixed point in time, and the column number corresponds to a fixed depth in the baffle filter. The discrete version of the model equations was adopted the simplest - differential - approximation of partial derivatives occurring in these equations by difference quotients:

$$\frac{C(k,i)-C(k,i-1)}{\Delta L} = -\lambda\big(\sigma(k,i)\big)C(k,i), \quad (7)$$

$$\frac{\sigma(k,i)-\sigma(k-1,i)}{\Delta T} = v(k-1)\frac{C(k-1,i)C(k-1,i-1)}{\Delta L} \quad (8)$$

$$\frac{p(k,i)-p(k,i-1)}{\Delta L} = k_1\sigma(k,i) + k_2, \quad (9)$$

Solving equations in the variables of the so-called more discreet argument is obtained:

$$C(k,\ i) = \frac{C(k,i-1)}{1+\Delta L\lambda(\sigma(k,i))} \quad (10)$$

$$\sigma(k,i) = \sigma(k-1,i) + \Delta t v(k-1)\lambda\big(\sigma(k-1,i)\big)C(k-1,i), \quad (11)$$

$$p(k,i) = p(k,i-1) + \Delta L k_1\big(\sigma(k,i)\big) + k_2, \quad (12)$$

For example, in the article analysis of the results for the concentration of contaminants in the fuel as a function of the thickness of deposition on baffle filter was made.

Marine diesel oils are purified in stages, which includes gravity sedimentation, filtration and centrifugation. Fuel, before the filtration, is stored in settling tanks. As a result of a long period storage of fuel, occurs the growth of microorganisms and consequently the level of microbial contamination of the fuel increases.

Depending on the amount of microorganisms in the fuel, there are three stages in the development of contamination [4, 8]:

– no contamination, low,
– growing, medium,
– very tall.

Progressive microbiological contamination affects the sedimentation contaminants on the filter baffle. If dirt particles are smaller than the pore diameter to penetrate with the fuel to the engine fuel system, causing rapid wear and, consequently, its malfunction. The simulation results of the filtration process in graph function C(d) were shown in Figure 1. Analyzing the form of the function C(d) it can be noted that at the beginning of the process linear increase in function has performed. The concentration contaminants was about $3\cdot10^{-6}$ g/ml at a depth 0.5 cm. Then this growth had exponential course and concentrations of pollutants reached the level about $4\cdot10^{-5}$ g/ml, the last stage again had linear course and concentration contaminants at a depth of 1.5 cm was around $4.5\cdot10^{-5}$ g/ml. Presented course may be related to the development of micro-organisms. At the beginning of a slight increase, because the level of microbial contamination is very low. In the second stage there is an increase of impurities, which results in faster deposition of the deeper layers of the filter increasing concentrations. In the last stage of the level of pollution it is very high, there is a blocking filter, which is contaminated with whole. Despite the development of contaminants, course characteristic is linear, because due to increasing contaminants the filtration process slowly stops, which will involve increasing pressure drop across the filter. In order to prevent to interrupt flow fuel, the filter should be cleaned or replaced. Therefore, to the fuel are added additives, including biocides, in practice rarely achieves the case.

Unfortunately biocide are compounds, synthetic or natural origin to combat harmful organisms, which unfortunately also destroy beneficial organisms and cause adverse changes in the composition of microorganisms. Despite a number of benefits arising from the use of biocides, it is now a strong tendency to limit their use [7]. They are caused by the fear of the harmful effects of highly concentrated substances on the environment. There is therefore a need to find new methods for to combat of microbial contamination, which will not destroy the useful microorganisms and they will be environmentally friendly.

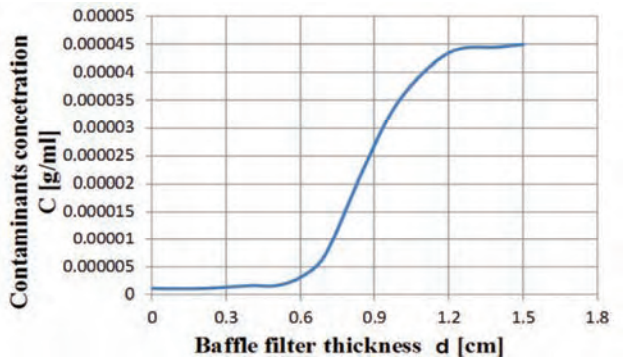

Fig. 1. Course of characteristic as a function of the concentration of contaminants in the deposition thickness of baffle filter

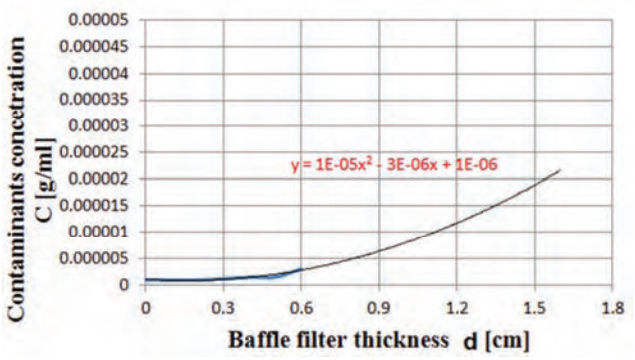

Fig. 2. Course of characteristic in the first stage of contaminants development together with the trend line and the development forecast after application of the countering microorganisms

Besides, for each stage of the filtration process trendline and the equation that describes it has been designated. They were also forecast, how would run characteristics, if at any stage the process of increasing contaminants would be stopped.

Forecasts show that the process of filter contamination is slower and contamination after the first stage is $2 \cdot 10^{-5}$ g/ml, in comparison with $4.5 \cdot 10^{-5}$ with the process without the use of additives, which is shown in Fig. 2.

5. Conclusions

1. With the development of industry and the wider automotive industry, it turned out that the problem of microbial contamination is still valid and it becomes more commonplace. Research showed that the activity of microbial life can lead to interference and even damage engines of vehicles, aircraft or ship.
2. Progressive microbial contamination has a significant impact, for example on the status of all fuel and lubricant systems components, causing the corrosion. Growing contamination cause excessive clogging of the filter barrier, resulting in a faster wear of the filter. If dirt particles are smaller than the pore diameter to penetrate with the fuel to the engine fuel system, causing rapid wear and, consequently, its malfunction
3. The development of the filtration model allows to simulate the effect of various pollutants on the efficiency of diesel oil filtration. In addition, this model allows you to check the performance of various additives in oils and to determine the potential for reducing the adverse effect of microorganisms on petroleum products.
4. It is necessary to develop effective methods for combating microbial contamination of fuels and oils, taking into account both the technical aspects and the specifics of the processes occurring in the fuel and lubricating systems by the means which will be environmentally friendly.

Bibliography

[1] DUDA, A. Problemy skażenia mikrobiologicznego w dystrybucji i magazynowania paliw naftowych. *Nafta-Gaz*. 2002, **58**(3), 160-167.
[2] GAYLARDE, C.C., BENTO, F., KELLEY J. Microbial contamination of stored hydrocarbon fuels and its control. *Revista de Microbiologia*. 1999, **30**.
[3] IVES, K.I. Mathematical models of deep-bed filtration. *Basis of Filtration Nordhoff International*. 1975 Leyden.
[4] JANDA, K. Mikrobiologiczne skażenie paliw. *Postępy mikrobiologii*. 2005, **44**, 157-169.
[5] KAISER, K. Filtry i filtracja (2). Filtracja i mechanizm filtracji. *Technika Chłodnicza i Klimatyzacyjna*. 2007, **5**, 202-204.
[6] KAULA, R. Podstawy automatyki. *Wydawnictwo Politechniki Śląskiej*. 2005.
[7] KLOFUTAR, B., GOŁĄB, J. Microorganisms in diesel and in biodiesel fuels. *Acta Chimica Slovenica*. 2007, **54**(4), 744-748.
[8] LASOCKI, J., KARWOWSKA, E. Wpływ mikroorganizmów bytujących w środowisku oleju napędowego i biodiesla na układ paliwowy pojazdów napędzanych silnikami o zapłonie samoczynnym. *Archiwum Motoryzacji*. 2010, **3**, 167-183.
[9] MARCINKOWSKI, L. Numeryczne rozwiązywanie równań różniczkowych. *Wydawnictwo Politechniki Warszawskiej*. 2011.
[10] NIEWCZAS, A., WRONA J., WRONA R. Zanieczyszczenia oleju smarującego oraz ich wpływ na trwałość silnika spalinowego. *Autobusy: technika, eksploatacja, systemy transportowe*, 2010, **11**(6), 1-5.
[11] SITNIK, L. Magnetyczne wspomagana filtracja oleju silnikowego. *Archiwum Motoryzacji*. 2009, **1**, 11-38.

Rafał Krakowski, DEng. – Faculty of Marine Engineering at Gdynia Maritime University.

e-mail: *R.Krakowski@am.gdynia.pl*

Article citation info:
GĘCA, M., HUNICZ, J., JAWORSKI, P. Numerical investigation into the effect of direct fuel injection on thermal stratification in HCCI engine. *Combustion Engines*. 2017, **169**(2), 137-140. DOI: 10.19206/CE-2017-224

Michał GĘCA
Jacek HUNICZ
Piotr JAWORSKI

CE-2017-224

Numerical investigation into the effect of direct fuel injection on thermal stratification in HCCI engine

Despite the fact that HCCI engines are distinguished by mixture homogeneity, some degree of stratification always appears inside a combustion chamber. It is especially applied to residual effect engines utilizing negative valve overlap. Mixture stratification is a result of the imperfect mixing of fresh air with trapped residuals. Direct fuel injection introduces stratification as well, due to fuel vaporization. As a consequence, the temperature within the combustion chamber is uneven. Thermal stratification affects auto-ignition timing and combustion evolution in a high extent. The purpose of this study was to evaluate a degree of thermal stratification in HCCI engine utilizing negative valve overlap. Investigations were performed using three-dimensional CFD model of the combustion system, made by using AVL FIRE software. Simulations were realized for various timings of fuel injection into the cylinder. It was found that fuel injection timing had a significant effect on the thermal stratification and resulting auto-ignition timing.

Key words: *HCCI, direct injection, thermal stratification, CFD*

1. Introduction

The problems of homogeneous charge compression ignition (HCCI) have been intensively investigated for last decades, as HCCI can be an interesting alternative to conventional spark ignition combustion. Because there is no flame propagation in the combustion chamber and fuel is highly diluted by air and re-circulated exhaust, low temperature combustion is obtained. It reduces NO_x emissions even to 98% when compared to conventional spark ignition combustion [6]. Additionally low temperature, lack of throttling and fast heat release rate provide good fuel economy [7, 13]. Fuel consumption can be reduced by 11–16% when compared to modern spark ignition engines [9].

However, in HCCI engine, ignition is not initiated by spark plug thus there are difficulties with controlling the ignition timing and combustion speed [10]. As a result HCCI engines have a much higher rate of pressure rise than conventional engines, especially when chemical energy introduced with fuel is high. A large rate of pressure increase in the cylinder is the reason for limitation of HCCI operation range. Therefore, control of the combustion process is a crucial issue in development of this combustion system. It cannot be realized directly, via spark discharge, but few indirect methods can be utilized, i.e. internal exhaust gas recirculation [1, 5, 11], valve timing control [8], stratification of the mixture and the temperature by controlling the injection strategy [2, 3, 11].The thermal stratification has a substantial impact on the combustion process. It affects the reaction rate of the combustible mixture. Thus, thermal stratification reduced heat release rate and pressure rise rate, enabling application of higher engine loads. Sjöberg et al. [12] found that a temperature difference even 30 K in the cylinder significantly influenced pressure release rate. These observations show that indirect combustion rate control can be achieved by thermal stratification. In engines using internal exhaust gas recirculation, some degree of thermal stratification appears due to the incomplete mixing of fresh air with gasses remaining after the previous cycle. Additional stratification can be achieved in direct injection engines due to thermal effects of fuel vaporisation.

This paper describes the investigations on the thermal effects of direct fuel injection and their impact on HCCI combustion. The experimental research was conducted on single cylinder engine. HCCI combustion was achieved with the use of negative valve overlap. Different split fuel injection techniques were compared. Combustion evolution was analysed on the basis of measured in-cylinder pressure. The observed trends were explained using 3D modelling of in-cylinder processes.

2. Experimental setup and conditions

The research engine is specified in Table 1. Engine was installed on a test bench equipped with a DC current dynamometer. The engine was equipped with a fully variable valve train with independent adjustment of valves lifts and timings. The valves lifts were adjusted with the hydraulic mechanism described in details in [4]. The fully variable valve train allowed to obtain internal EGR using the NVO technique. Valve timing and lift data are presented in Table 2.

The engine was operated at constant speed of 1500 rev/min. The pressure in the engine intake system was elevated to 1.5 bar absolute using a vane compressor. The total amount of fuel injected per cycle was 18 mg, which provided excess air ratio of 1.3. Engine load expressed by indicated mean effective pressure was approximately 0.5 MPa.

Fuel was injected into the cylinder with the use of single-stream swirl-type injector with fuel stream angle of approximately 70°. Analysed fuel injection strategies are shown in Fig. 1 and Table 3. In general half of the fuel was injected during NVO, whereas NVO fuel was split into two equal parts. The second half of fuel was injected during compression using different strategies, shown in Table 3, to achieve different degrees of stratification.

Table 1. Technical specification of SB 3.5 research engine

Displacement	498.5 cm^3
Bore/Stroke	84 mm/90 mm
Compression ratio	11.7
No. of valves	2
Intake cam profile	9.4 mm, 235 °CA
Exhaust cam profile	9.2 mm, 235 °CA
Intake valve lift	2.4–9.4 mm
Exhaust valve lift	2.2–9.2 mm
Boost system	Electrically driven vane supercharger
Fuel injector	Solenoid actuated swirl type
Fuel pressure	40–110 bar
Fuel	Gasoline 95 RON

Table 2. Valve timings and lifts

Intake valve opening /IVO	82°CA
Intake valve closing /IVC	212 °CA
Intake valve lift	3.6 mm
Exhaust valve opening /EVO	521°CA
Exhaust valve closing /EVC	640°CA
Exhaust valve lift	2.9 mm

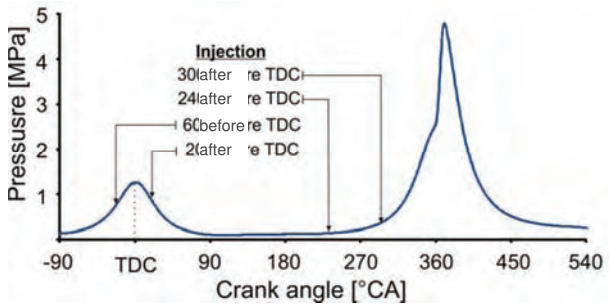

Fig. 1. Fuel injection strategy

Table 3. Fuel injection strategy and fuel quantities

Case	60° CA bTDC	20° CA aTDC	240° CA aTDC	300° CA aTDC
1	4.5 mg	4.5 mg	4.5 mg	4.5 mg
2	4.5 mg	4.5 mg	9.0 mg	–
3	4.5 mg	4.5 mg	–	9.0 mg

3. Engine model

In order to determine the influence of thermal stratification on the combustion process simulation software AVL FIRE was used. This is a specialized tool that uses numerical methods to solve fluid flow problems (CFD). The mathematical model geometry was the same as geometry of the experimental engine, shown in Table 1.

For computational purposes, a three-dimensional model of a test engine was prepared for which a mesh was constructed. Visualization of the resulting grid is shown in Fig. 2. The mesh needed to calculate the combustion process was done using the FIRE FAME Hexa module, which is a supplementary part of the FIRE software. The standard method was used to create the mesh. This method involves striving for obtaining maximum number of cubic cells. The maximum cell size was set at 1mm.Temperature distributions were computed for the three injection cases investigated experimentally. They were utilized for analysis of the thermal effects of fuel injection.

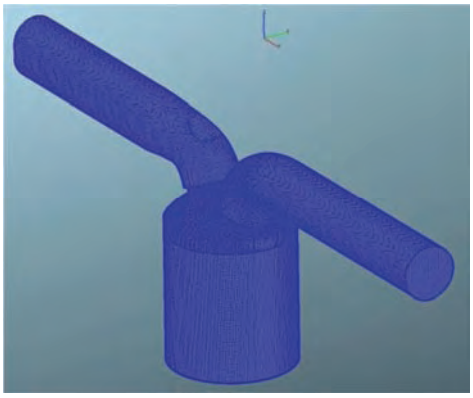

Fig. 2. Mesh model of the HCCI engine

4. Results and discussion

Experimental results are shown in Figs. 3 and 4. It can be noted that injection strategy indeed affects auto-ignition timing, however Fig. 4 shows that it does not affect peak HRR. It should be noted that ensemble averaged values presented in the traces are smoothed due to cycle-by-cycle variability. Actual values of combustion timing parameters and peak HRR, computed for each engine cycle separately are shown in Table 4.

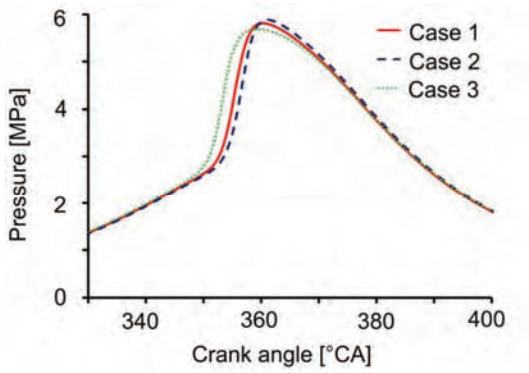

Fig. 3. Pressure in the cylinder for chosen cases (Table 4)

To illustrate thermal effects of each applied injection strategy, temperature distributions 10°CA after each injection are shown in Fig. 5. Temperature maps are shown for the plane in line with injection stream axis. The simulation results are presented for the Case 1, where mass of fuel was equally distributed among four injection timings.

Table 4. Combustion parameters

Case	5% MFB	5-95% MFB	Peak HRR
1	353.3 °CA	3.8 °CA	188 J/°CA
2	354.4 °CA	3.9 °CA	200 J/°CA
3	351.0 °CA	3.9 °CA	169 J/°CA

Fig. 5 shows decrease of temperature after fuel injection before TDC in NVO period, whereas if fuel was injected 20 °CA after TDC there was no temperature traces 10 °CA after injection. It is plausible, because close to TDC the re-compressed exhaust temperature was high, which enhanced vaporization, and additionally fluid velocity due to squish effect was higher, which enhanced mixing. Thus, the thermal effect of fuel injection disappeared quickly.

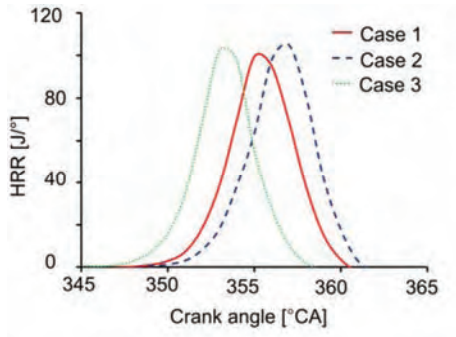

Fig. 4. Heat release rate for chosen cases (Table 4)

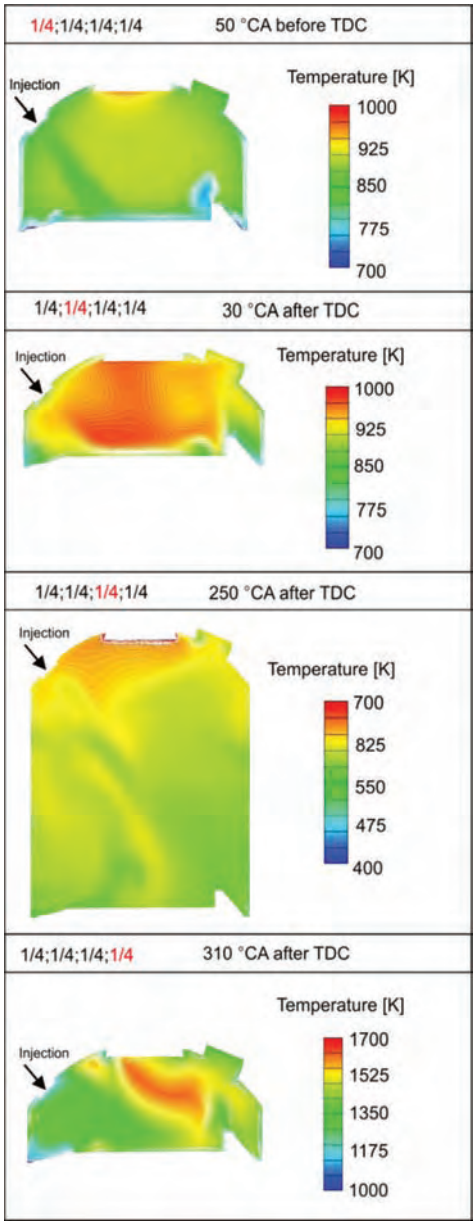

Fig. 5. Thermal stratification in the cylinder at different angles of injection

After fuel injection during the compression stroke thermal traces were clearly visible both for early and late injection, as shown in Fig. 5. It can be ascribed to longer vaporization process due to lower temperature. It should be noted that temperature fields in the bottom of the Fig. 5 indicate that exothermic reactions started. In fact, experimental results did not indicate any heat release at this timing. It is due to the fact that auto-ignition model was not validated properly, however, the present study is aimed at identification of temperature distribution before combustion rather that combustion process itself.

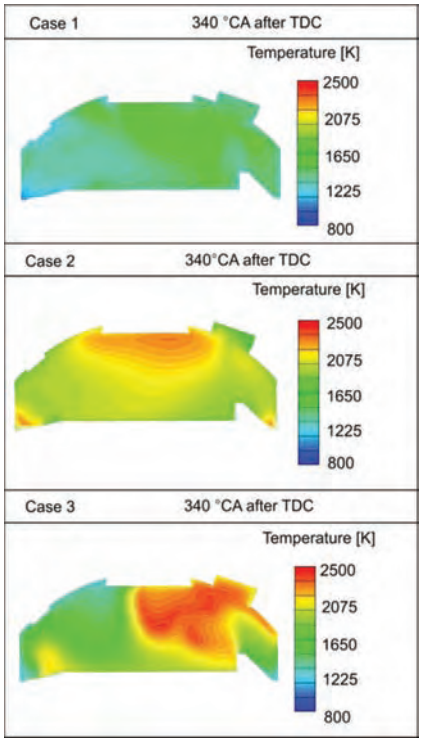

Fig. 6. Thermal stratification in the cylinder for 340 °CA after TDC

Figure 6 shows the in-cylinder temperature distribution at 340 °CA for all applied injection strategies. For Case 1 (even fuel distribution between two late injections) one can observe that temperature level is the lowest. However, it indicates that combustion process has already started. It can be also seen that the process is definirtelylow temperature combustion.

Among analysed cases experimental results provided the earliest start of injection for Case 3 and the latest for Case 2, as shown in Fig. 4. These results indicate that effects of fuel stratification and thermal stratification are not obvious. Experimental data show that the higher the stratification degree, the earlier the start of combustion. Despite the fact that in simulations combustion started to early, the observed trends can be explained by analysis of temperature maps in Fig. 5. In the Case 2, where injection was earlier lower stratification degree delayed start of combustion. In contrast, for Case 1 and Case 3 later injection provided higher stratification degree. As heat for fuel vaporisation was consumed locally, the temperature in the remaining volume was higher than average value. This region was the source of auto-ignition.

5. Conclusions

The effects of thermal stratification on auto-ignition timing and combustion in a gasoline fuelled HCCI engine were investigated. To provide insight into spatial temperature distribution in combustion chamber experimental results were complemented by 3D simulations.

Obtained experimental results showed that under investigated conditions higher amount of fuel injected later resulted in earlier start of combustion. Analysis of temperature distribution maps obtained from 3D modelling of the engine processes revealed that the more fuel was injected the later, the larger temperature span was observed. Larger thermal stratification resulted in appearance high temperature spots, which were the sources of auto-ignition.

It should be noted, however, that applied auto-ignition and combustion model was not properly validated for HCCI processes. Nevertheless modelling enabled analysis of the thermal effects of direct fuel injection locally and explained experimental results.

Acknowledgements

The research was funded by the National Science Centre, Poland, grant No. 2015/17/B/ST8/03279. The authors wish to thank AVL List GmbH for making simulation software available within a framework of AVL University Partnership Program.

Nomenclature

aTDC after top dead centre
bTDC before top dead centre
CA crank angle
CFD computational fluid dynamics
EGR exhaust gas recirculation
HCCI homogeneous charge compression ignition
HRR heat release rate
MFB mass fraction burnt
NVO negative valve overlap
TDC top dead centre

Bibliography

[1] ALEIFERIS, P., CHARALAMBIDES, A., HARDALUPAS, Y. et al. Modelling and experiments of HCCI engine combustion with charge stratification and internal EGR. *SAE Technical Paper*. 2005, 2005-01-3725.

[2] GUOHONG, T., ZHI, W., JIANXIN, W. et al. HCCI combustion control by injection strategy with negative valve overlap in a GDI engine. *SAE Technical Paper*. 2006, 2006-01.0415.

[3] HUNICZ, J., GĘCA M., KORDOS P. An experimental study of boosted gasoline HCCI engine under different direct fuel injection strategies. *Experimental Thermal and Fluid Science*. 2015, **4**.

[4] HUNICZ, J., KORDOS, P. Experimental study of the gasoline engine operated in spark ignition and controlled auto-ignition combustion modes. *SAE Technical Paper*. 2009, 2009-01-2667.

[5] KAWASAKI, K., HIROTA, K., NAGATA, S. et al. Improvement of natural-gas HCCI combustion by internal EGR by means of exhaust valve re-opening. *SAE Int. J. Engines*. 2010, **2**(2), 733-739.

[6] MASE, Y., KAWASHIMA, J., SATO, T., EGUCHI, M. Nissan's new multivalve DI diesel engine series. *SAE Technical Paper*. 1998, 981039.

[7] NAJT, P., FOSTER, D.E. Compression-ignited homogeneous charge combustion. *SAE Technical Paper*. 1983, 830264.

[8] OGURA, M., SASAKI, T., KAWAGUCHI, Y. HCCI combustion control by intake and exhaust continuous variable valve timing mechanism in premixed gasoline engine. *SAE Technical Paper*. 2004, 2004-32-0096.

[9] PULKRABEK, W.W. Engineering fundamental of the internal combustion engine 2nd edition. *Pearson Prentice-Hall*. Upper Saddle River, NJ, 2004.

[10] SJÖBERG M., DEC, J.E. Comparing late-cycle autoignition stability for single- and two-stage ignition fuels in HCCI engines. *Proceedings of the Combustion Institute*. 2007, **31**, 2895-2902.

[11] SJÖBERG, M., DEC, J., HWANG, W. Thermodynamic and chemical effects of EGR and its constituents on HCCI autoignition. *SAE Technical Paper*. 2007, 2007-01-0207.

[12] SJÖBERG, M., DEC, J.E., CERNANSKY, N. Potential of thermal stratification and combustion retard for reducing pressure-rise rates in HCCI engines, based on multi-zone modeling and experiments. *SAE Technical Paper*. 2005, 2005-01-0113.

[13] STANGLMAIER, R.H., ROBERTS, C.E. Homogeneous charge compression ignition (HCCI): benefits, compromises, and future engine applications. *SAE Technical Paper*. 1999, 1999-01-3682.

Michał Gęca, MSc. – Faculty of Mechanical Engineering at Lublin University of Technology.

e-mail: *Michal.Geca@pollub.pl*

Jacek Hunicz, DSc., DEng. – Faculty of Mechanical Engineering at Lublin University of Technology.

e-mail: *J.Hunicz@pollub.pl*

Piotr Jaworski, MSc. – Division of Aircraft Engines at Warsaw University of Technology.

e-mail: *Piotr.Jaworski@itc.pw.edu.pl*

Article citation info:
MIZUNO, H. Nissan gasoline engine strategy for higher thermal efficiency. *Combustion Engines*. 2017, **169**(2), 141-145. DOI: 10.19206/CE-2017-225

Hideaki MIZUNO

CE-2017-225

Nissan gasoline engine strategy for higher thermal efficiency

Rising highly concern about the environment has led to demands for the improvement of the efficiency of gasoline engines. Engine thermal efficiency will reach about 40% by technologies as boosted EGR, miller cycle and so on. This evolution trend will be continuously required to survive engines for the future. In this background, further improvement based on theoretical thermal efficiency of high compression ratio and specific heat capacity should be promoted. In addition, energy loss reduction such as represented by cooling loss and friction is also very important for the efficient and effective improvement. NISSAN's challenges will be introduced to solve these propositions.

Key words: *gasoline engine, downsizing turbo, variable compression ratio*

1. Introduction

In order to realize a sustainable society, the mobility solution promoted by Nissan is based on two pillars. The first one is the widespread use of "Zero Emission" vehicles that produce no tailpipe CO_2 emissions, and the second one is the thorough improvement of efficiency of vehicles equipped with internal combustion engines.

Regarding the widespread use of "Zero Emission" vehicles, Nissan aims for 25% sales ratio by 2025. However, simple manufacture and sale of the zero-emission vehicles is only a first step towards the widespread use of "Zero Emission" vehicles. The key factors to spread "Zero Emission" vehicles are the innovation in technology and the comprehensive effort in the construction of social infrastructure, including development and installation of quick-charging stations. Nissan focuses on promoting zero-emission mobility through these activities.

On the other hand, regarding the improvement of vehicles equipped with internal combustion engines, thermal efficiency of almost 40% will be achieved by generation change before 2020, but this is just a passing point. Due to the progress in lean-burn technologies such as turbocharging EGR, turbocharging Lean, the roadmap to the 45% thermal efficiency of internal combustion engines has already been seen. In order to have the internal combustion engines as valuable power source in the future, continuous effort to improve thermal efficiency is expected. The key for further continuous improvement of thermal efficiency is supposed to be the reduction of cooling loss and implementation of high compression ratio. However high compression ratio needs a long stroke that requires a geometrically unreasonable shape for an automobile internal combustion engine.

This is a major physical obstacle on the path to the high compression ratio engine. The link mechanism adopted by the new VC-T (Variable Compression-Turbo) engine developed by Nissan, in addition to enabling variable compression ratio functionality has the effect of changing the motion of the piston link. Because of this effect, the physical obstacle on the path to high compression ratio can be overcome and long stroke can be implemented geometrically and reasonably. In a sense, it can be said that by acquiring this link mechanism technology, internal combustion engines gain the evolution potential for another 100 years.

Although it seems a big challenge to aim for further significant improvement after thermal efficiency of internal combustion engines exceeds 45%, there are already cases of such high thermal efficiency being achieved in marine engines, power plants, etc. One of the key points is how the internal combustion engines is used. By narrowing down operating conditions, such as constant load operation, limiting rotation speed etc. further improvement can be expected.

In autumn 2016, Nissan launched a new electric powertrain "e-POWER", a new power unit combining a gasoline engine and a Battery Electric Vehicle (BEV) motor. The "e-POWER" has the potential to achieve a higher level of economic efficiency, because engine and tires are not directly connected mechanically; even when the internal combustion engine is used as engine for power generation it can operate with most effective rotation speed and load.

2. Nissan sustainability strategies

In order to realize sustainable society, Nissan adopted a long-term vision of reducing CO_2 emissions of new cars by 90% by 2050 comparing to 2000 (Fig. 1).

The widespread use of Battery Electric Vehicles (BEVs) that do not emit CO_2 and other exhaust gases when running is a major pillar supporting this long-term vision. Such vehicles have already entered mass-production and even more effort is going into development. By using technologies for improving the energy density of lithium batteries, reduction of running resistance etc. Nissan has already succeeded in development of technology that enables driving range per one charge comparable to that of ordinary gasoline vehicles [1]. However, at the present time, replacing all vehicles with BEVs looks problematic from both cost and technical points.

For example, the energy density of current lithium batteries is about 100 Wh/kg, and while there are technologies allowing in excess of 200 Wh/kg density in the future, in order to travel long distances heavier batteries must be carried continuously. Considering that the energy density of gasoline is about 12,000 Wh/kg, in order to make the selection of a BEV as a vehicle for long distance travel rational, further improvement of battery energy density is required in the future. In other words, even if BEVs become affordable and widespread, vehicles running on liquid fuel will continue to play an important role. There is no doubt, that to reduce the total amount of CO_2 emission globally, the improvement of fuel efficiency of vehicles equipped with internal combustion engines is extremely important.

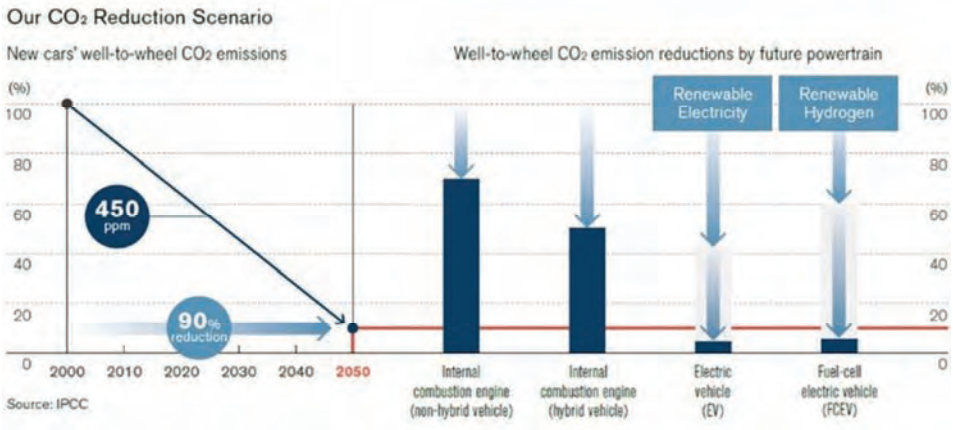

Fig. 1. Scenario for CO_2 emission volume reduction

Based on the above, the sustainable mobility solution promoted by Nissan is based on two pillars. The first one is the "Zero Emission" vehicles which produce no tailpipe CO_2, and the second one is "PURE DRIVE", the thorough improvement of efficiency of vehicles equipped with internal combustion engines (Fig. 2).

Fig. 2. The sustainable mobility solution based on two pillars

3. Evolution of PURE DRIVE

Nissan is focusing not only on Zero Emission vehicles, but also on improving efficiency of vehicles equipped with internal combustion engines using such technologies as downsizing turbocharging technology, CVT etc. The most important task required to further improve the efficiency of vehicles with internal combustion engines is the improvement of thermal efficiency of the internal combustion engine itself. The thermal efficiency of internal combustion engines used in passenger cars has continuously evolved from the past to the present without stopping (Fig. 3). In order to have the internal combustion engines as valuable power source in the future, continuous effort to improve thermal efficiency is expected.

Thermal efficiency of almost 40% will be achieved by generation change before 2020, but this is just a passing point. Due to the progress in lean-burn technologies, such as turbocharging EGR, turbocharging Lean, the roadmap to 45% thermal efficiency of the internal combustion engines has already been seen (Fig. 4). Even higher levels of thermal efficiency can be achieved by reducing cooling loss and further improving the compression (expansion) ratio. With the current level of cooling loss, significant improvement of thermal efficiency by improving compression ratio can not be expected, but there is still a place for thermal efficiency improvement by increasing the compression ratio while greatly reducing the cooling loss (Fig. 5).

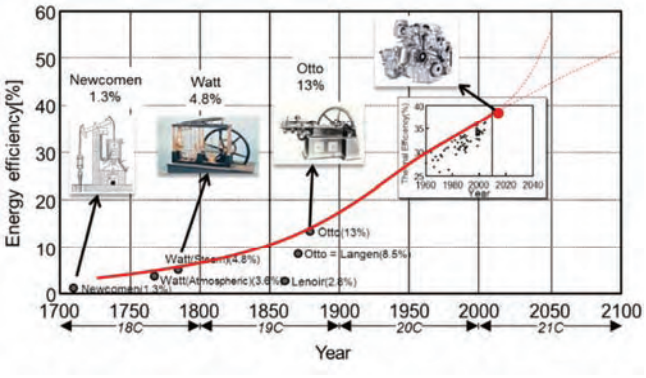

Fig. 3. Evolution of thermal efficiency of internal combustion engines

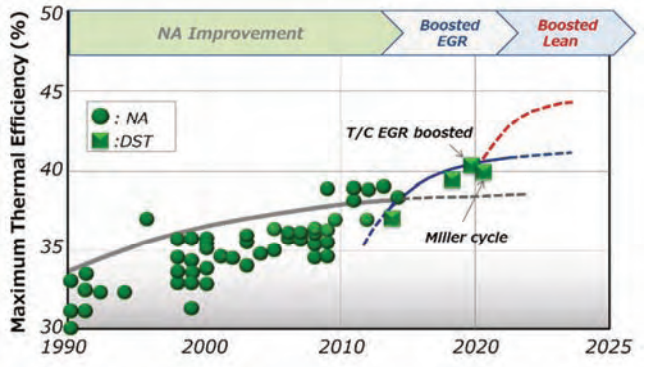

Fig. 4. What is the next key driver to evolve?

Research and development of high response heat insulating films and heat insulating materials has been advanced as a measure to further improve the cooling loss from the current level; these results are expected to achieve a breakthrough in reduction of the cooling loss in internal combustion engines [2]. On the other hand, when looking at history, the compression ratio has expanded together with the evolution of internal combustion engine, and it looks like the demand for improvement of compression ratio will continue as long as engine continues to evolve. In order to realize stable combustion at high compression ratio, a long stroke is required at the same time (Fig. 6).

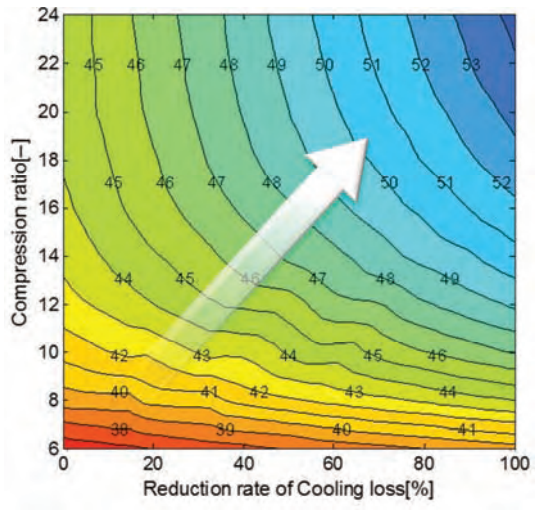

Fig. 5. Potential to improve thermal efficiency

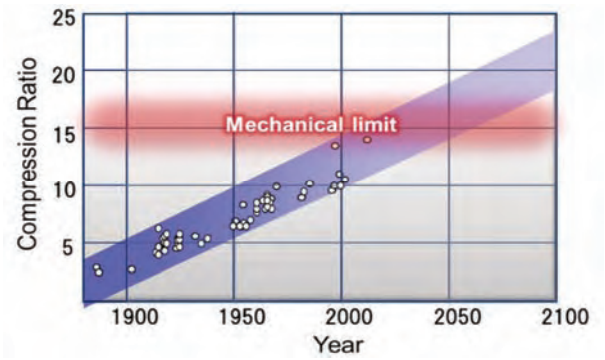

Fig. 6. Evolution of compression ratio of gasoline internal combustion engines

However, the long stroke necessary to achieve a compression above a certain level requires an extremely large engine height to realize it geometrically, which makes it an unsuitable shape for an automobile internal combustion engine. This is a major physical road block on the path to the high compression ratio engine.

At the 2016 Paris Motor Show Nissan presented the world's first innovative engine technology "VC-Turbo" from the Infinity brand (Fig. 7). The "VC-Turbo" engine adopts the world's first variable compression ratio technology using link mechanism (Fig. 8). This technology makes the 4 cylinder "VC-Turbo" engine an unprecedentedly advanced engine realizing the regular performance of a 6 cylinder gasoline engine with top-level thermal efficiency at the same time (Fig. 9).

The link mechanism adopted by the VC-Turbo engine, has in addition to enabling variable compression ratio functionality the effect of changing the motion of piston link [3, 4]. Because of this effect the physical obstacle on the path to high compression ratio can be overcome and long stroke implemented geometrically and reasonable (Fig. 10). In a sense, it can be said that by adopting this link mechanism technology, internal combustion engines gained the evolution potential for another 100 years.

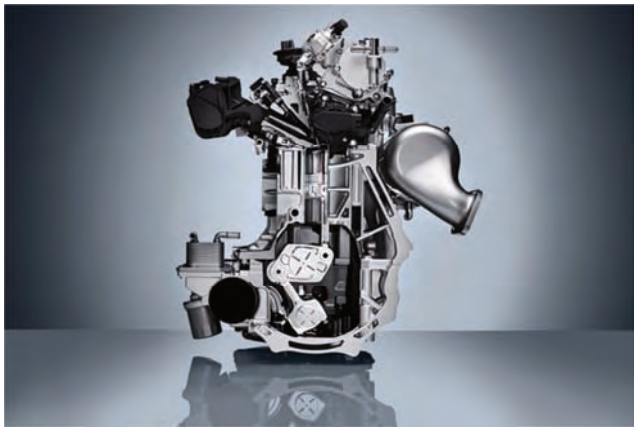

Fig. 7. INFINITI VC-Turbo

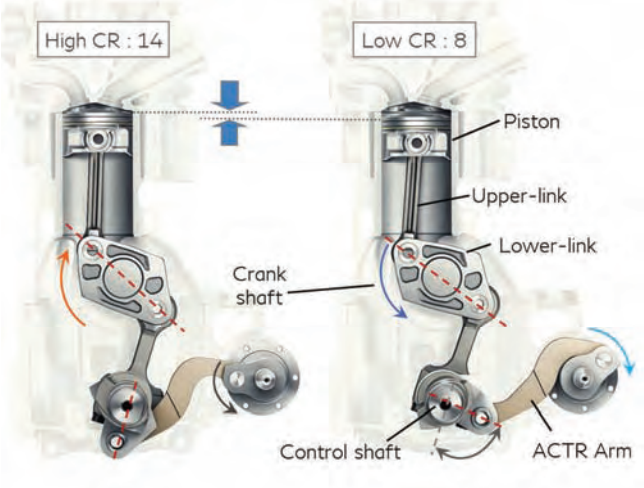

Fig. 8. Overview of the VC-Turbo engine

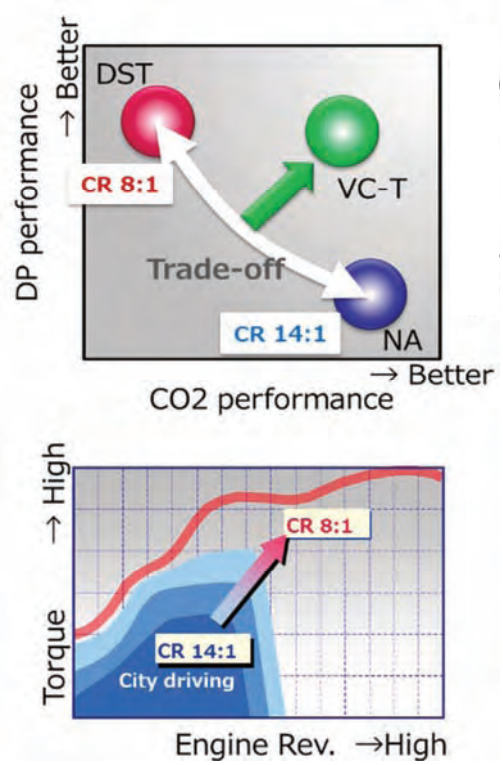

Fig. 9. Performances overview of the VC-Turbo technology

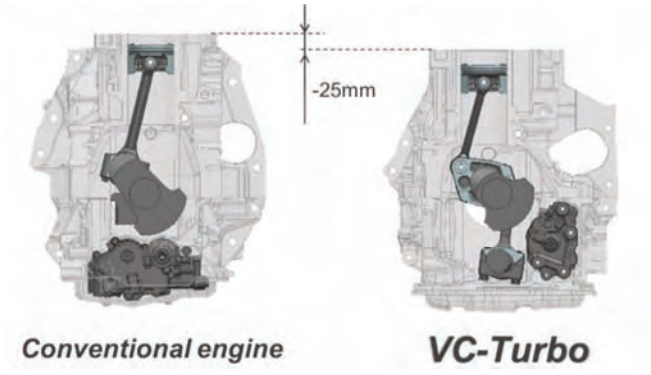

Fig. 10. Impact for engine height

4. Considerations for further evolution of PURE DRIVE combined with BEV technology

Although it seems a big challenge to aim for further significant improvement after thermal efficiency of internal combustion engines exceeds 45%, there are already cases of such high thermal efficiency in marine engines, power plants etc. One of the key points is how the internal combustion engines is used. By narrowing down operating conditions, such as constant load operation, limiting rotation speed etc. further improvement can be expected. As an internal combustion engine for electrified powertrain for automobiles, revision of specifications more specialized for power generation can be considered a major breakthrough (Fig. 11). However, in this case the use of the internal combustion engine in automobile also has to be changed.

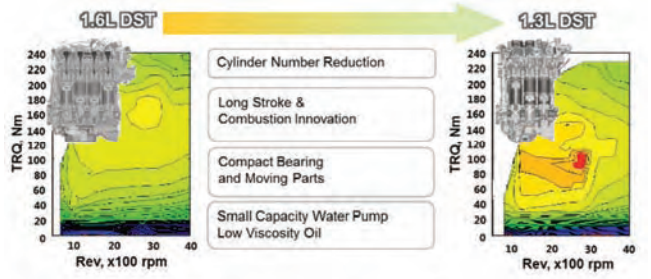

Fig. 11. Example of specialization for power generation

In autumn 2016, Nissan launched a compact car "NOTE e-Power" equipped with a new electric powertrain "e-POWER"; combining a gasoline engine and a BEV motor (Fig. 12). Although the power source of the "e-POWER" is an internal combustion engine, it is completely different from hybrid systems widely used in general compact cars because it is a new electric powertrain which has 100% motor driven EV operation (Fig. 13).

The "e-POWER" has the potential to acquire a higher level of economic efficiency, because the engine and tires are not directly connected mechanically, even when the internal combustion engine is used for power generation, it can operate with most effective rotation speed and load.

The following measures can be considered as examples of revisions to the internal combustion engine specification specially for power generation: reducing friction by lowering the maximum rotation speed, further downsizing by sacrificing responsiveness in the low rotation speed range, cylinder cutout incorporating measures against NVH, limiting operating rotation speed range, and so on. Radical improvement of compression (expansion) ratio is also important here, and realization of high compression (expansion) ratio by making super long stroke using link mechanism contributes to further efficiency improvement. While in this case there is a possibility that performance at high rotation speed may be sacrificed, this does not constitute a problem for the power generation function.

Fig. 12. Concept of "e-POWER"

Fig. 13. Fully integrated e-POWER powertrain

Considering the above changes, the thermal efficiency of the internal combustion engine can be further improved by about 5%; as a result, the thermal efficiency of the internal combustion engine will reach 50%.

5. Trend of downsizing

The ICE will be able to operate at most effective point (rev. torque) only if it specialized as a "generator" like e-power. Running time will be reduced because the ICE will always operate at its most effective point on demand dependent on driving situation. A key requirement will be to ensure that the internal temperature quickly increases at engine start timing in order to operate at most effective point. The energy for raising temperature will became an issue in the future as with improving BSFC the energy available will lessen [5].

Nissan assumes that making lower thermal energy capacity by reducing displacement will be effective via downsizing and will be focused on. As mentioned before, VC-T offers appropriate compression ratio depending on the operating situations by using unique link system. VC-T will be able to realize further downsizing, compared to conven-

tional ICE's due to avoiding knock in high power and high torque area by using low compression ratio (Fig. 14). Thus downsizing will be promoted more by using variable compression ratio or similar mechanism in order to minimize the warming up energy needed.

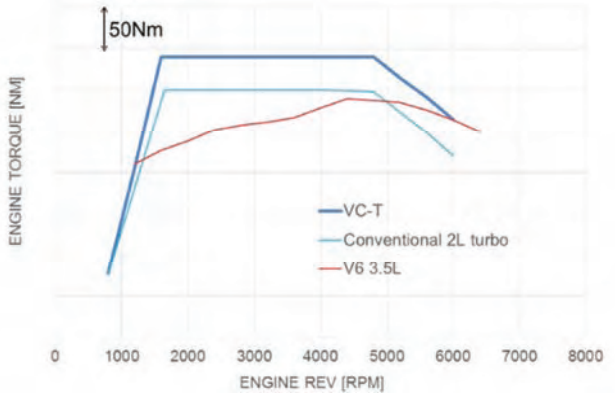

Fig. 14. Downsizing by VC-T

6. Summary

1) The mobility solution promoted by Nissan is based on the two pillars. The first one is the "Zero Emission" vehicles which produce no CO_2, and the second one is "PURE DRIVE", the thorough improvement of efficiency of vehicles equipped with internal combustion engines.

2) For "PURE DRIVE", Nissan will put our strength in technological development to continuously improve the thermal efficiency of the internal combustion engine and contribute to global reduction of CO_2 emission. The variable compression ratio technology for internal combustion engine using the link mechanism is one of the important key technologies for this purpose.

3) The e-POWER combined with the "Zero Emission" technology in vehicles equipped with internal combustion engines shows a new direction of "PURE DRIVE" evolution by operating the internal combustion engine as a power generator.

4) After making the breakthrough for the best BSFC, downsizing will be enhanced in order to reduce thermal energy capacity. Variable compression ratio technology will be an effective solution for this.

Nomenclature

BEV battery electric vehicle
BSFC brake specific fuel consumption
CVT continuously variable transmission
EGR exhaust gas recirculation
EV electric vehicle
ICE internal combustion engine
SI spark ignition
VC-T variable compression-turbo

Bibliography

[1] MIYAMOTO, T., WATANABE, Y., HIRAI, T., SASAKI, T. Development of high capacity lithium-ion battery for NISSAN LEAF. *SAE Technical Paper*. 2012, 2012-01-0664.

[2] MIZUNO, H., ASHIDA, K., TERAJI, A. et al. Transient analysis of the piston temperature with consideration of in-cylinder phenomena using engine measurement and heat transfer simulation coupled with three-dimensional combustion simulation. *SAE Journal Article*. 2009, 2009-01-0187.

[3] MOTEKI, K., AOYAMA, S., USHIJIMA, K. et al. A study of a variable compression ratio system with a multi-link mechanism. *SAE Technical Paper*. 2003, 2003-01-0921.

[4] TSUCHIDA, H., HIRAYA, K., TANAKA, D. et al. The effect of a longer stroke on improving fuel economy of a multiple-link VCR engine. *SAE Technical Paper*. 2007, 2007-01-4004.

[5] HIRAKU, R. Our tasks to make ICE surviving in the coming century. JSAE No.15FORUM-8. 20154338.

Hideaki Mizuno – Powertrain Engineering Division 1, Nissan Motor Co., Ltd.

e-mail: *Hid-Mizuno@mail.nissan.co.jp*

Article citation info:
KOMORSKA, I., WOŁCZYŃSKI, Z., BORCZUCH, A. Model-based analysis of sensor faults in SI engine. *Combustion Engines*. 2017, **169**(2), 146-151. DOI: 10.19206/CE-2017-226

Iwona KOMORSKA
Zbigniew WOŁCZYŃSKI
Artur BORCZUCH

CE-2017-226

Model-based analysis of sensor faults in SI engine

The article focuses on the fault not diagnosed by the OBD system. Apart from mechanical damages sensor faults are a serious group. Although the sensor values are constantly monitored, some errors are not detected. The article presents a diagnostic model of the air intake system of SI engine, which generates the control and work parameters of the engine for fault-free state. The parameters obtained from the reference model can be compared with the parameters measured for the engine in any operating condition. Based on the model the impact of sensor faults for other parameters was analyzed. Some errors can be masked by the adaptive control system of the engine, which changes the parameters of the engine control. Simulation tests were verified on the test bench.

Key words: *spark ignition engine, air-intake system, model-based diagnostics, engine sensor faults, residuals*

1. Introduction

Traditional diagnostic systems compare the measurement results with fixed limits. If the sensor signal voltage does not exceed the limit values, then the measurement is acceptable. Meanwhile, with the time the characteristics of the sensors are changed, leaks appear in the intake manifold, contacts become dirty and wet. It can change the indications of sensors, but signal voltage still does not reach the limits [8]. Adaptive control system of the engine will adjust the fuel dose - based on the lambda sensor indications – to new conditions. That is good, because the driver with any malfunction does not have to follow the service. Sometimes, however, the driver feels something is wrong with the engine, but the error is not detected [2, 3, 5, 13].

Another, also traditional approach to diagnosing, is hardware redundancy or multiplication of sensors. However, this is a costly solution, takes place and additionally weighs. Double potentiometric sensors are used for example in the gas pedal and throttle of engine.

Modern diagnostic systems [14, 15] use mathematical models to estimate measured physical quantities. These models act as virtual sensors. Based on the indications of other sensors recognised as efficient and relations of mathematical or statistical models, the rational indications investigated sensors are estimated and compared with an indication of the physical sensors [4, 10, 16, 17]. Virtual sensors can be divided into static – model-based, or dynamic – using observers [1, 18, 19]. This article defines virtual sensors in the air intake system.

2. Mean-value model of the air intake system

The state of the cylinder is defined by the mass and the internal energy of air contained in the cylinder. Fig. 1 shows a cross-section of the intake manifold. The throttle angle α controls the flow of air mass into the manifold.

The adiabatic flow across the throttle body/butterfly valve can be modeled as air flow from orifice. While modeling it is assumed that one-dimensional compressible flow has no friction and inertial effects in the flow and there is no change in temperature and pressure (lumped parameter approach) during the flow [6, 7, 9, 11].

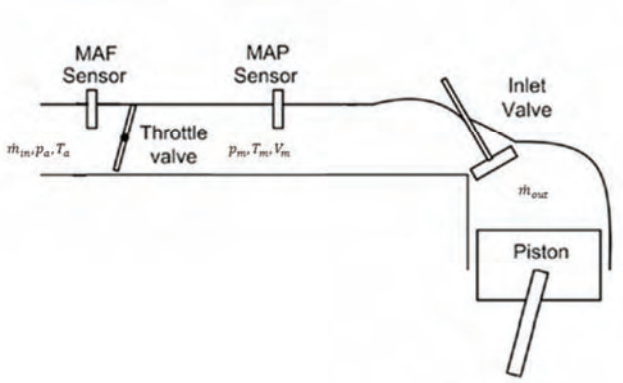

Fig. 1. Air intake system

Moreover, the fuel and temperature dynamics involved in air intake system are assumed to be uniform. The mass and energy of the air serves as inputs and outputs of the receivers. It is also assumed that no substantial changes occur in energy and no mass & heat transfers through the manifold walls. The manifold pressure dynamics can be modeled on the basis of filling and emptying of air behaving as perfect gas as shown in (1)

$$\dot{p}_m(t) = \frac{RT_m}{V_m}\left(\dot{m}_{in}(t) - \dot{m}_{out}(t)\right) \tag{1}$$

where: $\dot{p}_m$ – change of manifold pressure, T_m – manifold temperature, V_m – manifold volume, R – specific gas constant, $\dot{m}_{in}$ – air mass flow into the manifold, $\dot{m}_{out}$ – air mass flow out from the manifold.

The manifold absolute pressure sensor provides instantaneous manifold pressure information to the electronic control unit of engine. A fuel-injected engine may alternatively use a mass airflow sensor to find out the mass flow rate of air entering a fuel-injected internal combustion engine. The air mass information is necessary for the engine control unit to balance and deliver the correct fuel mass to the engine.

Air mass flow into the manifold is described as a function:

$$\dot{m}_{in}(t) = f(p_m, \alpha) \tag{2}$$

where p_m – manifold pressure, α – throttle angle, and air mass flow out from the manifold as a function:

$$\dot{m}_{in}(t) = f(p_m, n) \tag{3}$$

where n – engine speed.

At stationary engine operation it can be assumed that

$$\dot{m}_{in}(t) = \dot{m}_{out}(t) = \dot{m}_a(t) \tag{4}$$

where $\dot{m}_a$ – air mass flow rate measured with air flowmeter.

At stationary engine operation one of the engine load measure: throttle angle α, air flow $\dot{m}_a$, manifold pressure p_m, can be estimated from the remaining measurements and the rotational engine speed n [12].

The simple diagnostic model is presented in Fig. 2. Model was implemented in Matlab Simulink.

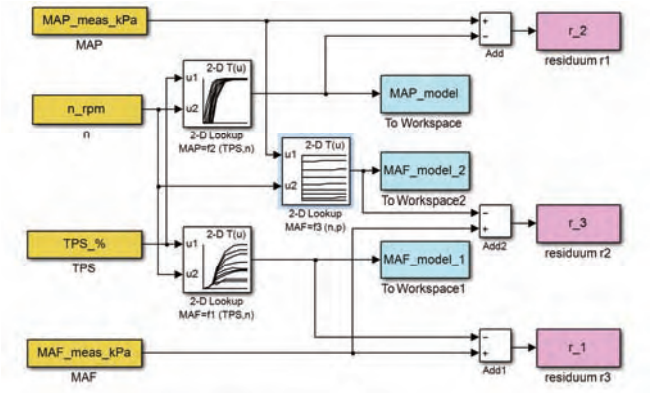

Fig. 2. Diagnostic model of air intake system

The inputs of the model are averaged values of signals: throttle position α, engine rotational speed n, manifold pressure p_m and air mass flow $\dot{m}_a$. In the model three lookup tables, that were taken in empirical way, were used:

$$\dot{m}_a = f_1(\alpha, n) \tag{5}$$

$$p_m = f_2(\alpha, n) \tag{6}$$

$$\dot{m}_a = f_3(n, p_m) \tag{7}$$

During simulations with the model for steady state, following residuals are generated:

$$r_1 = \dot{m}_a - f_1(\alpha, n) \tag{8}$$

$$r_2 = p_m - f_2(\alpha, n) \tag{9}$$

$$r_3 = \dot{m}_a - f_3(n, p_m) \tag{10}$$

The i-th residual indicator *R* is established in the following way:

$$R_i = \begin{cases} 0 & \text{if} \quad r_i \le u \\ 1 & \text{if} \quad r_i > u \end{cases} \tag{11}$$

where u is the model uncertainty.

The components of the model uncertainty are: measurement errors, uniqueness of working cycles of engine and model interpolation errors.

Based on the defined functions, three sensor faults (throttle angle sensor, air mass flowmeter, manifold pressure sensor or manifold leakage) can be detected. The engine speed sensor is not diagnosed, because it is monitored in other systems e.g. in the ABS system.

3. Model identification

To find the functions described in (5–7), a steady state experiment was performed. Investigations were conducted on the passenger car Mitsubishi Carisma with four-cylinder spark ignition engine of a gasoline direct injection (GDI) [20]. The solutions applied in this vehicle such as a design and engine equipment are commonly used in the automotive market. This substantiates the assumption as to the universality of the conclusions and trends resulting from the investigations. The car was positioned on a chassis dynamometer. It is possible to brake a vehicle with the given moment on wheels, or accelerated to the given speed. In such way the vehicle engine was loaded to the required and simultaneously constant speed *n* at various throttle openings α.

Tests were based on recording signals in 10-seconds stretches from selected sensors of the engine at stationery operation. Recording was performed by the computer system of collecting data consisted of the computer with the measuring equipment OCTOPUS CompuScope 8380 of the GAGE Company. This device allows sampling of all signals with a frequency from 1kHz to 10MHz and the resolution of 14 bits. The following voltage signals were recorded:

– crankshaft position sensor
– camshaft position sensor
– mass airflow (MAF) sensor
– throttle valve position (TPS) sensor
– manifold absolute pressure (MAP) sensor – an additional sensor not used as a standard in this car
– output signal of the analyser of the composition of combusted mixture, MEXA700λ of the HORIBA Company

In addition, temperatures of the liquid cooling the engine and of the sucked-in air were recorded, for each stationary engine operation point.

Tests were carried out for 9 equally spaced engine speeds (1000 to 5000 rpm) and throttle positions: 6-26% (without load), 34%, 53%, 70%, 83-87%, 90-100%. The throttle angle was expressed in percentages, where 0 means the total closing and 100% the total opening of the throttle. Since signals were recorded in steady states the average values of the above signals were determined for each second of the recording, it means 10 values for the given point (n, α).

The surfaces described by equation (5–7) are presented in Fig. 3, together with the marked measuring points.

To represent the functions f_1, f_2 and f_3, the interpolation in the maps or polynomial equations can be used. The identification quality of models was characterised by root mean squared errors.

a)

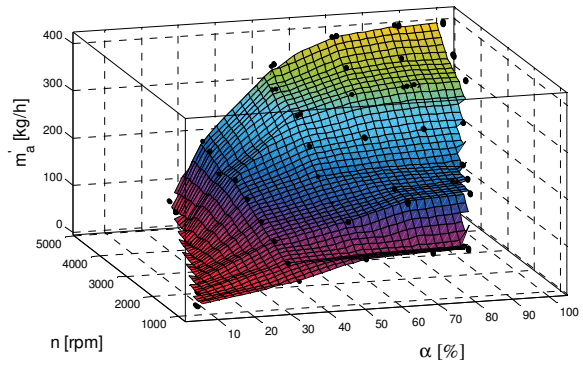

b)

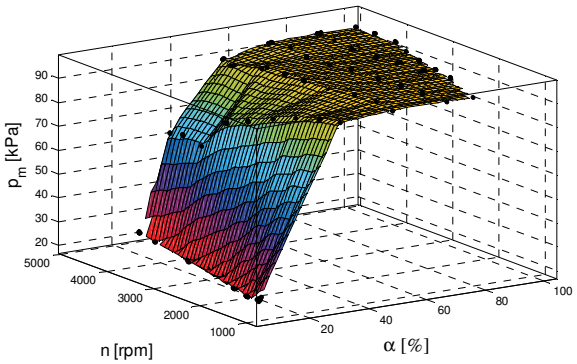

c)

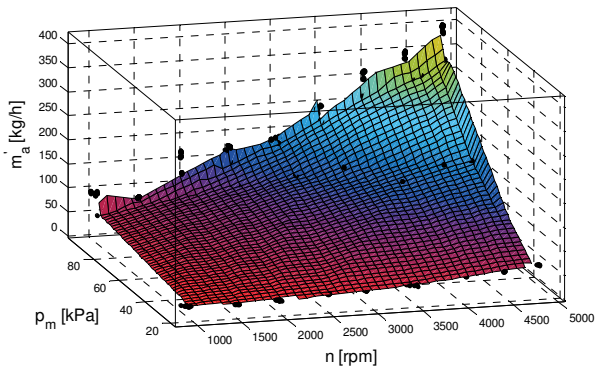

Fig. 3. Functions used in diagnostic model

4. Model validation

To validate the model, measurements and calculation procedures were repeated for three simulated faults:

1. Air mass flowmeter fault caused by chocking the part of the flow channel, from the air filter side.
2. Throttle angle sensor fault caused by characteristic change that occurring e.g. in a situation of wetting the electrical installation or sensor flooding.
3. Manifold air leakage.

In all these situations the on-board diagnostics (OBD) system did not record an error, while the user could notice the change in the engine operation in a form of roughness or a power loss at higher rotational speeds of the engine.

The throttle position sensor, the mass air flow sensor and the rotational speed sensor are installed as a standard in the tested engine. Whereas the manifold absolute pressure sensor was installed additionally in the intake manifold for diagnostics aims.

4.1. Fault of air mass flowmeter

Partial obscuration of the intake manifold has caused flow disturbances and malfunction of the Karman vortex air mass flowmeter. Large fluctuations in air mass index caused a oscillations in fuel dose and consequently uneven working of the engine. Consequently, this resulted in uneven rotational speed and variations in mixturecomposition (Fig. 4).

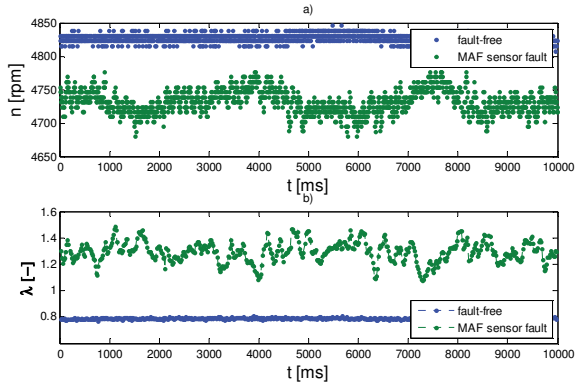

Fig. 4. Instantaneous values of a) engine speed and b) lambda coefficient, for fault-free and MAF sensor fault states at 85% throttle opening and 4800 rpm

The indicated flow is so small that the engine changes into supplying by a very lean mixture (recorded air-fuel ratio $\lambda > 1$). The adaptive control system will try to adjust the fuel dose based on the lambda sensor indication. Average air mass flow rate values are lower than at fault-free operation.

Fig. 5 shows the results of the measurements of intake manifold pressure and the mass air flow for the described failure at 85% of the throttle opening.

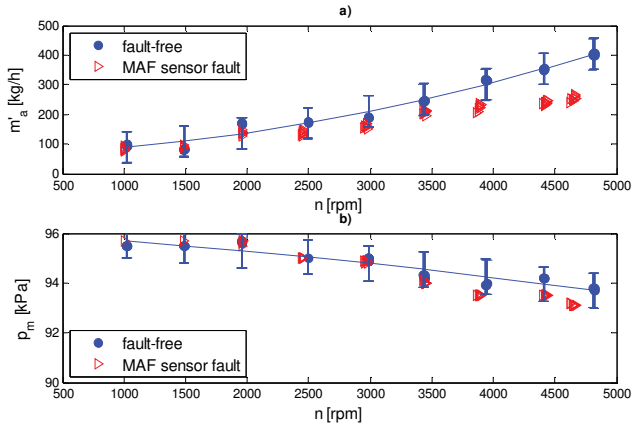

Fig. 5. Comparison of sensors indications for two states: fault-free and MAF sensor fault at throttle opening 85% a) MAF sensor, b) MAP sensor

Pressure in the intake manifold is within error limits of the model, while the mass air flow is lower than it results from the model for the whole range of engine loads.

4.2. Fault of throttle position sensor

In the second case – characteristic changes of the throttle angle sensor (Fig. 6) – the fault was simulated by bypassing the output of the second throttle channel with the resistor of 5.57 kΩ. This can correspond to the situation when the sensor is flooded or electrical installation wetted. A careful car user feels it as a small power decrease of the engine.

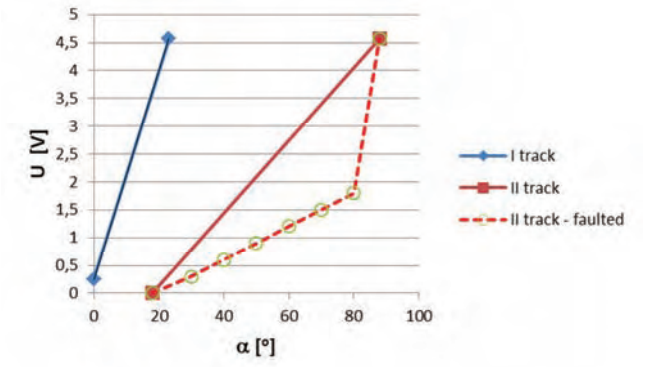

Fig. 6. Change of TPS characteristics caused by fault

Fig. 7 shows the results of measurements of the intake manifold pressure and the mass air flow for the described failure at 50% of the throttle opening. In this case, in a range of medium loads and high rotational speeds ($n > 4000$ rpm), a significant increase of signal indications from the pressure sensor as compared with the model sensor is observed, as well as a decrease of the mass air flow sensor indications as compared with the model.

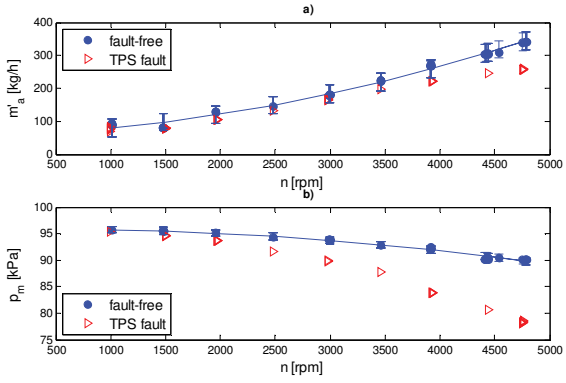

Fig. 7. Comparison of sensors indications for two states: fault-free and throttle position sensor fault at throttle opening 50% a) MAF sensor, b) MAP sensor

4.3. Leakage of the intake manifold

The third case constitutes air leakage of the intake manifold, which can cause such effects as: hissing noise, engine stumbling, rough or fast idling or stalling, poor gas mileage. Tests were performed at the small leakage, at which the onboard diagnostics system did not record any error. The mass air flow indicated the correct value, while the pressure sensor indicated underrated value as compared with the corresponding model, especially in the range of high loads.

Fig. 8 shows the results of measurements of the intake manifold pressure and the mass air flow for the described failure at 85% of the throttle opening.

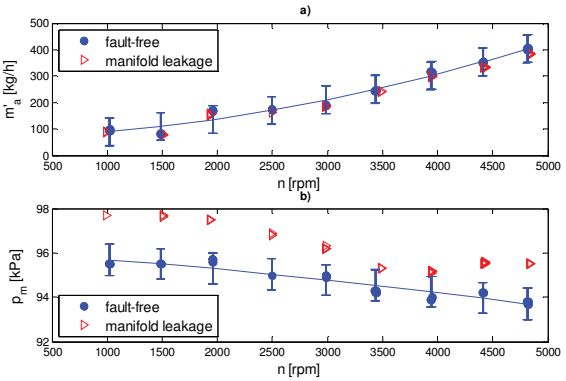

Fig. 8. Comparison of sensors indications for two states: fault-free and manifold leakage at throttle opening 85% a) MAF sensor, b) MAP sensor

The manifold pressure signal values in this case are larger than in fault-free state for all engine speeds, while the air mass values remain the similar. The fuel injection control of the tested engine is based on indications of MAF sensor. In this case the adaptive control system will try to adjust the fuel dose based on the lambda sensor indication.

4.4. Residuals analysis

During simulation of the model three residuals r_1, r_2, r_3, described with equations (8–10) are generated. It can be created multiple residuals, but in this simple example they do not provide any new information.

Residuals should be generated for several operation points at stationary condition. Fig. 9 shows the relationship between three indications describing the engine load: throttle position α, manifold pressure p_m and air mass flow rate $\dot{m}_a$ for engine speed n = 4500 rpm.

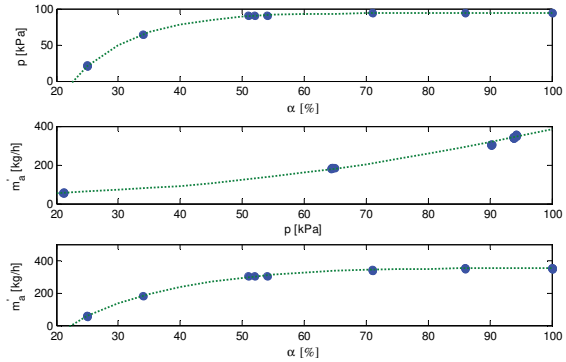

Fig. 9. Relationship between throttle position, manifold pressure and mass air flow for GDI engine at engine speed n = 4500 rpm

The simulation was performed for four states: fault-free, MAF sensor fault (fault 1), TPS sensor fault (fault 2), manifold air leakage (fault 3). It was assumed that only one fault can occur at the same time. For one selected engine operating point (n = 4500 rpm, α = 85%), the simulated results with measurements were compared (Fig. 10). Averaged values of manifold pressure signal and air mass flow rate signal were compared with the outputs of the model i.e. functions f_1, f_2, f_3 described in the equations (5–7).

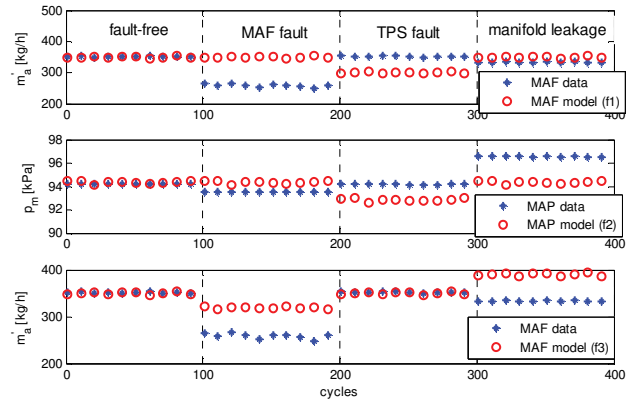

Fig. 10. Comparison of results of model simulation and measured data for four states of air intake system at 85% opening position of throttle valve and engine speed 4500 rpm

The residuals described in the formulas (8–10) were calculated and residual indicators described in formula (11) were summarised in Table 1.

Table 1. Residual indicators

	n = 4500 rpm, α = 85%			
Parameter	fault-free	MAF fault	TPS fault	manifold leakage
R1	0	1	1	0
R2	0	0	1	1
R3	0	1	0	1

The residuals takes two states: 1 means that the difference between data end model output surpasses the value of model uncertainty and 0 means that the difference lies within the limits of model error. In the simple case only three residuals are sufficient.

5. Conclusions

The article proposes the model-based method of diagnosing faults in the air-intake control system of engine not diagnosed by Mitsubishi Carisma OBD system. Incorrect measurement of airflow, change of throttle position sensor characteristics and leakage in intake manifold were tested. Based on simulation, residuals were generated.

The diagnostic method described here is based on measurements of all three physical quantities, which are a measure of the load on the engine: mass air flow, manifold pressure and throttle angle.

However, only two sensors are commonly installed in cars. In Mitsubishi throttle angle and mass air flow are measured. Based on measurements from two sensors, function f_3 cannot be determined. However, the TPS sensor error can be ruled out by comparing its indication with the second redundant TPS sensor.

This method has been verified for steady-state operation of the engine and illustrated for one operating point of engine. The residuals generation should be repeated for several steady-state operation condition (different rotational speeds and loads), as errors are not always reflected in measurements. Defect can be detected if the corresponding residuum is greater than the uncertainty of the model.

Nomenclature

SI spark ignition
GDI gasoline direct injection
MAP manifold absolute pressure
MAF mass air flow
TPS throttle position sensor
ABS anti-lock breaking system
OBD on-board diagnostics
α throttle position
n rotational speed of engine
p_m manifold pressure
$\dot{m}_a$ air mass flow rate

Bibliography

[1] AHMED, Q., BHATTI, AI., KHAN, Q., RAZA, M. Condition monitoring of gasoline engine air intake system using second order sliding modes. *International Journal of Vehicle Design*. 2013, **62**(2-4), 312-332.

[2] DĄBROWSKI, Z., MADEJ, H. Masking mechanical damages in the modern control systems of combustion engines. *Journal of Kones Powertrain and Transport*. 2006, **13**(3), 53-60.

[3] DĄBROWSKI, Z., ZAWISZA, M. Investigations of the vibroacoustic signals sensitivity to mechanical defects not recognised by the OBD system in diesel engines. *Mechatronic Systems, Mechanics and Materials. Solid State Phenomena*. 2012, **180**, 194-199.

[4] DUTKA, A., JAVAHERIAN, H., GRIMBLE, M. Model-based engine fault detection and isolation. *Proceedings of American Control Conference*. ACC '09. 2009, 4593-4600.

[5] FIGLUS, T., KONIECZNY, Ł., BURDZIK, R., CZECH, P. Assessment of diagnostic usefulness of vibration of the common rail system in the diesel engine. *Vibroengineering PROCEEDIA*. 2015, **6**, 185-189.

[6] FRANCHEK, M.A., BUEHLER, P.J., MAKKI, I. Intake air path diagnostics for internal combustion engines. *Journal of Dynamic Systems, Measurement and Control*. 2007, **129**(1), 32-40.

[7] GUZZELLA, L., ONDER, C. Introduction to modeling and control of internal combustion engine systems. *Springer*, ETH Zurich 2004.

[8] HERNER, A., RIEHL, H.J. Elektrotechnika i elektronika w pojazdach samochodowych. *WKiŁ*, Warszawa 2013.

[9] HEYWOOD, J.B. Internal Combustion Engine Fundamentals. *Mc-Graw Hill,* New York 1988.

[10] ISERMANN, R. Model-based fault-detection and diagnosis – status and applications. *Annual Reviews in Control*. 2005, **29**, 71-85.

[11] JONGENEEL,J., NIJMEIJER, H., MANZIE, C., NESIC, D. Input redundant internal combustion engine with linear quadratic Gaussian control and dynamic control allocation.

Internal Report. Eindhoven University of Technology, Eindhoven, Netherlands 2009.
[12] KIENCKE, U., NIELSEN, L. Automotive control systems. For engine, driveline, and vehicle. *Springer-Verlag*, Berlin Heidelberg 2005.
[13] KOMORSKA, I., PUCHALSKI, A. On-board diagnostics of mechanical defects of the vehicle drive system based on the vibration signal reference model. *Journal of Vibroengineering*. 2013, **15**(1), 450-458.
[14] MERKISZ, J., MAZUREK S. Pokładowe systemy diagnostyczne pojazdów samochodowych. *WKiŁ*, Warszawa 2006.
[15] MERKISZ, J., PIELECHA, J., RADZIMIRSKI, S. New trends in emission control in the European Union. *Springer* 2014.
[16] NYBERG, M., NIELSEN, L. Model based diagnosis for the air intake system of the SI-engine. *SAE Technical Paper*. 1997, 970209.
[17] NYBERG, M. Model-based diagnosis of an automotive engine using several types of fault models. *IEEE Transactions on Control Systems Technology*. 2002, **10**(5), 679-689.
[18] PUCHALSKI, A., KOMORSKA I. Online fault diagnosis of automotive powernets by kalman filtering. *Key Engineering Materials*. 2014, **588**, 209-213.
[19] WENZEL. T.A., BURNHAM, K.J., BLUNDELL, M.V. Kalman filter as a virtual sensor: applied to automotive stability systems. *Transactions of the Institute of Measurement and Control*. 2007, **29**(2), 95-115.
[20] WOŁCZYŃSKI, Z., KOMORSKA, I., BORCZUCH A. Wpływ uszkodzeń w układzie dolotowym powietrza na sterowanie silnikiem spalinowym. *Autobusy – Technika, Eksploatacja, Systemy transportowe*. 2016, **17**(12), 1487-1490.

Iwona Komorska, DSc., DEng. – Faculty of Mechanical Engineering at University of Technology and Humanities in Radom.

e-mail: *Iwona.Komorska@uthrad.pl*

Artur Borczuch, MEng. – Faculty of Mechanical Engineering at University of Technology and Humanities in Radom.

e-mail: *A.Borczuch@uthrad.pl*

Zbigniew Wołczyński, DEng. – Faculty of Mechanical Engineering at University of Technology and Humanities in Radom.

e-mail: *Z.Wolczynski@uthrad.pl*

Article citation info:
KOŁODZIEJ, S., LIGUS, G., MAMALA, J., AUGUSTYNOWICZ, A. Analysis of air flow velocity distribution in the intake system of an SI engine. *Combustion Engines*. 2017, **169**(2), 152-157. DOI: 10.19206/CE-2017-227

Szymon KOŁODZIEJ
Grzegorz LIGUS
Jarosław MAMALA
Andrzej AUGUSTYNOWICZ

CE-2017-227

Analysis of air flow velocity distribution in the intake system of an SI engine

The conditions of air flow in the intake determine power generated by the engine to a large extent. The biggest resistances in flow of the air sucked or pumped into the engine are generated by the throttle, which is at the same time the main component which allows for regulation of engine power. For the purpose of research conducted in this work, time density of engine work points in analyzed velocity profiles was determined with the use of Engine Road Load Simulator. Thanks to the knowledge of time velocity, it was possible to determine throttle positions at which the engine operates most frequently. With the use of image analysis methods, obtained parameters were experimentally researched, considering flow disturbances which are the effect of air flow through the throttle and uneven air distribution in the intake manifold of a four-cylinder engine.

Key words: *intake manifold, PIV, flow, throttle, filling ratio*

1. Introduction

The air flow process in the IC engine intake system affects the cylinder filling ratio, therefore affecting its performance. Power is one the main operation indicators of modern engines, and efforts to increase it are constantly undertaken. The main ways of obtaining more engine power are: getting more fresh air to the cylinders by increasing the air pressure in the manifold, lowering air temperature and minimizing flow resistances in the intake manifold. In a multi-cylinder engine it is also important to evenly distribute the air between cylinders. In IC engines where the fuel dosing system is situated at the beginning of the intake system (i.e. carburetors or Single Point Injection), uneven air supply results in uneven engine operation. In newer designs, equipped with Multi Point Injection systems, fuel is delivered separately to each cylinder, however its distribution is based on the measured air flow for all cylinders. In such cases, the uneven air distribution results not only in uneven engine operation, but also in increased harmful substance emissions, including carbon dioxide. The application of newest technologies, such as broadband lambda sensors (two per one cylinder in 4-2-1 exhaust systems) partially solves this problem. However, this design can naturally be implemented after the combustion process already took place. Moreover, in most cases a single, narrow-band lambda sensor is used. The main source of information about the quality of a combustion process is the quantity of free oxygen contained in exhaust gasses. The fuel dosage is adjusted so that a stoichiometric fuel-air ratio (λ = 1) is maintained. This means that the air-fuel ratio computed by the ECU is a mean value for all cylinders. Despite proper mean value of air-fuel ratio, a situation where lean burning occurs for some cylinders and rich burning occurs for the other ones.

Maintaining a stoichiometric air-fuel ratio for all cylinders on an IC engine is a challenge for many automotive research and science centers. One of the main solutions to this problem is an intake manifold designed with the following factors in mind:

1. Ensuring an even filling ratio for all cylinders,
2. Measure the mass of air delivered to each cylinder separately,
3. In the future- to use separate pressure sensors for each cylinder, which will allow to implement corrections in fuel dosage, taking into account both to engine operating parameters and engine wear.

In this work the authors on researching the phenomenon of air distribution in the intake manifold of an IC engine were focused.

2. Scope of research

The experimental research conducted on a real-life object are time consuming and costly. A way to reduce research costs and time is to implement simulation techniques. In the Chair of Road and Agricultural Vehicles at Opole University of Technology, a Road Engine Load Simulator was conceived. It utilizes a virtual engine, saved in a numerical form in computer memory, which allows for realization of simulation of drive cycles. Such simulations allow to facilitate recognition of key operating points in the scope of engine operating characteristics.

The main indicator of IC engine operation used by car manufacturers is the engine power, which in many cases exceeds 70 kW. However, power utilization in real-life driving conditions is significantly lower, rarely reaching the maximum value of engine power- which only occurs during very intense accelerations and near maximum vehicle speed.

Observation of simulation results shown on graphs in Fig. 2 it can be seen that mean power utilization for city driving cycles does not exceed 30 kW, being only slightly larger for out-of-city driving cycles, namely under 50 kW.

Management of engine power is realized mostly by means of lowering or increasing the cylinder filling ratio, which is possible due to changes in throttle position angle. Especially in SI engines, low filling ratio values are obtained for fully closed or only partially opened throttle. For researched driving cycles, it is possible to determine throttle operation points at different engine speeds which result from drivetrain operating conditions. Most densely occupied areas in Fig. 1 show most frequent engine operation fields during simulated driving cycles.

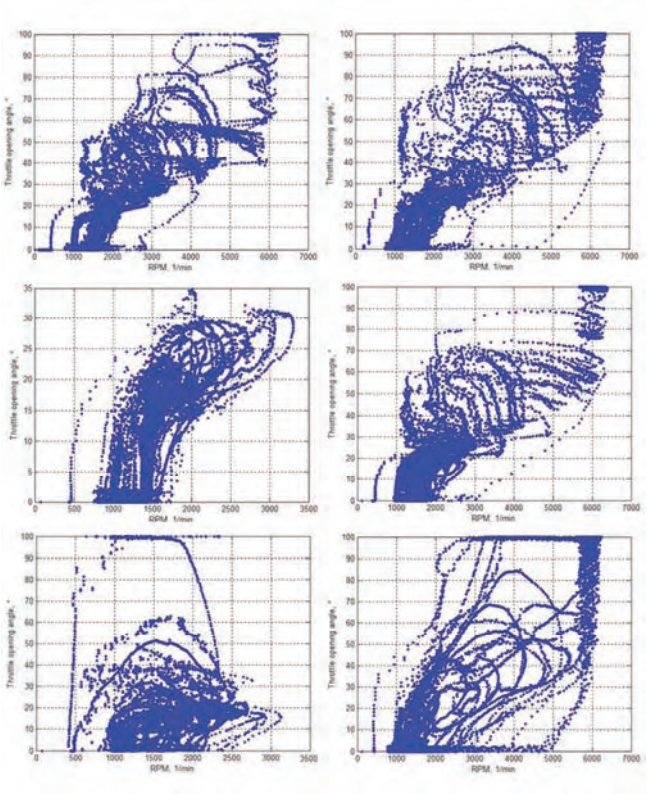

Fig. 1. Engine operation point density during realization of chosen driving cycles

The analysis of graphs presented in fig. 1 shows that the greatest density of engine operation points occurs at 10°, 20° and 30° throttle position and engine speeds of 1500 and 2000 RPM.

Each throttle position value for specific engine speed has a corresponding specific values of cylinder filling ratio, which is shown in Fig. 3.

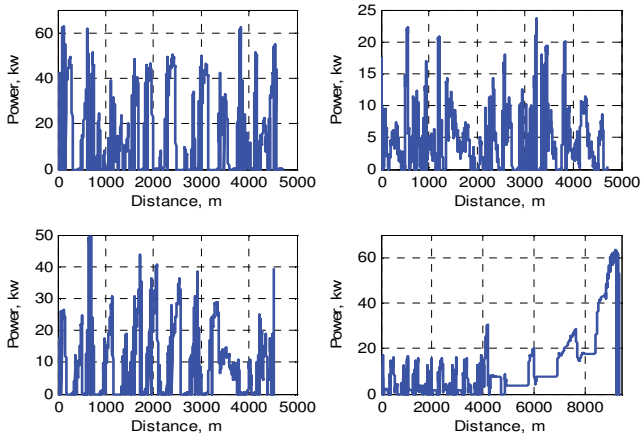

Fig. 2. Utilization of engine power during realization of chosen drive cycles

Despite the relations not being linear, it is clearly noticeable that with the increase in throttle position angle, filling ratio also increases. Biggest differences can be noted for throttle position angles between 0 and 45 degrees, while they are not so significant between 45 and 90 degrees.

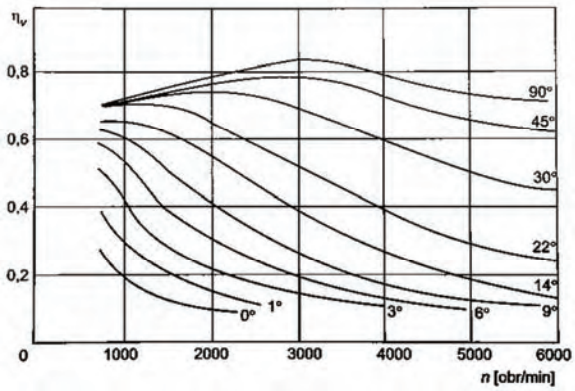

Fig. 3. Characteristics of cylinder filling ratio in relation to throttle inclination and engine speed [8]

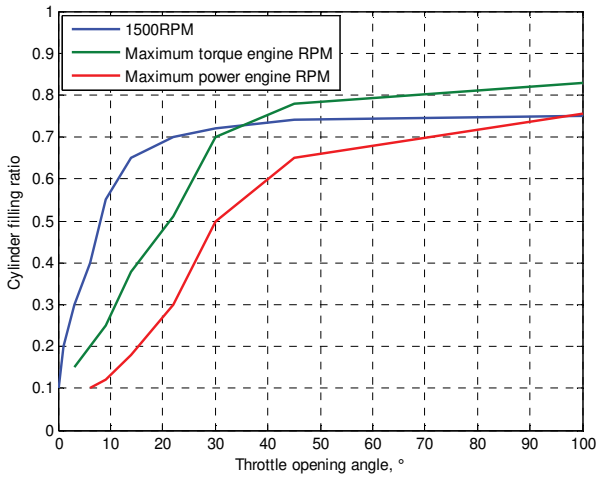

Fig. 4. Characteristics of cylinder filling ratio in relation to engine speed for chosen throttle repeal angles

By reading data from Figs 3 and 4, it can be inferred that the lower throttle position values have the biggest role in engine power management- this is especially evident in Fig. 4. At higher throttle position angles, the effect is not so prominent. This confirms the earlier observation, that engine operation points occurring at 10°, 20° i 30° throttle position and engine speeds of 1500 and 2000 RPM should be subject to further analysis.

For chosen parameters the amount of air flowing through the intake system was computed, taking into account the corresponding cylinder filling ratios.

$$V = V_s \cdot n \cdot 60 \cdot 2\,, \qquad (1)$$

where: V – volume of air, V_s – engine capacity, n – engine speed.

Table 1. Volume of air flowing through the intake at chosen operating points

	1500 RPM	2000 RPM
10°	37 m^3/h	40 m^3/h
20°	49 m^3/h	60 m^3/h
30°	52 m^3/h	71 m^3/h

3. Digital Particle Image Velocimetry

The literature study on the subject of an intake manifolds shows that most of the research is based on computer

simulations. The analysis of multiphase flow research methods has led the authors to conclude that it is possible to conduct experimental research of engine intake manifold through the use of DPIV (Digital Particle Image Velocimetry) method. The DPIV method relies on registering flow phenomena with the use of laser light sheet technique, for visualization of velocities vector fields, as shown in fig. 5. Lasers of different kinds (both constant and impulse-operating) are used as light sources. The use of laser light sheet technique allows to obtain a camera view area within a single chosen plane. In most cases of DPIV application, for calculation of the velocity vector field is also necessary to introduce additional inert seeding particles into circulation.

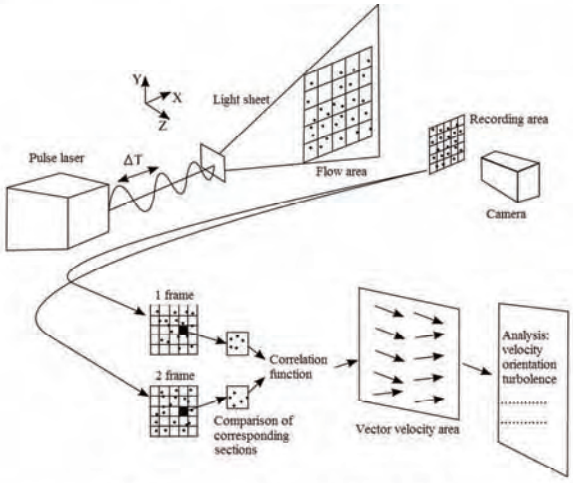

Fig. 5. Measurement scheme of DPIV method [11]

A video camera registers a series of images of flow area illuminated by the laser at a specified frequency and recorded images in double frame technology. In this technology every single image consists of two frames of image, separated by a time interval ΔT called the Time Between Pulse (TBP). Obtained images are being analysed in the aspect of changes the concentration of seeding particles suspended in the flowing gas. The result is that the seeding particle distribution from the first image is recognize in the second one, as shown in fig. 6. To find a mean seeding particles translation value, a Cross Correlation Function (CCF) method is used. Those computations are done according to Wiener-Kinchin law, which states that autocorrelation and power spectral density are equal to each other and linked by Fourier transform, given by equation below [5].

$$F(i,k) = \beta_O \sum_{m=0}^{M-1} \sum_{n=0}^{N-1} O(m,n) \exp\left(\frac{-j2\pi mi}{M}\right) \exp\left(\frac{-j2\pi nk}{N}\right) \quad (2)$$

for m = 0,1,…, M–1; n = 0,1,…, N–1
where:

$$O(m,n) = \beta_F \sum_{i=0}^{M-1} \sum_{k=0}^{N-1} F(i,k)_O \exp\left(\frac{j2\pi mi}{M}\right) \exp\left(\frac{j2\pi nk}{N}\right) \quad (3)$$

for i = 0,1,…, M–1; k = 0,1,…, N–1

$$\beta_O \cdot \beta_F = \frac{1}{M \cdot N} \quad (4)$$

The researched plane is divided into squares of known dimensions for the purpose of analysis. It is recommended to use sections of 32 x 32 pixels, assuming the translation of researched particles is no bigger than 33% of the analyzed square [9]. It is considered a good practice to run an initial research with the aim of estimating image capture time before beginning the main course of research. The assumption of excessively long image capture time would result in the seeding particle moving too far to be noticed by the computation algorithm, whereas a too short timespan would mean that the seeding particle would not change its position in the researched square. A correct choice of image capture time to be as short as possible while allowing the seeding particle to move, drastically increases measurement accuracy.

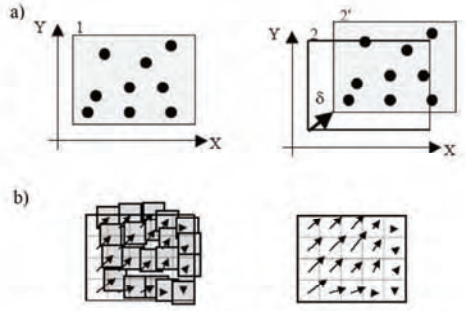

Fig. 6. (Division of captured images into sections - research ares and designation of movement vectors for each section. 1-image section 1, 2-image section 2, 2'image sections 1 found in section 2 δ-translation of section 2' in relations to section 1, conversion of translations to velocity vector field) [10]

Before captured images can be subject to verification by the DPIV algorithms mentioned above, it is recommended to carry out a series of image processing with the use of graphics software. In a situation where the area of interest does not fully fill the camera view area it is recommended to apply an image mask, which will exclude unwanted areas from the recorded image. Next, every pair of recorded images is subject to geometrical analysis, which searched for areas of pixel concentration that are constant in position (creation of background image). The generated background image is subtracted from all raw images of the recording session. The effect of this subtraction is a new series of images which show only moving seeding particles in interest area. Measurements which are prepared in such a way lower the risk of occurrence of hiss caused by uneven lighting etc. Generation of image depicting the flow of seeding particles which is free of interruptions requires capturing a series of images, conducting full calculations for each image, and then averaging of obtained results.

4. Experimental setup for research of phenomena in the intake manifold

To understand the real-life phenomena occurring in the intake, a series of experiments was conducted, utilizing a modified intake manifold from a Volkswagen 9A engine. The manifold was modified in a way that retains its original

geometry while allowing for the use of DPIV method. Front wall along with two side walls was removed to allow the use of the laser light sheet technique for flow visualization with the use of a camera. To ensure airtightness of the system, the missing walls were replaced with components made of transparent plastic. Flow direction consistent with real engine operating conditions was forced with the use of Helios MVZ315 fan, which sucked the air out of the manifold. The quantity of the air flowing through the system was regulated with the use of fan speed regulator and engine throttle mounted in its original position on the manifold. To preserve flow conditions similar to an on-engine situation, a stock intake pipe was installed before the throttle. Laser light sheet with the use of Nano L 200-15 PIV 1200mJ Laser produced by Litron Lasers was generated. A Dantec Dynamics FlowSense EO 4M camera perpendicularly to the laser light sheet was placed. Engine operating parameters and corresponding with them flow parameters chosen in previous chapters of this research, required specific TBP. Applied TBP value for each measuring series on volume of air and throttle position angle were depended. In the research the following values of TBP were finally adopted: for throttle position angle equal to 10 degrees and both values of volume of air assumed TBP equal to 60 µs, for others throttle position angle TBP only on the volume of air were depended and were respectively 40 µs (for 49 and 52 m^3/h) and 60 µs (for 60 and 71 m^3/h). Each double frame image in the measurement series with 10 Hz frequency were captured.

A Flow Visualization Components R700CE Flow Tracker which generates seeding particles of 2÷5 µm diameters was placed near the air inlet of the system. Aerosol of the Di-Ethyl-Hexyl-Sebacat (DEHS) was used as seeding particles for DPIV method.

Series of trials with the aim of determining a needed amount of seeding particles were carried out. The purpose was to determine an optimum outflow pressure from the Lasskin nozzle in the flow tracker to ensure a proper concentration of seeding particles in captured images of flow.

For better mixing of seeding particles with the drawn in air, a two-meter long circular pipe was installed before the intake manifold. A Siemens VDO 5WK97002 Mass Air Flow sensor was installed at the half of intake length to ensure a proper amount of the air flowing through the system. In the research all image analysis were carry out with the use of Dantec Dynamics Dynamic Studio 4.1 software.

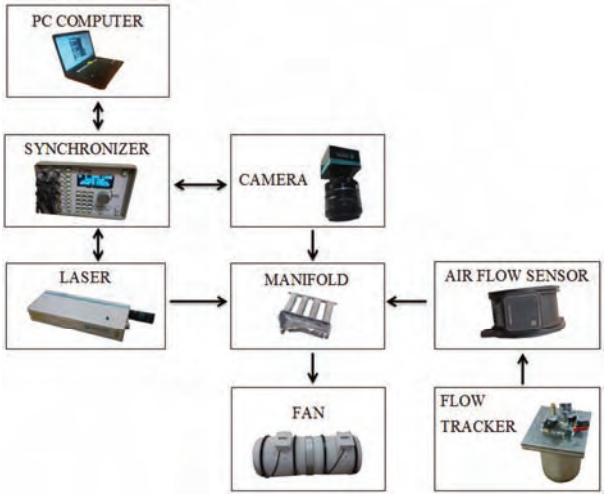

Fig. 7. Scheme of experimental setup

5. Research results

According to the DPIV method described in the chapter 3, it is assumed that the seeding particles move identically to the flowing air through the manifold. Therefore Velocity vector field generated by the computational algorithm illustrate real air flow through the investigated intake manifold (Fig. 8). Consequently colored vectors depict velocity and movement direction of air flow in manifold. The research describes the flow of medium in a plane corresponding to the center of intake canals distributing air to the cylinder head. It is common to use this localization for DPIV imaging [2, 4]. Some elements of the intake manifold made of original material (aluminum) reflected the laser light sheet, which significantly interfered with the research. In the effect reflecting green laser beam caused noise in those areas.This resulted in measurements being disturbed in the areas where the air flow is slower. Usual in such cases attenuation by shifting the histogram of the brightness of the image would become a barrier that would prevent recognition of the seeding particles at the present lower limit of brightness. For this reason, during the analysis an

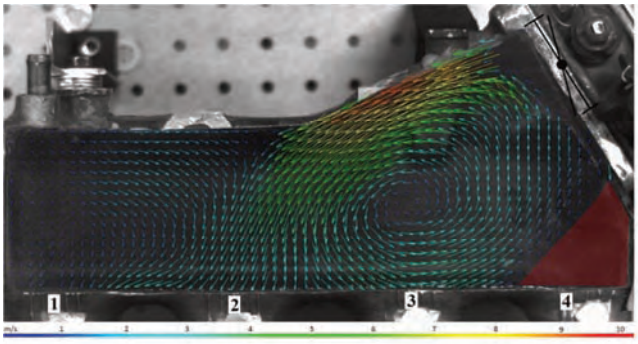

Fig. 8. Velocity vector distribution and air flow direction in the intake manifold at 1500 RPM engine speed and 10° throttle position angle

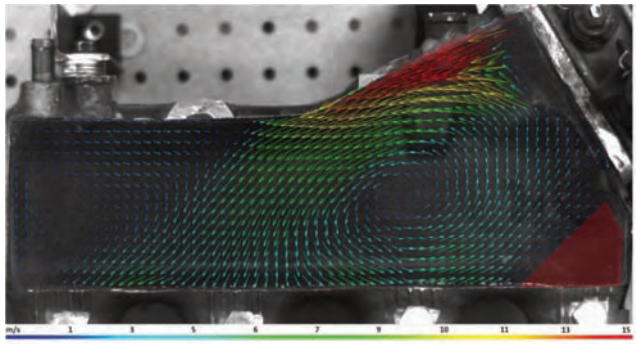

Fig. 9. Velocity vector distribution and air flow direction in the intake manifold at 2000 RPM engine speed and 10° throttle position angle

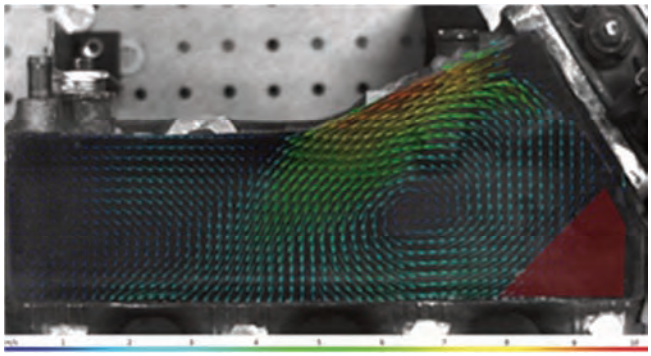

Fig. 10. Velocity vector distribution and air flow direction in the intake manifold at 1500 RPM engine speed and 20˚ throttle position angle

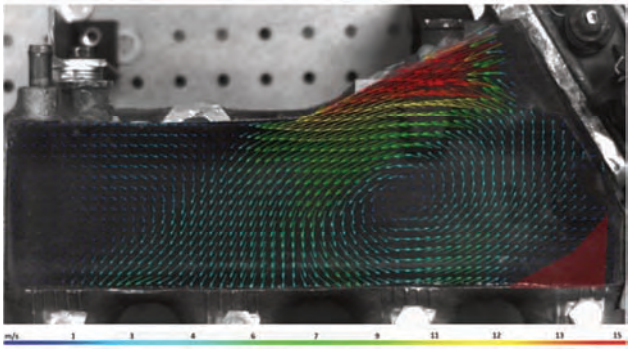

Fig. 11. Velocity vector distribution and air flow direction in the intake manifold at 2000 RPM engine speed and 20˚ throttle position angle

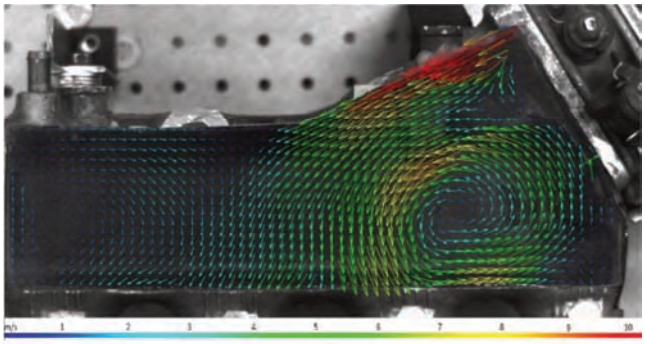

Fig. 12. Velocity vector distribution and air flow direction in the intake manifold at 1500 RPM engine speed and 30˚ throttle position angle

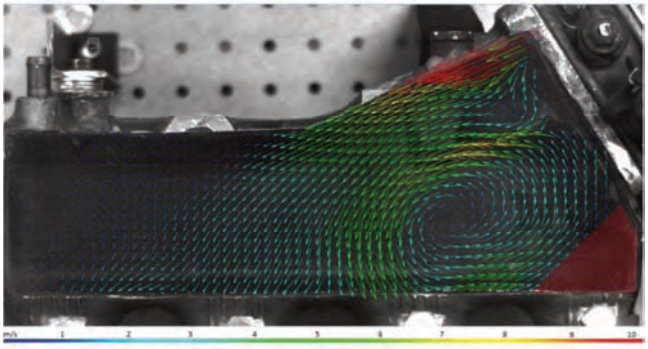

Fig. 13. Velocity vector distribution and air flow direction in the intake manifold at 2000 RPM engine speed and 30˚ throttle position angle

additional image mask was used. Image masking process had to be erased flawed areas in the DPIV computations algorithm. The procedure was also done in Dynamic Studio 4.1 software. The areas with errors resulting from such state of things were marked red in Figs 8–13. Markings used in the later parts of this work are shown in Fig. 8, which also naturally refer to Figs 9–13. By observing vector fields depicted in Figs 8–13, it can be clearly seen that for all of research parameters, significant whirl occur in the air collecting part of the intake manifold. It can be inferred that this adversely affects the air filling ratios of cylinders 1 and 4. For each researched case, biggest flow velocities occurred near the upper wall of the manifold, directly behind the throttle. It is assumed that this unevenness in flow between the sides of the throttle can be the effect of the air eddying in the original intake pipe placed before the throttle mechanism. The ejecting effect of the air particles moving with high velocity causes suction of the air flowing through the other side of the throttle plate and affects the formation of whirl visible above the inlets to cylinders 3 and 4. A clearly visible flow at both sides of the throttle is present only for throttle position angles of over 30 degrees.

It can be noticed that at these parameters the whirl diameter is significantly lower, as are flow velocity differences above inlets to cylinders 3 and 4.

It was seen that for each of the analyzed cases, the whirl formation also occurs in a part of the manifold situated at the opposing end of the throttle mechanism.

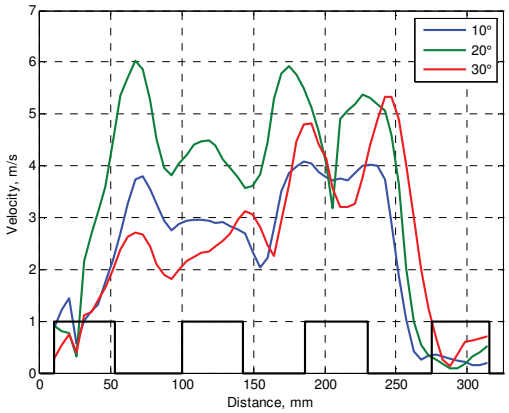

Fig. 14. Air velocity profiles in the manifold outflow plane for different throttle position angles at 1500 RPM

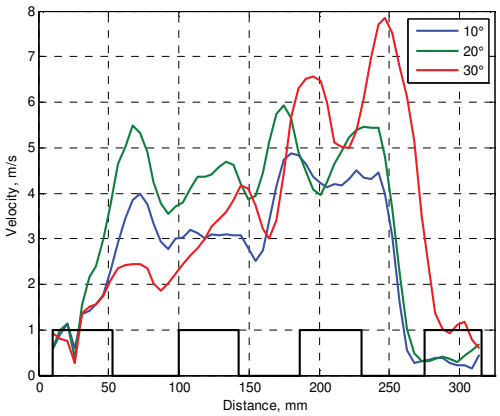

Fig. 15. Air velocity profiles in the manifold outflow plane for different throttle position angles at 2000 RPM

This results in air movement along the manifold walls in a direction opposite to the air stream entering the inlet. Therefore it can be concluded that redesigning the original intake pipe section (mounted before the throttle) and the section situated at the opposing end of the throttle mechanism would result in an improvement in this situation.

Figs. 14 and 15 shows experimentally obtained air velocity profiles for select engine speeds and throttle positions occurring just above the row of inlet canals of the manifold.

Black outlines drawn at the lower part of graphs schematically depict manifold shape while retaining real scale in X axis. Lines situated at value of 1 at velocity axis show the location of air outlet, while the remaining space corresponds to places where baffles between inlets are situated.

Highest velocities at manifold outlet areas for 1500 RPM engine speed occur at throttle position angle of 20 degrees, and highest inflow speeds were noted for cylinder 3. However, it has to taken into account that this velocity is the resultant velocity of inflow and whirl velocities.

Flow velocities obtained for 2000 RPM are characterized by bigger variations in value between cylinders and retain similar tendencies for all throttle positions. It is interesting that velocities of air particles are higher near inlet canal baffles, where the air flows between them, than at the manifold outlets. It is possible that redesigning outlet shapes would result in an improvement in air outflow conditions.

6. Summary

Both simulation and experimental results have shown that point of maximum engine power and torque are not the most commonly utilized engine working parameters.

DPIV technique is very sensitive to any neglect and inaccuracies that can occur during the course of research. Meticulously preparing the experimental setup in a way to provide as even lighting as possible without causing unnecessary flashes, as well as the need to experimentally verify image capture parameters multiple times for each flow velocity has elongated and complicated the whole research process. However, conducted measurement have shown that it is possible to use the DPIV technique for examination and analysis of engine intake manifold. The obtained results have shown significant differences in air distribution between cylinders. Variations in fresh air supply between cylinders can result in different values of air excess factors, therefore causing elevated harmful substance emissions to the environment.

The conducted research depicts free air flow through the intake manifold. They do not however fully show the real conditions of forced air flow in IC engines. Air momentum forced by the fan does not cause pulsations, which occur in real-life conditions due to piston operation and pulsating nature of valvetrain operation.

It can be assumed that shown measurement results give an overall outlook on flow processes in the intake manifold, showing differences in the air flow occurring within it. Conducting the research presented in this work was essential to develop methodology for quantitative and qualitative analysis of air velocity distribution in the intake manifold with the use of DPIV technique.

Bibliography

[1] NIGRO, A., ALGIERI, A., BARTOLO, C.D., BOVA, S. Fluid dynamic investigation of innovative intake strategies for multivalve internal combustion engines. *International Journal of Mechanical Sciences*. 2017**, 123**, 297-310.

[2] BODE, J., SCHORR, J., KRÜGER, C. et al. Influence of three-dimensional in-cylinder flows on cycle-to-cycle variations in a fired stratified DISI engine measured by time-resolved dual-plane PIV. *Proceedings of the Combustion Institute*. 2017, **36**, 3477-3485.

[3] MAMALA, J. The analysis of spark ignition engine short-time supercharging. *Combustion engines*. 2009, 139(4), 3-11.

[4] RABAULT, J., VERNET, J.A., LINDGRENC, B., HENRIK ALFREDSSON, P. A study using PIV of the intake flow in a diesel engine cylinder. *International Journal of Heat and Fluid Flow*. 2016, **62**, 56-67.

[5] BENDAT, J.S., PIERSOL, A.G., Random data: analysis and measurement procedures. 4th Edition. *Wiley, Hoboken*, 2010.

[6] CUPIAŁ, K., DUŻYŃSKI, A., GRZELKA, J. Wpływ pulsacji ciśnienia w układzie dolotowym na rozdział świeżego ładunku w silniku gazowym. *KONES 2000*. Nałęczów 2000, 31-36.

[7] ŚWIĘCICKI, K. Konstrukcja układu dolotowego silnika spalinowego. *Modelowanie Inżynierskie*, **57**, ISSN 1896-771X.

[8] ZAJĄC, P. Silniki pojazdów samochodowych. Podstawy budowy, diagnozowania i naprawy. *WKŁ* 2015.

[9] ADRIAN, R.J., WESTERWELL, J. *Particle image velocimetry*. Cambridge University Press, Cambridge 2011

[10] SUCHECKI, W., ALABRUDZIŃSKI, S. Metoda korekty wykresów pól prędkości w cyfrowej anemometrii obrazowej. *Inżynieria i aparatura chemiczna*. 2003, **42**(34), 3, 14-20.

[11] www.dantecdynamics.com/measurement-principles-of-piv, z dnia 25.02.2017.

Szymon Kołodziej, MEng., – Opole University of Technology.

e-mail: *S.Kolodziej@po.opole.pl*

Jarosław Mamala, DSc., DEng. – Opole University of Technology.

e-mail: *J.Mamala@po.opole.pl*

Grzegorz Ligus, DEng. – Faculty of Opole University of Technology.

e-mail: *G.Ligus@po.opole.pl*

Andrzej Augustynowicz, DSc., DEng. – Opole University of Technology.

e-mail: *A.Augustynowicz@po.opole.pl*

Article citation info:
ROJEWSKI, A., BARTOSZEWICZ, J. Usage of wing in ground effect to maintain lift force with reduced fuel consumption of aircraft. *Combustion Engines*. 2017, **169**(2), 158-161. DOI: 10.19206/CE-2017-228

Adam ROJEWSKI
Jarosław BARTOSZEWICZ

CE-2017-228

Usage of wing in ground effect to maintain lift force with reduced fuel consumption of aircraft

The main purpose of this article was to point out causes of reduced fuel consumption in aircraft jet engine when aircraft is in ground effect influence. Wing in ground effect occurs in the direct proximity of ground. The paper presents wing in ground effect description, with the numerical analysis of NACA M8 airfoil in three different conditions of flight. Numerical analysis was conduct in Ansys Fluent 17.2 software. The paper shows results of simulations which describes wing in ground effect influence on NACA M8 airfoil with two cases of jet engine exhaust gasses usage, first with exhaust gasses stream turns on upper airfoil surface, and second with exhaust gasses stream turns under lower airfoil surface. Results allow to define characteristics of NACA M8 airfoil in the influence of wing in ground effect which are lift coefficient, drag coefficient, drop of fuel consumption usage by the jet engine when lift force remains still in the wing in ground effect. The paper shows that in the wing in ground effect aircraft energy usage for flight in ground effect is smaller than for free air flight.

Key words: *ekranoplan, numerical analysis, fuel consumption, jet engine, energy consumption*

1. Introduction

When regular aircrafts fly at high altitude, there is a special kind which flies in the proximity of a ground. This kind of aircrafts is called "ekranoplan" and thanks to the wing in ground effect it makes great increase of aircraft lift force with reference to traditional aircrafts. WIG effect works in two ways, with positive angles of attack it makes lift force bigger in the proximity of ground, and for negative angles of attack, it makes greater downforce. Thus, WIG effect can be used in aeronautics, but also in automotive. The first ekranoplan was built by Rostislav Evgenievich Alexeyev in 1966, but in F1 WIG effect is present since 1979, where car front wing works in ground effect all the time.

WIG effect formation is simple, the most important factor is to reduce space between aircraft and ground. WIG effect provides to increase static pressure below the airfoil, what leads to the rise of lift force. Also, vortices made by higher pressure below and lower pressure above airfoil in WIG effect moves aside of wing tips, what provides to decrease of resistance and induced drag, also increases effective aspect ratio, what is shown in Fig. 1.

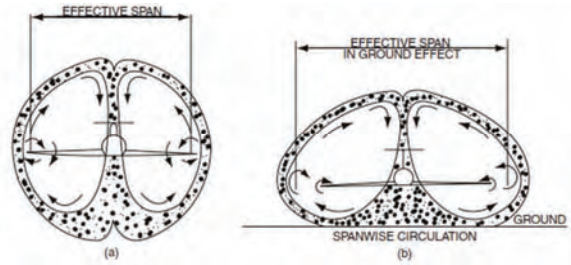

Fig. 1. Mechanism of WIG effect creation [1]

As it was written before, the most important factor, next to the angle of attack, is the height of flight. K.V. Rozhdestvensky [2] determines height coefficient for WIG crafts, this coefficient is the ratio of the height of flight above the sea level and length of airfoil chord. Moore N. [3], in his article about WIG effect wing geometry investigate that best value of height coefficient for WIG flight is 0,1; equation (1) shows height coefficient dependency:

$$\bar{h} = \frac{h}{c} \tag{1}$$

where: $\bar{h}$ – height coefficient; h – height of flight; c – length of airfoil chord.

2. WIG effect airfoil geometry

The most important part of every aircraft are wings, wing in WIG effect should provide high lift force and low drag force, but when aircraft operates in ground proximity airfoil should maximize static pressure under the wing. To choose right airfoil there was done series of numerical simulations for 10 different airfoils geometries [4]. The highest values of lift force were obtained for NACA M8 airfoil. Drag force for this profile was not the lowest one but the ratio of lift coefficient and drag coefficient which defines aerodynamic efficiency is biggest from investigated airfoils. For an optimal angle of attack (6°), when aerodynamic efficiency has the biggest value in WIG effect its value is equal to 16.56. It means that aircraft on 1 km altitude can fly without engines 16.56 km until it touches the ground. To compare regular flight and WIG effect flight, the same airfoil in free stream flight has aerodynamic efficiency equal to 5.15, so it is three times less. Influence of WIG effect is shown in Fig. 2 and in Table 1.

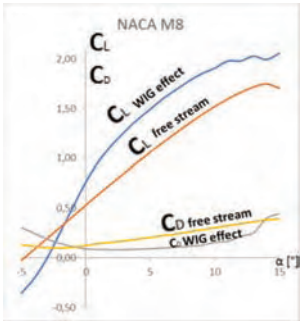

Fig. 2. Characteristics of NACA M8 profile [4]

Table 1. Lift and drag coefficient values for NACA M8 profile [4]

Angle of attack α [°]	Free stream flight lift coefficient	WIG flight lift coefficient	Free stream flight drag coefficient	WIG flight drag coefficient
–5	–0.02	–0.36	0.13	0.31
–4	0.09	–0.21	0.12	0.25
–3	0.2	0	0.11	0.19
–2	0.31	0.25	0.10	0.14
–1	0.42	0.51	0.11	0.11
0	0.53	0.76	0.13	0.09
1	0.64	0.97	0.15	0.08
2	0.75	1.13	0.16	0.08
3	0.86	1.26	0.17	0.08
4	0.96	1.39	0.19	0.08
5	1.06	1.49	0.21	0.09
6	1.16	1.6	0.23	0.10
7	1.25	1.69	0.24	0.11
8	1.35	1.78	0.26	0.12
9	1.44	1.85	0.28	0.13
10	1.52	1.91	0.30	0.15
11	1.6	1.98	0.33	0.16
12	1.66	1.98	0.34	0.22
13	1.72	2.03	0.36	0.25
14	1.75	2	0.38	0.40
15	1.7	2.06	0.39	0.45

3. Numerical analysis of WIG effect

3.1. ICEM CFD meshing software and models creation

Models, which were used in numerical analysis, were created in Autodesk Inventor Professional 2017, CAD software. For every type of simulation were used one model, so there are 4 models. In Fig. 3. there is a model for free stream flight simulation, with the yellow dotted line is marked out boundaries for WIG effect flight. There is also the view of NACA M8 airfoil geometry. Dimensions:

- **c** is the length of airfoil chord (3400 mm)
- **b** is the height of domain for free stream simulation (9**c**)
- **b'** domains height for WIG effect simulation (2.5**c**)
- **d** distance between the front side of the domain and leading edge of the airfoil for free stream flight (5**c**)
- **d'** distance between the front side of the domain and leading edge of the airfoil for WIG effect flight (1.8**c**)
- **e** distance between the front side of the domain and trailing edge of the airfoil for free stream flight (6.5**c**)
- **h** height coefficient for WIG effect flight (0.1**c**)

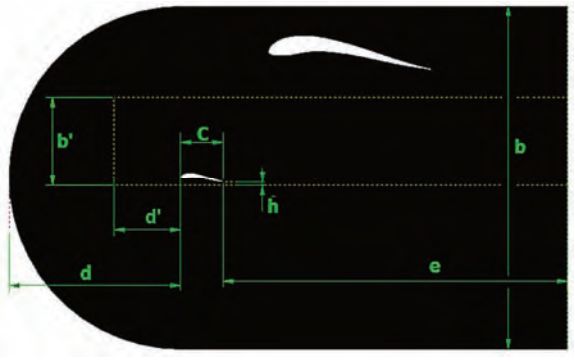

Fig. 3. Model created for simulation of free stream flight, with NACA M8 airfoil geometry

For every model, there were created a new structural 2D planar mesh in Ansys ICEM CFD meshing software. Every mesh is different, and the biggest difference is a number of cells. Mesh for free stream flight simulation has 19765 cells, mesh for WIG effect flight simulation has 35804 cells, mesh for WIG effect flight with exhaust gasses redirection above the airfoil has 29400 cells, mesh for WIG effect flight with exhaust gasses redirection to the lower surface of airfoil has 34344 cells and Fig. 4. shows display of this mesh. To create this kind of mesh, the first model should be divided into blocks, this creates edges on the surface. There is a possibility to set a number of elements for every edge on the surface, it is important to set the same number of element to parallel edges.

Also, in CFD simulation where turbulence equation is on, it is important to create boundary layer on important edges or surfaces. In this simulations, the first layer of cells on the airfoil has a height of 0,00032554 mm. This height is calculated in y+ calculator. y+ or dimensionless wall distance (2) is bonded with turbulence model (in this case k-epsilon) used in simulations, in this model of turbulence, y+ value should be between approximately 300-100 (in this simulation set as 100). Dimensionless wall distance equation:

$$y^+ = \frac{u_* y}{\upsilon} \tag{2}$$

where: u_* – friction velocity; y – distance to the nearest wall; υ – kinematic viscosity

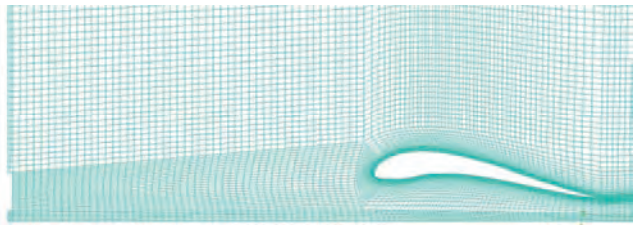

Fig. 4. View of mesh for WIG effect simulation with exhaust gasses redirection to the lower surface of airfoil

3.2. ANSYS Fluent simulations boundary conditions

Simulation conditions for all cases:

- solver set as density-based because velocity in this simulation is set above 0.3 of Mach number, above this value, there is need to consider flow as compressible
- pressure value set as 1 atm (101325 Pa)
- energy equation set on
- turbulence model set as k-epsilon, and it contains two equations in it, first the turbulent kinetic energy k, and second dissipation rate equation
- gas property set as ideal-gas, because the air in density based solver does not work with constant air density

Boundary conditions:

- for every case edges of domain sets as pressure far-field condition, with two exceptions, first for surface below airfoil in wing in ground effect cases, where ground condition was set as moving wall, with the speed of movement of air stream velocity, second for outlet from jet engine, where condition is set as mass-flow-inlet

(mass flow 66 kg/s, temperature 450 K, initial gauge pressure 1.3 atm, mass flow value is similar to value in F-100-PW-229 engine, from the nozzle behind last turbine stage – internal duct. The height of nozzle in 2D simulation is 600 mm)

– standard initialization for pressure far-field
– air stream velocity for free stream flight set as 0.4 of Mach number (139 m/s), for WIG effect flight set as 0.373 of Mach number (129.46 m/s), for both cases of exhaust gases redirection in WIG effect flight air stream velocity is set as 0.3 of Mach number (104.13 m/s)

In every simulation as the main condition of results, convergence is recognized stabilization of lift and drag coefficients in numerical analysis. It is shown in Fig. 5.

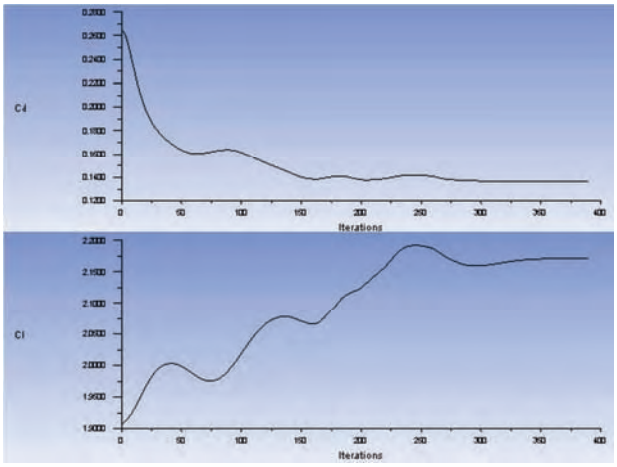

Fig. 5. Convergence of drag and lift coefficient

4. Numerical analysis results

To maintain lift force still in WIG effect flight it is necessary to reduce air stream velocity. Table 2 and Table 3. presents results of numerical simulations, as expected redirection of exhaust gasses in WIG effect above airfoil creates less lift force, but also less drag force. Even with smaller value lift force, as it is shown in Table 4. there is a big increase of lift coefficient for every case of WIG effect usage. With general thrust equation (3) it is possible to calculate thrust needed to propel aircraft, with values of thrust and on the assumption that thrust for free stream flight is 100% of jet engine power (F-100 engine), Table 5 presents needed thrust in the percentage of maximum engine thrust.

$$K = \dot{m}_2 * V_2 - \dot{m}_1 * V_1 \tag{3}$$

where: K – thrust; $\dot{m}$ – air stream mass flow (2 – outlet; 1 – inlet); V – air stream speed

Table 2. Lift force values for NACA M8 profile

Free air stream [N]	51482
WIG effect [N]	51529
WIG effect (exhaust gasses redirection above airfoil) [N]	39261
WIG effect (exhaust gasses redirection below airfoil) [N]	51609

Table 3. Drag force values for NACA M8 profile

Free air stream [N]	1197
WIG effect [N]	313
WIG effect (exhaust gasses redirection above airfoil) [N]	2513
WIG effect (exhaust gasses redirection below airfoil) [N]	3518

Table 4. Lift and drag coefficient values for NACA M8 profile

	Lift (CL) coefficient	Drag (CD) coefficient
Free air stream [N]	2.27	0.0528
WIG effect [N]	5.26	0.0317
WIG effect (exhaust gases redirection above airfoil) [N]	6.08	0.389
WIG effect (exhaust gases redirection below airfoil) [N]	8.09	0.552

Fig. 6. Shows absolute pressure distribution (measured relative to the absolute zero pressure), as expected pressure below the airfoil in WIG effect flight rises, this phenomenon provides to increase of lift force and lift coefficient but also, to decrease induced drag. In C section of Fig. 6. Pressure distribution for exhaust gasses redirection case below the airfoil is greater than in any other case.

Fig. 7. presents air stream velocity distribution around the airfoil in numerical simulations. With the rise of velocity in WIG effect flight, it is expected that air stream could create higher turbulences, what is possible to see after trailing edge in B section. Exhaust gasses in C-section creates high air speed area above the airfoil, what can provide to create a separation of the boundary layer.

Table 5. Thrust needed to propel aircraft

Thrust for free air stream flight	80 kN	100 %
Thrust for WIG effect flight	74.24 kN	92.81 %
Thrust for WIG effect flight with exhaust gases redirection	59.86 kN	74.82 %

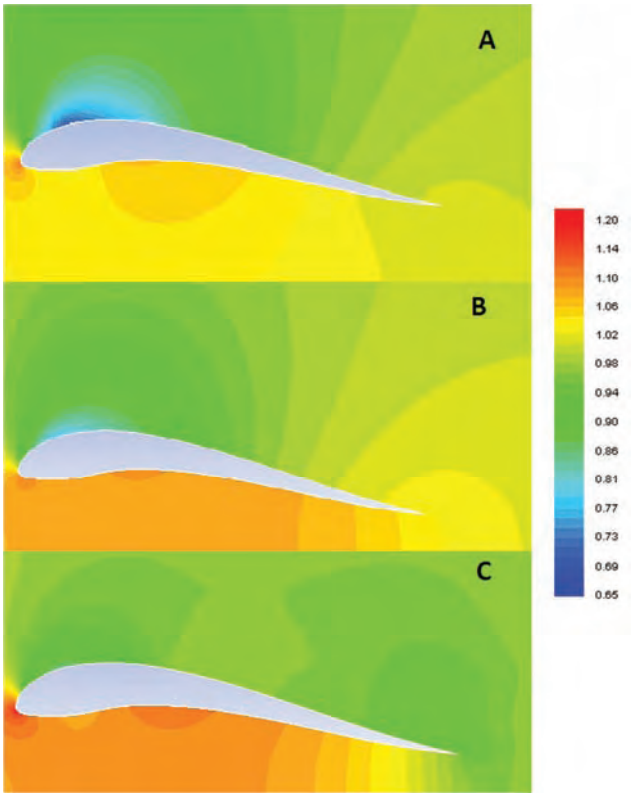

Fig. 6. Absolute pressure distribution: A – free stream flight; B – WIG effect flight; C – WIG with exhaust gasses redirection under airfoil [atm]

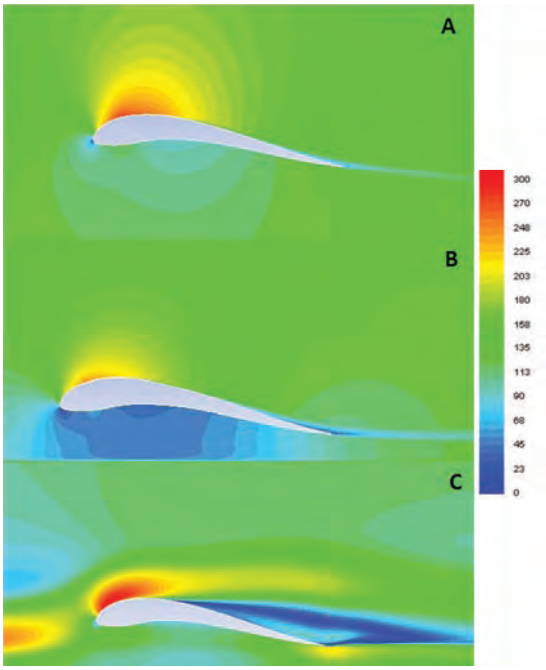

Fig. 7. Air velocity distribution: A – free stream flight; B – WIG effect flight; C – WIG with exhaust gasses redirection under airfoil [m/s]

Fig. 8 presents charts of specific fuel consumption rate in function of thrust, with flight in full power, which is 80 kN, the engine burns 21.5 mg/(s·N) of fuel. When the power to propel aircraft is smaller, like in WIG effect flight its need 21 mg/(s·N) of fuel. When to increase lift force aircraft uses exhaust gasses specific fuel consumption rate drops below 20 mg/(s·N).

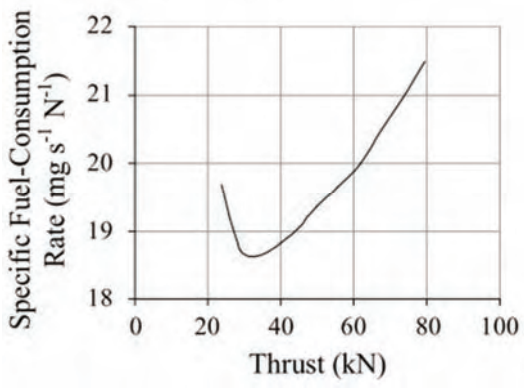

Fig. 8. The specific fuel consumption rate versus the thrust of F-100 jet engine [5]

5. Conclusion

WIG craft does not need a regular airports, it can start and takeoff from water. WIG effect produces more lift force what provides to less fuel consumption of aircraft, and it makes it cheaper. In automotive WIG effect is used to provide better traction. It makes both, automotive, and aeronautics safer, the stall of airfoil is not so catastrophic when it uses WIG effect. There is also a few disadvantages WIG effect produce more drag with negative angle of attack in automotive, particularly in F1, it cannot operate on the sea when waves are too high. It is important for aircraft to avoid negative angle attack, because it can provide to sudden lift force loss. It is necessary to conduct further research on WIG effect. NACA M8 profile is promising airfoil for WIG crafts.

Nomenclature

WIG wing in ground

Bibliography

[1] YUN, L., BLIAULT, A., DOO, J. WIG Craft and Ekranoplan, *Springer*. 2010.
[2] ROZHDESTVENSKY, K.V. Aerodynamics of a lifting system in extreme ground effect. 1st ed., *Springer-Verlag*. 2000, 63-67.
[3] MOORE, N., WILSON, P.A., PETERS, A.J. An investigation into wing in ground effect airfoil geometry, School of Engineering Sciences, *University of Southampton*, SO17 1BJ, UK 2002.
[4] ROJEWSKI, A. Ekranoplan – wstęp do projektu płatowca, MScEng Thesis, *Poznan University of Technology*, Poznan 2016.
[5] LEE, A.S., SINGH, R., PROBERT, S.D. Modelling of the performance of a F100-PW229 equivalent engine under sea-level static conditions. 45th AIAA/ASME/SAE/ASEE Joint Propulsion Conference & Exhibit, Denver, Colorado 2009.

Adam Rojewski, MEng. – Faculty of Machines and Transport at the Poznan University of Technology.
e-mail: *Adam.M.Rojewski@doctorate.put.poznan.pl*

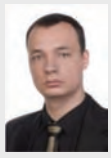

Jarosław Bartoszewicz, DSc., DEng. – Faculty of Machines and Transport at the Poznan University of Technology.
e-mail: *Jaroslaw.Bartoszewicz@put.poznan.pl*

Article citation info:
KRAKOWSKI, R. The emissions reduction possibility of sulphur compounds of vessels sailing in Emission Control Areas (ECA). *Combustion Engines*. 2017, **169**(2), 162-166. DOI: 10.19206/CE-2017-229

Rafał KRAKOWSKI

CE-2017-229

The emissions reduction possibility of sulphur compounds of vessels sailing in Emission Control Areas (ECA)

The article presents legal regulations, together with the characteristics of Emission Control Areas (ECA). It is connected with the new limit sulfur emissions in those areas. In this article , the advantages and disadvantages of various solutions, i.e. switching to low sulphur distillates, installing the marine scrubber device and using of liquefied natural gas (LNG) as ship's main fuel have been considered. Each of these solutions was described in respect of technological review, by the possibility of reducing harmful compound from exhaust gases, to investment costs. In another part of this thesis, there are the calculations of costs of fuel and necessary modifications for a selected passenger-car ferry. Costs were assessed for all of the mentioned solutions. The article was completed conclusions indicating which way is the most cost-effective.

Key words: *environmental protection, sulfur compounds, power engines, marine scrubbers, shipping*

1. Introduction

The development of technology throughout history has always been to facilitate the life of human. In shipbuilding, as a field of transport, there is also a gigantic technological leap. Ship propulsion has changed from simple ways like sail, steam engines to today's widely used diesel engines.

Such progress is unfortunately the price, and it is the degradation of the natural environment. Marine engines produce large amounts of toxic compounds to the atmosphere. The most commonly used heavy fuel oil (HFO) during combustion reactions in the engine emits mainly sulfur oxides (SO_x), oxides of nitrogen (NO_x) and carbon dioxide (CO_2). To limit the effects of human activities on the seas and oceans, the International Maritime Organization (IMO) has introduced Emission Control Area (ECA). Since January 1, 2015 new regulations have been introduced to limit the emission of sulfur compounds. According to new standards, the sulfur content of fuel in control zones may not be higher than 0.1% [7]. To meet these requirements, shipowners operating in these areas had to develop technical solutions to be able to move further in these areas. The easiest way is to switch from heavy fuel to more expensive marine diesel oil with reduced sulfur content (Marine Gas Oil). The disadvantage of this solution is the higher price and higher wear of the mechanical components of the engine. Another possibility is the installation of exhaust gas scrubbers, unfortunately this solution is expensive and it is not always possible to mount it on an existing vessel. Another alternative is to adjust the internal combustion engine to supply the liquefied natural gas (LNG), gas supply significantly reduce the emission of harmful compounds to the atmosphere and the fuel itself is cheaper. This solution is also not devoid of defects. And the biggest one is transport itself, hindered by the need to cool the liquefied gas to –163°C. In the case of new ships, there is no problem with the placement of suitable tanks, but in older structures it can be a serious challenge [4].

2. MARPOL Convention and characteristics of Emission Control Areas

The International Convention for the prevention of pollution from ships (MARPOL) is an international agreement which was adopted at the International Conference on Marine Pollution. The conference was organized by the IMO in October 1973. The Convention was modified in 1978 at the International Conference on Tanker Safety and Pollution Prevention. Convention is known as MARPOL 73/78. The next modification was made in 1997, when an Annex VI was added to deal with the prevention of air pollution by ships. Specific regulations describe the requirements for reducing nitrogen oxides (NO_x), sulfur oxides (SO_x), particulate matter (PM), volatile organic compounds (VOC) and substances that deplete the ozone layer. Regulations on the sulfur content of fuels in special and globally areas were detailed in the Annex. On January 1, 2015, the sulfur directive was amended to reduce the maximum sulfur content of marine fuels to 0.1% at Emission Control Areas [6]. Permissible sulfur content limits for fuel in particular years are shown in Table 1.

Special, sharper rules apply in defined special areas. Special area means a sea area where the use of extraordinary means of preventing marine pollution is required. This is due to a large number of ships and a greater risk of damage to the marine environment. Special areas for the purpose of this Annex are: The Baltic Sea, the Mediterranean Sea, the North Sea, the Black Sea, the Red Sea, the Antarctic area and the Caribbean region.

Table 1. Permissible limits of sulfur content in fuel [3]

Date	Limit of sulfur content in fuel [% m / m]	
	SO_x ECA	Global
2010 y.	1.5%	4.5%
07.2010 y.	1.0%	
2012 y.		3.5%
2015 y.	0.1%	
2020 y.		0.5%

For the need for new regulations, special emission control zones have been created. In these zones there are much more stringent ecological requirements. At first the zones were named as sulphur emission control area and NO_x emission control area, but they have been renamed as ECA and their meaning has been extended. Controlled areas are mainly around the most ecologically-polluted ports in the

world, ie the Baltic Sea, the North Sea and its approaches, and the English Channel.

Such zones also apply along the 200-mile wide coast of the United States and Canada. There are also talks on possible new ECAs such as the Mediterranean and Japan (Fig. 1). In Emission Control Areas, there are tightening of emissions to the atmosphere of such compounds as: such as SO_x, NO_x, PM, volatile organic compounds (VOC) [3].

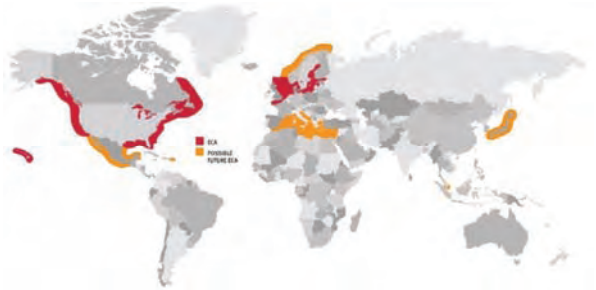

Fig. 1. Current areas ECA (red) and possible future zones (orange) [10]

One of the harmful substances entering the atmosphere with exhaust gases is sulfur oxides (SO_x). They are formed by oxidation (combustion) of marine fuel, where the sulfur content is up to 5%. Sulfur oxides, like nitrogen oxides, combine with water vapor in the atmosphere to cause acid rain, acidification of groundwater, water bodies and soil. Acidic groundwater flushes the potassium from the ground, and the effect is to reduce its fertility. In addition, heavy metals are dissolved. There are three basic groups of sulfur oxides: sulfur oxide II – (SO), sulfur oxide IV – (SO_2) and sulfur oxide VI – (SO_3). Sulfur oxides are also responsible for the corrosion of the equipment made of metal, in which combustion takes place, as well as in the surrounding environment. They also cause greater wear of mechanisms and machines. To the human body sulfur oxides get into the process of breathing, damaging the airways. After getting into the bloodstream, they accumulate in the liver, spleen and lymph nodes.

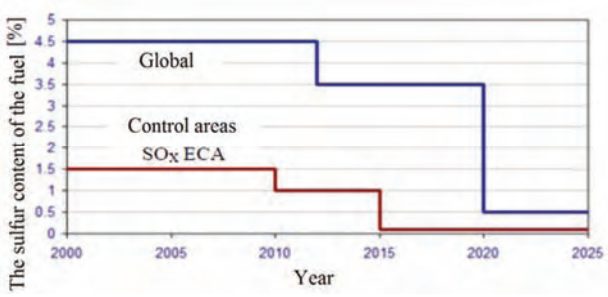

Fig. 2. Permissible sulfur content in fuel according to Annex VI MARPOL [3]

Limitation of the release of harmful sulfur oxides (SO_x) produced by burning of fuel on ships is carried out in accordance with the requirements of Regulation 14, Annex VI of the MAR-POL Convention by limiting the sulfur content of marine fuels (Fig. 2).

3. Possible solutions to reduce sulfur compounds emissions

The sulfur content of the fuel is strongly associated with the crude oil. During the combustion process, the sulfur is oxidized, producing SO_2 dioxide and SO_3 trioxide at a ratio of 15: 1. Sulfur oxide emissions are subject to limits as SO_x. The ways to limit the SO_x content can be the use of low sulfur fuels or exhaust gases cleaning by treating them in devices called scrubbers. These devices effectively remove sulfur oxides from the exhaust gases, but the problem is neutralization of waste. On the other hand, the transition to low-sulfur fuel is related to the economic factor – fuel prices are linked to sulfur content. The reason is the expensive desulphurisation process. The future solution for the reduction of sulfur oxide emissions is the supply of marine engines by liquefied natural gas (LNG) and methane. This is an interesting solution because it reduces SO_x emission, so it meets high requirements in ECA zones and is 20-40% cheaper than crude oil. Alkaline lubricant additives in the engine neutralize a small fraction of the sulfur contained in marine fuel, converting it into neutral calcium. However, the amount of neutralized sulfur is so small that it is not considered to be an effective way to reduce SO_x emissions [2].

4. Economic analysis of possible solutions to reduce emissions of sulfur

Considering the technical solutions to reduce emissions of sulfur oxides SO_x in ECA zones one of the more important issues is the costs associated with the required modernization of the fleet. Costs are the factor most influencing the decision of the shipowners. To approximate the financial issue of technological solutions to reduce SO_x emissions, you should make an example cost estimate for a given lifetime of the vessel.

To create cost estimates for individual construction solutions, the MF Stena Spirit passenger-car ferry on the Gdynia-Karlskrona route was selected (Fig. 3). This ferry has been chosen as an example of a ship for years in service, and the main task for shipowners is to adapt to the current standards just such units.

Fig. 3. MF Stena Spirit ferry [12]

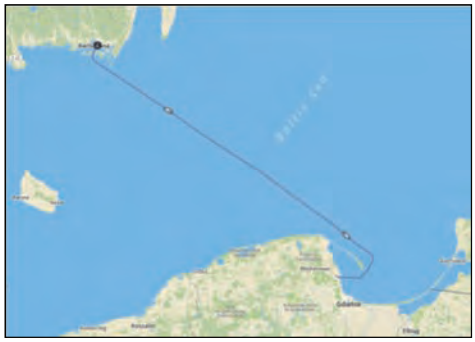

Fig. 4. MF Stena Spirit ferry route [13]

The ferry route is a permanent connection from Gdynia to Karlskrona in Sweden of 174 nautical miles (Fig. 4). The one-way journey takes about 10 hours, and the MF Stena Spirit ferry crosses this journey twice a day and 12 times during the week. As an example, sailing time for calculations was assumed to be 10 years.

4.1. Operation on low sulfur fuel

LSMGO low sulfur fuel used in ECA zones (ie throughout the route) was used for calculations. The specific fuel consumption of the main engine is g_e = 160 g/kWh, but by auxiliary engine is g_e = 175.5 g/kWh; In addition, the nominal power of the main engine equals N_n = 7355 kW and auxiliary engine N_n = 1265 kW [9].

Diesel oil consumption during the voyage

The nominal consumption of fuel by the main engine and auxiliary engines within one hour is determined by the formulas [5]:

$$G_g = g_e \cdot N_n \cdot 10^{-6} \text{ [t/h]} \quad (1)$$

$$G_p = g_{ep} \cdot N_n \cdot 10^{-6} \text{ [t/h]} \quad (2)$$

where: g_e – the actual specific fuel consumption by main engine, g_{ep} – the actual specific fuel consumption by auxiliary engine, N_n – the nominal power of the main engine, N_{np} – the nominal power of the auxiliary engine.

Accepted values were inserted into the formula for diesel oil according to (1) i (2):

$$G_g = 160 \cdot 7355 \cdot 10^{-6} = 1.18 \text{ t/h}$$
$$G_p = 175.5 \cdot 1265 \cdot 10^{-6} = 0.22 \text{ t/h}$$

If you assume that during the cruise of the MF Stena Spirit ferry all 4 main engines and two of the five power generators were running, the hourly fuel consumption will be as follows:

$$G_{gip} = 4 \cdot 1.18 + 2 \cdot 0.22 = 5.1 \text{ t/h}$$

Having the information that the ferry is on the route for 20 hours a day you can count daily consumption:

$$G_{gip} = 20 \cdot 5.1 = 102 \text{ t/h}$$

In this regard, that the ferry serves this route 6 times a week and a year consists of 52 weeks you can estimate fuel consumption for a year:

$$G_{gip} = 102 \cdot (6 \cdot 52) = 31824 \text{ t/year}$$

Assuming that the ferry will swim for 10 years, LSMGO fuel consumption in this term has been calculated:

$$G_{gip} = 31824 \cdot 10 = 318240 \text{ t/10 years}$$

Based on the assumption that the world price of low sulfur fuel is fixed and is 440 USD per ton [11], the fuel cost of a given period of time can be estimated:

$$318240 \cdot 440 = 140025600 \text{ \$}$$

The main engines and auxiliary engines have been able to supply diesel oil at the time of production, so in this case it is not necessary to replace fuel pumps and injectors. In this way, the investment costs for this solution practically does not exist.

4.2. Assembly of exhaust gas scrubbers

Considering the advantages and disadvantages of different types of scrubbers, it can be concluded that the most appropriate choice for the specifically selected passenger and car ferry will be wet scrubber in a closed circuit. This choice was dictated by the ferry route, where it is not possible to dump water from the wash circuit directly into the sea, which is possible with open scrubbers. Dry scrubbers do not reduce nitrogen oxides, which again would increase the cost of investing in equipment called Selective Catalytic Reduction (SCR).

The disadvantage of the solution chosen is the costs associated with the sludge generated during the rinsing process to the appropriate receiving facilities on land and the purchase costs of sodium hydroxide (NaOH) as a necessary means to operate the scrubber.

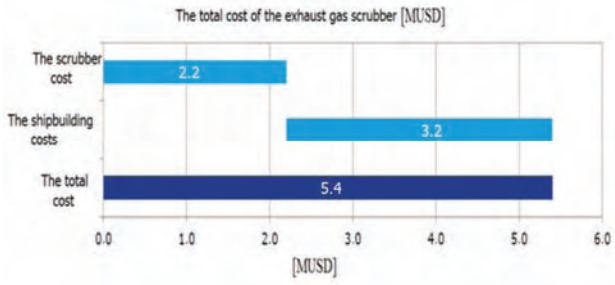

Fig. 5. The installing cost of the exhaust gas scrubber according to DNV GL [1]

The price of sodium hydroxide (NaOH) is 50–250 \$/m^3, which translates into an average cost of use of the scrubber of 20–50 \$ per metric ton of fuel burned. The amount of cash spent on the scrubber is 3–4 million USD depending on the manufacturer. Obviously, shipbuilding costs, such as assembly and necessary ship repairs, are included. Such costs are difficult to estimate due to market dependence. Some sources give about \$ 1 million, and others give up about \$ 3 million [3, 26]. The sample cost according to the classification society DNV GL is shown in Fig. 5.

The need of the analysis presented in the article, as the total cost of the exhaust gas scrubber together with shipbuilding costs \$ 5 million have been adopted. This amount will be added to the purchase price of heavy fuel used to power main engines and generating sets on the selected MF Stena Spirit.

Heavy fuel oil consumption during the voyage

The specific consumption of heavy fuel by the main engine is g_e = 164 g/kWh, while by auxiliary motor g_e = 180 g/kWh [9].

Accepted values were inserted into the formula for fuel according to (1) i (2):

$$G_g = 164 \cdot 7355 \cdot 10^{-6} = 1.21 \text{ t/h}$$
$$G_p = 180 \cdot 1265 \cdot 10^{-6} = 0.23 \text{ t/h}$$

As in the previous case, it was assumed that during the cruise of the MF Stena Spirit ferry all four main engines and two of the five generating sets were running. The hourly fuel consumption will be equal:

$$G_{gip} = 4 \cdot 1{,}21 + 2 \cdot 0.23 = 5.3 \text{ t/h}$$

As before, assuming that a ferry is on the route for 20 hours a day, daily consumption is calculated:

$$G_{gip} = 20 \cdot 5.3 = 106 \text{ t/h}$$

Annual fuel consumption (route operated 6 times a week, year ≈52 weeks):

$$G_{gip} = 106 \cdot (6 \cdot 52) = 33072 \text{ t/year}$$

So within 10 years the ferry will consume:

$$G_{gip} = 33072 \cdot 10 = 330720 \text{ t/10 years}$$

Assuming the world price of fuel is constant and is $ 248 per tonne [11], you can estimate the fuel cost of a given period of time:

$$330720 \cdot 248 = 82018560 \$$$

However, keep in mind the average cost of using a scrubber. It is $ 20-50 per metric ton of fuel burned. This is the cost of buying sodium hydroxide (NaOH) and leaving sludge in the ports. For the purpose of analysis, the cost of using a scrubber will be an average, that is $ 35 per ton of fuel. In this way, additional costs are generated:

$$330720 \cdot 35 = 11575200 \$$$

In the final account we also include the cost of buying and installing of the exhaust gas scrubbers as 5 million USD:

$$82018560 + 11575200 + 5000000 = 98593760 \$$$

This amount is lower than the use of low sulfur fuel in the same period of time.

4. 3. Reconstruction of the unit for liquefied natural gas supply (LNG)

The passenger/car ferry accepted for analysis can be adapted to work on liquefied natural gas (LNG) by replacing main and auxiliary engines for dual fuel engines (DF). The most similar dual-fuel engine is the 8L50DF with a power of N_n = 7600 kW. They were also chosen auxiliary engines with a nominal power of N_{np} = 1280 kW.

During dual-fuel operation, when natural gas and pilot fuel are used for the engine, the gas consumption is given in [kJ/kWh]. To determine the cost of gas to power the engine, calculate the gas consumption in m^3, using the gas heat rate given by the engine manufacturer:

$$7258 \text{ kJ/kWh} \cdot 7600 \text{ kW} = 55160800 \text{ kJ/h}$$

which means:

$$55160800 \text{ kJ/h} = 55160.8 \text{ MJ/h}$$

The liquefied natural gas consumption was calculated for calorific value of 34.43 MJ/m^3 for GZ-50 gas under normal conditions (temperature – 0°C, pressure 101.3 kPa). Hourly gas consumption in one main engine:

$$5516.8 \text{ MJ/h} : 34.43 \text{ MJ/m}^3 = 1602.11 \text{ m}^3\text{/h}$$

As with main engines, the gas consumption of auxiliary engines must be calculated:

$$7809 \text{ kJ/kWh} \cdot 1280 \text{ kW} = 9995520 \text{ kJ/h}$$

It means:

$$9995520 \text{ kJ/h} = 9995.5 \text{ MJ/h}$$

The liquefied natural gas consumption was calculated for a calorific value of 34.43 MJ/m^3 for GZ-50 gas under normal conditions:

$$9995.5 \text{ MJ/h} : 34.43 \text{ MJ/m}^3 = 290.31 \text{ m}^3\text{/h}$$

It should be noted, by burning gas, dual fuel engines consume certain amounts of liquid fuel as pilot fuel. These quantities will be included in the calculation.

The main and auxiliary engine fuel consumption for the hour was determined from the formula (1) and (2) for the specific fuel consumption by the main engine in dual fuel mode g_e = 1 g/kWh and for the specific fuel consumption by the auxiliary engine in dual fuel mode g_{ep} = 3.9 g/kWh:

$$G_g = 1 \cdot 7600 \cdot 10^{-6} = 0{,}0076 \text{ t/h}$$

$$G_p = 3.9 \cdot 1280 \cdot 10^{-6} = 0.0049 \text{ t/h}$$

We assume that all four main engines and two of the five generating sets were running during the cruise. The hourly consumption of liquefied natural gas is:

$$G_{gip} = 4 \cdot 1602.11 + 2 \cdot 290.31 = 6989.06 \text{ m}^3\text{/h}$$

The total hourly consumption of pilot fuel is:

$$G_{gip} = 4 \cdot 0.0076 + 2 \cdot 0.0049 = 0.04 \text{ t/h}$$

If we already have both values, that is the hourly gas burning and the dose of pilot diesel oil in the main and auxiliary engines, we can calculate the fuel consumption: daily, annual and within 10 years. Similar to previous calculations, we assume that the ferry is on the route for 20 hours a day:

LNG:

$$G_{gip} = 20 \cdot 6989.06 = 139781.2 \text{ m}^3\text{/h}$$

diesel oil:

$$G_{gip} = 20 \cdot 0.04 = 0.8 \text{ t/h}$$

Annual fuel consumption (route operated 6 times a week, year ≈52 weeks):

LNG:

$$G_{gip} = 139781.2 \cdot (6 \cdot 52) = 43611734 \text{ m}^3\text{/year}$$

diesel oil:

$$G_{gip} = 0.8 \cdot (6 \cdot 52) = 249.6 \text{ t/year}$$

This means that within 10 years the ferry will use:

LNG:

$$G_{gip} = 43611734 \cdot 10 = 436117340 \text{ m}^3\text{/10 years}$$

diesel oil:

$$G_{gip} = 249.6 \cdot 10 = 2496 \text{ t/years}$$

The price of liquefied natural gas is a moving value and depends on the place of purchase. For the calculation was adopted a price of 4.09 $/mmBTU (1 million British Thermal Unit), where 1 mmBTU ≈ 27.096 m^3. It follows that one cubic meter of liquefied natural gas costs $ 0.15. As the cost of diesel oil was adopted as before 440 US dollars per ton.

$$436117340 \cdot 0.15 + 2496 \cdot 440 = 66515841 \$$$

Difficult to determine is the conversion price of the analyzed passenger/car ferry. Due to lack of access to engine prices, auxiliary equipment and shipbuilding costs themselves, the conversion cost, to be included, is strongly estimated.

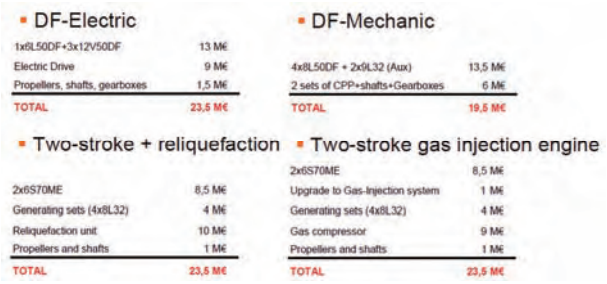

Fig. 6. Examples of engine prices [8]

As the cost of exchanging 4 main engines, 5 generating sets, LNG tanks and auxiliary equipment for the purpose of this article was accepted 20 million US dollars.

$$66515841 + 20000000 = 86515841\ \$$$

The final cost estimates for 10 years of sailing MF Stena Spirit ferry was shown in the following Table 2.

Table 2. Compare the cost of individual solutions

SO_x emission reduction method	Estimated cost [MUSD]
Use of low sulfur fuel	140
Exhaust gas scrubbers + HFO	99
Liquefied natural gas supply	87

All the above solutions have their advantages and disadvantages. Every shipowner should carefully analyze which solution is most beneficial in his case.

5. Conlusions

This article analyzes the available sulfur oxide emission reduction solutions on the example of a passenger-car ferry. Use of low sulfur fuel meeting emission standards, installation of exhaust gas scrubbers and modification unit for combustion of liquefied natural gas have been considered.

The main problem with the use of low sulfur fuels is its high price compared to heavy fuel oil (HFO), however, the lack of investment costs is an important issue for shipowners.

The use of exhaust gas scrubbers or unit conversion on LNG is a major investment and it is necessary to develop suitable space for the installation of new equipment and tanks. These solutions may be unprofitable on existing vessels whose planned life expectancy will be less than the time it takes to return the investment.

According to calculations in the article, in the case of the MF Stena Spirit ferry during the assumed operating period (10 years), the modification of the unit to liquefied natural gas and the investment in the exhaust gas scrubber will be returned. The use of low sulfur fuel during this time period would have been more expensive by 40 MUSD from the scrubber application and by 60 MUSD from the LNG supply. However, it should be borne in mind that fuel prices are not fixed and such assumptions can be variable.

Taking into account the large amount of time needed to return the investment and the complicated reconstruction of existing vessels, the option most likely to be chosen by the majority of shipowners is the use of low sulfur fuel. When building new units, the investment in exhaust gas scrubbers or LNG power is far more promising, and currently units are based on these technologies.

Nomenclature

DF dual fuel
DNV det norske veritas
ECA emission control area
HFO heavy fuel oil
IMO international maritime organization
LNG liquified natural gas
LSMGO liquified natural gas
MGO marine gas oil
PM particulate matter
SCR selective catalytic reduction
VOC volatile organic compounds

Bibliography

[1] DNV, G.L. ECA and emissions status and alternative solutions, Oslo 2014.
[2] KIDACKI, G., KRAUSE, P., RAJEWSKI, P. Techniczno-eksploatacyjne aspekty redukcji emisji SO_x na statkach. *Zeszyty naukowe Akademii Morskiej w Szczecinie.* 2006, **10**(82), 245-247.
[3] KOŁWZAN, K., ADAMKIEWICZ, A. Zapobieganie zanieczyszczaniu powietrza przez statki w świetle najnowszych wymagań Załącznika VI do Konwencji MARPOL. *Zeszyty naukowe Akademii Morskiej w Szczecinie.* 2009, **18**(90), 66-70.
[4] Merkisz, J., Pielecha I. Wymagania i kierunki rozwoju napędów zasilanych gazem ziemnym CNG/LNG, *Zeszyty Naukowe Politechniki Częstochowskiej. Mechanika.* 2006, **26**(162), 458-475.
[5] MICHALSKI, R. Siłownie okrętowe. *Wydawnictwo Uczelniane Politechniki Szczecińskiej*, Szczecin 1997.
[6] Międzynarodowa Konwencja o Zapobieganiu Zanieczyszczaniu Morza Przez Statki 73/78, Tekst jednolity, 2015, 299-338.
[7] WOJTYTO, Z. Problemy eksploatacji dwusuwowych silników okrętowych na paliwach niskosiarkowych według doświadczeń firmy MAN Diesel. *Silniki spalinowe*. 2006, **45**(3), 77-89.
[8] Wärtsila Dual Fuel LNGC, 2008.
[9] www.cleanmarine.no
[10] www.dupont.com
[11] www.shipandbunker.com
[12] www.shipspotting.com/gallery/photo.php?lid=1395782
[13] www.stenaline.pl

Rafał Krakowski, DEng. – Faculty of Marine Engineering at Gdynia Maritime Univesity.

e-mail: *R.Krakowski@am.gdynia.pl*

Article citation info:
JACH, A., CIEŚLAK, I., TEODORCZYK, A. Investigation of glycerol doping on ignition delay times and laminar burning velocities of gasoline and diesel fuel. *Combustion Engines*. 2017, **169**(2), 167-175. DOI: 10.19206/CE-2017-230

Agnieszka JACH
Ilona CIEŚLAK
Andrzej TEODORCZYK

CE-2017-230

Investigation of glycerol doping on ignition delay times and laminar burning velocities of gasoline and diesel fuel

Glycerol is a major by-product of biodiesel production. Per one tone of produced biodiesel, one hundred kilograms of glycerol is produced. Production of glycerol is increasing due to increase of demand for biodiesel. One of methods of glycerol utilization is combustion. Recent experimental studies with use of a diesel engine and a constant volume combustion chamber show that utilization of glycerol as a fuel results in lower NO_x emissions in exhaust gases. It combusts slower than light fuel oil, what is explained by higher viscosity and density of glycerol. Glycerol has low cetane number, so to make combustion in a diesel engine possible at least one of the following conditions need to be fulfilled: a pilot injection, high temperature or high compression ratio. The aim of the paper is to compare glycerol to diesel and to assess influence of glycerol doping on gasoline and diesel fuel in dependence of pressure, temperature and equivalence ratio. The subject of this study is analysis of basic properties of flammable mixtures, such as ignition delay times and laminar burning velocities of primary reference fuels (diesel: n-heptane and gasoline: iso-octane). Calculations are performed with use of Cantera tool in Matlab and Python environments. Analyses of influence of glycerol on ignition delay times of n-heptane/air and iso-octane/air mixtures covered wide range of conditions: temperatures from 600 to 1600 K, pressure 10-200 bar, equivalence ratio 0.3 to 14, molar fraction of glycerol in fuel 0-1 in air. Simulations of LBV in air cover temperatures: 300 K and 500 K, pressures: 10, 40, 100, 200 bar and equivalence ratio from 0.3 to 1.9. Physicochemical properties of gasoline, diesel and glycerol are compared.

Key words: *glycerol, ignition delay times, laminar burning velocities, Cantera, gasoline, diesel*

1. Introduction

Glycerol (chemical formula: $C_3H_8O_3$) is a major by-product of biodiesel production. Biodiesel is produced by transestrification of triglycerides (fats, oils, etc.) into fatty acid methyl esters [1]. The triglyceride reacts with an alcohol and a catalyst (i.e. sodium hydroxide) to produce FAME and glycerol (Fig. 1). Per one tone of produced biodiesel, one hundred kilograms of glycerol is produced. Depending on the process, the glycerol waste may contain variable amounts of alcohol, water, catalyst and other organic materials – soaps, fats, oils. Production of glycerol is increasing due to increase of demand for biodiesel. It is one of the most versatile chemical species. It is completely soluble in water and alcohols, but it is insoluble in hydrocarbons. It is widely used in the food industry, in pharmaceutical formulations and in cosmetics [2]. However, in order to utilize waste glycerol in this way it need to be purified, what requires more time and equipment. Instead, raw glycerol can be utilized as a fuel in an engine, by the way increasing a biofuel pool.

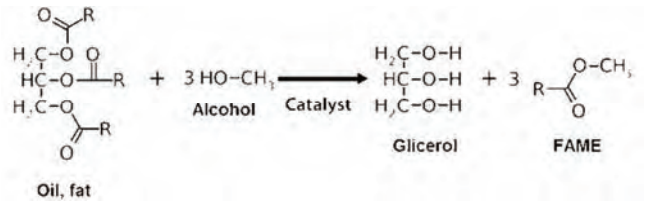

Fig. 1. Process of transestrification [1]

However, glycerol is much different from diesel fuel and kerosene. Main issues with using it in compression ignition engines is low cetane number and high viscosity [3]. A few researches on utilizing glycerol as a fuel were conducted. Rychlik et al. [4] presented the method of glycerine combustion in a diesel engine without necessity of using pilot fuel or additives improving the cetane number of a fuel in the form of glycerol. They used MTU V652 engine (12 MW power) and 98.5% technical glycerol. Reliable work of the diesel engine on glycerol was possible thanks to preheating of the fuel up to 98–105°C (kinematic viscosity dropped to ca 8 $mm^2/2$) and preheating of intake air in a heat exchanger by exhaust gas from 140°C to 190°C – 200°C (boost pressure dropped from 1.5 atm to 1.3 atm). Fuel consumption increased 2.25 times. McNeil [5] used glycerol in both naturally aspirated and turbo-charged engines with intake manifold heating. Natural aspiration required intake air heating to 144°C to sustain combustion compared to turbocharged operation at 100°C because glycerol has poor ignitability (cetane number = 0–5 [3, 5]). Lower energy density requires nearly double fueling rates to achieve equivalent power output compared to diesel fuel. Stelmasiak and Pietras [6] investigated effects of methanol and a blend of methanol and glycerin on parameters of automotive spark ignition engine of the Fiat 1100 MPI type (40 kW power). Addition of glycerin resulted in higher efficiency of the engine compared to pure methanol or gasoline E95. They tried to mix glycerin with diesel oil or gasoline. Despite of intensive mixing either a mixture with diesel oil or gasoline completely segregated after 15–20 minutes. Grab-Rogaliński and Szwaja [7] performed tests in a combustion research unit (a constant volume combustion chamber with injection system) with light fuel oil or glycerol. They concluded that glycerol combusts slower than LFO, because of poorer atomization due to higher viscosity and density of glycerol. Combustion of pure glycerol was not possible, a pilot injection of diesel fuel was necessary. Eaton et al. [8] showed glycerol/diesel emulsion can be produced using commercially available surfactants. Their research in a single-cylinder diesel engine with blends of

diesel oil and 10 vol.% or 20 vol.% of glycerol showed that combustion of the emulsion fuels at 900 rpm in a naturally aspirated engine resulted in nominal combustion delay, likely because of a lower cetane rating compared to diesel oil. Benefits of glycerol emulsification include increased thermal efficiency at high engine loads and reductions in NO_x and PM emissions of 5−15 and 25−50%, respectively.

The goal of this paper is to compare key thermo physical properties of glycerol to both gasoline and petroleum diesel oil in terms of combustion in engines.

2. Fuel properties

Ignition delay time and laminar burning velocity are fundamental properties characterizing a flammable mixture [9]. IDT and LBV are a direct reflection of fuel's chemical kinetics. The most important properties of a fuel for its application in an engine are kinematic viscosity, density, heating value, flash point, pour point, cloud point, cetane number etc. These properties directly influence engine's performance and emissions. The most common standard to define the limit of most of these properties for diesel is ASTM [10].

2.1. Ignition delay time

Glycerol has relatively low vapor pressure, i.e. 1 mm Hg in 125.5°C [2]. This makes investigation of IDT in a shock tube or a rapid compression machine difficult. Devices would need to be heated up to 200-300°C in order to reach a reasonable level of vapor pressure of glycerol to perform an experiment. For authors best knowledge there are no experimental information on IDT of glycerol in literature. Therefore a development of a detailed chemical kinetics mechanism for oxidation of glycerol was not trivial and only one scheme is found – POLIMI BIO 1412 [11–15]. Barker-Heming et al. [14] performed validation of their chemical scheme based on reduced-gravity experiments on combustion of propanol/glycerol mixture droplets [16]. Gasoline and diesel oil are complex blends of hydrocarbons. As surrogate fuels for chemical kinetic investigation iso-octane and n-heptane respectively are used. The mechanisms to be used in this investigations ought to contain either n-heptane/glycerol/air or iso-octane/glycerol/air chemistry. One mechanism fulfills this condition – POLIMI TOT 1412 [17] (which contains POLIMI BIO 1412 scheme).

Fig. 2 and Fig. 3 present a comparison of exemplary shock tube experimental ignition delay times [18, 19] with those simulated using POLIMI TOT 1412. Two data sets of IDT from shock tube experiments were collected for stoichiometric n-heptane/air and iso-octane/air. The first set is for 15, 20 and 38 bar for temperature from 727 to 1413 K [19] – 24 points in total. The second set is for pressures from 6.9 to 47.4 bar and temperatures from 713 to 1242 K [18] – 50 points in total. Ignition delay time simulations were performed in a constant volume reactor with adaptive time step in Cantera 2.3.0 [20] in Matlab R2016b environment. Initial conditions for simulations were experimental temperature and pressure behind a reflected shock wave and composition of a currently investigated mixture. Definition of IDT in simulations was the same as used in the experiments [18, 19]. It is worth to notice that for the second set of IDT experimental pressure varied from point to point, what influenced presentation of the comparison results on Fig. 3 (simulated points are not connected by a line). This brief validation of the mechanism shows that ignition delay time of iso-octane and n-heptane are well enough reproduced by POLIMI TOT 1412. The highest difference is visible for temperatures lower than 1000 K in the region of negative temperature coefficient. One can notice that the mechanism was not validated for blends of species investigated in this paper.

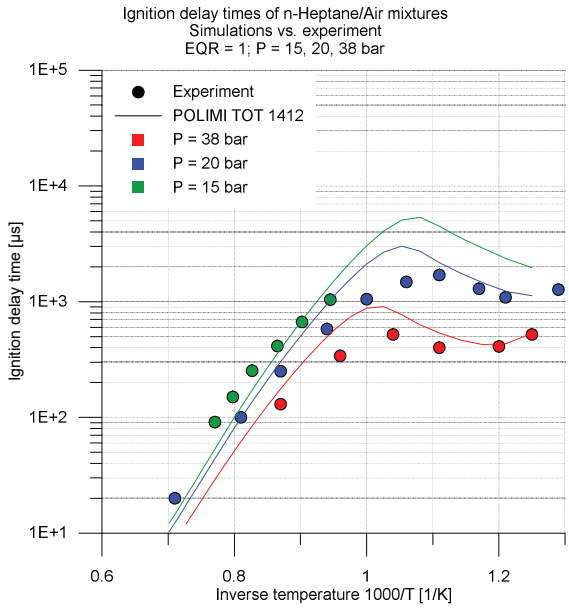

Fig. 2. Ignition delay times of stoichiometric n-heptane/air mixture for 15, 20, 38 bar: solid line – simulated IDT using POLIMI TOT 1412 mechanism, circles – experimental IDT [19]

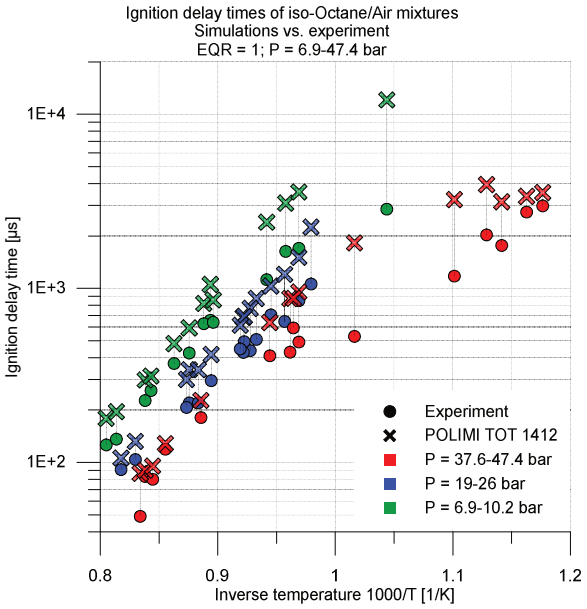

Fig. 3. Ignition delay times of stoichiometric iso-octane/air mixture for pressures 6.9-47.4 bar: solid line – simulated IDT using POLIMI TOT 1412 mechanism, circles – experimental IDT [18]

Analyses of influence of glycerol on n-heptane/air and iso-octane/air mixtures covered wide range of conditions:

temperatures from 600 to 1600 K, pressure 10-200 bar, equivalence ratio 0.3 to 14, molar fraction of glycerol in fuel 0-1 (from pure n-heptane or iso-octane to pure glycerol) in air. Assumed IDT definition is a time interval from the onset of simulation up to maximal gradient of temperature rise.

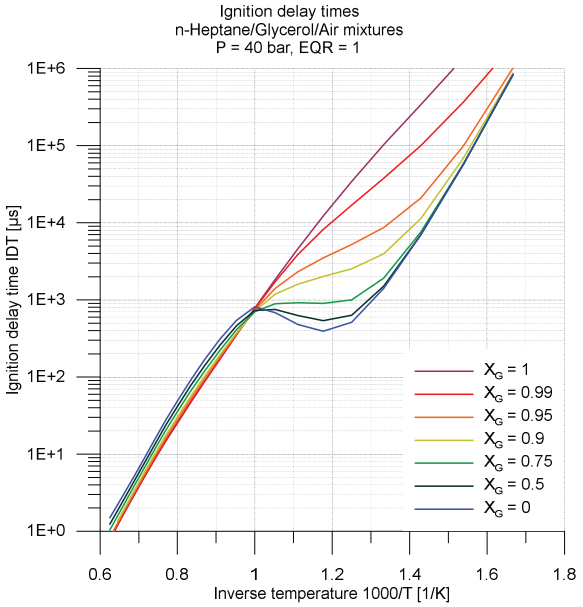

Fig. 4. Ignition delay time vs. inverse temperature of n-heptane – glycerol blends for 40 bar and equivalence ratio equal to 1 for different glycerol molar fraction in a fuel X_g

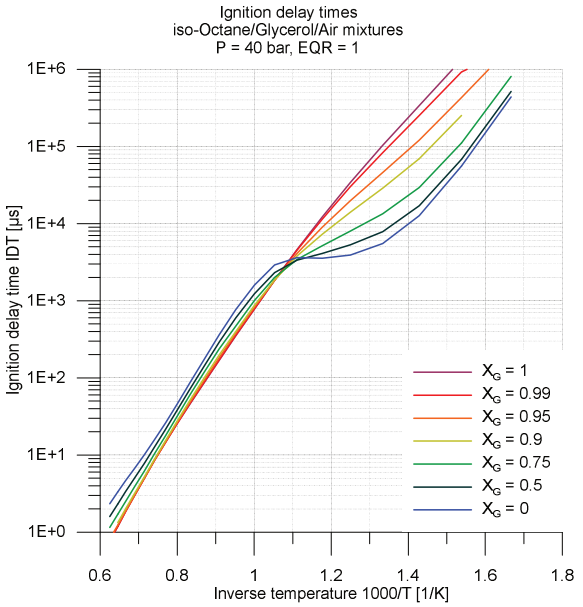

Fig. 5. Ignition delay time vs. inverse temperature of iso-octane – glycerol blends for 40 bar and equivalence ratio equal to 1 for different glycerol molar fraction in a fuel X_g

Fig. 4 and Fig. 5 present IDT of stoichiometric mixtures of n-heptane/glycerol/air and iso-octane/glycerol/air respectively for 40 bar. Glycerol does not have a negative temperature coefficient region as opposed to n-heptane and iso-octane. For high temperatures (T > 1000 K for n-heptane and T > 900 K for iso-octane) glycerol and blends with glycerol have shorter IDTs than n-heptane and iso-octane, but the difference is small. For lower temperatures (T < 1000 K for n-heptane and T < 900 K for iso-octane) lines intersect and then the difference is opposite. Glycerol and blends with glycerol have much longer IDT. The highest difference is present for NTC regions and may reach even 2 orders of magnitude for n-heptane and 1 for iso-octane.

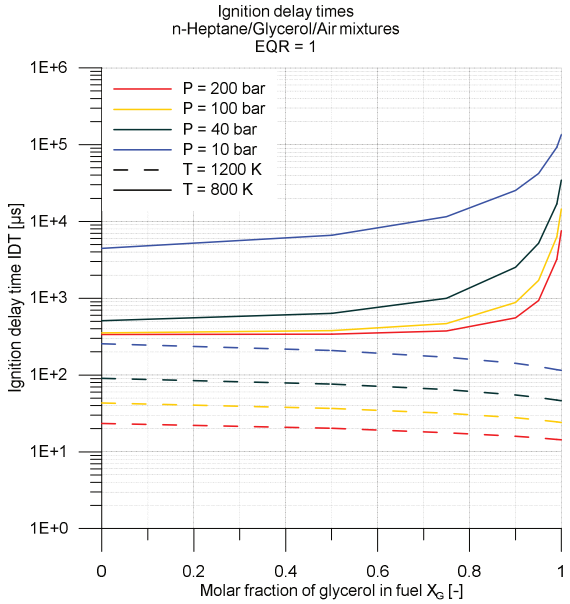

Fig. 6. Ignition delay time of stoichiometric n-heptane – glycerol mixtures vs. molar fraction of glycerol in fuel X_g for 4 pressures (10 bar – blue line, 40 bar – dark green line, 100 bar – yellow line, 200 bar – red line) and 2 temperatures (800 K – solid line, 1200 K – dashed line)

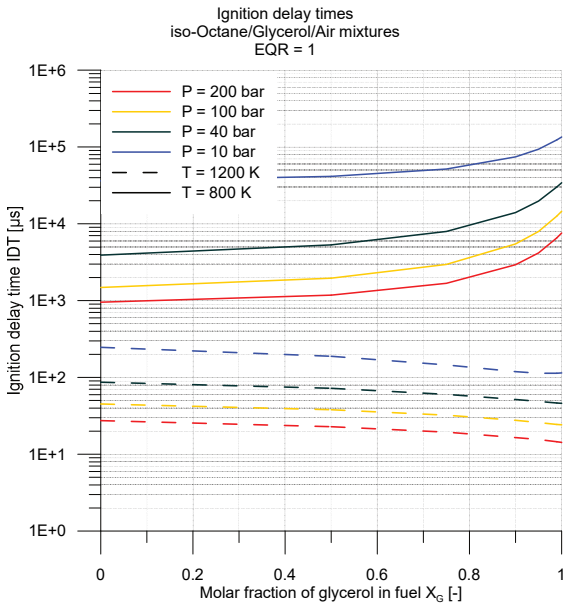

Fig. 7. Ignition delay time of stoichiometric iso-octane – glycerol mixtures vs. molar fraction of glycerol in fuel X_g for 4 pressures (10 bar – blue line, 40 bar – dark green line, 100 bar – yellow line, 200 bar – red line) and 2 temperatures (800 K – solid line, 1200 K – dashed line)

Next figures present IDT of stoichiometric mixtures of both n-heptane (Fig. 6) and iso-octane (Fig. 7) with glycerol vs. molar fraction of glycerol in a fuel X_g for 4 example pressures (10, 40, 100, 200 bar) and 2 temperatures (800 K

and 1200 K). IDTs are almost constant in a wide range of glycerol molar fraction. Shape of plots changes with pressure as NTC region moves with pressure. Glycerol is not a fuel additive. It is possible to preserve IDT of n-heptane or iso-octane for relatively high amounts of glycerol. Iso-octane is more prone for glycerol's influence than n-heptane. Behavior described in previous paragraph might be noticed here also. For n-heptane – glycerol and iso-octane – glycerol blends there is a temperature where a way of IDT's change switches – for very high temperatures glycerol has lower IDTs than both n-heptane and iso-octane, but still this difference is small.

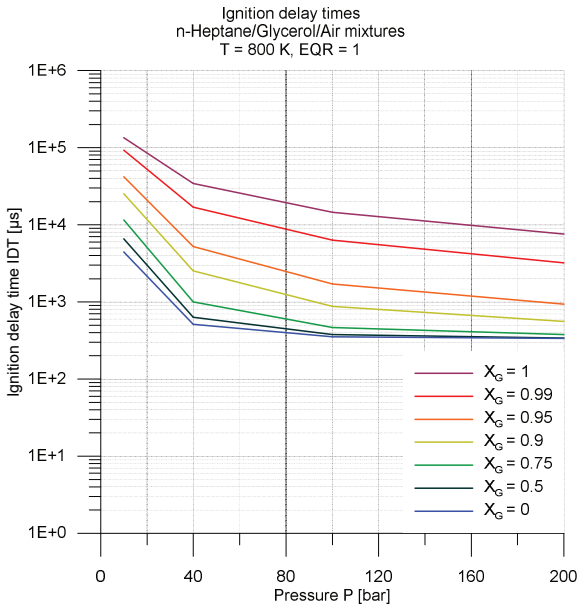

Fig. 8. Ignition delay time vs. pressure of stoichiometric n-heptane – glycerol blends for 800 K for different glycerol molar fraction in a fuel X_g

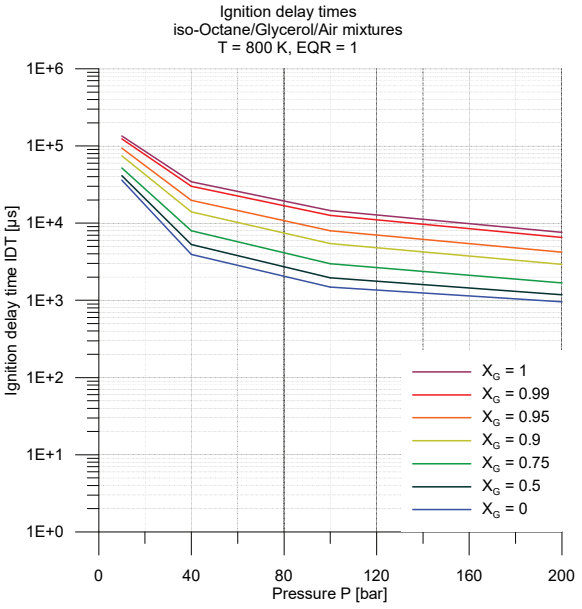

Fig. 9. Ignition delay time vs. pressure of stoichiometric iso-octane – glyc-erol blends for 800 K for different glycerol molar fraction in a fuel X_g

Fig. 8 and Fig. 9 show how ignition delay time changes with pressure for stoichiometric iso-octane/glycerol and n-heptane/glycerol blends for 7 glycerol molar fractions in a fuel for 800 K. IDT gets smaller when pressure increases. The difference between n-heptane and glycerol is higher than between gasoline and glycerol. The biggest difference for Fig. 8 is for 40 bar and n-heptane's IDT is 2 orders of magnitude higher than glycerol's. For gasoline the difference an order of magnitude of difference. Again, one can notice that n-heptane's and iso-octane's low IDT are persisted in a wide range of glycerol molar fraction in a fuel. The difference for both between $X_g = 0$ and $X_g = 0.5$ is negligible.

2.2. Laminar burning velocity

Laminar burning velocities are calculated in Cantera 2.3.0. in Python 3.5.3 environment using free flame model and automatic refinement of a grid. Diffusive mass fluxes due to the Soret effect are not included. Due to the high number of species and reactions in POLIMI TOT 1412 (451 species and 17848 reactions) 3 smaller chemical schemes are used. POLIMI BIO 1412 (137 species and 4522 reactions) for calculations of glycerol. Jerzembeck [21] reaction mechanism (99 species and 601 reactions) for n-heptane to simulate diesel fuel chemistry. Liu et al. [22] skeletal chemical kinetic model of iso-octane for internal combustion engines (33 species and 116 reactions). None of the three mechanisms handles chemistry of either glycerol/iso-octane or glycerol/ n-heptane blends, so calculations are performed only for pure species – pure glycerol, pure n-heptane and pure iso-octane. Simulations of LBV in air cover temperatures: 300 K and 500 K, pressures: 10, 40, 100, 200 bar and equivalence ratio from 0.3 to 1.9.

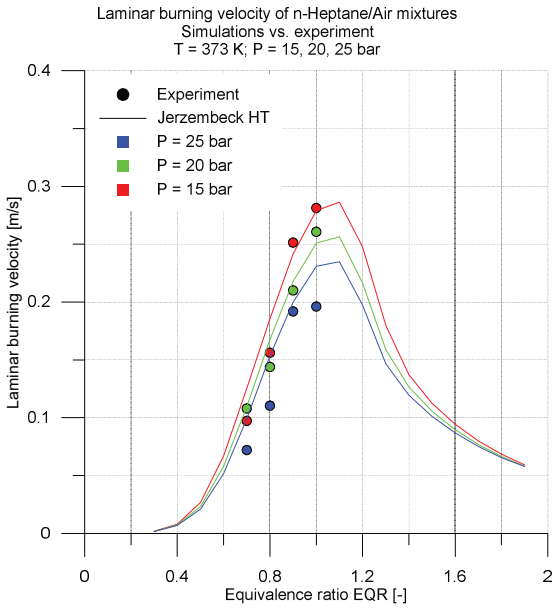

Fig. 10. Laminar burning velocities of n-heptane/air mixtures for pressures 15, 20, 25 bar: solid line – simulated LBV using Wisconsin ERC mechanism, circles– experimental LBV [21]

Fig. 10 and Fig. 11 present a brief comparison of experimental LBV with calculated ones for n-heptane/air and iso-octane/air mixtures using mentioned above mechanisms. Experimental LBV of glycerol/air blends are not present in literature. The chosen data set for n-heptane from Jerzem-

beck et al. [21] is for 373 K, pressures: 15, 20, 25 bar and EQR from 0.7 to 1.0. Jerzembeck mechanism predicts very well LBVs. Iso-octane/air experimental data from Jerzembeck et al. [21] are for the same conditions as n-heptane/air for EQR from 0.7 to 1.2. Liu et al. [22] mechanism's predictions are very consistent with experimental results for lean mixtures, for rich mixtures the mechanism's LBVs are ~20% smaller.

Fig. 12 and Fig. 13 compare LBV of n-heptane/air with glycerol/air mixtures for 500 K and 300 K respectively. N-heptane has higher LBVs. For near stoichiometric conditions the difference is ~15%. Change of temperature from 500 K to 300 K results in drop of LBV by 60% for both mixtures.

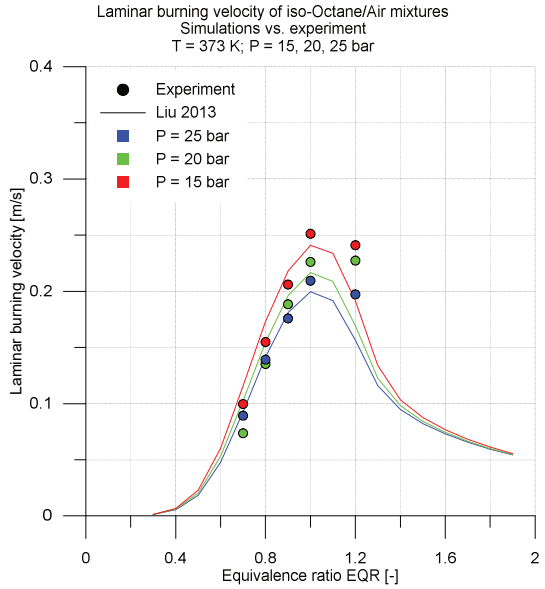

Fig. 11. Laminar burning velocities of iso-octane/air mixtures for pressures 15, 20, 25 bar: solid line – simulated LBV using Wisconsin ERC mechanism, circles – experimental LBV [21]

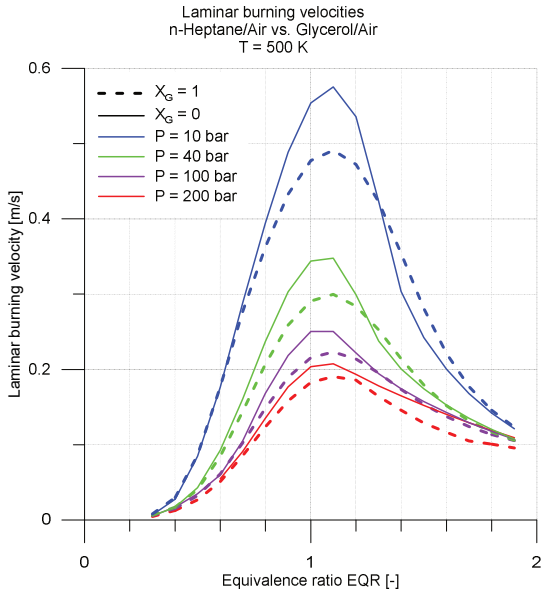

Fig. 12. Laminar burning velocity for n-heptane/air (X_g = 0, solid lines) and glycerol/air (X_g = 1, dashed lines) mixtures for 500 K and 4 pressures (10 bar – blue line, 40 bar – green line, 100 bar – violet line, 200 bar – red line)

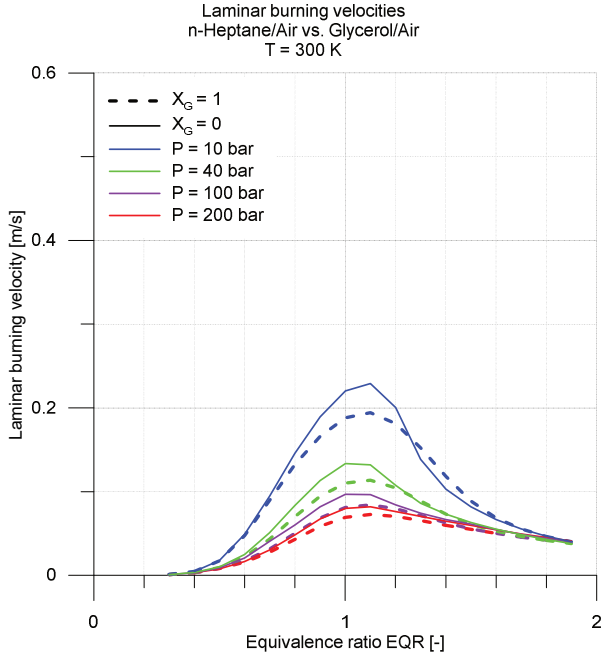

Fig. 13. Laminar burning velocity for n-heptane/air (X_g = 0, solid lines) and glycerol/air (X_g = 1, dashed lines) mixtures for 300 K and 4 pressures (10 bar – blue line, 40 bar – green line, 100 bar – violet line, 200 bar – red line)

Fig. 14 and Fig. 15 present a comparison of LBV between iso-octane-air and glycerol-air mixtures for 500 K and 300 K. For lean conditions LBVs are almost identical, for reach condition LBV of glycerol-air are higher, but as the brief valiadtion showed, in this range Liu mechanisms predicts too small LBV of n-heptane/air ~20%. This difference is diminished when pressure increases.

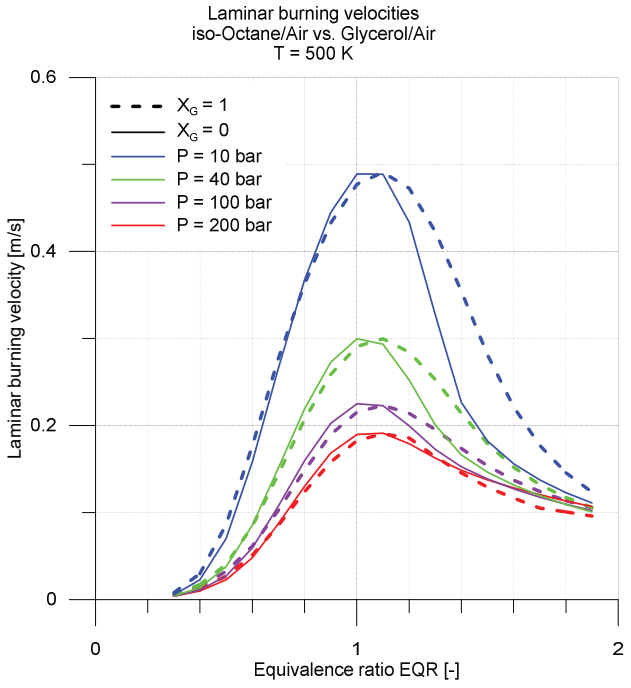

Fig. 14. Laminar burning velocity for iso-octane/air (X_g = 0, solid lines) and glycerol/air (X_g = 1, dashed lines) mixtures for 500 K and 4 pressures (10 bar – blue line, 40 bar – green line, 100 bar – violet line, 200 bar – red line)

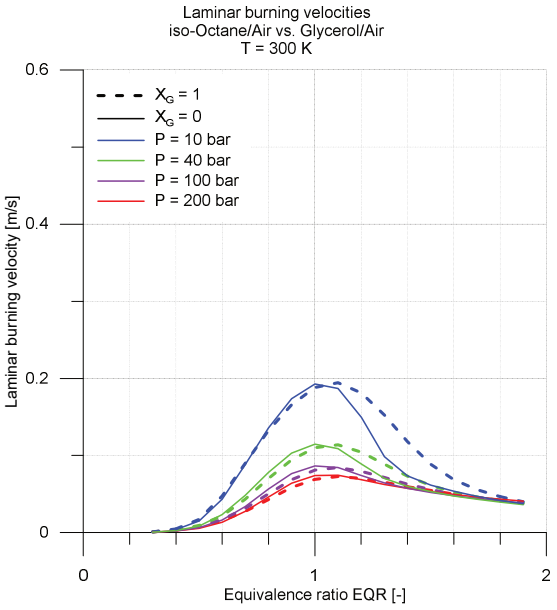

Fig. 15. Laminar burning velocity for iso-octane/air (X_g = 0, solid lines) and glycerol/air (X_g = 1, dashed lines) mixtures for 300 K and 4 pressures (10 bar – blue line, 40 bar – green line, 100 bar – violet line, 200 bar – red line)

2.3. Kinematic viscosity

Kinematic viscosity of the fuel directly governs fuel flow, spray and atomization, it impacts the performance of fuel injection system [10]. When kinematic viscosity is high fuel pump consumption is higher and atomization of the fuel poor. It can also cause damage of equipment – i.e. filter damage. If viscosity is too low pump and fuel systems can experience leakage, excessive wear and power loss.

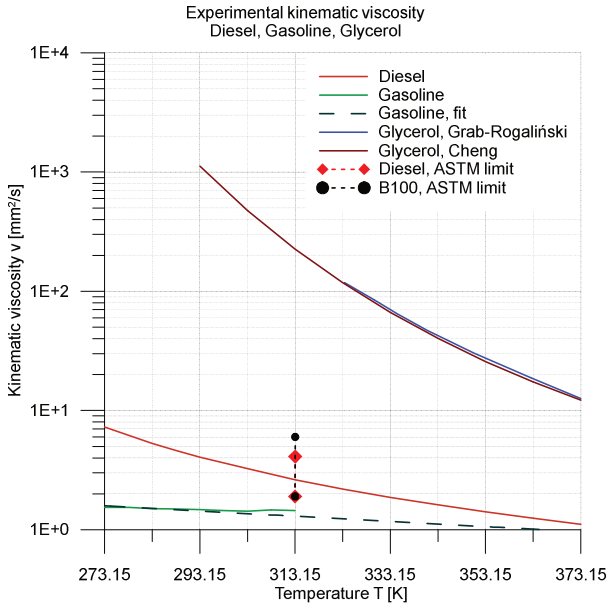

Fig. 16. Experimental kinematic viscosities of diesel oil [23], gasoline [24] and glycerol [25, 26] (ASTM limit for 40°C are marked for diesel oil and B100 – biodiesel)

Fig. 16 present experimental kinematic viscosities of diesel oil [23], gasoline [24] and glycerol [25, 26]. ASTM limits [10] for diesel oil (1.9–4.1 mm^2/s for 40°C) and B100, biodiesel (1.9–6 mm^2/s for 40°C) are marked by red rhomb and black circle respectively. Available literature data on gasoline's viscosity does not exceed 40°C. To enable further analysis the data are extrapolated up to 100°C. Viscosity is temperature dependent and i.e. obeys exponential model proposed firstly by Reynolds in 1888. In this case the exponential model of viscosity well enough fits the experimental data:

$$v_{gasoline} = 6.24826 \cdot \exp(-0.00502 \cdot T), R^2 = 0.958$$

Fitted function of $v_{gasoline}$ is presented on Fig. 16.

Glycerol is a very viscous liquid, whose melting point is 18.2°C [2]. It's viscosity is over 2 orders (20°C) to 1 order (100°C) of magnitude higher than diesel's. In comparison to gasoline it is almost 3 orders to 1 order of magnitude. It is outside limits suggested by ASTM for diesel and biodiesel. In order to make glycerol useful in engine applications it need to be heated up or mixed with a less viscous fuel.

As mentioned above, glycerol does not freely dissolve in hydrocarbons. These mixtures segregate after ~15 minutes, but it is possible to create a stable mixture with surfactant [8]. Next figures present kinematics viscosity of mixtures of diesel/glycerol and gasoline/glycerol.

In order to assess kinematic viscosities of these dual mixtures a mixing rule of Arrhenius [27] is applied:

$$\log v_{blend} = X_{v1} \cdot \log v_1 + X_{v2} \cdot \log v_2$$

which gave very similar results to validated Kanaveli's mixing rule with additional parameters [27]:

$$\ln v_{blend} = X_{v1} \cdot \ln v_1 + X_{v2} \cdot \ln v_2 + X_{v1} \cdot X_{v2} \cdot k$$
$$k = 0.053 \cdot \ln(\ln(v_1/v_2)) + 0.004$$

Fig. 17 and Fig. 18 present an influence of glycerol doping on diesel's kinematic viscosity. The mixtures complies with ASTM limit for biodiesel for glycerol molar fraction up to 19% and for diesel up to 10%. Fig. 19 presents kinematic viscosity of gasoline-glycerol blends. Gasoline has

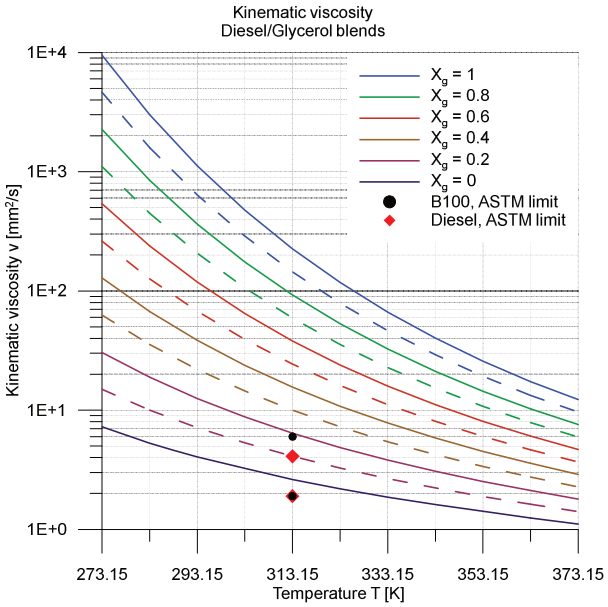

Fig. 17. Kinematic viscosity of diesel – glycerol mixtures vs. temperature. ASTM limits for diesel oil and biodiesel (B100) are marked by red rhomb and black circle respectively

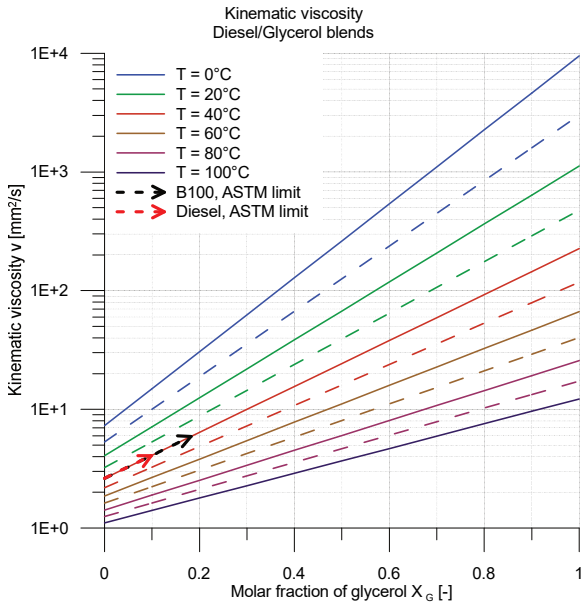

Fig. 18. Kinematic viscosity of diesel – glycerol mixtures vs. molar fraction of glycerol X_g. ASTM limits for diesel oil and biodiesel (B100) are marked by red arrow and black arrow respectively

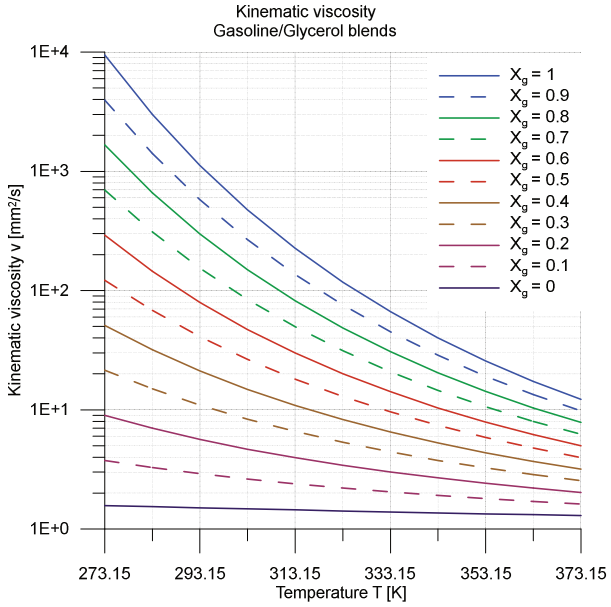

Fig. 19. Kinematic viscosity of gasoline – glycerol mixtures vs. temperature

lower viscosity than diesel oil. Glycerol has stronger influence in increasing viscosity of gasoline blends than of diesel blends.

2.4. The other properties

Table 1 summarizes the other important properties diesel, gasoline and glycerol. Glycerol has the highest density. Lower density decreases energy concentration of fuel, increses the risk of leakage. To high density may result in increase of enigne deposition and smoke [10].

Adiabatic flame temperature of glycerol is lower ~200 K than diesel's or gasoline's, this is the reason of lower NO_x of the engines switched to glycerol.

Heat of vaporization of glycerol is 3 times higher than diesel's and gasoline's. Utilization of glycerol as a fuel will result in cooling of the fresh charge (mainly in direct injection engines) during vaporization [28].

The flashpoint is the lowest fuel temperature at which the vapor above a fuel sample will momentarily ignite under the prescribed test conditions. Fuel with a higher flash point is considered safer and easier to store. Glycerol has high flash point so fire hazard is low even when exposed to heat or flame, but glycerine is still combustible [2]. ASTM limits of flash point for diesel oil is 130°C [10].

Cetane number of glycerol is 5 and is much lower than cetane number of diesel (52). ASTM limit for cetane number of biodiesel is min 47. A compression ignition engine cannot be switched to pure glycerol without any adaptation. Based on comparison of cetane numbers of glycerol and gasoline one can state that glycerol has anti-knocking property.

Table 1. Fuels properties (glycerol [3, 29], diesel [3], gasoline [30])

Property	Unit	Glycerol	Diesel	Gasoline
Molecular Weight	[g/mole]	92.09	150–250	60-150
Color	–	colorless liquid	amber	yellowish
Density	[g/cm^3]	1.260	0.832	0.67–0.8
Pour point	[K]	–	264.67	–
Cloud point	[K]	–	239	–
Melting point	[K]	290	264.9	252
Boiling point	[K]	563	450–463	312
Cetane number	–	5	52	12
Higher heating value	[MJ/kg]	18.6	46	45.4
Adiabatic flame temperature	[K]	2201	2413	2411
Heat of vaporization	[kJ/kg]	670	225–280	275–365
Flash point	[K]	450	422–644	227
Autoignition temperature	[K]	666	503	519–553
Low flammability limit	[vol.%]	3	0.6	1.4
High flammability limit	[vol.%]	19	5.6–6.5	7.4

The autoignition temperature of a substance is the lowest temperature at which it spontaneously ignites in normal atmosphere without an external source of ignition, such as a flame or spark. Glycerol has the highest autoignition temperature. The flammable limit is the range of a fuel concentration that will burn or explode if an ignition source is introduced.

Cloud point refers to the temperature below which wax in diesel or biowax in biodiesels forms a cloudy appearance. Pour point is the lowest temperature at wich the fuel can still be moved, before it has gelled [31]. For authors best knowledge there are no experimental information on pour points and cloud points of glycerol and gasoline in literature. Taking into account higher freezing (melting) temperature one can assume that both cloud point and pour point are higher than of gasoline and diesel.

3. Conclusion

The goal of this paper was to analyze the basic properties of gasoline, diesel and glycerol and their blends, such as ignition delay times and laminar burning velocities. Calculations are performed with use of Cantera tool in Matlab and Python environments. Validation the chemical kinetics mechanisms for reproduction of ignition delay times and laminar burning velocities of both n-heptane/air and iso-octane/air was performed. Interest in glycerol as a fuel is relatively new, therefore experimental data on ignition delay times and laminar burning velocities are not yet present in literature.

Analyses of influence of glycerol on ignition delay times of n-heptane/air and iso-octane/air mixtures covered wide range of conditions: temperatures from 600 to 1600 K, pressure 10–200 bar, equivalence ratio 0.3 to 14, molar fraction of glycerol in fuel 0-1 (from pure n-heptane or iso-octane to pure glycerol) in air. Simulations of LBV in air cover temperatures: 300 K and 500 K, pressures: 10, 40, 100, 200 bar and equivalence ratio from 0.3 to 1.9.

Glycerol has anti-knock properties for ignition temperatures lower than 900 K, based on calculated IDT of iso-octane/glycerol/air mixtures and cetane number of gasoline and glycerol. However to notice this influence molar fraction of glycerol in a fuel needs to be min. ~50%. LBV of glycerol and iso-octane is comparable.

Glycerol has longer IDT than n-heptane for temperatures lower than 1000 K. The highest difference is present for n-heptane/air negative temperature coefficient region. For local minimum (T = 830 K, n-heptane: IDT = 400 μs) it may reach even 2 orders of magnitude (glycerol: IDT = 20 ms). On the other hand, in order to change IDT of n-heptane using glycerol, glycerol molar fraction need to make up at least 50%. Small amounts of glycerol should not worsen ignitability. To fulfill ASTM limit for kinematic viscosity of diesel and biodiesel the amount of glycerol should not exceed 10% and 19% respectively. However, in the ASTM limit there is also requirement that maximal allowed fraction of glycerin in biodiesel does not exceed 0.24% mass and it is important in terms of injector depositions and filter plugging.

Nomenclature

IDT	ignition delay time
LBV	laminar burning velocity
LFO	light fuel oil
FAME	fatty acid methyl esters
PM	particulate matter
NOx	nitirc oxides
NTC	negative temperature coefficient
T	temperature
P	pressure
X	molar fraction
EQR	equivalence ratio
v	kinematic viscosity
k	parameter in Kanaveli's mixing rule
g	glycerol
B100	100% of biodiesel
E95	95% of ethanol and 5% of gasoline
ASTM	American Society for Testing and Materials
ERC	Engine Research Centre
POLIMI	Polytechnic University of Milan

Bibliography

[1] European Biofuels Technology Platform, Fatty Acid Methyl Esters (FAME). *Biofuel Fact Sheet*. 2011, **1**, 1-2.

[2] MINER, C., DALTON, N.N. Glycerine: an overview. *Chem Soc Monogr*. 1953, 117(212), 1-27.

[3] SETYAWAN, H.Y., ZHU, M., ZHANG, Z., ZHANG, D. Ignition and combustion characteristics of single droplets of a crude glycerol in comparison with pure glycerol, petroleum diesel, biodiesel and ethanol. *Energy*. 2016, **113**, 153-159.

[4] Rychlik A., Application of glycerine for powering piston diesel engines of large power. *Combustion Engines*. 2015, **162**(3), 644-648, 2015.

[5] MCNEIL, J., DAY, P., SIROVSKI, F. Glycerine from biodiesel: the perfect diesel fuel. *Process Saf. Environ. Prot.* 2012, **90**(3), 180-188.

[6] STELMASIAK, Z., PIETRAS, D. Utilization of waste glycerin to fuelling of spark ignition engines. *IOP Conf. Ser. Mater. Sci. Eng*. 2016, **148**, 12087.

[7] GRAB-ROGALINSKI, K.. SZWAJA, S. The possibility of use a waste product of biofuels production-glycerol as a fuel to the compression ignition engine. *J. KONES*. 2016, **23**(3), 157-164.

[8] EATON, S.J. et al. Formulation and combustion of glycerol-diesel fuel emulsions. *Energy and Fuels*. 2014, **28**(6), 3940-3947.

[9] ARBAB, M.I., MASJUKI, H.H., VARMAN, M. et al. Fuel properties, engine performance and emission characteristic of common biodiesels as a renewable and sustainable source of fuel. *Renew. Sustain. Energy Rev*. 2013, **22**, 133-147.

[10] KESLING, H.S., KARAS, L.J., LIOTTA, F.J. Diesel fuel. 1994.

[11] RANZI, E. et al. Chemical kinetics of biomass pyrolysis. *Energy & Fuels*. 2008, **22**(6), 4292-4300.

[12] DUPONT, C. et al. Biomass pyrolysis: kinetic modelling and experimental validation under high temperature and flash heating rate conditions. *J. Anal. Appl. Pyrolysis*. 2009, **85**(1-2), 260-267.

[13] CALONACI, M., GRANA, R., BARKER HEMINGS, E. et al. Comprehensive kinetic modeling study of bio-oil formation from fast pyrolysis of biomass. *Energy & Fuels*. 2010, **24**(10), 5727-5734.
[14] HEMINGS, E.B., CAVALLOTTI, C., CUOCI, A. et al. A detailed kinetic study of pyrolysis and oxidation of glycerol (propane-1,2,3-triol). *Combust. Sci. Technol.* 2012, **184**(7-8), 1164-1178.
[15] CORBETTA, M. et al. Pyrolysis of centimeter-scale woody biomass particles: kinetic modeling and experimental validation. *Energy & Fuels*. 2014, **28**(6), 3884-3898.
[16] DEE, V., SHAW, B.D. Combustion of propanol–glycerol mixture droplets in reduced gravity. *Int. J. Heat Mass Transf*. 2004, **47**(22), 4857-4867.
[17] RANZI, E. et al. Hierarchical and comparative kinetic modeling of laminar flame speeds of hydrocarbon and oxygenated fuels. *Prog. Energy Combust. Sci*. 2012, **38**(4), 468-501.
[18] HARTMANN, M., GUSHTEROVA, I., FIKRI, M. et al. Auto-ignition of toluene-doped n-heptane and iso-octane/air mixtures: high-pressure shock-tube experiments and kinetics modeling. *Combust. Flame*. 2011, **158**(1), 172-178.
[19] ZHANG, K. et al. An updated experimental and kinetic modeling study of n-heptane oxidation. *Combust. Flame*. 2016, **172**, 116-135.
[20] GOODWIN, D.G., MOFFAT, H., SPETH, R.L. Cantera: an object-oriented software toolkit for chemical kinetics, thermodynamics, and transport processes. 2017.
[21] JERZEMBECK, S., PETERS, N., PEPIOT-DESJARDINS, P., PITSCH, H. Laminar burning velocities at high pressure for primary reference fuels and gasoline: experimental and numerical investigation. *Combust. Flame*. 2009, **156**(2), 292-301.
[22] LIU, Y., JIA, M., XIE, M., PANG, B. Improvement on a skeletal chemical kinetic model of iso-octane for internal combustion engine by using a practical methodology. *Fuel*. 2013, **103**, 884-891.
[23] BARABÁS, I., TODORUŢ, I.A. Predicting the temperature dependent viscosity of biodiesel-diesel-bioethanol blends. *Energy and Fuels*. 2011, **25**(12), 5767-5774.
[24] KUMAR, P., KISHAN, P.A., DHAR, A. Numerical investigation of pressure and temperature influence on flame speed in CH4-H2 premixed combustion. *Int. J. Hydrogen Energy*. 2016, **41**(22), 9644-9652.
[25] CHENG N.-S. Formula for the viscosity of a glycerol−water mixture. Ind. Eng. Chem. Res. 2008, 47(9), 3285-3288.
[26] GRAB-ROGALINSKI, K., SZWAJA, S. The combustion properties analysis of various liquid fuels based on crude oil and renewables. *IOP Conf. Ser. Mater. Sci. Eng*. 2016, **148**, 12066.
[27] KANAVELI, I.-P., ATZEMI, M., LOIS, E. Predicting the viscosity of diesel/biodiesel blends. *Fuel*. 2017, **199**, 248-263.
[28] STEIN, R.A. et al. Effect of heat of vaporization, chemical octane, and sensitivity on knock limit for ethanol – gasoline blends. *SAE Int. J. Fuels Lubr*. 2012, **5**(2), 2012-01-1277.
[29] QUISPE, C.A.G., CORONADO, C.J.R., CARVALHO, J.A. Glycerol: production, consumption, prices, characterization and new trends in combustion. *Renew. Sustain. Energy Rev*. 2013, 27, 475-493.
[30] P. Information 3. *Chemical and Physical Information* 3.1, 1990.
[31] ALPTEKIN, E., CANAKCI, M. Characterization of the key fuel properties of methyl ester-diesel fuel blends. Fuel. 2009, 88(1), 75-80.

Agnieszka Jach, MSc. – Faculty of Power and Aeronautical Engineering at Warsaw University of Technology.

e-mail: *AJach@itc.pw.edu.pl*

Ilona Cieślak, MSc. – Faculty of Power and Aeronautical Engineering at Warsaw University of Technology.

e-mail: *ICieslak@itc.pw.edu.pl*

Prof. Andrzej Teodorczyk, DSc., DEng. – Faculty of Power and Aeronautical Engineering at Warsaw University of Technology.

e-mail: *ATeod@itc.pw.edu.pl*

Article citation info:
LEWKOWICZ, R., PIĄTKOWSKI, P., ŚCIEGIENKA, R., SZYMANIUK, B. The impact of starting process on wear of cylinder wall. *Combustion Engines*. 2017, **169**(2), 176-180. DOI: 10.19206/CE-2017-231

Ryszard LEWKOWICZ
Piotr PIĄTKOWSKI
Ryszard ŚCIEGIENKA
Błażej SZYMANIUK

CE-2017-231

The impact of starting process on wear of cylinder wall

The results of experimental research of cylinder wall wearing process were presented in this article. Researches were conducted on the basis of four strokes spark ignition one cylinder engine. The main goal of presented research was assessment of impact of cold start condition on intensity of cylinder wall wearing process. The new one and worn engine oil with grade 10W40 was used for experimental research. The experimental research was conducted on specially developed experimental stand. The wear of cylinder wall was assessed on the basis of cylinder diameter and wall roughness measurements.

Key words: *cylinder wall, oil grade, wear*

1. INTRODUCTION

The strain of engine's construction due to the gaseous forces, inertia forces and the temperature's gradients on the wall of combustion chamber are transferred to the crankshaft system. Among the parts of combustion engine which have a significant influence on energy losses and on the friction forces are piston, piston's rings and cylinder wall (TPC). It results on mechanical efficiency on the level of 45÷65%. Moreover, 75% of friction forces loses are results of piston rings and 25% of these are connected with friction between the piston and cylinder wall [7]. So the crankshaft-piston system is given to extremal thermic and mechanical strains. For decrease in friction loses it is necessary to obtain a good lubrication conditions between cylinder wall, piston and piston's rings. The modern engines with high output power and its trend to minimize of engine piston displacement (downsizing) are strongly given to thermic and mechanical strains. Engine cooling system and lubrication system are responsible for an optimal regulation of engine work conditions. As the cooling water is used for indirect thermal energy transfer to the air, the oil used in lubrication system directly flows through the zones where the friction appears. So the engine lubrication system have to lubricate the friction areas and have to transfer the thermal energy similar to the indirect cooling system [1, 2].

2. Engine start

The character of the engine's work conditions (especially the TPC system) are the one of the main of loses reasons for an engine. During the piston's move from TDC to BDC and non-stability of piston velocity with its stops have a negative impact on oil film achievement connected to the cylinder wall [7]. Moreover, it is impossible to obtain a regular distribution of stress made by piston's rings due to the cylinder shape changes and the friction wear of cylinder wall, especially during "cold" starts and very high engine load [9].

Due to the wedge-shaped zone from TPS system which appears during the engine work the oil film between on cylinder wall have been obtained. Thickness of oil film on cylinder wall isn't symmetric in cooperation to pressure resulted from piston ring. When the piston starts, the piston rings are changing its position and shape – what results in micro rings deformation and stress in oil film. These mechanical relation have an impact on pressure resulted from piston rings and oil film thickness.

Among the forces in TPC system can be indicated axial and radial direction forces [6]. The different values of engine crankshaft rotations disturb an oil film on cylinder wall. Significant influence in building of wedge-shaped oil film on cylinder wall have shape of piston rings.

Oil film between piston rings and cylinder wall have a hydrodynamic and elastic-hydrodynamic reactions. The hydrodynamic reactions results in piston rings and cylinder wall separating and lubrication.

Hydro-dynamic influence of oil film can be observed between piston rings and cylinder wall (Fig. 1), especially for TDC and BDC, when piston velocity decrease to zero. In these time the conditions for oil film generation have been done due to the transverse piston rings movement. It results in the worse of lubrication conditions [8].

As shows the results presented by Włodarski, the biggest cylinder wall wear appeared close to the TDC. Elastic and hydrodynamic reactions of cooperated friction parts results in resilience micro-deformation and changes in oil film thickness and pressure [7].

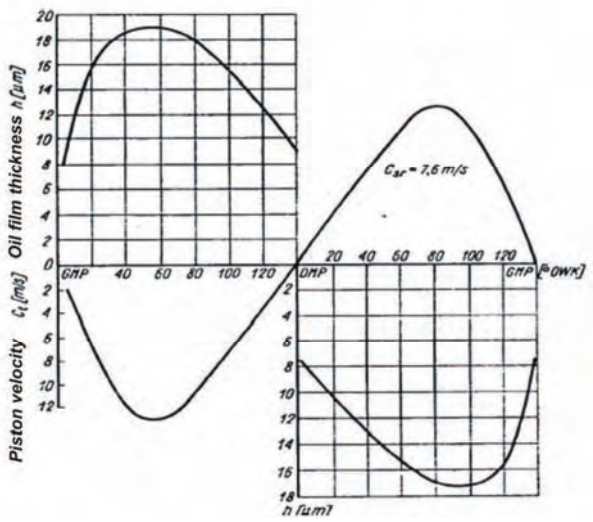

Fig. 1. The minimal oil film thickness by piston ring-cylinder wall system and the crankshaft position [8]

The mechanism of separation piston rings and cylinder wall was presented in Fig. 2. When the engine makes an intake stroke the oil ring has a contact with the fresh oil film (h_{ol}) and wiper and compression rings are moving on the rest of oil film (h_{wz}) and is a residue oil which leaved the oil ring. During the compression stroke there is a reverse process.

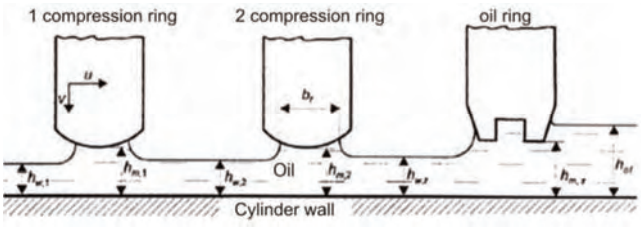

Fig. 2. The scheme of relation between the piston rings and cylinder wall [6]

Lubrication process of cylinder wall is created by oil splash and by the movement of piston ring during engine work. The oil pumping process is caused by the ring end movement for first stroke and start the engine, oil isn't pumped to combustion chamber. Moreover, the film created by cold oil on cylinder wall is quite unevenness. It have an impact on increase in wear of TPC system. Resistance forces depends mainly from a static friction coefficient and it is connected with the time calculated from the last engine start. The sources of these effect are decay of oil film and increase in micro adhesion between cooperated parts. The experiments conducted by Janecki and Gołąbek [5] indicates that 100 times of cold starting for engine (for diesel engine) is an equivalent of 200 hours of work.

The momentum of resistance during a starting process is mainly caused by forces of kinematic friction. This resistance covers from 70 up to 90% of total friction momentum for TPC system, as well in the main bearings of crankshaft and camshaft system. The momentum of kinematic friction resistance during a starting process depends from the construction factors, assembly parameters and form the temperature of oil in lubrication system.

For the first part of starting process, on cylinder wall can't be achieve a minimal thickness of oil film. It caused of increase in friction forces and wear of cooperated engine parts. Furthermore, there can appear a dry friction phase. When the engine starts, between parts of TPC system can be achieve wear process caused by adhesion forces, friction forces and corrosion. This situation was presented in Fig. 3.

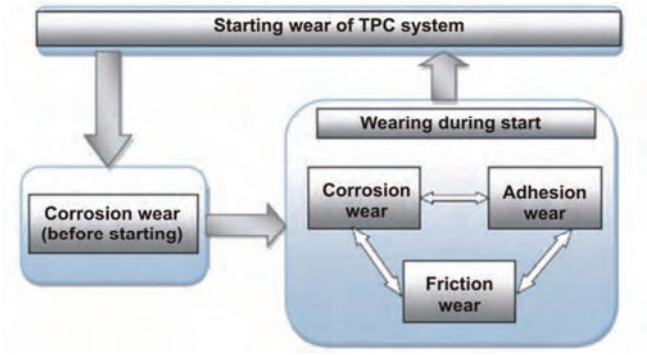

Fig. 3. The scheme of starting wear of TPC system [3]

The adhesion between TPC parts is caused by a broke micro-connection surfaces which worked for initial time of engine starting process.

One of the main factor which significantly results in a cylinder's wall friction wear during starting process is time gap where the engine didn't run. When this gap grow up, there can be observed increase in wear caused by electro-chemical corrosion and by gravity-flow of oil from cylinder wall to oil sump.

Temperature of the engine is also an important factor, which results in wear of TPC system. When the engine temperature grows an intensity of cylinder wall wear declines. It was presented in Fig. 4. For the engine cold start (temperature about 0˚C) the intensity of cylinder's wall wear is an equivalent of 80 kilometers, for the lower temperature for ex. –10°C – 100 kilometers.

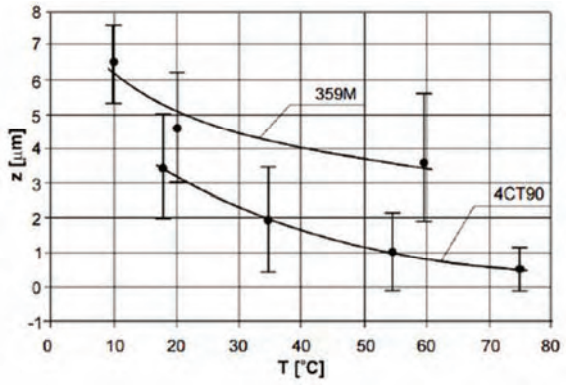

Fig. 4. The average cylinder wall wear (with standard error) for the diesel engine type 4CT90 and 359M dependence on temperature (T) after 1000 engine starts [4]

On the basis of literature's data we can write that engine starting process cause about 15% to 75% of total engine wear [3].

3. Experimental stand

Researches were conducted on the basis of specially developed experimental stand, where can mentioned:

– four strokes, one cylinder SI engine,
– electric engine with drive belt system,
– steering system,
– engine temperature measurement system,
– air temperature measurement system.

Table1. Technical data of engine 139QMA [10]

Parameter	Type/value
Starting system	manual/electric starter
Engine type	4 strokes
No. cylinder	1
The type of combustion chamber	Hemispheric
Cam system	Valve type, OHC, chain drive
Cylinder bore x piston stroke [mm]	39.0 x 41.4
Power [kW/min^{-1}]	2,2/7500
Torque [Nm/min^{-1}]	2,9/7000
Compression ratio	10.5:1
Lubrication system	Pressure-splash system with internally toothed pump and reticulated oil filter

The engine type 139QMA used for experiment was taken from motorcycle Baotian BT4QT. View of experimental stand was presented in Fig. 5 and the technical date was presented in Table.

The combustion engine was started by electric starter which was steered by electric time control system. Time of starting and time gap between next start were determined by operator. It lets us obtain very similar condition for engine cold start.

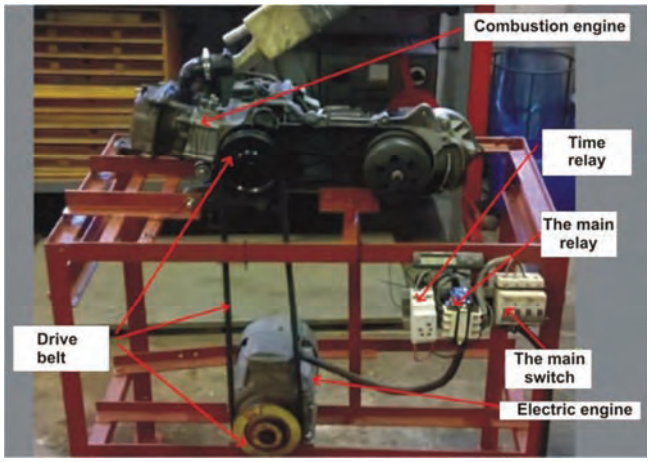

Fig. 5. The view of experimental stand with combustion engine and electric steering system

3.1. Experimental results

For conducting of research two set of nominal cylinder with piston and piston ring were used. The third nominal cylinder was assessed as a basis and it was presented in Fig. 7. In relation to nominal parts dimension (cylinder no. 3) the wear of two others were calculated.

Total time of starting process was 100 hours for each cylinder (with the new piston and piston rings) set. It was determined by steering system as:

– single starting time – 3 s,
– break between next starting – 15 s,
– number of starting cycles – 27000.

The scheme of experimental processing was presented in Fig. 6.

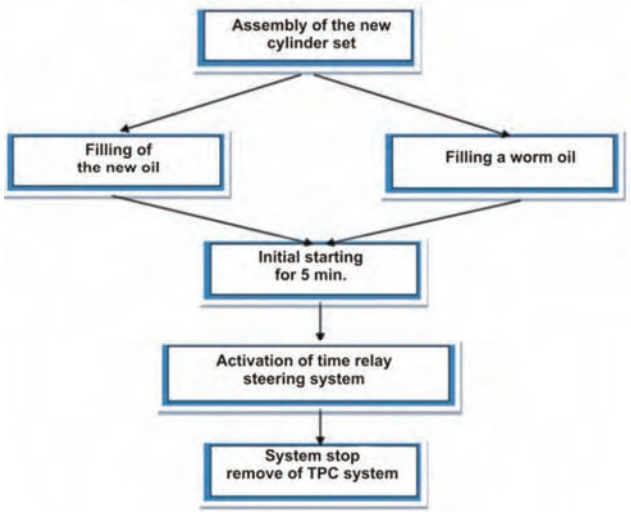

Fig. 6. The scheme of experiment processing

The air temperature in laboratory during conducted researches was about 18.5°C ±1°C with a relative humidity 61% ±5%.

Cylinder wearing was measured by increase its diameter. Other goal of conducted research was assessment of influence of oil grade on wearing process. For theses research the new oil (Mobil Super™ 2000) and worn-out oil with grade 10W40 was used. The worn-out oil was used after 1500 hours of engine work with nominal load. For the future research:

– basic cylinder was indicated as no. 1,
– cylinder worked with the new oil – no. 2,
– cylinder worked with worn oil – no. 3.

For accuracy of wear measurements a TRIMOS VERTICAL AUTOMATIC TVD 800A altimeter was used. The equipment of this device let us make some length measurements and shape deformation and localization error as well. The technical parameters of this device was presented in Table 2

Table 2. Altimeter TRIMOS VERTICAL AUTOMATIC TVD 800A – technical data [11]

Parameter	Value
Total scope [mm]	805
Scope without changing of measurement equipment [mm]	525
Total offset of metrological handle [mm]	240
Length measurement accuracy [µm]	5
Measurement pressure [g]	300
Total device height [mm]	845

Cylinder diameter measurements were conducted for three planes:

– below of TDC,
– up of BDC,
– in the middle of piston stroke,

and for two perpendicular direction. Localisation of measurement points were presented in Fig. 7.

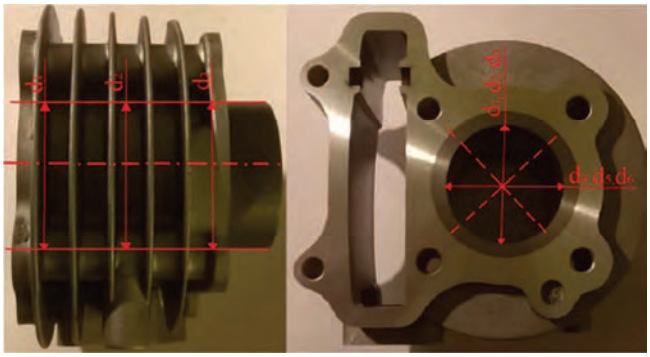

Fig. 7. Localization of measurement points for cylinders

Each measurement was repeated three time and on the basis of this arithmetic mean was calculated. The results of measurement and calculation were presented in Table 3 and diameter's differences in Table 4.

Table 3. Results of cylinder diameter measurement (arithmetic mean)

Cylinder no. 1					
d_1 [mm]	39.011	d_2 [mm]	39.011	d_3 [mm]	39.010
d_4 [mm]	39.010	d_5 [mm]	39.011	d_6 [mm]	39.010
Cylinder no.2					
d_1 [mm]	39.014	d_2 [mm]	39.012	d_3 [mm]	39.012
d_4 [mm]	39.015	d_5 [mm]	39.013	d_6 [mm]	39.015
Cylinder no.3					
d_1 [mm]	39.019	d_2 [mm]	39.018	d_3 [mm]	39.020
d_4 [mm]	39.021	d_5 [mm]	39.017	d_6 [mm]	39.019

Table 3. Differences in diameter's for nominal and worn cylinder

		Differences			
Cylinder no. 1		Cylinder no. 2		Cylinder no. 3	
d_1 [mm]	d_4 [mm]	d_1 [mm]	d_4 [mm]	d_1 [mm]	d_4 [mm]
39.011	39.010	0.003	0.005	0.009	0.012
d_2 [mm]	d_5 [mm]	d_2 [mm]	d_5 [mm]	d_2 [mm]	d_5 [mm]
39.011	39.011	0.001	0.002	0.006	0.008
d_3 [mm]	d_6 [mm]	d_3 [mm]	d_6 [mm]	d_3 [mm]	d_6 [mm]
39.010	39.010	0.002	0.004	0.009	0.010

These results (Table 2) were presented in Fig. 8. The scope of achieved measurements were from 39.010 mm up to 39.021 mm. Calculated standard error for diameter mean estimation was less than 0.5%.

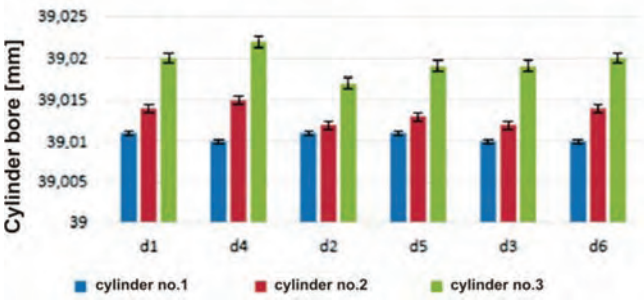

Fig. 8. Results of cylinder diameters measurements (arithmetic mean)

The measurements results presented in figure 8 let us state that the biggest cylinder wear was observed about TDC piston's position for both type of cylinder (no. 2 and 3). The lower wear of cylinders was observed close to BDC piston position. Significant impact of oil grade on cylinder wear intensity was observed during conducting an experiment. Lubrication of cylinder wall by worn engine oil results in increase of cylinder wear.

Another parts of our research were connected with measurement of cylinder's profile. The measurement were conducted by corner type profile meter HOMMEL TESTER T8000 made by HOMMELWERKE. This measurement stand was equipped by PC system, which allowed to make measurements of chosen profile indicators. This measurement system were based on Turbo Roughness computer application. It provided to achieve value the all normalized roughness parameters (R), undulations (W) and unfiltered parameters (P) agree with ISO, DIN and JIS standards.

Marking of cylinder were the same like during wear measurements. For all cylinders a length of measurement were 4.8 mm and was located close to the medium of stroke. The results of profile measurements were presented in Table 4. Receive profiles of cylinder wall were presented in Fig. 9–11.

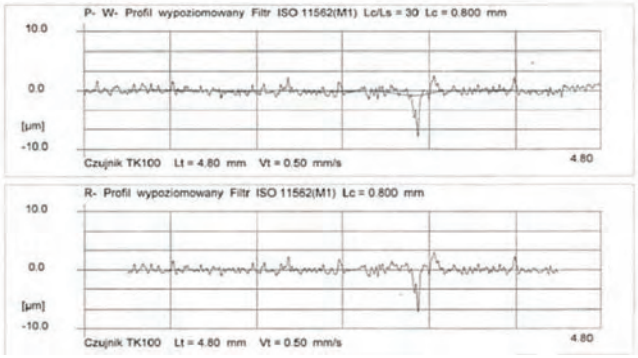

Fig. 9. Cylinder no 1 – wall's profile

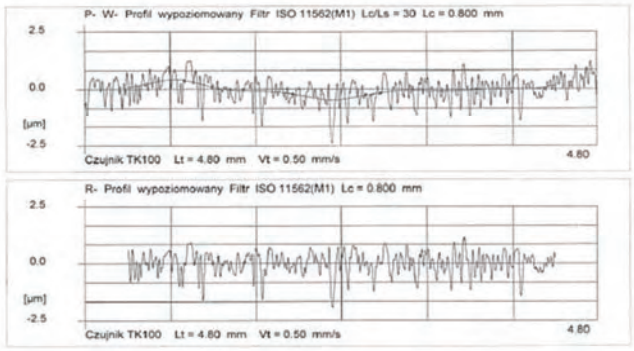

Fig.10. Cylinder no. 2 – wall's profile

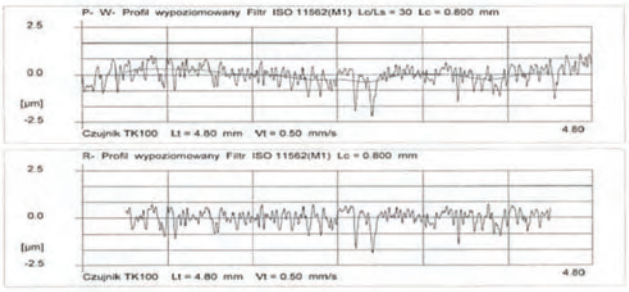

Fig.11. Cylinder no. 3 – wall's profile

Table 4. Results of measurements of cylinder wall roughness

	Cylinder no. 1	Cylinder no. 2	Cylinder no. 3
Ra [µm]	0.49	0.36	0.3
Rq [µm]	0.79	0.47	0.39
Rz [µm]	4.29	2.39	1.89
Rt [µm]	10.02	3.06	2.55
Pt [µm]	10.48	3.64	3.26
Wt [µm]	1.07	0.89	0.69

The results of profile parameters measurements let us state that reaching of TPC parts have an impact on decrease in roughness values. Third cylinder was characterized by the lowest value R_a, R_q, R_z, R_t which worked with worn engine oil. In this case the most intensive dry friction were observed. The effect of reaching process was observed for

the oil too. It was confirmed by decrease in Ra value. Decrease in roughness parameters were connected with cylinder surface smoothing and still left the superfinish rifts. It was presented in Fig. 9.

The biggest differences were observed for Rt parameter. This situation is caused by cooperation of cylinder wall and piston rings. It confirms that reaching process have significant impact on surface smoothing. Moreover, the superfinish of cylinder wall enhance this process.

Summary

On the basis of presented researches connected with cylinder wall wearing and roughness parameters for engine worked with the new and worn engine oil let us state that:

1. The oil grade and quality have a significant impact on cylinder wall wearing during engine starting, where the biggest wear was observed for cylinder which worked with worn oil.
2. During the experiment was observed similar character of cylinder wear process like it goes during normal engine work.
3. The oil quality have significant impact on friction's wearing what results in cylinder smoothing.
4. The biggest wear of cylinder wall was for the plane which is perpendicular to crankshaft axis.
5. Conducted research confirms that intensity of cylinder wear is caused by starting process, especially during cold start – what reflects in roughness decrease.

Nomenclature

TPC piston – cylinder – piston ring system
BDC Buttom dead center
TDC Upper dead center

Literatura

[1] BERNHARDT, M., DOBRZYŃSKI, S., LOTH, E. Silniki samochodowe. *WKŁ*, 1988, 489-516.
[2] BŁAŻEJ, A. Poradnik serwisowy – Vademecum stosowania olejów silnikowych, *Instalator Polski*. 2013, 14-25.
[3] DROŹDZIEL, P. Wybrane zagadnienia samochodowego silnika o zapłonie samoczynnym. *Polskie Naukowo-Techniczne Towarzystwo Eksploatacyjne*. 2007.
[4] DROŹDZIEL, P. Widmo rozruchu silnika o zapłonie samoczynnym jako kryterium oceny warunków użytkowania samochodu. *Polskie Naukowo-Techniczne Towarzystwo Eksploatacyjne*. 2009.
[5] GOŁĄBEK, S., JANECKI, J. Zużycie części i zespołów pojazdów samochodowych. *WKiŁ*. Warszawa 1979, 163-171.
[6] ISKRA, A. Rozkład filmu olejowego na gładzi cylindrowej silnika tłokowego. *Wydawnictwo Politechniki Poznańskiej*. Poznań 1987.
[7] KAŹMIERCZAK, A. Tarcie w ruchu posuwisto-zwrotnym zespołu tłok-pierścienie-cylinder. *Oficyna Wydawnicza Politechniki Wrocławskiej*. 2005, 23-52.
[8] WŁODARSKI, J.K. Tłokowe silniki spalinowe – procesy trybologiczne, *WKiŁ*. 1982.
[9] WRÓBLEWSKI, P. Ważne mikrometry. *AutoEXPERT* 2015, **5**, 30-31.
[10] www.49ccscoot.com/manuals/139QM_Engine_Manual.pdf
[11] www.auto-met.com/fowler/pdf/387.pdf

Ryszard Lewkowicz, DSc., DEng. – Faculty of Mechanical Engineering at Koszalin University of Technology.

e-mail: *Ryszard.Lewkowicz@tu.koszalin.pl*

Piotr Piątkowski, DSc., DEng. – Faculty of Mechanical Engineering at Koszalin University of Technology.

e-mail: *Piotr.Piatkowski@tu.koszalin.pl*

Ryszard Ściegienka, DSc., DEng. – Faculty of Mechanical Engineering at Koszalin University of Technology.

e-mail: *Ryszard.Sciegienka@tu.koszalin.pl*

Błażej Szymaniuk, MEng. – Mechanical Engineering at Koszalin University of Technology.

e-mail: *Blazej.Szymaniuk@gmail.com*

Article citation info:
SMOLEC, R., IDZIOR, M., KARPIUK, W., KOZAK, M. Assessment of the potential of dimethyl ether as an alternative fuel for compression ignition engines. *Combustion Engines*. 2017, **169**(2), 181-186. DOI: 10.19206/CE-2017-232

Rafał SMOLEC
Marek IDZIOR
Wojciech KARPIUK
Miłosław KOZAK

CE-2017-232

Assessment of the potential of dimethyl ether as an alternative fuel for compression ignition engines

The main problem that the automotive industry has been dealing with since the beginning of the XXI century is the need to reduce the exhaust emissions from piston combustion engines. Another, not at all less important problem is the depleting natural resources of crude oil. There are many concepts aiming at resolving of the said issues. One of them is the possibility of application of dimethyl ether (DME) in a classic engine. The paper characterizes this fuel, drawing attention to the aspects related to the adaptation of the engine to this type of fuel, presents the process of its atomization and relevant exhaust emissions.

Key words: *dimethyl ether, DME, alternative fuels, common rail, biofuel*

1. Introduction

The automotive sector is one of the branches of economy whose dynamics of advancement is tightly related to the development of industry. A constant increase in the widely understood production results in a need to transport a greater amount of raw materials and ready made products – therefore, the advancement of transport boosts the advancement of industry. The greatest dynamics in the growth of the number of vehicles in recent years has been observed in rapidly developing countries such as China or India (Fig. 1). It is forecasted that within the next 20 years, the number of vehicles worldwide will double.

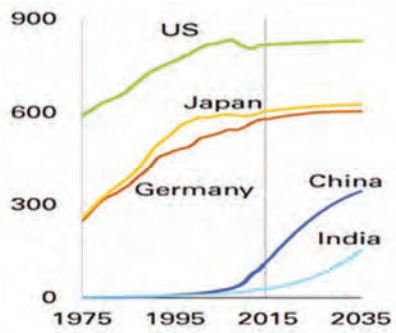

Fig. 1. Number of vehicles per 1 000 inhabitants in individual regions of the world [2]

Energy plays an important role in the discussed problems. In order to preserve the dynamics of the advancement of the automotive industry, it is necessary to provide proper quantity of the said energy. In the automotive sector, the energy used to propel vehicles comes from the fuel – mainly the product of distillation of crude oil. It is widely known that the world resources of fossil fuels such as crude oil coal or natural gas will eventually deplete. In order to provide sufficient amount of fuel guaranteeing an unrestrained advancement of the automotive industry, it is necessary to diversify the fuel resources. Therefore, greater emphasis has been put on the search for alternative sources of energy. Renewable fuels such as fatty acid methyl esters (FAME) are gaining in popularity. They are a product of estrification of oil obtained from rapeseed. This fuel is characterized by good energy related properties (the calorific value of this fuel is close to that of diesel fuel). This fuel however, has slightly different density and viscosity, which makes it difficult to apply in modern injection systems. Additionally, due to food deficit in some regions of the world, production of fuels from materials that can be used to manufacture food is reduced. This opens a window of opportunity for entirely new fuels referred to as second generation alternative fuels, dimethyl ether – DME being one of them.

2. Characteristics of dimethyl ether as a fuel

Dimethyl ether is an odorless and colorless organic compound belonging to the group of ethers. Under typical ambient conditions (pressure 0.1 MPa and temperature 25°C) it remains in the volatile phase. In a closed space under pressure of its own vapor it changes into liquid. Selected properties of DME and their comparison with diesel fuel and FAME have been shown in Table 1.

The density of volatile dimethyl ether is greater than that of air. In its liquid phase, it is approx. 80% of the density of diesel fuel and only 72% of the density of FAME. Given this parameter, in order to supply the same mass of fuel, it is necessary to provide 20% more volume of DME compared to conventional fuel and 25% more compared to FAME. Dimethyl ether is sparingly soluble in water. Its maximum mass share in the mixture does not exceed 6%. Carbon has the greatest mass share of 52.2% in a DME molecule. The share of hydrogen in the molecule mass is estimated at 13%. It is noteworthy that DME has better carbon to hydrogen ratio than diesel fuel (C/H). This results in a lesser amount of CO_2 and greater amount of H_2O generated following full combustion, which is the effect of the combustion of hydrogen. A DME molecule does not have direct bonds among the atoms of carbon – this facilitates full combustion, thus reducing the amount of carbon monoxide and particulate matter. Full combustion is also facilitated by a reduction of local oxygen deficits through the presence of this element in the molecule. Oxygen constitutes 34.8% of the molecule mass, which makes the calorific value of DME 40% lower compared to other fuels. Given the density and calorific value of other fuels, there is 18 409

MJ of energy stored in 1 m^3 of liquid dimethyl, 35 317 MJ of energy in 1 m^3 of diesel fuel and 36 312 MJ in 1 m^3 of FAME. In order to supply the same amount of energy, it is necessary to provide almost twice the volume of DME.

Due to the presence of the atom of oxygen, the stoichiometric air fuel ratio necessary for a full and complete combustion is also different. For the analyzed alternative fuel, this ratio is 9. It means that in order for the full combustion of 1 kg of dimethyl ether to take place, one needs only 9 kg of air. This amount is lower than that of diesel fuel, for which the mass of air needed for full combustion is 14.6 kg.

Table 1. Comparison of the properties of dimethyl ether with diesel fuel and fatty acid methyl esters FAME [1, 5, 15, 18]

Properties	Unit	Diesel fuel	Dimethyl ether DME	Methyl esters FAME
Critical pressure	[MPa]	3.00	5.37	8.1
Lower heating value	[MJ/kg]	42.5	27.6	39.5
Lower explosive limit	[% vol.]	0.6	3.2	–
Fluid density	[kg/m^3]	831	667	919.3
Upper explosive limit	[% vol.]	7	18	–
Fluid kinematic viscosity	[cSt]	3	<0.1	38
Cetane number		40–50	58	54-56
Mole mass	[g/mol]	170	46	296
Surface tension	[N/m]	0.027	0.012	0.352
Vapor pressure	[kPa]	<< 10	530	0.42
C/H ratio		6.14	4.01	6.41
Stoichiometric air fuel ratio		14.6	9	12.5
Chemical structure		–	CH_3–O–CH_3	–
Critical temperature	°C	434	126	239
Self ignition temperature	°C	249	234	261
Boiling temperature at 1atm	°C	176–370	–25	280-350
Oxygen content	[% mass]	0	34.8	1
Carbon content	[% mass]	86	52.2	77
Hydrogen content	[% mass]	14	13	12

3. Engine adaptation for dimethyl ether fueling

The fueling of a diesel engine with dimethyl ether is possible without any substantial modifications. Yet, due to its low boiling temperature of –25°C, it is necessary to store ether in an airtight container. The pressure generated by its vapor converts ether into a liquid under temperatures of 20 – 30°C (Fig. 2), which allows the application of the already existing LPG solutions for its storage (fuel tank) [10].

In the case of diesel engines used as power generators and pumps, the adaptation to DME fueling can be much easier. These engines operate under steady state conditions – constant engine speed and load, which allows the application of components from the second generation LPG systems – a pressure reducer and a mixer (or gas carburetor). The schematics of such a solution has been shown in Fig. 3. The application of such a simple system is possible thanks to the properties of DME. Low boiling temperature of dimethyl ether results in the fuel evaporating quickly and forming a homogenous mixture with air and its high cetane number and a relatively low self-ignition temperature facilitate the mixture ignition and the proper course of the combustion process.

Because it is impossible to precisely control the fuel dosage, the above solution is good only for engines operating under steady state conditions. As for the engines used in vehicles, in order to meet the required exhaust emission standards and ensure sufficient operating parameters, it is necessary to adapt the existing fuel systems to a fuel of different properties.

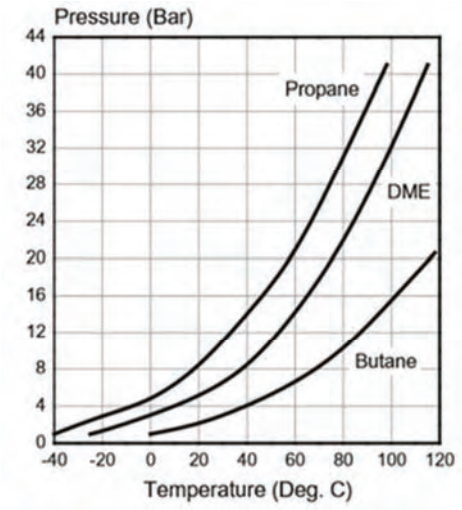

Fig. 2. Comparison of the vapor pressure of dimethyl ether and propane and butane [4]

The most commonplace fuel system in modern diesel engines is the common rail injection system. The application of an alternative fuel forces its supply in the liquid phase to the high pressure pump. Therefore, in the case of DME, it is necessary to use an additional pump sucking the liquid fuel from the tank – this allows the liquid phase to be pumped to the common rail high-pressure pump.

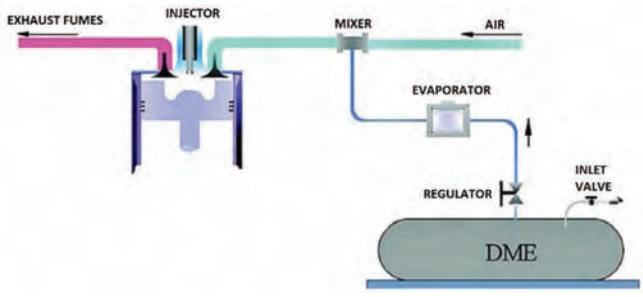

Fig. 3. Schematics of the system for the adaptation of a diesel engine to dimethyl ether fueling [6]

When applying dimethyl ether in modern fuel systems of diesel engines, one should remember that this compound is also a very good solvent and may have an adverse effect on the durability of the elastomer seals. When adapting the engine to DME fueling, it should, thus, be checked whether the seals in the system are DME proof. The application of

an alternative fuel of low viscosity, density and lubricity in a fuel system may result in unknown operating issues related to premature wear. Low values of viscosity and density result in more fuel passing through leakages in the pumping section or the control valves of the high-pressure pump, which is why, in order to perform the same work, greater flow is required. The greatest impact of the reduced density and viscosity is observed inside the injector where any leakage may result in a loss of control on the engine operation (fuel ingress into the combustion chamber).

In terms of the operational aspects, a significant problem is the DME's low lubricity, which may lead to premature wear of the surface layers of the mating components, which, in turn, may lead to increased leakage and, in extreme cases, damage the high pressure pump and the injectors. The problem of lubricity may be relatively easily resolved by the application of appropriate fuel additives.

4. DME atomization characteristics

Because of its low boiling temperature, dimethyl ether injected into the combustion chamber evaporates immediately forming a homogenous mixture with air. Research on the injection and atomization of dimethyl ether have been conducted by many research groups. Wakai et al. [17] have performed tests based on the Schlieren optical system. During the experiment, the alternative fuel was injected with a standard injector into the combustion chamber under the pressure of 1–15 bar. Sorenson et al. [14] have described the phenomena taking place during high-pressure injection of liquid DME with a lubricating additive.

During the injection of dimethyl ether into the combustion chamber, in which the pressure is lower than that of vapor saturation, the DME evaporates immediately. The penetration of the fuel spray front is close to conventional fuel, but the angle of the cone bifurcation and its volume are greater. The main reason for improved atomization is the occurrence of abrupt evaporation of oversaturated vapors. The boundary of the injected fuel spray of DME appears to be less regular compared to conventional fuel. The irregularity of the contour increases with the cylinder pressure [17].

As of the moment when the pressure of the dimethyl ether droplets reaches the supercritical area, the atomization becomes turbulent, which facilitates its good mixing with air. The atomization process may be turbulent as the fuel spray develops. If the fuel droplets are sufficiently small, their evaporation may take place already in the injection nozzle, which will affect further atomization stages. Wakai et al. [17] suggest that in areas of low pressure in the atomizer channels, cavitation may occur more easily compared with diesel fuel. It has also been confirmed that the mechanism of cavitation in the system may boost the atomization in the fuel spray, thus positively affecting the atomization of dimethyl ether. Other authors [7] suggest that the occurrence of gas-liquid flow of injected fuel significantly affects the bifurcation of the fuel spray cone. They, however, do not confirm the positive effect of cavitation on the process of fuel atomization. The comparison of atomization of dimethyl ether and diesel fuel under actual conditions of operation has shown that for high loads and engine speeds, the DME spray penetration is smaller compared with diesel fuel. This happens because of the longer duration of the injection and an increase in the angle of the fuel spray cone resulting from the high gaseous to liquid phase ratio in the injected spray. The analysis of dimethyl ether atomization shows that in order to obtain better mixing quality and better fuel combustion, a modification of the shape of the combustion chamber is recommended. The comparison of the atomization of dimethyl ether and diesel fuel has been shown in Fig. 4.

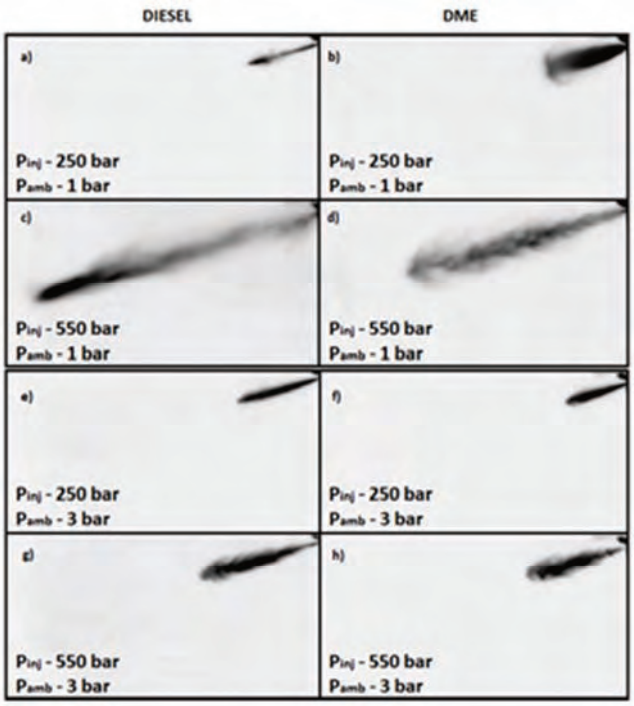

Fig. 4. Comparison of the atomization of DME and diesel fuel under different injection conditions [16]

5. Characteristics of DME emissions

Majority of published research results on exhaust emissions from diesel engines fueled with dimethyl ether indicates a significantly better emission performance compared to diesel fuel. Scarce emission of PM observed during DME combustion is most likely the result of combustion of the lubricating oil or the fuel lubricants. The reduced emission of particulate matter is mainly a result of the low boiling temperature that causes better evaporation of the fuel and its better mixing with air, simple composition of the molecule, presence of oxygen in the molecule and no direct bonds between the atoms of carbon. The comparison of smoke opacity tests performed on an engine fueled with different fuels has been shown in Fig. 5. Fig. 6 presents the results of particulate mass (PM) and particulate number (PN) tests performed on a diesel engine fueled with diesel fuel and DME. It is noteworthy that, in terms of mass, the engine fueled with DME generates much less particulate matter compared with diesel fuel but in terms of number the differences for both fuels are smaller and depend on the engine speed.

Numerous research in exhaust emissions performed by world renowned experts do not lead to clear conclusions as to the emission of NO_x. Part of the publication presents information that the share of this component in the exhaust gas during combustion of dimethyl ether is lower than that

of diesel fuel [3, 9, 21]. The reduction of the NO_x emission is said to result from the fact that DME has lower calorific value, higher cetane number and greater thermal capacity compared to diesel fuel. These characteristics reduce the ignition delay time, which results in a smaller amount of burnt fuel remains in the chamber, thus giving an effect similar to EGR [12].

Some of the scientists [2, 8] think that the short time of ignition delay and almost perfect evaporation of the alternative fuel adds to the rapid pressure and temperature increase during combustion, which facilitates the formation of nitrogen oxides. The positive effect of the operation of EGR has also been confirmed with numerous investigations. EGR much better inhibits NO_x formation when the engine is fueled with DME and does not increase the emission of PM (no need to apply SCR) [13].

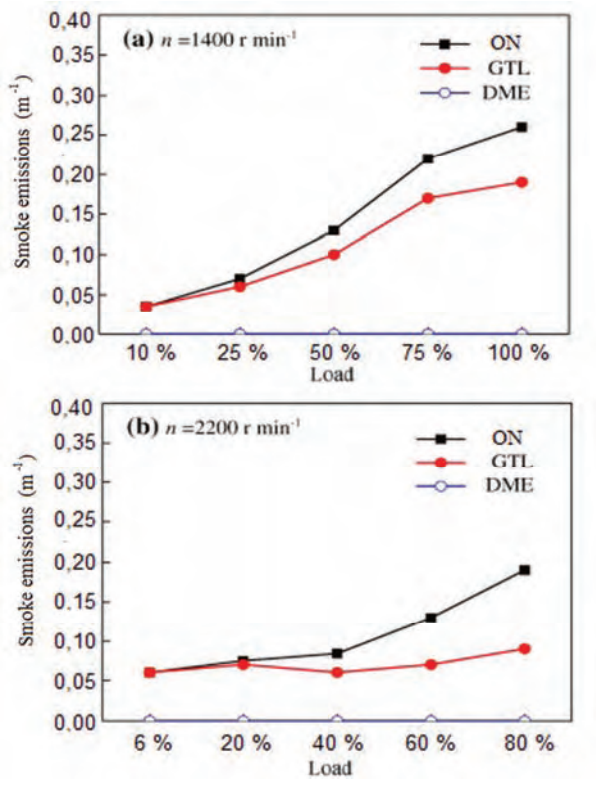

Fig. 5. Comparison of the smoke opacity when fueled with diesel fuel, GasToLiquid and DME under different conditions of engine operation [19]

The investigations of the exhaust emissions conducted by Youn et al. [20] have shown that the quantity distribution of the generated hydrocarbons depends on the moment of fuel injection into the combustion chamber. An increase in the injection delay results in greater HC emission (Fig. 7a). This relation is particularly conspicuous for higher engine speeds. Compared to diesel fuel, the combustion of dimethyl ether in a compression ignition engine is characterized by a lower emission of hydrocarbons for the entire range of injection time. An increased emission is visible only for very delayed injection and higher engine speeds. The main reason for such a low emission of HC is the composition of the molecule, the presence of oxygen as well as rapid and full evaporation of the injected fuel. This also pertains to residual fuel in the injector, constituting one of the main reasons for excess HC emission – increased evaporation rate allows better mixing of the fuel with air and facilitates full combustion.

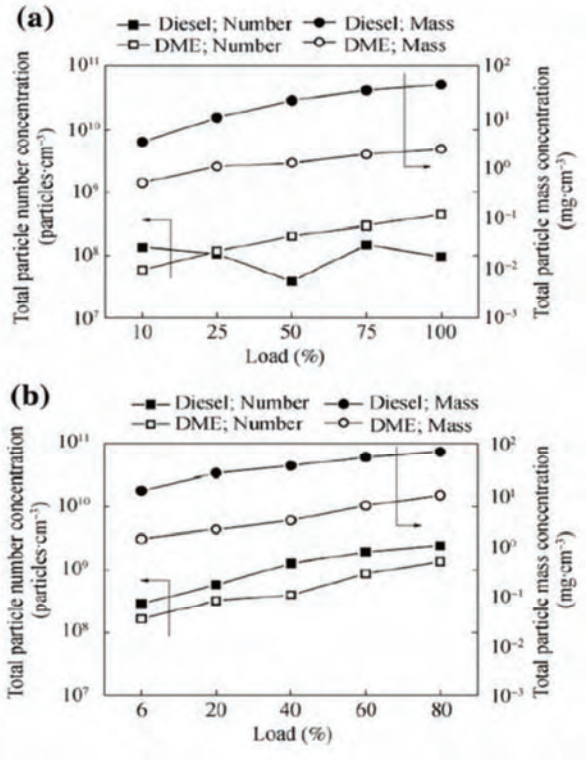

Fig. 6. The influence of the engine load and speed on the exhaust particle number and mass concentration for DME and diesel fueled engines; (a) 1400 rpm, (b) 2200 rpm

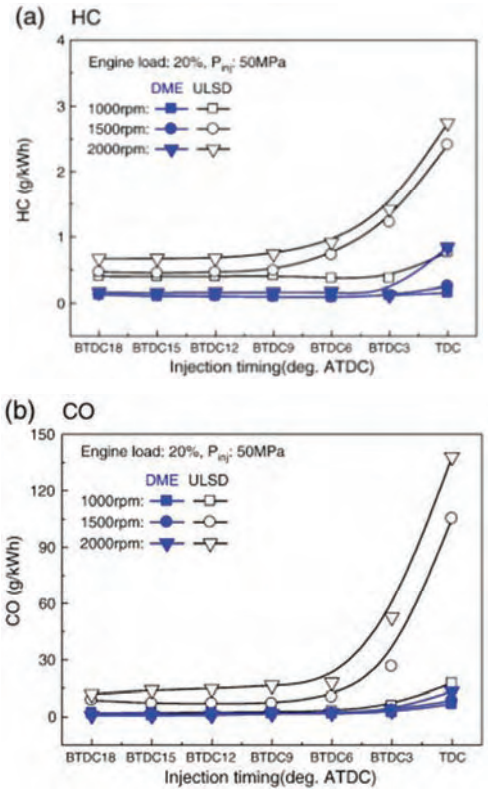

Fig. 7. Comparison of the emission of HC and CO for combustion of DME and diesel fuel [20]

Figure 7b presents the results of measurements of the emission of carbon monoxide. Similarly to the emission of HC, the emission of CO for dimethyl ether, turned out lower compared to diesel fuel. Only a slight increase has been observed for high engine speeds and late fuel injection. In the case of conventional fuel, an increase in the emission of CO under the said conditions is much more conspicuous. The formation of carbon monoxide is mainly attributed to local oxygen deficits and the occurrence of incomplete combustion. The amount of generated carbon monoxide during the combustion of DME is influenced by the presence of the atom of oxygen in the molecule, which reduces the amount of air necessary for full combustion.

4. Conclusions

Thanks to its chemical properties such as high cetane number, low boiling and ignition temperatures, dimethyl ether turns out to be a very good fuel for compression ignition engines. Dimethyl ether mixes with air well and is easily ignited even under sub zero temperatures. Its lower density, viscosity and lubricity compared to conventional fuels are potential downsides but may be cost-effectively eliminated by adapting of the injection systems and introducing fuel lubricity additives.

The potential of DME application in compression ignition engines has its environment related implications. Dimethyl ether has a very good carbon to hydrogen ratio, which generates more water vapor during combustion. Through no direct bond between the carbon atoms, formation of particulate matter is limited so that high exhaust gas recirculation rate is possible in order to reduce NO_x, which renders the application of any additional aftertreatment systems unnecessary. Because of good evaporation rate and the presence of oxygen atom in the molecule, the emission of carbon monoxide and hydrocarbons is also reduced, compared to diesel fuel. Besides, the adverse ecological impact of this fuel is reduced by a good CO_2 balance – DME may be manufactured from renewable materials such as wood chips, biomass or waste. Other than exhaust emissions the DME's environmental characteristics also include: no toxic, carcinogenic, teratogenic and mutagenic impact on the living organisms, safe decay products (water and carbon dioxide), short half-life in the troposphere and no impact on the stratosphere.

Proper adaptation of the infrastructure consisting in partial adapting of the existing solutions used in the LPG distribution may result in this fuel becoming increasingly popular and the group comprising Sweden, Denmark, USA, Japan, Korea and China, where DME road tests are in progress, will eventually expand.

Nomenclature

CI	compression ignition
CNG	compressed natural gas
DI	direct injection
LPG	liquified petroleum gas
SI	spark ignition

Bibliography

[1] ALAM, M., FUJITA, O., ITO, K. et al. Performance of NO_x catalyst in a DI diesel engine operated with neat dimethyl ether. *SAE Technical Paper*. 1999, 1999-01-3599.

[2] BP Energy Outlook 2016 Edition www.bp.com/energyoutlook (accessed 10.05.2016).

[3] EGNELL, R. Comparison of heat release and NO_x formation in a DI diesel engine running on DME and diesel fuel. *SAE Technical Paper*. 2001, 2001-01-0651.

[4] FLEISCH, T., MCCARTHY, C., BASU, A. et al. A new clean diesel technology: demonstration of ULEV emissions on a Navistar diesel engine fueled with dimethyl ether. *SAE Technical Paper*. 1995. 950061.

[5] HUANG, Z.H., WANG, H.W., CHEN, H.Y. et al. Study of combustion characteristics of a compression ignition engine fuelled with dimethyl ether. *Proc Instn Mech Engrs*. 1999, **213**, D, 647-52.

[6] JUNJUN, Z., XINQI, Q., ZHEN, W. et al. Experimental investigation of low-temperature combustion (LTC) in an engine fuelled with dimethyl ether (DME). *Energy & Fuels*. **23**, 2009.

[7] KAPUS, P., OFNER, H. Development of fuel injection equipment and combustion system for DI diesels operated on di-methyl ether. *SAE Trans J Fuel Lubr.* 1995, **104**(4), 54-59, 950062.

[8] KIM, M.Y., YOON, S.H., RYU, B.W., LEE, C.S. Combustion and emission characteristics of DME as an alternative fuel for compression ignition engines with a high pressure injection system. *Fuel*. 2008, **87**, 2779-2786.

[9] KONNO, M., KAJITANI, S., OGUMA, M. et al. NO emission characteristics of a CI engine fueled with neat dimethyl ether. *SAE Technical Paper*. 1999, 1999-01-1116.

[10] OWEN, K., COLEY, T., WEAVER, C.S. Automotive fuels reference book. 2nd ed. *SAE International Inc*. 1995.

[11] PARK, S.H., LEE, C.S. Applicability of dimethyl ether (DME) in a compression ignition engine as an alternative fuel. *Energy Conversion and Management*. 2014, **86**, 848-863.

[12] PARK, S.H., LEE, C.S. Combustion performance and emission reduction characteristics of automotive DME engine system. *Progress in Energy and Combustion Science.* 2013, **39**, 147-168.

[13] PARK, S.H., CHA, J., PARK, S., LEE, C.S. Simultaneous reduction in the exhaust emissions by a high exhaust gas recirculation ratio in a dimethyl-etherfuelled diesel engine at a low-load operating condition. *Proc Inst Mech Eng D – J Aut*. 2012, **226**(8), 1130-1142.

[14] SORENSON, S.C., GLENSVIG, M., ABATA, D. Di-metyl ether in diesel fuel injection systems. *SAE Trans J Fuel Lubr*. 1998, **107**(4), 438-449, 981159.

[15] SORENSON, S.C., MIKKELSEN, S.-E. Performance and Emissions of a 2.3 Liter Direct Injection Diesel Engine Fuelled with Neat Dimethyl Ether. *SAE Technical Paper.* 1995, 950064.

[16] TSUCHIYA, T., SATO, Y. Development of DME engine for heavy-duty truck. *SAE Technical Paper*. 2006, 2006-01-0052.

[17] WAKAI, K., NISHIDA, K., YOSHIZAKI, T., HIROYASU, H. Spray and ignition characteristics of di-methyl ether

injected by a DI diesel injector. *Proceedings of the fourth international symposium COMODIA'98*. 1998, 537-542.
[18] WANG, H.W., ZHOU, L.B. Performance of direct injection diesel engine fueled with DME/diesel blend. Fuel, *Better Air Quality in Asian and Pacific Rim Cities (BAQ 2002)*, 2002.
[19] XINLING, L., ZHEN, H. Emission reduction potential of using gas-to-liquid and dimethyl ether fuels on a turbocharged diesel engine. *Science of The Total Environment*. 2009.
[20] YOUN, I.M., PARK, S.H., ROH, H.G., LEE, C.S. Investigation on the fuel spray and emission reduction characteristics for dimethyl ether (DME) fueled multi-cylinder diesel engine with common-rail injection system. *Fuel Processing Technology*. 2011, 92(7), 1280-1287.
[21] FLEISCH, T.H., MEURER, P.C. DME – the diesel fuel for the 21st century?. *AVL Conference Engine and Environmental 1995*. Graz, Austria.
[22] THOMAS, G., FENG, B., VEERARAGAVAN, A. et al. Emissions from DME combustion in diesel engines and their implications on meeting future emission norms – a review. *Fuel Processing Technology*. 2014, **119**, 286-304.

Rafał Smolec, MEng. – Faculty of Machines and Transport at Poznań University of Technology.

e-mail: *Rafal.S.Smolec@doctorate.put.poznan.pl*

Wojciech Karpiuk, DEng. – Faculty of Machines and Transport at Poznań University of Technology.

e-mail: *Wojciech.Karpiuk@put.poznan.pl*

Prof. Marek Idzior, DSc., DEng. – Faculty of Machines and Transport at Poznań University of Technology.

e-mail: *Marek.Idzior@put.poznan.pl*

Miłosław Kozak, DSc., DEng. – Faculty of Machines and Transport at Poznań University of Technology.

e-mail: *Miloslaw.Kozak@put.poznan.pl*

This publication has been written within the project 'New generation of common rail injection pumps' in Lider V (Lider/015/273/L-5/13/NCBR/2014), financed by National Research and Development Centre.

Article citation info:
WOŁCZYŃSKI, Z. Evaluation of usefulness of mass flow meter to the survey of SI engine cylinder filling in one working cycle. *Combustion Engines*. 2017, **169**(2), 187-192. DOI: 10.19206/CE-2017-233

Zbigniew WOŁCZYŃSKI

CE-2017-233

Evaluation of usefulness of mass flow meter to the survey of SI engine cylinder filling in one working cycle

The article presents the technique of the usage of mass flow meter to the fill survey of a cylinder in the multicylinder engine, in each working cycles. The result of correctness of the survey was grounded on the comparison of air masses: the one registered with the usage of the flow meter and the other one calculated on the basis of mixture parameters. The flow meter was located in the consolidated part of suction system in front of the throttle valve. Mixture parameters were determined on the basis of time of fuel injection and measured λ_{zm} *factor of burnt mixture. The studies were carried out in the whole operating range of engine. Discrepancies between the measured and calculated values for 93% of all of the cycles fall within the ambit of ±3% of the actual value.*

Key words: *SI engine, the fill survey, mass flow meter, the phase of fill survey*

1. Introduction

Filling with the air of particular cylinders of multicylinder SI engine is inimitable in further working cycles. Its reason is a string of hard- and nonmeasurable phenomena e.g. outflow of fresh air parts to the outlet manifold during the valve overlap.

In the present article the following question was formed: Is it possible, with the usage of mass flow meter located in front of the throttle valve, to measure with requested correctness the air mass flowing to any cylinder in each of the working cycles. There was also a trial conducted of determining the correctness with which it is possible to measure the filling of this cylinder. Due to it the assumption was adopted that despite several nonmeasurable phenomena influencing the filling, the air mass suck to the cylinder is going to be proportional to the one measured with flow meter.

It enabled the implementation of proportionality factor between measured and actual air mass, called the k correction factor. Therefore, the k correction factor ought to be used to revise measured air mass to reach its actual value, i.e. the air mass suck to the cylinder.

Non-zero response time of flow meter and phenomena occurring in the suction system dictate to assume that the correction factor of measured air mass is going to have different values for each of the points of engine work. The decisive parameters from which the value of correction factor depends on are: n rotational speed and angle of the α throttle valve. Along with the change of n rotational speed wave phenomena in the suction system change as well and thereby the filling of engine cylinders. They also influence on flow meter indications located under the throttle valve. The location of the throttle valve influences on repression of flow and its pulsations. Therefore, decisive meaning of the opening angle of the α throttle valve to the k correction factor comes from it. Named parameters, i.e. n and α, also influence on the delay of signal of air mass flow m_a rate in proportion to the air flow filling the engine cylinder. Therefore, these parameters decide about the range in which on the basis of m_a signal the air mass is measured. In terms of above phenomena the method of air mass survey flowing to any cylinder in every filling and the way of their verification were developed.

2. The method of air mass survey and its verification

Presented method is used to the air mass survey filling a cylinder of four-cylinder SI engine by way of mass flow meter located in the consolidated part of suction system in front of the throttle valve. The essence of this survey method was graphically presented on the basis of signal processes in the Fig. 1. This picture shows signals in the system of controlling SI engine necessary to determining air mass in further and successive working cycles.

The survey consists of several phases. The first one determines once every turn in TDC piston: n rotational speed of engine and opening angle of the α_{zm} throttle valve according to the dependencies:

$$n = \frac{60000}{t_0} \tag{1}$$

where: t_0 – time of rotation

$$\alpha_{zm} = \frac{\sum \alpha}{\text{l.p.}} \tag{2}$$

where: l.p. – number of samples of α signal.

Just before the opening of inlet valve the angle of the beginning of phase of ϕ_{pn} fill survey is determined. For the engine which the studies were made on it is the angle of 672° of the previous cycle. Its value is read from a „map" on the basis of rotational speed and opening angle of the throttle valve. In the moment of the accomplishment with crankshaft the ϕ_{pn} location the M_{Azm} air mass survey flowing to the engine cylinder begins which finishes half of the rotation later. M_{Azm} survey is an integration after the time of signal of air mass flow m_a rate according to the formula:

$$M_{Azm} = \int_{\phi_{pn}}^{\phi_{pn}+180} dm_a dt \tag{3}$$

It is equivalent with determining a zone under the curve of m_a strength (in the Fig. 1 – bold with the half of the sky-blue curve) in the designated borders. Simultaneously durance of injection pulses of engine is measured and after the finishing the each of them a mass of injected fuel is calculated.

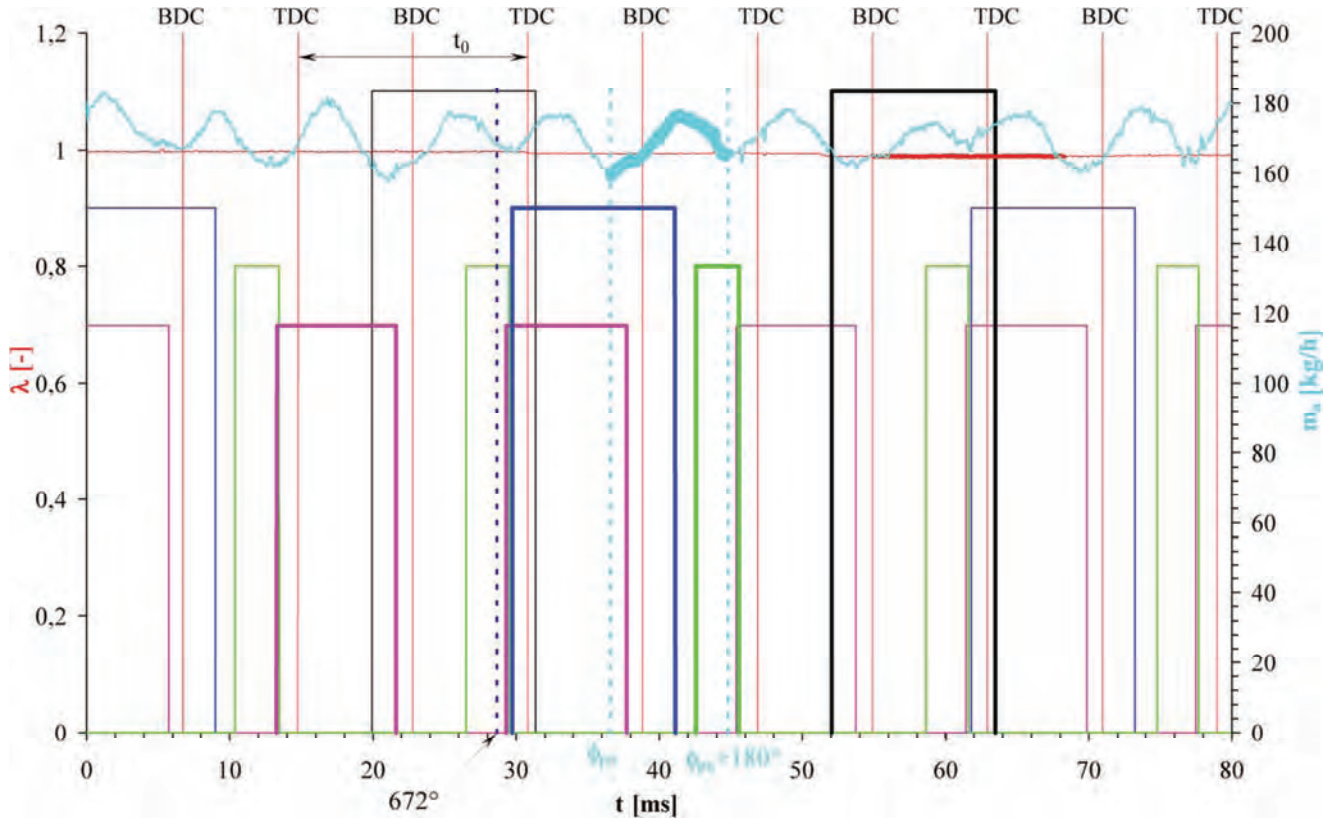

Fig. 1. Processes of chosen signals in the control system of SI engine necessary to determining air mass in each of the cycles of chosen cylinder

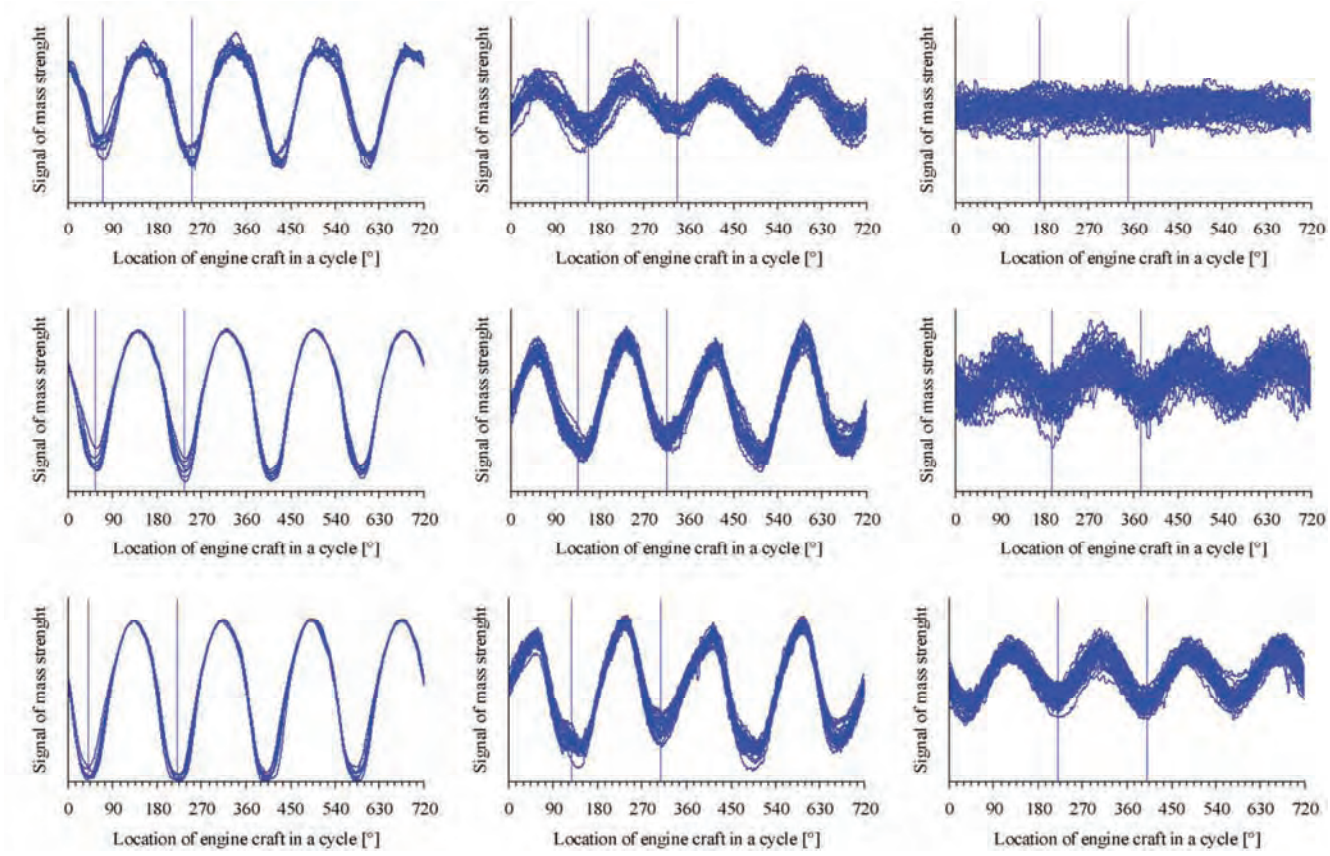

Fig. 2. Timing of m_a signal of the function of crankshaft for different rotational speeds and openings angle of the throttle valve (in the columns: „small", „medium", „big" rotation speed; in the rows: „small", „medium", „big" opening angle of the throttle valve)

$$t_w = t_{w2} - t_{w1} \tag{4}$$

where: t_w – time of injection, t_{w1} – time of the beginning of injection, t_{w2} – time of the finishing of injection

$$M_{Fl;F2} = 1.842 \cdot t_w - 1.411 \tag{5}$$

Each of the injections is assigned to particular working cycle.

The fuel injected during the opening of M_{F2} inlet valve (in the Fig. 1 it is a range shown with the bold blue line) and during the injection on the closed inlet valve in the previous M_{Fl} cycle (in the Fig. 1 these are pulses shown with the bold pink line) creates fueled-airy mixture with the air which mass was measured in specific cycle.

$$M_F = M_{Fl} + M_{F2} \tag{6}$$

where: M_F – mass of injected fuel per a cycle, M_{F1} – mass of the first injection of fuel in a cycle, M_{F2} – mass of the second injection of fuel in a cycle.

As a result of burning of mixture exhaust gas are going to appear which analysis will allow to determine λ factor of burnt mixture. The exhaust gas will drain during the opening of exhaust valve (in the fig. 1 it is a range shown with the bold black line). The average value of λ signal from the analyzer (bold part of red curve) equals the λ_{zm} factor of burnt mixture in particular cycle according to the formula:

$$\lambda_{zm} = \frac{\sum_{540^\circ}^{120^\circ} \lambda}{\text{l.p.}} \tag{7}$$

where: l.p. – number of λ signal samples in the range of counting the average, i.e. from 540° of particular cycle to 120° of the following one.

The delay with which the average value of λ signal in proportion to the range of the opening of exhaust valve is calculated results from the time necessary for the outflow of exhaust gas and their analysis.

On the basis of fuel mass in particular cycle and λ factor of mixture in the same cycle M_{Ao} air mass as an actual air mass was measured according to the formula:

$$M_{Ao} = M_F \cdot 14{,}7 \cdot \lambda_{zm} \tag{8}$$

The proportion of calculated M_{A0} mass to measured M_{Azm} mass equals the k correction factor:

$$k = \frac{M_{Ao}}{M_{A_{zm}}} \tag{9}$$

The presented method of the air survey was developed as a result of the observation of influence of rotational speed and the opening angle of the throttle valve on the process of flow meter signal. It was observed that these borders submit to displacement along with the rotational speed of engine and the opening of the throttle valve. This displacement is different for the particular points of engine work and is connected with wave phenomena in the suction system. It was also noticed that for each of the points of engine work variability time of m_a signal equals 180° of rotation of crankshaft. Therefore, this signal was plotted in many points involving the entire zone of engine work and the angle of the beginning of the ϕ_{pn} fill survey phase was determined in each of them (Fig. 2).

The angle of the end of the fill phase is located 180º further. It is a result of this that flow meter signal during a cycle (two rotations – four filling of cylinders) holds four characteristic parts of process. They represent the fillings of the following four engine cylinders. On the basis of ϕ_{pn} value in many points of work there was created a „map" of this angle for tested engine cylinder as dependency from n rotational speed and α_{zm} opening angle of the throttle valve (Fig. 3).

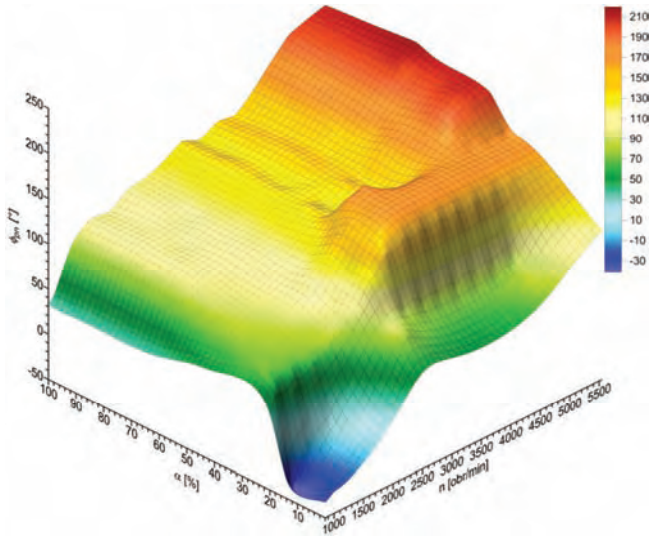

Fig. 3. „Map" of fill survey phase

Similarly, i.e. for many points of engine work there was created a „map" of the k correction factor (Fig. 4) determining its value according to the dependency (9).

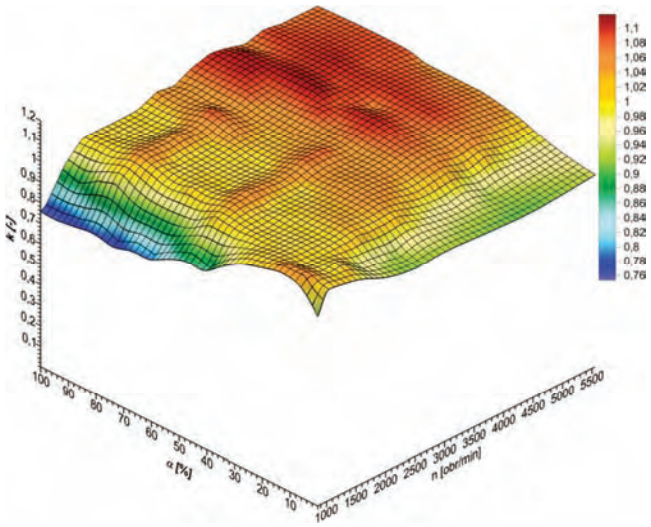

Fig. 4. „Map" of the k correction factor

3. Studies

In order to develop the map: the angle of the beginning of the ϕ_{pn} fill survey phase and the k correction factor and determining an error of air mass survey with the use of mass flow meter the studies were planned and carried out. The measurement site was built (Fig. 5).

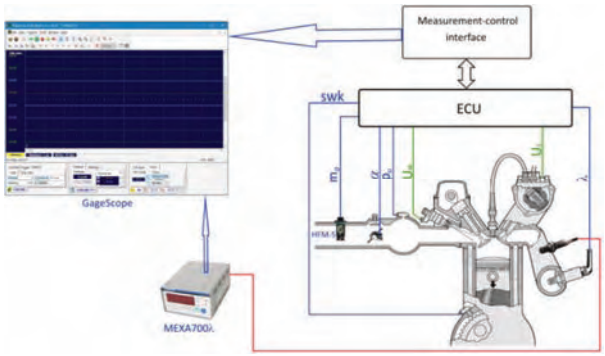

Fig. 5. Measurement site

Manufactured in series SI engine with multipoint, indirect injection of fuel with the capacity of 1600 cm^3 was the object of study. It was installed on the stationary measurement site and was managed with the factory control system. Control system was equipped with measuring-controlling interface enabling a survey of all of the signals occurring in it. Interface belongs to the equipment of measurement site. Furthermore in the suction system of engine between air filter and throttle valve additionally HFM-5 mass flow meter of BOSCH company was installed. The broadband lambda sensor was the second additional sensing device installed. It was used as a sensing device of analyzer of the composition of MEXA700λ burnt mixture of HORIBA company. It was installed in the branch of outlet manifold of the fourth cylinder.

The PC computer equipped with the OCTOPUS CS8380 measuring card with eight measuring channels and GageScope software of GAGE company was used to the registration of any signals in the time function. Each of the measuring channels is equipped fourteen-bit A/D converter. The studies were carried out on the entire zone of points of engine work determined with the rotational speed and the opening angle of the throttle valve, i.e. in 215 points (Fig. 6).

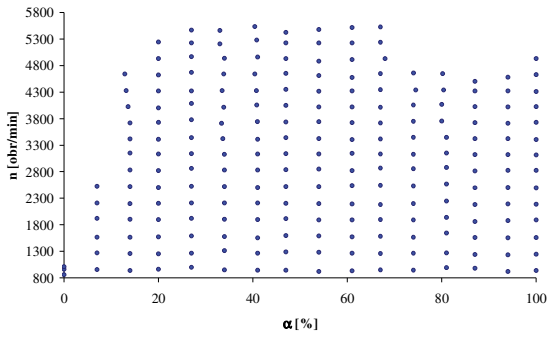

Fig. 6. Points of engine work in which the studies were carried out

Signals mentioned below were being registered in every point. They were sampled by 10 μs during 1 s, i.e. one hundred thousands of samples of every signal. The following voltage signals in the function of time were registered (Fig. 7):

– λ – composition of burnt mixture measured in the branch of outlet manifold of the fourth cylinder.
– m_a – air mass flow rate
– p_u – negative pressure in the intake manifold
– α – angle of the throttle valve measured with TPS sensing device which is a part of the control system
– M – torque on the brake shaft
– U_w – voltage signal of controlling the power of injector of the first or the fourth cylinder
– U_z – voltage signal of controlling the current in the primary winding of ignition coil for the first and the fourth cylinder
– swk – transformed with equipment into the bistate signal of the location of engine crankshaft.

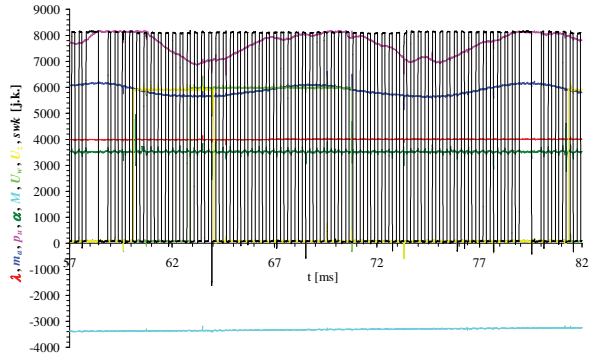

Fig. 7. Exemplary process of registered signals

4. The results of studies

Registered in the studies signals were submitted for initial modifications in order to prepare them for further analysis:

– bistate signals: U_w, U_z, swk were transformed into zero-one signals (Fig. 8)
– the remaining signals (analogue ones) were averaged with the use of method of average from 20 samples (Fig. 9)
– on the basis of the swk zero-one signal the angle of the location of shaft in the working cycle (0–720°) was assigned to every sample of registered signals (Fig. 10).

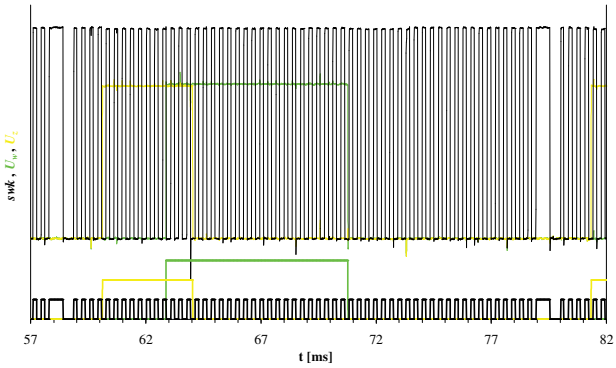

Fig. 8. Bistate signals before and after transformations into zero-one signals (on the upper part of figure registered bistate signals, on the lower part corresponding to the zero-one signal)

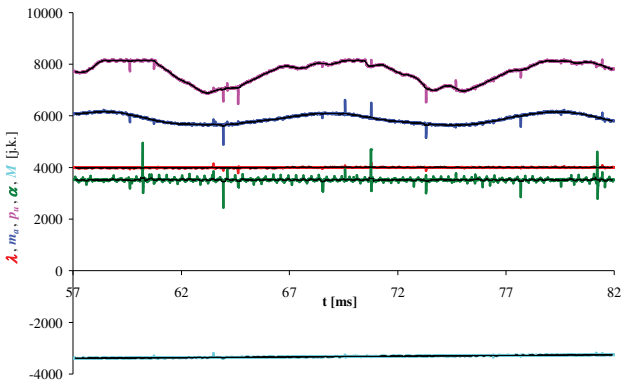

Fig. 9. Analogue signals before and after averaging with the use of method of average from 20 samples (black lines represent averaged processes)

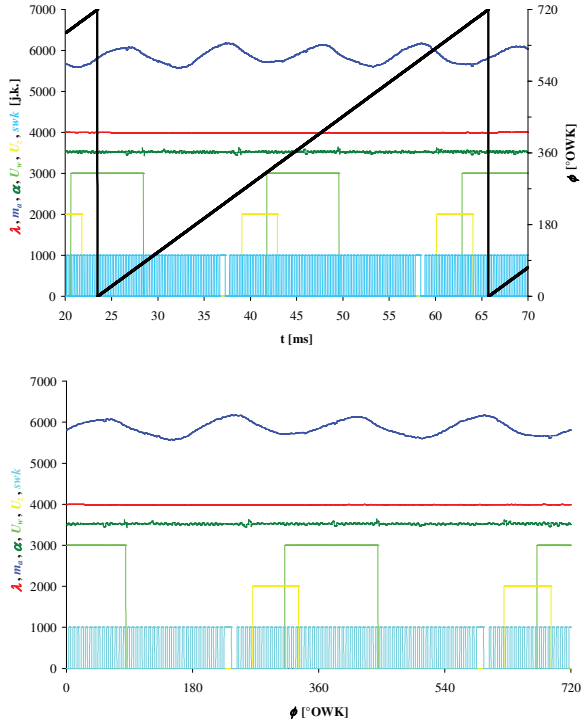

Fig. 10. Assignment of registered in time samples of signals to temporary angular position of engine shaft (chart above presents value of angle of ϕ crankshaft in a cycle against the background of registered in time samples of signals, chart below present the same samples of signals in the function of ϕ angle)

Modifications mentioned above enabled carrying out of analysis of registered signals for every entire working cycle. This analysis consists in determining all of the parameters of a cycle necessary to the calculation of air mass on the basis of m_a signal and error of determination of this mass. They are:

- n rotational speed [rpm] for a rotation (from TDC to TDC) on the basis of swk according to (1),
- angular location of the α_{zm} [%] throttle valve on the basis of signal from TPS (0% - entirely closed, 100% - entirely open] according to (2),
- the opening angle of ϕ_{pn} and the end of ϕ_{pn}+180° of the phase of air mass survey [°] (retrieved from „map" on the basis of n and α_{zm}),
- time of injection of t_w fuel [ms] on the basis of U_w signal and corresponding to this time dose of injected M_F fuel [mg] according to (4), (5), (6),
- mass of measured M_{Azm} air [mg] on the basis of m_a signal from HFM-5 flow meter in designated borders of survey according to (3),
- measured value of excess air α_{zm} [-] factor on the basis of λ signal from MEXA700λ meter according to (7),
- measured air mass $k \cdot M_{Azm}$ rectified with the correction factor.

Later on air masses were compared: the measured one with the actual one and the error of survey in every entire registered cycle was calculated according to the formula:

$$\delta_{M_A} = \frac{k \cdot M_{zm} - M_{Ao}}{M_{Ao}} \cdot 100\% \qquad (10)$$

The results of this error are shown in the Fig. 11.

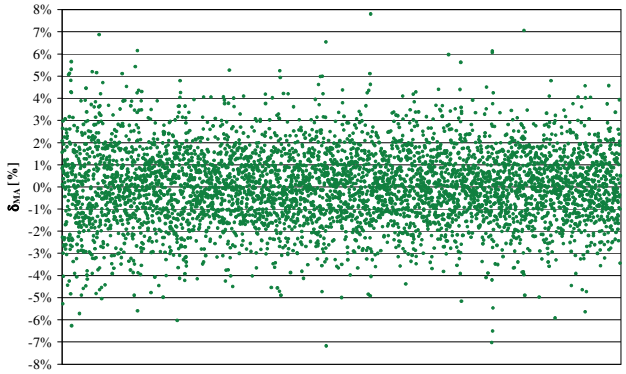

Fig. 11. Errors of air mass survey suck to the studied engine cylinder

Every point in the picture represents the value of error of air mass survey in one filling cycle. The picture includes values of error of survey for 4895 filling cycles.

The number of cycles for particular ranges of error was shown in the Fig. 12. Cycles in which error of survey is bigger than 3% represents less than 7% of all of them.

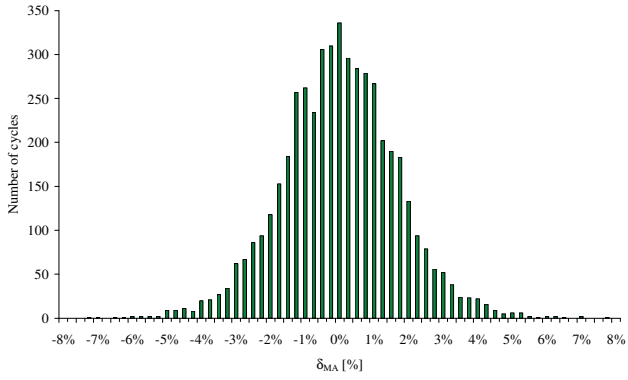

Fig. 12. Layout of the number of cycles for which error of survey falls within the ambit of particular borders

5. Conclusions

1. With the usage of mass flow meter located in the consolidated part of suction system in front of the throttle

valve it is possible to measure air mass filling one engine cylinder in each of the working cycles.
2. The analysis of flow meter signal have to take place in the angular range of the rotation of crankshaft ancillary to the rotational speed of engine and the opening angle of the throttle valve.
3. For all of the analyzed work cycles from the entire zone of engine work the error of air mass survey did not pass 8%.
4. Measuring air mass with the usage of presented method the error of survey is less:
   – from 3% for 93% of cycles,
   – from 4% for 98% of cycles,
   – from 5% for 99,4% of cycles.

Nomenclature

SI	spark ignition
n	rotational speed
α	signal of location of the throttle valve
α_{zm}	opening angle of the throttle valve
M	moment on the brake shaft
m_a	air mass flow rate
M_{Azm}	measured air mass
M_{A0}	actual air mass
ϕ	angular position of crankshaft in a cycle
ϕ_{pn}	opening angle of the filling survey phase
t_w	time of injection
t_{w1}	time of the beginning of injection
t_{w2}	time of the finishing of injection
M_F	fuel mass in a cycle
M_{F1}	fuel mass injected in the first injection per a cycle
M_{F2}	fuel mass injected in the second injection per a cycle
λ	signal of mixture composition with MEXA700λ analyzer
λ_{zm}	measured value of mixture composition
U_w	voltage signal of controlling the injector of the first or the fourth cylinder
U_z	voltage signal of controlling the ignition coil for the first and the fourth cylinder
swk	signal from the sensing device of crankshaft
p_u	negative pressure in the intake manifold

Bibliography

[1] NITA, J. Niepowtarzalność cyklowego składu mieszanki w silniku GDI. *Czasopismo techniczne*. 2012, **5M**, 229-241.
[2] PRZYBYŁA, G., POSTRZEDNIK S. Niepowtarzalność cykli pracy silnika przy jego wysokiej prędkości obrotowej oraz różnym obciążeniu. *Czasopismo techniczne*. 2008, **7M**, 151-159.
[3] DYKIER, M., FLEKIEWICZ, M. Analiza częstotliwości drgań czynnika roboczego w układzie dolotowym silnika SI. *Czasopismo techniczne*. 2008, **8M**, 173-183.
[4] NITA, J., WOŁCZYŃSKI Z. Ocena fluktuacji składu mieszanki wysterowanej z cyklu na cykl w silniku z pośrednim wtryskiem benzyny. *Silniki Spalinowe*. 2013, **3**, 1002-1010.
[5] KOMORSKA, I. (red.) Eksperymentalna ocena możliwości poprawy sprawności silnika benzynowego zasilanego LPG poprzez optymalizację jego sterowania. *UTH Radom*. 2016, 18.

Zbigniew Wołczyński, DEng. – Faculty of Mechanical Engineering at Kazimierz Pulaski University of Technology and Humanities in Radom.

e-mail: *Z.Wolczynski@uthrad.pl*

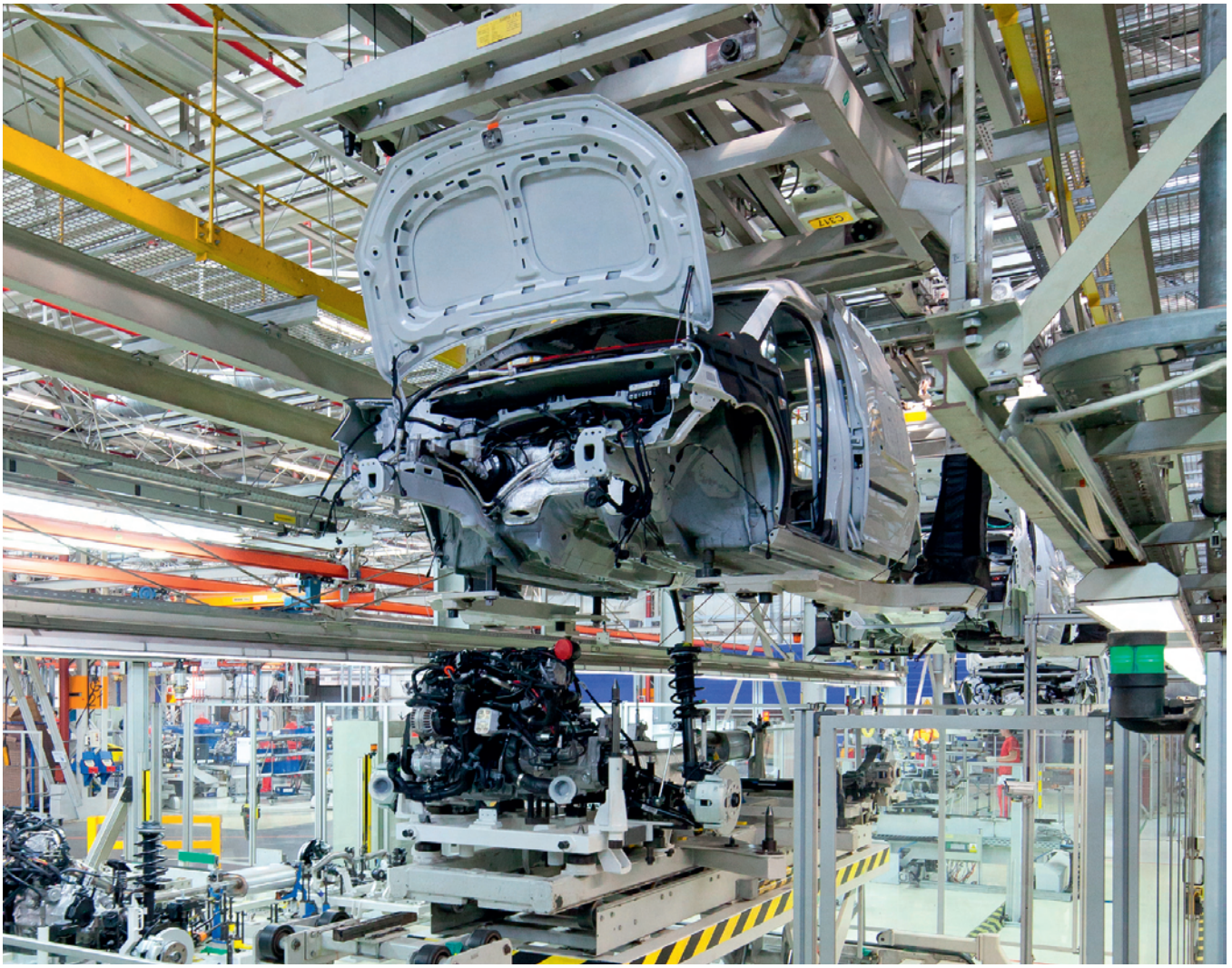

Volkswagen Poznań

to nowoczesna fabryka samochodów użytkowych i komponentów

Od blisko 25 lat Volkswagen Poznań jest największym prywatnym pracodawcą w Wielkopolsce zapewniając miejsca pracy dla 10.000 pracowników. Od roku 2003 w Poznaniu produkowane są modele samochodów użytkowych Caddy oraz Transporter, a od 2016 w fabryce we Wrześni model VW Crafter. W roku 2016 firma wyróżniona została tytułem „Pracodawca Przyjazny Pracownikom".

Volkswagen Poznań

is a modern factory manufacturing commercial vehicles and components

For almost 25 years Volkswagen Poznan has been the biggest private employer in the Wielkopolska region providing jobs for 10.000 employees. Since 2003 the commercial vehicles models Caddy and Transporter have been manufactured in Poznan and since 2016 the new Crafter in the new factory in Września. In 2016 the company was awarded the title "The friendly employer".

Volkswagen Poznań Sp. z o.o., 61-060 Poznań, ul. Warszawska 349
www.volkswagen-poznan.pl

Samochody Użytkowe

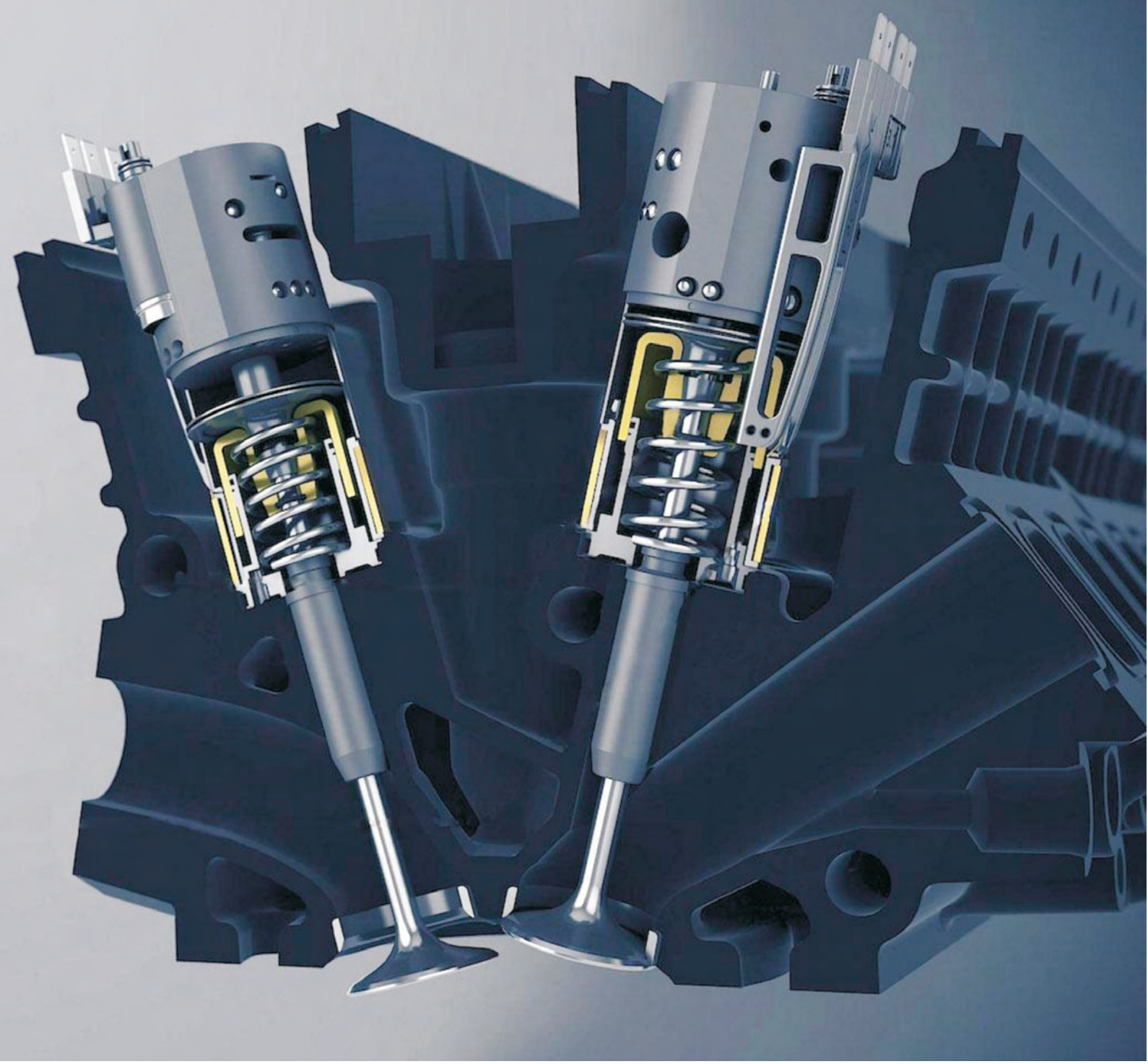

Publisher:

Polish Scientific Society of Combustion Engines

Combustion Engines

Polskie Towarzystwo Naukowe Silników Spalinowych

ISSN: 2300-9896

www.combustion-engines.eu